A UNITED STATES DEPARTMENT OF COMMERCE PUBLICATION

U.S. DEPARTMENT OF COMMERCE
Environmental Science Services Administration

COLLECTED REPRINTS–1969
Volume II

ATLANTIC OCEANOGRAPHIC
AND METEOROLOGICAL LABORATORIES
PACIFIC OCEANOGRAPHIC LABORATORIES

U. S. DEPARTMENT OF COMMERCE
Maurice H. Stans, Secretary

ENVIRONMENTAL SCIENCE SERVICES ADMINISTRATION
Robert M. White, Administrator
RESEARCH LABORATORIES
Wilmot N. Hess, Director

Collected Reprints–1969
Volume II

ATLANTIC OCEANOGRAPHIC AND METEOROLOGICAL LABORATORIES
PACIFIC OCEANOGRAPHIC LABORATORIES

ISSUED SEPTEMBER 1970

Atlantic Oceanographic and Meteorological Laboratories
Miami, Florida 33130

Pacific Oceanographic Laboratories
Seattle, Washington 98105

For sale by the Superintendent of Documents, U. S. Government Printing Office, Washington, D. C. 20402
$3.75

FOREWORD

Knowledge of the ocean and its processes develops slowly. It is the result of the work of many researchers in this country and throughout the world. To be useful, however, each new increment of knowledge must be disseminated so that the other workers will know of it and be able to build upon it.

Because the published results of the scientific and technical work of ESSA's Atlantic Oceanographic and Meteorological Laboratories and Pacific Oceanographic Laboratories are scattered through the literature, they are being brought together in a series of annual publications. These publications provide to researcher and to interested layman alike a convenient summary of the results of the work of these two Research laboratories of the Environmental Science Services Administration of the U. S. Department of Commerce.

This volume, the fourth in the series, holds the published papers for the year 1969.

Harris B. Stewart, Jr.
Director
Atlantic Oceanographic and
Meteorological Laboratories

TABLE OF CONTENTS

Volume I

GENERAL

MARINE GEOLOGY AND GEOPHYSICS

12. Dietz, Robert S., Primitive earth: A marine geologist's appraisal: The Primitive Earth Symp., Miami Univ., Oxford, Ohio, special publ. D1-D11.

13. Dietz, Robert S., Book review of "History of the Earth's Crust" ed. R. Phinney, Princeton Univ. Press: J. Marine Technol. Soc., <u>3</u>, No. 5, 30.

14. Dietz, Robert S., Robert Fudali, and William Cassidy, Richat and Semsiyat domes (Mauritania): Not astroblemes: Geol. Soc. Am. Bull., <u>80</u>, No. 7, 1367-1372.

15. Dietz, Robert S., and Knebel, Harley J. First deep sea sounding: Sea Frontiers <u>15</u>, No. 4, 212-218.

16. Erickson, Barrett H., and Paul J. Grim, Profiles of magnetic anomalies south of the Aleutian Island Arc: Geol. Soc. Am. Bull., <u>80</u>, No. 7, 1387-1390.

17. Grim, Paul J., Heat flow measurements in the Tasman Sea: J. Geophys. Res. <u>74</u>, No. 15, 3933-3934.

18. Grim, Paul J., SEAMAP deep-sea channel: ESSA Tech. Rept. ERL 93-POL 2, Jan.

19. Grim, Paul J., and Barrett H. Erickson, Fracture zones and magnetic anomalies south of the Aleutian trench: J. Geophys. Res. <u>74</u>, No. 6, 1488-1494.

20. Grim, Paul J., and Frederick P. Naugler, Fossil deep-sea channel on the Aleutian abyssal plain: Science <u>163</u>, No. 3865, 383-385.

21. Harbison, Reginald N., Possible morainal deposits in the Gulf of Maine: Maritime Sediments, <u>5</u>, No. 1, 19-21.

22. Keller, George H., Book Review of "Marine Geotechnique": Marine Geol., <u>7</u>, No. 2, 176-181.

23. Keller, G. H., Radioisotopes and Oceanography: Isotopes and Radiation Tech. <u>6</u>, No. 4, 376-381.

24. Malloy, R. J., and G. F. Merrill, Vertical crustal movement associated with the Prince William Sound, Alaska, earthquake: The Prince William Sound, Alaska, Earthquake of 1964 and Aftershocks <u>II</u>, Part C, U. S. Government Printing Office, 329-338.

25. Malahoff Alexander, and Barrett H. Erickson, Gravity anomalies over the Aleutian Trench: E⊕S, Trans, Am. Geophys. Union 50, No. 10, 552-555.

26. Mathewson, Christopher C., Bathymetry of the north insular shelf of Molokai Island, Hawaii, from surveys by the USC&GSS McArthur, Data Report No.14, HIG-69-21, Sept.1969.

27. Peter, George, and O. E. DeWald, Geophysical Reconnaissance in the Fulf of Tadjura: Deep Sea Research, Geol. Soc. Am. Bull., 80, 2313-2316.

28. Peter, G., and R. Lattimore, Magnetic structure of the Juan de Fuca-Gorda Ridge area: J. Geophys. Res. 74, No. 10, 586-593.

29. Rona, Peter A., Linear "lower continental rise hills" off Cape Hatteras: J. Sedimentary Petrology 39, No. 3, 1132-1141.

30. Rona, Peter A., 1969, Comparison of continental margins of eastern North America at Cape Hatteras and northwestern Africa at Cape Blanc: Am. Assoc. Petroleum Geologists Bull. 54, No. 1, 129-157.

31. Rona, Peter A., Middle Atlantic continental slope of United States: Deposition and erosion: Am. Assoc. Petroleum Geologists Bull. 53, No. 7, 1453-1465.

32. Rona, Peter A., Possible salt domes in the deep Atlantic off Northwest Africa: Nature, 224, No. 5215, 141-143.

33. Sproll, Walters, and Dietz, Robert S., Morphological continental drift fit of Australia and Antarctica: Nature, 222, No. 5191, 345-348.

METEOROLOGY

34. Anthes, Richard A., Numerical experiments on ring convection and effect of variable resolution of cellular convection: ESSA Tech Memo ERLTM-NHRL No. 86, June.

35. Carlson, Toby N., Hurricane genesis from disturbances formed over Africa: Mariner's Weather Log, 13, No. 5, 197-202.

36. Carlson, Toby N., Some remarks on African disturbances and their progress over the tropical Atlantic: Monthly Weather Rev. 97, No. 10, 716-726.

37. Carlson, Toby., Synoptic histories of three African disturbances that developed into Atlantic hurricanes: Monthly Weather Rev. 97, No. 3, 256-276.

38. Chase, P., A note on drawing probability sectors: Monthly Weather Rev. 97, No. 8, 602-603.

39. Gentry, R. Cecil, Project STORMFURY: WMO Bull., XVIII, No. 3, 146-154.

40. Gentry, R. Cecil, Project STORMFURY: Bull. Am. Meteorol. Soc. 50, No. 6, 404-409.

41. Koss, Walter J., Note on the accumulated error in the numerical integration of a simple forecast model: Monthly Weather Rev. 97, No. 12, 896-901.

42. Miller, Banner I., Hurricane: in McGraw-Hill Yearbook of Science and Technology, McGraw-Hill, New York, 193-196.

43. Miller, Banner I., Experiment in forecasting hurricane development with real data: ESSA Tech. Memo. ERLTM-NHRL 85, Apr.

44. Rosenthal, Stanley L., Experiments with a numerical model of tropical cyclone development. Some Effects of radial resolution: ESSA Tech. Memo. ERLTM-NHRL 87. Aug.

45. Rosenthal, Stanley L., Numerical experiments with a multi-level primitive equation model designed to simulate the development of tropical cyclones. Experiment 1: ESSA Tech. Memo. ERLTM-NHRL 82, Jan.

46. Staff, Office of the Director, National Hurricane Research Laboratory, "Project STORMFURY" Annual Report, 1968.

47. Sheets, Robert C., Some mean hurricane soundings: J. Appl. Meteorol. 8, No. 1, 134-146.

48. Sugg, Arnold L., and Robert L. Carrodus, Memorable hurricanes of the United States since 1873: ESSA Tech. Memo. WBTM-SR-42, Jan.

49. Hebert, Paul J., and Banner I. Miller, Hemispheric circulation and anomaly patterns observed when tropical storms reach hurricane intensity: ESSA Tech. Memo. WBTM-SR-46, May.

TABLE OF CONTENTS

Volume II

EXPERIMENTAL METEOROLOGY

61. Simpson, Joanne, William L. Woodley, Howard A. Friedman, Thomas W. Slusher, R. S. Scheffee, and Roger L. Steele, An airborne pyrotechnic cloud seeding system and its use: ESSA Tech. Memo. ERLTM-APCL 5, Feb.

62. Woodley, William L., Precipitation results from a pyrotechnic cumulus seeding experiment: ESSA Tech. Memo. AOML 2, Aug.

63. Woodley, William L., and Alan Herndon, A rain gage evaluation of the Miami reflectivity-rainfall rate relation region: ESSA Tech. Memo. ERLTM-AOML 3, Sept.

64. Woodley, William L., A. Herndon, and R. Schwartz, Large-scale precipitation effects of single cloud pryotechnic seeding: ESSA Tech. Memo. ERLTM-AOML 5, Nov.

65. Woodley, William L., and Jose Partagas, Radar and photographic documentation of convective developments on May 16, 1968: ESSA Tech. Memo. ERLTM-APCL 7, April.

66. Cantilo, Luis M. H., and William L. Woodley, Cloud photogrammetry from air-borne time-lapse photography. Preprint No. 105-52, 105th Techn. Conf. Soc. of Motion Picture and Television Eng., April 20-25, Miami Beach, Florida.

* Simpson, Joanne, Modification experiments on tropical cumulus clouds, Paper presented at Cloud Weather Modification and Cloud Physics Conf., Tbilisi, Georgia, USSR, May.

* Woodley, William L., The effect of air-borne silver iodide pyrotechnic seeding on the dynamics and precipitation of supercooled tropical cumulus clouds: A dissertation submitted to the Graduate School of Florida State Univ. in partial fulfillment of the requirements for the Degree of Doctor of Philosophy.

---

* Reprints not available.

PHYSICAL OCEANOGRAPHY

67. Byrne, Robert J., Field occurrences of induced multiple gravity waves: J. Geophys. Res. 74, No. 10, 2590-2596.

68. Cartwright, David, Walter Munk, and Bernard Zetler, Pelagic tidal measurements: EØS Trans., American Geophys. Union, 50, No. 7, 472-477.

69. Hansen, Richard T., Charles J. Garcia, Shirley F. Hansen, and Harold G. Loomis, Brightness variations of the white light corona during the years 1964-67: Solar Phys. 7, 417-433.

70. Hansen, Richard T., Shirley F. Hansen, and Harold G. Loomis, Differential rotation of the solar electron corona: Solar Phys. 10, 135-149.

71. Laird, Norman P., Anomalous temperature of bottom water in the Panama Basin: J. Marine Res. 27, No. 3, 355-357.

72. Laird, N. P. and T. V. Ryan, Bottom current measurements in the Tasman Sea: J. Geophys. Res. 74, No. 23, 5433-5438.

73. Larsen, J. C., Long waves along a single step topography in a semi-infinite uniformly rotating ocean: J. Marine Research 27, No. 1, 1-6.

74. McAlister, E. D., and William McLeish, Heat transfer in the top millimeter of the ocean: J. Geophys. Res. 74, No. 13, 3408-3414.

75. Nelson, Raymond M., The potential application of remote sensing to selected ocean circulation problems: in Oceans from Space, Gulf Publishing Co., Houston, Texas 38-45.

76. Ostapoff, Feodor, A fourth brine hole in the Red Sea?: in Hot Brines and Recent Heavy Metal Deposits in the Red Sea, Ed. Egon T. Degens and David A. Ross, Springer-Verlag, New York, 18-21.

77. Reed, R. K., Deep water properties and flow in the Central North Pacific: J. Marine Res. 27, No. 1, 24-31.

78. Shaw R. P., and Courtine D. F., Diffraction of a plane acoustic pulse by a free orthogonal trihedron (3-D Corner): J. Acoustic Soc. Am. 46, No. 5, 1382-1384.

79. Shaw, R. P., and Bugl P., Transmission of plane waves through layered linear viscoelastic media: J. Acoustic Soc. Am. 46, No. 3, 649-654.

80. Sokolowski, T. J., and M. H. Manghnani, Adiabatic elastic moduli of vitreous calcium aluminates to 3.5 Kilobars: J. Am. Ceramic Soc. 52, No. 10, 539-542 (also HIG 287).

81. Smith John A., Bernard D. Zetler, and Saul Broida, Tidal modulation of the Florida current surface flow: Marine Technol. Soc. J. 3, No. 3, 41-46.

82. Wunsch, C., D. V. Hansen, and B. D. Zetler, Fluctuations of the Florida current inferred from sea level records: Deep Sea Res. 16, Suppl. 447-470.

83. Zetler, B. D. Tides, 1-74 to 1-81, Tide Forecasting, 11-109 to 11-113, and 11-119: in Handbook of Ocean and Underwater Engineering, © North American Rockwell, Inc., McGraw-Hill Inc. New York.

84. Zetler, Bernard D., Computer applications to tide and current analysis in the Coast and Geodetic Survey: Proc. Symp. on Tides organized by the Intern. Hydrographic Bureau, Monaco, 28-29 April 1967, 75-77.

85. Zetler, Bernard D., Shallow water tide predictions: Proc. Symp. on Tides organized by the Intern. Hydrographic Bureau, Monaco, 28-29 April 1967, 163-166.

86. Zetler, Bernard D., Tide-talk: monthly column, GO Boating Miami, January through October.

Reprinted from Quarterly Journal Royal Meteorological Society 95, No. 403, 120-147

551.543.1 (265/266) : 551.576.31 : 551.577.31 : 525.624

Tropical cloudiness and rainfall related to pressure and tidal variations

By G. W. BRIER and JOANNE SIMPSON
Environmental Science Services Administration

(Manuscript received 20 October 1967; in revised form 9 September 1968)

Summary

A definitive statistical relationship is established between tropical cloudiness and rainfall and the semi-diurnal solar (S_2) atmospheric tide, as manifested in the semi-diurnal surface pressure variation. Pressure and weather data are used from Batavia (seventy years) and Wake Island (twelve years). The S_2 tidal effect is shown to enhance cloudiness and rain near sunrise and sunset, and to suppress them shortly after midday and midnight. The analysis is based on (a) the fact that the S_2 amplitude varies by 15-20 per cent between months and by more than 100 per cent from day to day and (b) the amplitude of the S_2 wave as computed from the pressure data at a station is closely related to the 5-6 hourly pressure changes during the periods around 4-5 a.m. to 10 a.m., from 10 a.m. to 4 p.m., etc. The crux of the analysis is the demonstration that days with large 5-6 hourly pressure changes during these periods have large cloudiness changes (in the sense described above) during these same periods relative to days with small 5-6 hourly pressure changes.

Possible mechanistic connections between S_2 pressure tendencies and cloud properties are examined. The varying convergence-divergence field is suggested as the main link. It is shown how the concentration of active cloud updraughts in the Tropics can permit cloudiness to be extremely sensitive to small divergence fields.

Finally, large-scale simultaneous pressure changes over the Pacific Ocean area are shown and related to cloudiness changes. A need for re-examination of the nature and origins of tropical disturbances is shown to exist, using the concept that possible small (terrestrial or extra-terrestrial) triggers may set off significant changes in weather both locally and on the synoptic and global scales.

1. Introduction

Tropical cloudiness and rainfall patterns exhibit different time and space scales and different relationships to the other atmospheric variables than do those in temperate latitudes. For many years it has been suspected that tropical oceanic clouds and rain exhibit maximum amounts and frequency during the hours of darkness, compared to the hours of daylight. This suspicion has been confirmed by recent studies from a research vessel (Garstang 1964; Holle 1968) and several tropical atolls (Lavoie 1963). In addition to a diurnal periodicity, a superimposed semi-diurnal periodicity has been increasingly indicated by observational analyses (LaSeur and Garstang 1964; Kiser, Carpenter and Brier 1963; Malkus 1964). The main features of the semi-diurnal effect appeared to be a cloudiness and rain maximum near dawn, with a weaker maximum near sunset.

The existence, causes and distribution of tropical cloudiness and rainfall variations are important to seek and document, not only for forecasting local weather in the Tropics but for understanding disturbance growth, the energy sources of the large-scale global circulation and for progress towards eventual weather modification. The frontal and air mass models of cloud and precipitation control were long ago shown inapplicable to the Tropics (Palmer 1951). More surprisingly, the satellite era has begun to suggest that progressive travelling waves or vortical perturbations in the wind field, while often present and of major importance, may not be the main or most common controls upon tropical cloudiness and rainfall variability (Simpson, Garstang, Zipser and Dean 1967). It is timely to re-examine these controls and their degree of predictability. We have chosen the semi-diurnal variation in the belief that the documentation and greater understanding of this one scale of variation, which is currently tractable, may open the door to understanding and prediction of cloudiness on other important but currently less tractable scales.

Various causes, all radiative, have been advanced for the diurnal cloudiness cycle (e.g. Kraus 1963). The semi-diurnal cycle has been more controversial and more difficult to establish. The reasons are, firstly, that its amplitude is small compared to interdiurnal changes, amounting to a range of roughly 5-15 per cent in cloudiness and perhaps a slighter larger percentage in rainfall. This low signal to noise ratio requires many years of data to form an adequate sample. Secondly, nearly all observations have been made from land masses; even small islands introduce their own daily régimes which vary as the large-scale flow varies. Thirdly, visual cloud observations are very difficult at night. Systematic bias can be argued related to the phase of the moon, for example, no matter how long the data sample.

Numerous workers have hypothesized a relationship between the 12-hour atmospheric solar tidal oscillation, called the S_2 wave, and the cloudiness and rainfall cycle (Gold 1913; Riehl 1947; LaSeur and Garstang 1964). The semi-diurnal S_2 surface pressure wave is one of the outstanding features of the tropical atmosphere. It has pressure maxima near 10 a.m. and p.m. local time and minima near 4 a.m. and p.m. The mean annual amplitude is about 1-2 mb, decreasing with higher latitude and varying with season (Stolov 1955; Haurwitz and Sepúlveda 1957). This regular twice-daily barometric change is clearly due to the sun but it has become established practice in meteorology to refer to it as 'tidal' without specifying what portion is thermally or gravitationally induced. A small associated tidal wind variation in the tropical easterlies can be extracted by statistical analysis from long series of wind data. An example is the surface tidal wind at Eniwetok Atoll (11·30N; 162·15E) presented by Lavoie (loc. cit. 1963). The tidal wind range was about 30 cm sec^{-1}, with easterly wind maxima and minima corresponding to those in pressure. Putting together these indications, Malkus (1964) postulated the pressure-convergence-cloudiness relation illustrated schematically in Fig. 1. Maxima in cloudiness correspond with maxima in convergence or pressure tendency which lead the pressure maxima by three hours or 45° in phase.

Two main problems faced the evaluation of the proposed relation between the S_2 wave and cloudiness. The first lay in the factual demonstration that the relation exists, which is difficult due to the high noise level and several types of data inadequacy. The fact that the low-level convergence associated with the S_2 tidal wave is not likely to be greater than 1-5 $\times$ 10^{-7} sec $^{-1}$ led most meteorologists to dismiss its importance for many years, since storm and sea-breeze scale convergence exceed this amount by 1-3 orders of magnitude. The main purpose of this paper is to establish a conclusive relation between the S_2 wave and semi-diurnal cloud and rainfall variations. The matter of mechanism is still not resolved; some suggestions will be considered in the closing Sections.

If the diurnal march of cloudiness and rainfall is affected by the S_2 wave, a midday suppression should be noted around the hours of noon and early afternoon and another suppression shortly after midnight. The noon and early afternoon suppression is strong and readily detectable on ships and most small islands, but on larger land masses it is usually at least partly obscured or overcome by the sea-breeze and land effect (Riehl 1947, 1954; LaSeur and Garstang 1964; Holle 1968). Verification of the after-midnight suppression was regarded as critical in confirming the S_2 relationship; neither a radiative nor sea-air exchange hypothesis of cloudiness variations could account for a mid-nocturnal diminution in cloudiness or rain. Unfortunately, documenting this nocturnal suppression in cloudiness faced the problem of observer bias, while no oceanic rainfall records were available until the *R. V. Crawford* cruises by Garstang (Garstang 1964; LaSeur and Garstang 1964). These cruises, albeit with a small data sample, showed a very large after-midnight diminution in both rainfall and 3 cm radar echoes. Oceanic satellite radiation measurements reported by Merritt and Bowley (1966) provide confirmatory evidence in diminished cloudiness and heights of tops just after midnight.

Despite these encouraging pieces of evidence, the S_2-cloudiness relation still lacked firm statistical support. The demonstration has now been made possible and forms the main subject of this paper. The key links are (i) documentation (Holloway, Holt, Mauchly and Woodbury 1955) of fairly large monthly variations in the amplitude of the S_2 wave, (ii) the demonstration by Brier (1967) of a statistical relation between these monthly variations and the magnitude of the six-hour pressure changes (from 0400-1000 hr, 1000-1600 hr local time, etc.) and (iii) the establishment of a correlation between pressure change and cloudiness variations of proper magnitude and direction consistent with the observed S_2-cloudiness relation. This paper is mainly concerned with this link.

The data at Batavia show differences of 15-20 per cent in S_2 amplitude between the same month of different years and for single days amplitude variations may exceed 100 per cent. Wake Island and other typical stations show similar variations. Very little is known about the nature of these changes, their spatial distribution and propagation as a wave phenomenon, or the extent to which they may represent variations in either the 'migratory' or 'standing' component of the S_2 wave. Present theory has little or nothing to say about them. It is known that the diurnal component S_1, which is smaller in amplitude, is quite variable and influenced by local weather. However, since by mathematical definition S_1 and S_2 are orthogonal, it does not seem possible to account for long term variations in S_2 as a direct consequence of variations in S_1. For the present, many of these questions must remain unanswered, and here we shall refer to the semi-diurnal pressure oscillation at a station as a tidal or S_2 component, without attempting to specify what portion is thermally induced or results from resonance phenomena of the atmosphere. Although the amplitude of the S_2 pressure wave as determined from the data at a particular station shows considerable variation in time, the phase of the wave remains remarkably constant. This means that a month with an average S_2 amplitude higher than normal will have larger than normal pressure rises from 4 a.m. to 10 a.m., larger pressure falls from 10 a.m. to 4 p.m., etc. This, of course is the reason for the statistical relationship reported by Brier (1967). But it is also clear than on an individual day a rise in pressure during a six hour period, say from 4 a.m. to 10 a.m., will increase the amplitude of the S_2 wave estimated by harmonic analysis, even though the variation in pressure is not sinusoidal

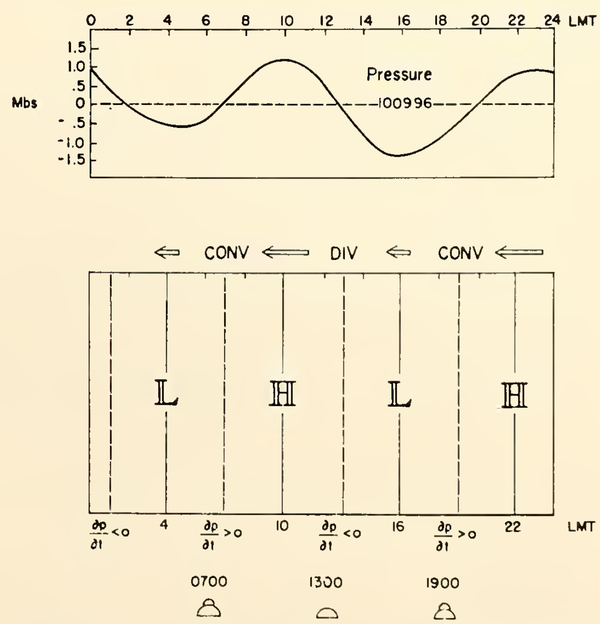

Figure 1. Schematic illustration of hypothesized relations between diurnal pressure wave, convergence field and cloudiness over tropical oceans or small atolls. Top curve shows observed mean annual diurnal pressure oscillation at Eniwetok atoll (after Lavoie 1963) as a function of local mean time.
Arrows above bottom diagram show qualitative predicted (Stolov 1955) and observed (Shibata 1964) variation in the tropical easterlies due to the S_2 component of the atmospheric tide and the associated convergence-divergence.
Diagram shows lows (L) and highs (H) spread around the clock (or globe) and associated pressure tendencies. See Bjerknes (1948) for diagrams explaining antibaric character of tidal winds.
Cloud symbols below indicated cloudiness variations and local times of extremes if maximum cloudiness is in phase with maximum convergence and vice-versa.

in wave form or may be produced by non-tidal perturbations. However, if large six hour pressure changes were distributed uniformly and randomly throughout the day, there could be no net contribution to the mean S_2 wave and the pressure changes could not be considered as tidal since they are not phased in with the 24 hour clock. The statistical relation between the magnitude of the S_2 wave and the six hour pressure changes means, *on the average*, a larger six hour pressure change is associated with a larger value of S_2, but it does not necessarily imply that an anomalous change during a *particular* six hour period is tidally produced. The six hour pressure change is a convenient measure or index of the amplitude of the S_2 wave but, more important in the analysis here, it makes it possible and easy to study in greater detail the fluctuations that take place in periods much shorter than 24 hours.

The pressure-convergence-cloudiness relation postulated earlier and illustrated schematically in Fig. 1 requires that rising pressure from 4 a.m. to 10 a.m. (4 p.m. to 10 p.m.) should be associated with increasing cloudiness. If this view is essentially correct, then one should expect to find a greater increase in cloudiness on days when the pressure rise during this period was greater than normal, and a smaller increase in cloudiness on days when the pressure rise was smaller. Likewise, during the period 10 a.m. to 4 p.m. one should expect to find the greatest suppression of cloudiness on days when the fall in pressure was relatively greater. If a statistically significant relation is found between cloudiness (or rainfall) and the magnitude of the pressure changes during these intervals, then strong support is provided for a physical link between S_2 and weather, regardless of whether we know the direction or the mechanism of the causality or reason for variations in the amplitude of S_2. The evidence would be even more convincing if the relationship was pronounced, suggesting that the tropical atmosphere was very sensitive to small pressure changes.

2. The data used and the analysis procedure

Two data samples were used in this study, the first from Batavia (now called Djakarta) and the second from Wake Island. Pressure trends are to be correlated with trends in cloudiness and rainfall for selected 5 and 6-hour periods of the 24-hour day. Batavia (6·80°S; 106·45°E) is located at the north-west extremity of Java, in the Malay Archipelago. Fig. 2 shows that Java is a mountainous island extending about 600 miles approximately east-west and about 100 miles north-south. Numerous peaks exceed 2,000 m and several exceed 3,000 m elevation. The mean annual rainfall at Batavia is 184 cm per year. Java is in the south-east monsoon in its winter which is the dry season. The rainy season occurs in summer (October through March) when Java lies in the equatorial trough. The surface pressure at Batavia is practically always rising from 4 a.m. to 9 a.m. local time and from 4 p.m. to 10 p.m. The pressure is always falling from 9 a.m. to 4 p.m.

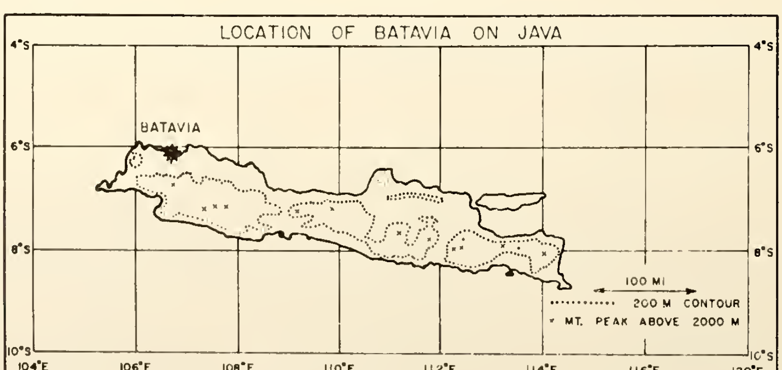

Figure 2. Location of Batavia on island of Java in Malay Archipelago and schematic illustration of orography.

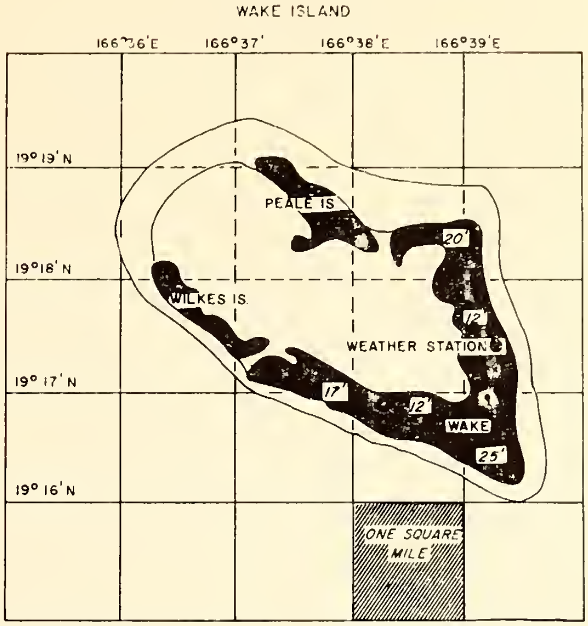

Figure 3. Outline map of Wake Island (after Kiser *et al.* 1963). Dark areas depict dry land; clear outlines show outer margins of barrier reef. Numbers in boxes are elevations in ft.

Six hour changes may be nearly 6 mb at times or as small as 2 mb at other times. The annual mean amplitude of the semi-diurnal pressure variation is about 1·38 mb. The average diurnal march of cloudiness and rainfall shows a dawn and sunset maximum, with a secondary maximum just after noon. For presentation, we have analysed a sample from 16 months of summer season data for the years 1924-1944, used earlier by Brier (1966). The dry season has also been studied; it shows similar but less pronounced results.

Wake Island (19·29°N; 166·65°E) typifies a contrasting tropical situation. Fig. 3 shows that it is a truly oceanic atoll, less than 4 by 3 miles in total extent. The atoll lies in the northeast trades the year round, but disturbances of temperate origin occasionally affect it during the drier winter season. The mean annual rainfall at Wake is 94 cm per year, about half that at Batavia. Twelve years of data were available on magnetic tape, subdivided into four seasons. Winter is defined as December through February, spring as March through May, etc. The mean semi-diurnal variations in these data had previously been related to mean atmospheric tides by Kiser, *et al.* (loc. cit., 1963).

The surface pressure at Wake is normally rising between 5 a.m. and 10 a.m. local time and also between 4 p.m. and 10 p.m. The annual average amplitude of the semi-diurnal pressure wave at Wake is 0·93 mb, or only 67 per cent of that at Batavia, in poor agreement with the 79 per cent ratio calculated from the cosine-cubed decrease with latitude found empirically by several workers (Haurwitz 1956; Simpson 1918). The ratio of daily and monthly variations to the mean are comparable at both locations. The mean cloud cover at Wake shows peaks at dawn and sunset, with a weak midday suppression. In contrast with most other small tropical islands (e.g. LaSeur and Garstang 1964; Lavoie 1963) the mean visually recorded cloudiness is smaller during the night-time than during the daylight hours. The mean rainfall frequency shows a maximum between 0300-0600 with a secondary peak near sunrise.

Figs. 4 and 5 illustrate the reason why a definitive relation between weather and S_2 wave has been so difficult to establish. In the mean daily marches of the weather variables, land-sea effects and their interaction with synoptic disturbances cannot be subtracted out, nor can the night versus day observers' bias in cloudiness be assessed.

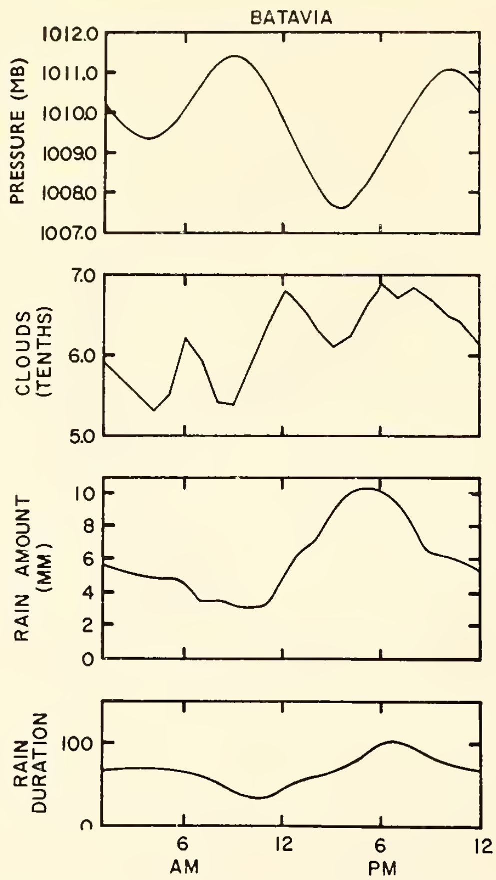

Figure 4. Diurnal marches of pressure, cloudiness and rain amount and duration at Batavia, Java. Averaged over the year for 70 years of data. Rain amounts are hourly. Rain duration (in minutes) was summed for each hour for each month for the seventy years. The curve shown is the average of all monthly curves. Note that on this and succeeding figures the abscissa value at the origin (left) is 1 a.m.

An interesting example of ' heated island ' effect is seen by comparing the cloudiness and rainfall curves in Fig. 4. The cloudiness curve has a strong midday peak, absent in the rainfall. Experience suggests the midday island-produced clouds are less likely to precipitate due probably to the rise in cloud base height resulting from the heating (Malkus 1964).

The primary means by which the present study attempts to establish a definite relation between atmospheric tides and weather variables is to segregate days of abnormally large from days of abnormally small S_2 pressure component and to compare the semi-diurnal cloudiness and rainfall variation on these two classes of days with each other. This is accomplished by selecting days on the basis of pressure change during 5-6 hour periods, since we are interested in studying pressure-weather relationships on a much shorter time scale than an entire day. Furthermore, this avoids the serious ambiguity in interpretation that would result from a direct comparison between the amplitudes of the semi-diurnal components of pressure and weather computed from a 24 hour period. It would be possible, for example, for a large S_2 pressure component to result from an anomalous rise in pressure from 4 a.m. to 10 a.m. while a large semi-diurnal component in cloudiness might be produced by a large rise in cloudiness from 4 p.m. to 10 p.m. Since any correlation resulting from such an analysis might be misleading or spurious, it makes more physical and statistical sense to concentrate on weather variations *concurrent*

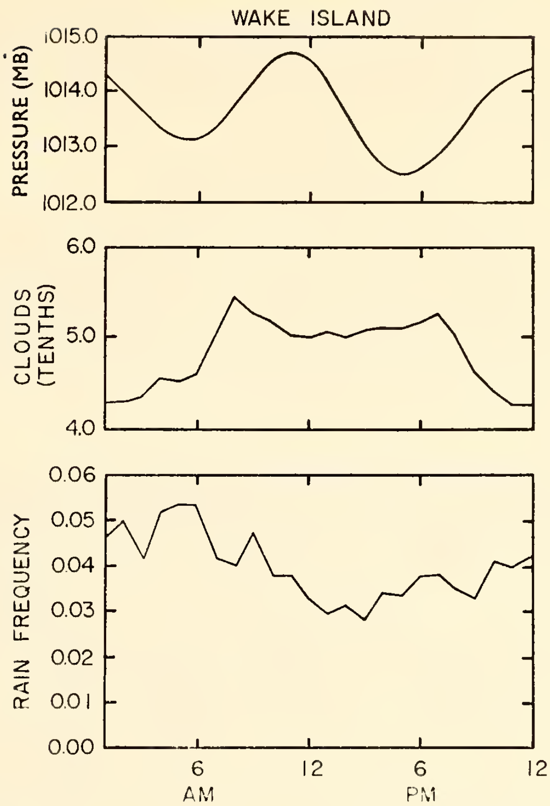

Figure 5. Diurnal marches of pressure, cloudiness and rain frequency at Wake Island. Averaged over the year for twelve years of data.

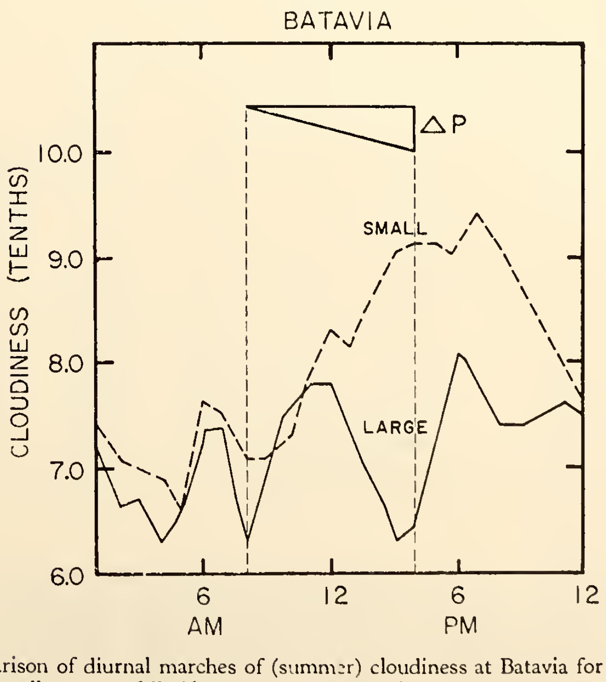

Figure 6. Comparison of diurnal marches of (summer) cloudiness at Batavia for large pressure falls (solid and small pressure falls (dashed) in midday period from 9 a.m. to 4 p.m. local time.

with the pressure changes. Statistical averaging over a number of samples will reduce the effect of local variations, or noise due to pressure changes that are non-tidal or random with respect to the time of day, since they cannot contribute, in the long run, to the average S_2 pressure oscillation determined at a station.

3. Results and discussion

Table 1 summarizes the analysis procedures and results. Three periods of the day were examined for Batavia and two for Wake, corresponding to both S_2 tidal pressure rises and including the midday fall period for Batavia. Large and small pressure changes are defined as follows for Batavia: From 0400 to 0900 increases equal to or exceeding 3 mb were called 'large.' Increases equal to or less than 1·8 mb were called 'small' changes.

TABLE 1. Statistical results

Differences in weather variations with large and small pressure changes at Batavia and Wake Island. Pressures normally rise in morning and evening and fall during midday hours. Greater cloudiness-precipitation *increases* in morning and evening and *decreases* during midday are found on all large pressure change days than on small pressure change days except the one (very small) exception in parenthesis

Identification	Period of day	Initial cloud conditions (tenths)	Number of cases: Large pressure changes	Number of cases: Small pressure changes	Difference of pressure change (mb)	Weather variations: Difference of cloudiness changes in period	Weather variations: Difference in change in probability of rain from beginning to end period	Weather variations: Difference in mean precipitation amount during period (mm)
Batavia (6·08°S; 106·45°E	4 a.m. to 9 a.m.		94	82		1·28	0·06	7·33
	4 p.m. to 10 p.m.		178	87		2·11	0·18	8·65
	9 a.m. to 4 p.m.	1, 2, 3	10	11	2·31	5·50		
		4, 5, 6	7	4	1·49	2·20		
		7, 8, 9	15	15	2·18	1·80	(all groups)	(all groups)
		10	17	18	2·50	2·10	0·29	6·58
Wake Island (19·29°N; 166·65°E								
Winter	5 a.m. to 10 a.m.		54	54	1·96	0·13	0·03	
Spring			54	54	2·32	0·42	0·04	
Summer			54	54	1·81	0·84	0·09	
Autumn			54	54	2·13	(0·08)*	0·03	
Winter	4 p.m. to 10 p.m.		54	54	2·15	0·56	0·06	
Spring			54	54	2·03	0·38	0·03	
Summer			54	54	1·80	1·29	0·03	
Autumn			54	54	2·11	0·25	0·11	

* Change in opposite sense

For the p.m. rise period the corresponding boundaries were 4 mb and 3 mb, respectively. For the midday fall period, the three greatest pressure falls in each month were classified as 'large' changes, while the three least falls were called 'small' changes. For Wake, only the rise periods were studied. The three greatest rises in each month were called 'large' changes while the three smallest rises in each month were called 'small' changes.

To understand the pressure-weather relationship established by Table 1, it is necessary to keep in mind that the entries under 'Weather variations' are the *differences* between the cases of large and small pressure change. For example, during the morning pressure rise period at Batavia, the 'large rise' days exhibited a greater increase in cloudiness between 4 a.m. and 9 a.m. than did the 'small rise' days, by 1·28 tenths; they exhibited an increase in rain occurrence probability 0·06 greater than the 'small rise' days and a 7·33 mm larger rainfall amount in the five-hour period. We define the rain occurrence probability as the number of rain occurrences divided by the total number of cases.

Qualitatively similar relationships are inferred for both rise periods in both locations. During the falling pressure period of the day at Batavia, the S_2 effect should act to suppress cloudiness and rainfall if the tide-weather relationships work as hypothesized in Fig. 1. However, Java is a large land mass. Sea-breeze effects are working in the midday hours to build clouds against any suppressive influence. The best method of isolating the S_2 effect is to compare weather trends on the large and small pressure change days in the same location.

From the work of Haurwitz (1955), it could be argued that the heated land mass effect is uncorrelated with the amplitude of the S_2 wave and is cancelled out in the comparison just described. Haurwitz's work, however, concentrated on the small island of Bermuda (32.18 N; 64.78 W). The greater size of Java suggests a possible feed-back relationship between the land mass effect and cloudiness. Because clouds diminish insolation at the ground, a three-way coupling between disturbances, sea-breeze and S_2 effect could occur. This might also involve an interaction with the S_1 component of pressure. We cope with this problem by sub-dividing the cases by initial cloudiness conditions. The results are striking, as shown in Table 1 for the 9 a.m. to 4 p.m. period at Batavia.

Relatively much greater suppression (or smaller enhancement of weather by the heated land mass effect) occurs on large pressure change days than on small ones. When the initial cloudiness is 1-3 tenths at 0900, the cloudiness decrease is more than five tenths greater during the large pressure change middays than during those with small pressure falls. Clearly this means that small S_2 days have midday *increases* in cloudiness, since cloud amount cannot decrease below zero tenths. This result implies that most cases of greatly increasing daytime cloudiness at Batavia are days of weak S_2 wave. That is, 'island' effect and S_2 amplitude are inversely related. Fig. 6 shows that the sea-breeze or island effect is able to produce a noon cloudiness peak at Batavia on both classes of day, but when the S_2-associated divergence is strong at 1300 hours, the cloudiness is not able to go on developing during the afternoon as it does on weak S_2 days.

Conversely, Table 1 shows that days which start off disturbed (10 tenths cloudiness at 0900) show midday suppression due to the S_2 effect. Physically, these initially disturbed days contrast with the initially fair days in experiencing a minimal heated island effect. Therefore large S_2 effect superimposes upon disturbances to suppress cloudiness during the day by two tenths more than small S_2 effect does.

Wake Island also exhibits a significant and similar relationship between the S_2 tidal component and the weather variables. But the difference in cloudiness changes at Wake are much less than those found at Batavia; they are in fact relatively much smaller than the one-third decrease in amplitude of the S_2 pressure wave at Wake compared to Batavia. It may be that the interaction of land mass effects with S_2 (or S_1) variations increase the cloudiness sensitivity to the latter. However, it is likely that a factor in the difference is simply the larger mean cloudiness at Batavia in summer. To explain the difference further it may be necessary to assess the relative frequency of cloud types and elevations.

In the morning the autumn season at Wake shows a very small S_2-cloudiness relation in the opposite sense from that generally prevailing. Even in that case, however, the relationship for rain occurrence turned out positive, consistent with the rest of the results. Thus the one negative value in Table 1 might well be a statistical accident that a larger data sample would reverse. It is noteworthy that only in summer does the S_2-weather relation-

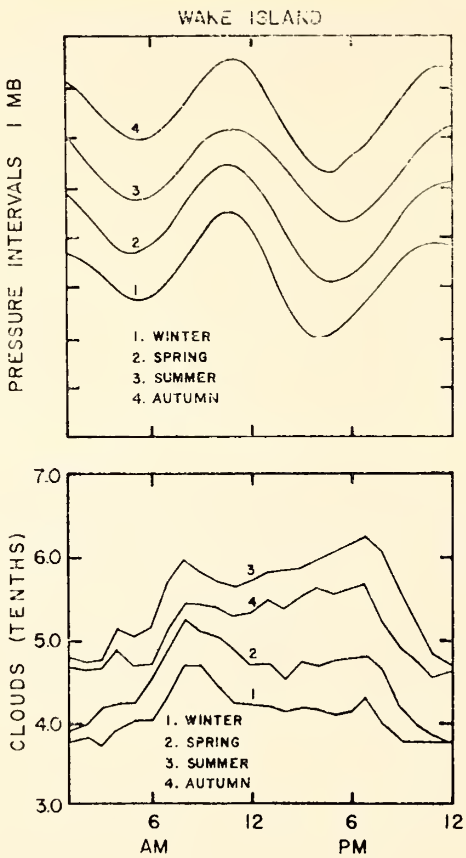

Figure 7. Seasonal change in daily marches of pressure and cloudiness at Wake Island. On the cloudiness (lower) curves note the seasonal migration of the mean peak from morning to afternoon in good agreement with the *slopes* of the pressure (upper) curves. Pressure curves not plotted on absolute scale. Interval is 1 mb (see Fig. 5).

ship at Wake exhibit comparable strength to that shown at Batavia in summer. Fig. 7 compares the seasonal change in the march of mean pressure wave and cloudiness at Wake. Surprisingly, the pressure wave shows maximum amplitude in winter. Haurwitz and Sepúlveda (1957) in fact showed that in January the S_2 wave has its maximum amplitude at 15°N while in July it is a maximum at the Equator. Thus the maximum S_2 amplitude is displaced latitudinally from both the overhead solar position and that of the equatorial trough in all seasons, a mystery which has not been explained. For present purposes, it is most important to note only that the strength of the S_2-cloudiness relation at any place is dependent upon factors other than the mean amplitude of the S_2 wave. Fig. 7 shows these factors are more complex than just the average cloudiness, since at Wake the autumn cloudiness is greater than that in spring. The autumn cloudiness, however, is likely both to occur at higher levels and to exhibit a greater ratio of stratiform to cumuliform than in spring. Section 4 on mechanistic linkages suggests ways to pursue these interesting questions further. The seasonal trend in Fig. 7 which shows the main cloudiness peak advancing with season from morning in winter to late afternoon in summer seems to be at least partially explained by a similar trend in the slopes of the pressure curves. This indicates that variations in the S_1 pressure component are related to cloudiness in the same way that S_2 is related, thus confirming the relationship between pressure trends and cloudiness changes.

The main result of Table 1 is that out of the 28 entries in the last three columns, 27

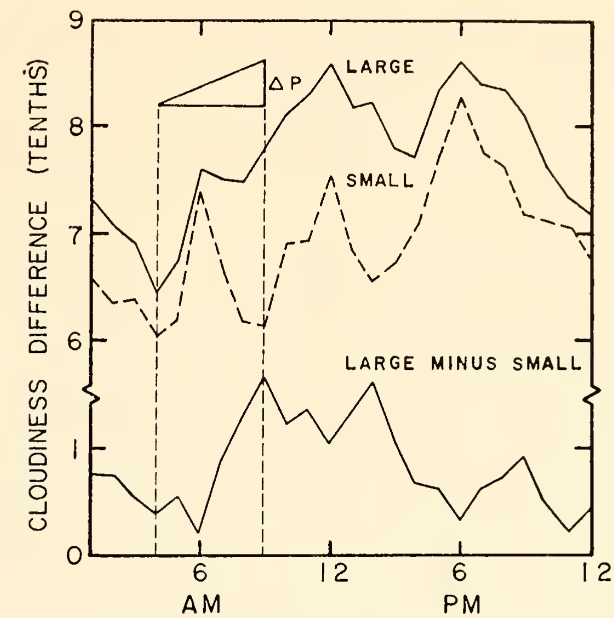

Figure 8. Comparison of daily march of summer cloudiness at Batavia for large (solid) versus small (dashed) morning (4 a.m. to 9 a.m. local time) pressure rises. The lower curve is the difference between the two upper curves and shows the greatest *increase* during the 4 a.m. to 9 a.m. period when pressure was increasing the most rapidly in the large Δp group compared with the small Δp group. Note absence of any noticeable 24-hour trend in the variables.

of them are positive. By chance one would expect one-half of them to be negative. Fourteen separate or independent groups (six for Batavia and eight for Wake) were analysed for cloudiness and only one of these shows a negative value (which is very small or close to zero). The chances are less than one in ten thousand that one or fewer negative signs will turn up in 14 randomly distributed differences. Thus there is no doubt about the

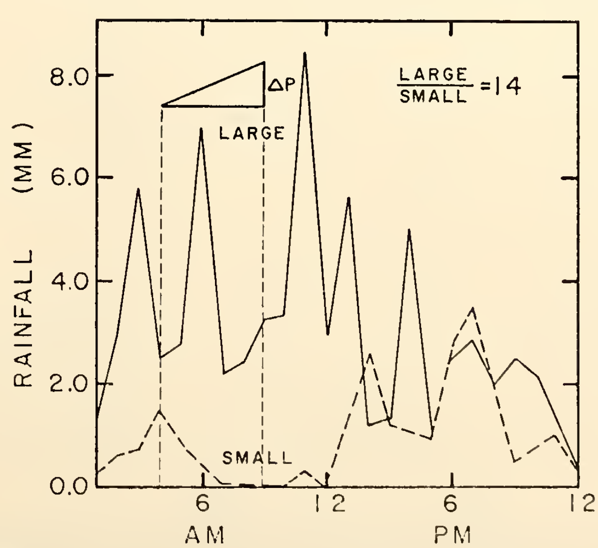

Figure 9. Comparison of hourly summer rainfall amounts for large (solid) and small (dashed) morning pressure rises at Batavia. As indicated in Table 1, the difference in precipitation amount was 7·33 mm while the ratio of the amounts during the 4 a.m. to 9 a.m. period is 14 to 1 ! Note also the downward trend in amount for the small pressure rise cases, in contrast with the upward trend in the large pressure rise cases.

statistical significance and physical reality of the relationship between pressure change and weather. Significance would have been attained if only 6, instead of 14, separate groups had been analysed. The values in the two rain columns in Table 1 are not independent of the results of the cloudiness column since more frequent rain and greater amounts will tend to be associated with increasing cloudiness. However, the functional and quantitative relationship between cloudiness, vertical cloud development, rain frequency and rain amount are just beginning to be documented in the Tropics (LaSeur and Garstang 1964; Holle 1968).

If there is no entry in the table, it means that the analysis was not performed either because the data were not conveniently available or because it was felt that the data sample was too small give meaningful results. For example, the rainfall analysis was made only on the combined groups for the Batavia 9 a.m. to 4 p.m. period because of the few cases and high natural variability in rainfall.

A second important result of this study is that with this separation into large and small pressure change cases (correlated to large and small S_2) the S_2-weather relation becomes so pronounced and consistently above the noise level that it is apparent from visual inspection of the graphs and can be demonstrated even with relatively few observations. Figs. 8-15 show a few selected graphs from the Batavia results. Differences between individual curves are generally highly significant but standard errors are not

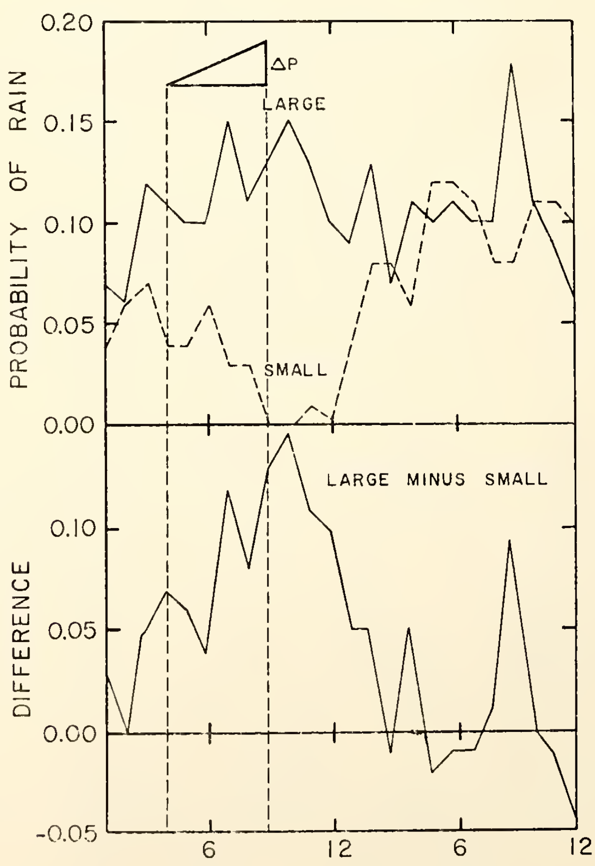

Figure 10. Comparison of hourly rainfall probability for the summer season in Batavia for large (solid) and small (dashed) morning pressure rises. The lower curve is the difference between the two upper curves. The greatest increase in rainfall probability is during the period of rising pressure. The abscissa refers to the rainfall measured up to the end of the hour.

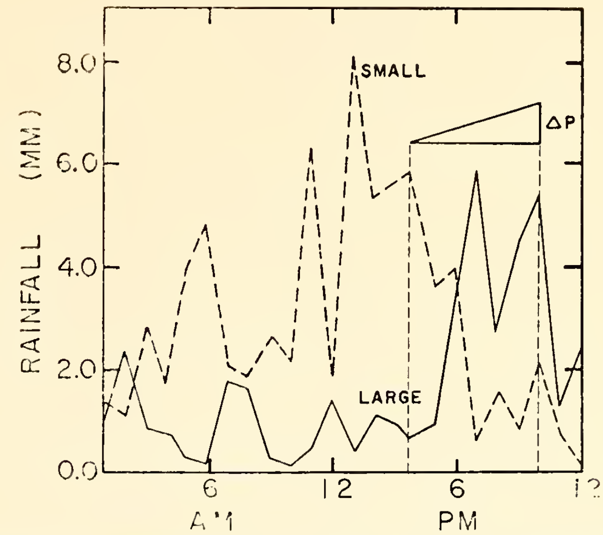

Figure 11. Rainfall amount comparison for the evening pressure rise period for Batavia in summer. The rise period considered is 4 p.m. to 10 p.m. local time. Large pressure rise cases (solid) show much more precipitation in the period than do the small pressure rise cases (dashed).

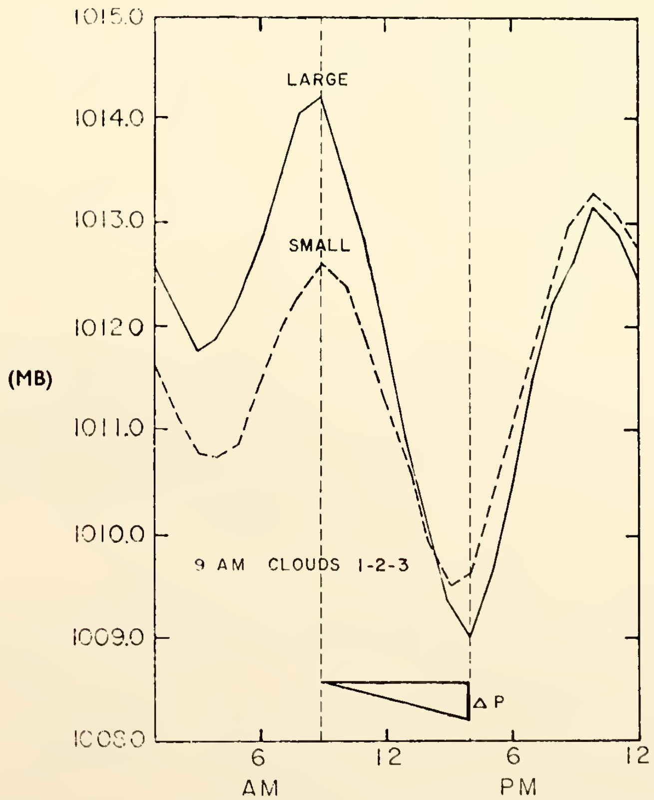

Figure 12. Diurnal march of pressure at Batavia on large (solid) and small (dashed) pressure fall days. Note that the pressure falls between 9 a.m. and 4 p.m. local time on both classes of days, but about 67 per cent more on 'large' fall days. Note that 'large' midday fall days are also days of large rises in the a.m. and p.m. periods, graphically illustrating Brier's (1967) correlation between S_2 amplitude and 5-6 hourly pressure changes. Other pressure régime curves are similar.

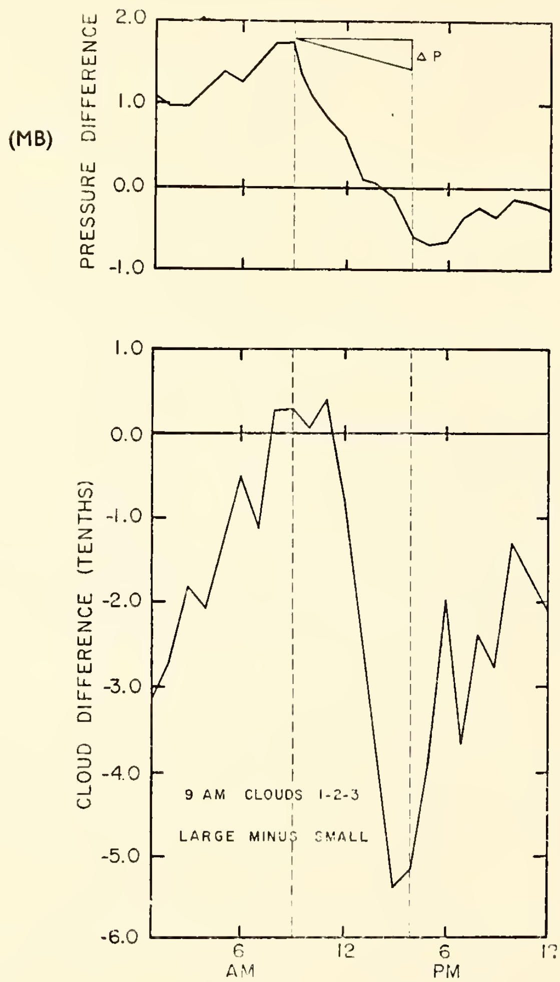

Figure 13. Difference in cloud régimes on days with large versus small midday pressure at Batavia in summer, when the 9 a.m. cloudiness is 1-3 tenths. The period considered is 9 a.m. to 4 p.m. local time. The upper curve is the difference in the pressure fall between the large fall and small fall cases (Fig. 12). The lower curve is the difference in cloudiness *change* between the two sets of cases. Note that the greatest and in fact the only consistent and large *decrease* in cloud anomaly is during the period of *falling* pressure anomaly. Since cloudiness cannot decrease by five-tenths if it is initially three-tenths or less, the results are contributed mainly by the increased cloudiness that takes place when the pressure *falls* much *less* than it normally does during the period 9 a.m. to 4 p.m. (see Fig. 6).

given because they would be misleading in view of the lack of independence of the observations from one hour to the next. Fig. 8 compares the diurnal cloudiness march for large and small pressure rises in the morning period from 4 a.m. to 9 a.m. Both cases show the three peaks of Fig. 4, but the large morning pressure rise cases show a higher rate of cloudiness increase in the morning and a less sharp noonday cloudiness peak.

It is important to note that there is relatively little change in 24 hours in all curves, so that situations with long period trends are not influencing the results. Very small or zero 24-hour trends were found for all data sub-divisions reported in Table 1. Fig. 9 compares the corresponding daily marches of mean hourly rainfall amounts for Batavia. The aggregate mean rainfall for the period is in the ratio of 14 to 1 for the case of large versus small pressure rise. For the ' small ' pressure change, the trend in precipitation is downward during the period, indicating a suppression of activity. The same

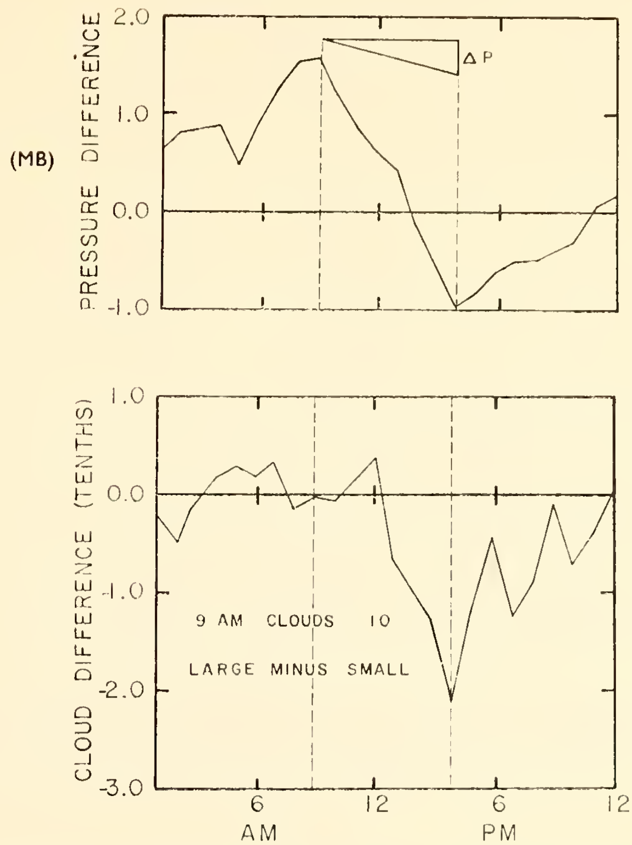

Figure 14. Difference in cloud régime on days with large versus small midday pressure fall at Batavia in summer when the 9 a.m. cloudiness is 10 tenths. A greater midday suppression is found on the large pressure fall days.

suppression was found in rainfall probability (Fig. 10). Fig. 9 and the location of Batavia (Fig. 2) suggest that a late nocturnal land-mountain breeze dominates the precipitation régime in the early morning hours on 'small' pressure change days. The island effect is largely overcome by the tidal effect on 'large' pressure change (large S_2) days.

Fig. 11 shows the corresponding rainfall amount comparisons for the 4 p.m. to 10 p.m. pressure rise period. The dominance of the island effect is striking on the 'small' pressure change days, as is the dominance of the S_2 effect on the 'large' pressure change days. Figs. 12-15 examine the midday régimes at Batavia with very low and very high initial cloudiness at 9 a.m. Fig. 12 illustrates graphically the correlation between 5-6 hour pressure change and semi-diurnal S_2 amplitude which was established statistically by Brier (1967, loc. cit.). Even with only 10-18 cases making up each graph, the strikingly greater suppression on the 'large' pressure fall (large S_2) days is obvious. Fig. 13 illustrates the different effect of large versus small S_2 on the midday cloudiness peak on days which start off fair. The midday cloudiness peak has five-tenths more sky cover on weak S_2 days. Fig. 14 examines the same midday differences on days which start off overcast. Large S_2 days show a noonday reduction in sky cover two-tenths more than do small S_2 days. Fig. 15 compares midday rainfall amounts. The amount of rain from 9 a.m. to 5 p.m. during the 'small' pressure falls exceeds that during the 'large' pressure falls by a factor of three. This ratio again supports the hypothesis regarding the varying relative strengths of tidal versus island effect.

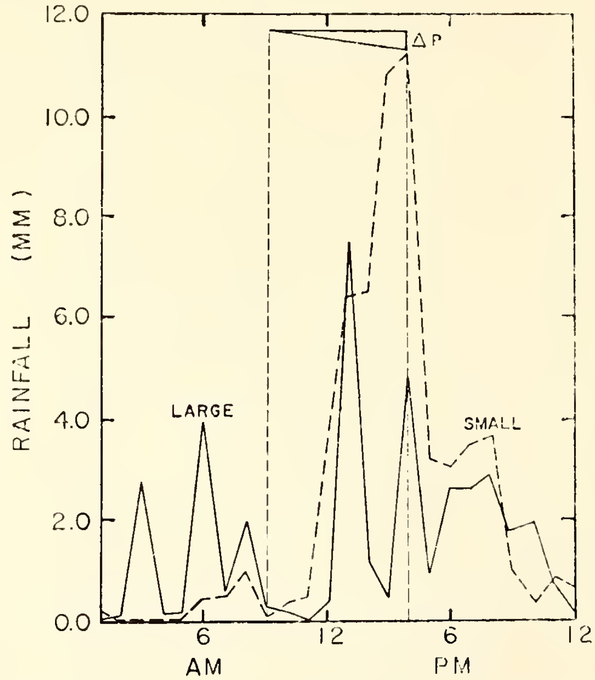

Figure 15. Comparison of rainfall amounts at Batavia in summer during days of large midday pressure fall (solid) and small midday pressure fall (dashed). Note the far bigger afternoon peak on the small pressure fall days.

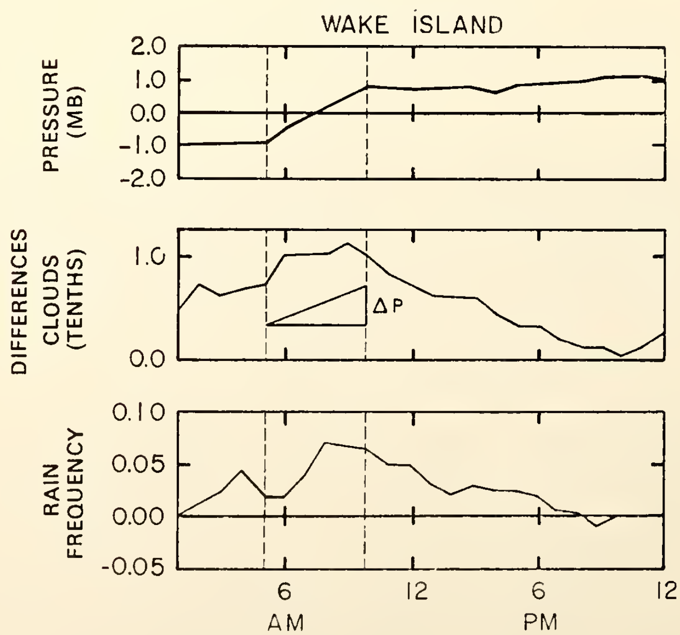

Figure 16. Comparison for Wake Island. Differences in pressure rise, cloudiness increase and increase in rain for the morning pressure rise period from 5 a.m. to 10 a.m. Small rise values have been subtracted from large rise values (all seasons).

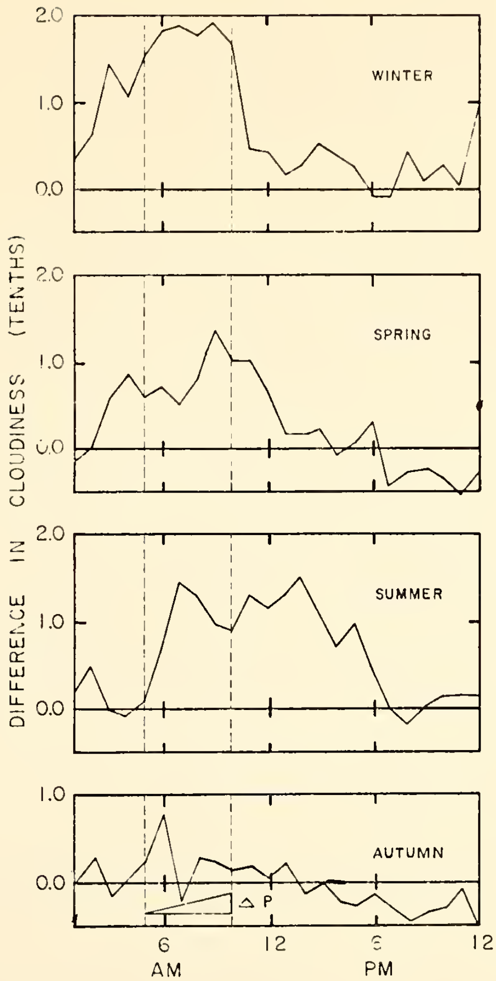

Figure 17. Cloudiness comparison for Wake Island for morning pressure rise period, broken down by seasons. Small rise values have been subtracted from large rise values. Note pronounced excess in cloudiness increase on large pressure rise cases for all seasons except autumn.

Diagrams for Wake Island for the morning (5 a.m. to 10 a.m.) pressure rise period are shown in Figs. 16-18. In Fig. 16, it is important to note that the pressure difference curve does not necessarily mean that the pressure fell from midnight to 1 a.m. It means that days with large pressure rises from 5 a.m. to 10 a.m. had lower initial pressures than the small pressure rise days. Most noteworthy is the observation that when the pressure stopped rising rapidly around 10 a.m., the cloudiness and rainfall stopped increasing and actually decreased. This emphasizes that we are dealing with variations on a time scale of a half day or less and not twenty-four hour trends, for if the latter were involved the cloudiness and rainfall would have continued to increase, or at least levelled off, past 10 a.m. The morning relative cloudiness peak for the 'large' pressure rise days is pronounced in all seasons except autumn. The latter season, nevertheless, has a strong relative peak in rainfall. This peculiarity is equally evident in the afternoon diagrams for autumn (not shown). At this time no explanation is evident, but if the peculiarity were confirmed in a larger data sample, a reason might first be sought in the seasonal changes in cloud types, elevations and origin. Some evidence of 24-hour trends is present in the autumn data at Wake. Climatologically, this season might be the most prone to travelling disturbances.

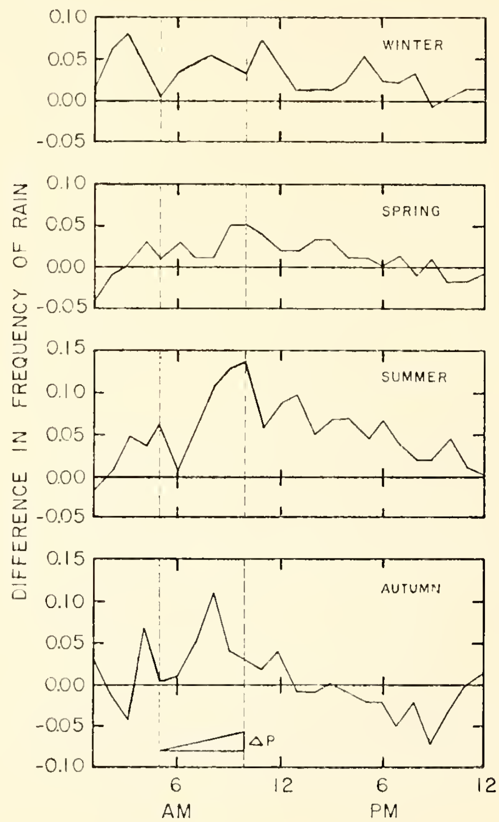

Figure 18. Rain frequency comparison for Wake Island, for morning pressure rise period, broken down by seasons. Small rise values have been subtracted from large rise values. Pronounced excess in increased rain probability is found for the large rise cases for all seasons.

4. Possible mechanistic connections between S_2 atmospheric tide and cloudiness and rainfall

Fig. 1 hypothesized a physical connection between the S_2 pressure wave and clouds by means of the convergence and divergence concomitant with the rising and falling pressure. It was also mentioned that most meteorologists have regarded the magnitude of the S_2-associated convergence as too small to affect clouds and precipitation. However, the hypothesized S_2-weather relationship has now been established statistically. It therefore becomes desirable to examine possible mechanistic links and to inquire about their necessary magnitude and method of operation. We shall first estimate the magnitude of the convergence-divergence likely to be associated with the S_2 wave and then inquire as to how it might affect clouds and precipitation.

A basic physical relation is found in the tendency equation, viz :

$$\frac{\partial p}{\partial t} = -\underbrace{\int_z^\infty g\rho \, \nabla \, . \, \mathbf{v}_H \, dz}_{A} - \underbrace{\int_z^\infty g \, \mathbf{v}_H \, . \, \nabla_H \, \rho \, dz}_{B} + \underbrace{g\rho w_z}_{C} . \qquad (1)$$

The symbols have their usual meanings; $\partial p/\partial t$ is the local pressure tendency at level z (for example as measured by a barograph). A is the horizontal velocity divergence term. B is the horizontal density advection term. C is the vertical motion term where w_z is the vertical air motion at level z, positive upwards. At the surface ($z = 0$), $w = 0$. Density advection plays no part in the semi-diurnal pressure cycle. Since the tropospheric density ρ has only one maximum and one minimum around the globe, we must explain the surface pressure oscillation in terms of the vertically integrated divergence field. From Eq. (1) an average divergence field (from the surface to levels of 12-15 km) of the order of 10^{-7} sec^{-1} would produce a surface pressure oscillation with an amplitude of about 1 mb at the surface.

Since the atmosphere is commonly divided into superimposed layers of divergence and convergence the net integrated value, however, may tell us little about what a given layer is experiencing. Average cloud layer divergences of 1-3 $\times$ 10^{-7} sec^{-1} are in good agreement with results from tidal theories and observations, as reviewed by Shibata (1964). If the main tidal divergence producing the pressure change were confined to the lowest three kilometers, it would average about 3 $\times$ 10^{-7} sec^{-1} for Batavia and 2 $\times$ 10^{-7} sec^{-1} for Wake. Thus for the 'large' pressure change days at Batavia, the cloud layer convergence could be in the neighbourhood of 6 $\times$ 10^{-7} sec^{-1}, or more if there were compensating layers aloft.

Clearly the magnitude of the S_2-associated convergence cannot be resolved without a determination of the tidal ' wind.' These S_2 winds have been studied successfully with rockets and meteor trails in the ionosphere where they are large (Elford 1959; Greenhow and Neufeld 1961; Kashcheyev and Lissenko 1961). But in the high density troposphere, whence the main contributions to surface tendencies must originate, the measurement problem has been very difficult. The mean horizontal tidal winds corresponding to a divergence field of about 2·5 $\times$ 10^{-7} sec^{-1} are about 80 cm sec^{-1}. The surface wind evaluated by Lavoie (1963) at Eniwetok atoll (11·30°N; 162·15°E) is much smaller than this, but the magnitude might well be expected to increase upward away from the surface.

It is necessary to determine the amplitude and phase of the S_2 tidal wind as functions of altitude, a very difficult task. Small wind variations must be isolated from far bigger inter-diurnal changes. A large around-the-clock sample must be sought on one or more atolls. This sampling presents a nearly impossible data requirement since rawinsondes are normally made at 12-hour intervals. One of the rare opportunities with more frequent soundings was provided at Lajes Field, Azores, in 1956-1958. Using these data, Harris, Finger and Teweles (1962) made a fine study of the semi-diurnal tidal winds (and other variables) at thirty levels between the surface and 10 mb. The east-west component increases rather uniformly from about 28 cm sec^{-1} at 850 mb to about 1 m sec^{-1} at 15 mb (29 km) with little change in phase. Unfortunately, the Azores are extra-tropical (38.73 N; 27.07 W).

The only opportunity for a similar study on a tropical atoll was provided by the Marshall Island bomb tests in the 1950's, when a series of six-hourly upper wind measurements were made. There was also a helpful shift in observation time within the series, permitting an adequate 3-hourly sample over the 24-hour period at some stations. These data were analysed, in most detail for Eniwetok, by Shibata (1964, loc. cit.). He found mean tidal winds consistent with Fig. 1 and the mean divergence figures quoted here. A maximum east-west component of 80 cm sec^{-1} was found at 1 km (just above mean cloud base) with a probable error of $\pm$ 9 cm sec^{-1}. There was also some evidence of a phase shift beginning above 2 km. By 3 km, the tidal wind had apparently reached a 6-hour phase lead relative to that in the lower cloud layer, although the data were rapidly thinning with height. It would be important to determine whether this difference from the results of Harris *et al.* (1962) is real and due to location difference, or whether it is fictitious. Some upper atmospheric studies (cf. Greenhow and Neufeld 1961) suggest that the ionospheric (80-100 km) tidal wind and pressure oscillation are, in some seasons, almost exactly out-of-phase with those at the surface. From Fig. 1, this implies that the upper divergence field may be out of phase with that lower down. Tropical studies (e.g. Riehl 1954) have shown that the most favourable conditions for clouds and rain consist of convergence in the lower cloud layer and divergence at its top. Thus determination of the existence and height of any phase shifts in semi-diurnal tidal wind and pressure oscillation is important. Harris *et al.* (1962, loc. cit.) show that a two-year series of six-hourly wind soundings could provide the necessary information.

We must next ask whether and how these small convergence-divergence fields could cause the documented variations in cloudiness and rainfall. A divergence of 10^{-6} sec^{-1} is roughly the value of the prevailing mean divergence in the trade-wind cloud layer, associated with an average subsidence of several hundred metres per day. The subsidence was shown (by Riehl *et al*, 1951) to be a major brake against cloudiness. Thus if the large S_2 days are associated with oscillating divergence-convergence magnitudes of 25-75 per cent of this amount, we might expect a significant effect upon cloud growth. The prevailing divergence is to a large extent removed near sunrise and sunset and greatly increased during the midday hours. In the equatorial trough zone, mean convergence prevails and analogous reasoning would apply. To understand the effect of these small changes on clouds, however, we must keep in mind the concentration of convergence and active cloudiness in the Tropics. A study of the equatorial trough by Riehl and Malkus (1958) suggested that the mean ascent there is not a gradual, widely spread slow movement of all the air, but that the up motion is highly concentrated in a few active cloud groups, and within these in a few active cloud towers.

An analysis by Kuo (1961) provides an important theoretical foundation for this concentration. He showed that if the stratification is unstable for ascending motion over an infinite area and stable for descending motion, and small random perturbations of various scales are introduced, the final disturbance evolved will have the dimension of a cumulus cloud. The stable stratification in the descending region has the effect of increasing the critical lapse-rate and narrowing the ascending region and making the descending motion widespread, so that centres of the ascending region are further apart. The distances estimated from Kuo's theoretical analysis agree favourably with cloud row spacing obtained from satellite observations. In this way the weak, large-scale tidal perturbation can cause the atmosphere to react on the cumulus scale. We postulate that this concentration of vertical motion is a key to the relation between S_2 tidal convergence and weather.

In the quantitative calculations, we shall be conservative and consider the effect of a convergence-divergence amplitude of only $2{\cdot}5 \times 10^{-7}$ sec^{-1}. This amplitude agrees with the mean tidal winds found by Shibata (1964) at Eniwetok and also with theoretical values and the observed mean pressure changes in the Marshall Islands region. By continuity, a convergence field of $2{\cdot}5 \times 10^{-7}$ sec^{-1} would be associated with an overall average ascent of $0{\cdot}1$ cm sec^{-1} at 3 km (near the top of the normal undisturbed cloud layer in the trade-wind region). The mean cloudiness at this level is 35 per cent and the mean is made up by about half the sky being clear and the other half being occupied by cloud groups with about 70 per cent cloudiness. We assume that the average ascent of $0{\cdot}1$ cm sec^{-1} over the whole area is brought about by no ascent in the clear zones, with $0{\cdot}2$ cm sec^{-1} confined entirely to the cloudy zones.

Table 2 shows how an oscillation of $\pm$ $0{\cdot}2$ cm sec^{-1} in the average vertical motion can lead to a 10 per cent cloudiness variation. The figures in Table 2 are based on typical values taken from years of aircraft observations by Malkus (1958a). A small mean additional vertical motion is able to contribute such a relatively large cloudiness change because of the concentration of the active updraughts into 2-3 per cent of the whole area, so that most clouds seen or photographed are inactive or decaying. This concentration of active updraught has in fact been confirmed by years of observations and has also been found in tropical hurricanes (Malkus 1958b; Malkus, Ronne and Chaffee 1961).

The calculations in Table 2 are intended to be illustrative rather than definitive; they are both conservative in assumptions and insensitive to reasonable variations in them. Examining the results in more detail, we find that they depend on the following three features of cumulus clouds, which have been documented observationally.

(i) Comparable vertical speeds in active updraughts and active downdraughts, which together occupy only a small per cent of the total cloudy area. In the example, the

TABLE 2. CLOUDY AREA (3 km ELEVATION)

Average over 24 hours	
5 per cent Active updraught	274 cm sec^{-1}
5 per cent Active downdraught	− 150 cm sec^{-1}
60 per cent Inactive cloud	− 8 cm sec^{-1}
30 per cent Intercloud spaces	− 1 cm sec^{-1}
	$\overline{w} = +$ 1·1 cm sec^{-1}
Max. conv. ($2{\cdot}5 \times 10^{-7}$ sec^{-1})	
5·5 per cent Active updraught	274 cm sec^{-1}
5·5 per cent Active downdraught	− 150 cm sec^{-1}
66 per cent Inactive cloud	− 8 cm sec^{-1}
23 per cent Intercloud spaces	− 1 cm sec^{-1}
	$\overline{w} = +$ 1·3 cm sec^{-1}
Max. Div. ($2{\cdot}5 \times 10^{-7}$ sec^{-1})	
4·5 per cent Active updraught	274 cm sec^{-1}
4·5 per cent Active downdraught	− 150 cm sec^{-1}
54 per cent Inactive cloud	− 8 cm sec^{-1}
37 per cent Intercloud spaces	− 1 cm sec^{-1}
	$\overline{w} = +$ 0·9 cm sec^{-1}

updraught speed is not quite twice that of the downdraught, which is a typical lifetime average for the upper parts of a cloud (Malkus 1954; 1955).

(ii) Equal or nearly equal areas on the average occupied by active updraught and downdraught (not necessarily in the same cloud).

(iii) Nearly constant ratio between area occupied by active cloud draughts (up and down) and inactive or decaying cloud matter.

Table 2 suggests that a 20 per cent cloud-group cloudiness variation, or an overall 10 per cent variation, can readily result at 3 km from a convergence amplitude as small as $2{\cdot}5 \times 10^{-7}$ sec^{-1}. Aircraft observations suggest that the cloudiness variation at 1-2 km would be as large or larger. Active updraughts and downdraughts have very nearly the same r.m.s. amplitude near cloud base, since the updraughts increase upward and the downdraughts downward. Therefore, at lower levels a smaller mean updraught may permit as large a cloudiness increase as that shown by Table 2 for about 3 km.

There is also evidence of a 'tidal' variation in the height of the trade-wind inversion and the thickness of the moist layer, which vary as the pressure tendency*. These variations are probably caused by the semi-diurnal variation in the vertical development of trade cumuli and are thus unlikely to be a critical link in the causal chain between S_2 tendency, cloudiness and rainfall. A semi-diurnal variation in the cloud base height, however, could be a critical link in the causal chain, if the cloud base were found to be lower near sunrise and sunset and higher just after noon and after midnight. Some evidence of a systematic semi-diurnal variation of about 100 m in magnitude was found by Holle (1968) analysing photographs from the *R. V. Crawford* (13·00°N; 55·00°W). Cloud base had double minima near dawn and sunset. This variation could be explained in terms of sea-air transfer effects, if substantiated. No night-time cloud base information was available with which to see whether the critical post-midnight rise was present. Holle's sample was only 3 weeks, moreover, and the error in cloud base measurement may have been comparable to its variation. A further study of oceanic cloud base variations is important. The reason is that on most typical tropical soundings a 100 m (10 mb) lowering of cloud

* Personal conversation with Professor Herbert Riehl of The Colorado State University.

base would result in tops that are higher by 0·5-1·0 km and buoyancies increased by 50-100 per cent, if the in-cloud lapse rates are unchanged.

Without the necessary observations, it is only possible to inquire here whether a convergence-divergence of roughly $2{\cdot}5 \times 10^{-7}$ sec^{-1} in the sub-cloud layer could cause a variation of the order of 100 m in the height of cloud base and how it would operate to do so. Convergence of this magnitude in the sub-cloud layer corresponds to a net inflow of about 10 per cent of the air which is ascending through cloud base, if at this level one-tenth of the area is occupied by ascent at 25 cm sec^{-1} or if one-twentieth of the area is ascending at 50 cm sec^{-1}. In any case it is noteworthy that a fairly conservative estimate of the average tidal convergence represents a significant fraction of the air rising through cloud base. Although this does *not* explain how cloud base is or could be lowered by tidal effects, it does point to a need for systematic investigation of oceanic cloud bases and the mechanisms controlling their height.

At present it appears probable that dynamic factors (horizontal wind convergence) are an important mechanistic link in the relation between S_2 tendency and cloudiness and rain. It can be postulated that the convergence acts to produce slightly stronger updraughts, lower cloud bases, greater vertical development and a higher cover of cumuli. Thus our proposal to assess the variation in cloud levels and types with season at Wake is clarified. Stratus-type clouds should be less affected by these mechanisms, as should very tall cumulonimbus in disturbed situations, particularly if the tidal convergence shifts phase above about 3 km. None of these links is as yet firmly established. The next Section attempts to discuss the questions concerning mechanisms relating tropical weather and pressure tendency by a brief look at variations on different time and space scales.

5. Scales of tropical pressure changes and their relations to cloudiness

A major result of this study is the confirmation that cloudiness increases with rising 5-6 hour pressure tendency and decreases with falling 5-6 hour pressure tendency. This relation was found statistically at two widely separated tropical stations with different orography and climatology. Although tropical forecasters have long used the relation between rising pressure and increasing clouds, this correlation may surprise some temperate-latitude meteorologists who associate increasing clouds and rainy weather with the approach of travelling low pressure centres.

In the Tropics, the hierarchy of pressure change scales, their causes and their relations to weather show increasing dissimilarities to those in higher latitudes as knowledge of them increases. The most obvious scales of pressure change as seen on a tropical barograph (not in order) are: the 12-hour S_2 wave, the 24-hour S_1 wave (smaller than S_2), large-scale inter-diurnal changes, progressive inter-diurnal changes due to travelling synoptic-scale windfield perturbations and sub-synoptic or meso-scale variations. Preliminary tests indicate that the relation between rising pressure and cloudiness can be expected to be valid statistically on all scales, although many more detailed studies need to be made.

The relative contribution of the different scales of pressure variations to tropical weather has not been specifically documented. The advent of satellites will now permit this to be begun in the case of cloudiness. Twenty years ago it was a common belief that most tropical rain occurred in wave-like or vortical perturbations travelling with speeds comparable to those of the 'basic current' in which they were embedded or with the equatorial trough and its fluctuations. The well-known 'easterly wave model' of a class of travelling disturbances does indeed predict convergence and maximum cloudiness on the east or rising-pressure side of the easterly wave. The passage of travelling disturbances, however, did not contribute significantly to the results in this paper. The relation between the time of disturbance passage and local time is random. Furthermore, we showed that 24-hour changes were negligible in almost all of our figures.

Satellite implementation of tropical weather analysis (e.g. Simpson *et al.* 1967, loc. cit.) has suggested that many large rain-producing disturbances in the Tropics are not recognizable as travelling perturbations in the low-level windfield. Instead, they grow and die *in situ* with no major change in the three-dimensional windfield as represented by the synoptic networks, even when those networks with the best coverage, such as in the Caribbean area, are further supplemented by research aircraft and other special observations. This puzzle together with the S_2-weather relation established here led to the construction of Figs. 19-21.

Fig. 19 shows the surface pressure at the midnight observation during July 1955 for three Pacific islands. Eniwetok is about 900 km from Wake Island and Kwajalein is about 1,100 km from Wake. The general trend in pressure at all three stations is downward to about 14 July, upward to about 24 July, downward to 26 July and upward again to the end of the month. The peaks and tendencies appear to be in phase at all three stations with little evidence of disturbances progressing with the winds. Fig. 20 shows the cloudiness at the same stations for the same period. There is a general downward trend in mean daily cloudiness until around the 13th or 14th. After that the trend is upward, reaching a maximum around 22 July and then decreasing to a minimum around the 25th or 26th. Comparison with Fig. 19 shows clearly that the cloudiness is decreasing in the pressure fall periods and increasing in the pressure rise periods. Nor is there evidence of any substantial or consistent time lag between events at the three stations.

Finally Fig. 21 shows simultaneous hourly pressure anomalies at even more widely separated Pacific stations. These anomalies are still largely in phase, despite a longitudinal

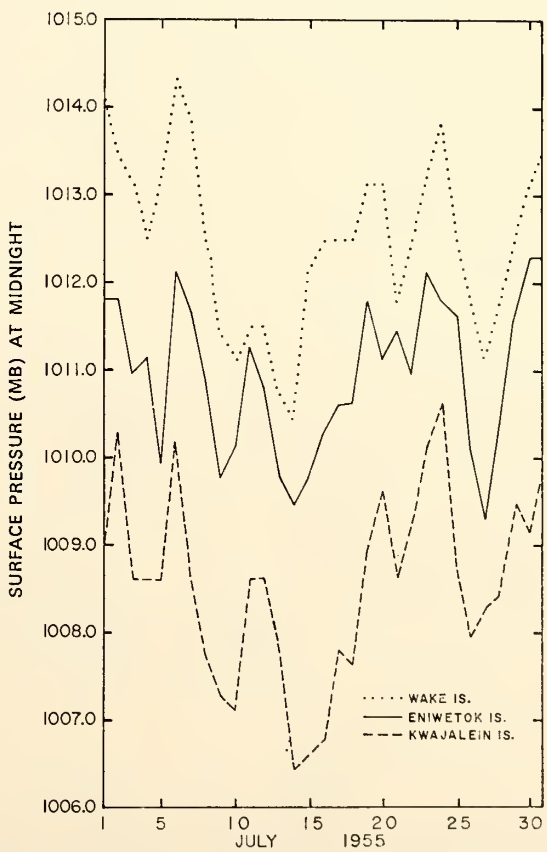

Figure 19. The surface pressure at the midnight observation during July 1955 for the three Pacific atolls of Wake (19·29°N; 166·65°E), Eniwetok (11·30°N; 162·15°E) and Kwajalein (9·15°N; 167·30°E). Eniwetok is approximately 900 km from Wake and Kwajalein is about 1,100 km.

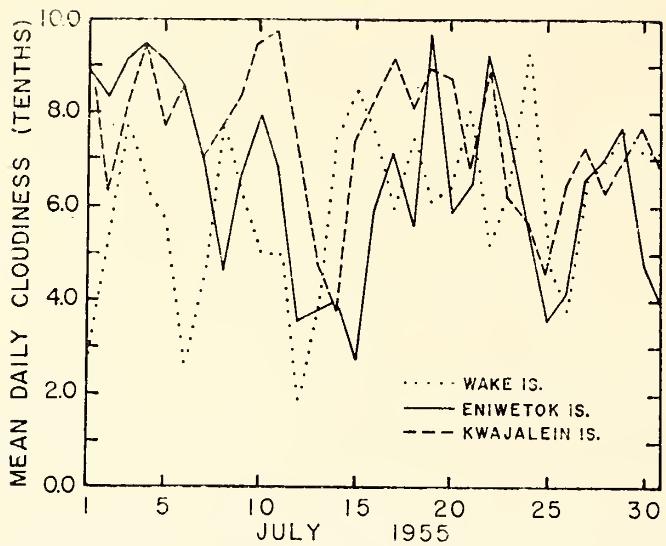

Figure 20. The mean daily cloudiness at the three Pacific island stations of Fig. 19 during July 1955. Note the similarity in cloudiness and pressure trends.

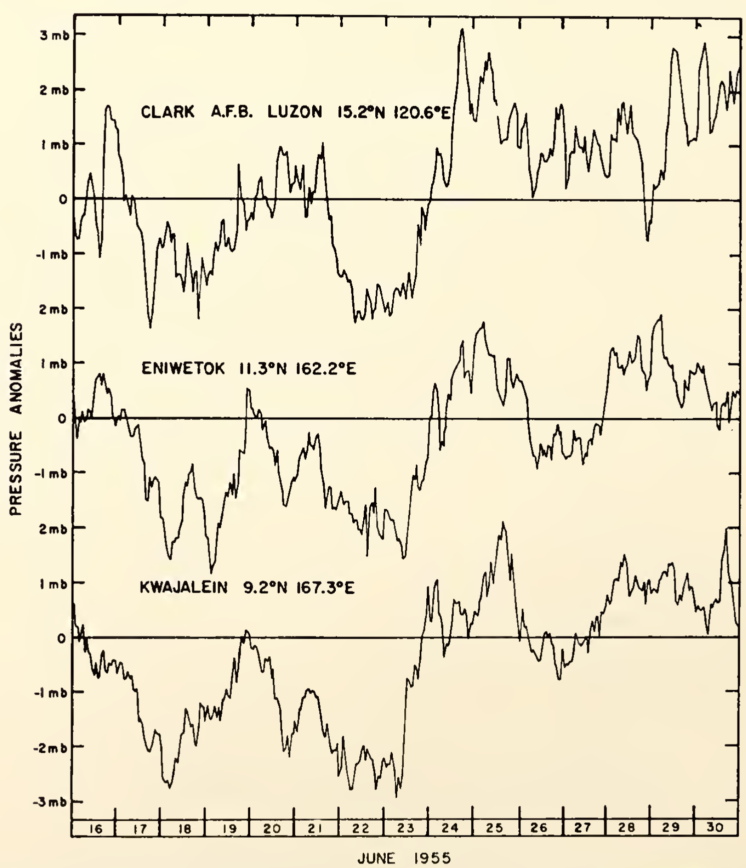

Figure 21. Simultaneous hourly pressure anomalies 1-15 June 1955 for Kwajalein Island, Eniwetok Island and Luzon, Philippines. The diurnal and semi-diurnal variations have been removed by using departures from the monthly means of hourly values.

separation of 47 degrees and a latitudinal separation of 6 degrees. The latter precludes a northward surge of the equatorial trough, another frequent synoptic-scale cause of change in tropical pressures and weather. Similar in-phase changes over widely separated (by latitude *and* longitude) Caribbean and Atlantic stations were carefully documented by Frolow a quarter century ago (Frolow 1942). A stationary 6-day period was analysed but not explained by him. Nor do we have any explanation for the changes shown in Figs. 19-21 in terms of either a terrestrial or extra-terrestrial origin. We do postulate, however, their importance to tropical weather and suggest a further study using satellite observations.

Nor do we deny the existence or importance of migratory perturbations in the wind-field. These play an important role in the atmosphere's water, momentum and energy budgets, and in their severe form both wreak destruction and bring important rainfall as tropical storms. It is, however, time to reassess quantitatively the controls upon tropical weather and the pressure change-weather relations on a hierarchy of scales. Furthermore, we believe that the tendency-weather relationships that we have documented on one scale and suggested on others may be an important step to a further understanding of tropical disturbances.

6. Concluding remarks

A statistical relation between S_2 atmospheric tide and a semi-diurnal variation in tropical cloudiness and rain has been established. 'Large' 5-6 hour pressure change days have been shown to have larger semi-diurnal variations than 'small' 5-6 hour pressure change days at Batavia and Wake Island. Using a previously established correlation between 5-6 hour pressure changes and S_2 amplitude (see Brier 1967 and Fig. 12 (a)) we deduced that the S_2 effect acts to increase cloudiness and rain near sunrise and sunset and to suppress them near midday and just after midnight. The pressure-weather relationship demonstrated here shows that pressure changes of around two or three millibars, associated with the mean S_2 oscillation, are quite adequate to account for the observed increase of 5-15 per cent in mean cloudiness and rainfall near dawn and sunset. Statistically significant relations were found for per cent cloudiness, rain probability and rain amount for each station for each season, except for cloudiness at Wake in Fall.

The mechanism relating S_2 and weather is not yet resolved although a strong observationally-based argument exists in favour of its being dynamic, through the effect of the changing tidal convergence-divergence field upon cloud development and possibly upon cloud base height. The direction of the causality is not yet firmly established, since anomalies in the S_2 variation (cf. Haurwitz and Sepúlveda 1957) imply a feedback to S_2 amplitude from atmospheric variables, possibly from the clouds themselves. Cloudiness variations could be at least partially controlled by other factors, such as sea-air interaction. The causal linkages must be left open for further investigation, building upon the firm association established here. We do not know of any physical theory to support the alternative suggestion that the mean S_2 pressure wave is primarily a consequence of the semi-diurnal cloudiness cycle. Any such theory must explain how a semi-diurnal cloudiness cycle with an amplitude of 5-15 per cent can produce a S_2 oscillation with an amplitude of 1-2 millibars and at the same time show for example, why stations with a pronounced midday cloudiness peak like Batavia fail to show a corresponding pressure maximum a a few hours later.

We have also briefly presented data suggesting important linkages between larger-scale pressure rises and increased cloudiness. These pressure changes are found to occur almost simultaneously over wide belts of latitude and longitude and their possible effects would have to be considered in a synoptic or statistical investigation of the world-wide distribution and propagation of the S_1 and S_2. These relationships are among a number of factors compelling reassessment of the definition, nature and origin of tropical disturbances and how these might be forecast or controlled.

A possibly important clue is provided by Brier's (1967) study of the cause of the amplitude variation in the S_2 wave. He showed that S_2 amplitude variations are correlated with lunar gravitational tides, in a beat fashion, so that large amplitude S_2 occurs when the lunar tide acts in phase with the S_2 tide and small amplitude S_2 occurs when they are out of phase. Although the mechanism of this interaction between the thermal and gravitational tides is not understood, the important point is that a small trigger can force a large response in marginally balanced atmospheric systems, as demonstrated in a different context by Brier (1965). Evidence has also begun to come in (Brier and Carpenter 1967) which suggests that the tropical atmosphere may be more prone to the development of synoptic-scale disturbances when the S_2 wave has a large amplitude.

It is important to explore these tide-weather relations further and also to inquire whether any significant contributions to the large-scale pressure anomalies shown in Fig. 21, or documented much earlier by Frolow (1942), may be associated with lunar or solar tides or their interaction. Increasing evidence favours the association of very large scale as well as large amplitude response to very small forcing functions. For example, the 26-month shift in upper winds around the whole tropical belt may be related to a beat frequency between solar and lunar tides, in which a mechanistic linkage has been suggested via the latent heat release by large tropical clouds (Brier 1966). An important start at pursuing many of the questions raised here has been made using rainfall records and results from a hierarchy of special field programmes on Barbados in the West Indies (Garstang and Visvanathan 1967).

Undoubtedly there are inherent and perhaps even unpredictable instabilities in the ocean-atmosphere system itself, which contribute some or possibly even most of the tropical pressure and weather variations. Nevertheless, if any predictable outside forcing functions, such as tides, can be shown to cause even a measurable fraction of the variations, then some aspects of tropical weather become more understandable, predictable and even perhaps controllable than they were previously.

Furthermore, if a predictable small-scale, small amplitude trigger can be shown to interact with and set off large-scale instabilities in the atmosphere itself, such as synoptic-scale storms or a 26-month shift on global upper winds, then those globally important phenomena become more tractable to modelling, prediction and conceivably modification through understanding the small triggers and how they operate.

Acknowledgments

We wish to thank our colleagues Thomas H. Carpenter and William L. Kiser for their assistance with the data analysis and computations. Mr. Robert N. Powell drafted the drawings and Mrs. Peggy M. Lewis prepared the manuscript. We are grateful for their contribution.

References

Bjerknes, J. 1948 'Atmospheric tides,' *J. of Marine Res.*, **7** (3), pp. 157-162.

Brier, G. W. 1965 'Diurnal and semi-diurnal atmospheric tides in relation to precipitation variations,' *Mon. Weath. Rev.*, **93**, pp. 93-100.

1966 Evidence for a longer period tidal oscillation in the tropical atmosphere,' *Quart. J. R. Met. Soc.*, **92**, pp. 284-289.

1967 Reply to J. R. Probert-Jones on 'Evidence for a longer period tidal oscillation in the tropical atmosphere,' *Ibid.*, **93**, pp. 127-131.

Brier, G. W. and Carpenter, T. 1967 Comment on 'A study of a non-deepening tropical disturbance,' *J. Appl. Met.*, **6**, pp. 425-426.

Elford, W. G. 1959 'A study of winds between 80 and 100 km in medium latitudes,' *Planet. Space Sci.*, **1**, pp. 94-101.

Frolow, S. 1942 'On synchronous variations of pressure in the tropics,' *Bull. Amer. Met. Soc.*, **23**, pp. 239-254.

Garstang, M.	1964	'The distribution and mechanism of energy exchange between tropical oceans and atmosphere,' Dept. of Met. Florida State Univ., Tallahassee, Florida, U.S.A. Doctoral Dissertation.
Garstang, M. and Visvanathan, T. R.	1967	'Solar and lunar influences on rainfall,' *Final Rep.* Part I to the U.S. Environmental Science Services Admin., Grant No. E-18-67(G).
Gold, E.	1913	Discussion of S. C. Russell's ' Results of monthly and hourly cloud form frequencies at Epsom 1903-1910,' *Quart. J. R. Met. Soc.*, **39**, pp. 271-293.
Greenhow, J. S. and Neufeld, E. L.	1961	'Winds in the upper atmosphere,' *Ibid.*, **77**, pp. 598-626.
Harris, M. F., Finger, F. G. and Teweles, S.	1962	'Diurnal variation of wind, pressure and temperature in the troposphere and stratosphere over Azores,' *J. Atmos. Sci.*, **19**, pp. 136-149.
Haurwitz, B.	1955	'The thermal influence on the daily pressure wave,' *Bull. Amer. Met. Soc.*, **36**, pp. 311-317.
	1956	'The geographical distribution of the solar semi-diurnal pressure oscillation,' *Met. Pap.*, **2** (5), pp. 1-36. New York Univ.
Haurwitz, B. and Sepúlveda, G. M.	1957	'Geographical distribution of the semi-diurnal pressure oscillation at different seasons,' *J. Met. Soc. of Japan*, 75th Anniversary Vol., pp. 149-155.
Holloway, L., Holt, A., Mauchly, J. and Woodbury, M.	1955	'Topics in statistical meteorology,' *Final Rep.* Met. Statistics Project, Inst. Cooperative Res., Univ. Pennsylvania.
Holle, R. L.	1968	'Some aspects of tropical oceanic cloud populations,' *J. Appl. Met.*, **7**, pp. 173-183.
Kashcheyev, B. L. and Lissenko, I. A.	1961	'Investigation of atmospheric circulation at the height of 80-120 km,' (In Russian), 'Ionospheric Researches,' No. 9, *Acced. Sci.*, U.S.S.R.
Kiser, W. L., Carpenter, T. H. and Brier, G. W.	1963	'The atmospheric tides at Wake Island,' *Mon. Weath. Rev.*, **91**, pp. 566-572.
Kraus, E. B.	1963	'The diurnal precipitation change over the sea,' *J. Atmos. Sci.*, **20**, pp. 546-551.
Kuo, H. L.	1961	'Convection in conditionally unstable atmosphere,' *Tellus*, **13**, pp. 441-459.
LaSeur, N. E. and Garstang, M.	1964	'Tropical convective and synoptic scale weather systems and their statistical contribution to tropical meteorology,' *Final Rep.* on the Observational Field Programme to U.S. Army Electronics Res. and Devel. Lab. Grant No. DA-SIG-36-039-62-G23 and U.S. Army Res. Office Grant No. DA-ARD-49-092-63-G23.
Lavoie, R. L.	1963	'Some aspects of the meteorology of the tropical Pacific viewed from an atoll,' Hawaii Inst. of Geophysics, *Rep. No.* 27.
Malkus, J. S.	1954	'Some results of a trade cumulus cloud investigation,' *J. Met.*, **11**, pp. 220-237.
	1955	'On the formation and structure of downdraughts in cumulus clouds,' *Ibid.*, **12**, pp. 350-354.
	1958a	'On the structure of the trade-wind moist layer,' *Pap. Phys. Ocean. Met.*, Woods Hole Ocean. Inst. and Mass. Inst. of Tech., **13** (2), 47 pp.
	1958b	'On the thermal structure of the hurricane core,' *Proc. Tech. Conf.* on *Hurricanes*, Miami Beach D3, 1-2 (1958).
	1964	'Convective processes in the tropics,' *Proc. Symposium Tropical Met.*, W.M.O. and Int. Un. of Geodesy and Geophysics. Rotorua, New Zealand, Nov. 1963, pp. 247-277.
Malkus, J. S., Ronne, C. and Chaffee, M.	1961	'Cloud patterns in hurricane Daisy, 1958,' *Tellus*, **13**, pp. 8-30.
Merrit, E. S. and Bowley, C. J.	1966	'Analyses of diurnal variations in Tiros VII 8-12 μ window radiation over Indonesia and Malaysia,' *Second Quarterly Rep.*, Contract No. NAS-10151, N.A.S.A., Goddard Space Flight Centre, Greenbelt, Maryland, U.S.A.
Palmer, C. E.	1951	'Tropical meteorology,' *Compendium of Meteorology*, Amer. Met. Soc., Boston, Mass., U.S.A., pp. 859-880.
Riehl, H.	1947	'Diurnal variation of cloudiness over the subtropical Atlantic Ocean,' *Bull. Amer. Met. Soc.*, **28**, pp. 37-40.

Riehl, H. 1954 *Tropical meteorology*. McGraw-Hill Book Co., New York, Toronto, London, pp. 392.

Riehl, H., Yeh, T. C., Malkus, J. S. and LaSeur, N. E. 1951 'The northeast trade of the Pacific Ocean,' *Quart. J. R. Met. Soc.*, **77**, pp. 598-626.

Riehl, H. and Malkus, J. S. 1958 'On the heat balance in the equatorial trough zone,' *Geophysica*, **6**, 3-4, pp. 503-538.

Shibata, E. 1964 'The atmospheric tide hypothesis on the diurnal variation of cloudiness in the tropics,' M.A. dissertation, Dept. of Met. Univ. of California (Los Angeles), 82 pp.

Simpson, G. C. 1918 'The twelve-hourly barometer oscillation,' *Quart. J. R. Met. Soc.*, **44**, pp. 1-19.

Simpson, J., Garstang, M. Zipser, E. J. and Dean, G. A. 1967 'A study of a non-deepening tropical disturbance,' *J. Appl. Met.*, **6**, pp. 237-254.

Stolov, H. L. 1955 'Tidal wind fields in the atmosphere,' *J. Met.*, **12**, pp. 117-140.

U.S. DEPARTMENT OF COMMERCE
Environmental Science Services Administration
Research Laboratories

ESSA Technical Memorandum ERLTM-AOML 4

THE EFFECT ON RAINFALL OF CLOUD CONDENSATION NUCLEI FROM VEGETATION FIRES OVER SOUTH FLORIDA DURING SPRING DROUGHTS

Ronald L. Holle

Experimental Meteorology Laboratory

Atlantic Oceanographic and Meteorological Laboratories
Miami, Florida
October 1969

TABLE OF CONTENTS

THE EFFECT ON RAINFALL OF CLOUD CONDENSATION NUCLEI FROM VEGETATION FIRES OVER SOUTH FLORIDA DURING SPRING DROUGHTS

Ronald L. Holle

ABSTRACT

Cloud condensation nuclei (CCN) at cloud base strongly affect the droplet concentration at cloud base, which in turn influences the life history of a cloud. Continental nuclei counts are much higher over large fires, which thereby may keep much of a cloud's water in small droplets that do not grow to raindrop size during a cloud's lifetime. Consideration of the vegetation cover in South Florida led to the choice of four sources of most smoke particles produced during droughts: (1) muck (peat), (2) algae, (3) saw grass, and (4) mixed leaves from common trees and bushes. These were burned at 0.75 percent supersaturation in the laboratory and all were found to produce between 10^9 and 10^{10} nuclei per g burned. A sample calculation assuming reasonable burn rates for these materials resulted in 4600 CCN cm^{-3} when mixed uniformly to cloud base.

The extreme dryness between 1 April and 15 May of 1967 over Florida was found to be related predominantly to synoptic-scale dryness and northerly winds aloft. There was no significant large-scale lag in rainfall caused by lingering CCN from fires, since dynamic causes easily explain the timing of rainfall. Individual cloud rainfall may have been affected by high CCN counts, as suggested by cumulus height populations and cumulus model calculations. Liquid water fallout from small clouds is affected to a greater degree than from tall clouds.

1. INTRODUCTION

Cloud condensation nuclei (CCN) have been considered an important factor in determining several aspects of cloud growth. It is generally recognized (Mason, 1962; Braham, 1968) that the available CCN count at cloud base determines to a significant extent the cloud droplet concentration at cloud base. Twomey and Warner (1967) found a correlation coefficient of over 90 percent between airborne measurements of these two parameters. Cloud droplet concentration subsequently influences cloud growth by changing the diffusive growth rate of cloud-size particles (10 to 20 μ) and by determining partially their later potential for collision and coalescence growth, and thus their ultimate size. Nuclei concentrations are major variables in mathematical models of droplet growth by Howell (1949), Mordy (1959), and Twomey (1959).

As the concentration of CCN, and thereby the cloud base droplet concentration, grows several important changes occur in the cloud. Less water grows to raindrop size (generally $>400\mu$), and more remains as cloud droplets that have low terminal velocities and collection efficiencies (Twomey, 1959). In this context, Kessler (1965) has referred to "cloud conversion", where in a uniform cloud of cloud-sized droplets, such droplets may collide with one another to form raindrops, even when no larger drops are available initially. This is, however, a slow process. If the original nucleus is a large 500μ salt particle, by contrast, the condensed droplet may have a large terminal velocity - while a small droplet may hardly fall at all. Under these circumstances the coalescence time for a raindrop to form, when many CCN are present to share the available water, may greatly exceed the lifetime of the cloud. Twomey (1959) showed most clearly that in a simplified model with 1 g m^{-3} liquid water and starting with a normal distribution of droplet radii, less than one-tenth as much water is collected by coalescence for a "drought" CCN count of 1350 cm^{-3} compared with a "maritime" value of 50 cm^{-3}. His model also predicted that precipitation only could be initiated heterogeneously by salt particles, for example, in a continental cloud with 400 droplets cm^{-3} and 1 g m^{-3} liquid water. For clouds of 800 droplets cm^{-3} or more, inordinately long times and depths are necessary.

The highest published count of CCN is 4300 cm^{-3} near the Marshall Islands (Twomey and Wojciechowski, 1969). Usually, numbers do not exceed about 2800 cm^{-3}. This approximate figure is the highest reported by Squires and Twomey (1966) over the Australian continent, by Meteorology Research, Inc., (MRI) over Puerto Rico in July 1967 (unpublished notes from Experimental Meteorology Branch (EMB) project), and by both MRI and Naval Research Laboratory (NRL) aircraft during May 1968 over Florida (unpublished notes). Average continental CCN counts are often several hundred cm^{-3}, but variable. Squires and Twomey (1966) found counts over Colorado in summer to vary from 13 to 1309 cm^{-3} (at 0.75 percent supersaturation) in the first 6,000 feet above surface. Comparable numbers over the Caribbean during August ranged from 60 to 360 cm^{-3}. These do not include Aitken nuclei, which at times reached over 10^4 cm^{-3}. Such particles, however, are too small to become activated and condense water that will later grow to raindrop size under normal ambient supersaturations.

It is generally agreed that natural mechanisms of CCN formation over land are (as yet) much more important than anthropogenic production around the world (Twomey, 1960; Twomey, 1963; and Twomey and Wojciechowski, 1969). However, on a smaller time and space scale the counts are much more variable. Schaefer (1969) convincingly presents observations of many types of inadvertent weather modification that are brought about through changes in CCN, freezing nuclei, and Aitken nuclei. During a flight over Africa, Schaefer (1958) saw clouds reaching 35,000 feet that did not produce any surface rainfall. These clouds were in the vicinity of large bush and forest fires occurring before the rainy season began. Schaefer hypothesized that the clouds did not rain because so many CCN were being entrained into them that coalescence was ineffective among the numerous small droplets, and thus no raindrop-sized particles developed. No data were presented for this case concerning the type and amount of material burned, its effectiveness as CCN, or the observed CCN concentrations in the area.

Sugar cane fires are prolific sources of CCN, which Warner and Twomey (1967) found to reach a maximum of 2580 cm^{-3} near cloud base during a fire in Australia. Their concentrations measured over the sea were lower than over land when fires were occurring, but still higher (average of 280 cm^{-3}) than normal maritime counts. Hobbs and Radke (1969) measured airborne CCN caused by a simulated forest fire in Washington. They found that CCN increased from 100 cm^{-3} before ignition to well over 1000 cm^{-3} a few hours later. Feininger (1968) suggests that rainfall over the Amazon has been reduced over the last 15 years because the natural tree cover in the region has been extensively cut. This may have allowed an increase in CCN because of wind transport from exposed ground, which thereby affected precipitation. The widespread forest fires over Alaska shown by Parmenter (1969) also may reduce summer rainfall to some degree.

These studies suggest situations where larger CCN counts may have affected rainfall when events on the surface caused large amounts of pollutants to enter the atmosphere. Warner (1968) found apparent rainfall reductions over several decades that resulted from cane fires increasing the CCN counts downstream over parts of Australia. An interesting comparison to these results can be made during a drought period over the Florida peninsula. In this region prolonged shortages of rain in spring sometimes change the surface from mostly water-covered swamp to rather continental, as surface water evaporates and the water table lowers. There also is extensive radar, rain gage, and radiosonde information available. In particular, the period of April and May 1967 was extremely dry over Florida. Since the preceding winter also had been rather dry, surfaces that normally were wet became quite continental with respect to potential for CCN production, and numerous fires occurred until the drought effectively was ended by rainfall in mid-May. The question is asked then whether the fires produced effective CCN that were active at realistic supersaturation values, and whether such nuclei can be detected to have had any effect on rainfall. This could be effected by (1) prolonging the drought over a large region through mixing the CCN produced by all fires up to cloud base, for example, or by (2) reducing the amount of rain that might have fallen from individual clouds that formed near CCN-producing fires during the drought. We will examine first the nuclei in terms of their source, effectiveness, and amount. Then we will study the synoptic conditions to delineate time periods when CCN could have had an effect on the physics of clouds, real or hypothetical, during the drought.

Although droughts over South Florida initially result from reduced rainfall, the extent of fires in recent drought years apparently has been greater than during previous years. In 1968 again, numerous fires occurred during several dry weeks in late April and early May. Whited (1968) suggested that "it isn't really the lack of rain that's drying up and burning up the Everglades. It's man." He continues, "We are lowering our level of ground water outside the Everglades National Park. We are drying the muckland... and the stuff is catching fire more often. As the muckland burns, heavy smoke pollutes our air." This is then a rather unique variation on the many types of possible inadvertent weather modifications by man.

2. CHARACTERISTICS OF FIRE-PRODUCED CCN IN THE ATMOSPHERE OVER SOUTH FLORIDA

It is not true that during a drought, a steady increase in CCN count occurs over land only, until rainfall clears the air. Concentrations depend on time and location of fires, wind trajectories, and ultimately location of the clouds. During the spring of 1967, however, there was a much more continental character to the sky than is often the case over Florida. Visibility was sometimes reduced in the horizontal direction by heavy haze in the lower levels, which usually indicates an inversion and trapping of small particles and water droplets. Such haziness was probably greater than normal in Miami between 1 April and 15 May 1967. Smoke particles spread over populated areas on several days during the drought. Such instances were noted by the author in Coral Gables on 19 April and 10, 27, and 28 May. Figure 1 shows the 10 May late afternoon sky over Coral Gables. At this time a layer of dense smoke was sufficiently heavy to obscure the sun in the absence of clouds about 2 hours before sunset. The smoke is not uniform, shown by the lightening in the upper left corner.

2.1 Sources of Smoke During South Florida Droughts

What are the available sources of smoke in South Florida during a drought? Figure 2 shows the natural vegetation cover in Florida drawn by Davis (1967). Only five major types that occur within 100 n mi are portrayed here. Table 1 explains the characteristics of the major plants growing in the lettered areas. Saw grass covers a very large area. Based on descriptions

Figure 1. Smoky sky in late afternoon of 10 May 1967 in Coral Gables, Florida.

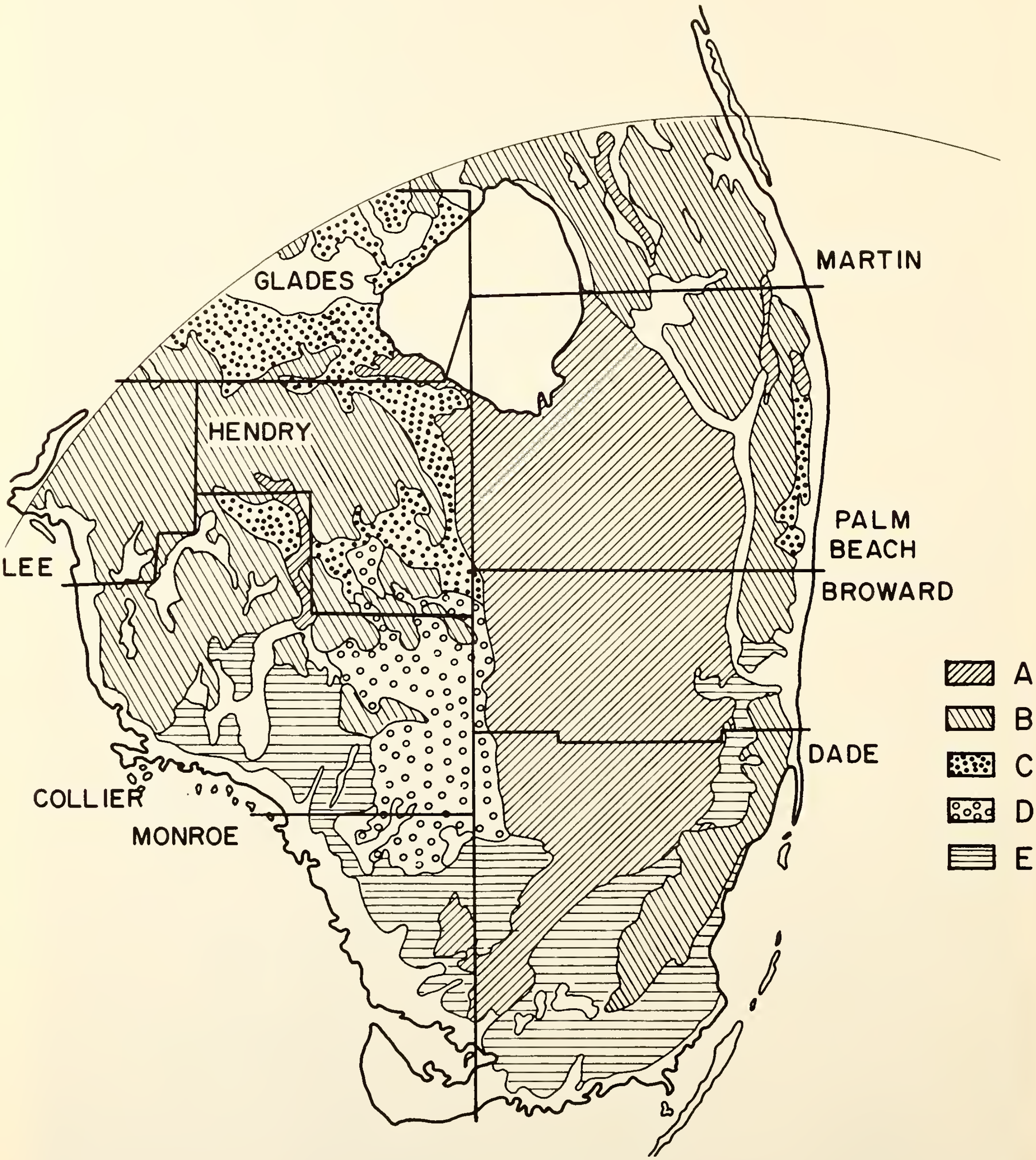

Figure 2. Location of counties and natural vegetation cover types over South Florida within 100 n mi of Miami (after Davis, 1967). Description of types is given in table 1.

in table 1 saw grass of some extent (types A and E) covers about 3,000 square nautical miles. Grassland and pasturelands of other grasses (C and E) cover a total of about 750 n mi^2. Non-hardwood trees, bushes, and palmettoes cover part of the 3000 n mi^2 of types B and D, while pine, cypress, and other tropical hardwoods in hammocks then comprise the rest of the area.

This analysis of vegetative areas does not show completely the proportional amounts of combustibles in droughts. Conversations with members of fire control agencies in South Florida have led to the addition of two important biological sources of smoke: peat(muck) and algae. The Everglades Fire Control (state agency) specializes only in control of muck fires, mostly in Broward and Palm Beach counties. Mr. Charles Rogers (personal communication) of EFC indicated that when the water table lowers, or the surface of the muck dries out, up to 6 in. may burn off, with an average fire burning about 2 or 3 in. deep. The muck is 10 to 50 percent decomposed organic materials and contains its own oxygen (Howard, 1965), such that muck will burn under, in, and floating on water. Further evidence of its unusual character is that the muck evaporates (oxidizes) at a rate of about 1.5 in. per year (besides fires) in the Lake Okeechobee region. According to Howard (1965), rainfall of less than 0.25 in. has little effect on a muck fire, while over 1 in. may stop a shallow fire. Estimation of the land area with muck is difficult. In figure 2 we see that parts of all vegetative types, except B, have muck at the surface. It is always present to some extent in saw grass, pasture, and other grass lands, since these plants grow from nutrients in the muck. These areas alone comprise about 3,450 n mi^2. There is also muck in cypress and marshes with trees and bushes, but these areas do not burn easily or often.

Table 1. Area and Description of the Five Major Vegetation Types within 100 n mi of Miami (After Davis, 1967)

Letter	Area	Vegetation
A	2635 n mi^2	EVERGLADES MARSHES. Some of these areas consist only of saw grass marshes of varying density, while some other regions have herbs and bushes mixed with saw grass. Some tree islands, sloughs and other marshes also.
B	2500 n mi^2	PINE FORESTS. Open woodlands of pine, partly on rock. Many herbs, saw palmettoes, shrubs, other hardwoods and tropical hammocks. Also includes some cypress swamps, prairies, and bay tree swamps.
C	650 n mi^2	GRASSLANDS OF PRAIRIE TYPE. Includes wet prairies on seasonally flooded lowlands, and dry prairies, on seldom flooded flatlands. Much has been converted to pasture land.
D	500 n mi^2	REGION OF OPEN SCRUB CYPRESS. Mostly on rock and marl soils that are often flooded. Some palm and hardwood hammocks.
E	1105 n mi^2	WET TO DRY PRAIRIE-MARSHES ON MARL AND ROCKLAND. Some are mostly thin saw grass; also other bushes and grasses

Algae are also significant smoke sources in saw grass areas. When the surface is covered with water, algae can cover up to 50 percent or more of the water to a depth of about 1 in. When drought comes and the water table lowers, the algae dries, clings to, and then burns with the saw grass. Since the area involved is sometimes quite large in grass fires, algae must also be considered significant smoke sources.

2.2 Effectiveness of Common South Florida Vegetation As CCN Sources During Fires

The effectiveness of smoke particles from vegetation fires as CCN sources will be presented in terms of results of laboratory tests made on samples, which were supplied to MRI. The only previous comparable data were collected by Warner and Twomey (1967) and Hobbs and Radke (1969), who gave CCN counts which were caused by vegetation burning but did not include any specific data on the combustibles. Four samples of vegetation were collected in the Dade County Everglades on 9 May 1969 to represent the combustibles during droughts in the area. Based on actual fire reports for 1967, it was decided that hardwoods did not comprise a significant proportion of the smoke that was produced. Also, the pasture grass and other non-saw-grass plants in flatlands were considered sufficiently similar to saw grass to warrant testing only that kind of grass. Data concerning the four samples are shown in table 2. The "mixed leaves" category represents several rather different, but common, plants found in hammocks among many of the vegetation types listed in table 1. They may not, in fact, be the best three in terms of volume burned. The "peat" entry is representative of only one of three different common types of muck found in South Florida.

The complete test procedure is given in the report by Green (1969), included as the appendix to this paper. Briefly, the test instrument is similar to the aircraft-borne condensation nuclei (CN) counter developed by MRI and used for the 1967 EMB project, as described by Mee and Takeuchi (1968). The four samples were first dried out completely at MRI. Then two burn modes were

Table 2. Source and Composition of Four Samples Collected in Everglades to be Tested for Effectiveness as CCN

Sample	Location	Remarks
Algae	Shark Valley Rd., Everglades National Park	Collected from canal surface among saw grass plants.
Mixed leaves (bushes)	Near intersection of US 41 and 27	Combination of leaves from 3 common bushes: 1. About 40 percent of samples from leaves and branches of coastal plain willow tree (*Salix longipes*). 2. About 40 percent from saw palmetto fronds (*Serenea repens*). 3. About 20 percent of sample from leaves and branches of southern wax myrtle, or bayberry tree (*Myrica cerifera*).
Muck (peat)	Frog City on US 41	Collected from edge of road in swampy saw grass region.
Saw grass	Near canal along US 41	Some live and dead blades, some tips and roots mixed.

tried, one with abundant oxygen supplied and the other was a partially-covered fire with smoldering combustion. These were designed to simulate open and confined burning in the real atmosphere. The samples were burned in a large chamber with a volume of 100 liters, then either 20 or 100 cm^3 of gas and smoke were taken from this volume and put into a smaller chamber with an 11-liter volume. Air from this chamber was injected into the MRI CN counter (volume of .024 cm^3), where between 20 and 100 nuclei were found for each sample.

Results are remarkably uniform for all materials in both modes of burning. The particles were found to be between 0.4 and 1.2μ in diameter, which is within the normal range of CCN. Test results are shown in table 3.

Table 3. Average and Standard Deviation of the Number of Condensation Nuclei Active at 0.75 Percent Supersaturation for Four Types of Combustibles*

	Saw Grass	Mixed Leaves	Peat	Algae
Rapid Burning	(2)† $2.9 \pm 1.1 \times 10^9$ CN/g	(2) $3.5 \pm 0.1 \times 10^9$	(2) $2.9 \pm 0.2 \times 10^9$	(2) $4.8 \pm 0.9 \times 10^9$
Smoldering or Slow Burning	(4) $5.85 \pm 5.1 \times 10^9$	(3) $4.9 \pm 1.6 \times 10^9$	(2) $4.7 \pm 3.7 \times 10^9$	(2) $11.5 \pm 0.7 \times 10^9$
Ash	5%	5%	35%	50%

*(after Green, 1969).

† Number of samples burned shown in parentheses

The immediate impression is that all of these materials are significant producers of activated CCN. The counts range from 2.9×10^9 to 1.15×10^{10} CN per gram of burned material, active at 0.75 percent supersaturation. The materials were not particularly good sources of Aitken nuclei. Algae are twice as productive as the other three combustibles, perhaps because they contain some of the limestone that usually underlies the water containing the algae. Rather small numbers of samples were burned for most materials, hence the large standard deviations. These deviations were not mass-weighted, although some samples were smaller than others. More samples should have been tested, but part of the materials was used to bring the CN count to within the range of the instrument. Ash content was estimated visually and applies to both burn modes.

Several variables must be considered when applying table 3 to the atmosphere. A choice is available between rapid and slow burning rates in that a hot flame will reignite the smoke and remove it from the CCN count. A lower burn temperature produced larger particles; nevertheless, the tests show more CCN for smoldering fires. From personal conversation with forestry and fire-control personnel, it appears that most fires with these 4 materials burn rapidly at a high temperature.

A greater potential variable is the change of CCN with supersaturation. Twomey and Wojciechowski (1969) have shown this variation with several parameters, but when only one value of supersaturation could be used, 0.75 percent was chosen because CCN counts are considered most accurate then. Also they indicated that for an updraft of 3 m sec^{-1} (reasonable for continental Florida cumuli) the supersaturation is about 0.75 percent. Numerous studies have shown that as supersaturation increases by a factor of 10 the CCN count increases by 5 to 10. Hobbs and Radke (1969) showed that different supersaturation spectra of CCN existed before and during their simulated forest fire, with 47 percent more CCN present during than before, at 0.75 percent supersaturation. Data from real clouds are needed to learn the proper value for Florida cumuli in spring droughts, however.

2.3 Estimation of Amounts of Fire-Produced Nuclei Over South Florida During Spring, 1967

The most difficult link in the chain of reasoning, which starts with knowing surface vegetation distributions and ends with how many CCN may have entered a cloud, is how to handle the data on observed fires in a certain period. Information is difficult to obtain, interpret, and summarize. Most of the fire data used here came from the Everglades Fire Control (EFC). Original ranger reports were scanned for location, duration, area, and type of fire whenever such facts were reported. Their data were searched for fires of 3 acres or more in April and May of 1967 for the counties, which cover most of the land area within 100 n mi of Miami. Additional data for Dade County were obtained from the Florida Forest Service (FFS) for all fires larger than 1 acre. Most of these were small fires in wooded land near populated regions. One interesting variable is the diurnal variation of observed fires during these 2 months. The highest fire frequency is at 1600 EST, during highest temperature and lowest relative humidity on a drought day. This coincides with the highest cloud tops in the late afternoon (see fig. 14) over Florida and suggests that maximum CCN counts can affect cumuli when they are at their most active stage of the day.

Some idea of the area involved in fires can be gained from table 4, which shows the FFS data for Dade County and EFC reports for all counties within 100 n mi of Miami. Clearly, there is not a monotonic increase of fire activity with time. Although this gives an average of 55 acres per fire, 70 of the 95 fires were 100 acres or less in size, and only 6 were over 1,000 acres. These 6 contributed 80 percent to the total area burned. Figure 3 shows that four of them were in northern Broward County and two in southern Palm Beach County. It should be noted that all six were located in the area of vegetation type A (figure 2), which is the Everglades marsh with saw grass and tree islands. Figure 3 also shows the location of most of the other large fires during April and May 1967 that are listed in table 4. The larger fires in Broward and Palm Beach Counties are again found mostly in saw grass and

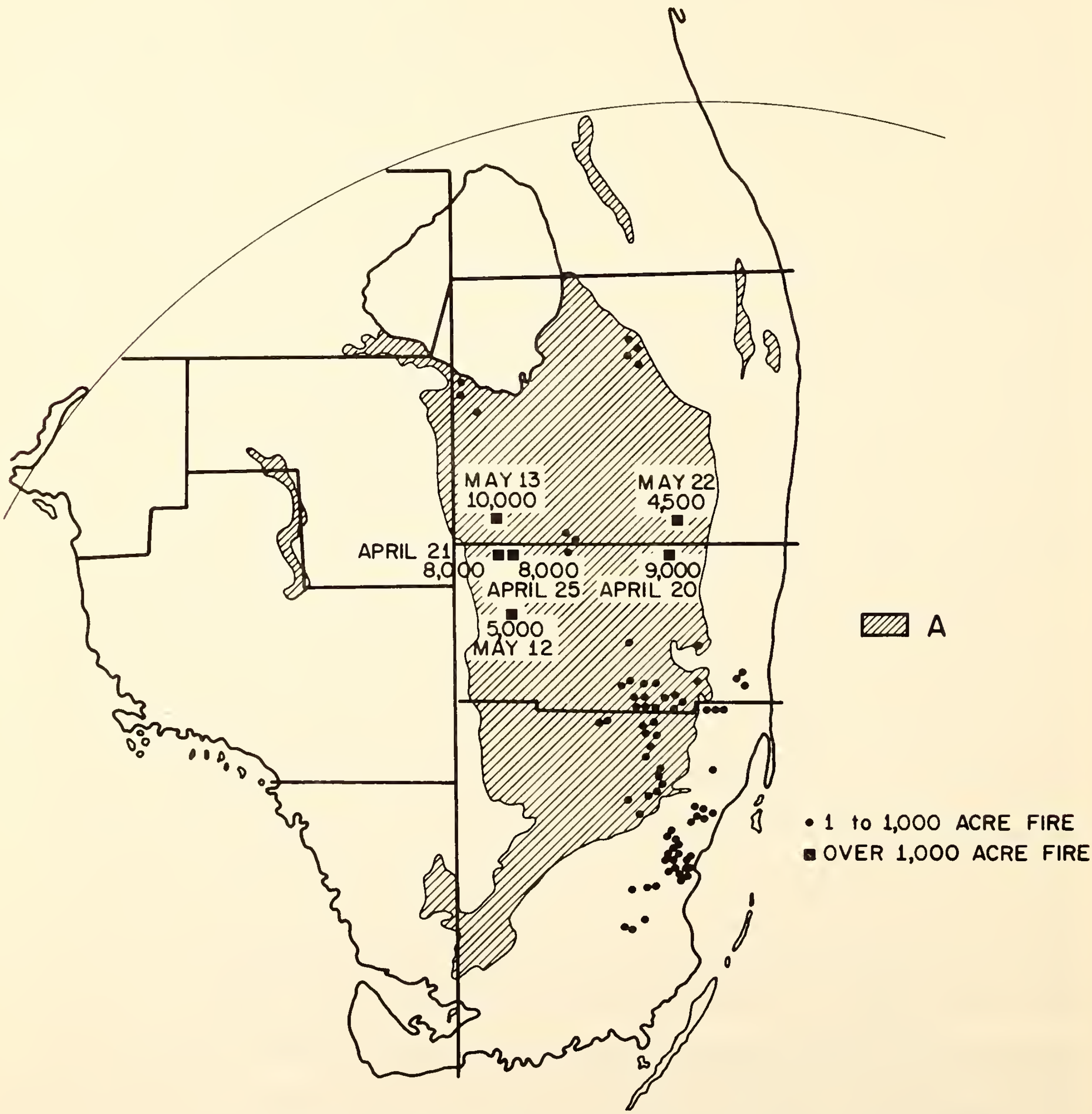

Figure 3. Locations of fires over South Florida during April and May 1967. Dates and acreages of the 6 largest are shown.

Table 4. Number of Fires and Acreage Burned in April and May 1967 within 100 n mi of Miami

	April		May		Total
	1-15	16-30	1-15	16-31	
Acreage Burned	1,973	30,264	16,864	2,801	51,902 Acres
Number of Fires	12	33	33	17	95 Fires

muck areas. During the spring of 1967 EFC personnel estimate (personal communication) that 5 percent of the private land and 10 percent of the public land with muck bottoms burned in these two counties. One of the six large fires on May 13th (10,000 acres) is identified on the ranger report as "mostly saw grass and some muck," but no others are this specific. The exact composition of the combustibles is not critical, however, since the test data show that a fire in mixed undergrowth alone, for example, produces about the same number of CCN as saw grass or muck; or 80 percent of the area burned produces about 80 percent of the CCN in smoke, regardless of vegetation. It should be noted that the estimated area of a large fire is only the area inside a perimeter enclosing all smaller fires that are out of control during the lifetime of the large major fire. The following computation, nevertheless, places into perspective how much a large-scale approach can contribute to CCN production, and how easily an order of magnitude may become lost. The factors are chosen to be reasonable values but are far from being well established.

Consider a 5,000-acre fire. Assume 0.33 g of muck actually burns for each cm^3 of moist peat, which is only a guess, then table 5 shows a sample calculation based on estimates and the test data of how many CCN are produced.

Table 5. Sample Calculation of CCN Produced by a 5,000-Acre Fire Based on Assumed Burn Rates and Test Data for CCN Production

	Assumed Rate of Burn	Total Burn Volume (g)	CCN Produced for Rapid Burning (CN/g)	Total Nuclei (CN)
Muck	1 in. deep*	1.94×10^{10}	2.9×10^{9}	5.63×10^{19}
Saw Grass	1 ton/acre	4.54×10^{9}	2.9×10^{9}	1.32×10^{19}
Algae	1/10 ton/acre	4.54×10^{8}	4.8×10^{9}	1.57×10^{18}
Mixed leaves	1/10 ton/acre	4.54×10^{8}	3.5×10^{9}	2.16×10^{18}
Total:				7.33×10^{19}

*More likely would have 3 in. of muck burning over 1/3 of whole area.

Then assume that the 7.33×10^{19} CN calculated in table 5 to have been produced over the 5,000 acres are spread evenly up to a 700-m cloud base. The total volume of air is 1.60×10^{16} cm^3, which results in 4600 CN per cm^3.

It should be very clear that these assumptions are uncertain. Nevertheless, even if the concentration is 460 cm^{-3}, this is probably greater than the average background CCN count over South Florida. At any rate, knowledge of the test figures removes some doubt from one step of the calculation. There is obviously no substitute for measurement of CCN in the real atmosphere during a drought. Actually, high concentrations may well be limited to small regions near the active fires, as will be discussed in section 4.

3. RAINFALL AND SYNOPTIC SITUATION IN SOUTH FLORIDA DURING SPRING OF 1967

In terms of rainfall the months of April and May are quite variable from year to year over South Florida. Normals over the south half of Florida during April range from 2.5 to 4.4 in. and during May from 4.0 to 6.5 in.

Some idea of the cloud populations and their variability can be gained from radar data summarized in figures 4 and 5. The curves show the cumulative daytime maximum tops within 100 n mi of Miami in daytime (07-18 EST) and are a fairly good measure of the rainfall. For April (fig. 4) there have been 2 years markedly wetter than the average, two years drier, and three years near the average; 1967 was the driest April since at least 1963. In general, the same is true for figure 5 and the month of May, although May was drier in 1965 than in 1967.

Spring of 1967 will now be examined in detail. Figure 6 shows the cumu lative normal and observed rainfalls from 22 March to 31 May 1967 for two portions of Florida within 100 n mi of Miami. An average of six stations with 30-year means was used for the "Lower East Coast" and five such stations for the "Everglades and Southwest Coast" as found in the Monthly Climatological Data of the U. S. Weather Bureau. The normal mean rainfall from 22 March to 31 May is 10.15 in. for the Lower East Coast and 7.75 in. for the other area. (Monthly means were linearly distributed from the start to the end of each month.) Observed rainfall in 1967 fell at only two times of consequence: once in late March and again during the last half of May. Average observed precipitation from 1 April to 16 May was between 0.15 and 0.30 in., which is extremely low. Starting on 16 May, a line drawn to the end of the month is little different from the slope of the normal, thus the drought can be considered to be confined to 45 days from 1 April to 15 May. This drought in Florida was probably greater in extent during 1967 than the previous severe one in 1945.

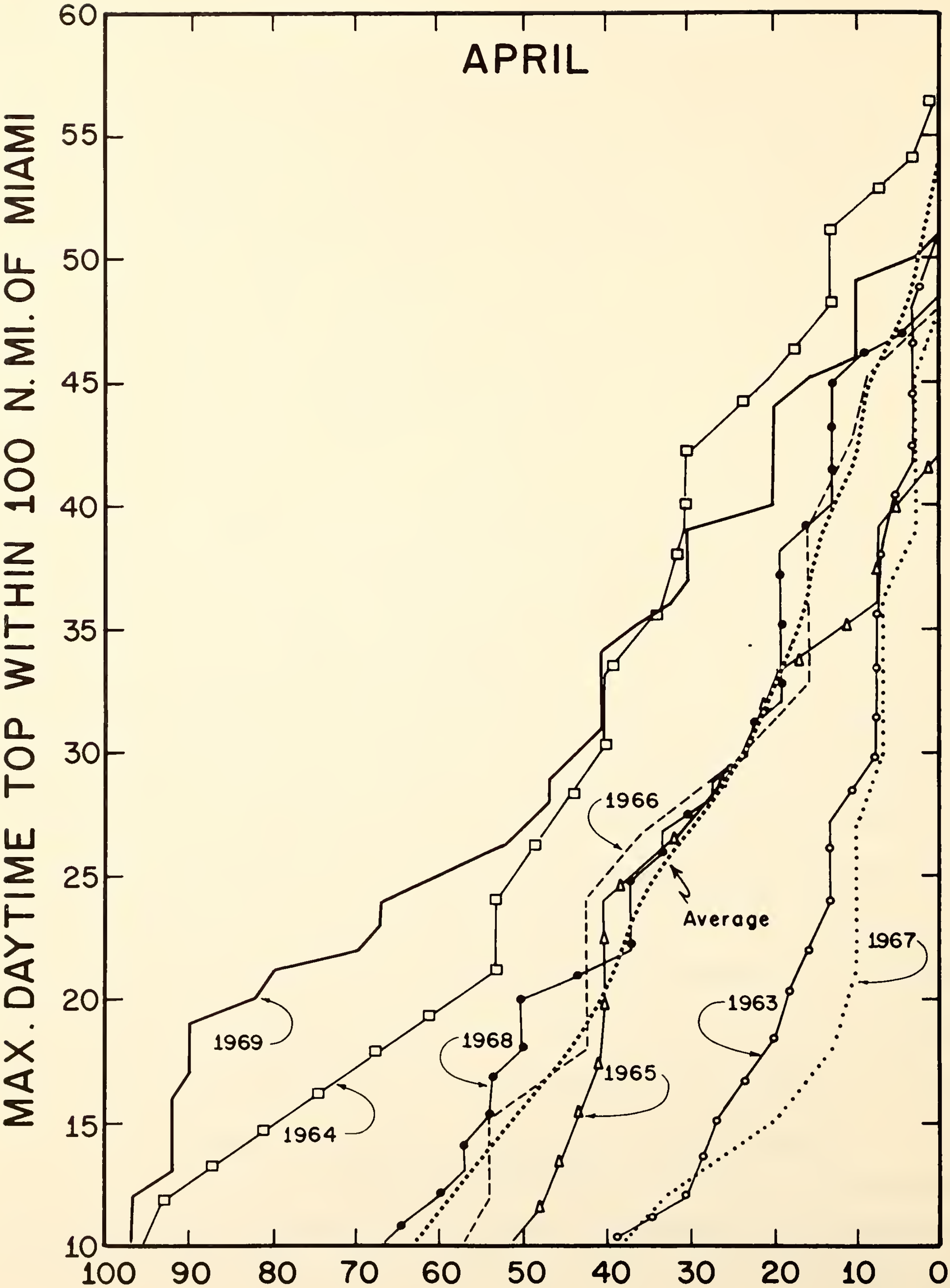

Figure 4. Cumulative daytime (07 to 18 EST) maximum tops in thousands of feet within 100 n mi of Miami during each April from 1963 to 1969, and the average of these years.

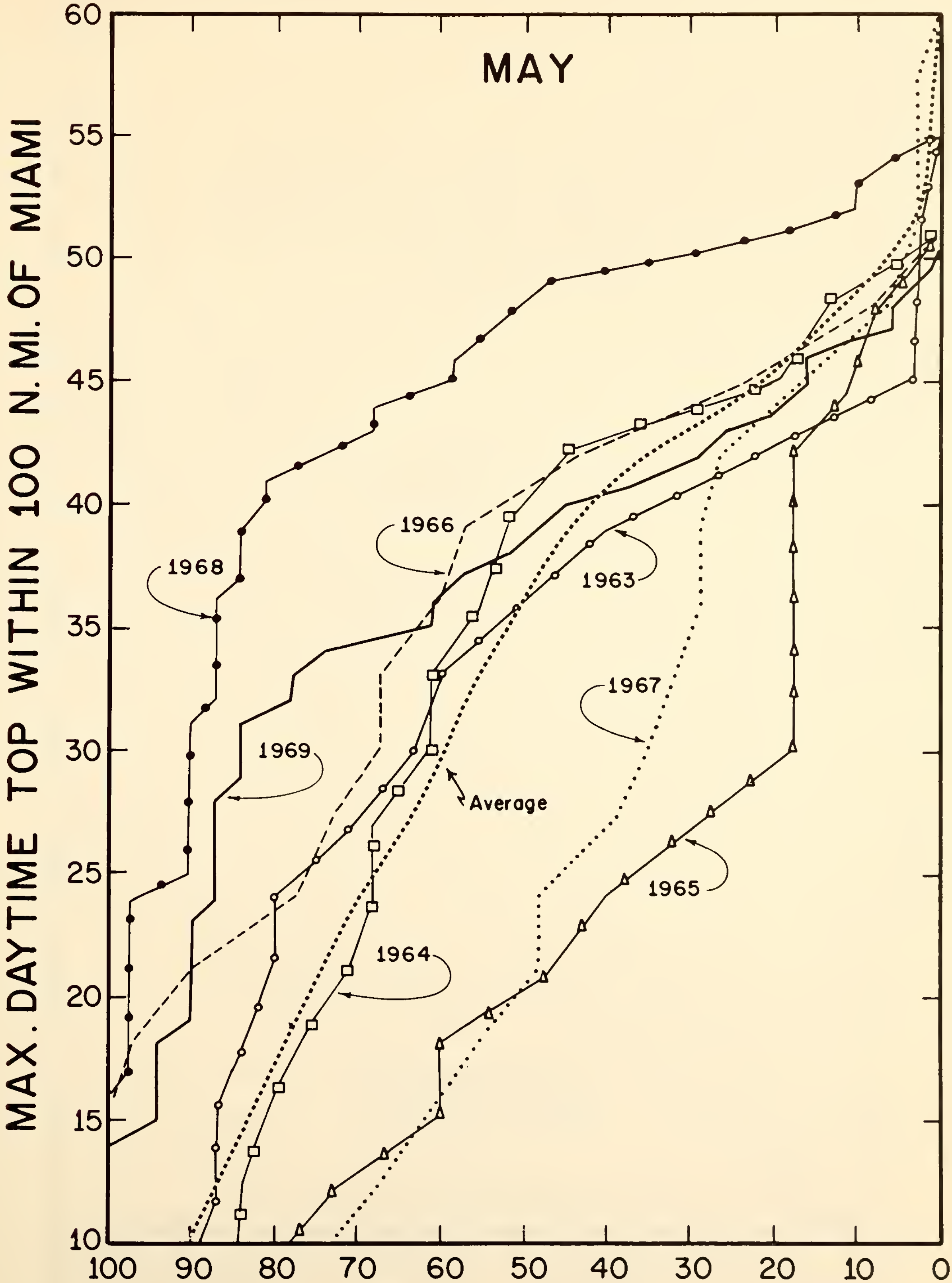

Figure 5. Cumulative daytime (07 to 18 EST) maximum tops in thousands of feet within 100 n mi of Miami during each May from 1963 to 1969, and the average of these years.

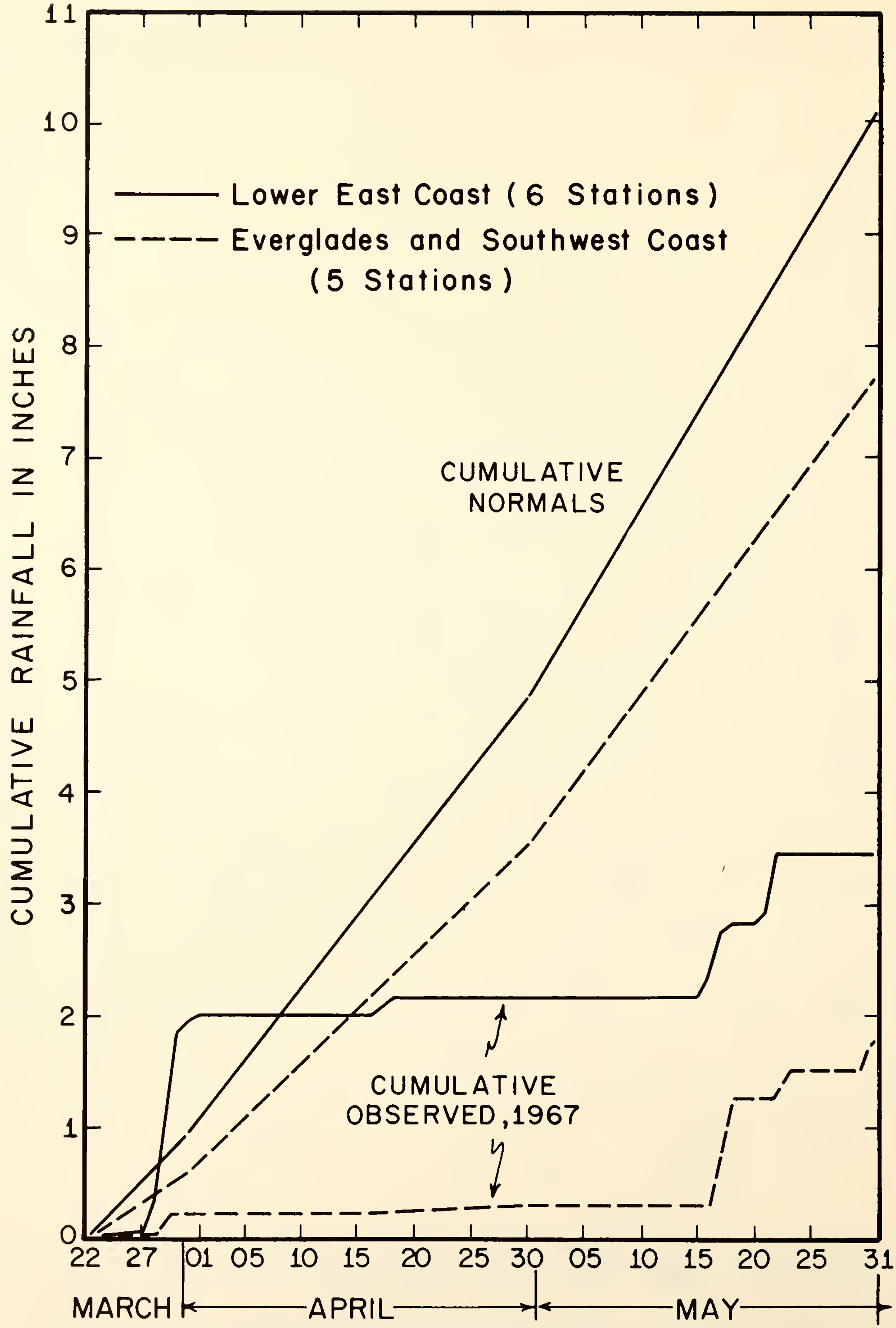

Figure 6. Cumulative normal and observed (1967) rainfall over South Florida during late March, April, and May.

Observed precipitation over the entire state is shown for April (fig.7), 1 to 15 May (fig. 8), and 16 to 31 May (fig. 9). Areas with less than 0.05 in. are lightly shaded, while those with more than 2 in. are heavily shaded. In April, many stations reported no rain or a trace, and few exceeded 0.50 in. except to the north. Some of the rain along the east coast probably fell from shallow cumuli during easterly flow. But the absence of significant rainfall in the western two-thirds of the peninsula, except at one station, indicates that almost no large afternoon cumuli developed all month from land heating. Rainfall north of 29° was caused by a frontal system. Virtually no rain fell from 1 to 15 May south of 28° (fig. 8). North of 28° there were spotty heavier rains, but no organized systems prevailed. Figure 9 shows that the areas with less than 0.05 in. during 16 to 31 May were small, while some locations exceeded 2 in. This pattern is more typical of a summertime map for half of one summer month in Florida, except that amounts are still somewhat low.

How much of this great reduction in rainfall could have been effected by increased CCN counts caused by the fires discussed in the previous section? Is the relation direct, indirect, or obscure? Much insight can be gained by considering the large-scale circulations and then the vertical time-sections for Miami. A strong ridge at 700 mb was centered in the eastern Gulf of Mexico during April, and extended eastward across the peninsula in May to form a long ridge centered at 25°N from the Gulf to the Central Atlantic. Heights at 700 mb over South Florida were 50 to 100 ft above normal in April and 30 ft above in May (Stark, 1967; and Green, 1967). Northwest or west-northwesterly flow is indicated on mean charts for both months. It is interesting to note that

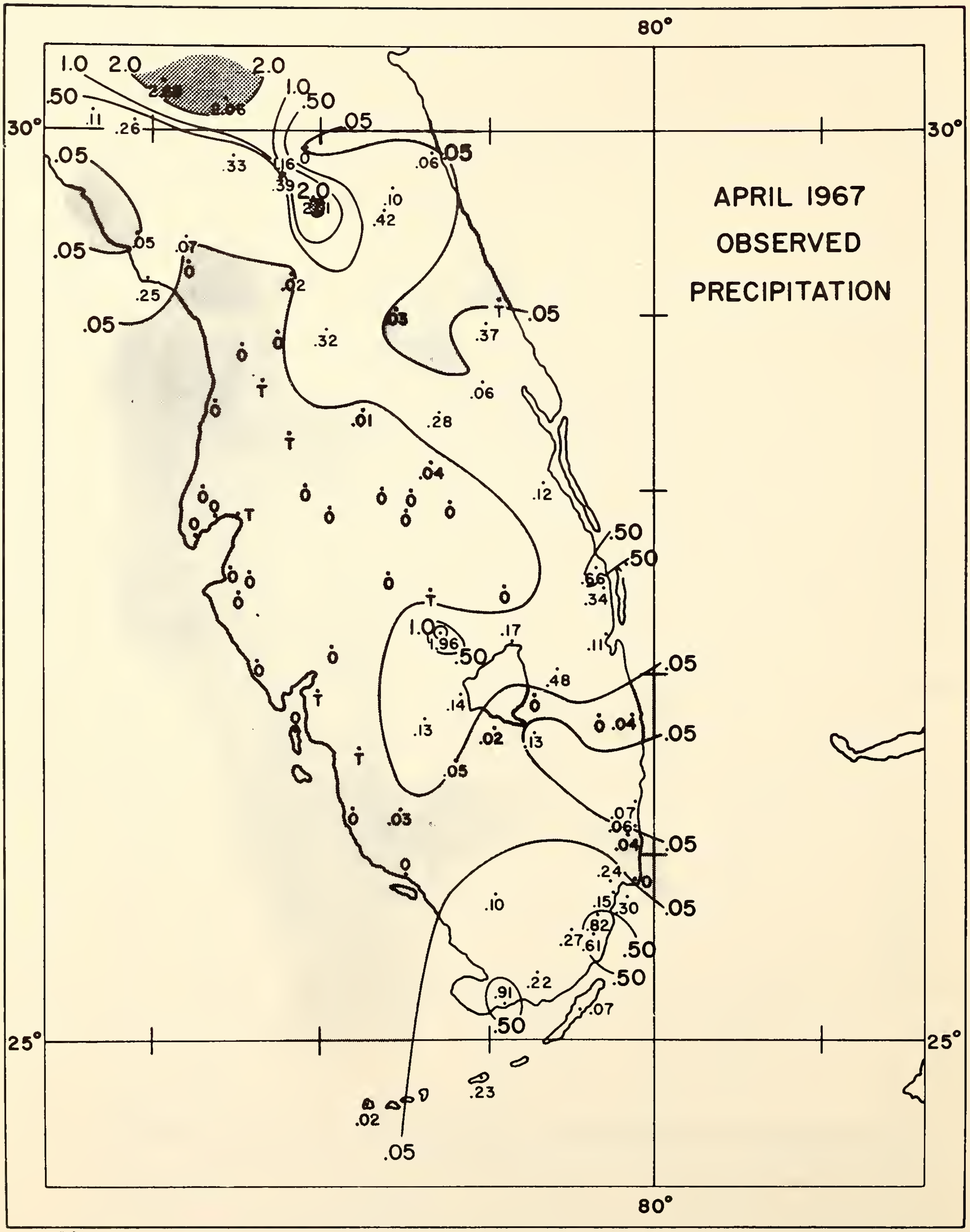

Figure 7. Observed precipitation during April 1967 over peninsular Florida.

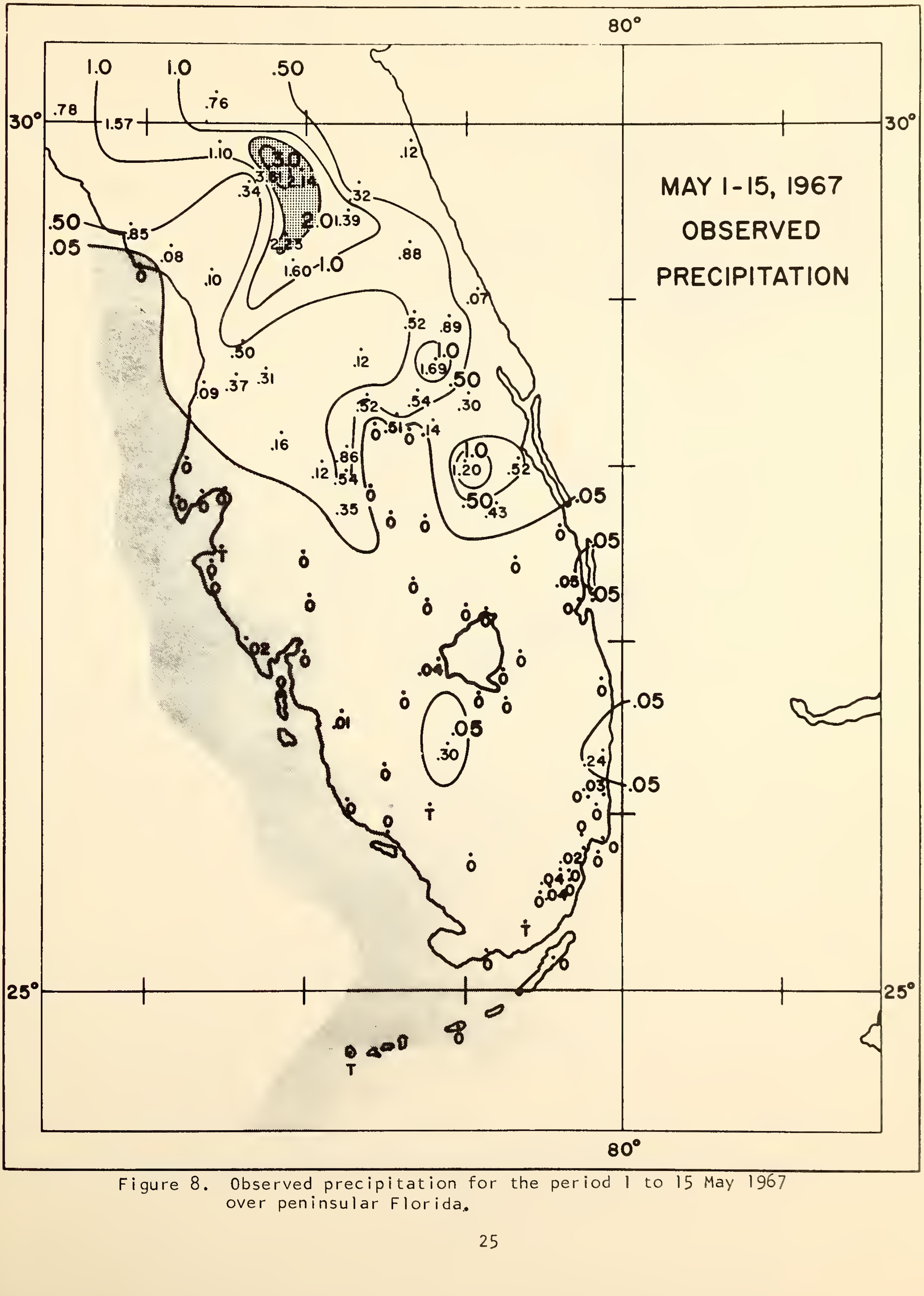

Figure 8. Observed precipitation for the period 1 to 15 May 1967 over peninsular Florida.

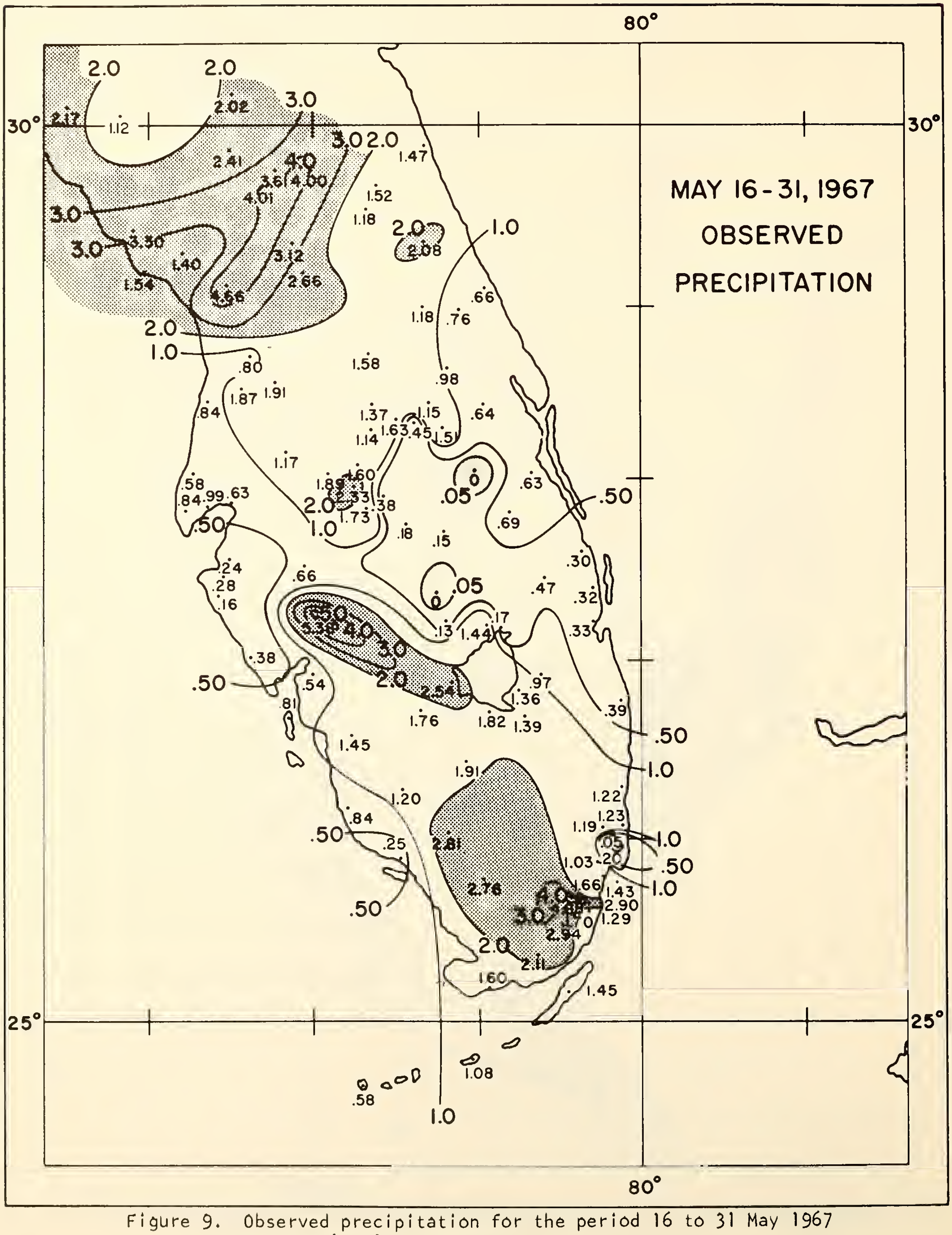

Figure 9. Observed precipitation for the period 16 to 31 May 1967 over peninsular Florida.

coincident with the end of the Florida drought on 16 May, "Great circulation changes occurred from the first half of May to the last half..." over much of North America (Stark, 1967; p. 591).

Time-height cross sections at Miami were constructed for wind direction and dew-point depression from the surface to 40,000 ft between 27 March and 31 May 1967 with data at 10 wind levels and 3 moisture levels. Besides giving some idea of the nature of the wind and moisture structure during the drought, the charts were prepared to show whether there were any effects of the smoke-produced CCN on rainfall. It may be hypothesized that if CCN were effective in inhibiting rainfall, the beginning of more normal rains in Florida would come later than the dynamic changes of wind and temperature. By this hypothesis, then, a wetter and less subsident regime would move in, but little or no rain would fall, possibly for a day or two because of large CCN counts preventing precipitation-sized droplets from growing in large numbers.

Two key representative factors were found to be reasonably well related to rainfall during the period. These two are (1) presence of winds with a northerly component above about 15,000 ft, which probably were subsiding and (2) a dew-point depression of 20°C or greater at 700 mb. Frank and Smith (1968) also found that the humidity at 650 mb is related to Florida radar echoes better than at any other level. These factors are often closely related. From 27 to 31 March the 700-mb dew-point depression was 10 to 20°C, except that it decreased from 15°C on the 28th and 30th to 1°C on the 29th. At the same time as the moisture intrusion, west-southwest winds occurred from 10,000 to 18,000 ft, and rainfall was observed. It is important to note, however, that two days earlier, no moisture accompanied extensive southwest winds and no rain fell (see fig. 6). Northwesterly winds were increasingly common in April and early May; so much so that from 21 April to 10 May, winds were from the northwest during 95 percent of the time above 15,000 ft and often reached near the surface. Strongest winds were at 200 mb and sometimes reached 75 k or more from the west-northwest. The dew-point depression at 700 mb between 21 April and 5 May was seldom less than 18°C. In general, then, rainfall was well related to moisture and accompanied winds with a southerly component fairly closely.

With these general comments of the time cross sections in mind, we examine the section at Miami from 11 to 20 May. Figure 10 shows wind direction and 700-mb dew-point depression during this period of onset of rainfall (see fig. 6). Isogons in upper figure 10 show a basic northwesterly current aloft, with northeast and southeast winds between it and the surface easterlies. The satellite photographs during the dry period for several days up to 15 May are quite similar; for example, figure 11 shows that there was no significant cloudiness near South Florida on 15 May. On this date no radar echoes were reported over peninsular Florida, but southwesterly flow ahead of a trough was moving into northern Florida (Halter, 1967). By comparison, note that southwest winds (with speeds under 20 k) are found through a 15,000 ft depth on 16 May. Lower figure 10 usually shows a dry layer above 700 mb, except that dew-point depressions down to 6°C at 700 mb are found on the 16th and 17th. The time sections show that winds with a southerly component advected a deeper moist layer over Miami on 16 May. The ESSA 3 picture on 16 May, figure 12, shows a large band of cloudiness over South Florida, which was associated with a frontal trough. Numerous well-developed cumuli and some cumulonimbi were observed (Halter, 1967). Since this band of cloudiness and the onset of

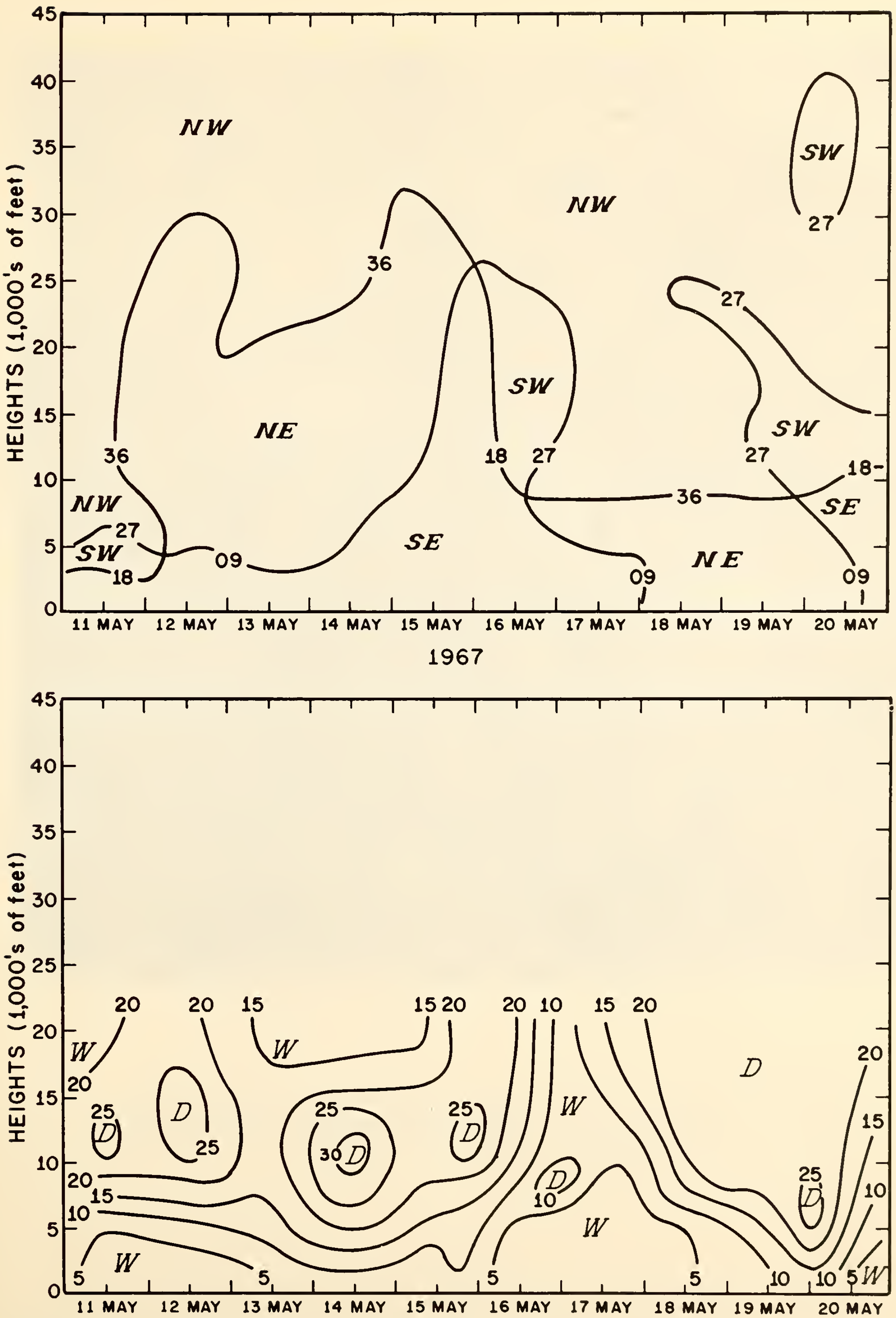

Figure 10. Time cross section at Miami of dew-point depression in degrees C (lower panel) and wind direction (upper panel) from 11 to 20 May 1967.

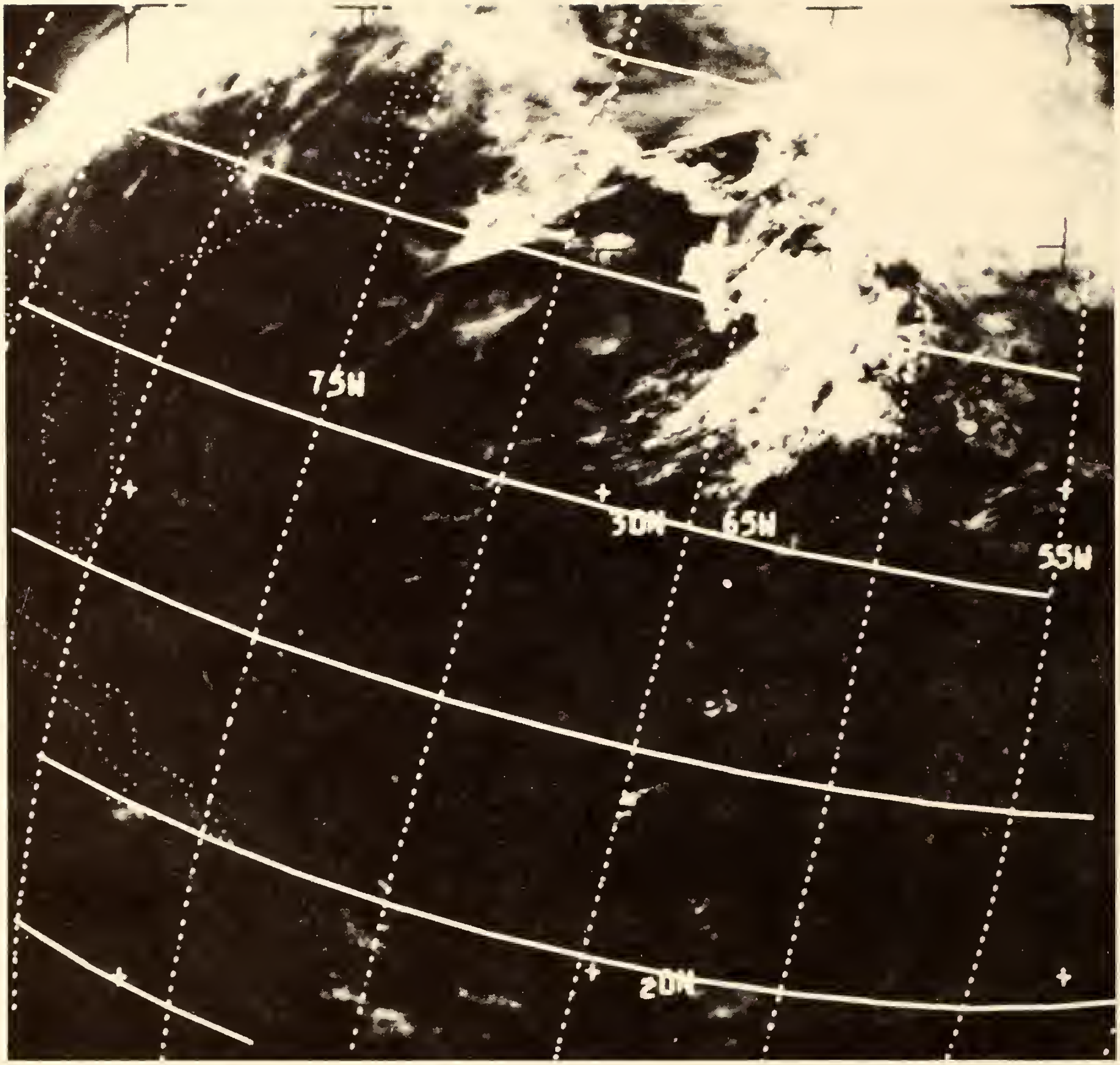

Figure 11. ESSA 3 photograph at 1742 GMT on 15 May 1967.
Florida is in upper left portion of picture.

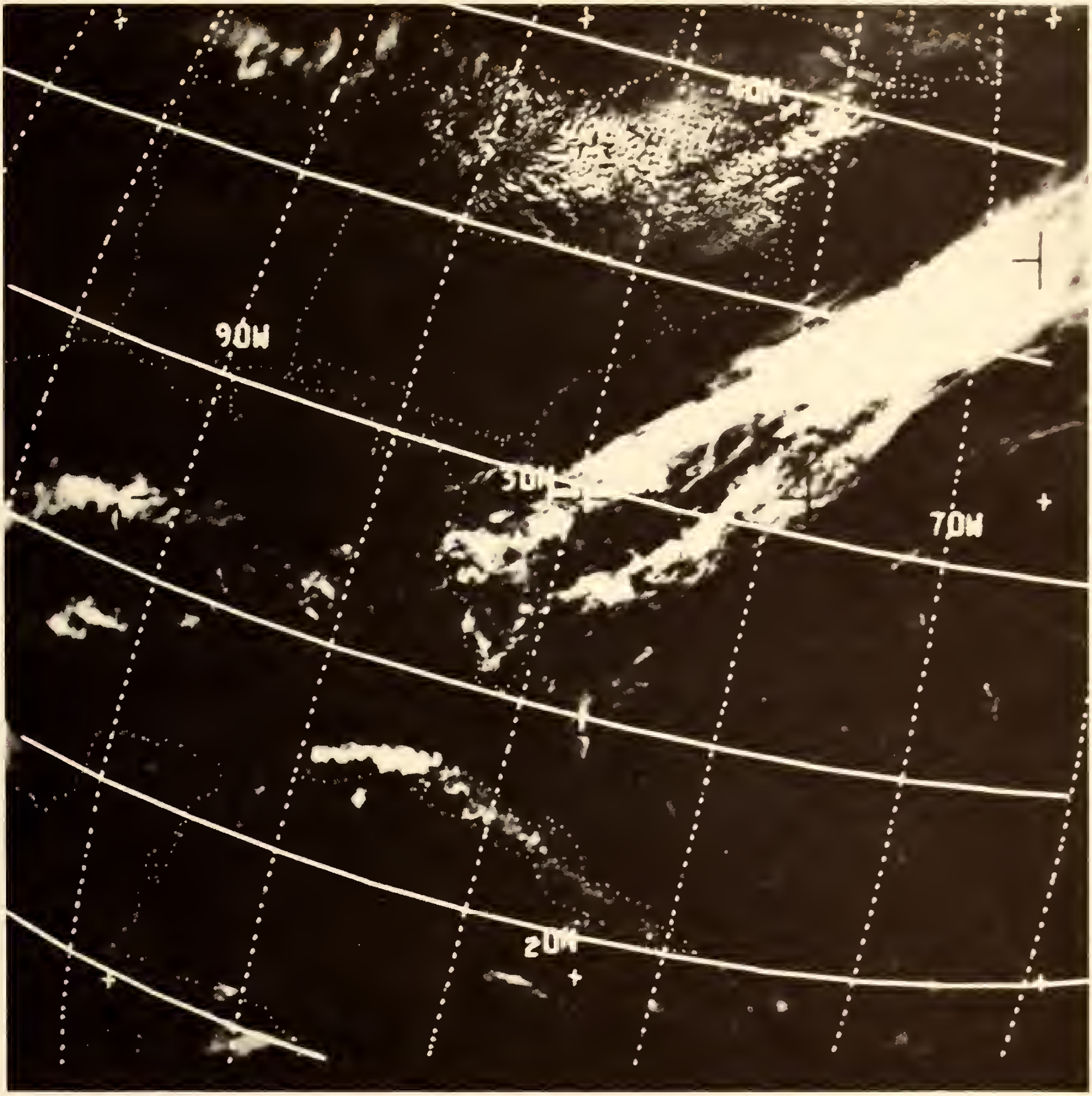

Figure 12. ESSA 3 photograph at 1833 GMT on 16 May 1967. Florida is in center of picture.

moisture and southwest wind coincides with the onset of rain, it is clear that no lag whatsoever existed that may be caused by the hypothesized CCN effect, at least on a large scale approach. The rapid return to dryness at 700 mb on the 18th is accompanied by more northwest winds (fig. 10) as the trough moved offshore, and no rain of consequence fell from 19 to 23 May (fig. 6). (Most of the rain on 18 May came early in the morning.)

No "lag effect" of CCN in large scale terms apparently occurred in mid-May 1967, since the dynamic changes were quite strong. Large CCN counts did not have much opportunity to act on clouds nevertheless, because winds over southeastern Florida up to 5,000 ft were from the open ocean for many days before May 16. Fire records show that from 14 to 15 May a total of only 30 acres burned. The larger fires of 10,000 acres on 13 May in Palm Beach County and 5,000 acres on 12 May in Broward County came several days before changes in dynamics took place,such that the smoke had probably settled and been diffused by the wind, mostly to the northwest. It is interesting to speculate that a CCN effect could only have been important on a large scale if (1) large fires were burning on the day when meteorological conditions changed,and (2) these conditions kept the smoke over land and carried the CCN into the clouds which began to grow. Such a combination on a large scale is rather unlikely to occur on the particular day when a drought is ending, as on 16 May 1967.

4. POSSIBLE EFFECTS OF FIRE-PRODUCED CCN ON INDIVIDUAL CLOUDS

The result of the previous section does not negate the possibility that fire-produced CCN reduced rainfall from individual clouds during spring of 1967. How much rain a cloud produced during a drought versus what it may have made with no smoke in the vicinity only can be determined by theoretical models, direct aircraft measurements, or calibrated radar studies. In fact the very premise that the cloud forms first and then is modified by the greater CCN count is uncertain. Some photos have shown large cumuli that formed over forest fires because of the fire location (see cover pictures of <u>Weatherwise</u>, August 1962; and <u>Science</u>, 17 January 1969).

The concept of influencing an individual cloud over a fire may be understood better by considering the Gaussian plume numerical diffusion model of Milly et al. (1969). This model was developed originally to predict the diffusion of cloud seeding nuclei produced by ground generators. Since we are interested in CCN counts at a cloud base of 700 m, while their results showed distributions at 1500 m, only qualitative comparisons may be drawn. Nevertheless, a fire over South Florida would be a sort of seeding in reverse, and distributions would be quite analogous to their low-stability, high output rate case. For the 10-mph wind used in this diffusion model, considerable variation was found which depended primarily on rate of output from the generators, number of generators and stability in the lowest 4 m. Applied to a single forest fire under Florida meteorological conditions, this model would imply that a strong CCN concentration would be produced at 700 m fairly near to the fire, downstream, and in only one area. The distribution of concentrations cannot be estimated but maximum values over a small area certainly would exceed the subcloud layer figure of 4600 CN cm^{-3}, which resulted from the large-scale approach given in section 2.3. It is quite possible that a CCN count much smaller than the maximum would effectively reduce precipitation fallout. Much could be learned by running such a model as that of Milly et al. (1969)

for one generator, a comparable output rate, and stability as is found in Florida, and for a 700-m height, although some consideration must be made of the different fall velocities of CCN compared to AgI particles.

Some idea of the effect that larger CCN counts have on individual cumuli, regardless of whether they form over a fire or simply entrain some of the ambient CCN in the general vicinity of the fire, may be gained by varying the nuclei count in a cumulus model that includes both dynamics and cloud physics. The model described by Simpson and Wiggert (1969) was run for Miami soundings on 15 and 17 May 1967. Variations were made in N_b, the concentration of drops at cloud base, from 50 to 5000 cm^{-3}. This concentration is closely related to CCN concentrations, as mentioned earlier. The relative dispersion D_b was taken to be 0.1083, a smaller value than that used in the "Berry Florida" version of the model, since for large N_b most nuclei would be from one source and of one size over a fire. For the dry day of 15 May at 1200 GMT only calculations for $N_b = 50\ cm^{-3}$ were made. Even for this marine-type cloud there was no fallout of liquid water (summed over all height steps of the buoyant element) because of the very dry sounding (fig. 10). For a 700-m cloud base, the cloud top for a radius of 500 m was only 1450 m, while for a 1500-m radius, the top was 2500 m. Nothing short of a huge radius apparently would have made a significant cumulus on this day, and no rain was observed to fall over the southern two-thirds of Florida. It is interesting to note, however, that at 1600 EST on 15 May a cloud reached 12,000 ft over water within 100 n mi of the Miami WSR-57 radar. Either the dry layer aloft was missing near this cloud, or a meso-scale convergence had produced a very large radius.

The calculations for Miami on 17 May at 1200 GMT were made for a cloud base of 600 m and D_b = 0.1083. The Berry Florida version always had D_b =0.1460 and N_b = 500 cm^{-3}. Table 6 shows the results for liquid water and table 7 shows top heights. Calculations for a cloud base of 700 m gave somewhat

Table 6. Fallout of Liquid Water for Varying Tower Radii R and Cloud Base Drop Concentrations N_b for Miami on 17 May 1967 at 1200 GMT

		R		
		500 m	1000 m	1500 m
	50 cm^{-3}	2.13 g m^{-3}	4.17	4.26
N_b	500 cm^{-3}	1.21	3.87	3.88
	5000 cm^{-3}	0.44	3.37	3.27
Berry Florida		1.28	3.83	3.86

Table 7. Same as Table 6, Except for Cloud Heights

		R		
		500 m	1000 m	1500 m
	50 cm^{-3}	4400 m	7150 m	8850 m
N_b	500 cm^{-3}	4250 m	7000 m	8700 m
	5000 cm^{-3}	4200 m	6800 m	8500 m
Berry Florida		4250 m	7000 m	8700 m

smaller values than in tables 6 and 7, but did not change the relationships in any case.

On 17 May rainfall was reported to exceed 0.50 in. almost everywhere in Florida. Tops reached 40,000 ft over land within 100 n mi of Miami at 1400 EST, and tops over water exceeded 20,000 ft every hour of the day. Even with this moist sounding,however, some reduction in top heights is seen when CCN are numerous. Particularly interesting is the liquid water fallout being greatly affected for small radii. In this situation a 10^2 increase in N_b reduced the fallout to 20 percent of the fallout for a maritime CCN count. Perhaps this is why clouds of 10,000 to 15,000 ft over land seem to rain less sometimes than clouds of a similar size over water. Because of their smaller volume small clouds may entrain proportionally more CCN into their core region of ascent. Radke and Hobbs (1969) indicated that growing clouds also may absorb CCN from the surrounding area. Then a larger proportion of the liquid water in a 500-m radius cumulus may be condensed onto the numerous CCN and little water can grow to raindrop size. Note also that fallout from the larger 1500-m cloud is reduced by 23 percent.

It may be possible to see some effects of occasionally larger CCN counts during fires over land by comparing 1967 populations to those during a wet year. A quick review of population statistics shown in Holle (1968) can be gained by examining figures 13 and 14. The distributions of daytime maximum tops within 100 n mi of Miami in May of 1966 and 1967 are divided into those tops occurring over land and over water in figure 13. May 1966 was a wet month (see fig. 5) and the land curve shows, for example, that heights exceeded 20,000 ft in daytime on 80 percent of those May days.

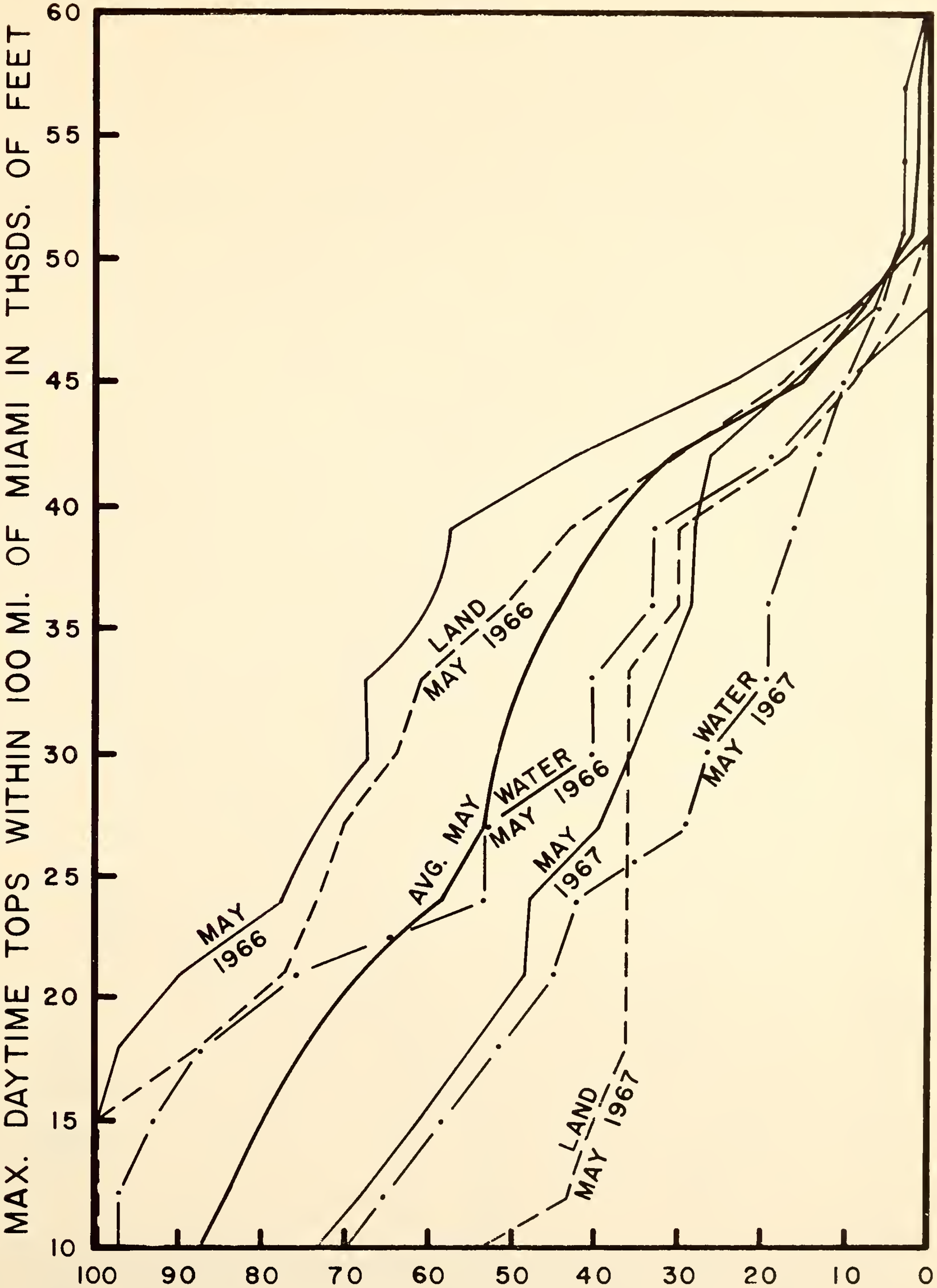

Figure 13. Cumulative percentages of maximum cumulus heights during daytime (07 to 18 EST) over land and water during May 1966 within 100 n mi of Miami (after Holle, 1968).

Clouds over water also were fairly large, but had fewer tops over 20,000 ft than clouds over land areas. In 1967 clouds over water were definitely smaller, but the curve does not differ from 1966 by more than 15 percent above 20,000 ft and 25 percent down to 10,000 ft. Clouds over land in 1967 show a large reduction in frequency for tops below 30,000 ft. In May 1966 a cloud over land reached 15,000 ft on every day, whereas the clouds were this high on only 40 percent of the days in 1967.

Figure 14 shows the diurnal frequency of land and water clouds in 1966 and 1967 in terms of echo presence. Some echoes were seen over water during about 85 percent of all hours in May 1966 and about 50 percent of May 1967 hours, a reduction to 60 percent of 1966 values. Land clouds in 1967, however, reduced to between 30 and 50 percent of 1966 frequencies. From 1200 to 1800 EST, when fires were most frequent , echoes were seen on 40 percent of the days in 1967 over land compared to 90 percent in 1966. In other words, the "drought" was more pronounced over land in 1967 than over water. Similar conclusions were found in Holle (1968) comparing another dry year (1965) to 1966. Since figure 13 shows that smaller clouds formed proportionally less often over land in 1967 (compared to large clouds) than in 1966, it should be recalled that large CCN counts affect smaller clouds more than large clouds (see tables 6 and 7). It does not appear possible, nevertheless, to expect that a large CCN count could stop some clouds completely from growing to precipitation stage, which might have grown otherwise. The 15 May calculation showed no fallout even for an oceanic N_b of 50 cm^{-3}, since the environment was unfavorable for any cloud growth on that day. The 17 May calculation showed that on a moist day more CCN only reduced the liquid water fallout

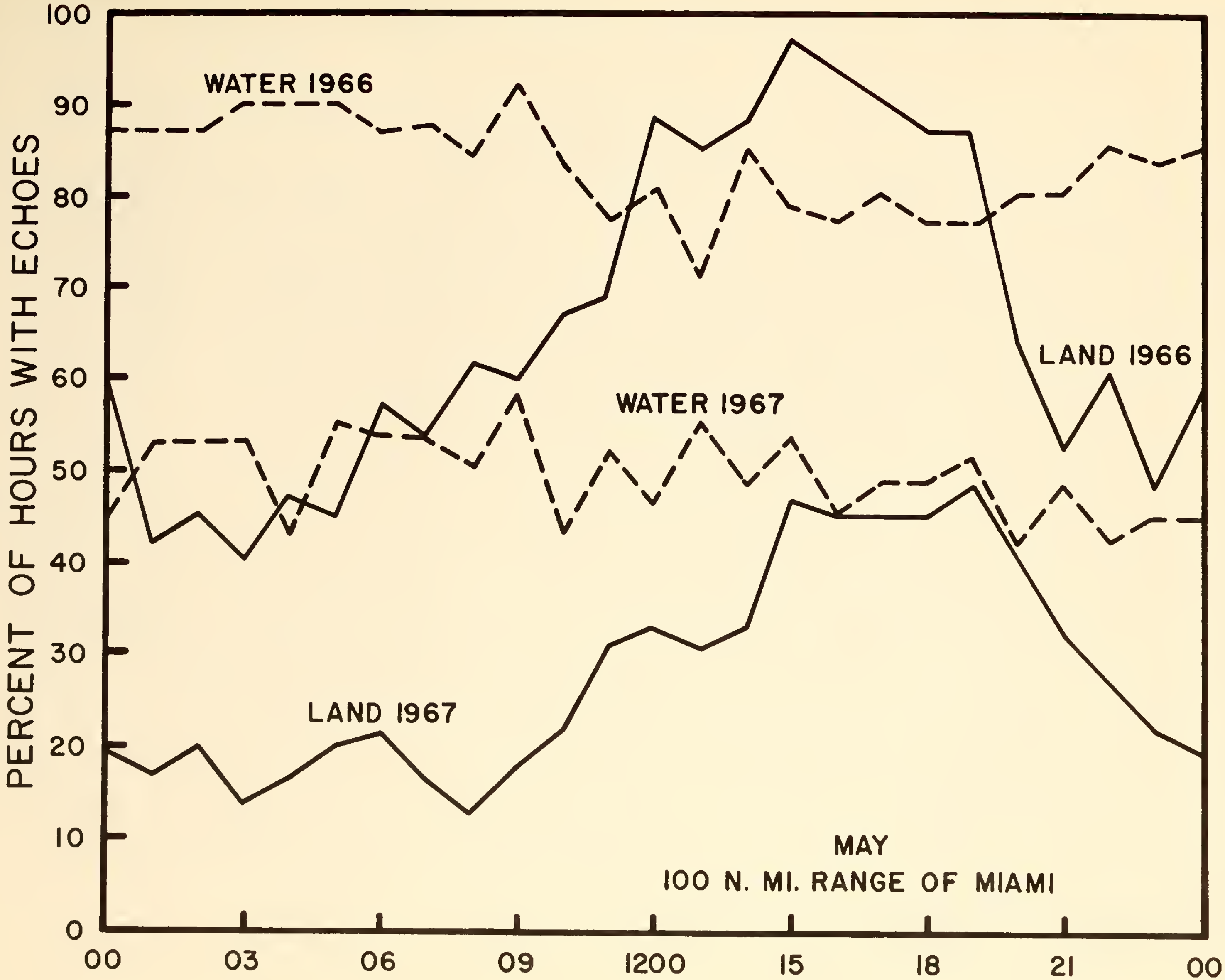

Figure 14. Diurnal variations in echo frequency over land and water during May 1966 and 1967 within 100 n mi of Miami (after Holle, 1968).

significantly for smaller clouds. The large CCN concentration obviously did not keep a cloud from attaining liquid water fallout; no critical threshold for reasonable CCN counts was found.

The most likely effects of CCN on individual clouds in 1967, then, appear to be that fallout from large cumuli was reduced slightly and rainfall from smaller clouds may have been significantly reduced if they were in the immediate vicinity of fires. Larger clouds tended to form in moister periods when there happened to be no large fires over South Florida. Since the exact history of all clouds and trajectories of fire-produced CCN cannot be determined accurately from historical data, it is obvious that field data during a drought would be the only way to test these conclusions.

5. CONCLUSIONS AND SUGGESTIONS

The following conclusions can be drawn from this investigation:

(1) Laboratory tests show that four common vegetative combustion sources from South Florida fires produce between 10^9 and 10^{10} active condensation nuclei per gram of material burned at 0.75 percent supersaturation. These particles are in the normal size range of CCN. There is no great difference in resulting concentrations between the different combustibles; however, slower burn rates produce about twice as many nuclei as fast burning.

(2) Large areas of vegetation may burn and produce CCN over South Florida during a spring drought. In April and May 1967, for example, at least 52,000 acres burned within 100 n mi of Miami.

(3) No lag effect was seen at the end of the long drought in mid-May of 1967. Precipitation was not inhibited noticeably by fire-produced CCN after more favorable dynamic conditions brought more convection over Florida on the large scale.

(4) Calculations with a numerical cumulus model show that large CCN concentrations may significantly affect individual clouds by reducing the liquid water fallout for most sizes of cumuli, especially smaller ones. It cannot be shown that the overall rainfall during the drought of 1 April to 15 May 1967 was noticeably reduced by the production of CCN in fires reducing fallout from many individual cumuli, although it is possible.

Several suggestions have been made about uncertainties in measuring the relations between clouds and fires that can only be accomplished by studying the real atmosphere from instrumented aircraft and calibrated radar. Only then can some estimates be made of the effects of inversions and wind on smoke plumes, mode of burning of the vegetation, whether specific clouds form in preferred locations along trajectories from fires and other factors. Further examination of the following may yield useful results:

(1) Examination of the 1967 and 1968 CCN data collected by MRI and NRL during EMB programs may give some indications of causes of natural variations. Counts ranged from 0 to 2670 cm^{-3} in 1968 over Florida during only a 10-day period.

(2) Study with the diffusion model of Milly et al. (1969) would delineate approximately how large an area around a fire may receive sufficient CCN to affect a nearby growing cloud.

(3) Better understanding of the burning conditions of surface materials would be useful. It is not well established how much tonnage per acre burns, what the proportions of materials are, or many other factors. Additionally, the fire reports themselves are not easily interpreted.

(4) Flying an airborne CCN counter through smoke plumes from sugar cane fires could give some idea of the supersaturations in adjacent Florida cumuli. Such fires normally are set between November and April. In 1968 about 168,000 acres of cane were burned in Palm Beach County alone.

(5) Some rangers mentioned wind sources of aerosols as a major pollutant in South Florida. The three most common sources seem to be oxidized muck, marl (chalk-like crushed limestone), and dried algae. Wind-borne sources could be interesting because of their effects all year long, if not their high CCN counts.

(6) It was suggested by Green of MRI (personal communication) that 15 to 200 lbs of salt particles per acre may be deposited along an oceanic coastline. These large particles also could be activated and carried upward in significant amounts during a fire.

(7) Fire distributions and atmospheric dynamics during the droughts of 1965 and 1968 also should be investigated for similar results to those presented for 1967.

(8) The effect of surface fires on ice nuclei variations is a separate subject and deserves attention.

(9) With this better combination of data, it can be visualized that a statistical analysis of downstream effects from surface fires could be made. Radar, rather than rain gage data, would be preferable. Comparison of known individual smoke trajectories with large numbers of randomly chosen "control" plumes, where no fires occurred, could be made in a similar manner to AgI studies. Warner (1968) did this on a long-time basis but did not explore the question of the plume characteristics on shorter time and space scales.

(10) Artificial introduction of CCN at cloud base from airborne generators may be an interesting test of cloud dynamics in the absence of fires. MRI now has available a simple generator that produces ammonium chloride nuclei that are 0.5 μ in diameter; and droplets formed on them only will reach 5 to 10 μ .

6. ACKNOWLEDGMENTS

This research was supported by the Office of Atmospheric Water Resources, Bureau of Reclamation, U.S. Dept. of the Interior, under Contract 14-06-W-176. Many other individuals contributed to this study. The efforts of Mr. William Green of MRI were indispensable in providing the preliminary results and a final report. The assistance of Mr. William Hardy of EML is greatly appreciated in expediting the arrangements with MRI. Victor Wiggert of EML provided knowledge of the cumulus model in picking appropriate variables for testing. Mr. Robert Ruskin of NRL kindly provided advice concerning supersaturations. Appreciation is due the staff of the Applications Group of the National Environmental Satellite Center for their preparation of a series of ESSA 3

photographs of Florida during May 1967. Several individuals in South Florida patiently explained many of the features of fires and vegetation in the region: among these are Ralph Neely, ranger with Everglades National Park, Homestead; Charles Rogers, chief of the Everglades Fire Control, Belle Glade; and Jim Keene, Dade County Chief of the Florida Forest Service, Princeton.

7. REFERENCES

Braham, R. (1968), Meteorological bases for precipitation development, Bull. Amer. Met. Soc. 49, 343-353.

Davis, J. (1967), General map of natural vegetation of Florida, Ag. Exp. Sta., Univ. of Florida, Gainesville; map, 1 p.

Feininger, T. (1968), Less rain in Latin America, Science 160, No. 3823, 13 - 14.

Frank, N. L., and D. L. Smith (1968), On the correlation of radar echoes over Florida with various meteorological parameters, J. Appl. Meteorol. 7, 712-714.

Green, R. (1967), The weather and circulation of April 1967 - numerous temperature extremes and extensive blocking, Monthly Weather Rev. 95, 491-496.

Green, W. (1969), Condensation nuclei measurements on four types of combustibles from the Florida Everglades, Final report on work performed by MRI for EMB, 15 May 1969, 6 pp.

Halter, B. (1967), Untitled study for EMB of Florida radar and satellite data during May, 1967, 19 pp.

Hobbs, P., and L. Radke (1969), Cloud condensation nuclei from a simulated forest fire, Science 163, No.3864, 279-280.

Holle, R. L. (1968), Frequency and height populations of convective radar echoes over South Florida during May, ESSA Tech. Memo. ERLTM-APCL 4, 27 pp.

Howard, F. (1965), Rural and woods fire tactics, Florida State Fire College, 43 pp.

Howell, W. (1949), The growth of cloud drops in uniformly cooled air. J. Meteorol. 6, 134-149.

Kessler, E. (1965), Microphysical parameters in relation to tropical cloud and precipitation distributions and their modification, Geofisica Intern. 5, No. 3, 79-88.

Mason, B. J. (1962), Clouds, rain and rainmaking (Cambridge Univ. Press, Cambridge), 145 pp.

Mee, T. and D. Takeuchi (1968), Natural glaciation and particle size distribution in marine tropical cumuli, Final report on work performed under Contract No. E22-30-68(N) by MRI for ESSA, 71 pp.

Milly, G., J. T. Ball, and D. B. Spiegler (1969), A numerical experiment on the spatial distribution of cloud seeding nuclei, J. Appl. Meteorol. 8, 83-91.

Mordy, W. (1959), Computations of the growth by condensation of a population of cloud droplets, Tellus 11, 16-44.

Parmenter, F. C. (1969), Picture of the month - Alaskan forest fires, Monthly Weather Rev. 97, 683.

Radke, L. and P.Hobbs(1969),Measurement of cloud condensation nuclei, light scattering coefficient, sodium-containing particles, and Aitken nuclei in the Olympic Mountains of Washington, J. Atmospheric Sci. 26, 281-288.

Schaefer, V. (1958), Cloud explorations over Africa, Trans. N.Y. Acad. Sciences 20, 535.

Schaefer, V. (1969), The inadvertent modification of the atmosphere by air pollution, Bull. Amer. Met. Soc. 50, 199-206.

Simpson, J. and V. Wiggert (1969), Models of precipitating cumulus towers, Monthly Weather Rev. 97, 471-489.

Squires, P. and S. Twomey (1966), A comparison of cloud nucleus measurements over Central North America and the Caribbean Sea, J. Atmospheric Sci. 23, 401-404.

Stark, L. P.(1967), The weather and circulation of May 1967 - strong blocking and record cold in the East, Monthly Weather Rev. 95, 587-592.

Twomey, S. (1959), The influence of droplet concentration on rain formation and stability in clouds, Bull. de L'Obs. du Puy de Dome, 33-41.

Twomey, S. (1960), On the nature and origin of natural cloud nuclei, Bull. de L'Obs. du Puy de Dome, 1-19.

Twomey, S. (1963), Measurements of natural cloud nuclei, J. Rech. Atmospheriques 1, 101-105.

Twomey, S. and J. Warner (1967), Comparison of measurements of cloud droplets and cloud nuclei, J. Atmospheric Sci. 24, 702-703.

Twomey, S. and T. A. Wojciechowski (1969), Observations of the geographical variation of cloud nuclei, J. Atmospheric Sci. 26, 684-688.

Warner, J. (1968), A reduction in rainfall associated with smoke from sugar-cane fires - an inadvertent weather modification? J. Appl. Meteorol. 7, 247-251.

Warner, J. and S. Twomey (1967), The production of cloud nuclei by cane fires and the effect on cloud droplet concentration, J. Atmospheric Sci. 24, 704-706.

Whited, C. (1968), What's really drying Glades, Miami Herald, 1 May 1968.

APPENDIX

CONDENSATION NUCLEI MEASUREMENTS ON FOUR TYPES OF COMBUSTIBLES FROM THE FLORIDA EVERGLADES

by

William D. Green

INTRODUCTION

The objective of the tests described in this report was to determine the number of cloud or meteorological condensation nuclei produced by the burning of four types of combustibles from the Florida Everglades.

PROCEDURES

The four types of materials, listed below, were burned in a closed chamber under conditions simulating open burning with abundant oxygen or confined burning resulting in slow combustion or smoldering. Following the burning, a measured sample of the smoke and gases was withdrawn from the chamber and injected into a second dilution volume containing filtered air. The sample to be counted in the MRI Cloud Condensation Nuclei Counter was drawn from this chamber.

The four types of materials submitted were

Sawgrass

Mixed Leaves

Mud-Peat

Algae

The materials, as received, were dried in an oven at 120°C for 24 hours before processing.

One-half to two grams of the material was weighed out in a glass dish and the dish was then placed in the combustion chamber. A fragment of the sample was ignited outside the chamber to avoid a contribution of nuclei from the match or torch. The fragment was then blown out and the glowing coal was placed on the sample in the dish. The chamber was closed and an oxygen line in the chamber was used to ignite the sample.

In the slow burning or smoldering mode, the resulting fire was rapidly extinguished and the oxygen was used only to maintain the smoldering of the resulting brands.

In the open or rapid burning mode, the oxygen was used to maintain open flames and combustion.

After 50 to 75% of the sample had burned, the combustion was smothered by covering the dish.

The combustion chamber had a volume of 105,000 cubic centimeters. From this volume, either 20 or 100 cc of gas and smoke were withdrawn with a syringe and injected into a volume containing 11,200 cc of filtered air. After corrections for the small background in both chambers, the resulting concentration of condensation nuclei in the last chamber was about equal to the natural background of 10^3 nuclei per cc. Within the counting volume of the condensation nuclei counter (0.024 cc), the count was in the range of 20 to 100 for each of the samples. The above dilution procedure was calibrated several times with both the CN counter and an Aitken Nuclei counter and the contributions from residual nuclei in the chambers were always less than 10 percent. The final results were corrected for this small background.

RESULTS

CN Measurements

The number of condensation nuclei per gram of material burned (loss of weight) is reported in the following table. In all cases, the number was between 10^9 and 10^{10} CN per gram. The number in parentheses is the number of individual samples burned in the particular mode. An estimate of the ash or unburnable fraction is given at the bottom of the table.

With the exception of the algae, which produced about twice as many nuclei per gram burned, all the materials were comparable. The higher count for the algae may be due to a close association with limestone or calcium carbonate which might be activated by the burning process.

Table I

CONDENSATION NUCLEI ACTIVE AT 0.75 PERCENT SUPERSATURATION FROM FOUR TYPES OF COMBUSTIBLES

	CN/Gram (Burned) x 10^9			
	Sawgrass	Mixed Leaves	Peat	Algae
Rapid Burning	(2)	(2)	(2)	(2)
	2.9 ± 1.1	3.5 ± 0.1	2.9 ± 0.2	4.8 ± 0.9
Smoldering or	(4)	(3)	(2)	(2)
Slow Burning	5.8 ± 5.1	4.9 ± 1.6	4.7 ± 3.7	11.5 ± 0.7
Ash	5%	5%	35%	50%

NOTE: The large deviations noted on smoldering of sawgrass and peat are due to errors introduced by the burning of one small sample (0.2 - 0.3 grams) in each case.

Slow burning, as suspected, produced more smoke and nuclei.

Size Distribution

The maximum size of the particles produced can be calculated from the relationship $N \frac{4}{3}\pi v^3 \rho = 1$ assuming all the sample burned is converted to nuclei active at 0.75 percent. Assuming $\rho = 1.5$, 5×10^9 particles per gram would have an average diameter of 6 microns; 11×10^9 particles per gram would average 2 microns. Since it is unlikely that more than 20 percent of the samples were converted into nuclei active at 0.75 percent, the particles would average between 0.4 and 1.2 microns in diameter, or within the range for cloud or meteorological condensation nuclei, $0.4 < d < 2$ microns diameter (Borovikov, Khrgian, et al., 1961, p 9).

Condensation vs. Aitken Nuclei

A comparison between the relative number of condensation and Aitken nuclei ($< 0.4\,\mu m$) was made for a sample of ambient air and diluted smoke from a burned sawgrass sample.

At the lowest saturation in an Aitken nuclei counter (sensitive to particles around $0.2\,\mu m$ diameter) ambient air yielded 5×10^4 per cc while the sawgrass smoke yielded 1.5×10^4 per cc. In the condensation nuclei counter, ambient air yielded about 1×10^3 per cc while the smoke read 2.8×10^3 per cc. These results are summarized in Table II

Table II

COMPARISON BETWEEN AITKEN AND CONDENSATION NUCLEI IN AMBIENT AIR AND SMOKE

	Nuclei/cc	
	Ambient Air	Sawgrass Smoke
Aitken Nuclei	5×10^4	1.5×10^4
Condensation Nuclei	1×10^3	2.8×10^3

The smoke does not appear to be a rich source of Aitken nuclei. These measurements support the assumption that many of the Aitken nuclei in the atmosphere are derived from gas-gas reactions such as the combination of ammonia and oxidized sulfur dioxide to form ammonium sulphate rather than from direct combustion of materials.

Mass of Vegetation Burned per Acre

The following figures for the mass of material burned per acre were obtained from U. S. Forest Service personnel at the Riverside, California Fire Laboratory. They apply to California vegetation but can be extrapolated to certain situations in Florida.

Table III

MASS OF VEGETATION BURNED PER ACRE

(Tons per Acre)

Type of Cover	Fuel Loading per Acre	Percent Burned	Total Burned per Acre
Grass - Wild Oats	1/2 - 2 tons	100%	1/2 - 2 tons
Chapparal (Brush)	10 - 12 tons	40 - 50%	4 - 6 tons
Scrub Oak	40 tons	15 - 20%	6 - 8 tons

CONCLUSIONS

1. Rapid open burning produces approximately half as many condensation nuclei as slow burning or smoldering.
2. The number of nuclei from sawgrass, mixed leaves, and peat were comparable in both modes of burning.
3. Algae produced approximately twice as many nuclei as the other materials burned.

4. Condensation nuclei counts ranged from 2.8 x 10^9 to 1.1 x 10^{10} per gram of material burned.

5. Calculation of average particle sizes, assuming 10-20% of the burned samples were converted into nuclei active at 0.75% supersaturation placed the nuclei in the cloud nuclei range.

6. Comparisons between Aitken and condensation nuclei in ambient air and sawgrass smoke indicate that the smoke is not a major source of Aitken nuclei.

REFERENCES

Brierly, W. B., 1965: Atmospheric sea-salts - design criteria areas. J. Environ. Sci., 8, 5, 15-23.

Borovikov, A. M., et al., 1961: Cloud Physics, Israel Program for Scientific Translations, U. S. Dept. of Commerce-NSF, 392 p.

Reprinted from Bulletin of American Meteorological Society
Vol. 50, No. 3, 157-161.

[Reprinted from BULLETIN OF THE AMERICAN METEOROLOGICAL SOCIETY, Vol. 50, No. 3, March, 1969, pp. 157–161]
Printed in U. S. A.

correspondence

Observations and comments on two simultaneous cloud holes over Miami

H. M. Johnson and Ronald L. Holle, *Environmental Science Services Administration, Coral Gables, Fla.*

A pair of large, almost perfectly circular cloud holes were observed and photographed during their formation, growth and dissipation directly over Miami, Fla., on 1 December 1967. These were strikingly similar to the "Hole-in-Cloud" cases reported in recent issues of WEATHERWISE (Vol. 21, Nos. 4, 5, 6) and in the BULLETIN OF THE AMS (Vol. 49, No. 10). The two holes formed in a rather high and thin layer of altocumulus (altocumulus stratiformis translucidus perlucidus), a water droplet cloud. The Miami radiosonde data for 1200 GMT (0700 EST) indicate a temperature inversion and a moisture maximum at about 450 mb, or 21,000 ft, our estimated height of the cloud layer. At this level the temperature was about −16C, and the wind was from the west-northwest with a speed of 25–30 kt. The layer was an apparently isolated, notably homogeneous, rather large patch or band of altocumulus, with an approximately WSW-ENE long axis. It formed a "broken" sky condition at 0830 EST (when its central part was overhead), and was moving southeastward fairly rapidly (at an estimated 25 kt). The ESSA VI satellite picture for about 1545 GMT showed the presence of a rather indistinct formation of thin middle clouds mainly east of Miami which were connected with the western limit of a narrow, oceanic, cold frontal cloud band.

Evidence of the anomalous condition that later resulted in the large circular holes was well observed at 0830 EST. At that time small cirrus tufts (heads) with characteristic tapering tails below, and the beginnings of the holes, surrounding the central cirrus heads, were noted fairly far to the west. At about this time one of us independently noted a distinct downward protrusion of what appeared to be middle cloud below the base of the otherwise uniform altocumulus layer. By 0900 EST the holes were conspicuous almost perfect circles. The sketch of the southern hole (designated hole B), Fig. 1, depicts conditions observed at about 0845 EST. A well-developed cirrus tail extended down from this hole, and trailed off approximately west-northwestward, thus indicating a downward decrease in wind speed. Nothing but cirrus was visible in this hole and cirrus filaments extended radially to the edge of the hole. The top of the cirrus formation (head) appeared clearly to rise a little above the level of the altocumulus layer. By the time the northern hole (hole A) was nearly overhead little remained of its cirrus tail. It contained mainly remnants of the cirrus filaments and what was left of the central tuft. From 0910 to 0930 EST the visible cirrus disappeared almost completely, and the holes continued to grow in size slowly, finally to meet, and then to overlap. By 0945 EST the overlapping was about 20% of

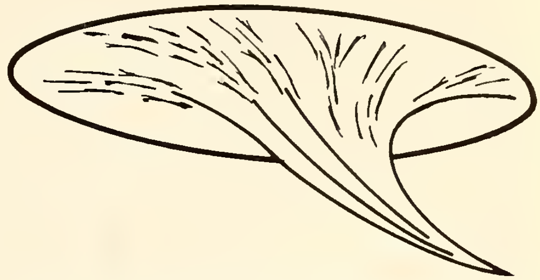

FIG. 1. A sketch of early stage of the southern cloud hole (hole B) at 0845 EST.

the area within each circle, and a substantial amount of altocumulus had reformed within each circle. When last observed, at 1000 EST, fairly far to the east, each hole was about half filled with thin cellular altocumulus, and a third hole with a good cirrus tail was noted to the west. Observation was terminated, and the three holes not observed again, because of the press of other duties.

Fig. 2 is a mosaic of photographs taken at cloud hole A when it was nearly over the University of Miami campus in Coral Gables at about 0905 EST. At this time the circle had not yet reached its maximum clearing, and cirrus remained quite widespread. Some altocumulus can be seen in the lower part of the circle (downstream side). Since this view looks nearly overhead, and the tail is much reduced, it is not possible to see the extent to which the cirrus extends below the layer cloud, a condition well observed earlier. Fig. 3 shows cloud hole B at almost the same time as that of hole A in Fig. 2. Note that hole B has already passed its time of maximum clearing and, although the cirrus has mostly disappeared, altocumulus is reforming in the hole. The next mosaic, Fig. 4, shows circle A again after additional clearing of altocumulus, probably between 0905 and 0910 EST. Only a few small lines of altocumulus cloud are evident inside the perimeter. Note that the eastern edge is quite sharp, and that much cirrus is still present in the center. The diameter is estimated to be about 4 miles at this stage.

By 0915 EST more altocumulus was apparent in this hole. Fig. 5 shows hole A at 0918 EST, looking downstream from Coral Gables. Hole B was consistently in the direct sunlight at this time and could not be photographed easily. The remnant of the central "cirrus" formation of hole A appears to consist at least partly of water droplets. Additional water droplet cloud (altocumulus) is reforming near the edge. Fig. 6 shows hole A about 10 minutes later. The thicker clouds in the upper right extend to near the center, where a water droplet cloud layer is reforming and cirrus is decreasing. Fig. 7 shows hole A on the left and a portion of hole B on the right (still partly in the sun) a few minutes

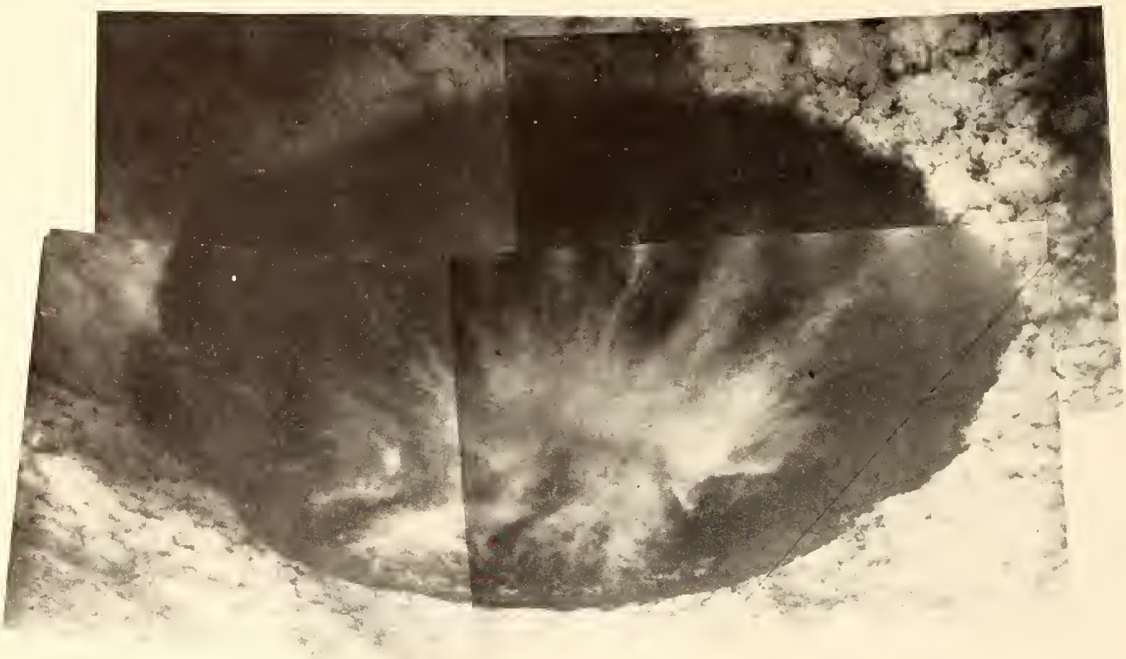

FIG. 2. A mosaic of photographs showing cloud hole A at about 0905 EST when it was almost directly over Coral Gables.

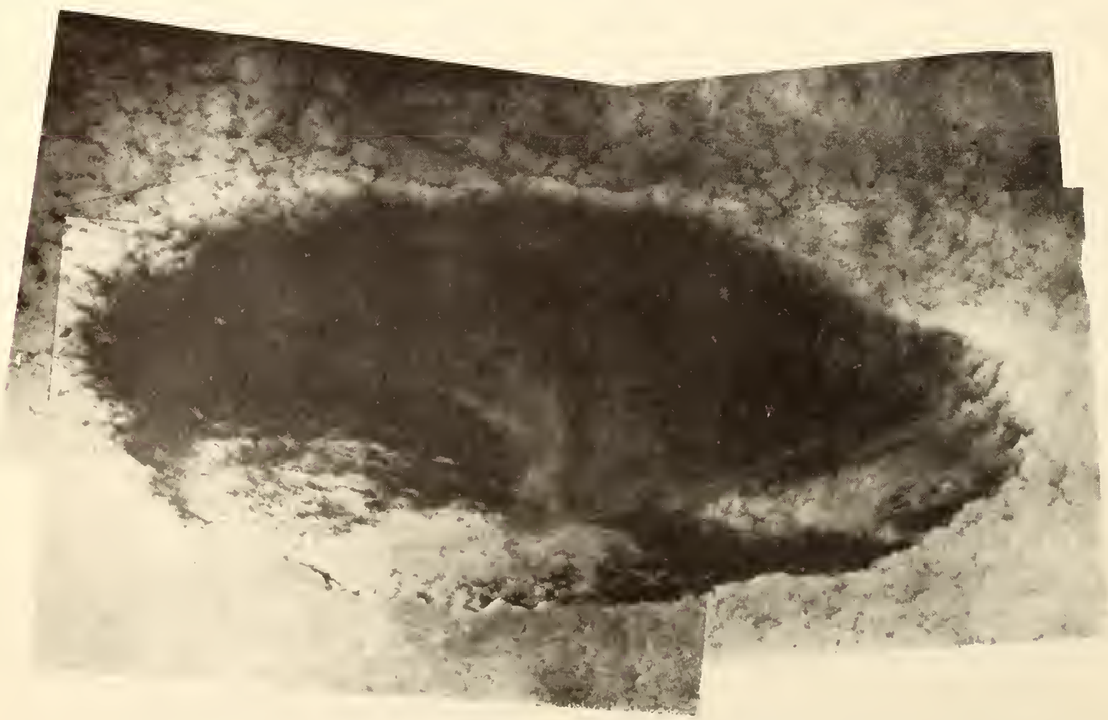

FIG. 3. Mosaic of photographs showing cloud hole B at about 0905 EST.

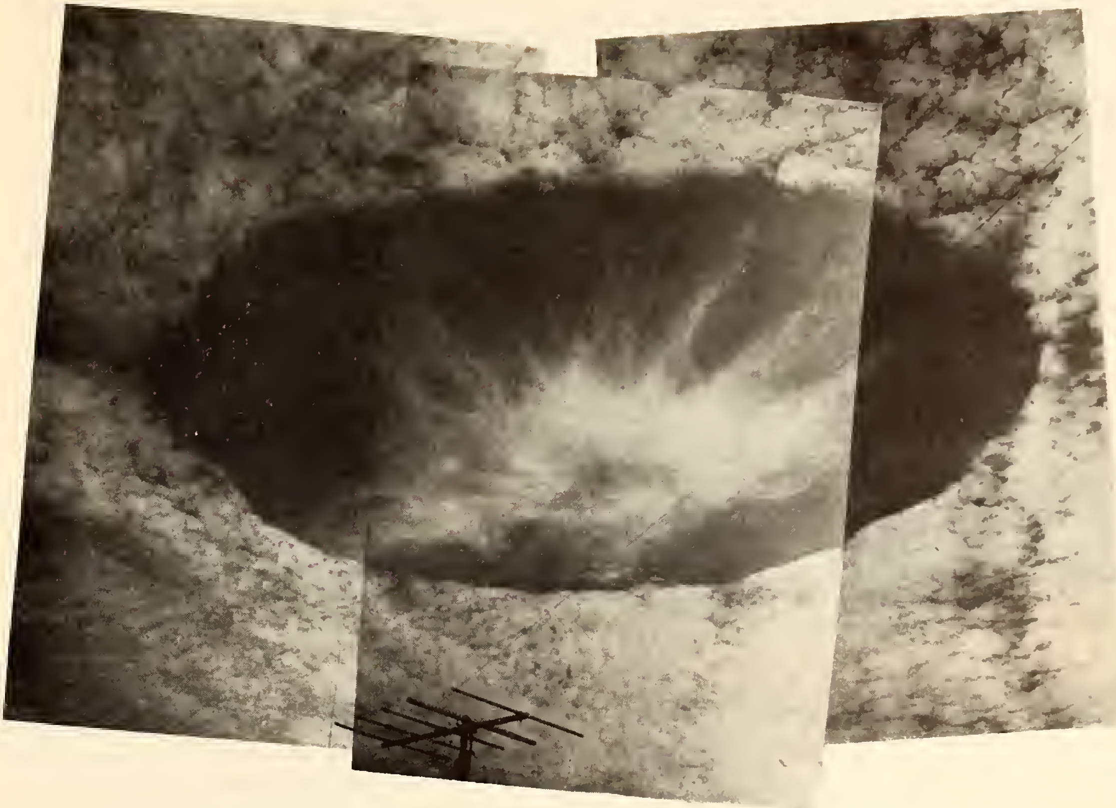

FIG. 4. Mosaic of photographs showing cloud hole A between 0905 and 0910 EST.

later, or about 0930 EST. Both circles were visible downstream until at least 1000 EST, or 90 minutes after they were first observed. By 1000 EST the diameters had increased to at least 5 miles. Because of increasing distance, and decreasing viewing angle, detail became increasingly difficult to see, but the major features remained clearly visible when observation was terminated.

The primary cause of the sequence of developments just presented seems fairly clear, except that a strong case cannot be made for or against natural or artificial initiation of the holes. The altocumulus layer in which the holes grew had a markedly cellular structure and was clearly composed of water droplets. By chance, the required nucleation conditions, possibly a natural (or artificial) concentration of appropriate nuclei, initiated the nearly simultaneous freezing of two small portions of the altocumulus layer at points about 4 miles apart. Such initiation events must be exceptional, that is, very infrequent, otherwise more holes would have been observed and holes of this type would not be so rare.

After initiation the supercooled water droplet cloud converted into a central ice crystal cirrus formation, and cirrus developed progressively outward from this initiation point. Before long ice crystals began to fall from the central mass giving rise to the cirrus below altocumulus which was observed near 0830 EST. After the first ice particles were produced they provided the heretofore missing freezing nuclei which led to the lateral growth of cirrus filaments,

FIG. 5. Cloud hole A at 0918 EST, now downstream from Coral Gables.

perhaps by contact freezing of supercooled water droplets, or perhaps by a somewhat more complex process involving the sublimation of water vapor onto the ice crystals from the water droplets. Whatever the details of the process the cirrus clearly propagated slowly outward. While the cirrus was propagating laterally, other ice crystals were falling down-

FIG. 6. Cloud hole A at about 0925 EST; picture taken from downtown Miami.

ward from the central cirrus formation, thus removing water from this zone. These falling crystals soon evaporated below, the innermost falling farther before evaporation, thus producing the characteristic tapering cirrus tail illustrated in Fig. 1. The observations suggest that the central tuft may not have completed conversion to ice, so that the central cloud may have, in fact, remained partly a water droplet cloud. Figs. 2 and 4 of hole A show fairly well the approximately radial appearance of the lateral cirrus at two stages of this hole. It is noteworthy that most of the photographs illustrating the holes reported in WEATHERWISE and the BULLETIN also show this radial cirrus structure, and show as well that cirrus extends below the altocumulus.

At least three processes appear to be of major importance in determining the lateral growth of the holes and their ultimate size. The first, already mentioned and most easily observed, is the radial propagation of cirrus filaments as water droplet altocumulus is converted into ice crystal cirrus. This process appears to go rapidly at first, then more slowly, finally becoming generally ineffective so that it produces little or no additional cirrus. During this last stage the cirrus already formed decreases or disappears, presumably by descent and evaporation of the ice crystals. Thus the visible cirrus filaments may be considered to be the net result of two opposing processes, one generating and the other decreasing the cirrus. The second, or cirrus reducing, process would appear to be dominant during the last stage (of ineffective net production).

The third process became clearly evident during this 1 December case when the circular boundaries of the two holes met and then overlapped. At this time the fact that the hole diameters were increasing was made evident not by the advancing outward limit of the lateral cirrus filaments and the associated altocumulus edge, as previously, but instead by the process of overlapping, and the advance of an apparent "edge," a quasi-discontinuity or marked change in cellular pattern of the altocumulus. Within the zone of overlap no cirrus was observed, and for the most part the altocumulus did not dissipate but persisted and remained little changed. Thus the outer limits or "edges" of the circles, only partly "holes" at this time, were revealed at the overlap zone not by the presence and absence of altocumulus, as formerly, but by distinct structural differences within the altocumulus. These well-marked limits were clearly still increasing during the observation period. They were moving outward slowly as a wave-like progression of a minor discontinuity or anomaly in the otherwise remarkably homogeneous cellular altocumulus pattern. Possibly what was moving outward was merely a progressive extension of the zone of weak downward motion that surrounded, and partly compensated for, the central zone of weak ascent. However, near the perimeters of the circles these downward motions should be extremely weak. Thus it is notable that the moving "edge" appeared to be a small but real wave perturbation propagating outward from a central initiation area, as along an interface, and may well have been such a wave. It would appear that holes of this type represent a rather complex combination of thermodynamic and dynamic conditions, which remain, as yet, not properly measured and inadequately understood.

The sequence of events described above could conceivably be initiated by entirely natural "seeding" processes, or could be a result of the activities of man. Ice crystals falling from overlying cirrus formations with well-developed tails have been observed by one of us from aircraft on several different occasions to produce similar but smaller near-circular openings in the cellular altocumulus below. Thus seeding from cirrus can initiate such holes. Cirrus tails have also been observed to initiate development of a substantial convective system, producing precipitation, by seeding supercooled altocumulus (Braham, 1967). However, during the period of observation on 1 December no cirrus of any kind was visible above the altocumulus. Ice crystals falling from almost invisible thin cirrus, or persisting from dissipated cirrus remnants, might possibly have provided the necessary nuclei. Such initiation would appear to be unlikely, though the Miami sounding does show a fairly pronounced moisture maximum and a significant temperature inversion at about 28,000 ft, and a lesser moisture maximum at 33,000 ft (so that a thin cirrus layer could have been present), and though cirrus crystals have been observed to fall considerable distances through quite dry air and still effect nucleation of middle clouds (Braham and Spyers-Duran, 1967). Initiation by other natural falling particles also remains a possibility, as does initiation by particles due to activities of man. Since the holes began to form just west of Coral Gables, neither rockets nor vertically-moving aircraft appear to have been involved. Approximately horizontally-moving aircraft might have produced suitable freezing nuclei either while in flight above or while passing through the cloud layer. Such aircraft were not observed near the area of interest during the 90-min observation period, nor were any holes observed to the north where air traffic was fairly heavy. No aircraft were observed for over an hour above or near the initiation point of the third hole. Natural nucleation, perhaps by a chance concentration of sufficient appropriate nuclei, would appear to be the most likely alternative.

FIG. 7. A view of both cloud holes A (left) and B (right) as they appeared southeast of Coral Gables at about 0930 EST.

In summary, it may be noted that a basic requirement for circular hole development appears to be a very particular type of cloud—a high, thin, cellular, rather homogeneous, relatively strongly supercooled, water droplet cloud. A second basic requirement is successful initiation by appropriate nuclei. Although the details of initiation remain undetermined, initiation is clearly a rare event, quite possibly a rare natural event. Once initiation occurs a central cirrus head develops quite rapidly, giving rise to a central zone of weak upward motion, a gradually widening surrounding zone of weak descending motion, a lateral propagation of cirrus filaments, and a central tail of falling ice crystals. A slowly outward-moving wave-like perturbation is also present. The holes, and these associated conditions, would appear to be observed rarely because the required altocumulus conditions occur infrequently, at least where most observation takes place, and because even when these conditions are present the required initiation events occur rarely.

Acknowledgments. The authors are grateful to the following individuals whose photographs add much to this note and led to its preparation: Thomas E. McCaughan of the National Hurricane Center, ESSA, Coral Gables, Fla., for Figs. 2, 3, 4 and 7; Charles True of the National Hurricane Research Laboratory, ESSA, Coral Gables, Fla., for Fig. 5; and Bill Kuenzel of the *Miami Herald* for Fig. 6.

References

Braham, R. R., Jr., 1967: Cirrus cloud seeding as a trigger for storm development. *J. Atmos. Sci.*, **24**, 311–312.

——, and P. Spyers-Duran, 1967: Survival of cirrus crystals in clear air. *J. Appl. Meteor.*, **6**, 1053–1061.

Reprinted from Tellus
Vol. XXI, No. 3, 331-340.

The transport of moisture into the antarctic interior

By B. LETTAU, *ESSA*, *Silver Spring*, *Maryland*

(Manuscript received June 25, 1968)

ABSTRACT

The magnitude of the moisture transport by the atmosphere into the Antarctic interior is determined from a mass transport model which allows a longitudinal variation in the annual flux values. It is indicated that the use of monthly mean transport and temperature values underestimates the annual moisture transport required by observed accumulation values in the interior, consequently a relatively much larger fraction of the annual moisture transport must occur in conjunction with positive temperature deviations from mean monthly values. This relation is examined at Byrd station where it was found that during the austral summer 1957–8 the threeday period with the highest 700 mb temperature accounted for nearly 20 % of the annual moisture transport. The variation of the moisture transport with altitude is examined and its effect as a constraint upon the maximum central height that the ice sheet may attain is briefly discussed.

Introduction

One of the more important, but heretofore generally neglected aspects of Antarctic meteorology is the mechanism by which the large amounts of precipitable water required to nourish the inland ice sheet are transported into the continent. Since the annual increments of the net snow accumulation are fairly easily identified by stratigraphic methods (e.g. Gow, 1965), estimates of the annual ice mass budget are generally made without reference to meteorological or climatological conditions, although their inclusion would very likely give a better definition of the dynamic situation which is interacting with the underlying surface.

The problem that will be considered here is simply to determine how and where the mass of water enters the Antarctic continent and is carried into the interior. This will involve analysis of the mass flow over the continent and consideration of the probable moisture content of the air. Some implications of the results will also be discussed, particularly with reference to the problem of whether the total ice mass is presently increasing or decreasing.

The flow of air over the Antarctic continent also is an important parameter in the study of a number of related questions concerning the heat balance of the continent and the role that the continent plays in affecting the climate at lower latitudes.

Since the routine measurement of atmospheric moisture content at very low temperature is both difficult and imprecise, the direct evaluation of the total moisture transport will not be attempted, except for a short analysis of the actual temperature-moisture covariance at one station, but rather the feasibility of moisture transport will be considered in combination with various Antarctic circulation models. Such a general treatment of course only yields limiting conditions and possible mechanisms, but does provide an insight into the ice mass balance of the Antarctic interior.

The two-layer circulation model

The most recent treatment of the mass budget of the Antarctic atmosphere is that of Rubin & Weyant (1963), which presents a consistent pattern of outflow in the lower troposphere and inflow in the upper troposphere and stratosphere, involving a balanced flux of 65×10^{12} gm/sec. This conceptually simple model of upper level inflow, sinking motion, and low level outflow is similar to one proposed for Greenland by Hobbs (1945), and is in agreement with that postulated for the Antarctic from ozone transport values (Wexler *et al.*, 1960). Furthermore it provides an adiabatic heat source to offset the large continental radiative losses. However such a model cannot be reconciled with the transport of water vapor since on the average it suppresses precipitation, and assigns the mass influx to such a high altitude that little moisture can be transported into the interior. Apparently the peripherally averaged situation is never actually realized, and the mathematically determined mean state may not be equated to a physical equilibrium or steady state.

The Rubin-Weyant model utilizes a circular equivalent continent with a radius of 2000 km, and was developed from coastal station data. It therefore includes an edge effect which places the boundary between inflow and outflow at a much lower altitude than can be expected in the interior. As one goes inland from the coast, the zero net transport level should rise approximately as the ice surface, and the already difficult moisture transport process will be confined to more hostile altitudes.

An alternate hypothesis, which seems more reasonable from a synoptic point of view is that large deviations of the meridional wind components from their average values exist in space or time. Either supposition however, produces a mass transport pattern that is unlike the mean peripheral pattern.

The tabulated values of the circumferential monthly mean meridional winds given by Rubin & Weyant allow a determination of the temporal variability, although not of the spatial variability of the mean mass flux. These show that there was, on the average, outflow at and below 700 mb and inflow at and above 500 mb around the periphery of the Antarctic continent in every month included in the study. It follows therefore that longitudinal variations in the mass flux must exist, and that there must be preferred sectors of inflow and outflow on the Antarctic continent.

A consideration of the water vapor transport required to produce the observed snow accumulation in the interior leads to the conclusion that the preferred sectors of inflow must necessarily transport relatively large amounts of water vapor and that the inflowing air must therefore be relatively warm. This of course is also required from considerations of the total atmospheric heat budget. If it is assumed that the mean annual precipitation amount over the Antarctic interior is roughly 10 cm of water, then a flux of 0.04×10^{12} gm/sec of water vapor into the equivalent continent is required. In conjunction with the previously given value of the mass flux, this loss implies a decrease in mixing ratio of 0.62 gm/kg for the inflowing air during its residence time over the continent, which is an appreciable change in the Antarctic. Mean conditions at Amundsen–Scott station for example produce a saturation mixing ratio at the surface of only about 0.66 gm/kg, thus stated very simply, air flowing into the interior must be saturated, while air flowing out of the interior must be dry, a condition that is difficult to achieve in practice.

Peripheral variation of the mass flux

The peripheral variation of the mean annual mass flux was computed for Rubin and Weyant's equivalent circular continent, using actual radial wind components rather than meridional wind components, although this refinement is only of moderate importance since the greatest angular difference between the radial and meridional direction does not exceed 23°. The analysis was carried out from the surface to 50 mb in three increments: Sfc to 600 mb, 600 to 350 mb, and 350 to 50 mb.

The mean annual, vertically integrated mass flux values for the peripheral stations are given in Table 1. Since the stations are not spaced equally on the perimeter of the equivalent continent, mass flux values are presented for a unit area defined as a one centimeter wide strip extending from the top to the bottom of each layer. Mass outflow has been defined as positive. The distribution of the annual net mass flux is also shown in Fig. 1 with the stations identified by their number in Table 1.

Examination of Table 1 shows that preferred sectors of inflow and outflow definitely exist. On the average the mass flux is positive in Wilkes Land and in the Weddell Sea region, and negative in the eastern Ross Sea, Marie Byrd Land and much of East Antarctica. Maximum values of mass inflow occur at Byrd and Mirny, while maximum values of mass outflow occur at Hallett and Dumont d'Urville. The outflow at Hallett could be due to the large angle between the boundary of the equivalent

Table 1. *Distribution of the net annual mass flux around the periphery of the Antarctic continent*

Index	Station	Mass flux intensity (10^4 gm/cm/sec) Sfc–600 mb	600–350 mb	350–50 mb
1	Norway Base	4.0	2.7	−4.8
2	Halley Bay	−0.4	2.3	3.8
3	Ellsworth	2.5	2.0	4.7
4	Byrd	−11.2	−8.4	2.0
5	Little America V	−0.5	−3.0	7.1
6	Hallett	10.7	5.6	15.1
7	Dumont d'Urville	5.2	4.4	5.2
8	Wilkes	−4.1	−0.1	−2.6
9	Mirny	−1.6	−1.4	−5.0
10	Davis	−6.0	−4.0	−3.1
11	Mawson	4.0	3.7	−4.7
12	Molodezhnaya	−0.3	3.1	−6.3
13	Roi Baudouin	2.8	−2.9	−5.6
14	Lazarev	6.9	−0.2	−6.0
Integrated mass exchange		31.7×10^{12} −32.2	20.3×10^{12} −20.2	33.4×10^{12} gm/sec −33.2
Total exchange 85.4×10^{12} gm/sec				

Data sources: Stations 1–9, 14, U.S. Navy Marine Climatic Atlas of the World, Vol. VII, Antarctic, NAVWEPS 50-1C-50, Sept. 1965. Stations 10–13, U.S. Dept. of Commerce Weather Bureau, Monthly Climatic Data for the World.

continent and latitude lines, so that circumpolar flow would appear to have a radial component, however since there is no corresponding inflow at Ellsworth, this effect seems to be a minor one.

This distribution of inflow and outflow may be modelled schematically by an elongated region of low pressure centered approximately on the south pole, with one trough extending roughly along the zero meridian and the other along

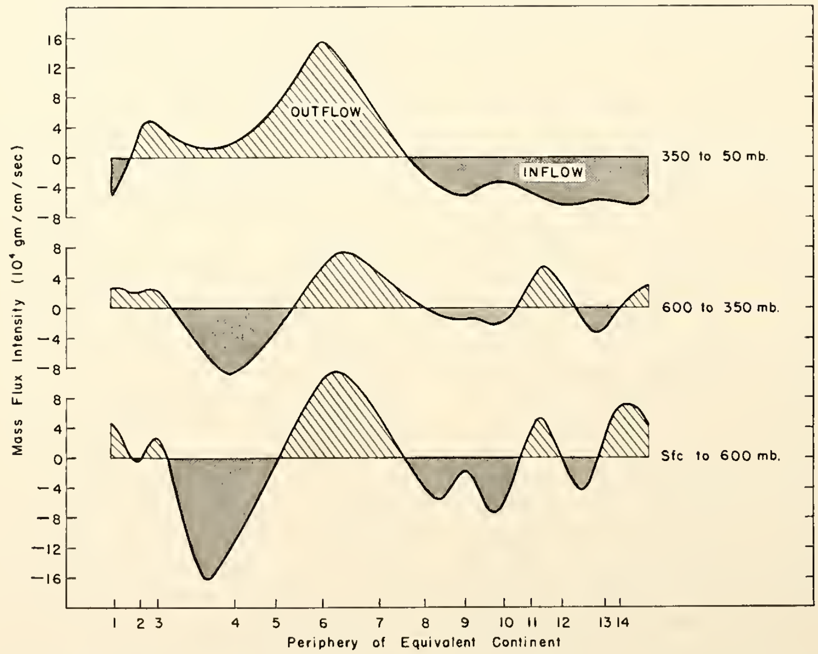

Fig. 1. Peripheral distribution of the annual net mass flux for the equivalent continent.

160° E longitude, which coincides in fact with one of the two basic types of atmospheric circulation found in the Antarctic by Astapenko (1964).

The empirically determined total mass exchange of the Antarctic atmosphere (cf. Table 1), is 85.4×10^{12} gm/sec, which is roughly 30% higher than the value 65×10^{12} gm/sec obtained from the Rubin–Weyant circulation model. That the two values are unequal is not surprising, and in fact the higher value found here is more desirable from the standpoint of moisture exchange.

A seasonal variation of the basic pattern is evident at some stations. For example at Byrd, Dumont d'Urville and Wilkes, the mass flux changes sign during the year, being negative (inflow) in summer and positive (outflow) in winter. At Little America V there is less inflow in winter than in summer, and at Hallett there is less outflow in winter than in summer, indicating a seasonal variation in the Ross Sea circulation. At Mirny there is a semi-annual variation with inflow in summer and winter, but zero flux at the time of the equinoxes. These variations are of course only reflections of the seasonal shifts of the mean pressure distribution around the Antarctic perimeter, but for the purpose of this paper, it should be noted that the austral summer, which is the period during which the upper limit of the moisture transport is high, is also one of wide-spread low-level inflow into the continent, with outflow being confined to the Hallett and Ellsworth sectors.

Mass flux in the interior

In order to determine whether or not the observed mass flux values represent only a coastal phenomenon, a second arbitrary volume was constructed, extending from the surface to 100 mb, and roughly encompassing Amundsen–Scott, Vostok II, and Plateau stations. The circular base has a radius of about 720 km, and is centered at 83.5° S, 66° E. Plateau station has only been used as a residual to balance the mass flux at Vostok II and Amundsen–Scott, since data for it is not now available. The mass flux values for these stations show that generally the peripheral conditions extend substantially inland. Thus the inflow at Amundsen–Scott and Plateau is a continuation of the mass inflow at Byrd and Roi Baudouin, while the outflow at Vostok II is a source for the mass flux at Hallett and Dumont d'Urville. The magnitude of the mass exchange is 22.1×10^{12} gm/sec, which is an appreciable fraction (26%) of the total mass flux through the equivalent continent, in spite of the fact that the inner volume is little more than one tenth that of the equivalent continent. Such a rapid exchange of air is of course very favorable for the deposition of sizeable amounts of moisture at very low temperatures.

Loewe (1962) determined that the total water vapor content over the higher parts of the Antarctic ice cap would have to be replaced at least every fifth day in order to provide an accumulation of 7 to 8 cm per year. The above calculations indicate that this requirement is fulfilled since the representative residence time of a parcel of air in the inner volume, determined by taking the ratio of the mass within the volume to the exchange rate, is only about 5.7 days.

The transport of moisture

The largest fraction of the lower level annual mass influx occurs in the Byrd–Amundsen–Scott sector, consequently it may be presumed that a similarly large fraction of the moisture transport is carried through this sector. Since the actual moisture transport is difficult to measure, monthly values of the saturation mixing ratio will be considered, with a weighting factor of 60% relative humidity applied for transport values. The assumption of such a value is quite good for Byrd throughout the year.

The average annual amount of precipitation observed on the Antarctic continent is of the order of 10 cm, requiring an annual water vapor flux of 1.26×10^{18} gm into the interior. (A summary of flux values obtained by other investigators, which vary from 0.8 to 2.8×10^{18} gm/year is given in Wexler (1961)). With the previously determined mass exchange value, this requires, on the average, a minimum mixing ratio of 0.47 gm/kg. In Fig. 2 a time section at Byrd is presented, which gives monthly mean saturation mixing ratio values converted from temperature data. Also indicated is the seasonal variation in the level of zero mass flux. It is evident, particularly in the austral summer, that the inflowing air is potentially quite moist although with an average relative humidity of

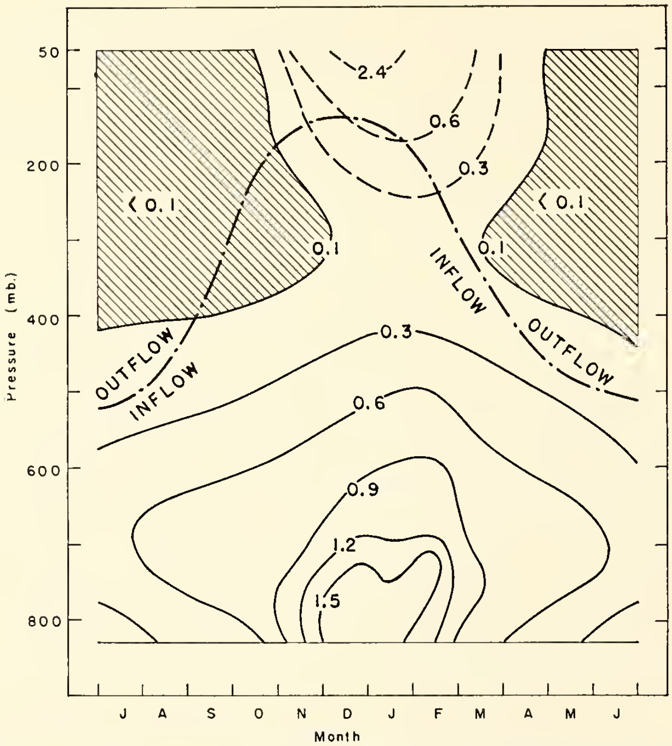

Fig. 2. Time vs. altitude section showing isopleths of saturation mixing ratio from monthly mean temperatures at Byrd. Also indicated is the boundary between net annual inflow and outflow.

60% the actual mean annual mixing ratio does not quite reach 0.3 gm/kg The high saturation mixing ratio values above 200 mb are solely a result of stratospheric. warming, and are not indicative of high moisture content. A computation of the total annual water vapor transport through the Byrd sector with these mean values yields a value of 0.30×10^{18} gm water, which is roughly twentyfive percent of the total transport required for the entire continent, however since the annual mass flux through the Byrd sector amounts to forty percent of the total mass exchange, the water vapor transport falls short of the minimum required to explain the observed inland accumulation by a factor of about two.

There are two means of resolving this difficulty. One is that the inward moisture transport at Byrd is abnormally low relative to that at other peripheral stations, which does not seem very likely because of the lower coastal elevations in West Antarctica than in East Antarctica. The other is the assumption that the bulk of the moisture is carried by inflowing air warmer than the monthly mean temperatures, which seems reasonable because of the exponential variation of the saturation mixing ratio with temperature. This relationship will be investigated in a later section.

At Amundsen–Scott the transport of water vapor by the inflowing air, on an average basis, is nearly equal to the minimum required to explain the observed inland accumulation. The potentially greatest moisture carrying capacity of the air does occur near the surface where outflow from the interior is observed, however the mean saturation mixing ratio of the inflowing air above 550 mb reaches approximately 0.15 gm/kg (cf. Fig. 3). Although the actual mixing ratio of the inflowing air will therefore only be of the order of 0.10 gm/kg, such a low value is roughly sufficient to produce the quite small accumulation values of the Antarctic interior.

Assuming a mean annual deposition of 5 gm/cm^2 water equivalent over the inner area

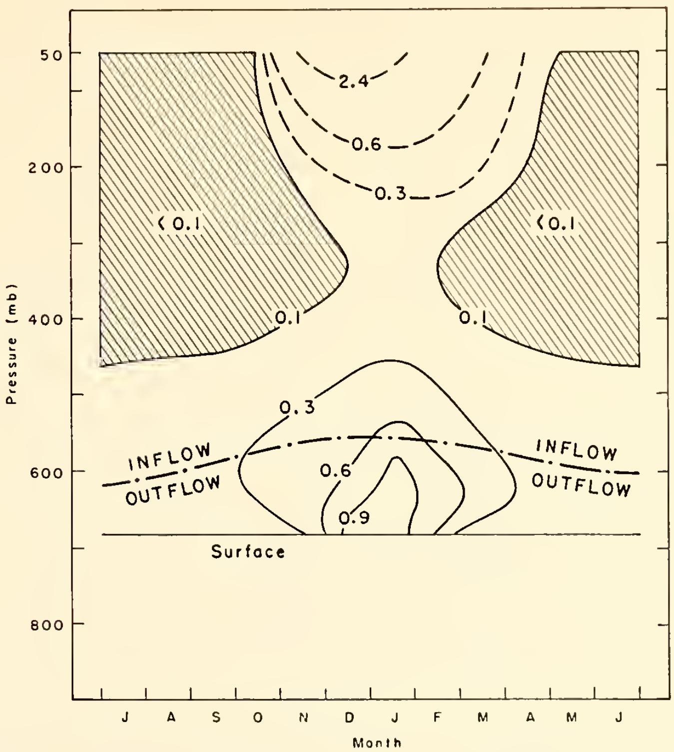

Fig. 3. Time vs. altitude section showing isopleths of saturation mixing ratio from monthly mean temperatures at Amundsen–Scott. Also indicated is the boundary between net annual inflow and outflow.

of radius 720 km, an annual water mass influx of 0.68×10^{18} gm is required, which must enter through the Amundsen–Scott and Plateau sectors. The annual mass exchange through these sectors is 7.0×10^{20} gm, thus the requisite mean mixing ratio need only be 0.11 gm/kg.

The situations at Byrd and Amundsen–Scott may be characterized as being respectively meteorologically and climatologically controlled. The influx of sufficient water vapor at Byrd is apparently dependent upon positive departures of the air temperature from its mean; thus if the short-term variability of the summer temperature (meteorological variation) were to decrease, the mass of water vapor transported into the interior through the Byrd sector would similarly decrease. At Amundsen–Scott such a mechanism is not required; a change in the variability of the air temperature about the monthly mean values would not affect the influx of sufficient water vapor to maintain the present mean accumulation rate. It would be affected only if the monthly mean temperatures themselves were to decrease.

The temperature-moisture covariance at Byrd

The hypothesis that the bulk of the moisture is carried by the warmest air is consistent with the fact that the moisture transport calculated from average values is too low to explain the observed inland accumulation, and is strengthened by the exponential increase of the saturation mixing ratio with temperature at any given pressure level. The hypothesis may be tested by plotting the moisture flux against temperature. If the resulting cloud of points shows definite deviations from a straight line, then it may be assumed that the hypothesis is correct.

Such a computation was carried out for Byrd Station from October 1957 to April 1958. Fig. 4 shows individual daily moisture transport values as a function of temperature at 700 mb. The graph definitely shows that the moisture transport increases approximately exponentially with temperature, and that positive departures from the mean temperature (about −20°C) correspond to much greater positive

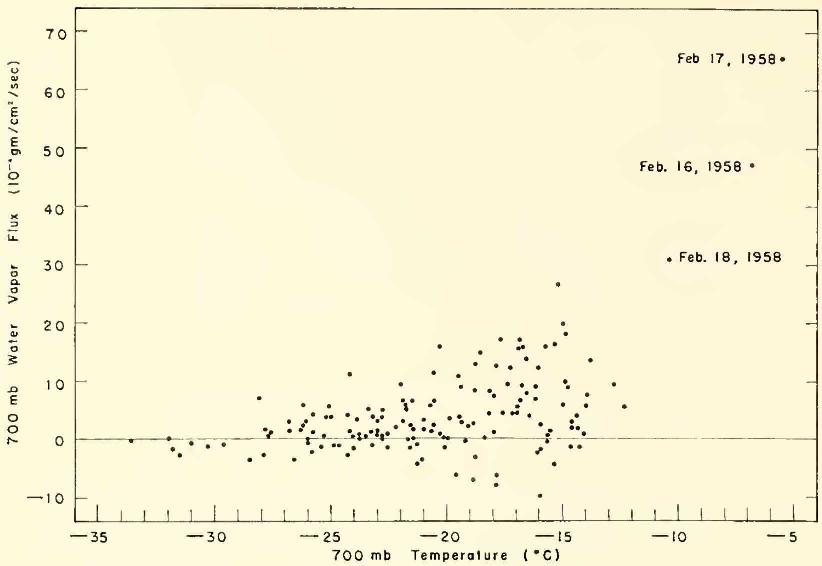

Fig. 4. Moisture flux as a function of the 700 mb temperature at Byrd station, October 1957–March 1958. Each dot represents a day on which data was available.

departures from the mean moisture transport value. At low temperatures (less than $-28°C$) the moisture transport is essentially independent of themperature and very elose to zero. At more moderate temperatures (between $-28°C$ and $-20°C$) there is a definite tendeney toward moisture transport into the interior and toward higher transport values. At temperatures above $-20°C$ the moisturo transport inereases rapidly and reaehes values that are an order of magnitude greater than those observed at lower temperatures.

The total moisture transport for the summer season is given in Fig. 5 on a monthly basis together with the eumulative total through the summer. It is immediately evident that at least in 1957–58 the moisture transport did not follow a regular progression, but rather was quite variable throughout the season. While the Oetober and April values are low, as would be expeeted from temperature observations, the January value is anomalously low, particularly when contrasted with the high February value.

The eumulative total transport reaehes a value of 0.36×10^{18} gm by the end of April, whieh, on the assumption that the five winter months eontribute very little to the moisture flux into the interior, may be taken as nearly the annual value. While it exeeeds that eomputed from the mean monthly data by twenty percent, it is less than that required to explain a mean preeipitation value of 10 em over the equivalent continent. (Since the mass flux at Byrd was 40% of the Antaretic total, the moisture flux should be 40% of $1.26 \times 10^{18} = 0.5 \times 10^{18}$ gm.) This of eourse is not a serious diserepaney beeause it is the result of a eomparison between the observed transport in one year and an arbitrarily designated representative value, which may not refleet the aetual precipitation value for any given year.

The meteorologieal eontrol of the magnitude of the moisture transport at Byrd is very well shown by the February value, whieh is largely the result of one three-day period (February 16–18) during whieh a low pressure area was situated near Little Ameriea and warm moist maritime air was moving into the continent. The moisture transport during these three days, which are marked in Fig. 4, amounted to 40% of the monthly total, whieh itself amounted to nearly half the annual total. Therefore approximately one-fifth of the total annual moisture transport in the Byrd sector oeeurred during this particular three day period.

Sineo only one set of sueh high transport values was observed (cf. Fig. 4), it is apparent that this favorable synoptie situation appeared

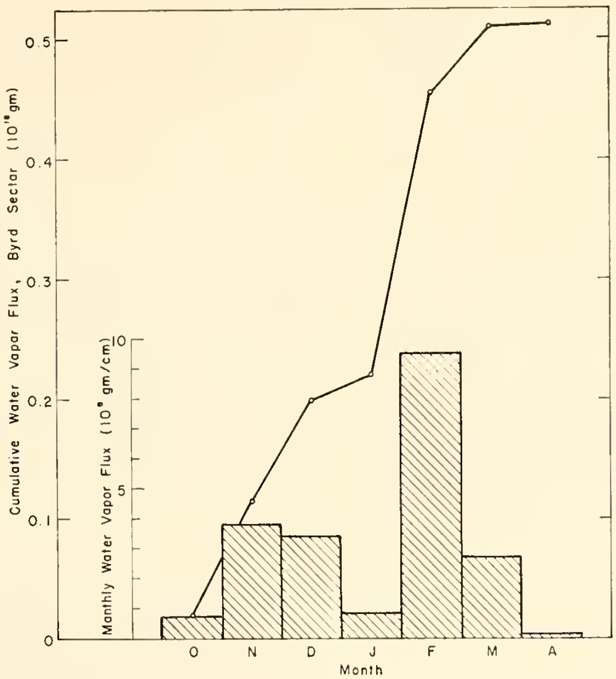

Fig. 5. Histogram of the monthly net moisture transport through the Byrd sector during the austral summer 1957–8. Also shown is the cumulative total moisture transport.

only once during the summer of 1957–58. There is however no reason to suppose that it cannot recur one or several times during one summer, but on tho other hand, there is also no reason to assume that it need to occur at all. Then, because of the great influence of this situation on the total annual moisture transport, one would expect a high interannual variability in the moisture transport values. Furthermore it would follow that the observed annual accumulation amounts, which represent a rough measure of the annual moisture transport, should similarly be highly variable. This latter effect is indicated in a study by Giovinetto & Schwerdtfeger (1966), who found that the one-year lag correlation in the snow accumulation record over 200 years at the South Pole was very nearly zero, so that the annual succession of snow accumulation amounts is very nearly random. The accompanying standard deviation values indicate that individual annual values may vary from the mean by a factor of 2, producing a relatively large range of observed values, in accord with the moisture transport thypothesis at Byrd.

Effect on ice mass balance

The mass balance of the interior ice sheet is a function of the ablative effects at its edge and its surface, and the accumulative effects of the precipitation pattern on its surface. Since neither its rate of gain nor its rate of loss can be calculated very precisely, the difference in the two rates, which determines whether the ice mass is increasing or decreasing is also not very well defined. It is however possible to place rough limits on the amount of ice that can be accumulated.

The detailed moisture transport values at various pressure levels at Byrd show that to a very good approximation these vary logarithmically with pressure, such that the transport is halved for a pressure decrease of 100 mb. This empirical observation is related to the fact that at Byrd a 100 mb pressure decrease corresponds to an increase in altitude of approximately 1500 m, through which distance the moist adiabatic lapse rate will produce a temperature decrease of approximately 10°C which in turn corresponds approximately to a decrease in the saturation mixing ratio of a factor of 2. On the further assumption of horizontal flow, and because of the generally sloping surface, one can say that for every 100 mb decrease in the surface pressure on a track from Byrd station to Amundsen–Scott the total annual moisture transport will be decreased by a factor of two. Since the mean pressure difference between Byrd and Amundsen–Scott is 126 mb, the moisture transport at Amundsen–Scott will be roughly 40% of that at Byrd. In the present case that would be 0.12×10^{18} gm/year, which somewhat exceeds the amount necessary for a mean precipitation rate of 5 cm/year computed previously. The mean precipitation rate may be greater than 5 cm/year however, and the computed transport value at Amundsen–Scott is a slight overestimate because the simple model that has been postulated above is not strictly correct. It does not, for example, take into account the fact that some moisture will be advected through the sides of the volume extending inland from Byrd and so will be lost as far as this analysis is concerned.

Although the assumptions which underlie this simple latitudinal transport decrease model are open to question, the model itself is quite useful for rough calculations. The highest ice surface elevation in the Antarctic interior is about 4000 m (550 mb) which, if it were uniformly applicable to the Amundsen–Scott–Vostok–Plateau area, would reduce the moisture transport to 10% of that at Byrd, and produce a mean annual precipitation value of about 1 cm. This value is so small that it appears very unlikely that the ice sheet could maintain itself at such an altitude for very long before wind-produced ablation and the outward movement of the ice sheet would initiate a thinning process. The existence of an appreciably thicker ice sheet than the present one seems therefore excluded on meteorological grounds.

This conclusion of course assumes a climate not much different from the present one. Climatic amelioration does occur and should be considered in any discussion of such a slow process as the variation in thickness of the interior ice sheet. In general, the moisture transport will vary directly with the temperature, although the atmospheric mass flux may change with the climate and must also be considered. It should be noted however, that an increase in the mean temperature, for example, must occur at least throughout the troposphere for the moisture transport to increase by a noticeable amount, and that climatic variations which are confined to the surface layers will have a negligible effect on the mass balance of the ice.

Résumé

La magnitude du transport de vapeur de l'eau dans l'intérieure de l'Antarctique par l'atmosphère est detérminée par une modèle du transport de masse qui permette une variation longitudinale en le valeur de la fluxe annuelle. Il est indiqué que l'usage des moyennes mensuelles en le transport et la température sousestime le transport annuel de vapeur de l'eau exigés par les valeurs observés de l'accumulation de glace en l'intérieure. Par suite il faut que la plupart du transport annuel de vapeur de l'eau se trouve avec les déviations positives de la température à partir des moyennes mensuelles. On examine ce rapport pour le station Byrd où on trouve qu'en été austral 1957–8 l'espace de trois jours a la température la plus grande à 700 mb produisée à peu près 20% du transport annuel de vapeur de l'eau. On examine aussi le variation altitudinal du transport de vapeur de l'eau et on discute en peu de mots son effet comme constrainte sur la élévation centrale que peut atteindre la mer de glace

REFERENCES

Astapenko, P. D. 1964. *Atmospheric Processes in the High Latitudes of the Southern Hemisphere* (tr. by Israel Program for Scientific Translations, Jerusalem), 286 pp.

Giovinetto, M. B. & Schwerdtfeger, W. 1966. Analysis of a 200 year snow accumulation series from the South Pole. *Arch. f. Met. Geophys. and Biokl.*, *15*, 2, 228–249.

Gow, A. J. 1965. On the accumulation and seasonal stratification of snow at the South Pole *J. Glaciology*, *5*, 40, 467–478.

Hobbs, W. H. 1945. The Greenland glacial anticyclone. *J. Meteorology*, *2*, 3, 143–153.

Loewe, F. 1962. On the mass economy of the interior of the Antarctic ice cap. *J. Geophys. Res.*, *67*, 13, 5171–5177.

Rubin, M. J. & Weyant, W. S. 1963. The mass and heat budget of the Antarctic atmosphere. *Monthly Weather Review*, *91*, 487–493.
Wexler, H. 1961. Ice budgets for Antarctica and changes in sea level. *J. Glaciology*, *3*, 29, 867–872.
Wexler, H., Moreland, W. B. & Weyant, W. S. 1960. A preliminary report on ozone observations at Little America, Antarctica. *Monthly Weather Review*, *88*, 43–54.

ПЕРЕНОС ВЛАГИ ВО ВНУТРЕННИЕ ОБЛАСТИ АНТАРКТИКИ

Определяется величина переноса влаги в атмосфере внутрь Антарктики путем использования модели переноса массы, которая учитывает долготные изменения в годовых величинах потоков. Указано, что использование среднемесячных значений переноса массы и температуры занижает годовой перенос влаги, требуемый наблюдаемыми значениями аккумуляции во внутренних областях. Следовательно, существенная часть годового переноса влаги должна происходить при наличии положительных отклонений температуры от среднемесячных значений. Эта связь проверялась для станции Бэрд, где было найдено, что в течение лета 1957–58 гг. для трех дней с наибольшими температурами на поверхности 700 *мб* перенос влаги составил почти 20% от годового переноса. Исследуется изменение переноса влаги с высотой и кратко обсуждается ограничительное его влияние на максимальную высоту, которой может достичь ледяной покров.

Reprinted from Annalen der Meteorologie
NF No. 4, 30-34.

DK 551.510.522:551.554

Wind structure in the equatorial maritime friction layer

von

B. LETTAU

Abstract

The vertical wind structure in the equatorial maritime friction layer is related to parameters derived form pressure and density gradients, frictionalstresses, and the rotation of the Earth. The analytic expressions for the free-air wind and wind shear, obtained by latitudinal differentiation of the geostrophic approximation, are used to define surface wind components analogous to the midlatitude surface geostrophic wind and gestrophic deviation vectors.

Two assumptions are made in the analysis: 1. The free-air wind and vertical wind shear vectors are determined by macro-scale meteorological patterns which are persistent for relatively long periods of time, and 2. The vertical wind structure of the equatorial friction layer is determined by the momentum exchange mechanism at the air-sea interface and by local synoptic temperature (density) variations. The use of the latitudinal gradients of the coriolis force and the pressure gradient force obviates the problem of a vanishing coriolis parameter at the equator, and as a result the model in its detailed application is analogous to that of the wind structure in an extra-tropical baroclinic boundary layer. The model is tested with observed surface temperature values and wind profiles obtained in the Arabian Sea by the 1967 "OCEANOGRAPHER" expedition, and in the equatorial Atlantic Ocean by the 1925—7 "METEOR" expedition. Relevant climatological pressure and temperature fields have been taken from published summaries and atlases. The observed behavior of the wind profiles can be related quite well to the ambient distributions of thermodynamic parameters: The observed shear vectors may be separated into a thermal component related to local synoptic temperature variations, and a frictional component related to the vertical variation of the shearing stress. Since these generally oppose one another, and the frictional shear vectors decrease with height, the total shear vector increase to a non-zero asymptote, producing the typically observed maritime pattern.

Zusammenfassung

Die vertikale Windstruktur in der äquatorialen maritimen Reibungsschicht hängt ab von Parametern, die aus den Druck- und Dichte-Gradienten, den Reibungskräften und der Rotation der Erde abgeleitet sind. Die analytischen Ausdrücke für den Wind in der freien Atmosphäre und die Windscherung, die durch breitengerechte Differenzierung der geostrophischen Näherung erhalten wurden, werden benutzt, um die Bodenwind-Komponenten ähnlich den Vektoren des geostrophischen Bodenwindes und der geostrophischen Abweichung für die Mittelbreiten zu bestimmen.

Zwei Annahmen werden in der Analyse gemacht: 1. Die Vektoren des Windes in der freien Atmosphäre und der vertikalen Windscherung werden bestimmt durch ein makro-meteorologisches Feldgepräge, das über relativ lange Zeitabschnitte andauert, und 2. Die vertikale Windstruktur der äquatorialen Reibungsschicht wird durch den Mechanismus des Impuls-Austausches an der Grenzfläche Luft — See durch lokale synoptische Temperatur-(Dichte-) Änderungen bestimmt. Die Benutzung der Breiten-Gradienten der Coriolis-Kraft und der Druckgradient-Kraft beugt dem Problem eines am Äquator verschwindenden Coriolis-Parameters vor, und es ergibt sich, daß das Modell in seiner Anwendung im einzelnen dem der Windstruktur in einer außertropischen baroklinen Grenzschicht ähnlich ist. Das Modell wird an Hand der Bodentemperaturen und Windprofile geprüft, die im Arabischen Meer auf der „Oceanographer"-Expedition 1967 und im äquatorialen Atlantischen Ozean auf der „Meteor"-Expedition 1925—27 beobachtet wurden. Hinreichend belegte klimatologische Druck- und Temperaturfelder wurden den veröffentlichten Zusammenstellungen und Atlanten entnommen. Das beobachtete Verhalten der Windprofile kann recht gut zu den umgebenden Verteilungen der thermodynamischen Parameter in Beziehung gebracht werden: Die beobachteten Scherungsvektoren können aufgeteilt werden in eine thermische Komponente, die zu den lokalen synoptischen Temperaturänderungen in Beziehung steht, und eine Reibungskomponente, die zu der vertikalen Änderung der Scherungskraft in Beziehung steht. Da diese im allgemeinen einander entgegengesetzt sind und die reibungsbedingten Scherungsvektoren mit der Höhe abnehmen, so wächst der gesamte Scherungsvektor asymptotisch gegen einen von null verschiedenen Wert und läßt die beobachtete, für maritime Verhältnisse typische Form entstehen.

It is the purpose of this report to examine the vertical wind distribution within the maritime friction layer both in geostrophic terms, that is in a rotating system with a welldefined Ekman layer, and in non-geostrophic terms, that is in an equatorial non-rotating system in which the analytical framework is not as simply defined. Additionally it is intended to examine the manner in which the system passes from the geostrophic to the non-geostrophic mode.

It has been established that in middle and high latitudes of the northern and southern hemisphere, where the coriolis parameter has an appreciable magnitude, the effect of the surface stress is to produce a satisfyingly veering wind vector through the boundary layer, although quite often the simple spiral is distorted by an accompanying geostrophic wind shear (JOHNSON (1), B. LETTAU (2)). Essentially the same technique has been used by CHARNOCK et al (3) with reasonable success.

The obvious next step then was to attempt similar analyses at approximately 10°N, and at the equator. The results reported here at 10°N are not successful if success is defined as obtaining inconsistent answers with standard techniques; the results at the equator on the other hand indicate that it is possible to interpret some of the observations within a new framework fitted more reasonably to the ambient conditions.

In the spring of 1967 a series of wind profiles were obtained by USCGS OCEANOGRAPHER off the Somali coast in the region of a persistent wind maximum within the boundary layer, which had been called the Somali Jet by BUNKER (4). Although the individual wind velocities observed on this cruise did not reach the high values observed by Bunker, the general decrease in the wind speed with height was observed and appears in the mean wind profile.

The wind as a function of height is given in figure 1 in a coordinate system oriented parallel and normal to the surface wind vector. In such a coordinate system the

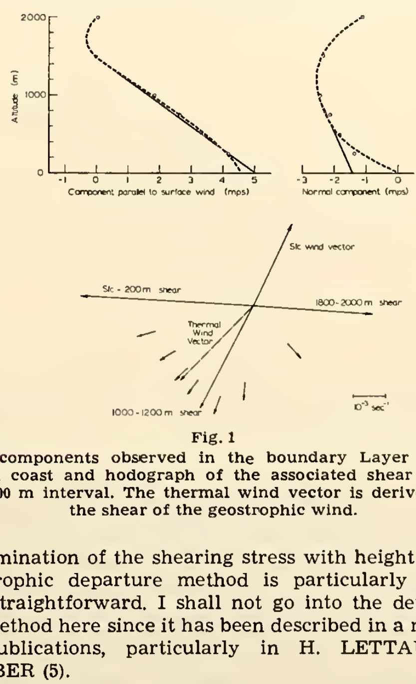

Fig. 1
Wind components observed in the boundary Layer off the Somali coast and hodograph of the associated shear vectors over 200 m interval. The thermal wind vector is derived from the shear of the geostrophic wind.

determination of the shearing stress with height by the geostrophic departure method is particularly simple and straightforward. I shall not go into the details of the method here since it has been described in a number of publications, particularly in H. LETTAU and HOEBER (5).

The shearing stress is described in this situation by the progressive (and additive) deviation of the observed wind profile from the geostrophic wind profile, down to the surface stress, τ_0, which is proportional to the total integrated profile deviation.

The weakest point of this technique is the determination of the shape of the geostrophic wind profile. The hypothesis that the wind at the top of the planetary boundary layer is in fact geostrophic offers one constraint, while a second is obtained from the characteristics of the shearing stress profile in the chosen coordinate system.

In the absence of further information (e.g. the surface pressure gradient) it is safest to assume a linear geostrophic profile as has been done here, resulting in an angle of 17° between the observed surface wind and the surface geostrophic wind. The computed surface stress value is 0.11 dynes/cm^2, the geostrophic drag coefficient is 0.4 x 10^{-3}, and the friction velocity is 9 cm/sec. All of these are of course equivalent, derivable from each other, and only subject to personal preference. The values are low as surface friction parameters go, but fall reasonably well into the summaries of these parameters as given by ROLL (6).

Occasionally independent observations either of the surface pressure distribution (surface geostrophic wind) or of the temperature distribution (thermally produced wind shear) are available which indicate that the true situation is likely to be more complex than that shown here. For example the average wind profiles obtained by CHARNOCK, FRANCIS, and SHEPPARD (3) at Anegada included the surface geostrophic wind as an observed parameter. An examination of their diagrams shows quite clearly that a linear geostrophic profile will not satisfy all three constraints, hence the geostrophic profile must be curved. It is encouraging to note however that the curvature of the profile decreases upward indicating that the horizontal temperature contrast is greatest at the surface. In their case the surface stress is higher at 0.32 dynes/cm^2, the angle between the geostrophic and observed wind at the surface is less at 13°, while the geostrophic drag coefficient is nearly the same at 0.3 x 10^{-3}.

One can see from this that results which do not conflict with previous experience can be obtained from techniques involving the coriolis parameter in regions where the geostrophic approximation can no longer represent the observed wind field.

The situation changes somewhat however at the equator itself. Here the equivalence between geostrophic departure and shearing stress no longer holds because neither the geostrophic wind nor the factor of proportionality are defined. It is however possible to apply those concepts and techniques that are independent of latitude. For example, it is reasonable to assume that a free region and a friction layer exist and that their boundary lies at approximately the same altitude as in mid-latitudes.

The following analysis is based on a series of pilot balloon ascents from the 1925-7 METEOR expedition, between 5° N and 5° S latitude in the Atlantic Ocean. The data are old but usable, and illustrate the relevant dynamic processes very well.

An examination of the individual ascents showed that the variation in wind direction decreased with height, orlooking from the top down, the wind at 2000 m was typically from the northeast; the wind at 1000 m from somewhat south of east, with the surface wind from a variety of directions. As a first step therefore it was decided to group the profiles by surface wind direction at two point intervals, and to construct mean profiles by averaging the component parallel and normal to the surface wind at standard levels. The gross structure of the five resultant classes is shown in figure 2 which gives the surface wind vector, the sfc-

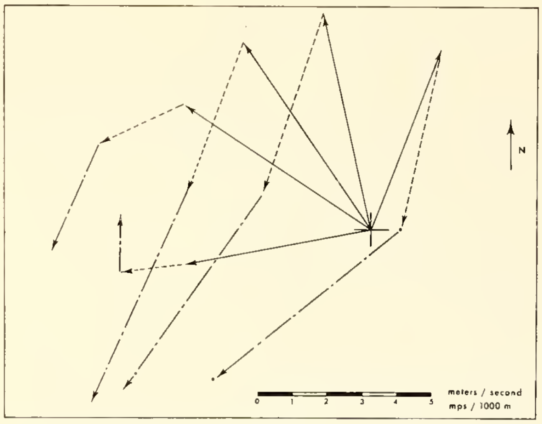

Fig. 2
Surface wind vectors (solid), surface — 1000 m shear vectors (dotted), and 1000—2000 m shear vectors (dot-dashed), in the atmospheric boundary layer of the equatorial Atlantic Ocean.

1000 m shear vector, and the 1000-2000 m shear vector for each group. Quite plainly there is a tendency for the shear to increase with veering of the surface wind, and also for the shear vector to increase with height. This last effect is quite generally observed in the trade wind zone where it is due to the opposition of the pressure and temperature gradient, producing anti-parallel wind and wind shear vectors. In the equatorial region however one must look for an alternate explanation since the normal thermal wind is not defined. It seems reasonable however that the extremely variable deriation of the sfc wind vector from the 2000 m wind, vector, which ranges roughly from 0° to 180° among separate groups is caused by an equally variable thermodynamic parameter within the boundary layer; and it is difficult to imagine this parameter to be anything other than the horizontal temperature distribution. One may say then that there exists an as yet undefined equatorial thermal wind which has the same characteristics as the normal midlatitude thermal wind.

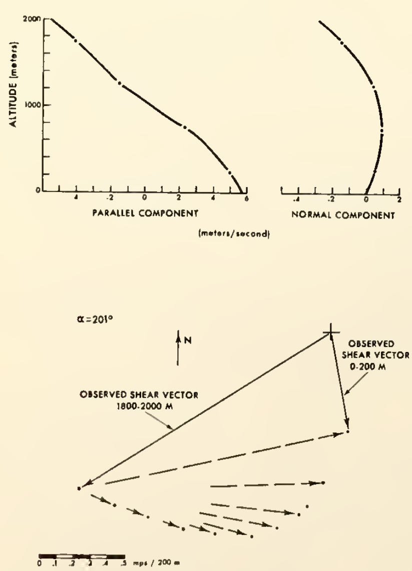

Fig. 3
Wind components in the equatorial boundary layer and associated shear vector. The mean azimuth of the surface wind is 201°.

Figure 3 shows the mean profiles of the group with the individually largest sfc deviation ($\alpha = 201°$). The components of the profile are again parallel and normal to the surface wind. The parallel component decreases continuously and nearly linearly from a sfc value of 6mps to 5mps at 2000 m. The normal component is comparatively small and is directed to the right of the sfc wind in the lower part of the profile and to the left in the upper part. The lower part of the diagram presents the smoothed shear vector one two hundred meter intervals in hodograph form, and shows clearly its increase in magnitude and veer with height. Since the shearing stress very likely does not increase with height, and in fact most likely has gone to zero at 2000 m, the observed shear vector from 1800 to 2000 m has been arbitrarily taken as the equatorial thermal wind and has been assumed constant through the boundary layer. The vector difference between the 1800-2000 m shear and the observed shear then represents an effect which is large near the surface and goes to zero at 2000 m which looks very much like the effect of surface stress. The stress vector turns to the right with height in this case, and as you may note appears to reach a non-zero asymptotic value, indicating that the assumption of a constant thermal wind is not quite correct.

The next group with a mean surface wind azimuth of 168° (fig. 4), looks very much like the previous one

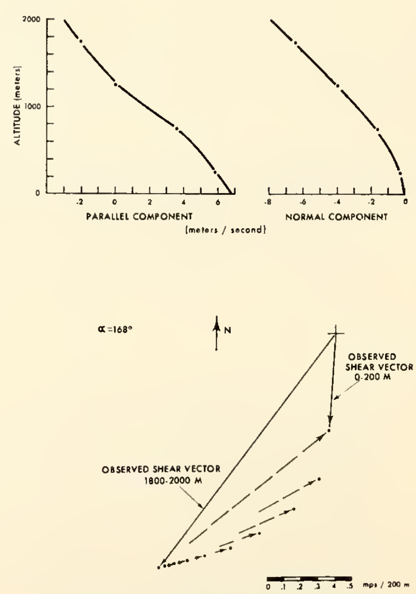

Fig. 4
Wind components in the equatorial boundary layer and associated shear vector. The mean azimuth of the surface wind is 168°.

except that the turning of the stress vector with height is not quite so great as for the first group, and that its magnitude goes smoothly to zero at 2000 m.

The third group, with a mean surface wind azimuth of 146° (fig. 5), again is very similar to the other two except that the wind shear is not as great. Although the slope of the profiles appears to be the same or greater than the others, the wind scale has been expanded by a factor of two. The observed shear still increases with height, however the stress vector has practically no curvature, but again goes smoothly to zero at 2000 m.

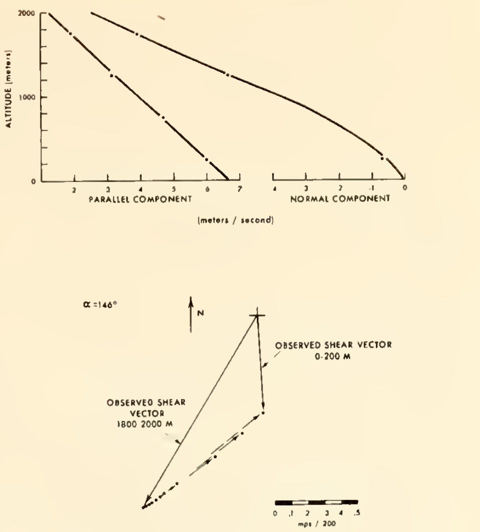

Fig. 5
Wind components in the equatorial boundary layer and associated shear vector. The mean azimuth of the surface wind is 146°.

Figure 6 shows the mean wind profiles of the fourth group in which the mean surface wind azimuth approaches that of the upper winds, and the wind speed varies

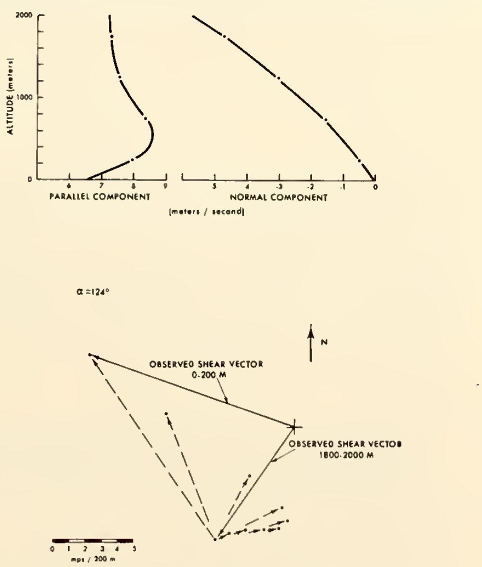

Fig. 6
Wind components in the equatorial boundary layer and associated shear vector. The mean azimuth of the surface wind is 124°.

relatively little, particularly in the parallel component. The observed shear decreases with height which is something new and there is some doubt that the 1800—2000 m shear vector is the appropriate one to define as the thermal wind since the stress vector turns first to the right and then to the left with height. Directional consistency may be preserved if the top of the boundary layer is taken to be approximately 1200 m, and the curvature in the upper part of the profile is assumed to be due to vertical variating in the equatorial thermal wind. It is possible to reach the same conclusion by considering the idea that the direction of the stress vector is the lowest 200 m of the boundary layer (the first shear vector) should be roughly the same as that of the surface wind. If the top of the boundary is taken as approximately 1200 m, then the azimuths of the two vectors agree quite well.

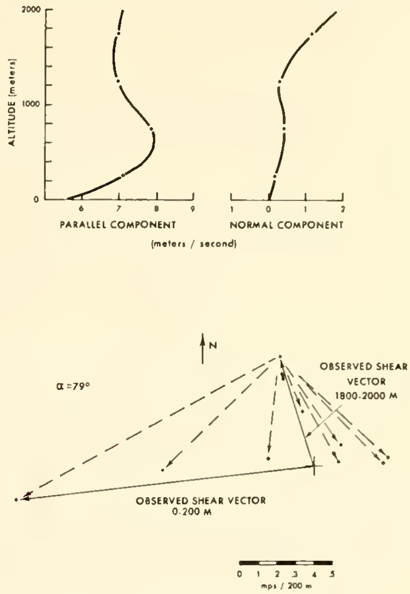

Fig. 7
Wind components in the equatorial boundary layer and associated shear vector. The mean azimuth of the surface wind is 79°.

The fifth group (fig. 7) has generally the same profile curvature for the parallel component, but a quite different normal component. The direction of turning is generally to the right, with the shear increasing with height, although the mean shear over the 2000 meter height interval is quite small. There is again some doubt that the 2000 m level is in fact the top of the boundary layer, the azimuth of the near-surface stress vector becomes 80°, again in good agreement with the surface wind direction.

We may summarize the so-called stress vectors on one diagram (fig. 8) and examine the vertical variation of the shearing stress. To a certain extent this is illusory because the shift from a shear vector to a stress vector involves the unknown eddy dynamic viscosity. In a limited situation such as this one cannot hope to do better than to apply uniformly a typical value, and this has in fact been done. This scheme has some merit however, since it allows comparison with shearing stress values obtained in other experimental situations. The typical value incidentally was 15000 cm²/sec for the eddy dynamic viscosity or Austaugh coefficient, or alternatively 0.4×10^{-3} for the shear stress coefficient The surface stress values obtained here, ranging from 0.12 to 0.28 dynes/cm², are of a reasonable magnitude and compare quite well to those found by Charnock at Anegada, under presumably similar conditions, but from the geostrophic departure method. The peculiar inflection point at about 800 meters in two of the profiles is directly related to the previously mentioned possible error in the height of the boundary layer, and would disappear if the height were adjusted.

Returning now to the equatorial thermal shear mentioned previously, it became apparent in this study that the surface wind direction was highly sensitive, in a predictable manner, to variations in the surface temperature. Figure 9 shows the surface wind direction as a function of the observed station temperature, and

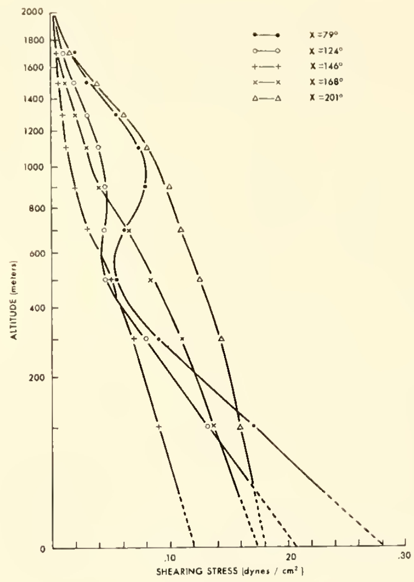

Fig. 8
Vertical variation of the stress vector for the five separate groups. The values shown represent the difference in shear between any level and the top of the boundary layer.

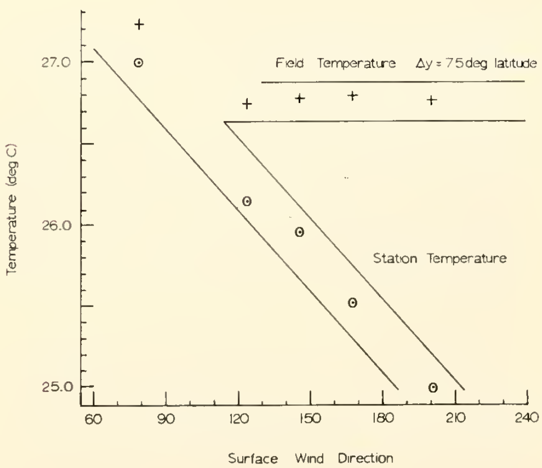

Fig. 9
Conjectural field temperatures (see text) as a function of observed mean surface temperatures and mean surface wind directions.

it is quite evident that the direction veers by roughly 60° for every degree centigrade decrease in the station temperature. For surface temperature near 27° C (the climatological mean value), the surface wind direction is approximately parallel to that at the top of the boundary layer, while by extrapolation for a temperature of 24° C, the surface wind is oppositely directed to the upper winds. One can obtain an analytic expression for the horizontal wind in equatorial regions by differentiating the geostrophic relationship with respect to latitude. If both the horizontal wind shear and the horizontal density gradient are small, the result is an equatorial wind, analogous to the geostrophic wind, with β as the angular parameter and $\delta p/\delta y$ as the stream function. It is possible to obtain the vertical variation of this equatorial wind in terms of the horizontal variation of $\delta p/\delta y$, which may then be related to the vertical temperature structure. The salient parameter is $\delta^2 T/\delta y^2$ interpreted as a local deviation from a linear meridional temperature gradient in the equatorial region. The sense of the relationship is such that a local hot spot will produce an eastward directed shear, that is, the wind at height is more westerly than at the surface, while a local cold spot will produce a westward directed shear, that is, the wind at height is more easterly than at the surface. The magnitude of the zonal shear is proportional to the relative intensity of the temperature deviation.

If now the second derivative is replaced by a finite difference, and as a first approximation it is assumed that the observed station temperatures are the result of a uniform but unknown field temperature minus a deviation due to local causes, then the local deviation, over a suitable horizontal distance, is the only unknown in the equatorial thermal wind equation. This scheme has been applied to the zonal components of the five individual thermal shear vectors with the results shown in the same figure. With a horizontal scale of 7.5 degrees of latitude — roughly the dimensions of traveling disturbances in tropical regions — the computed deriation in each case brings the field temperature to an approximately uniform value, which is a gratifying result in itself. In addition, this value is quite close to the climatological surface temperature of the region under consideration.

In conclusion I would like to state that the analysis presented here suffers greatly from lack of supporting data. On the other hand it seems reasonable to conclude that the structure of the boundary layer in equatorial regions is not very much different from that in mid-latitudes, and that even if the geostrophic departure method of obtaining the shear stress vector is invalid at the equator, the free air wind vector, the stress vector, and the boundary layer all retain theier normal meaning.

It should also be remembered that this has been a heuristic examination — that the conclusions follow from the assumptions, and that only the similarity between deduction and observation can be pointed out. One can only hope that future expeditions will have the foresight to plan for detailed enough appropriate observations so that the relationships suggested here may be adequately tested.

References

(1) JOHNSON, W. B., Jr.: Climatology of atmospheric boundary layer parameters and energy dissipation. Studies of the three-dimensional structure of the planetary boundary layer. Dept. Meteor. Univ. Wisconsin (1962).

(2) LETTAU, B.: Thermally and frictionally produced wind shear in the planetary boundary layer at Little America, Antarctica. Monthly Wheater Rev. 95 (1967) S. 9.

(3) CHARNOCK, H.; FRANCIS, J. R. D.; SHEPPARD, P. A.: An investigation of wind structure in the trades. Phil. Trans. Roy. Soc. London A 249 (1956).

(4) BUNKER, A. F.: A low-level jet produced by air, sea, and land interactions. In: Proc. Sea-Air Interaction Conference, Tallahassee, Florida. Techn. Note 9-SAIL-1 (1965).

(5) LETTAU, H. H.; HOEBER, H.: Über die Bestimmung der Höhenverteilung von Schubspannung und Austausch-Koeffizienten in der atmosphärischen Reibungsschicht. Beitr. Phys. Atmosph. 37 (1964) S. 2.

(6) ROLL, H. U.: Physics of the marine atmosphere. New York (1965).

MONTHLY WEATHER REVIEW
VOLUME 97, NUMBER 9
SEPTEMBER 1969

UDC 551.511.2

ON THE KINETIC ENERGY SPECTRUM NEAR THE GROUND

ABRAHAM H. OORT
Geophysical Fluid Dynamics Laboratory, ESSA, Princeton, N.J.
ALBION TAYLOR
Atlantic Oceanographic Laboratory (SAIL), ESSA, Silver Spring, Md.

ABSTRACT

For six stations in the northeastern United States, the spectrum of horizontal wind speed was analyzed using 10 yr of 1-min averaged, hourly surface reports. The fast Fourier transform technique was employed to estimate the spectrum between 1 cycle/2 hr and 1 cycle/2 yr.

The kinetic energy spectra show two major spikes at periods of 24 hr and 1 yr. However, most of the energy is contained in the traveling cyclones and anticyclones with periods between 2 and 7 days. The apparent discrepancy between Van der Hoven's results and our results concerning the existence of an important diurnal cycle in the kinetic energy can be explained by Blackadar's theory of the diurnal wind variation with height. Van der Hoven's spectrum represents conditions near the top of the surface layer, while our data were taken well within the surface layer. A line-by-line investigation of the diurnal peak reveals a very sharp line at 2400 hr with two side lobes 3.9 min away from the main line. These side lobes are probably caused by an annual modulation of the diurnal cycle.

The spectra tentatively corrected for aliasing give some indication of the existence of a spectral gap between small-scale turbulence and mesoscale phenomena.

1. INTRODUCTION

Van der Hoven (1957) made a detailed analysis of the power spectrum of the horizontal wind speed in which he analyzed measurements taken at Brookhaven National Laboratory, Long Island, at a height of about 100 m. By piecing together various sets of observations, he was able to present a composite picture of the contribution to the total variance of the wind speed from different frequency ranges. The kinetic energy spectrum thus determined covered periods from 4 sec to about 2 mo. He convincingly showed that most of the variance of the wind speed can be explained by the passage of large, synoptic scale pressure systems with periods of about 4 days. Turbulence of the order of minutes also gave some contribution, although it was much smaller. However, between these two regions he found a broad section of the spectrum centered near the period of 1 hr with very little energy connected with it; this last portion of the spectrum was therefore called the "spectral gap" region. His analysis further showed a small rise in the spectrum for periods of about 12 hr, but surprisingly there was not much energy near the 24-hr period.

More recent investigations by Bysova et al. (1967) using 40 hr of wind speed data from a 300-m tower at Obninsk (U.S.S.R.) also show a pronounced minimum in the spectrum between the turbulent and mesometeorological wind fluctuations.

Recently, 10 yr of hourly wind records have become available on magnetic tape for several weather stations in the United States. This made it feasible to repeat and extend Van der Hoven's analysis to include the spectrum from periods of a few hours up to a few years. Another contributing factor was the advance in data analysis made possible by the introduction of the "fast Fourier transforms" (FFT), recently developed by Cooley and Tukey (1965) for calculating the Fourier components directly from a long time series in very little computation time. This practically eliminates the difficulties connected with the piecing together of various portions of the spectrum.

In contrast to Van der Hoven's work, our analysis shows a major spike in the wind spectrum at a period of 24 hr. Therefore, an important part of this paper will be concerned with an investigation of the diurnal variability in the kinetic energy.

2. DATA AND DATA ANALYSIS

In 1965, records of hourly surface data for several U.S. stations covering the period Jan. 1, 1949, through

Dec. 31, 1958, were stored on magnetic tape at The Travelers Research Center, Inc., Conn., under contract for the U.S. Air Force.

DATA

A group of three stations (Caribou, Old Town, and Portland) in Maine, representing the northeastern part of the United States, and another group in the Great Lakes Region (Detroit and Sault Sainte Marie, both in Michigan, and Duluth, Minn.) have been investigated. The climate at all of these stations is influenced to a high degree by the proximity of water, with the exception possibly of Caribou. As we shall see later, there appear to be no major differences in the shape of the spectrum at the stations considered. Therefore, in this paper we have arbitrarily selected Caribou for a more detailed study. In a future study we intend to include other groups of stations having a more continental climate as well as stations at a lower latitude.

TABLE 1.—*Climatological information from "Local Climatological Data—With Comporative Data" published by the U.S. Weather Bureau (1958)*

	Station identification	Lat. (° N.)	Long. (° W.)	Station elevation above sea level (ft)	Wind instruments above ground (ft)	Reported changes in exposure of wind instruments
Caribou, Maine	CAR	46.9	68.0	620	33	none
Old Town, Maine	OLD	44.9	68.7	124	27	(1)
Portland, Maine	PWM	43.7	70.3	61	55	none
Detroit, Mich	DET	42.4	83.0	619	81	none
Sault Ste. Marie, Mich.	SSM	46.5	84.4	721	33	(2)
Duluth, Minn	DLH	46.8	92.2	1409	55	(3)

[1] We could find no reports on the height of the wind instruments before 1954. It is, however, more likely that the height was not changed during the 10 yr of record.

[2] On June 15, 1949, the wind instruments were relocated on another building. The elevation above ground was changed from 43 ft to 33 ft on the same date.

[3] On July 1, 1950, the wind-recording equipment was moved from the city to the Duluth Airport.

The wind observations were taken 1 hr apart and represent 1-min averages. The height of the wind sensor is not the same for all stations but varies from 30 to 80 ft above the ground. Other factors that make the results for the different stations not strictly compatible are 1) differences in station elevation above sea level and 2) differences in exposure of the wind sensor due to, e.g., neighboring buildings. In some cases the location of the wind sensor was appreciably changed during the 10 yr of record. However, we have included all 10 yr in our analyses.

Although Caribou is located only 150 mi from the Atlantic coast, its climate can be classified as a typical continental type. Old Town and Portland have an "east coast" maritime climate; the winds are generally light.

The climate of the group of stations in the Great Lakes Region has some maritime characteristics because of the location of the stations close to the Great Lakes. Rather frequent changes in the weather pattern occur, since nearly all atmospheric disturbances that move eastward across the country pass close enough to affect the weather.

Further climatological information is given in table 1.

DATA ANALYSIS

In the present study we are interested in the contribution from different frequency bands to the variance of the horizontal wind speed (i.e., in the kinetic energy spectrum). The contribution from each frequency range is estimated by calculating the sum of the squares of the coefficients in the cosine and sine transforms (the Fourier coefficients) at the particular frequency. Recently a method for efficiently computing these coefficients, called the fast Fourier transform (FFT), has been reported by Cooley and Tukey (1965). This method produces savings of up to 99 percent of computer time over conventional methods of finding the Fourier coefficients. The FFT apparently not only reduces the computation time but also slightly reduces round off errors associated with these computations. The computation time is reduced by a factor of $(\log_2 N)/N$ where N is the number of data points in the time series (Group on Audio and Electroacoustics (G–AE) Subcommittee on Measurement Concepts, 1967). For further details the reader is referred to the papers in a special issue of the *IEEE Transactions on Audio and Electroacoustics* (June 1967), entitled "On Fast Fourier Transform and Its Application to Digital Filtering and Special Analysis."

A fast Fourier transform subroutine was coded for the Univac 1108. This subroutine replaces a time series of length 2^m (m an integer) with the Fourier coefficients for the time series. Since the maximum value of m allowed by the program equals 14, the time series may contain a maximum of 16,384 data points. In the case of hourly data, one can analyze a series of at least 1 yr in one pass (8,760 points). In order to analyze a series of 10 yr, we shall replace the values in the original time series by the averages over 6 hr. The number of data points is then reduced from 87,600 to 14,600.

Because of the finite length record, it is impossible to resolve Fourier coefficients corresponding to frequencies separated by less than a certain amount. This limit of resolution measured by ΔF has the value of 1 over the period of the entire data record, i.e., 1 cycle/1 yr or 1 cycle/10 yr, according to whether a 1-yr or a 10-yr period is being analyzed.

In order to clarify these statements, let us follow the reasoning given by Bingham et al. (1967, pp. 57–58). The finite Fourier transforms resolve exactly any combination of sine terms and cosine terms of frequencies F_0, F_1, F_2, . . . , F_j, . . . $(=0, \Delta F, 2\Delta F, \ldots, j\Delta F \ldots)$. Thus, if a component $c_j \cos(2\pi F_j t+\phi_j)$ were added to the time series, the transform would be affected in the coefficients a_j and b_j (the coefficient a_j would be replaced by $a_j+c_j \cos \phi_j$, and b_j by $b_j+c_j \sin \phi_j$), but the other coefficients a_k and b_k, where $k\neq j$, would not be affected. However, if a component $c \cos(2\pi Ft+\phi)$ were added to the time series, with F *not* equal to one of the F_j, all Fourier coefficients would be affected by an amount proportional to $(|F-F_j|/\Delta F)^{-1}$ for $|F-F_j|>2\Delta F$. Thus the influence of a sinusoidal term at frequency F is largest for frequencies F_j nearest F, although its influence extends to coefficients at frequencies F_j many times ΔF away. This "spill-over" of the influence may be decreased by decreasing ΔF (which means considering longer records).

Another means of sharpening the resolution lies in a filtering procedure known as "hanning" the Fourier coefficients (see Blackman and Tukey, 1958, pp. 14–15). This may be done directly by applying the hanning weights $-\frac{1}{4}$, $\frac{1}{2}$, $-\frac{1}{4}$ to the coefficients at frequencies $F-\Delta F$, F, $F+\Delta F$, respectively, or indirectly by multiplying the original time series by a *data window* function before processing the data. If the time t runs from 0 to T, a data window can be obtained by multiplying the data series by a cosine bell:

$$(1-\cos 2\pi t/T)/2.$$

This curve has a maximum value of 1 in the middle of the series and falls off smoothly to 0 at the beginning and at the end of the series. After applying the window, the influence of a sinusoid of frequency F on the other coefficients tends to $(|F-F_j|/\Delta F)^{-3}$ for $|F-F_j|>4\Delta F$. That is, the influence of a line at frequency F is now restricted to a smaller neighborhood of that frequency.

Prior to applying the data window, the mean of the series and a least-squares linear trend were computed and subtracted from the series. The presence of such long-term variations would tend to bias the spectrum by introducing extra variance in the lower frequencies.

After the data were conditioned by the mean and trend removal and by the data window, the time series was extended by adding sufficient zeros to attain the number of 2^{14} data points required by the subroutine. As a result, the number of Fourier components computed increased from half of 8,760 (or half of 14,600) to 8,193 at frequencies that divide the frequency interval $0\leq F \leq 1/(2\Delta t)$ into 8,192 equal parts (in our case Δt equals 1 hr or 6 hr). Thus, we have an apparent increase in resolution over this interval. The increase in resolution is not real, however, since the Fourier coefficients are no longer independent, but must be related to each other in such a manner as to produce the extra zeros. This introduces an interaction between components similar to the spill-over mentioned above and emphasizes the need of hanning the data with the cosine bell.

A plot of the individual power estimates versus frequency will in general be very "rough" showing many individual small peaks. Often, the location and magnitude of these peaks is climatologically insignificant, being due to *sampling fluctuations* rather than any systematic physical interaction. It is thus desirable to average out these peaks to obtain a more useful presentation. Of course, we then give up much detail in resolution. However, with a long time series covering nearly three decades of frequency, the resolution is generally one or two orders of magnitude greater than required in any case.

There are two possible means of performing the averaging to account for sampling fluctuations. One method is to break up the entire record into several parts of equal length, next to compute spectral estimates for each part, and finally to average these estimates at the corresponding frequencies. In effect, this corresponds to taking several samples. An alternative method, which we actually use here, is to calculate the Fourier coefficients and then to average estimates in several frequency bands (Hinich and Clay, 1968). Incidentally, the loss of resolution in the frequency domain produced by this averaging tends to compensate for the fictitious increased resolution produced by the subtended zeros.

In our case, we have split up the frequency scale into about 80 bands. We distributed the band limits according to a logarithmic scale between the lowest and highest frequencies attainable. The lowest frequency is evidently $1/(N\Delta t)$, and the highest (the Nyquist or folding) frequency $1/(2\Delta t)$, where N is the total number of observations and Δt is the time interval between observations. For example, for a 10-yr record the resolution in the vicinity of 1 yr is about one-tenth of a year or 36 days; however, near periods of 1 day the resolution is approximately 1/3650 day or 24 sec. In our logarithmic scale with 80 bands, the power in the band near 1 day represents the average over several hundred individual estimates (see table 3 in the Appendix), while in the bands near 1 yr only one or two estimates are included.

In order to have some assurance that significant information is not being averaged out along with variations due to sampling fluctuations, some form of *confidence statistics* would be useful. If the individual estimates within each band are distributed very tightly around the mean for the band, more confidence would be attached to that mean than if the individual estimates were widely scattered. Again, more confidence is attached to a mean if many estimates are used to compose it.

A statistic with these properties is given by

$$\mathrm{DF}=n\, M^2/(M^2+V)$$

where n is the number of estimates in the band, M is the mean, and V the variance. The quantity DF is referred to as the number of *equivalent degrees of freedom* and, according to Blackman and Tukey (1958, pp. 21–25) the chi-square distribution with DF degrees of freedom has the same mean-variance relation as the estimates in that band.

It should be emphasized that a low number of degrees of freedom does not mean that the data in this band is unreliable, but merely that the computed mean does not represent the estimates in the band very well. Thus, if resonance, for example, produces a very large, narrow peak inside the band, say at the 24-hr period, the degrees

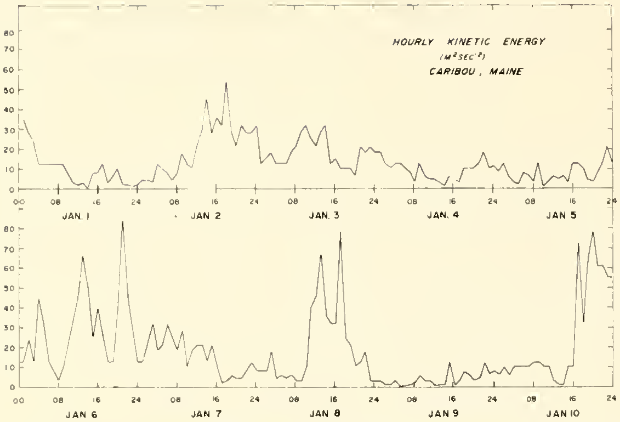

FIGURE 1.—Hourly kinetic energy at Caribou, Maine, for the first 10 days of January 1949.

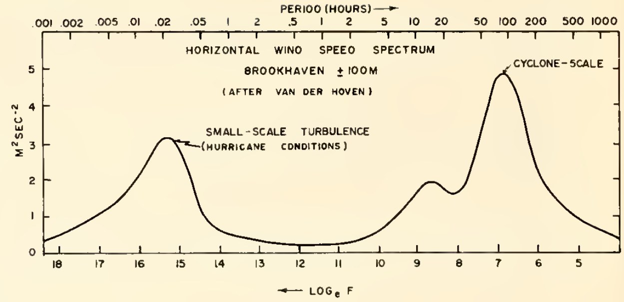

FIGURE 2.—Spectrum wind speed at Brookhaven National Laboratory, Long Island, at about 100-m height (after Van der Hoven, 1957). Frequency F in cycles/4096 days.

TABLE 2.—*Spectral intensity in small-scale turbulence maximum as a function of roughness length*

		Caribou	Old Town	Portland	Detroit	Sault Ste. Marie	Duluth
z	(ft)	33	27	55	81	33	55
V	(m sec^{-1})	5.75	3.85	4.59	4.95	4.61	6.35
$(P\times F)_{max}$	(m^2 sec^{-2}) (z_0=20 cm)	.36	.18	.18	.17	.23	.34
$(P\times F)_{max}$	(m^2 sec^{-2}) (z_0=50 cm)	.60	.31	.28	.26	.39	.53
$(P\times F)_{max}$	(m^2 sec^{-2}) (z_0=100 cm)	1.00	.54	.42	.38	.64	.82

z =observation height above ground.
V =mean horizontal wind speed.
$(P\times F)_{max}$ =product of power density and frequency in small-scale turbulence maximum.
z_0 r=oughness length.

of freedom estimate for that band is sharply reduced (see, e.g., table 3 in the Appendix of this paper). In such cases a close, line-by-line examination of this band may be indicated.

3. THE ALIASING PROBLEM

As mentioned earlier, the reported wind speeds represent 1-min averages and are spaced 1 hr apart. Figure 1 shows a plot of the reported hourly kinetic energy for Caribou, Maine, for the first 10 days of January 1949. The graph gives evidence of high-frequency fluctuations in the data.

This intuitive conclusion is backed up by Van der Hoven's results at Brookhaven (fig. 2) which show that the energy in wind fluctuations below 2 hr cannot be neglected. The power in the frequency range between 1 cycle/2 hr and 1 cycle/1 min causes an aliasing problem. However, the aliasing is not as bad as it might appear from figure 2. The observations in the high-frequency part of the spectrum were taken during the passage of a hurricane near Brookhaven. A more normal situation would certainly give lower values for the maximum in the minute range; a maximum value between 0.5 and 1.0 m^2 sec^{-2} might be expected (table 2) instead of the value of 3.0 m^2 sec^{-2} shown in figure 2.

In the present data sample the power in the nonresolvable frequencies between 1 cycle/2 hr and 1 cycle/1 min is added to and cannot be distinguished from the real power in the resolvable range of frequencies between 1 cycle/10 yr and 1 cycle/2 hr. The higher frequencies that are aliased into a resolvable frequency F are:

$$2F_N-F, 2F_N+F,\ 4F_N-F,\ 4F_N+F,\ 6F_N-F,\ 6F_N+F, \text{ etc.,}$$

where F_N=Nyquist or folding frequency=1 cycle/2 hr. For example, the power in periods of approximately 72, 51, 33, 28, 21, 19, 15.6, 14.4, 12.4, 11.6, 10.3, 9.7, 8.8 min, etc. will be added to the power in a period of 6 hr.

Before going into more detail, let us first discuss the form in which the spectra in this paper will be presented. For each frequency band, the value of the product of the mean power density (P) and the mean frequency (F) will be plotted as the ordinate and the natural logarithm of the mean frequency ($\log_e F$) as abscissa. This commonly used scale gives perhaps a better illustration of the contribution of the various ranges of meteorological interest than a curve of simply the mean power density versus the frequency. In both cases, the area under the curve between the two frequencies F_1 and F_2 gives that portion of the total variance (kinetic energy) that is explained by phenomena in this frequency range

$$\int_{\log_e F_1}^{\log_e F_2} (P\times F) d \log_e F = \int_{F_1}^{F_2} P\, dF.$$

In our graphs we chose to let the frequency decrease from left to right, in order to have the time scale increase in that direction.

Let us assume that the aliased part of the spectrum between 1 cycle/1 min and the folding frequency of 1 cycle/2 hr resembles *white noise*, i.e., the power is not a function of frequency. The effect of aliasing will then be to add to the true power between the folding frequency and 1 cycle/2 yr a constant amount, independent of frequency. Aliasing as described above is, of course, independent of the way in which the spectrum is represented. However, different representations of the spectrum might give different impressions of the effect of aliasing. In the graphs in this paper, the product of the power and the frequency (not the power itself) is plotted along the y-axis. Each time that one decreases the frequency by e (in other words, the value of the x-coordinate in the graphs is decreased by 1), the contribution to the y-coordinate (power $\times$ frequency) due to aliasing will decrease by e, simply because the frequency decreases by e. Thus, the effects of aliasing tend to show up mostly near the folding frequency of 1 cycle/2 hr. If the true spectrum were to show a *decrease* of power with increasing frequency near the folding frequency instead of being independent of frequency, the effects of aliasing would be still more concentrated near this frequency.

For a better understanding of the aliasing effect, we have performed two experiments for Caribou, Maine. In the first experiment we used all hourly surface reports and analyzed the spectrum in the range from the Nyquist frequency of 1 cycle/2 hr up to 1 cycle/2 yr. In the second experiment we only used one observation every 6 hr and could, therefore, determine only the spectrum between the new Nyquist frequency of 1 cycle/12 hr and 1 cycle/2 yr. In this last experiment, the power between 2 hr and 12 hr is aliased further into the rest of the spectrum. The results shown in figure 3 indicate that most of the distortion is confined to the spectrum in the vicinity of the Nyquist frequency, i.e., to the range from 12 hr up to about 2 days. In the next section we shall make use of this result in order to make a rough correction to the spectrum of Caribou for the effects of aliasing from the range of periods of 1 min to 2 hr.

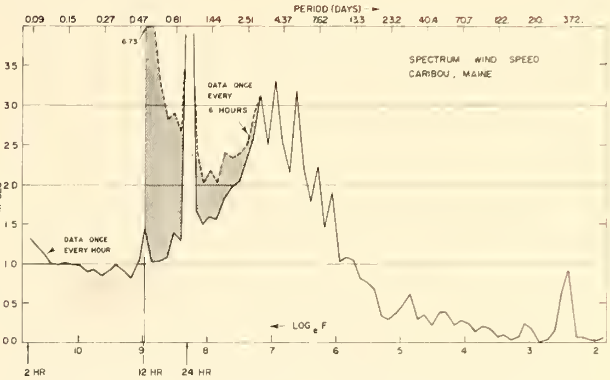

FIGURE 3.—Example of the effects of aliasing on the wind speed spectrum. Dashed line gives the spectrum at Caribou, Maine, if power between 2 and 12 hr is aliased. Frequency F in cycles/4096 days.

4. THE KINETIC ENERGY SPECTRUM

In this section, power spectra of the surface wind speed will be presented which cover cycles from 1 cycle/2 hr to 1 cycle/2 yr. A split up of the spectral analysis in two parts was necessary because of the limitation in the total number of data points in the computer program for the fast Fourier transform.

METHOD OF ANALYSIS OF THE SPECTRUM

The spectrum for periods of 24 hr and up was obtained by an analysis of the 10 yr of record. The hourly data were first averaged over nonoverlapping 6-hr intervals. Next, these 6-hr averages were used as input data for estimating the spectrum from 12 hr and up. The averaging process reduces the amplitude of each wave in the spectrum by

$$R(F)=\sin(\pi FT)/(\pi FT)$$

where $R(F)$=the response function for a wave with frequency F, F=frequency in cycle/hr, and T=the filtering interval=6 hr (Holloway, 1958). The original spectral power was restored by multiplying the computed power at each frequency by $1/R^2(F)$.

The spectrum for periods between 2 hr and 1 day was obtained by analyzing each year of the 10 yr of record separately and then averaging the spectral estimates thus obtained. In general, the effects of aliasing are most severely felt in this part of the spectrum, i.e., close to the Nyquist frequency.

THE HIGH FREQUENCY PART OF THE SPECTRUM

Our concern at this point is to estimate what the most probable shape of the spectrum will be between periods of 2 hr and 1 min. Since Van der Hoven made his study, further evidence has been accumulated that there exists a broad gap in the spectrum. For example, Bysova et al. (1967) analyzed a continuous record of 40 hr of wind velocity fluctuations measured at Obninsk (U.S.S.R.). Their analysis shows at all levels (25, 75, 150, and 300 m) a pronounced spectral gap between periods of about 15 min and 7 hr. This gap, which separates the mesoscale phenomena (periods of the order of a few hours) from the high-frequency turbulence (periods of the order of minutes), appears to be centered at a period of about 1 hr.

The value of the high-frequency maximum of $P\times F$ can be estimated using a general relationship found by Busch and Panofsky (1968) for the maximum

$$(P\times F)/u^{*2}\simeq 1$$

where u^*=friction velocity=$kV/(\log_e z/z_0)$ in neutral air, k=von Kármán constant=0.4, z_0=roughness length, z=height observation above ground, and V=mean wind speed. For simplicity, effects of stability have been neglected in the formula for the friction velocity. Table 2 gives the calculated values of $P\times F$ in this maximum, assuming several different values of the roughness length.

In the case of Caribou, we rather arbitrarily selected a value of 0.8m^2 sec^{-2} in the high-frequency maximum

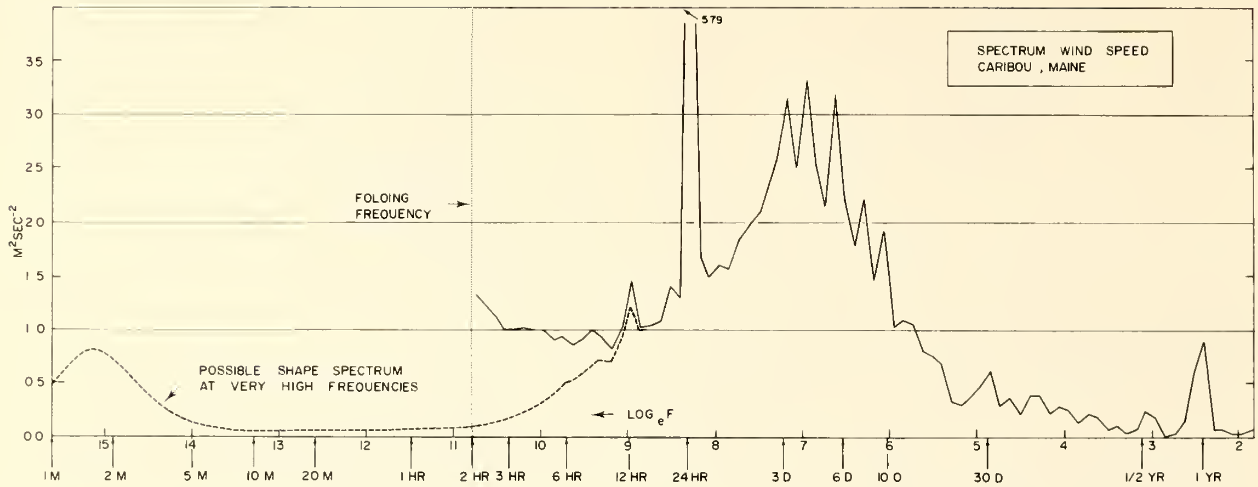

FIGURE 4.—Results of an attempt to correct the spectrum at Caribou, Maine, for the effects of aliasing from periods between 1 min (the basic averaging period of the wind reports) and 2 hr (the Nyquist frequency). Frequency F in cycles/4096 days.

corresponding with a roughness length between 50 cm and 100 cm. The location of the maximum does not seem to be very well fixed. For higher wind speeds it generally shifts to higher frequencies. Again arbitrarily, but perhaps not unreasonably, we selected a location of about 1 cycle/2 min. Having fixed the height and the location of the high-frequency maximum, we drew freehand a hypothetical line for the "true" spectrum (see dashed line in fig. 4). This line gives our estimate of how the spectrum would look if measurements were available for 10 yr with a 1-min instead of a 1-hr separation. In drawing the dashed curve, we used the following guidelines:

1) The conservation of variance of the wind speed. In other words, the area under the dashed curve between the basic averaging frequency of the data (1 cycle/ 1 min) and the folding frequency F_N (1 cycle/2 hr) should be approximately equal to the area between the solid (computed) and dashed curves to the right of F_N.

2) The assumption of an approximately white power distribution in the aliased portion of the spectrum to the left of F_N. The contribution to the spectrum at the right of F_N due to aliasing will then decrease by e, if F decreases by e (see discussion in section 3). This consideration rather limits the range of acceptable possibilities in drawing the true spectrum curve to the right of F_N. If one would assume, e.g., significantly more power to the left of F_N than is done in figure 4, the dashed curve would become negative near the folding frequency—an impossible situation. After having drawn the dashed curve in the way described, the total amount of aliased power is directly determined. However, considerable freedom is still left in constructing the shape of the spectrum between the folding frequency and 1 cycle/1 min; more information is needed.

3) The assumption of the existence (which seems to be well proved, Busch and Panofsky, 1968) and next of the magnitude and location of the high-frequency maximum as tentatively derived above in table 2. Finally, one can infer that very little energy is left to be distributed between the high-frequency maximum and the folding frequency.

Although our method of estimating the true spectrum is of course very approximate, the final curve in figure 4 shows that our results using a very long time series are certainly compatible with the existence of a spectral gap in the vicinity of 1 cycle/2 hr.

DETAILED DISCUSSION OF THE SPECTRUM

Starting on the left side of figure 4 for Caribou, Maine, one notices first the rise in the spectrum in the vicinity of a period of 2 min due to small-scale turbulence with a maximum value of 0.8 m^2 sec^{-2}. Then there follows the spectral gap region with intensities of the order of 0.1 m^2 sec^{-2} or less between roughly 10 min and 2 hr. Next, in the range from 2 hr up to 2 days, the level of activity starts to rise from the low values in the spectral gap up to a very high level in the "cyclone rise."

Superposed on this part of the spectrum is a minor peak at 12 hr and a major peak at 24 hr. A high, broad plateau of activity of about 3 m^2 sec^{-2} connected with the traveling cyclones and anticyclones is found at periods between approximately 2 and 8 days. After this, the level of activity drops quite rapidly and shows only minor (probably not significant) bumps near periods of 1 and 2 mo. Finally, we reach periods of one-half and 1 yr where again important peaks are found.

A striking feature of the "cyclone rise" is the appearance of spikes. By making the resolution coarser (or by a little smoothing on the spectrum) it is relatively easy to get rid of the spikes. However, we think the picture as it is may give the reader more insight into the inaccuracies (or rather the effects of sample fluctuations on the spectrum). These fluctuations play a role even when one analyzes a very long sample such as 10 yr of data. It is clear that one should not interpret the peaks (at 3.1, 3.9, and 5.5 days) as true periodicities comparable to the diurnal and annual periods or to their higher harmonics. If one looks at the hundreds of individual power estimates that make up each peak, one soon realizes that each band consists of a large number of peaks and valleys. The high average value in a band means only that the general level of activity is high in that portion of the spectrum. If one studies the spectra for individual years, spikes seem to occur each year but not necessarily at the same frequencies. Averaging of the 10 individual years would largely smooth out these spikes.

F n more detailed information on the spectrum for Caribou, e.g., the number of equivalent degrees of freedom for each band, the reader is referred to table 3 in the Appendix.

In figure 5, the measured kinetic energy spectra for the six stations considered in the present study are plotted, both with (full line) and without (broken line) applying a correction for aliasing. The area under each solid curve was normalized; and, because the total variance is not the same for the different stations, the scale along the y-axis is also different. The general shape of these spectra is quite similar, in spite of apparent differences in detail. For example, in the case of Caribou and Duluth the intensity in the cyclone rise appears to be much larger than in any of the other stations. On the other hand, Detroit shows an exceptionally pronounced annual cycle.

The *intensity in the cyclone rise* for Caribou and Duluth has a value between 2 and 3 $m^2 sec^{-2}$, while for the other stations the intensity is only 1 to 1.5 $m^2 sec^{-2}$. According to the description in the *Local Climatological Data—With Comparative Data* (U.S. Weather Bureau, 1958), Caribou Airport is located on the top of high land which is about on the same level as most of the surrounding, gently rolling hills. The exposed location of this airport probably causes the greater activity in the cyclone and anticyclone scale, while in the case of Duluth Airport the large value must be related to its high elevation above sea level (see table 1). The differences in intensity can thus be explained by assuming that the observations at Caribou and Duluth are more representative of the conditions at higher levels in the atmosphere.

One can expect that, in general, the *annual period* in the kinetic energy will show up most prominently at continental stations and at stations located at high latitudes. Since the six stations considered in this study are located in a relatively narrow latitude belt between 42° N. and 47° N., only the effect of continentality might be noticeable. However, there is no clear indication of this effect in the graphs given in figure 5, possibly because the stations are all located close to either the Atlantic Ocean or to the Great Lakes.

One other important point is that—if one allows for the effects of aliasing (see dashed curves in fig. 5)—all spectra tend to show low values near the Nyquist frequency of 1 cycle/2 hr.

COMPARISON WITH VAN DER HOVEN'S RESULTS

If we compare figures 2 and 4, good qualitative agreement is generally found between the spectrum at Brookhaven, Long Island, determined by Van der Hoven, and our spectrum for Caribou, Maine. As we have pointed out before, the small-scale turbulence maximum in the minute range has an abnormally large value in the case of Brookhaven, due in part to hurricane conditions present in its determination. The difference in magnitude of the cyclone peak, i.e., 5 $m^2 sec^{-2}$ for Brookhaven and less than 3 $m^2 sec^{-2}$ for Caribou, could be related to the difference in location. However, it appears more likely that it is mainly due to the difference in elevation above ground level at which the observations were taken (respectively, 100 m and 10 m). Another contributing factor may be that Van der Hoven's observations were made during the winter half year, while ours are representative of the entire year.

One important qualitative difference, however, is the surprising lack of a diurnal peak in the Brookhaven data even though there is a semidiurnal peak of comparable magnitude. The most probable reason for this discrepancy lies in the fact that the Brookhaven observations were taken at a height of 100 m, which is near the top of the surface layer (see fig. 6, taken from a report by Singer and Raynor, 1957), while our data represent conditions within the surface layer. Both Van der Hoven's results at the top of the surface layer and our results within the surface layer are in very close agreement with Blackadar's description (1959) of the typical diurnal wind variation with height.

5. THE DIURNAL CYCLE IN THE KINETIC ENERGY

In table 4 (see Appendix) the hourly kinetic energy averaged for each of the 10 yr is given as a function of local time (see also fig. 7). For each station and for each year there is a large and systematic diurnal variation. The maximum value is found between 2 and 3 p.m., and the minimum in the early morning. The phase of this diurnal variation changes rather rapidly with height. Singer's measurements (fig. 6) show that around 120 m the phase of the diurnal cycle is shifted by 180° compared to the phase at the surface. At this height the maximum wind speed is observed at night, and a minimum around midday.

The change of wind speed with elevation and time of the day was clearly explained by Blackadar (1959) as being related to the *coupling* and *decoupling* of the surface and upper layers. Because of the frictional drag exerted

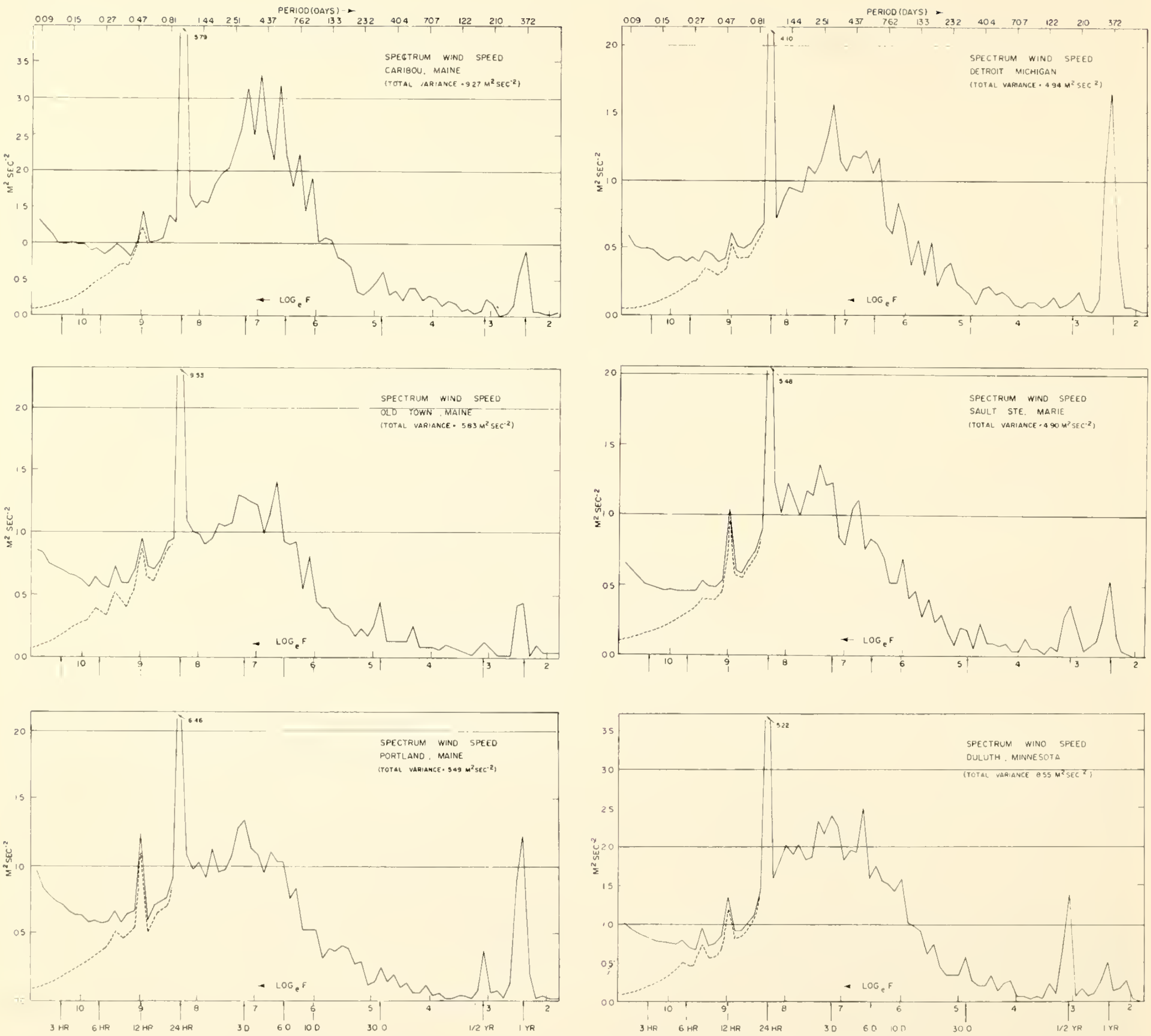

FIGURE 5.—Spectra wind speed determined from 10 yr of hourly wind reports. The dashed curves represent a rough estimate of the spectrum corrected for the effects of aliasing. Frequency F in cycles/4096 days.

on the air by the earth's surface, the wind speed generally increases with height above the ground. During the day, convective mixing will transfer momentum from higher levels to the surface layer. The wind speed in this layer will thus increase until an equilibrium is reached between the supply of momentum from above and the loss due to friction with the earth's surface; but this same process will slow down the upper layers during the daytime. However, at night convective mixing stops; and the surface and upper layers become effectively decoupled by the formation of a temperature inversion. The air near the surface then slows down, while the air in the upper layers speeds up.

The spectra presented by Bysova et al. (1967) for heights of 25, 75, 150, and 300 m seem also to show an important contribution at frequencies near 1 cycle/24 hr, the highest contributions being found at 300 m.

The diurnal variation presented in table 4 for the different stations shows a remarkable variability from year to year. We have the impression that all this variability cannot be explained away by changes in exposure of the wind instruments and that there may well be a

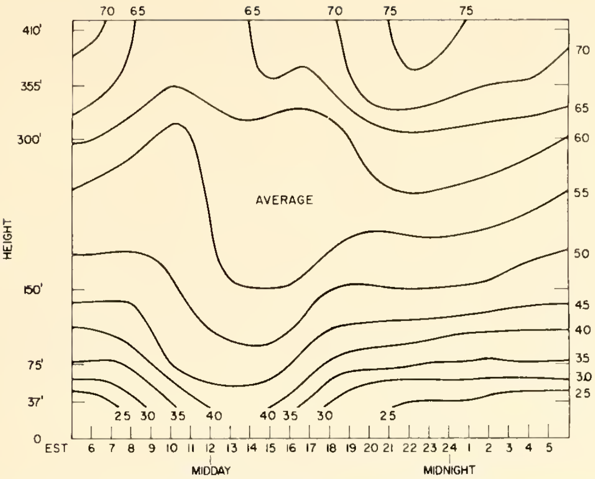

FIGURE 6.—Diurnal variation of wind speed (m sec^{-1}) with height at Brookhaven National Laboratory, Long Island (after Singer and Raynor, 1957).

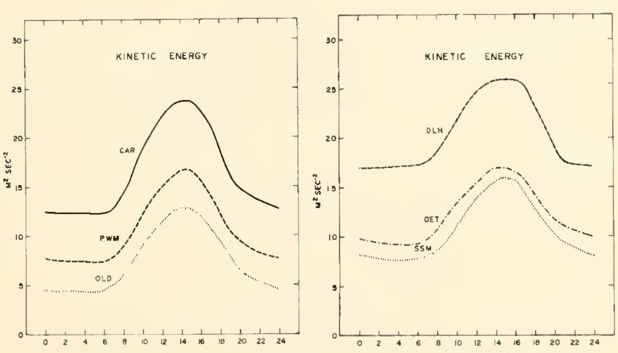

FIGURE 7.—Ten-year average of the kinetic energy as a function of local time at Caribou, Old Town, and Portland, Maine; Detroit and Sault Sainte Marie, Mich.; and Duluth, Minn.

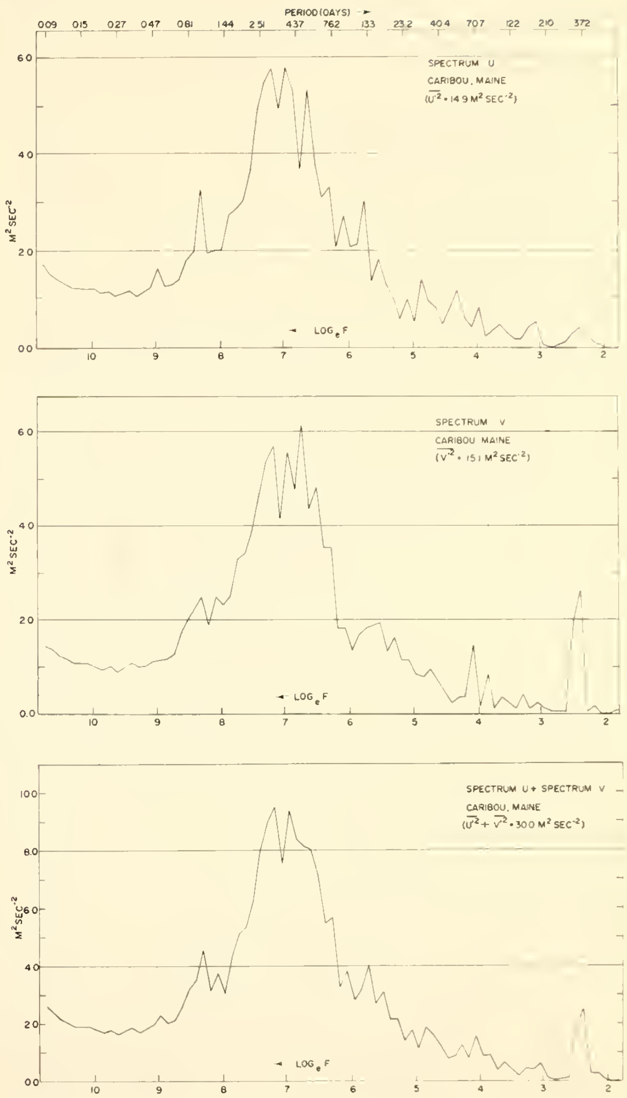

FIGURE 8.—Spectra of the west-to-east (u) and the south-to-north (v) components of the wind for Caribou, Maine, determined from 10 yr of hourly wind reports. Frequency F in cycles/4096 days.

long-term cycle superposed. However, we do not want to pursue this topic further since this is beyond the aim of our present investigation. Our purpose in showing the results for the different years is to make clear that the diurnal cycle shows up in the results for *each* year.

THE LACK OF A DIURNAL CYCLE IN THE SPECTRUM OF THE ZONAL AND MERIDIONAL WIND COMPONENTS

It may be of interest to compare the present results with the spectrum obtained from separate analyses of the west-to-east (u) and the south-to-north (v) components of the wind (fig. 8). In the second type of analysis there is a significant increase (by a factor of 3) in total variance because the wind direction adds a new degree of freedom. However, the most interesting difference (compare figs. 4 and 8) lies in the fact that the diurnal peak does not show more prominently in the u- and v-spectra.

The lack of an important diurnal cycle in the zonal and meridional wind components is indeed very surprising. The interpretation is probably that the wind direction at the stations considered is—at least near the surface—highly variable and that it does not change systematically during the course of a day. The 10-yr mean u- and v-components and the total wind speed as a function of the time of the day are shown in figure 9. If stations with strong land- and sea-breeze effects had been selected

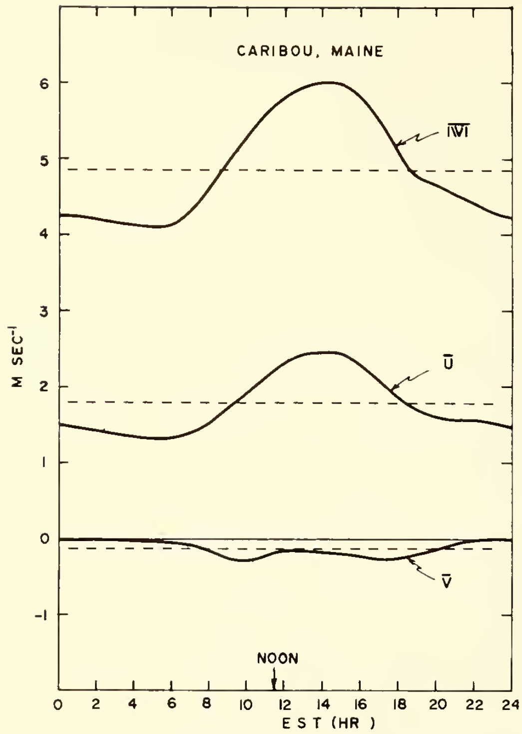

FIGURE 9.—Ten-year average of the zonal (u), the meridional (v) wind component and the total wind speed ($|\mathbf{v}|$) as a function of local time.

in this study, the diurnal cycle would certainly have been more prominent in their u- and v-spectra.

We might also mention the strong annual periodicity in the v-component of the wind, which does not show up in the u-component. The same is true for the other stations in Maine (not shown here). However, in the cases of Detroit and Sault Sainte Marie the annual period is most dominant in the u-component, while for Duluth both the u- and v-components show an important annual cycle. It is not obvious what causes these differences in the u- and v-spectra.

THE DIURNAL SPIKE IN THE KINETIC ENERGY SPECTRUM

From the kinetic energy spectra as shown in figure 5, the diurnal band was selected for further study. The logarithm of the *individual* power estimates (not multiplied by the frequency) is graphed on a linear frequency scale in figure 10.

A sharp spike at exactly 24 hr dominates the picture. However, a little distance away from this spike the intensity drops off rapidly. In addition to the main peak, there are on both sides secondary maxima of about equal intensity. A plausible explanation for the occurrence of these side lobes, which are located at a distance of about 4 min from the peak, seems to lie in an analogy with the "beating" phenomenon in acoustics. Our basic assumption is that the amplitude A of the diurnal cycle in the kinetic energy is not constant throughout the year, but has an annual variation

$$A = A_1 + A_2 \cos(2\pi t/T),$$

where t is measured in days and $T=365.25$ days. A spectral analysis would show at 24 hr the intensity of that part (A_1) of the diurnal cycle which is constant. However, the remaining signal would be interpreted as being the sum effect of two cycles at $(1+1/365.25)$ and $(1-1/365.25)$ cycles per day, corresponding with periods of respectively 24.066 hr and 23.934 hr. These frequencies are indicated in figure 10 by arrows.

$$\begin{aligned} A\cos(2\pi t) &= (A_1 + A_2\cos(2\pi t/T))\cos(2\pi t) \\ &= A_1\cos(2\pi t) + (1/2)A_2\cos 2\pi t(1+1/T) \\ &\quad + (1/2)A_2\cos 2\pi t(1-1/T). \end{aligned}$$

With some imagination one can also detect a weaker semiannual modulation of the diurnal cycle at periods of 24.13 hr and 23.87 hr. The meaning of this effect is that the modulation during the year is not a pure sine wave but that also higher harmonics are involved.

In order to test our hypothesis for this beating phenomenon, we investigated the diurnal cycle in January and in July (fig. 11). Indeed, the results show that there is a strong annual modulation of the diurnal cycle. The largest amplitude is found during July, when there is the strongest convective exchange between the surface and higher levels.

Finally, we would like to comment on one other interesting feature shown in figure 10, i.e., the close correspondence in magnitude and shape of the diurnal spike and to a lesser degree of the side lobes between the different stations. One would expect that the intensity in the diurnal cycle would be strongly dependent on the latitude and longitude of the station, in the sense that the intensity would increase with decreasing latitude and also with increasing continentality. However, the stations used in this study are not particularly suitable for investigating these questions.

6. SUMMARY AND CONCLUSIONS

The spectrum of horizontal wind speed was analyzed using 10 yr of 1-min-averaged hourly surface reports for a group of stations in the northeastern United States and another group near the Great Lakes.

The fast Fourier transform technique was used to estimate the spectrum between periods of about 2 hr and 2 yr. The results were compared with the earlier work of Van der Hoven (1957) for Brookhaven, Long Island.

It was found that most of the effects of aliasing are confined to frequencies between the folding frequency of 1 cycle/2 hr and 1 cycle/12 hr. After assuming a reasonable shape for the small-scale turbulence maximum in the

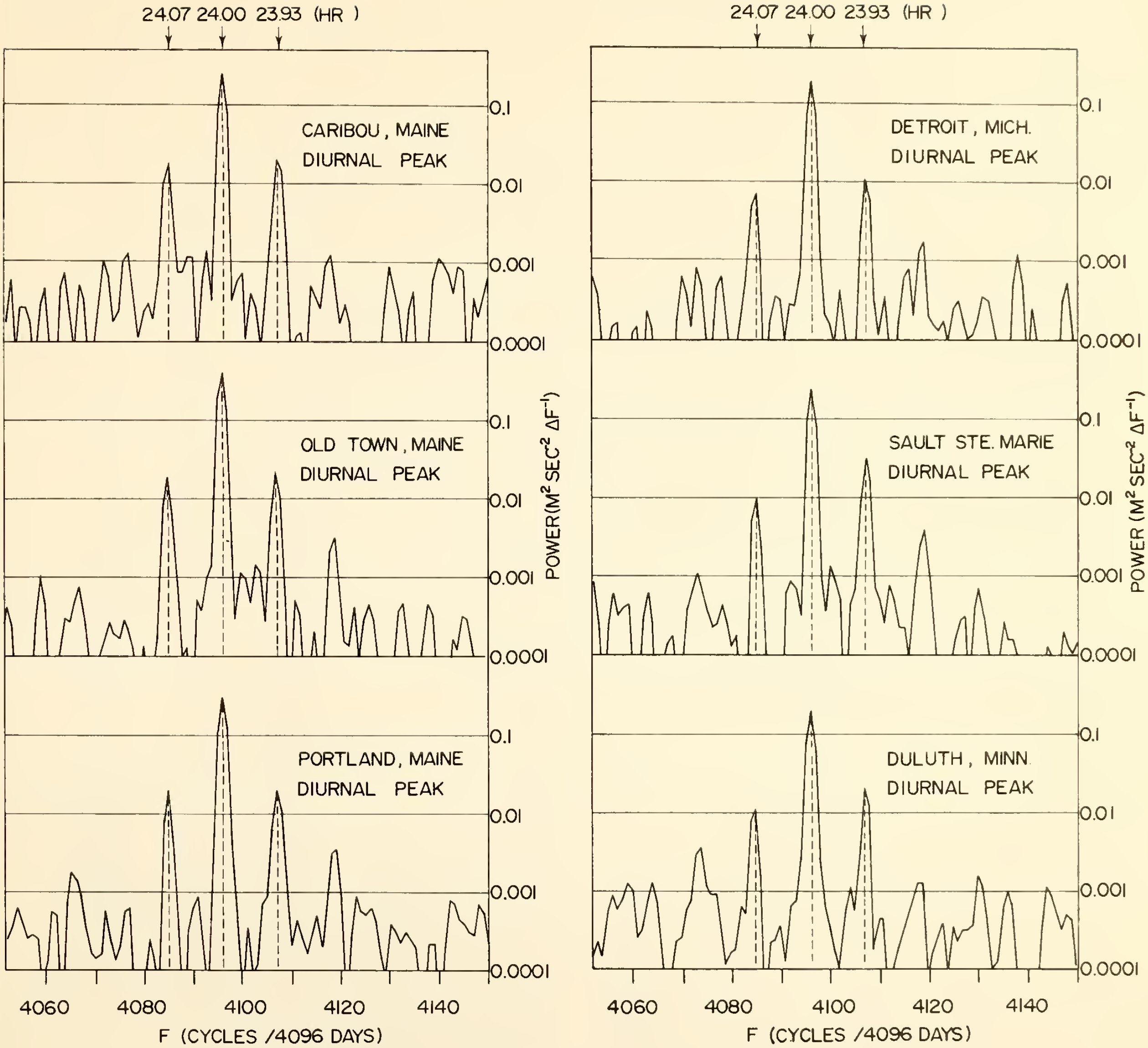

FIGURE 10.—Plot of the individual power estimates ($m^2 sec^{-2}$ per elementary frequency interval) versus frequency near the diurnal period

minute range, the spectrum for Caribou, Maine, was corrected for the aliasing from frequencies between 1 cycle/1 min and 1 cycle/2 hr.

With regard to the final form of the spectrum as shown in figure 4, the following comments can be made:

1) Any reasonable method of correcting for the effects of aliasing seems to lead to quite small values for the spectrum near the folding frequency of 1 cycle/2 hr. This finding is compatible with the existence of a wide spectral gap between the small-scale turbulence maximum near a period of 2 min and the mesoscale phenomena at periods of a few hours. The existence of such a gap in the spectrum was first discussed by Van der Hoven (1957) and has been most extensively documented by the atmospheric turbulence group at The Pennsylvania State University under Professor Hans A. Panofsky. The present study shows that there is some evidence for a spectral gap even if one uses a very long time series.

2) Most of the variance of the wind speed is explained by the activity of traveling cyclones and anticyclones at periods roughly between 2 and 7 days. This agrees quite well with Van der Hoven's results.

3) A large peak in the kinetic energy spectrum was found at the diurnal period and a minor peak at the semi-

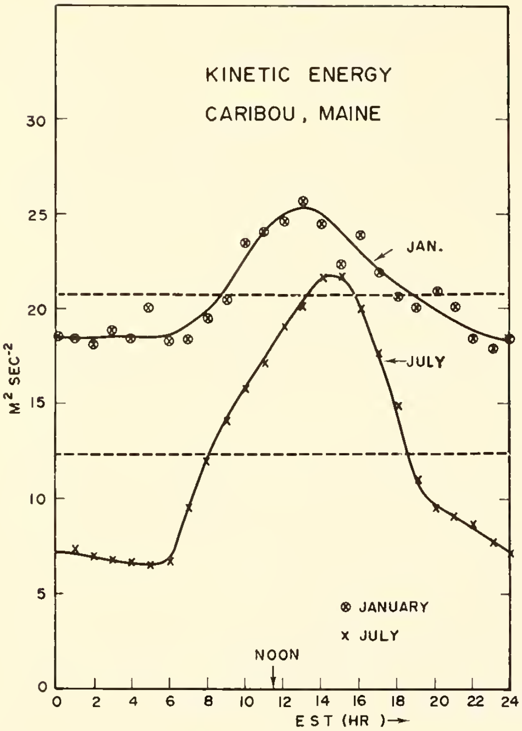

FIGURE 11.—Ten-month mean kinetic energy for January and for July as a function of local time at Caribou, Maine.

TABLE 3.—*Data on the power spectrum of the horizontal wind speed at Caribou, Maine. Hourly data cover the period Jan. 1, 1949, through Dec. 31, 1958.*

Band	N	$\overline{PE}$ (days)	$\mathrm{Log}_e\overline{F}$	$\overline{P}$	$\overline{P}\times\overline{F}$ (m^2 sec^{-2})	DF
1	8630	0.09	10.75	0.03	1.33	4346
2	7710	.10	10.64	.03	1.22	3923
3	6900	.11	10.53	.03	1.13	3287
4	6180	.12	10.42	.03	1.00	2929
5	5520	.14	10.30	.04	.99	2796
6	4950	.15	10.19	.04	1.02	2388
7	4420	.17	10.08	.04	.98	2236
8	3960	.19	9.97	.05	.98	1945
9	3540	.21	9.86	.05	.90	1752
10	3170	.24	9.75	.05	.94	1567
11	2840	.27	9.64	.06	.86	1351
12	2530	.30	9.53	.07	.91	1284
13	2270	.33	9.42	.08	1.00	989
14	2040	.37	9.31	.08	.92	996
15	1810	.42	9.19	.08	.83	883
16	1630	.47	9.08	.12	1.03	777
17	1450	.52	8.97	.19	1.47	243
18	1310	.58	8.86	.14	.96	614
19	1160	.65	8.75	.17	1.04	618
20	1040	.73	8.64	.19	1.07	508
21	940	.81	8.53	.28	1.41	476
22	830	.91	8.42	.28	1.30	388
23	442	1.03	8.29	1.45	5.79	6
24	396	1.15	8.18	.45	1.61	201
25	354	1.29	8.07	.45	1.42	182
26	317	1.44	7.96	.55	1.56	148
27	284	1.61	7.85	.58	1.49	129
28	253	1.80	7.73	.77	1.76	142
29	227	2.01	7.62	.93	1.89	104

TABLE 3.—Continued

Band	N	$\overline{PE}$ (days)	$\mathrm{Log}_e\overline{F}$	$\overline{P}$	$\overline{P}\times\overline{F}$ (m^2 sec^{-2})	DF
30	204	2.24	7.51	1.07	1.96	99
31	181	2.51	7.40	1.38	2.26	98
32	163	2.80	7.29	1.71	2.51	82
33	145	3.13	7.18	2.32	3.04	65
34	131	3.50	7.07	2.05	2.41	66
35	116	3.91	6.96	3.08	3.23	63
36	104	4.37	6.84	2.61	2.45	55
37	94	4.88	6.73	2.46	2.06	55
38	83	5.46	6.62	4.10	3.08	44
39	75	6.10	6.51	3.15	2.12	32
40	67	6.82	6.40	2.88	1.73	34
41	59	7.62	6.29	4.03	2.17	35
42	54	8.52	6.18	2.90	1.40	29
43	48	9.52	6.06	4.29	1.85	25
44	42	10.6	5.95	2.57	.99	22
45	39	11.9	5.84	3.05	1.05	21
46	34	13.3	5.73	3.28	1.01	23
47	31	14.9	5.62	2.78	.77	21
48	27	16.6	5.51	2.92	.72	11
49	25	18.6	5.40	2.96	.66	17
50	22	20.8	5.29	1.68	.33	11
51	19	23.2	5.18	1.49	.27	11
52	18	25.9	5.06	2.22	.35	10
53	16	29.0	4.95	3.14	.44	8
54	14	32.4	4.84	4.61	.58	9
55	12	36.1	4.74	2.58	.29	5
56	12	40.4	4.62	3.53	.36	8
57	10	45.3	4.50	2.33	.21	7
58	9	50.6	4.39	4.65	.38	5
59	8	56.6	4.28	5.42	.39	4
60	7	63.1	4.17	3.44	.22	4
61	7	70.7	4.06	4.84	.28	5
62	5	78.8	3.95	4.93	.26	4
63	5	87.2	3.85	2.61	.12	5
64	5	97.6	3.74	5.17	22	4
65	4	109.	3.62	4.54	.17	----------
66	4	122.	3.51	2.11	.07	----------
67	3	137.	3.40	3.86	.12	----------
68	3	152.	3.29	1.83	.05	----------
69	3	171.	3.18	2.34	.06	----------
70	2	191.	3.07	10.70	.23	----------
71	2	210.	2.97	9.80	.19	----------
72	2	234.	2.86	.65	.11	----------
73	2	265.	2.74	2.22	.03	----------
74	2	304.	2.60	9.50	.13	----------
75	1	341.	2.48	48.94	.59	----------
76	1	372.	2.40	80.85	.89	----------
77	1	410.	2.30	7.97	.08	----------
78	1	455.	2.20	6.01	.05	----------
79	1	512.	2.08	3.40	.03	----------
80	1	585.	1.95	2.51	.02	----------
81	1	683.	1.79	10.86	.01	----------

N=number of spectral estimates in frequency band.
$\overline{PE}$=mean period in band (days).
$\overline{F}$=mean frequency in band (cycles per 4,096 days).
$\overline{P}$=mean power density in band ($m^2\,sec^{-2}$ per elementary frequency interval, where elementary frequency interval=1 cycle/4,096 days).
$\overline{P}\times\overline{F}$=mean spectral intensity in band ($m^2\,sec^{-2}$).
$\mathrm{Log}_e\overline{F}$=natural logarithm of mean frequency in band.
DF=number of equivalent degrees of freedom for estimate of $\overline{P}$ in band and $=N\overline{P^2}/\overline{P}^2$ (see Blackman and Tukey, 1958, p. 24).
Note that the following relation should hold:

$$\text{total variance wind speed}=\sum_{j=1}^{81}\overline{N}_j\times\overline{P}_j=0.111\sum_{j=1}^{81}\left(\overline{P}\times\overline{F}\right)_j,$$

where the constant 0.111 represents the band width in $\log_e F$ units.

diurnal period. Van der Hoven (1957) did not find the diurnal peak, probably because his data were taken near the top of the surface layer (about 100 m). Blackadar's

TABLE 4.—*Hourly kinetic energy* ($m^2\ sec^{-2}$)

Station	Year	1	2	3	4	5	6	7	8	9	10	11	12	13	14	15	16	17	18	19	20	21	22	23	24	Daily average
CAR	1949	15.7	15.1	14.4	15.1	15.2	15.2	16.3	17.9	21.3	23.6	24.2	25.6	27.0	27.0	27.9	25.7	23.7	20.7	17.9	16.7	15.7	15.3	15.5	15.0	19.5
46.9° N.	1950	18.7	18.2	18.1	19.0	18.7	19.3	21.0	22.2	26.5	29.1	31.2	33.6	34.7	35.5	32.6	33.1	29.6	25.7	22.1	22.1	21.3	22.5	21.0	19.3	24.8
68.0° W.	1951	13.4	13.5	13.0	12.3	12.5	12.7	13.7	14.9	17.4	19.3	19.7	20.9	21.6	22.1	22.2	21.0	19.4	16.5	14.9	14.4	14.3	12.9	13.0	12.9	16.2
(EST)	1952	10.9	10.8	10.6	10.4	10.8	10.7	11.7	13.5	15.6	17.8	18.9	20.1	21.6	21.5	21.9	20.1	18.4	15.5	13.6	13.0	11.8	11.9	11.6	11.0	14.7
	1953	11.7	11.2	10.7	10.9	10.7	10.5	11.5	13.7	16.2	17.6	19.7	20.0	20.8	21.0	21.9	21.0	18.9	16.0	13.4	13.7	13.0	12.2	11.8	11.0	15.0
	1954	11.4	11.8	11.0	11.4	10.8	11.7	12.2	13.8	15.5	16.9	18.9	19.5	20.2	21.3	19.9	18.7	17.3	15.8	14.5	14.2	12.7	12.5	12.1	11.3	14.8
	1955	11.6	11.9	11.7	12.2	11.8	11.6	11.9	13.4	15.5	17.7	19.9	21.2	22.6	21.8	20.9	18.6	18.1	15.3	13.9	13.1	12.5	12.1	11.1	11.2	15.1
	1956	10.3	11.2	11.6	10.3	10.7	10.7	11.6	12.8	16.3	17.6	19.9	20.8	21.0	21.8	21.3	20.3	19.1	15.9	12.5	12.4	11.0	11.1	10.5	10.7	14.6
	1957	11.8	12.0	11.6	11.5	11.7	11.4	13.2	14.0	16.4	18.1	20.0	22.4	23.4	24.2	24.1	23.2	20.0	17.0	14.7	13.1	12.7	12.3	11.8	11.5	15.9
	1958	12.5	11.8	11.2	11.5	11.6	11.1	11.6	14.4	15.6	18.6	20.1	21.7	21.8	22.6	22.5	21.4	18.9	17.3	15.2	14.7	13.9	13.0	12.2	12.2	15.7
	10-yr average	12.8	12.7	12.4	12.4	12.5	12.5	13.5	15.1	17.6	19.6	21.2	22.7	23.5	23.9	23.5	22.3	20.3	17.6	15.3	14.7	13.9	13.6	13.1	12.6	16.6
OLD	1949	3.9	4.0	3.6	3.7	3.8	4.0	5.0	5.5	7.1	7.9	8.6	9.4	10.2	10.7	11.0	10.5	9.4	7.5	6.1	5.0	4.6	4.2	3.6	3.9	6.4
44.9° N.	1950	5.7	5.9	5.8	5.6	6.0	6.3	7.3	9.5	11.1	14.3	15.4	16.5	18.6	17.4	17.9	17.1	14.2	12.0	9.7	7.7	7.6	6.8	6.7	6.3	10.5
68.7° W.	1951	4.5	5.2	4.8	4.9	4.8	5.0	6.1	7.0	8.7	10.6	11.9	13.0	13.4	13.9	13.2	11.8	10.4	8.6	6.5	6.0	5.3	5.1	5.2	4.9	7.9
(EST)	1952	4.6	4.7	4.6	5.0	4.8	5.2	5.8	7.5	8.5	10.2	11.8	12.5	13.5	13.9	13.2	12.4	11.3	8.8	7.4	6.9	6.1	5.8	5.0	4.8	8.1
	1953	3.7	3.6	3.5	3.4	3.4	3.6	4.3	5.9	7.3	8.3	10.8	10.7	11.6	11.8	11.8	10.4	9.6	8.0	6.1	5.9	4.7	4.4	4.2	3.7	6.7
	1954	3.5	3.7	3.8	3.4	3.7	3.7	4.5	5.9	7.1	8.5	9.2	10.1	10.3	10.5	10.7	9.8	8.2	7.0	6.0	4.9	4.7	4.2	3.9	3.8	6.3
	1955	4.3	4.3	4.5	4.5	4.8	5.1	5.5	6.6	8.3	10.7	11.4	13.0	13.5	14.3	13.2	13.0	11.2	9.1	7.1	6.6	5.7	5.1	4.6	4.2	7.9
	1956	3.6	3.4	3.4	3.4	3.4	3.6	4.3	5.2	6.4	7.6	9.1	10.0	10.3	10.6	10.8	9.9	8.7	7.5	6.2	5.5	4.9	4.3	3.9	4.1	6.3
	1957	4.2	4.3	4.1	4.2	3.8	4.1	4.5	6.0	7.4	8.3	9.3	10.5	11.1	12.2	12.0	11.5	10.4	8.7	7.1	6.6	5.4	4.8	4.7	4.6	7.1
	1958	4.8	4.6	4.8	4.9	4.7	4.8	5.1	6.2	7.5	8.8	10.3	10.9	11.9	11.8	11.3	11.0	10.2	8.9	7.9	6.9	5.8	5.4	5.5	4.9	7.5
	10-yr average	4.3	4.4	4.3	4.3	4.3	4.5	5.2	6.5	7.9	9.5	10.7	11.6	12.4	12.7	12.5	11.7	10.4	8.6	7.0	6.2	5.5	5.0	4.7	4.5	7.5
PWM	1949	4.0	4.1	4.3	4.6	4.4	4.2	4.7	5.6	6.8	8.1	8.5	9.5	10.9	11.1	10.7	10.4	8.4	6.3	5.0	4.9	4.4	4.7	4.2	4.0	6.4
43.7° N.	1950	5.0	5.4	5.2	5.3	5.6	5.2	5.7	6.7	7.2	8.2	9.6	10.4	11.8	12.5	12.0	12.0	10.4	8.7	7.7	6.7	6.3	6.2	5.7	5.8	7.7
70.3° W.	1951	6.3	6.3	6.6	6.8	7.0	6.8	7.1	8.3	9.5	10.9	11.5	13.2	13.7	14.6	14.2	13.4	11.7	10.0	8.9	7.8	7.4	7.0	6.7	6.3	9.2
(EST)	1952	6.5	6.7	6.6	6.7	6.3	6.3	6.9	7.9	9.4	10.9	12.2	12.9	14.3	14.1	14.2	13.5	11.9	9.7	8.7	8.1	7.2	7.0	6.8	6.8	9.2
	1953	7.9	8.2	7.8	8.1	8.1	7.7	8.3	9.5	11.5	14.5	15.8	16.7	17.8	18.2	18.3	16.2	14.5	13.1	10.9	9.7	9.2	8.5	8.5	8.1	11.5
	1954	8.2	7.9	7.5	7.6	7.8	7.9	8.7	9.6	11.5	13.6	14.8	16.4	16.4	17.7	17.3	15.9	14.2	11.7	10.3	9.2	8.7	8.5	8.7	8.7	11.1
	1955	8.2	8.2	8.7	8.4	8.4	9.0	9.2	11.1	12.4	13.5	15.7	17.5	18.5	18.4	18.1	17.3	15.5	12.4	11.0	10.8	10.3	9.2	9.0	8.3	12.0
	1956	7.1	7.3	7.0	7.1	6.7	7.1	7.3	8.6	9.3	11.1	12.2	13.4	13.9	13.6	13.5	12.8	11.8	10.5	9.4	8.5	8.0	7.5	7.4	7.1	9.5
	1957	9.1	9.0	8.5	9.3	8.4	9.2	9.6	10.6	12.5	14.6	17.4	19.7	21.3	22.3	22.3	21.7	19.8	16.7	13.7	12.5	10.3	10.2	9.6	9.0	13.6
	1958	11.8	11.9	11.9	11.9	11.7	12.0	13.2	14.0	16.8	18.9	20.7	21.0	21.6	23.8	24.1	22.6	21.1	18.7	15.4	13.6	13.3	12.4	12.8	12.3	16.1
	10-yr average	7.4	7.5	7.4	7.6	7.4	7.5	8.1	9.2	10.7	12.4	13.8	15.1	16.1	16.6	16.5	15.6	13.9	11.8	10.1	9.2	8.5	8.1	7.9	7.7	10.7
DET	1949	9.6	9.4	10.0	9.5	9.1	9.5	9.3	10.3	11.7	13.3	14.7	15.4	16.6	18.0	18.1	17.4	16.9	14.7	14.2	11.7	10.6	10.8	10.7	10.0	12.6
42.4° N.	1950	9.3	9.1	9.2	8.4	9.1	8.6	9.0	9.8	10.5	11.3	12.3	13.1	13.9	14.6	15.0	14.8	14.3	13.6	12.4	11.1	10.7	9.8	10.2	10.2	11.3
83.0° W.	1951	9.3	8.8	8.8	9.0	8.6	8.3	8.5	9.0	9.8	11.4	12.6	12.9	14.0	14.5	14.4	14.2	13.8	13.4	11.6	10.7	9.7	9.9	9.8	9.6	10.9
(EST)	1952	8.9	8.6	8.3	8.5	8.4	8.4	8.6	9.1	10.8	11.8	13.4	13.9	15.0	16.0	16.2	15.9	15.4	14.9	12.5	11.7	11.0	10.2	9.5	9.7	11.5
	1953	9.4	9.9	9.3	8.9	9.3	8.9	9.3	10.2	10.7	11.8	12.8	13.9	14.7	15.8	16.1	16.0	14.8	13.6	12.2	11.6	10.7	10.4	10.2	9.6	11.7
	1954	10.1	9.5	9.5	9.0	9.4	8.8	9.7	10.3	11.4	13.6	14.7	15.3	15.6	16.9	17.6	18.0	16.9	15.7	13.7	12.1	11.0	11.0	10.3	10.3	12.5
	1955	9.1	8.8	8.4	8.4	8.9	8.6	9.0	9.7	11.2	12.3	13.7	14.5	15.3	16.5	16.8	16.3	15.8	15.0	13.0	11.7	10.7	10.6	9.6	9.3	11.8
	1956	8.8	9.0	8.7	8.5	8.7	8.8	9.0	9.7	10.9	12.2	13.6	14.5	14.8	15.9	15.8	15.9	15.1	14.1	12.7	11.1	10.5	10.0	9.4	9.3	11.5
	1957	11.3	10.7	10.4	10.6	10.2	10.3	10.6	11.2	12.8	13.7	15.1	16.9	17.7	17.9	18.7	18.7	18.3	17.1	15.8	14.0	13.3	12.5	12.2	11.6	13.8
	1958	12.0	11.7	11.7	11.5	11.1	10.7	11.0	11.3	12.8	14.3	16.3	18.3	19.4	20.6	21.1	20.9	21.0	20.2	18.2	16.7	15.1	13.6	13.2	12.3	15.2
	10-yr average	9.8	9.6	9.4	9.2	9.3	9.1	9.4	10.0	11.2	12.6	13.9	14.9	15.7	16.7	17.0	16.8	16.2	15.2	13.6	12.2	11.3	10.9	10.5	10.2	12.3
SSM	1949	8.9	8.5	8.0	8.5	8.3	8.4	8.6	9.4	9.9	11.0	12.6	14.8	16.4	16.9	17.1	17.1	17.0	15.4	13.1	11.8	10.3	9.9	9.9	8.9	11.7
46.5° N.	1959	7.9	8.6	8.1	8.1	7.7	8.1	7.8	8.7	8.7	10.6	11.6	13.1	13.7	14.9	14.7	14.7	13.9	12.3	10.9	9.8	9.5	8.8	8.3	7.9	10.3
84.4° W.	1951	7.7	7.7	7.9	7.5	7.8	7.8	7.5	7.5	8.1	9.6	10.4	11.8	12.9	13.6	15.1	14.4	13.9	12.7	11.1	9.8	8.7	8.8	8.3	7.6	9.9
(EST)	1952	7.8	7.0	7.3	6.9	7.4	6.9	7.3	7.6	8.6	9.6	10.8	12.5	13.8	14.9	14.9	14.8	14.5	13.2	11.2	10.0	8.6	7.9	8.1	7.7	10.0
	1953	7.7	7.3	7.8	7.3	7.8	7.4	7.4	7.5	8.3	9.5	10.5	11.7	13.0	14.0	14.5	14.3	14.0	13.0	11.1	10.1	9.0	8.3	8.0	7.5	9.9
	1954	7.7	7.3	6.9	6.7	7.2	7.5	7.6	8.1	8.9	10.2	11.1	12.3	13.8	15.3	15.2	15.0	14.8	13.1	11.6	10.4	8.7	8.0	7.7	7.6	10.1
	1955	7.7	7.6	8.1	7.8	7.3	7.3	7.4	8.1	9.0	10.2	11.4	12.8	14.1	14.9	15.8	16.0	15.5	13.1	11.3	10.2	9.3	8.7	8.4	8.3	10.4
	1956	7.3	7.4	6.9	7.2	7.1	7.2	7.5	7.6	8.4	9.1	10.6	11.9	12.8	13.2	13.7	14.6	14.6	12.5	11.3	10.4	9.1	8.5	7.8	7.6	9.8
	1957	9.1	8.6	8.4	8.3	8.2	8.1	8.5	8.8	9.6	11.0	12.5	13.8	16.6	17.4	19.0	19.2	18.8	17.0	15.3	13.8	11.9	10.8	10.0	9.5	12.3
	1958	8.9	9.0	7.9	7.9	7.8	7.7	7.9	8.4	9.5	10.4	12.0	13.4	15.3	16.8	18.0	18.6	18.7	17.2	16.1	14.7	11.6	10.6	10.4	9.6	12.0
	10-yr average	8.1	7.9	7.7	7.6	7.7	7.7	7.8	8.2	8.9	10.1	11.4	12.8	14.3	15.2	15.8	15.9	15.6	13.9	12.3	11.1	9.7	9.1	8.7	8.2	10.6
DLH	1949	25.6	26.7	26.4	26.4	26.6	26.5	26.9	26.8	28.8	30.7	33.3	34.7	34.8	36.7	36.9	36.7	35.5	31.8	28.2	27.1	24.0	24.8	26.2	24.8	29.4
46.8° N.	1950	20.7	20.6	21.2	22.3	23.7	22.9	23.6	24.8	25.6	25.8	26.1	27.4	27.8	27.9	27.7	27.9	28.4	26.5	23.9	22.4	20.1	20.7	21.8	21.3	24.2
92.2° W.	1951	13.5	13.4	13.3	12.8	12.7	13.3	13.9	14.2	15.1	16.4	19.0	20.6	20.7	21.7	21.2	21.1	20.4	18.8	16.6	15.2	13.5	13.0	13.8	13.4	16.2
(CST)	1952	14.3	15.1	13.7	14.3	15.0	14.7	13.9	15.0	15.6	17.9	20.0	21.4	21.9	23.3	22.3	23.1	22.4	20.4	18.1	16.2	14.9	14.8	14.4	14.0	17.4
	1953	14.9	14.6	14.2	14.4	14.8	14.0	14.5	16.1	18.3	19.7	22.0	22.9	23.4	24.4	24.7	24.4	24.1	22.5	20.5	18.4	16.1	15.6	15.5	15.0	18.5
	1954	16.8	16.1	15.4	15.5	16.1	15.9	16.0	17.3	19.1	20.6	23.3	23.8	24.3	25.0	25.6	24.4	24.6	22.8	20.9	19.3	16.9	16.5	16.5	16.3	19.5
	1955	17.8	17.3	17.0	17.0	16.5	16.5	16.8	17.3	19.1	19.7	21.5	23.5	24.5	25.1	24.1	24.7	24.4	22.0	20.1	18.7	17.2	17.0	17.3	17.7	19.7
	1956	16.4	16.1	16.5	16.9	16.5	16.4	17.5	18.1	19.5	21.6	22.6	24.2	24.7	26.2	25.1	25.1	25.1	23.1	21.9	19.9	18.4	17.8	17.6	16.7	20.2
	1957	15.2	14.7	14.3	14.8	15.4	14.9	15.6	16.3	17.4	18.6	20.8	22.5	23.6	25.0	24.3	24.8	24.3	22.8	20.5	18.1	16.3	15.4	16.1	15.3	18.6
	1958	15.3	15.7	16.5	17.1	16.2	15.8	16.2	17.1	17.9	19.3	21.1	23.1	24.9	25.5	25.0	25.5	24.7	23.3	21.9	19.3	16.4	15.3	15.7	15.1	19.3
	10-yr average	17.0	17.0	16.9	17.1	17.4	17.1	17.5	18.3	19.6	21.1	23.0	24.4	25.1	26.1	25.7	25.8	25.4	23.4	21.3	19.4	17.4	17.1	17.5	17.0	20.3

theory (1959) adequately explains the differences between Van der Hoven's and our results.

4) At low frequencies in the spectrum beyond the cyclone rise, most activity is found in the annual and semiannual periods.

The stations used in this study are confined to a latitude belt between 42° N. and 47° N. One may expect that there will be a general shift in importance of the diurnal and annual peaks and of the cyclone rise, if one would study stations at a different latitude.

Through a comparison with the spectra of the zonal and meridional wind components, it is shown that the diurnal cycle in the wind speed is not accompanied by a similar cycle in the wind direction. The diurnal variation in the kinetic energy near the surface with a maximum between 2 and 3 p.m. is in evidence at each of the six stations and for each of the 10 yr.

A closer look at the individual estimates that make up the diurnal peak in the spectrum shows, in addition to the mean spike at 24 hr, side lobes which are probably due to the annual modulation of the diurnal cycle. The diurnal cycle is found to be more pronounced in July than in January. This is what one might expect with a more intense vertical exchange of kinetic energy between the surface and upper levels during the summer.

APPENDIX

Table 3 supplies more detailed information on the spectral estimates and their accuracy for Caribou, Maine. Table 4 gives the average kinetic energy as a function of time of the day for the six stations and the 10 yr studied.

ACKNOWLEDGMENTS

Copies of the data tapes used in this study were kindly supplied to us by Mr. Howard M. Frazier of the Travelers Research Center, Inc. We would like to acknowledge the help of the following people at the Geophysical Fluid Dynamics Laboratory, ESSA: Mr. Henry Stambler for writing the unpacking program for the data tapes, Mr. Richard Stoner for drawing the figures, and Mrs. C. T. Morgan for typing the manuscript.

REFERENCES

Bingham, C., Godfrey, M. D., and Tukey, J. W., "Modern Techniques of Power Spectrum Estimation," *IEEE Transactions on Audio and Electroacoustics*, Vol. AU-15, No. 2, June **1967**, pp. 56–66.

Blackadar, A. K., "Periodic Wind Variations," *Mineral Industries*, Vol. 28, No. 4, College of Mineral Industries, The Pennsylvania State University, University Park, Jan. **1959**, pp. 1–5.

Blackman, R. B., and Tukey, J. W., *The Measurement of Power Spectra*, Dover Publications, Inc., New York, **1958**, 190 pp., (see pp. 14, 15, and 21–25).

Busch, N. E., and Panofsky, H. A., "Recent Spectra of Atmospheric Turbulence," *Quarterly Journal of the Royal Meteorological Society*, Vol. 94, No. 400, Apr. **1968**, pp. 132–148.

Bysova, N. L., Ivanov, V. N., and Morozov, S. A., "Characteristics of the Wind Velocity and Temperature Fluctuations in the Atmospheric Boundary Layer," *Proceedings of the International Colloquium on the Fine-Scale Structure, Moscow, June 15–22, 1965*, Izdatvo Nauka, Moscow, **1967**. pp. 76–92.

Cooley, J. W., and Tukey, J. W., "An Algorithm for the Machine Calculation of Complex Fourier Series," *Mathematics of Computation*, Vol. 19, No. 91, Apr. **1965**, pp. 297–301.

Group of Audio and Electroacoustics, Subcommittee on Measurement Concepts, "What Is the Fast Fourier Transform?" *IEEE Transactions on Audio and Electroacoustics*, Vol. AU-15, No. 2, June **1967**, pp. 45–55.

Hinich, M. J., and Clay, C. S., "The Application of the Discrete Fourier Transform in the Estimation of Power Spectra, Coherence, and Bispectra of Geophysical Data," *Reviews of Geophysics*, Vol. 6, No. 3, Aug. **1968**, pp. 347–363.

Holloway, J. L., Jr., "Smoothing and Filtering of Time Series and Space Fields," *Advances in Geophysics*, Vol. 4, **1958**, pp. 351–390.

Singer, I. A., and Raynor, G. S., "Analysis of Meteorological Tower Data April 1950–March 1952 Brookhaven National Laboratory," *Brookhaven National Laboratory Report* No. BNL 461 (T-102), Contract No. (AFCRC-TR-57-220), Upton, N.Y., June **1957**, 93 pp., (see p. 34).

U.S. Weather Bureau, *Local Climatological Data—With Comparative Data*, for the stations Caribou, Maine, Portland, Maine, Detroit, Mich., Sault Sainte Marie, Mich., Duluth, Minn., published in Asheville, N.C., 1958.

Van der Hoven, I., "Power Spectrum of Horizontal Wind Speed in the Frequency Range from 0.0007 to 900 Cycles Per Hour," *Journal of Meteorology*, Vol. 14, No. 2, Apr. **1957**, pp. 160–164.

[Received February 24, 1969; revised April 10, 1969]

CORRECTION NOTICE

Vol. 97, No. 3, March 1969, p. 286, next to the last sentence: "Moscow Airport in Idaho reported −50°F, on the 30th, the coldest December temperature of record in the State." is incorrect and should be deleted.

Reprinted from Journal of Applied Meteorology, The American Meteorological Society, Vol. 8, No. 1, 92-104. 56

The Importance of Natural Glaciation on the Modification of Tropical Maritime Cumuli by Silver Iodide Seeding

ROBERT I. SAX

Atmospheric Physics and Chemistry Laboratory, ESSA, Coral Gables, Fla.

(Manuscript received 21 August 1968, in revised form 7 November 1968)

In order to determine if natural glaciation proceeds rapidly or extensively enough in tropical maritime cumuli to influence attempts to modify their dynamical behavior by seeding with silver iodide, a detailed study was made of the clouds observed during the 1965 Project Stormfury experiments. From photographic coverage, notes on visual observations, and instrumentation on-board penetrating aircraft, data were compiled on cloud liquid water content, volume-median drop size, in-cloud temperature profile, and the dynamical life histories of both seeded and non-seeded clouds. The validity of applying Koenig's numerical splintering model to tropical maritime cumuli, as well as an assessment of the effectiveness of silver iodide seeding, were determined by comparing the dynamical behavior of paired seeded and non-seeded clouds with glaciation times predicted by the model. Dynamical studies were initiated on two independently developed parametrized numerical cumulus models, and an excellent correlation between predicted and observed cumulus growth was found if no natural glaciation at temperatures >-15C was assumed.

The results of this study suggest that natural glaciation does not proceed rapidly and/or extensively enough in the critical cloud updraft areas to alter the effectiveness of modifying tropical maritime cumuli by causing artificial glaciation with silver iodide.

1. Introduction

The technique of modifying supercooled cumuli by silver iodide seeding is based on the idea that silver iodide particles will act as freezing nuclei at a much higher temperature than naturally-occurring nuclei. Instead of remaining liquid until temperatures of the order of -25C have been reached, the seeded cloud can freeze and release its latent heat of fusion in the temperature range of -4 to -8C, thus gaining additional buoyancy. The cumulus growth resulting from the increased buoyancy can best be demonstrated on days when an existing inversion layer is strong enough to prevent penetration by the natural, unseeded cumuli, but not sufficiently strong to prevent penetration by the warmed, seeded cumuli. Explosive cumulus growth can occur if the atmosphere above such an inversion is unstable and not too dry.

Such a seeding modification hypothesis based on a growth increase caused by buoyancy from fusion heating fundamentally assumes that the organized updraft region of the cloud remains essentially liquid until the time of seeding. The effectiveness of artificial seeding would be drastically reduced if a significant portion of the water content in an updraft area is rapidly consumed by ice from natural glaciation at temperatures >-15C. In the extreme case of rapid natural glaciation of updraft water content near temperatures of -5C, no change in growth behavior between seeded and non-seeded clouds could be expected.

From a cumulus modification viewpoint, therefore, observations of ice particles existing in cumuli topping below the -15C level are particularly important. A great deal of evidence has accumulated during the past decade giving credence to the idea that ice occurs far more frequently at temperatures >-15C in the free atmosphere than previously thought possible, and apparently in greater concentrations than can be explained by the presence of natural freezing nuclei. Murgatroyd and Garrod (1960) found significant quantities of ice in British cumuli whose tops were no colder than -11C. Koenig (1963) showed evidence from the University of Chicago's Project Whitetop experiments indicating that approximately 30% of the cumulus clouds studied in Missouri completely glaciated, apparently naturally, at temperatures >-10C. Mossop *et al.* (1968) report finding ice crystals in an Australian cumulus cloud which never reached a temperature <-4C. Koenig (1968) sampled ice particles in Californian orographic clouds which failed to grow above the -9C isotherm. The author himself has observed evidence of ice particles at "warm" temperatures during an ESSA cloud physics project in Puerto Rico during the summer of 1967.

Although the presence of some isolated large ice particles at temperatures >-10C can be explained by a stochastic freezing process (Gokhale, 1965), a complete and rapid glaciation of natural clouds would certainly require a more efficient process. Hypothesizing that large water droplets eject splinters of ice as they freeze, and that such splinters can act as freezing nuclei for other liquid droplets which, in turn, eject more splinters as they freeze, Koenig (1966), using laboratory

Table 1. Theoretical time for natural cloud glaciation by the ice-splintering mechanism as a function of cloud liquid water and mean drop size (after Koenig, 1966).

% of cloud LWC glaciated	Cloud LWC (g/m)^3	Average Drop Diam. (microns)	Time (seconds)	Average Drop Diam. (microns)	Time (seconds)	Average Drop Diam. (microns)	Time (seconds)
10	0·5	30	760	60	550	90	500
10	1·0	30	420	60	320	90	300
10	2·0	30	240	60	Not Computed	90	180
50	0·5	30	860	60	640	90	600
50	1·0	30	460	60	380	90	340
50	2·0	30	270	60	Not Computed	90	210
95	0·5	30	1280	60	910	90	880
95	1·0	30	660	60	520	90	500
95	2·0	30	400	60	Not Computed	90	280

data on splinter production as studied by Latham and Mason (1961), devised a numerical model for a chain-reaction type of ice-multiplication glaciation in cumuli topping at temperatures > -10C. His computed glaciation times are a function of the cloud's liquid water content and drop-size distribution, but turn out to be remarkably insensitive to the number of initial ice particles present in the cloud. A summary of his results, based on an initial $10\,\mu$ ice particle concentration of $1\ \mathrm{m}^{-3}$, is given in Table 1.

The above computations have strong implications on dynamical cumulus modification by silver iodide seeding. The predicted time for 95% glaciation by a natural ice-multiplication mechanism in a cloud with a broad drop-size distribution is within the 5–10 min needed for complete artificial glaciation by silver iodide seeding. It would appear to follow that trying to induce artificial glaciation by seeding clouds possessing a broad drop size distribution, such as tropical maritime cumuli, should be ineffective in altering the life history of such clouds since almost complete natural glaciation by an ice-multiplication mechanism is predicted to occur in approximately the same time interval. This study is an attempt to determine if natural glaciation occurs both significantly and rapidly enough in tropical maritime cumuli to impair the effectiveness of cumulus modification by artificial seeding techniques.

2. Analytical procedure and acquisition of data

All data were obtained from the 1965 Project Stormfury cumulus modification experiments during which randomized seeding operations were conducted on 23 tropical maritime cumuli in the Caribbean. Only 14 of the clouds were actually seeded, the remainder being used as control clouds. Two ESSA DC-6 aircraft, equipped to measure such physical parameters as liquid water content, volume-median drop size, ambient temperature, humidity, wind speed and direction, and vertical accelerations, made cloud penetrations at 10,000 and 19,000 ft, and a Naval Research Laboratory aircraft, equipped with a Formvar replicating device (Averitt and Ruskin, 1967) penetrated clouds at the 17,000-ft level. The cloud's life history was carefully analyzed from 16-mm color motion pictures taken from the command and control aircraft (a radar-equipped WC-121) and from 35-mm movies taken from both sides of the two DC-6 penetrating aircraft. Color slides and Hasselblad pictures, along with the original notes taken by meteorologists on board the various participating aircraft provided a clear reconstruction of the cloud's growth from time of first visual sighting.

The liquid water data were obtained by means of a Johnson-Williams meter in combination with a hot wire instrument described in detail by Levine (1965). Essentially, this system consists of a nickel-iron wire loop cloud unit sensitive to drops $\lesssim 100\,\mu$ in diameter, and a rain instrument made of the same kind of wire wound on a grooved ceramic cone and sensitive to drops $> 100\,\mu$ in diameter. Because the responses of the two instruments are dependent upon drop size, the volume-median drop diameter can be determined if a drop distribution is assumed.[1]

In order to test the applicability of the splintering model to the Stormfury clouds, it was necessary to focus attention on an analysis of physical parameters such

[1] An exponential log-normal distribution was assumed, both for calibration of the instrument and for the actual clouds. In this case the volume-median corresponds closely with the mean, and the two terms can be interchanged without introducing a large error.

TABLE 2. Liquid water contents and volume-median drop sizes for nine clouds studied during Project Stormfury. (JW refers to the Johnson-Williams meter.)

Date (1965)	Cloud	Run	Seed or No Seed	Average JW LWC (g/m^3)	Average Total LWC (g/m^3)	% LWC greater than JW size drops	Average Volume Median Drop Size (microns)	Maximum LWC (total) g/m^3	Flight Altitude (feet)
28 July	1	1	No Seed	0·31	1·07	71	67	3·1	19,000
	3	1	Seed	0·27	0·79	66	83	1·6	19,000
29 July	1	2	Seed	0·31	1·13	73	85	2·1	19,000
	1	2	Seed	0·13	1·08	88	99	1·7	10,000
	2	1	No Seed	0·12	0·50	76	132	1·0	19,000
3 August	4	2	Seed	0·14	0·46	70	109	0·6	19,000
5 August	3	1	Seed	0·13	0·43	70	120	1·6	19,000
	1	1	No Seed	–	0·15	–	–	0·3	19,000
10 August	2	1	No Seed	0·29	1·30	78	89	2·1	19,000
	3	1	Seed	0·19	0·79	76	105	1·8	19,000

as cloud liquid water content profile, volume-median drop size, cloud life history, and environmental conditions. This also served to point out any internal physical differences between the control and seeded Stormfury clouds. In order to determine if natural glaciation is important enough to alter the effectiveness of silver iodide seeding in tropical maritime cumuli, the behavior of the Stormfury clouds was analyzed by using two independently developed dynamical models, both of which assumed no natural glaciation at temperatures >-15C. If natural glaciation is as rapid and widespread in the updraft regions of tropical maritime cumuli as the splintering model seems to imply, the dynamical models would not be expected to give a good correlation between predicted and observed cloud top heights, particularly for the non-seeded cases.

3. Discussion of the physical analysis

Reliable physical data from the Levine instrument could only be obtained at the 19,000-ft penetration level for nine of the Stormfury clouds, five of which were seeded.[2] A complete summary of the data obtained is shown in Table 2. With the exception of the 5 August control cloud, these cases had water contents and volume-median drop sizes comparable to those used in Koenig's calculations (Table 1), thus enabling their time of glaciation by an ice-multiplication mechanism to be easily predicted. A good test for the validity of Koenig's model could be made by determining if natural glaciation occurred in these clouds in the time and to the extent predicted by the model.

Because the NRL aircraft could not fly above 17,000 ft, the Formvar replicator was sampling at temperatures too warm for mixed phase conditions except on 5 August when the freezing level was exceptionally low and the sampling took place at -4C. Except for 5 August, therefore, direct evidence of the extent of cloud glaciation could not be obtained, and an indirect deductive means of determining natural glaciation had to be used. If a cloud fails to grow above a certain level for a substantial period of time (15–20 min), and is then seeded, any sudden growth of the cloud can most likely be attributed to additional buoyancy caused by the latent heat release of freezing water. Significant growth can only occur if a large percentage of the cloudy updraft area is supercooled liquid water at the time of seeding. Also, if a seeded cloud can grow, while an unseeded cloud, possessing the same physical properties, is unable to grow in an identical environment, such behavioral difference can most likely be attributed to fusion heat release and rules out the possibility of rapid natural glaciation in the unseeded case. Such an analysis of the dynamical behavior of the Stormfury clouds was used as the primary means of assessing the rate and importance of a natural glaciation mechanism and its effect on the modification of tropical maritime cumuli by silver iodide seeding.

4. The cloud data

Table 3 summarizes the important data analyzed for each of the nine clouds thought to have reliable Levine water measurements. Fig. 1 gives the temperature pro-

[2] Because of the abundance of large drops in tropical cumuli, the Levine cloud instrument wire frequently broke and data were lost; the problem of preventing such breakage is currently being studied by ESSA's Research Flight Facility.

Table 3. Supercooling times and cloud growth histories for nine clouds studied during Project Stormfury.

Date (1965)	Action	Time of First observation T_o (GMT)	Top Temp at T_o (°C)	Time of Action T_1 (GMT)	Top Temp at T_1 (°C)	Time Supercooled until Action Time (min)	Growth to Action Time (ft)	Growth after Action Time (ft)	Total Time of Supercooling Control Cases (min)
28 July	Control	2010:00	−6·0	2033:00	−8·0	23·0	1500	2500	30·0
	Seed	2202:30	−7·5	2217:30	−5·0	15·0	−1500	17500	(Seeded)
29 July	Seed	1755:00	−9·0	1810:30	−19·0	15·5	4000	14000	(Seeded)
	Control	1920:00	−9·0	1929:30	−14·0	9·5	2500	None	15·0
3 August	Seed	2142:00	−19·0	2158:30	−22·0	16·5	2500	10500	(Seeded)
5 August	Control	1641:00	−9·0	1657:30	−14·0	16·5	2000	4000	21·0
	Seed	1747:30	−12·0	1805:30	−18·0	18·0	4000	11000	(Seeded)
10 August	Control	1913:00	−11·0	1916:00	−11·0	Unknown	None	None	Unknown
	Seed	1940:00	−8·0	1957:30	−17·0	17·5	4000	14000	(Seeded)

file through each cloud (except for the 5 August control) as measured at 19,000 ft by the vortex thermometer on board the DC-6. The 5 August control cloud was penetrated incorrectly at the edge instead of through the center, thus accounting both for its extreme dryness and for the temperature profile omission. The following brief analysis of each cloud has been given in much greater detail by Sax (1967).

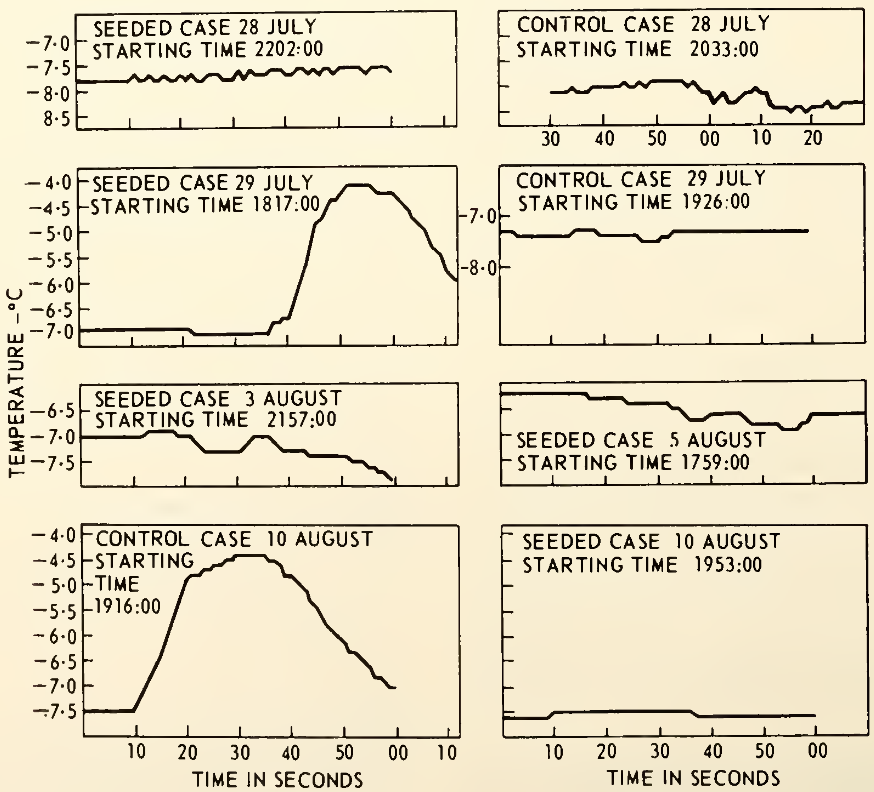

Fig. 1. Temperature profiles at the 19,000-ft level for eight of the Stormfury clouds.

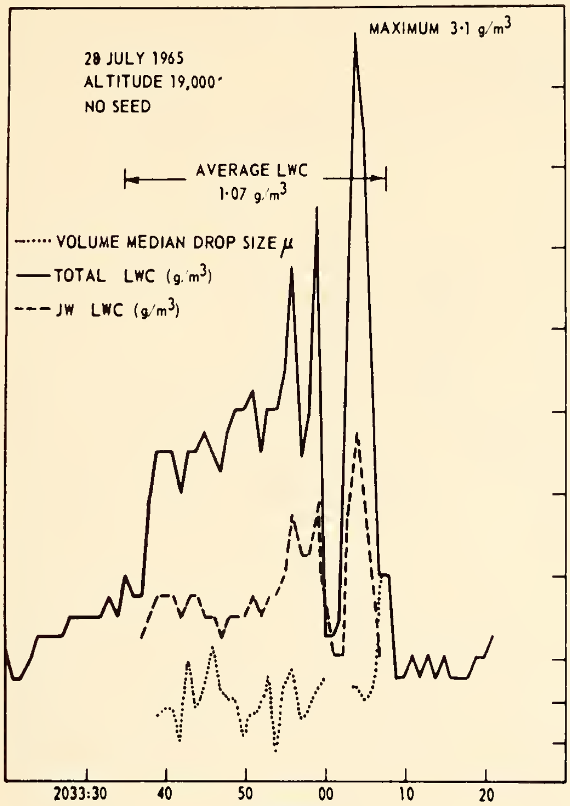

Fig. 2. Physical profile at the 19,000 ft level; 28 July control cloud.

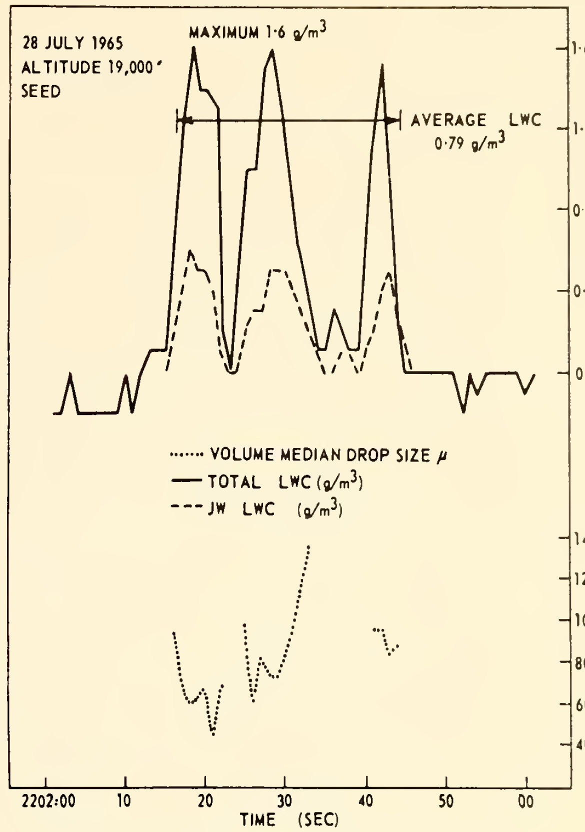

Fig. 3. Physical profile at the 19,000-ft level; 28 July seeded cloud (before seeding).

a. 28 July

Good physical measurements were obtained for both a seeded and a control cloud on this day, the control cloud's 19,000-ft physical profile being shown in Fig. 2. This cloud was observed to exist with its upper level at a temperature < -6C for 23 min prior to penetration, and a further 7 min after penetration, but the cloud could grow no higher than to the 24,000-ft level (-18C). The steadiness of the temperature profile (Fig. 1) indicates the absence of a strong warm updraft in the upper portion of the cloud. Assuming that a few "primary" ice particles (1 m^{-3}) were able to form early in the cloud's existence as it approached the -10C isotherm, the splintering calculations predict that about 9 min would be sufficient time for this cloud to achieve 95% glaciation. If such glaciation actually did occur in this short time interval in the control cloud, then 24,000 ft should represent an upper limit to the growth of a seeded cloud possessing similar physical characteristics

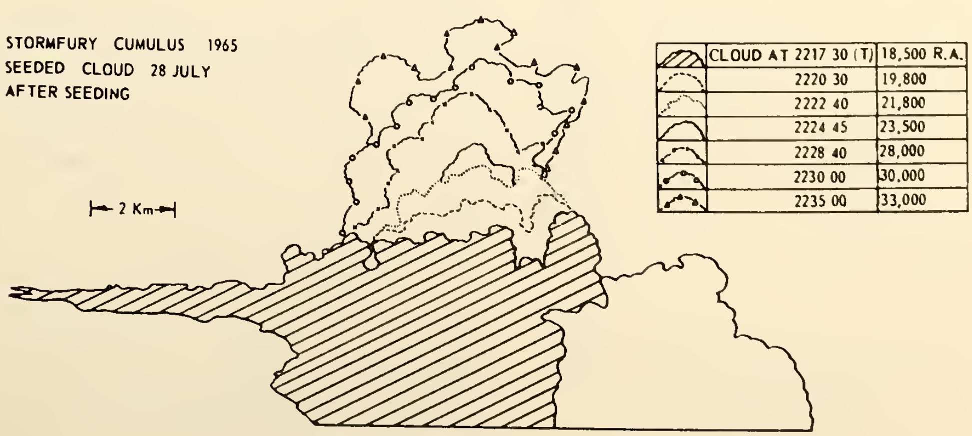

Fig. 4. Growth of the 28 July seeded cloud.

and existing in nearly the same time and place as the control.

Fig. 3 shows the profile of the seeded cloud which developed 2 hr after the control and in an area approximately 100 n mi distant. The cloud top was in an active state with new turrets forming and old ones collapsing. Although the cloud top pushed above 19,000 ft (−7C) when it was first sighted, by seeding time, 15 min later, no part of the cloud was above 17,500 ft (−5C). Upon seeding, however, the cloud grew explosively to 35,000 ft in the next 18 min as illustrated by Fig. 4.

Because apparently a large amount of fusion heat was released by the silver iodide, such dynamical behavior suggests that the organized updraft area of the cloud was essentially liquid at the time of seeding. Although the splintering calculations predict that the seeded cloud should have been 95% glaciated some 5 min before it was seeded (clearly an impossibility if seeding caused the growth), it is quite possible that, since the cloud top never became colder than −7C prior to seeding, primary ice particles may not have been present in sufficient quantities to initiate the chain-reaction multiplication mechanism.

A comparison of the dynamical behavior of the two clouds studied on this day strongly indicates that the updraft areas of the control cloud could not glaciate naturally as efficiently as could the updraft areas of the cloud which was artificially seeded. The seeded cloud's 11,000 ft height gain relative to the control points out the effectiveness of silver iodide seeding in tropical maritime cumuli. Apparently, the splintering calculations resulted in far too short a glaciation time for this day's control cloud, since 95% glaciation in 9 min should have permitted such efficient release of fusion heat as to give growth compatible with that of the seeded cloud.

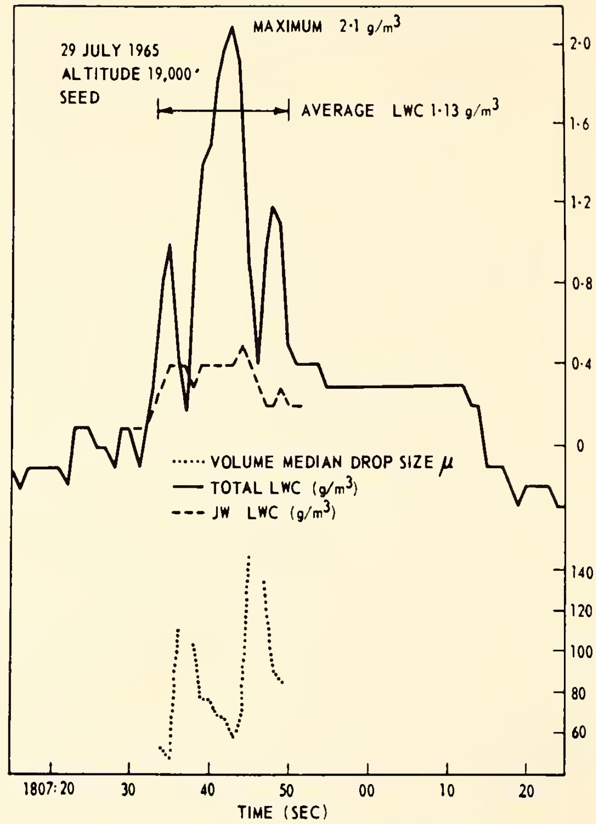

Fig. 6. Physical profile at the 19,000-ft level; 29 July seeded cloud (before seeding).

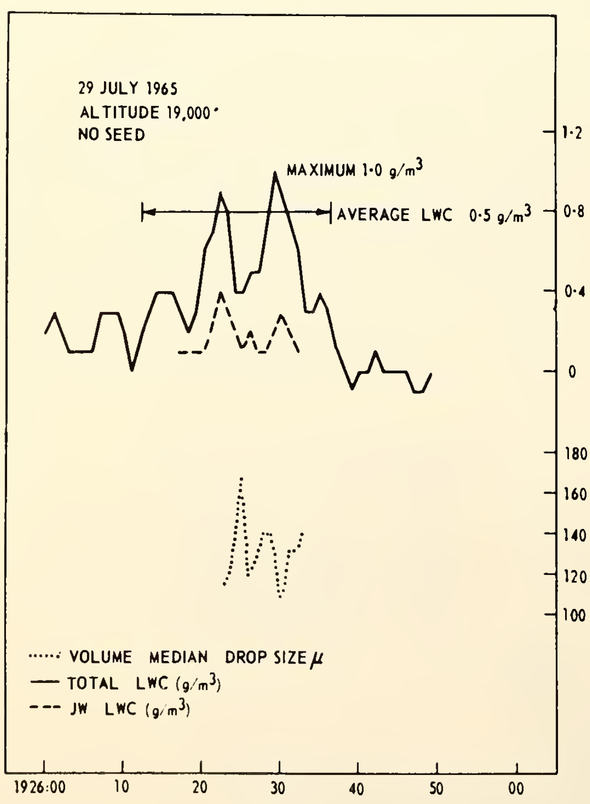

Fig. 5. Physical profile at the 19,000-ft level; 29 July control cloud.

b. 29 July

The control cloud for this day was first observed to have a height of 20,000 ft (−9C), but it could grow no higher than 22,500 ft (−15C) before it began to decay 15 min later. From the cloud's physical profile, shown in Fig. 5, it can be calculated from Table 1 that 95% natural glaciation should have occurred in about 14 min; the cloud, however, failed to exhibit any buoyancy gain.

In contrast, the seeded cloud for this day, initially observed at 20,000 ft (−9C), had grown to 24,000 ft (−19C) 15 min later, at which time it was seeded. During the following 18 min, the seeded turret grew spectacularly to 38,000 ft, shearing off from the main body of the cloud which died without further growth. Although the seeded cloud existed in the same environmental conditions as the control, it was considerably wetter than the control cloud, as can be seen from the profile in Fig. 6. An examination of the 19,000-ft temperature profile (Fig. 1) reveals a strong increase in temperature in the seeded cloud's interior, thus indicating an actively growing turret with a substantially warm updraft. Evidence of such activity could not be found in the control cloud.

The dynamical behavior of the two clouds on this day does not lend itself to an easy single explanation. The San Juan radiosonde data indicated the presence of a weak stable layer between 21,000 and 23,000 ft. It appears that the seeded cloud, being wetter and more active than the control, was just able to penetrate this layer prior to seeding, while the control could not. It is therefore possible that the seeded cloud would have grown independently of seeding, particularly since its top temperature just prior to seeding was near −20C. Because the seeded cloud was able to grow 4000 ft prior to seeding, it might be argued that the additional growth after seeding was just an acceleration of an already established process of natural fusion heat release.

Koenig's splintering calculations predict that 10 min should have been sufficient time for 95% of the seeded cloud to have glaciated naturally before seeding. Even allowing for the warm updraft, droplets in this cloud were supercooled at −10C or colder for at least 10 min before seeding, but substantial, almost explosive, growth did not commence until after the cloud was seeded. Such dynamical behavior suggests a liberal release of fusion heat upon seeding, thus requiring an essentially liquid updraft region at the time of seeding. By a similar analysis, this day's control cloud should have completely glaciated according to the splintering model, but its failure to grow indicates ineffective fusion heat release in its updraft region. Calculations similar to those described by Wexler and Donaldson (1966) predict that 3% of all drops >2.5 mm radius should freeze at −10C in 25 sec, and 50% of such drops should freeze in the same time at −14.5C. The large volume-median drop sizes in both the seeded and control cases (Fig. 5 and Fig. 6) would seem to indicate that such large droplets should have been present in these clouds to provide an adequate source of primary ice particles for ice-multiplication initiation. This would be particularly true in the case of the seeded cloud with its strong supporting updraft.

The failure of the seeded cloud on this day to exhibit much growth prior to seeding, and the failure of the control cloud to grow at all, even though both clouds were supercooled at temperatures < −10C for a sufficient amount of time to completely glaciate according to the splintering model, indicates that the model calculations greatly overpredicted the extent and/or rate of natural glaciation in these clouds. The 15,500-ft growth increase in the seeded turret indicates that natural glaciation does not proceed efficiently enough to interfere with the effectiveness of the artificial seeding of tropical maritime cumuli.

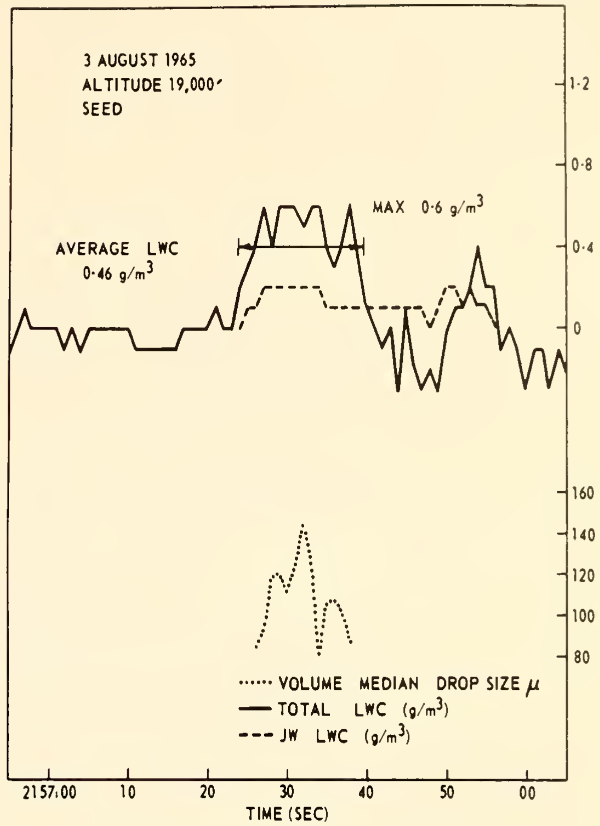

FIG. 7. Physical profile at the 19,000 ft level; 3 August seeded cloud (before seeding).

c. 3 August

The only case available for this day was a seeded cloud which had its upper 4000 ft supercooled well below −15C for $16\frac{1}{2}$ min prior to seeding, but managed to grow only 2500 ft during that time. After seeding, however, the seeded turret grew 10,500 ft in 14 min and separated from the main cloud mass. Comparing the cloud's physical profile shown in Fig. 7 with the splintering criteria in Table 1, it can be seen that this cloud should have been 95% glaciated at least a full 3 min before it was seeded. The dynamical behavior of the cloud, however, strongly refutes the idea that it had completely glaciated before seeding. The sudden increase in cloud buoyancy shortly after seeding can reasonably be attributed to warming caused by a mass amount of fusion heat release, an impossible condition for a cloud already fully glaciated. The cloud's long supercooling time at such a low temperature should theoretically insure a primary ice concentration of 1 m^{-3}, but the ice apparently could not propagate throughout the cloud as rapidly as predicted by the splintering model. The extent of natural glaciation in this cloud was apparently not sufficient to interfere with the effectiveness of the silver iodide seeding.

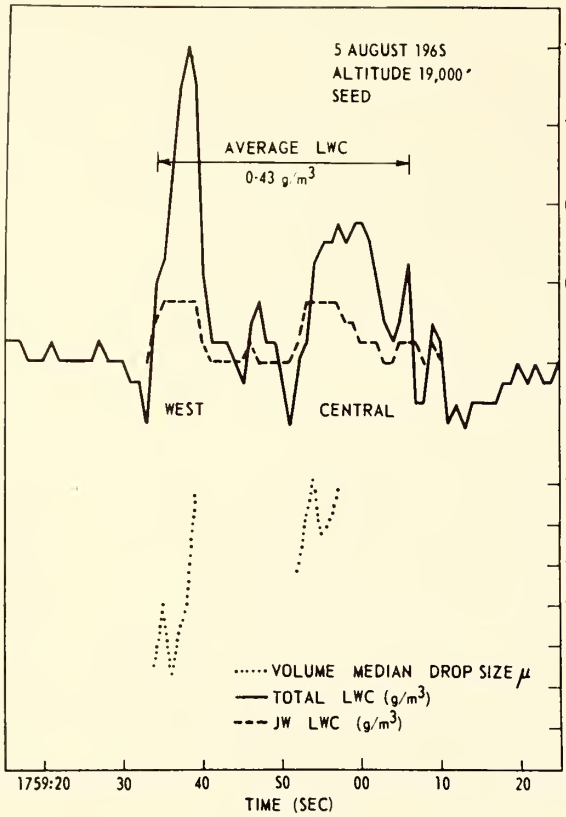

FIG. 8. Physical profile at the 19,000 ft level; 5 August seeded cloud (before seeding).

d. 5 August

The control cloud for this day topped at 26,000 ft (−14C) and was supercooled below −9C for at least 21 min. Unfortunately, the DC-6 penetration of this cloud was incorrectly made through an extremely dry edge instead of through the center, thus making it impossible to compare the physical characteristics of this cloud with the splintering criteria presented in Table 1.

In contrast, a great deal of work has already been published about the seeded cloud for this day (Ruskin, 1967; Simpson 1967). As can be seen from Fig. 8, this cloud possessed two distinct turrets, a rather wet western turret and a dry central turret. The central turret was the oldest part of the cloud and had existed above the 21,000 ft level (−12C) for at least 18 min before beginning to dissipate near the time of seeding. As can be seen from Fig. 9, the western turret was a young, growing area which had existed above 19,000 ft (−7C) for 6 min at the time of seeding. The splintering calculations (Table 1) predict that, at the time of seeding, the central turret should have been 95% glaciated while the western turret should have been about 10% glaciated.

Formvar replication data were available for the western turret at the 17,000 ft level (−4C) shortly before the time of seeding. Using a method similar to Averitt and Ruskin (1967), a detailed ice-to-water percentage area analysis was made from the Formvar sections which did not contain large graupel pellets or shattered liquid droplets. As Fig. 10 indicates, the average concentration of ice in the western turret just before seeding time was 20%, but a localized pocket of up to 50% ice existed in a small area near the cloud edge. This is roughly in agreement with a similar analysis on the same cloud performed by Ruskin (1967). The low water content of the central turret made a quantitative estimate of ice impossible for that portion, but, in small areas where good data were available, the central turret appeared somewhat more glaciated than the western.

The presence of significant quantities of ice in the young western turret lends support to a multiplication mechanism since the number of natural freezing nuclei active at −8C cannot account for the large amount of ice throughout the turret. However, the old central

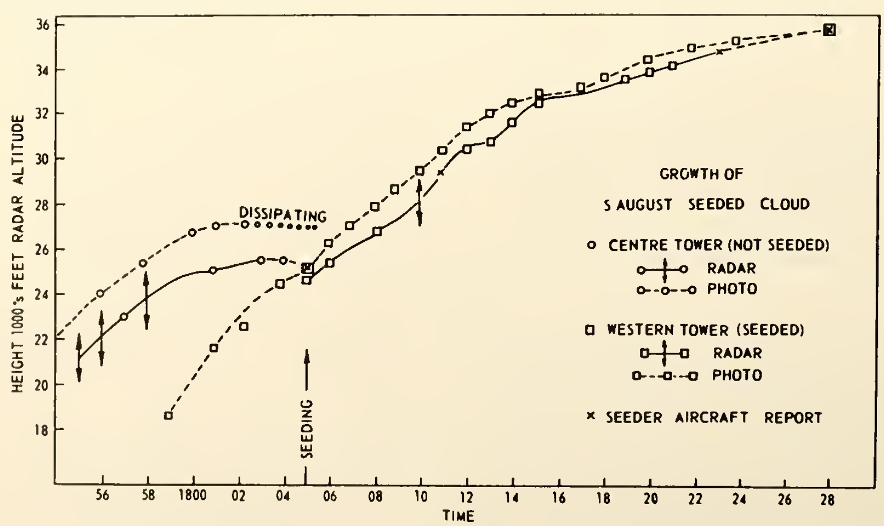

FIG. 9. Growth of the 5 August seeded cloud.

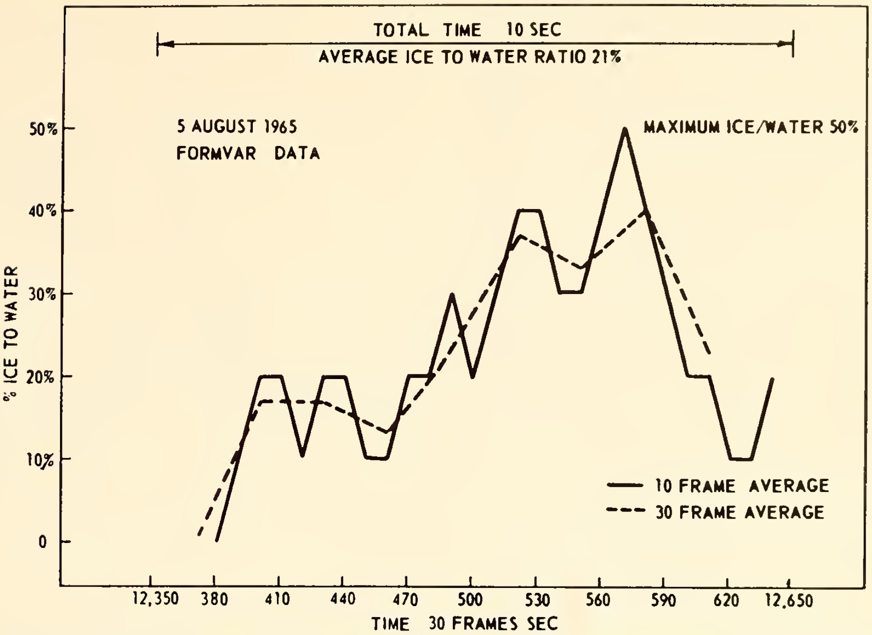

FIG. 10. Ice-to-water area percentage from Formvar data for 5 August seeded cloud. Abscissa is in frame number, 30 frames being equivalent to 1 sec or 100 m.

turret had reached the −18C level by the time of the Formvar sampling, and there is a possibility that the western turret was contaminated by ice particles filtering down from above. It is also not clear just how much of the observed ice was actually liquid freezing on impact with the cold Formvar. Although not conclusive, the presence of small pockets of up to 50% ice concentration in this cloud at −4C may be indicative of a multiplication mechanism working on a localized scale near the edges of the cloud, but not necessarily spreading throughout the entire cloud.

In any event the dynamical behavior of the two turrets works against an efficient *large scale* natural glaciation theory. According to the formvar evidence from a penetration just after seeding, the western turret was able to completely glaciate within 5 min after the silver iodide was released, and it managed to grow 10,500 ft higher than the unseeded central turret. If natural glaciation proceeded as rapidly and as extensively through tropical maritime cumuli as envisaged by the splintering model, it would be very difficult to explain the failure of the central core to grow in a similar manner as the seeded turret.

It is interesting to observe that arguments for some kind of an ice-multiplication process working on a less extensive scale and proceeding less rapidly than envisioned by Koenig can be advanced from a study of this cloud. This is especially significant in view of the fact that this was the only Stormfury case that had good Formvar replication data at the required temperature.

e. 10 August

Although the only two Stormfury clouds randomly selected for intensive study on this day were both seeded, excellent physical data were obtained on a penetration through a non-seeded cloud. Particularly noticeable in this control cloud's physical profile shown in Fig. 11 is the large volume-median size of the drops. This is consistent with observations of rain falling from cloud base during the entire 5 min it was under observation. Although the cloud topped at −11C (about −7C in the active, warm updraft core) when first observed, it quickly rained out and began to dissipate. Unfortunately, the cloud's history prior to the first observation is not known, thus making it impossible to determine the total time of supercooling and relating its behavior to the splintering hypothesis.

Good physical data were not obtained on penetrations of this day's first seeded cloud, but the second seeded case provided the profile shown in Fig. 12. First observed topping near −8C, this cloud grew 4000 ft to the −17C level in the 18 min leading up to the time of seeding. In 30 min following seeding, the cloud's growth rate accelerated as it grew an additional 14,000 ft.

The splintering calculations predict that this seeded cloud should have been 95% glaciated some 8 min before the time of seeding. However, the cloud's dynamical behavior is not consistent with such a prediction. The pronounced acceleration of cloud growth after seeding strongly implies fusion heat release through silver iodide nucleation, a condition requiring an essentially supercooled liquid state in the seeded area at the time of seeding. The large height increase of the seeded cloud again serves to point out the effectiveness of artificial glaciation under the right conditions in tropical maritime cumuli.

5. Discussion of the dynamical modeling

Although it is both useful and interesting to try to evaluate the efficiency of ice multiplication by physically and dynamically examining a cloud's life history in retrospect, a much more effective way of determining the importance of natural glaciation on cumulus modification is to predict beforehand the behavior of a certain size cloud in a given environment assuming the complete absence of natural glaciation and then testing the predictions on actual clouds. Likewise, from a suitable numerical model of cumulus dynamics it should be possible to predict the effects of seeding before the actual seeding experiment is conducted. If the clouds, after seeding, behaved as predicted by a model that assumes no natural glaciation at a temperature warmer than −15C, and if the unseeded clouds also behaved as predicted by such a model, it would be very hard to understand how natural glaciation at temperatures warmer than −15C could be a significant process in altering the dynamics of cumuli.

Two such independently developed numerical models were used to predict the behavior of all 23 clouds studied in the 1965 Project Stormfury experiments. The model used by the Experimental Meteorology Branch (EMB) of ESSA has been described by Simpson *et al.* (1965).

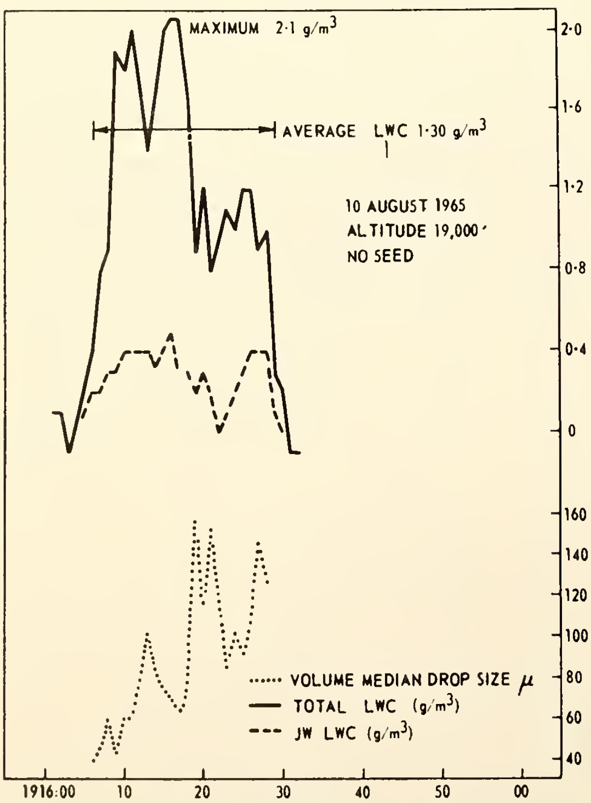

Fig. 11. Physical profile at the 19,000 ft level; 10 August control cloud.

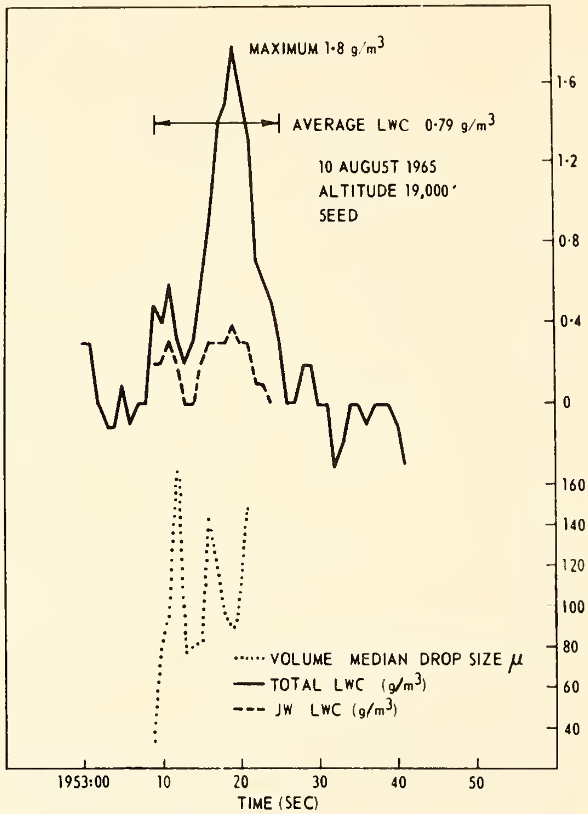

Fig. 12. Physical profile at the 19,000-ft level; 10 August seeded cloud (before seeding).

The model used at The Pennsylvania State University (PSU) is a steady-state modification of a time-dependent model developed and described by Weinstein and Davis (1968).

Essentially, the EMB model calculation consisted of integrating the vertical equation of motion for the rising cloud tower, which is assumed to behave as a rising plume with a vertically circulating cap, entraining environmental air at a rate inversely proportional to its horizontal dimension. The vertical acceleration of the center of the cloud tower is expressed as the difference between buoyancy and drag forces. The buoyancy force is a function of the temperature excess of the cloud over the environmental air, and is reduced by entrainment and by the weight of the condensed water within the cloud. The drag forces consist of momentum exchange from entrainment and a small aerodynamic effect. One-half of the cloud's liquid water was assumed to fall out of the cloud at each integration step. The model has recently been modified to include microphysical interactions (Simpson *et al.*, 1968).

The PSU model does not deal directly with the vertical acceleration of a cloud turret, but rather with conversion of kinetic energy to updraft velocity. The production of energy is again a function of the temperature excess of the cloud over the environmental air, the drag of the cloud's liquid water, and an entrainment parameter. A constant vertical mass flux through the cloud is assumed, thus allowing the updraft radius to be a function of the vertical velocity. The cloud's liquid water is partitioned into cloud water and hydrometeor water by assuming autoconversion and accretion rates, and all of the hydrometeor water is carried until the cloud reaches its maximum height, at which time it is released.

Although the two models approach the energetics of cloud growth from slightly different directions, the thermodynamic and entrainment calculations are handled in roughly the same manner. Both models require an environmental sounding, cloud base height, and the appropriate cloud radius as input data, and both compute cloud temperature excess, liquid water content, vertical velocity profiles, and maximum cloud height as output.

In practice, neither model assumes glaciation to occur naturally at temperatures $>-15C$. If the cloud were seeded, a subroutine was introduced which allowed the latent heat of fusion to be released linearly between -4 and $-8C$ (EMB model), or completely at $-6C$ (PSU model). Both models then assumed ice saturated conditions, thus accounting for additional warming as water vapor sublimed onto the ice instead of condensing into water.

Given an environmental sounding and the cloud base height, it was thus possible to predict cloud top heights of both the seeded and the non-seeded Stormfury clouds on both models if an in-cloud updraft radius could be chosen for the PSU model corresponding to the turret radius used in the EMB model.

6. Results of the dynamical modeling

A composite summary of the modeling results is given in Table 4. The chosen PSU model radius is an extrapolation into the cloud body of the turret radius

TABLE 4. Comparison of the EMB cumulus model with the PSU model: Results from the 1965 Project Stormfury experiments.

Time	Cloud	Action	Cld Radius		EMB Model Predict		PSU Model Predict		Obs Max Top (Km)	EMB Diff (km)	PSU Diff (km)
			EMB	(m)PSU	Unfroz Cld Ht	Seed (Km)	Unfroz Cld Ht	Seed (Km)			
28 July											
2058	1	Contr	500	1400	6·4	9·8	14·2	14·4	6·3	+0·1	+7·9
2217:30	2	Seed	550	2850	6·7	10·5	15·6	15·7	10·5	0	+5·2
2033	3	Contr	650	2000	7·8	11·9	14·9	15·1	7·4	−0·4	+7·5
29 July											
1810:30	1	Seed	1150	1700	7·6	12·4	6·6	12·1	11·6	+0·8	+0·5
1929:30	2	Contr	1100	1700	7·0	11·9	6·6	12·1	6·8	+0·2	−0·2
2044:30	3	Contr	1150	2000	7·6	12·4	8·2	12·9	7·8	−0·2	+0·4
2126:30	4	Seed	800	1350	5·4	5·4	5·2	5·2	5·4	0	−0·2
2205:30	5	Seed	800	1350	5·4	5·4	5·2	5·2	5·0	+0·4	+0·2
1 August											
2013:30	1	Seed	800	1500	6·0	6·0	5·7	5·9	6·2	−0·2	−0·3
3 August											
2158:30	1	Seed	1000	1800	9·4	11·1	10·0	11·2	11·2	−0·1	0
4 August*											
1825:30	1	Contr	950	1500	8·5	10·4	8·2	10·2	9·9	−1·4	−1·7
2144:30	2	Seed	550	1100	6·3	7·1	6·7	7·5	7·4	−0·3	+0·1
5 August											
1657:30	1	Contr	1000	1500	8·4	12·9	7·5	12·9	8·4	0	−0·9
1805:30	2	Seed	850	1250	7·0	11·9	6·3	11·9	11·0	+0·9	+0·9
8 August											
1636:30	1	Contr	1200	2300	7·2	8·6	6·1	7·0	7·0	+0·2	−0·9
1703:30	2	Seed	900	2100	6·4	6·5	5·9	6·4	6·4	+0·1	0
9 August											
1727:30	1	Contr	700	1200	8·4	9·8	8·7	11·1	8·3	+0·1	+0·4
1740:30	2	Seed	850	1250	9·5	11·2	9·2	11·4	11·2	0	+0·2
1847:30	3	Contr	1200	1400	6·8	7·5	5·3	5·3	6·5	+0·3	−1·2
1944:30	4	Seed	700	2100	8·4	9·8	13·7	13·9	10·2	−0·4	+3·7
2022:30	5	Seed	1300	2000	7·1	9·2	5·8	6·8	8·7	+0·5	−1·9
10 August											
1813:30	1	Seed	900	1300	8·6	10·6	7·9	10·2	10·2	+0·4	0
1957:30	2	Seed	1100	1500	9·7	12·0	8·3	11·2	11·4	+0·6	−0·2

* The apparent discrepancies in both models in predicting the 4 August control case could be resolved if the cloud naturally glaciated at $-15C$; in that case the EMB model predicts a top height of 10.0 km, while the PSU model predicts a top height of 9.8 km. The cloud grew to 9.9 km. This is the only case for modeling support for natural glaciation at temperatures $>-15C$.

used by the EMB model. Although admittedly this is a very subjective technique, it was performed prior to the model calculations to eliminate bias.

As can be seen from Table 4, the PSU model cloud top heights were generally in good agreement both with those predicted by the EMB model and with the actual observed cloud heights, with the notable exception of the three clouds on 28 July. A careful re-examination of the cloud photographs for this day revealed that the radii chosen for the PSU model were almost a factor of 2 too large, and this error was compounded by an unstable environment above 20,000 ft which allowed very buoyant clouds at that level to grow naturally all the way to the tropopause. Because the cloud's buoyancy, computations are a function of entrainment, which in turn is a function of the cloud's horizontal dimension, the error in choosing the cloud radii on this day was critical and caused the PSU model to overpredict cloud growth by an embarrassing 50%.

The statistical results of the modeling are graphically portrayed in Figs. 13 and 14. If the EMB model predictions are compared with the observed maximum heights of all 23 Stormfury clouds, a correlation coefficient of 0.98 is established by the results. Excluding the three clouds on 28 July from the analysis, the correlation coefficient between the PSU model predictions and the observed maximum height of 20 Stormfury clouds is 0.92.

Such results strongly imply that natural glaciation

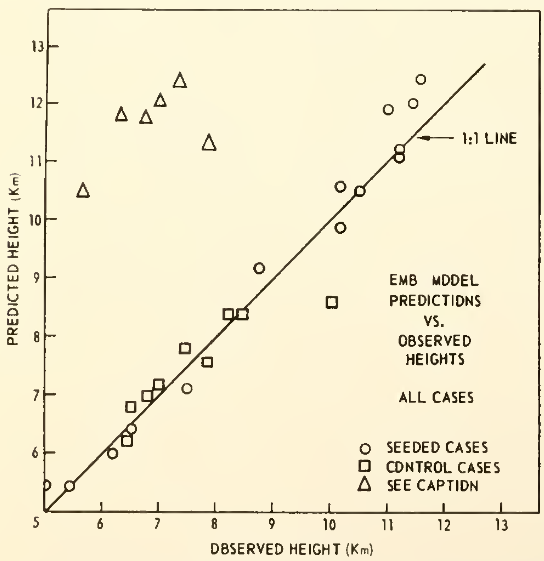

Fig. 13. Experimental Meteorology Branch (EMB) model predicted cloud top heights vs observed cloud top heights for all 23 Stormfury clouds. The correlation coefficient is 0.98. The triangular symbols give the EMB model predicted cloud top heights for natural glaciation at −8C (of the extent predicted by the splintering model) vs the observed cloud top heights. Only the six Stormfury clouds with long, documented life histories and good microphysical data cloud were used in this particular analysis. The correlation coefficient between predicted heights and observed heights for these six cases is a rather poor 0.43, indicating that the splintering model glaciated these clouds too rapidly.

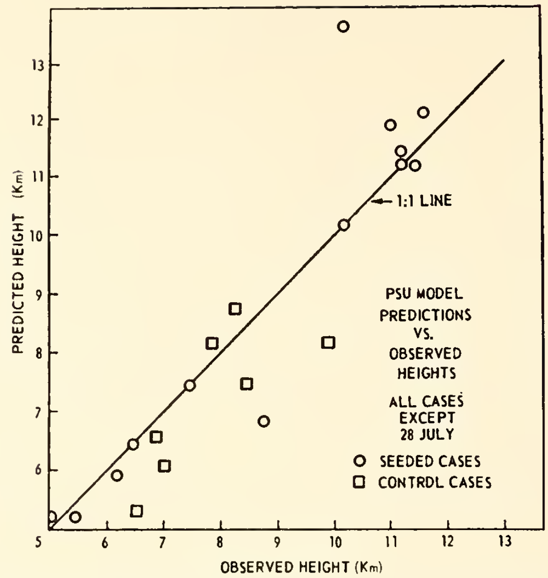

Fig. 14. Pennsylvania State University (PSU) model predicted cloud top heights vs observed cloud top heights; three cases on 28 July excluded from analysis. The correlation coefficient for these 20 clouds is 0.92.

does not affect the dynamical behavior of tropical maritime cumuli, at least at temperatures $> -15C$. Only for one cloud (control case of 4 August) do both models predict cloud heights better if natural glaciation is assumed at $-15C$. Using a slightly different technique of analyzing the results of the model predictions, Simpson *et al.* (1967) demonstrate a very good correlation between seeding and growth which strongly indicates that natural glaciation is not nearly as efficient as artificial seeding by silver iodide in modifying the dynamical behavior of tropical maritime cumuli.

7. Summary and conclusions

In order to test the validity of Koenig's (1966) ice splintering model, and in order to determine if natural glaciation is important enough in tropical maritime cumuli to influence modification attempts by silver iodide seeding, a detailed study was made of cumuli observed during the 1965 Project Stormfury experiments. Physical data involving the water and temperature profiles within the clouds were analyzed, and dynamical studies were initiated on two independently developed numerical cumulus models.

In the physical analysis it was found that all of the seeded clouds studied grew at least 10,000 ft higher than a paired control cloud in the same environment, thus indicating a strong cause-and-effect relationship between seeding and growth. A very strong correlation between seeding and growth was later confirmed in the dynamical analysis. Some direct evidence of partial glaciation in a cloud topping at no colder than $-5C$ was found, but all of the clouds behaved dynamically in a manner indicating that their vital updraft areas did not glaciate as rapidly as predicted by the splintering model. The evidence suggested that the updraft core of a typical tropical maritime cumulus cloud can remain in a supercooled liquid state at temperatures of -10C and colder for periods $\geqslant 20$ min, and natural glaciation in such a cloud is not extensive enough to significantly influence its dynamical behavior. On the other hand, the results of the study indicate that artificial glaciation induced by silver iodide seeding is an effective means of modifying the dynamical behavior of such clouds by converting the cumulus updraft areas from supercooled water to ice at temperatures $\lesssim -5$C.

The primary conclusion to be drawn from this study is that natural glaciation does not proceed rapidly and/or extensively enough in the critical cloud updraft areas to alter the effectiveness of modifying tropical maritime cumuli by causing artificial glaciation with silver iodide.

8. Future studies

Evidence now suggests that the occurrence of ice in clouds topping at temperatures near -10C is far more prolific than can be explained by assuming a one-to-one relationship with active freezing nuclei. From the results of this study, however, apparently the ice is not evenly distributed throughout the cloud body, as the vital updraft areas remain essentially supercooled liquid for long periods of time. It is possible that some kind of an ice-multiplication mechanism may be able to work near the cloud edge to glaciate local pockets, but cannot work effectively in the wetter updraft core.

A better physical understanding of the behavior of freely-falling freezing water droplets in realistic atmospheric conditions is essential to the interpretation of an ice-multiplication mechanism. It now seems likely that the original laboratory work on splintering performed by Mason and Maybank (1960) may have greatly overestimated the efficiency of such a mechanism in the free atmosphere. Both Dye and Hobbs (1968) and Johnson and Hallett (1968) have failed to find copious splintering under more reasonable atmospheric conditions using rather large (1 mm) suspended drops, but more work now needs to be concentrated on both the freezing of small droplets in free fall and the importance of a riming mechanism on ice multiplication.

Acknowledgments. The author is sincerely grateful to Dr. Joanne Simpson and the personnel of the Experimental Meteorology Branch for making the Stormfury data available for this study, and for offering much helpful advice on a wide variety of topics related to the splintering mechanism and computer modeling. R. E. Ruskin and J. M. Averitt of the Naval Research Laboratory provided the Formvar tapes used in the analysis of the 5 August seeded cloud, and both devoted a great deal of their time in assisting with the interpretation of the data. The author wishes to express a special note of thanks to Dr. Larry G. Davis of The Pennsylvania State University faculty for initiating interest in the topic, and for providing much-needed encouragement and guidance on attacking the problem.

REFERENCES

Averitt, J. M., and R. E. Ruskin, 1967: Cloud particle replication in Stormfury tropical cumulus. *J. Appl. Meteor.*, **6**, 88–94

Dye, J. E., and P. V. Hobbs, 1968: The influence of environmental parameters on the freezing and fragmentation of suspended water drops. *J. Atmos. Sci.*, **25**, 82–96.

Gokhale, N. R., 1965: Dependence of freezing temperature of supercooled water drops on rate of cooling. *J. Atmos. Sci.*, **22**, 212–216.

Johnson, D. A., and J. Hallett, 1968: Freezing and shattering of supercooled water drops. *Quart. J. Roy. Meteor. Soc.*, **94**, 468–482.

Koenig, L. R., 1963: The glaciating behavior of small cumulonimbus clouds. *J. Atmos. Sci.*, **20**, 29–47.

——, 1966: Numerical test of the validity of the drop-freezing/splintering hypothesis of cloud glaciation. *J. Atmos. Sci.*, **23**, 726–740.

——, 1968: Some observations suggesting ice multiplication in the atmosphere. *J. Atmos. Sci.*, **25**, 460–463.

Latham, J., and B. J. Mason, 1961: Generation of electric charge associated with the formation of soft hail in thunderclouds. *Proc. Roy. Soc. (London)*, **A260**, 537–549.

Levine, J., 1965: The dynamics of cumulus convection in the trades: A combined observational and theoretical study. Woods Hole Oceanographic Institution, Ref. No. 65-43, 129 pp.

Mason, B. J., and J. Maybank, 1960: The fragmentation and electrification of freezing water drops. *Quart. J. Roy. Meteor. Soc.*, **86**, 176–186.

Mossop, S. C., R. E. Ruskin and K. J. Heffernan, 1968: Glaciation of a cumulus at approximately -4C. *J. Atmos. Sci.*, **25** 889–899.

Murgatroyd, R. J., and M. P. Garrod, 1960: Observations of precipitation elements in cumulus clouds. *Quart. J. Roy. Meteor. Soc.*, **86**, 167–175.

Ruskin, R. E., 1967: Measurements of water-ice budget changes at -5C in AgI-seeded tropical cumulus. *J. Appl. Meteor.*, **6**, 72–81.

Sax, R. I., 1967: Natural and artificial glaciation of tropical cumuli. NSF Rept. No. 9, Dept. of Meteorology, The Pennsylvania State University, 85 pp.

Simpson, J., 1967: Photographic and radar study of the Stormfury 5 August 1965 seeded cloud. *J. Appl. Meteor.*, **6**, 82–87.

——, G. W. Brier and R. H. Simpson, 1967: Stormfury cumulus seeding experiment 1965: Statistical analysis and main results. *J. Atmos. Sci.*, **24**, 508–521.

——, R. H. Simpson, D. A. Andrews and M. A. Eaton, 1965: Experimental cumulus dynamics. *Rev. Geophys.*, **3**, 387–431.

——, V. Wiggert and T. Mee, 1968: Models of seeding experiments on supercooled and warm cumulus clouds. *Proc. First Natl. Conf. Weather Modification*, Amer. Meteor. Soc., Albany, N. Y., 251–269.

Weinstein, A. I., and L. G. Davis, 1968: A parametrized numerical model of cumulus convection. NSF Rept. No. 11, Dept. of Meteorology, The Pennsylvania State University, 44 pp.

Wexler, R., and R. J. Donaldson, Jr., 1966: The spread of ice in cumulus clouds. *J. Atmos. Sci.*, **23**, 753–756.

Reprinted from Medical Opinion & Review Vol. 5, No. 10, 39-58.

Cloud Building and Breaking

Joanne Simpson, Ph.D.

Seeding clouds with silver iodide has been going on for more than twenty years, and, during all that time, controversy has been raging about it. Recently, the Experimental Meteorology Laboratory of the Environmental Science Services Administration (ESSA) jointly with the Naval Research Laboratory has been conducting research to clear up the controversy.

To understand what is new and different about our approach to cloud seeding, we must know something of the history of the subject. Cloud seeding dates back only to 1946, when Vincent Schaefer, at the General Electric Company, discovered that small pellets of dry ice could convert a supercooled water cloud into an ice cloud—at least, it could in his laboratory.

The concept of supercooling is central to the theory of cloud seeding. Water may be cooled to a temperature below its freezing point but still not crystallize. When some nucleus is present around which the ice may grow, then crystallization will proceed in the familiar manner. After his laboratory work, Schaefer experimented in the real atmosphere, where he used dry ice to convert supercooled fogs and stratus clouds. He was frequently able to precipitate snow streamers, and many people still remember the impressive race-track patterns carved out by GE aircraft in supercooled stratus decks.

JOANNE SIMPSON *is Director of the Experimental Meteorology Laboratory, U.S. Department of Commerce Environmental Science Services Administration, and Adjunct Professor of Atmospheric Science at the University of Miami, Coral Gables*

Silver Preferred

Only a year later, in 1947, Bernard Vonnegut, also of GE, discovered that silver iodide was nearly as good a cloud nucleator as dry ice, presumably because its crystal structure so closely resembles that of ice. Vonnegut and his successors showed that silver iodide could be produced chemically in ground or airborne generators, making it logistically more convenient than dry ice for seeding experiments. We are still using silver iodide.

Schaefer and Vonnegut have explained their cloud conversion in terms of the colloidal instability of a cloud of supercooled water. At temperatures colder than freezing, the saturation vapor pressure is higher over water than over ice, so that the introduction of ice crystals into a supercooled cloud releases the colloidal instability—that is, the ice crystals grow at the expense of the water drops until the cloud is glaciated. In the atmosphere, supercooled clouds are common because of scarcity of nuclei.

The rain-making idea, originated

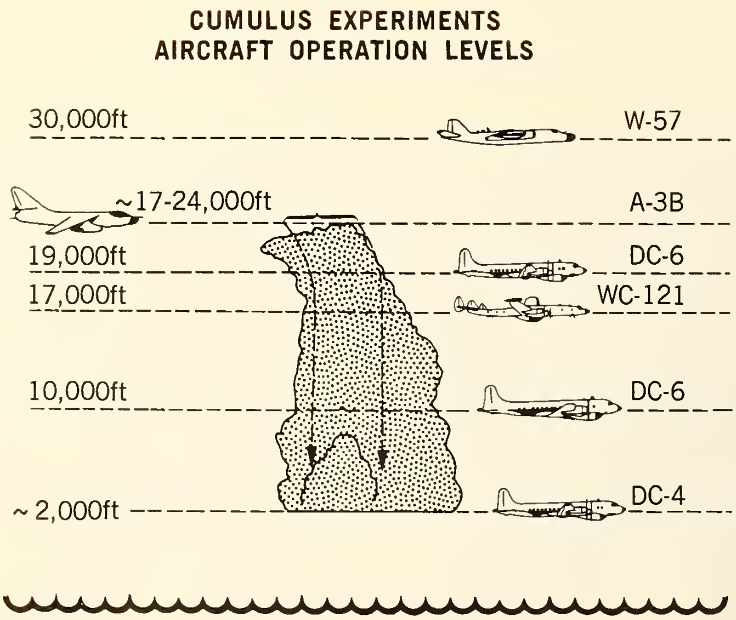

Figure 1. *Experimental design for cumulus-seeding experiment. Several aircraft are heavily instrumented with probes to measure temperature, humidity, winds, cloud water, rain water, particle habit and spectrum. Pyrotechnic seeding-devices are dropped by jet aircraft at 100-meter intervals within bracketed arrows.*

by Schaefer and his colleague, Nobel Prize winner Irving Langmuir, went like this: in order for a cloud to rain, about one million tiny cloud drops, each about a thousandth of a centimeter in diameter, must somehow combine into one raindrop of about a millimeter in diameter. Relative to the cloud, the drop can then fall and reach the ground without evaporation. One way to achieve this artificially would be to introduce one to ten artificial freezing nuclei per million supercooled droplets, or about one nucleus for each one to ten liters of cloudy air. The ice will fall as rain when it melts at a lower altitude. Let us call this the "static" theory of precipitation growth by seeding, since it ignores the motion structure of the cloud and possible cloud changes.

Since an average cumulus might contain about ten trillion liters of supercooled cloudy air, and silver iodide generators provide roughly ten trillion nuclei per gram of

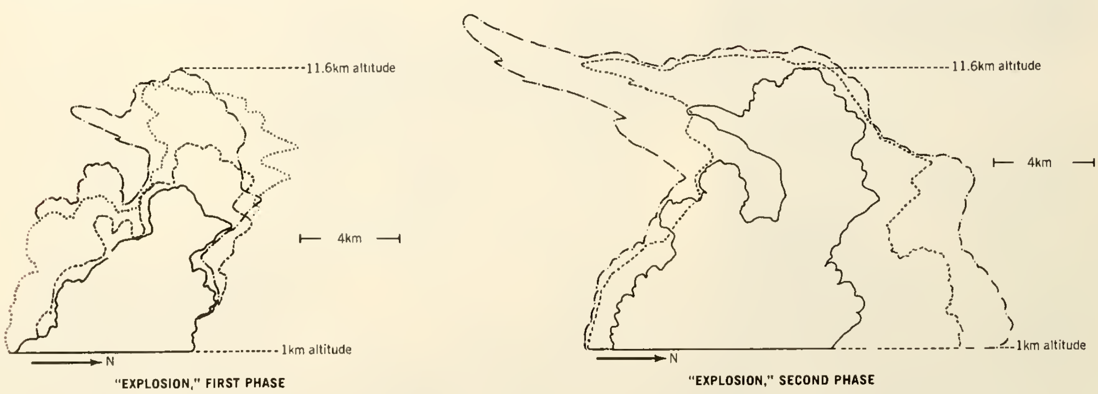

Figure 2. *Scale outlines of the growth of a cloud following seeding. First phase of the explosion is shown at the left; second phase, at the right. The outlines were made every three to four minutes by photogrammetry from the command and control aircraft that were boxing the cloud.*

smoke, we need something like a few *grams* of silver iodide per cloud. This requirement is well within the capacity of the ground and airborne generators that have been in use for many years.

One of the most carefully designed of the experiments based on the "static" hypothesis was Project Whitetop, a five-year program for seeding of summer cumulus clouds over Missouri. Project Whitetop was directed by an eminent meteorologist, Roscoe R. Braham, Ph.D., of the University of Chicago. Statistical controls were applied both in space and time.

Two disturbing results were obtained: first, the seeding apparently *decreased* rainfall by about 21 percent over an area of 100,000 square miles; second, Dr. Braham found that many rather warm, but still supercooled, cumuli had plenty of natural ice already in them. In fact, he often found about one ice particle per liter in unseeded clouds. Our ESSA group has duplicated these results over Florida and the Caribbean.

Since the one ice particle per liter that Dr. Braham and we found was the amount supposed to be introduced by seeding, there should have been precipitation. If the theory were correct, there would be no point to introducing much larger injections of ice nuclei, since these would result in "overseeding" the cloud. If too many ice nuclei were

Figure 4. *Typical "cutoff" tower growth regime following seeding: A, cloud at seeding time: B, 10 minutes later; C, 18 minutes after seeding, when tower has reached 36,000 feet and cut off.*

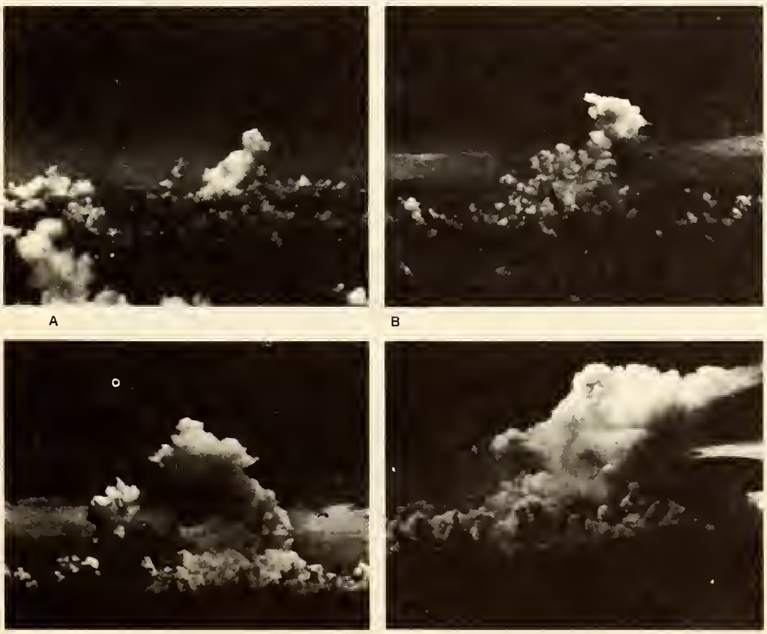

Figure 3. *Explosive growth of same seeded cloud as shown in Figure 2. Typical GO cloud (A) is shown at time of seeding, 9 minutes later (B), 19 minutes after seeding (C), and 38 minutes after seeding (D), when the cumulonimbus is fully developed, top about 40,000 feet.*

introduced, it was believed, the cloud water would be shared among many small ice particles, and none of them would grow large enough to precipitate.

In our own work, we chose a different approach; ironically enough, overseeding was just what we decided to aim at because we intended to rapidly release the heat of freezing (fusion) in the supercooled water. We intended to increase the cloud buoyancy and hence enhance its updraft and vertical growth. When we first started our modification experiments, back in 1963, we were not directly concerned with increasing rainfall, although it was soon clear that increased rainfall was a likely by-product of the invigorated cloud dynamics.

Figure 5. *Typical "no-growth" regime. At 12 minutes after seeding, cloud looks unchanged except that top has glaciated.*

So we have proposed the "dynamic" theory. From years of study of cumulus clouds, we had learned that their life cycle is a fierce struggle for existence, with the forces of growth and destruction in near balance. Because it is very difficult to study by measurement a nearly balanced natural phenomenon, we wanted to upset the balance. This, we thought, would enable us to improve our numerical models of cumulus clouds.

Floating on Air

The main growth force in a cumulus is buoyancy. The air of the cloud has a lower density than the surrounding air. Gaseous water condenses into the liquid droplets that make up the cloud; in the process, heat is released; thus the average tropical cumulus is warmer than its environment by about 0.5 to 1.0°C. Freezing its liquid water content of one to two grams per cubic meter can about double this excess and thereby double its buoyancy—if the freezing is done suddenly in the cloud's ascending region. A "seeding subroutine" that models this release of heat was introduced into our computer.

For a real-life experiment, the technical means first appeared in 1963, when, for the first time, the massive-seeding techniques became available. These had been invented at the Naval Ordnance Test Station in California. The innovation consisted of generating silver iodide smoke by pyrotechnics or fireworks. These Navy pyrotechnic silver iodide generators released 1.2 *kilograms* of silver iodide each. Moreover, they could be dropped by an aircraft from above directly into the business portion of the cloud.

In August, 1963, we conducted a preliminary pyrotechnic seeding experiment in the Caribbean area. Six clouds were seeded with about twenty kilograms of silver iodide per cloud—about one nucleus per cloud drop instead of one or a few per million, as the static theory required. Four of the seeded clouds showed a spectacular or explosive growth following seeding; moreover, it appeared that our model could predict which clouds would grow, which would not.

The validity of the results was viewed with some justifiable skepticism by the meteorological community: there is a large, natural variability in clouds; the sample was small; and there was a possibility of bias in the selection of clouds (clearly, the clouds just might have grown as well by themselves, without seeding).

Control System

We had to apply statistical control and randomization, in the same manner as in medical or biological research. The simplest randomization technique would be tossing a coin—heads you seed, tails you don't, but you do observe the cloud as a control. A series of sealed envelopes were prepared for us by a statistician and provided to the pilot of the seeder aircraft. He then followed the "seed–no-seed" instruction without informing the project scientists what his action had been for any given cloud.

In 1965, an extensive randomized-seeding experiment was undertaken with seven aircraft in the Caribbean area (see Figure 1). A stack of five instrumented aircraft make one penetration of the "GO" cloud before seeding and many penetrations after seeding to develop a complete picture of its before-and-after structure. The jet seeder flies through cloud top between the first two measuring runs; it drops pyrotechnics at 100-meter intervals, so that the smoke plumes completely fill the supercooled portion of the cloud top. A seventh aircraft (not shown in Figure 1) boxes the cloud and directs all the others on its radar scope. It also takes radar and

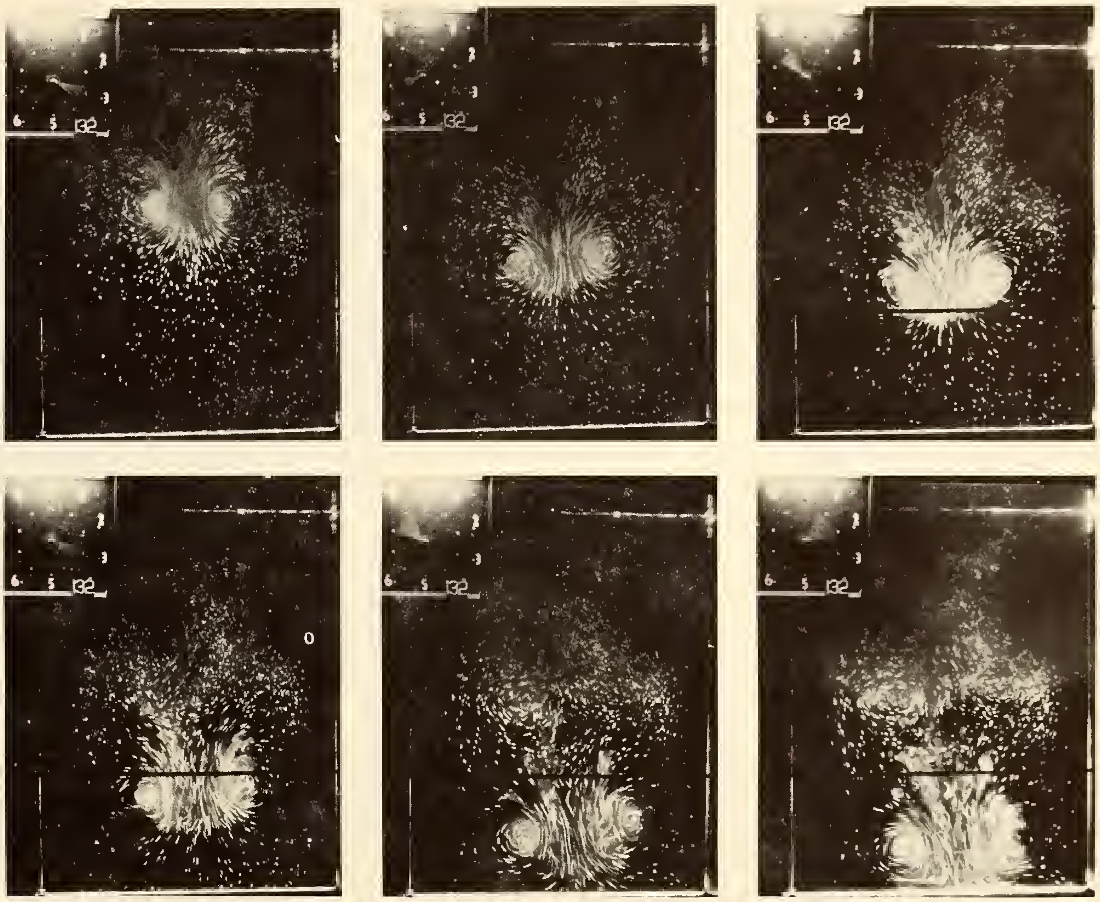

Figure 6. *Development of tank "cloud" as function of time. Note circulationlike vortex ring as indicated by white streaks. The computer model of a cumulus—a set of equations predicting vertical rate of rise of a buoyant plume or bubble—was originally developed from laboratory experiments, such as this, carried out at the Imperial College in London and at the Woods Hole Oceanographic Institution in Massachusetts. Here a laboratory cloud, which consists of a blob of salt solution, is released into a resting tank of pure water. The cloud, being denser than its surroundings, moves downward. Its vortexlike circulation is made visible by neutral-density, white-painted particles. These experiments led to the laws of cloud-tower circulation and of mixing between cloud and its drier surroundings, which in nature is the main brake against buoyancy.*

motion pictures on time-lapse, so that the cloud growth can later be reconstructed (Figure 2).

In 1965, we obtained twenty-three GO clouds, of which fourteen were seeded and nine were studied identically as controls. This experiment established definitively that massive silver iodide seeding could increase cloud growth, but *under specifically initial conditions of the cloud-environment system.* The italics contain the meat of the result, which clarifies some of the seeding controversy. Seeding could lead to three quite different growth regimes, depending on the conditions (Figures 3–5). The first is explosive growth, where the cloud grows greatly in both height and size and becomes a full-fledged cumulonimbus after twenty to thirty minutes (Figure 3). With this regime, we suspected that the rain falling from the cloud must have been considerably increased. In the second regime (Figure 4), the seeded tower grows to great heights, but it cuts off from the main cloud body, which may then dissipate prematurely. We suspected a decrease of rainfall in these cases. The third regime displays little or no growth (Figure 5), and so we might expect either no change or lessened rainfall from seeding.

The version of the computer model we used in 1965 did very well in predicting the difference between the growth and no-growth cases (Figure 7), however it was too simple to say anything about precipitation—but then, we had no way to measure rainfall over the Caribbean anyway. Since then, we have improved the model so that it begins to predict the growth and fallout of precipitation, and we can measure rainfall with the University of Miami's calibrated radars.

In May, 1968, our first overland experiment was run in South Florida, again a cooperative venture of ESSA and the Naval Research Laboratory. The Air Force, the University of Miami, and Meteorology Research, Inc., also participated. For a land experiment, ESSA had special pyrotechnic flares developed commercially. These burn out completely by 10,000 feet and so are safe to use over populated areas. Extensive laboratory and field tests have been made of these flares (Figures 8 and 9), which put out fifty grams of silver iodide each. Their efficiency was sufficiently high so that twenty units per cloud were injected.

This time, the results were even more successful. Thirteen of the fourteen seeded clouds grew explosively following seeding. The seeded clouds grew an average of 11,400 feet higher than the control

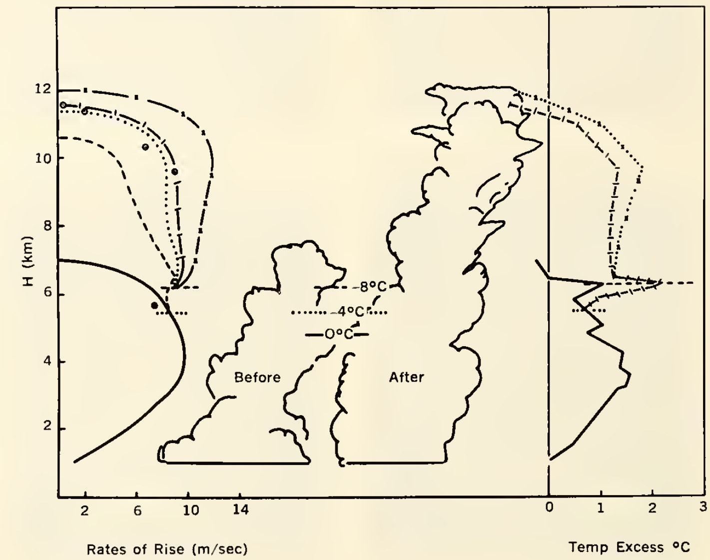

Figure 7. *Model results for cloud of Figures 2 and 3. Right-hand curves are temperature excess of cloud over environment, and are proportional to buoyancy. Left-hand curves are rate of rise of cloud tower as function of height. Growth ceases at level where rate of rise goes to zero. Unseeded-tower properties are shown by solid lines. Seeded properties are shown by dashed and dotted lines. Different seeded curves are results of slightly different seeding subroutines, some allowing for tower expansion. Note increased temperature excess (buoyancy) caused by seeding.*

clouds. The odds against that being a chance occurrence are one in two hundred. A main reason for this improvement was that the computer model was run each morning in advance of the seeding operation. If the model predicted that all clouds would grow to great heights naturally—or that no clouds could grow even after seeding—the day's operation was cancelled; thus nearly all "dud" cases were avoided. Also, the cutoff growths were eliminated, presumably as a result of the "two-shot" seeding technique, where the seeder aircraft make two successive passes at right angles to each other.

Figure 8. Loading of pyrotechnic flares on rack under wing of jet seeder-aircraft. Rack is in down position, aircraft nose is on left. Each of two racks carries 56 50-gm flares. Each flare is 3.75in long and about 1.5in in diameter.

One of the most important results of the experiment (Figure 10) is a combination theoretical, statistical, and observational graph plotting seedability against seeding effect. "Seedability" is defined in kilometers—it is the difference between the model-predicted seeded top and the predicted unseeded top. A seedability of 4km means that the seeded cloud should grow 4km higher than the same cloud if left unseeded. "Seeding effect" is the difference (again in kilometers) between the observed maximum cloud top and the predicted unseeded top. If the data follow the model, the numerical results for the seeded clouds should be found to lie on a slanting line with slope one, because for them seedability and seeding effect should be exactly equal. The unseeded control clouds, however, should lie along the horizontal line with zero slope, because they should show no seeding effect regardless of their seedability.

The two populations separate clearly, even to the satisfaction of the statisticians, and the effect of massive seeding on vertical cloud growth is again definitively established.

But we were able to take a further important step and relate rainfall to both cloud growth and predicted seedability. To do this, first the water production in ten-minute intervals had to be calculated for all clouds, both seeded and unseeded. A prerequisite for this evaluation was a careful calibration of all components of the radar. A comparison was made with the extensive rain-gauge network of South Florida, so that a measured radar-echo intensity can be read as a rate of rainfall (Figure 11).

There was a high day-to-day and cloud-to-cloud variability, but, on the average, the seeded clouds rained twice as much as the controls. The average difference was 100 to 150 acre-feet per cloud, which is quite a lot of water. Unfortunately, the large variability and small sample reduced the statistical significance of the rainfall increases, depending on the particular test used, to where the odds were only one in five to one in twenty against the results having

Figure 9. Nighttime test of five pyrotechnic flares, 1968 Florida seeding-program. Straight line is aircraft landing-light, left on for 4,000ft travel. Each flare falls 12,000ft before burnout (80 seconds); forward travel is only about 1,500ft.

come about by chance. This level of significance is not adequate, and the experiment must be repeated one more time with the same result in order for it to be completely definitive.

There is an important result of this experiment that pertains to rainfall modification—the vertical growth following seeding and the predicted seedability are both highly and significantly correlated to the production of water by a seeded cloud. This supports the dynamic theory of seeding, which hypothesized that invigorating the cloud growth was the way to increase rainfall.

Quantity, Not Quality

Confirmation of this came from the detailed aircraft penetrations: the precipitation sampling instruments showed that the rainfall rate, spectrum, and structure were not perceptibly different in seeded and unseeded clouds, both at the 20,000-foot elevation and at cloud base. Rather, it was the increased size and prolonged life of the seeded clouds that caused them to rain more, and not the microstructural changes the older theories had supposed. Also, we now have the ability to predict in advance the potential water-production from seeding, since the numerical model can predict seedability when atmospheric temperature, moisture, and initial cloud-diameters are known.

In general, there is good seedability when there are just a few isolated thunderstorms over South Florida; both drier and much wetter days are generally less favorable. The probable number of favorable days in the various seasons is now being investigated. If ten clouds could be seeded on each suitable day, then, at 100 to 150 acre-feet per cloud, the water production would be considerable. In an operational seeding program, which would be much less expensive than our experimentation, each cloud could be seeded for less than $500, including pyrotechnics and aircraft time. With irrigation water costing about $48 per acre-foot, we would get about a ten-to-one cost-benefit ratio—*if* these results can be extended from single clouds to groups of clouds over a larger area.

The implications of this experiment are more far-reaching, however, than the immediate practical consequences of rain augmentation. We have learned to predictably and controllably manipulate one aspect of the convective, or buoyant, process, and that is a key process in the atmosphere. If we control one aspect of cumulus activity, then why not others in the foreseeable future?

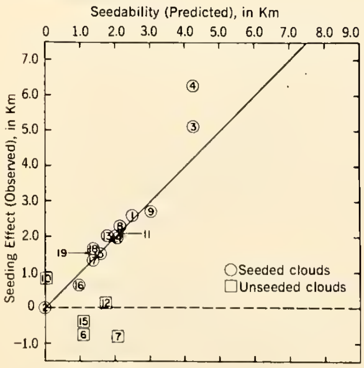

Figure 10. *Seedability versus seeding effect, Florida, 1968 (see text).*

Cumulus clouds are important in several ways equally as vital as their rain production. Clouds like these are the driving mechanism of severe storms such as the squall line, hailstorm, tornado, and hurricane. A hurricane-seeding program, Project Stormfury, is building on the techniques and models described here to seek a way to mitigate the destruction of the furious hurricane winds, which do nearly 300 million dollars damage annually in the United States alone, aside from a tragic loss of life and human suffering, as hurricane Camille recently demonstrated.

Forestalling Storms

At present, in the Soviet Union, an area half the size of Switzerland is being protected from hail damage. There, rockets and artillery shells are guided by radar to fire massive quantities of silver iodide into the wettest part of potential hail clouds. An apparently spectacular reduction of hailstone size and damage has resulted.

Finally, cumulus clouds play a crucial role in maintaining the large-scale wind systems in the atmosphere—they drive the trade winds, convert the fuel in the global fire-box zone near the equator, and affect the earth's radiation budget over large portions of the globe, so that their effects must be incorporated in the computer forecast-programs that the weatherman uses daily to predict the air flow. The knowledge gained from controlled experiments and numerical cumulus models are being introduced into large-scale forecast schemes

Figure 11. *Radar echo (at cloud base) for a cloud that exploded following seeding. Time from seeding, in minutes, is under the echo tracing.*

leading to the more realistic simulation of global weather changes.

But what of possible large-scale weather and climate modification? Since cumulus clouds fuel large wind systems, drive storms, and control exchange of radiant energy, could not altering cumuli over wide areas perhaps change storm and weather patterns? This might sound today like a far-fetched science-fiction daydream, but that's the way a manned moon-voyage sounded in the 1930s. END

Reprinted from Deep Sea Research
Vol. 16, Suppl. 447, 233-361.

Deep-Sea Research, 1969, Supplement to Vol. 16, pp. 233 to 261. Pergamon Press. Printed in Great Britain.

On some aspects of sea–air interaction in middle latitudes

JOANNE SIMPSON*

Abstract—Sea–air exchange is related to travelling frontal cyclones in middle-latitudes. The distribution of energy and momentum transfer relative to the cyclone model is first described. Then the role of sea–air exchange in cyclogenesis is analyzed in terms of the concentration and production of vorticity. Observational cases are supplemented by numerical model results. It is tentatively concluded that the direct effect of oceanic heating upon cyclone growth is small but that the indirect effect, via convection, may be very large. A beginning attempt is made to analyze how and under what conditions turbulent exchange sustains deep convection and how, in turn, the convection acts to produce or enhance cyclone development.

1. INTRODUCTION

LIKE THE weather, the main characteristic of sea–air interaction in these regions is fluctuation. A typical sample from Atlantic Station C (52°45′N; 35°30′W) is shown in Fig. 1. The graphs are time sequences of sensible and latent heat exchange, Q_s and Q_e, and shearing stress, τ. These were computed from the ship's three-hourly observations using the Jacobs exchange formulas in the form published by MALKUS (1962).

The figure shows that the exchange fluctuations are not random but quite organized. The main organization is on a time scale of 2–3 days, with superposed mesoscale variations of a few hours. In the period shown, 4·35 cm (net) of sea water evaporated into the atmosphere at Sta. C and 58% of the evaporation took place in just one-sixth of the time intervals, while 84% was achieved in one-third of them. The shearing stress imposed on the ocean and the sensible heat flux were similarly concentrated. The significant air–sea exchange in mid-latitudes is thus restricted almost entirely into synoptic-scale " disturbances." It requires little daring to identify these with the travelling frontal cyclones which dominate the weather maps of these regions. This exchange pattern contrasts with that in the tropics, where the major energy exchange is effected by the strong and steady trade winds.

In Fig. 1, the shape of the exchange curves permits deductions about the weather pattern and its stage of development. In the sequence February 2–4, a surge in stress (wind) coincided with negative heat flux abruptly changing to positive just before midnight on February 2. Then the evaporation and heating of the air persisted for about a day after the strong winds diminished. These features suggest a simple cold front or young warm-sector cyclone wave, with warm air flowing northward first, followed by a sudden cold outburst over the sea. Figure 2a shows that this was indeed the chain of events. A front is as much an " exchange discontinuity " as it is an air mass transition.

A deeper, older and more occluded cyclone is suggested by the exchange pattern for January 27–29. The greater deepness is indicated by the stronger stress and the age by the lack of surface warm air advection (negative heat exchange) ahead of the

*Environmental Science Services Administration and University of Miami, Coral Gables, Florida.

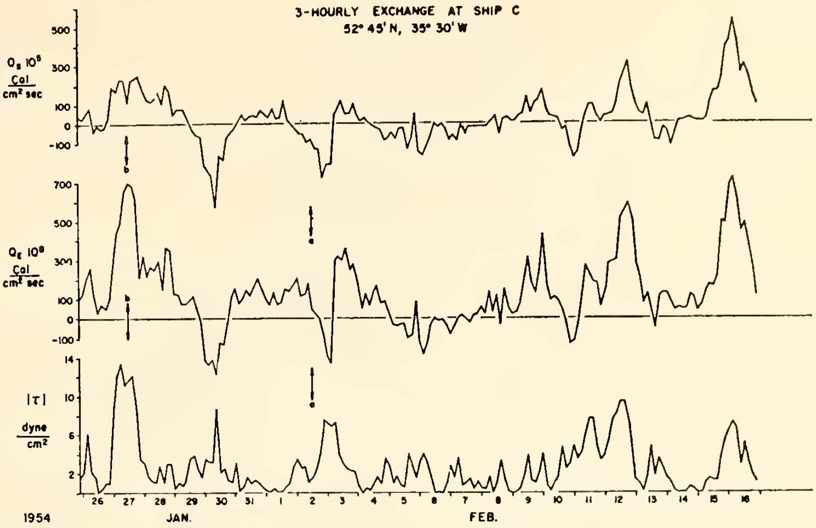

Fig. 1. Three-hourly exchange at Atlantic Ship C(52°45′N; 35°30′W) from Jan. 26–Feb. 16, 1954. Values of Q_s (sensible heat flux), Q_e (latent heat flux) and τ (shearing stress) computed from ship observations using Jacobs-type formulas. Top curve is Q_s in cal cm^{-2} sec^{-1} $\times$ 10^5; middle curve is Q_e in same units; bottom curve is shearing stress in dynes cm^{-2}. The " a " denotes time of weather map in Fig. 2a; the " b" denotes time of weather map in Fig. 2b.

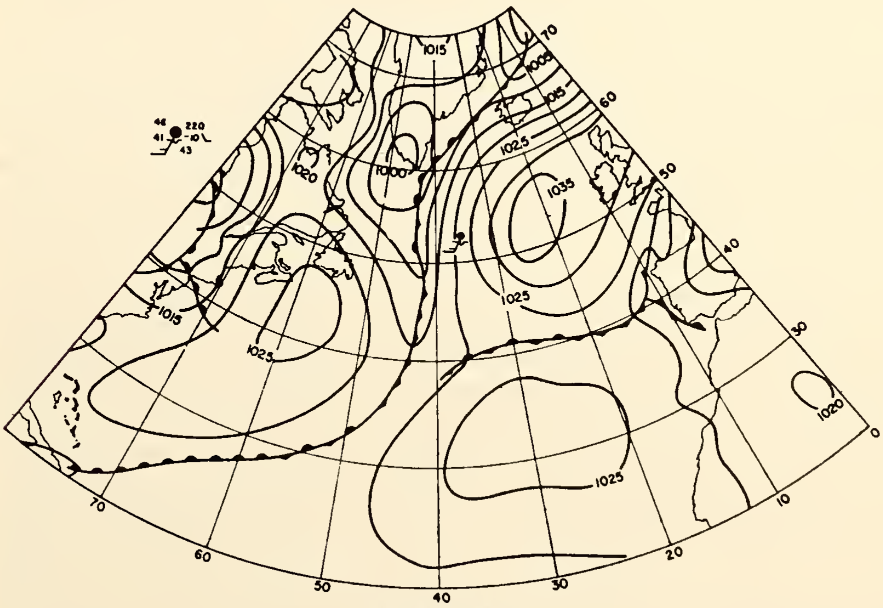

Fig. 2a. Surface weather map for February 2, 1954, 1230 GMT. Adapted from Daily Series Synoptic Weather Maps published by U.S. Weather Bureau. Only station shown is Weather Ship C. Sea temperature (°F) appears to lower right of station symbol. Remaining notation standard.

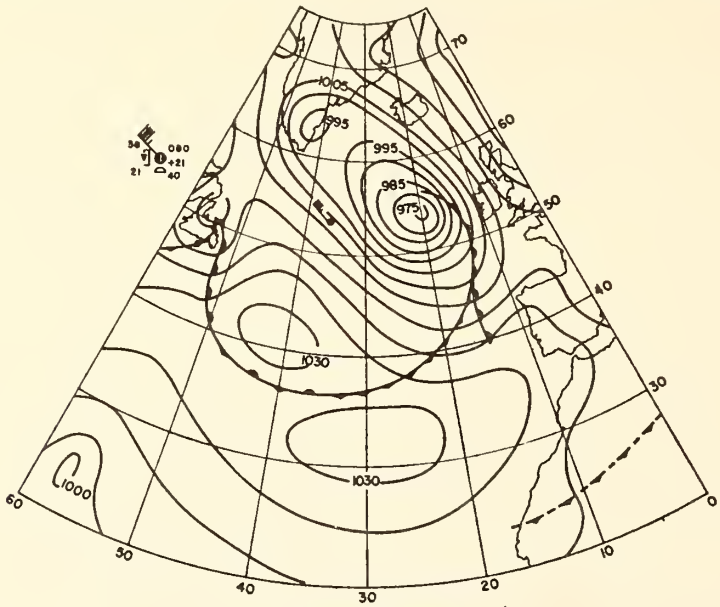

Fig. 2b. Surface weather map for January 27, 1954, 1230 GMT. Adapted from Daily Series Synoptic Weather Maps published by U.S. Weather Bureau, in same way as Fig. 2a.

storm. However, the skew-shaped Q_s and Q_e curves, with positive heat flux and evaporation lasting beyond the wind maximum, again suggests a cold-air outbreak behind the system. Figure 2b bears out these deductions.

The deepening cyclone is an outstanding feature of the mid-latitude atmosphere. It both characterizes the instability of the westerly winds and releases the energy that maintains their motion. The cyclone problem has consumed the greatest minds and effort in meteorology. And this is rightly so. Cyclones are not only the elements of planetary energy exchanges across these latitudes and the solution to one of the most fascinating (unsolved) stability problems in geophysics, but they condition the natural environment of most of human civilization. Figure 1 suggests that they also control sea–air interaction over the extra-tropical oceans, at least on the short time scale.

Models of the deepening wave cyclone were evolved early in the century by the great Norwegian meteorologists (see Petterssen, 1956, Chap. 12 and references). These models described and explained physically the three-dimensional distributions of wind, cloud and weather patterns as a " typical " frontal system goes through its life history. It is thus fitting that successors of these great Norwegians (Petterssen, Bradbury and Pedersen, 1962) have incorporated the sea–air interaction distribution into the cyclone model, so that exchange becomes quantitatively and coherently related to the developing disturbance and its processes.

Perhaps even more exciting, a possibility has concomitantly emerged of an important feedback of sea–air interaction upon the growth of the cyclones themselves. The enhanced exchange which oceanic cyclones have at their disposal apparently can, under propitious circumstances, cause them to be unstable where they would not be so over land. Thereby they may sometimes deepen violently and even disrupt the planetary flow pattern of an entire hemisphere. If further research substantiates this linkage, the oceans will indeed have become a vital part of still another crucial aspect of mid-latitude meteorology. As well as their long-recognized role in producing an anomalously warm Europe, they may through local sea–air interaction affect the stability of the planetary westerlies to disturbances. Before discussing this intriguing possibility, we shall first examine the relationship of exchange to the cyclone model.

2. HOW THE WEATHER PATTERN CONTROLS EXCHANGE

PETTERSSEN, BRADBURY and PEDERSEN, (1962) constructed a composite oceanic cyclone in each stage of development and documented the distribution of exchange in relation to its winds and weather pattern. The synoptic situations were chosen to be typical of the various stages of cyclone development, as proposed by BJERKNES and collaborators (1918; 1922; 1933). These stages are: the nascent cyclone wave, the warm-sector cyclone, the partly occluded cyclone, the full occlusion, and the frontless cold core low. In addition, the typical features of arctic outbreaks were similarly investigated.

Fifty-one individual cases during the winter of 1956–1957 were selected for the compositing. In each, analyses were drawn for the pertinent variables. The sea–air transfer was computed from these with the Jacobs formulas at grid points oriented with respect to the cyclone center. These were then transferred to a master grid constructed for each of the five stages of development.

Charts A in Figs. 3–6 show the sequence of pressure distributions and frontal structures at sea level for the developing wave cyclone. Figures 7 and 8 show the same calculations for the frontless cold core low and arctic air outbreak.

The young wave (Fig. 3) is generously supplied with tropical air dragged north from the trade wind belt, which is perturbed in tune with the wave disturbance. Charts B show the rate of kinetic energy dissipation at the ocean–atmosphere interface, or the surface shearing stress times the windspeed. The maximum stress is found in the warm sector of the open wave, while it increases and moves to the cold air in the rear as the storm develops. (cf. Fig. 1).

The patterns of energy exchange (Charts C and D) exhibit remarkable peaks associated with the cold air. These peaks are developed by and locked into the cyclone pattern as it progresses. Typical maxima of the sensible flux were about 1 cal cm^{-2} min^{-1} (or 1440 cal cm^{-2} per day) and maximum isopleths of latent heat flux were about 1·4 times this. Still higher peaks were found in single cases. Except over the cold coastal waters (which prohibit large sea–air humidity differences), the fluxes Q_s and Q_e are highly correlated, as can be seen by comparing Charts C and D with Chart E which shows their sum. The net upward radiative fluxes from sea to air were computed to be in the much lower range of 0·00 to 0·10 cal cm^{-2} min^{-1} (GODBOLE, 1961).

Standing above any doubts about the Jacobs formulas, the main feature of cyclone exchange is its large size coupled uniquely to the moving system. In the extreme case the oceanic heat loss to the atmosphere amounted to 2·5 cal cm^{-2} min^{-1}. This is about twenty times the average absorption of shortwave radiation at latitude 50°N in winter and more than *forty* times the net balance that the sea surface has in the radiation bank! Consequences to the ocean of these huge spasmodic heat losses have

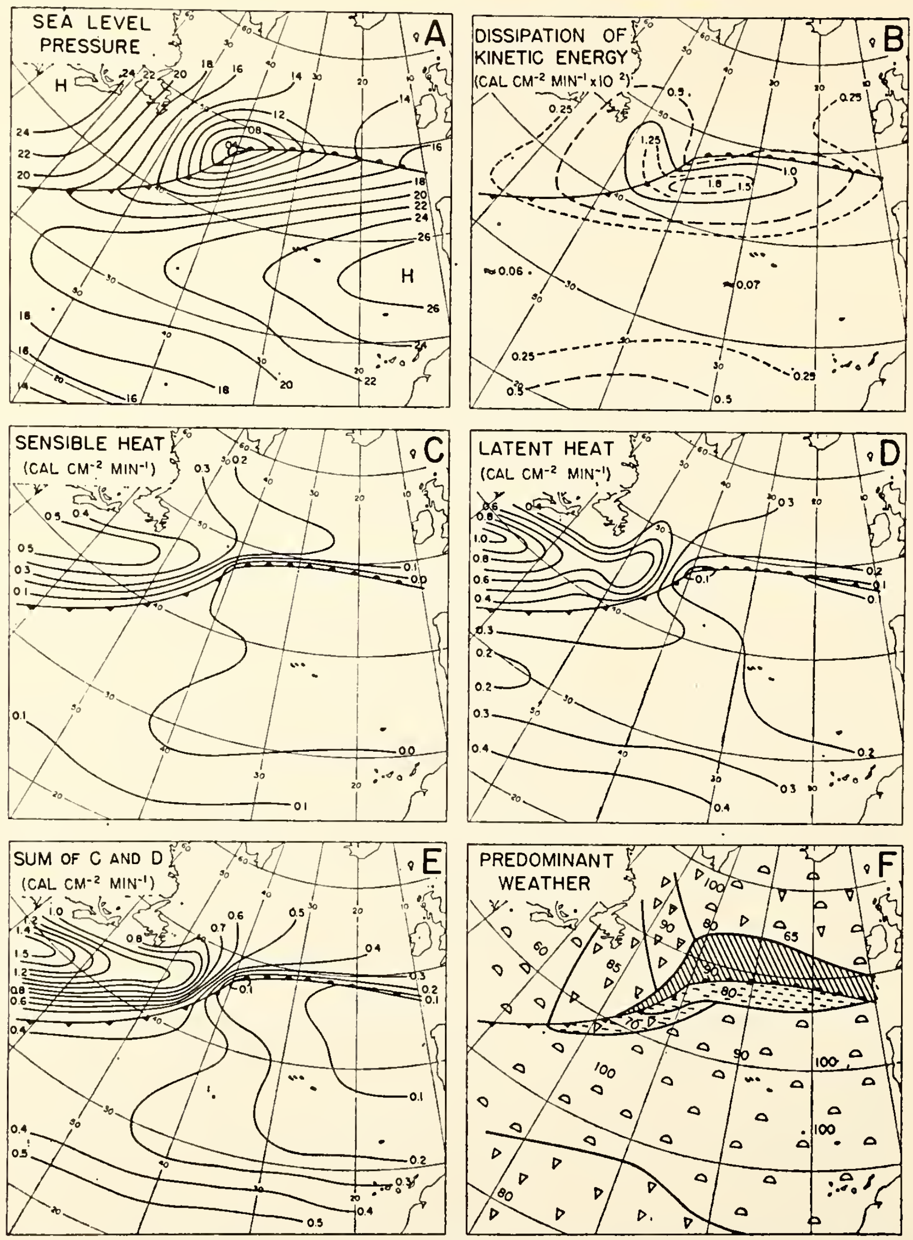

Fig. 3. (After PETTERSSEN, BRADBURY and PEDERSEN, 1962). Models of nascent cyclone waves. Note that the values in Chart B have been multiplied by 100.

been difficult to isolate. Here we will be concerned mainly with the role of these exchanges in the cyclone processes themselves.

3. EXCHANGE AND CYCLONE STRUCTURE

In the warm air, the figures show negligible sensible heat exchange and slightly positive latent heat gain by the atmosphere. As in the tropics, small cumuli prevail in this sector, with their upward development stopped by the trade inversion. But here the tropical air is cooling at a rate of about 5°C per day! Computations by GODBOLE (1961) showed that this is effected by huge radiative losses at cloud top (~ 800 mb) which help in maintaining the steep cloud layer lapse rate and upward convective heat flow.

In the cold air portion of the system, peak amounts of sensible and latent heat are absorbed, with consequences for European rainfall and perhaps for the future of the

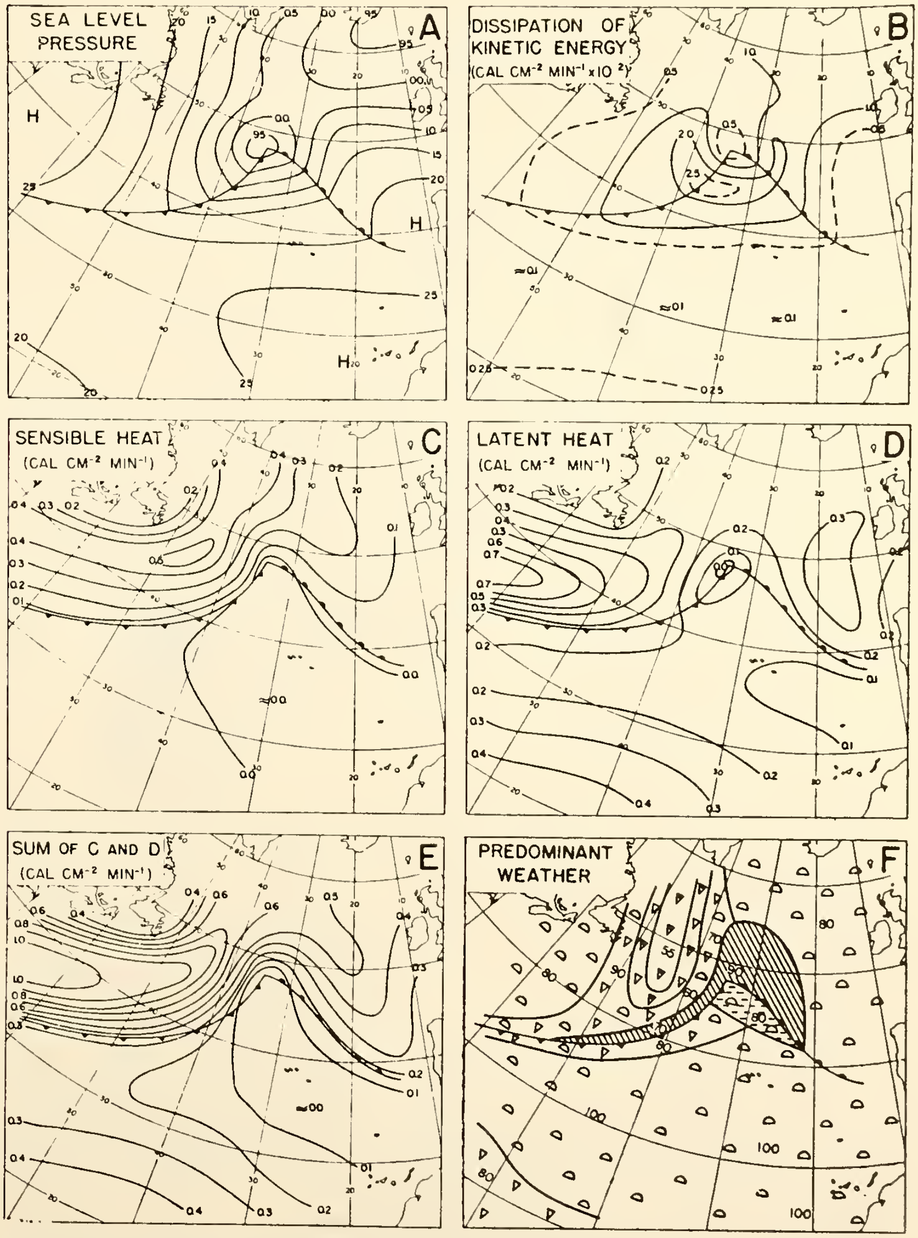

Fig. 4. (After PETTERSSEN, BRADBURY and PEDERSEN, 1962). Models of warm sector cyclones.

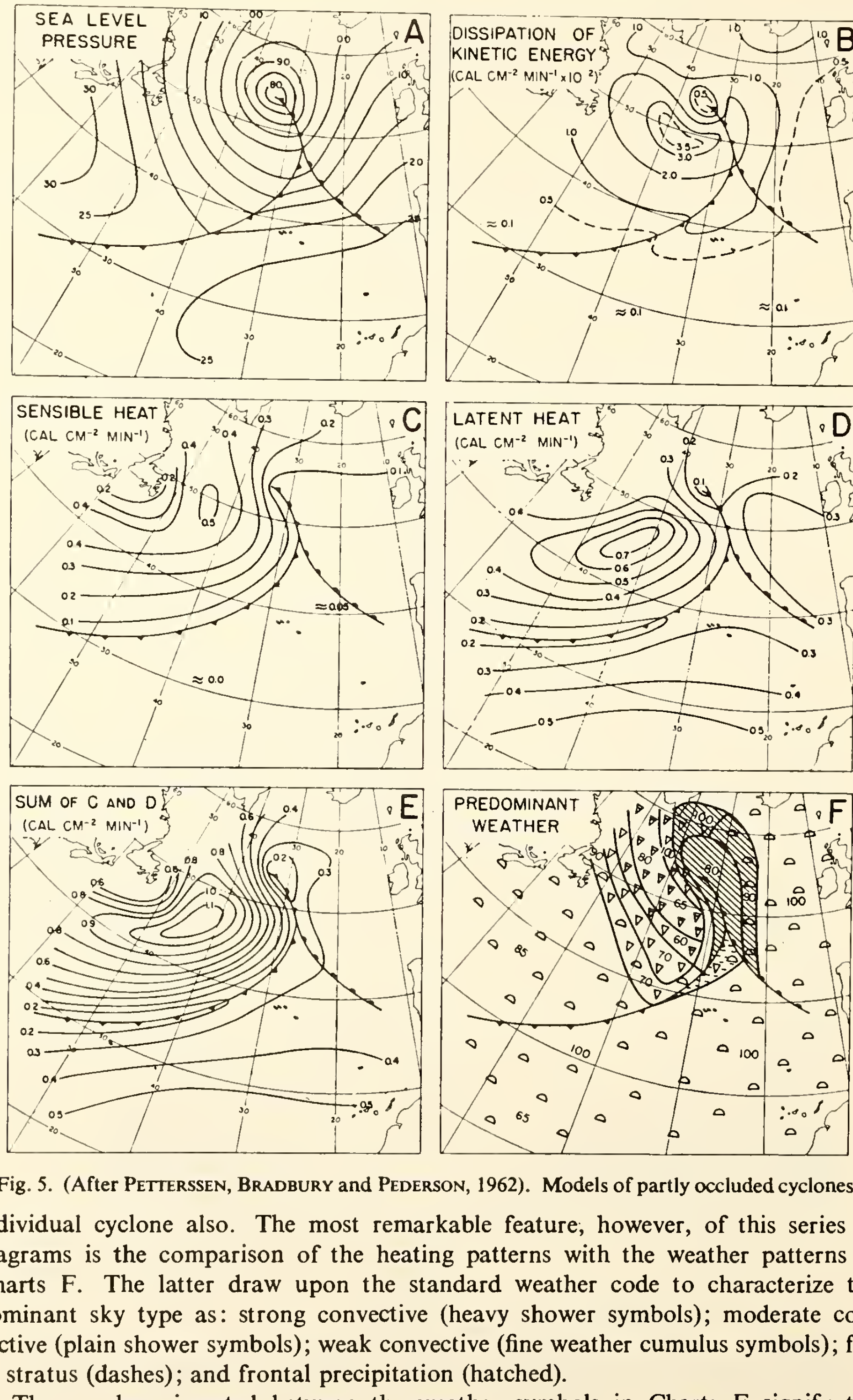

Fig. 5. (After Petterssen, Bradbury and Pederson, 1962). Models of partly occluded cyclones.

individual cyclone also. The most remarkable feature, however, of this series of diagrams is the comparison of the heating patterns with the weather patterns in Charts F. The latter draw upon the standard weather code to characterize the dominant sky type as: strong convective (heavy shower symbols); moderate convective (plain shower symbols); weak convective (fine weather cumulus symbols); fog or stratus (dashes); and frontal precipitation (hatched).

The numbers inserted between the weather symbols in Charts F signify the probability of occurrence of that weather type. The heavy lines which mark the border between neighboring predominant weather types represent the 50% probability of occurrence of either of the adjacent types. The zone of transition between two adjacent types is normally quite narrow and the losing type soon drops below the 10% frequency level. The high probability within large regions and the remarkable continuity from one stage of development to the next are noteworthy.

Even more noteworthy are the relationships on Charts C, D and E. *The axes of*

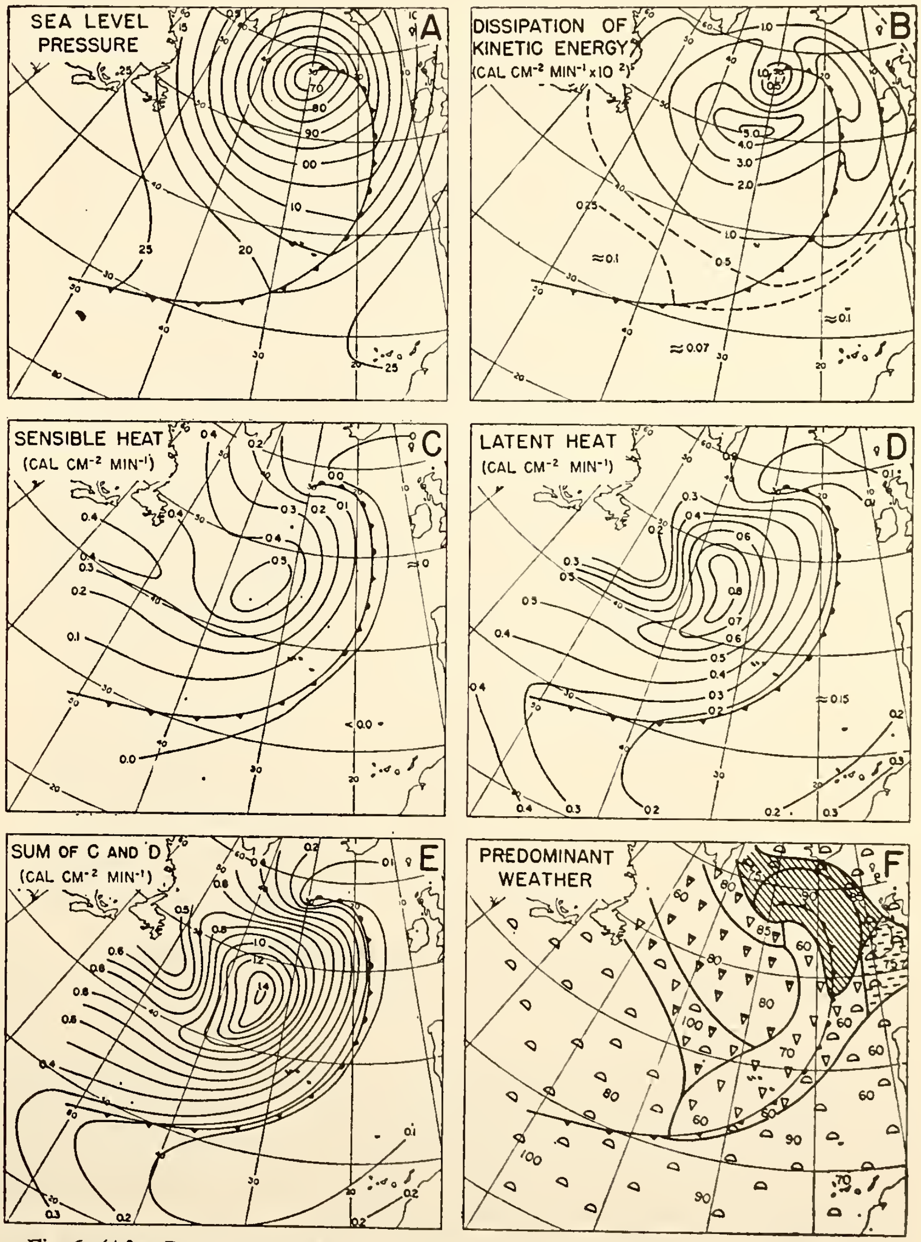

Fig. 6. (After PETTERSSEN, BRADBURY and PEDERSEN, 1962). Models of full occlusions.

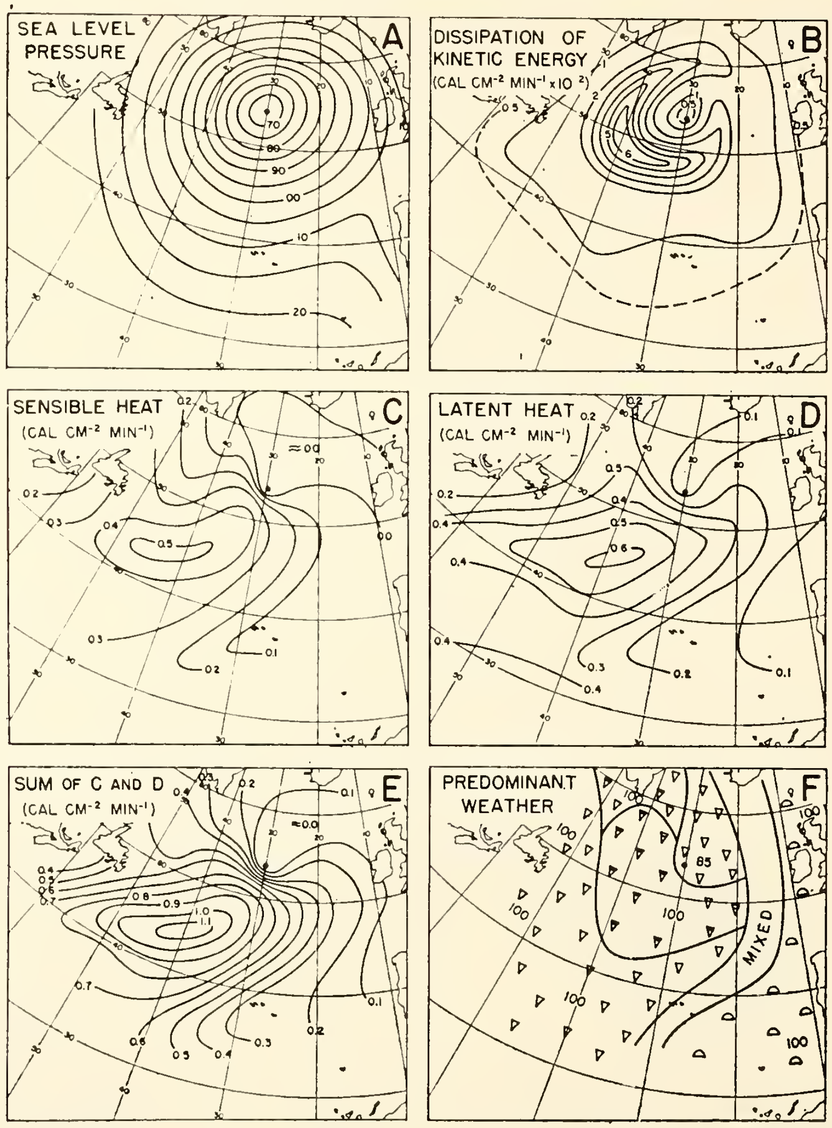

Fig. 7. (After Petterssen, Bradbury and Pedersen, 1962). Models of cold core frontless cyclones.

the heavy convective areas are oriented at right angles to the heating pattern. The conditions shown in Fig. 3 are typical. A band of moderate to heavy convective activity is present to the northwest of the apex of the wave where the rate of heating is moderate. The convective activity decreases to moderate south of Newfoundland where the rate of heating is quite large. Still farther to the west only flat cumulus and stratocumulus develop although the heat inputs by exchange reach a maximum in this area. The features shown in Fig. 3 are maintained throughout the life history of the model cyclone except that the area with heavy convective activity enlarges as the storm deepens and moves toward Europe.

Comparison of Charts F, E and A in Figs. 3–8 shows that heating from the underlying surface always results in some convective activity. However, unless the air takes part in a cyclonic circulation, moderate and heavy convection (with precipitation) will not take place even if *the surface heating is very intense.* Petterssen, Bradbury and Pedersen conclude that as far as the " state of the sky " is concerned, there is a greater difference between cyclonic and anticyclonic air masses than there is between those warmed versus cooled from below. A similar conclusion regarding tropical sky types was reached by MALKUS and RIEHL (1964). From aerial photographs over the tropical Pacific they devised a set of seventeen sky code numbers and found these could be better related to large-scale vorticity tendencies than to any other feature of the atmosphere. This dynamic control upon convection, when understood, could prove to have powerful implications to the oceans. Cyclonic disturbances form a critical link and here we shall examine the joint role of the oceans and of convection in their development.

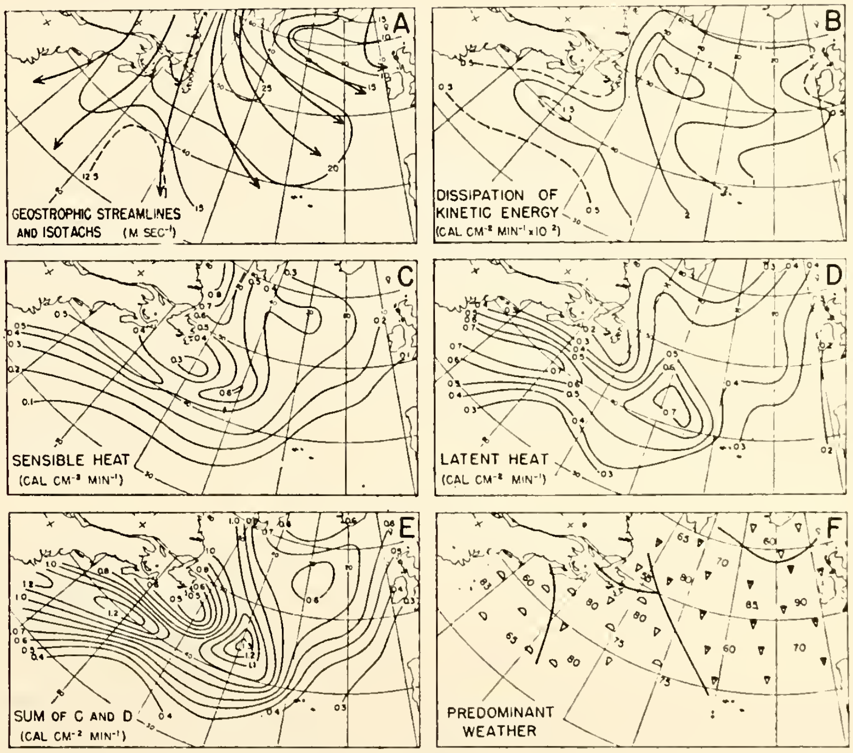

Fig. 8. (After PETTERSSEN, BRADBURY and PEDERSEN, 1962). Composite chart showing the characteristics of outbreaks of arctic air in different parts of the North Atlantic region.

4. HEAT SOURCES AND THE GROWTH OF MARINE CYCLONES

Cyclone development over the oceans apparently needs different ingredients than those usually found to catalyze it on land. Over continents, a proper setup for the concentration of vorticity by advection seems to precede most cases of deepening. Over the Atlantic, Petterssen, Bradbury and Pedersen, usually found that the setup for vorticity advection was not adequate to explain development. As compared with similar structures over the North American mainland, there was remarkably little evidence of a well- developed upper trough with strong vorticity advection ahead of it which could overtake the young marine wave cyclone. Some other initial mechanism must then be sought in oceanic developments. It is our purpose next to as sess the possible role of sea–air interaction in this exciting puzzle.

The question is to discover how cyclonic vorticity either creates or concentrates itself in the developing low-level disturbance.

Petterssen develops the vorticity relations, beginning with the vorticity equation on a constant pressure surface derived directly from cross-differentiation of the horizontal equations of motion, viz:

$$\frac{\mathrm{d}\eta}{\mathrm{d}t} = - D\eta \tag{1}$$

where η is the absolute vertical vorticity (composed of the relative vorticity ζ and the Coriolis parameter f), D is the two-dimensional velocity divergence in the pressure surface, nearly equal to the horizontal velocity divergence on a level surface. So far, only the twisting terms have been ignored.*

The pioneer numerical forecasting models (see, for example, THOMPSON, 1961, Chap. 7) largely used this equation with the right side assumed zero, so that the absolute vertical vorticity is conserved and only redistributed by horizontal advection. As we mentioned, this appeared roughly adequate to predict cyclogenesis over continents. But much evidence points to the divergence D as somehow providing the missing ingredients for marine developments. It is clear from (1) that to grow a cyclone we want convergence at low levels, which from continuity implies divergence aloft. In several papers, PETTERSSEN and his collaborators (1955; 1959) have been concerned with developing quantitative connections between heat source distributions, convergence and vorticity production. The development is implemented by postulating a level of non-divergence in the middle or high troposphere where $\mathrm{d}\eta/\mathrm{d}t = 0$. Then if we break down all variables into surface and shear values, viz:

$$|V = |V_0 + |V_s,\ D = D_0 + D_s\ \eta = \eta_0 + \eta_s = \zeta_0 + f + \zeta_s \tag{2}$$

where $|V$ is the horizontal wind vector and the shear is taken between 1000 mb and the level of nondivergence, the vorticity equation at the level of nondivergence is

$$\frac{\partial\zeta_s}{\partial t} + \mathbf{V}\cdot\nabla\zeta_s + \mathbf{V}_s\cdot\nabla\eta_0 = D_0\,\eta_0 = -\frac{\mathrm{d}\eta_0}{\mathrm{d}t}. \tag{3}$$

The vorticity advection is represented as

$$A_\eta = -\,\mathbf{V}\,\nabla\cdot\,\zeta_s - \mathbf{V}_s\cdot\nabla\eta_0. \tag{4}$$

Its evaluation in numerical forecasting models has been described at length (c.f THOMPSON, 1961).

Therefore

$$-\frac{\mathrm{d}\eta_0}{\mathrm{d}t} = \eta_0\,D_0 = \frac{\partial\zeta_s}{\partial t} - A_\eta. \tag{5}$$

*The solenoid term does not appear explicitly in the vorticity equation in pressure coordinates, due to slightly different definitions of vertical vorticity ξ in pressure vs. height systems. For clarification, the reader is referred to PETTERSSEN (1956), p. 135 ff.

The right side of (5) is a measure of the rate of destruction of vorticity at the 1000 mb level. Since η_0 is positive, development of the cyclonic absolute vorticity is proportional to the negative magnitude of the right side of (5). Following SUTCLIFFE and FORSDYKE (1950), we use D_0 as a measure of development and attempt to relate D_0 to sea–air interaction through $\partial\zeta_s/\partial t$.

PETTERSSEN (1955) set up a quasi-geostrophic, hydrostatic framework to relate $\partial\zeta_s/\partial t$ quantitatively to the heat source distribution.

With these assumptions we have

$$\zeta_s = \frac{\nabla^2 h}{f} \tag{6}$$

where h is the geopotential thickness between the level of nondivergence and 1000 mb and f is the Coriolis parameter.

Using the integrated hydrostatic equation and the first law of thermodynamics we obtain

$$\frac{\partial h}{\partial t} = R \ln \frac{p_0}{p} \left[\frac{1}{c_p} \frac{\overline{\mathrm{d}Q}}{\mathrm{d}t} + \overline{\omega\,(\Gamma - {}_a\Gamma)} + \overline{A_T} \right]. \tag{7}$$

Where p is the pressure at the level of nondivergence and p_0 is 1000 mb. $\overline{\mathrm{d}Q}/\mathrm{d}t$ refers to the heating rate per unit mass. The vertical velocity is $\omega \equiv \mathrm{d}p/\mathrm{d}t$, Γ_a is the dry adiabatic lapse rate and Γ the actual lapse rate in pressure coordinates.

$$A_T \equiv -u\frac{\partial T}{\partial x} - v\frac{\partial T}{\partial y} \tag{8}$$

where A_T is the thermal advection. The bars denote averages with respect to intervals of ln p.

And finally, since

$$\frac{\partial\zeta_s}{\partial t} = \frac{\nabla^2}{f}\left(\frac{\partial h}{\partial t}\right) \tag{9}$$

we have

$$-\frac{\mathrm{d}\eta_0}{\mathrm{d}t} = \eta_0\, D_0 = \frac{R}{f}\nabla^2\left\{ \ln\frac{p_0}{p}\left[\overline{A_T} + \frac{1}{c_p}\frac{\overline{\mathrm{d}Q}}{\mathrm{d}t} + \overline{\omega\,(\Gamma_a - \Gamma)} \right] \right\} - A_\eta. \tag{10}$$

The immense complexity of the development process is apparent from (10). Development at the 1000 mb level comes out as an unbalance between the vorticity advection and the Laplacian of certain interrelated thermal contributions. The thermal contributions derive from advection, non-adiabatic heating, and vertical motion times stability or buoyancy. The last term is a measure of convective heat release when the air is saturated and conditionally unstable. Over the oceans, the first two terms may be established or controlled by the sea–air interaction. As the cyclone models showed (Figs. 3–8), $\overline{\mathrm{d}Q}/\mathrm{d}t$ and convection are related but not uniquely. For oceanic heating to set off intense buoyant convection in the overlying air, the initial vorticity must already be cyclonic. This additional requirement in terms of initial conditions perhaps accounts, at least partly, for the vast variety of marine developments.

In the work described on Atlantic cyclones, PETTERSSEN, BRADBURY and PEDERSEN, (1962 *loc. cit.*) computed the direct effects of heating upon the thickness changes in the vicinity of ten cyclones, using equation (7). Specifically, they evaluated $\overline{dQ/dt}$ and $\overline{\omega (\Gamma_a - \Gamma)}$ and compared these with other factors causing thickness change. But drastic assumptions were required in so doing. For one thing, the depth of the heated layer and the vertical decay of the flux curve had to be assumed arbitrarily. The latent heating had to be taken from an area-mean ascent rate, which would indeed be fortunate if it correctly approximated convective release.

The main result of the ten computed cases was that the $\overline{dQ/dt}$ contributed non-negligible thickness changes, up to one-third or even one-half those from other sources. However, all were in a sense of height rises, or reduced falls. The tentative conclusion is that including sensible heating from the sea may be necessary for a good forecast, but that it does not contribute directly to cyclone intensification. On the whole the ten cases chosen contained rather small amounts of precipitation due to large-scale vertical motion, with the result that the height changes due to released latent heat were small.

The main effects of sea–air interaction may lie in the instigation of large convective precipitation, or in more subtle dynamic convective effects via the forcing of an ageostrophic mass inflow (convergence). This effect probably cannot be explicitly studied in a large-grid, geostrophic hydrostatic framework as the foregoing; even the twisting term may become important in the vorticity equation at an early stage, as in tropical developments (cf. YANAI, 1961).

Furthermore, the seaward position of Petterssen's growing cyclones may have obscured matters, since cyclonic vorticity would coincide with heating more frequently just off the American continent in the preferred planetary trough position. After leaving the coast, anticyclonic vorticity is more likely to dominate the cold air. We suggest that the coastal waters are cyclogenetic not just because of the thermal impact but because this impact frequently coincides with a trough position and initial cyclonic vorticity. Two contrasting sets of observational evidence are next introduced for preliminary evaluation of this hypothesis.

5. CONTRASTING OBSERVATIONAL CASES

On January 22, 1955, the Woods Hole Oceanographic Institution's research aircraft flew from the island of Bermuda (32°20′N; 64°44′W) to a location in Rhode Island (41°38′N; 71°30′W) on the U.S. East Coast. The path of the aircraft (Fig. 9 inset) cut through a young wave cyclone that had generated on a cold front in the Gulf Stream area off Cape Hatteras and was accelerating over the ocean in a northeasterly direction. An opportunity was thus provided to measure the turbulent fluxes of momentum and heat directly and to relate them to the structure of the cyclone and its air masses. The work has been described in detail by BUNKER (1957).

All the observations and computations are summarized in Fig. 9. The outstanding feature of the cold air mass was its very high static stability,which must have been maintained by strong subsidence. Beneath the levels of the aircraft observations, great instability must have existed, since the ocean was 6°C warmer than the air. The only turbulence observation taken in the cold air showed decreased turbulence and a downward heat flow at 100 m elevation (80 km behind the cold front). The shearing stress measured was about 3 dynes cm^{-2}.

The downward flux of heat in an air mass flowing over 6°C warmer water requires comment in connection with Petterssen's cyclone models. It re-emphasizes that a

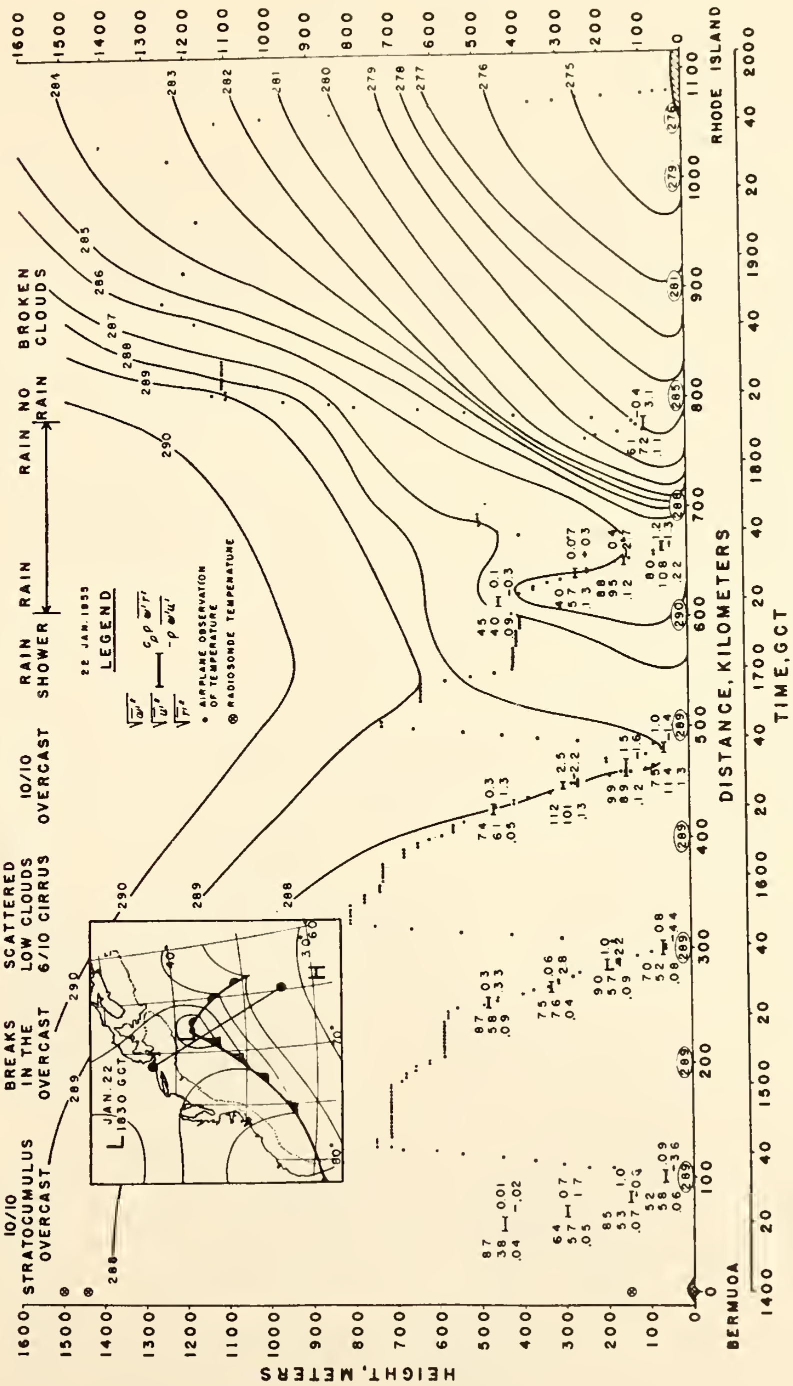

Fig. 9. (After Bunker, 1957). Vertical cross section from Bermuda to Rhode Island, along line shown in inset map. Observations entered from aircraft study, January 22, 1955. Ordinate is height in meters, double abscissa in distance and time from flight origin at Bermuda. Solid lines are isopleths of air potential temperature, labeled in °A. Turbulence parameters, as indicated in legend at observation points; shearing stress component along flight in lower right position.

large boundary transfer does not imply large heat addition to a deep air layer. Bunker's case permits quantitative estimation of the balance of the heat transfer processes at work, namely buoyant convection, mean subsidence and eddy diffusion. Using the method of PRIESTLEY (1954), Bunker estimated the maximum upflux of heat due to buoyant convection to be 0·4 m cal cm^{-2} sec^{-1}. This flux was obtained assuming the mixing rates for momentum and heat to be equal and using the observed root-mean-square temperature deviations. At the same time, he computed a downward flow of heat by eddy diffusion of 1 m cal cm^{-2} sec^{-1} with the conservative value of 50 g cm^{-1} sec^{-1} for the eddy conductivity. As the airplane detects the net heat flow in the vertical, it is apparent that a downward flux should be obtained from its records, as it was.

Thus a strong mean subsidence behind the front preserved the great stability and resulted in a net downward flow of heat by advection and diffusion even under conditions of large sea–air temperature difference and slight turbulence. The very lowest air is heated by the ocean, becomes unstable and rises in small buoyant " thermals " which penetrate a short distance into the stable air. The heat transport by this convection process was, in this case, small compared to the downward flow. This air mass was heated more by warm stable air aloft than by the warm ocean!

It is noteworthy that Bunker's disturbance failed to deepen but died soon as an open wave. Restriction of the role of exchange by dynamic factors (subsidence) probably played a role in this failure. The exchange was working against strong anticyclonic vorticity in most of the cold air (cf. inset Fig. 9). We suggest that the anticyclonic vorticity worked its effect through subsidence, which prevented the heating from setting off deep convection. To support this we contrast a case where the exchange encountered an initially cyclonic planetary pattern, with a dramatically different outcome.

The Gulf of Alaska is frequently the scene of rapid cyclone intensification. Many times the cyclogenesis occurs on such a large scale that the basic planetary wave pattern is radically altered in a few days, with effects even reaching half a hemisphere downstream toward the east. NAMIAS and CLAPP (1944) attributed this type of deepening to the rapid modification of cold Arctic air masses pouring over the warmer waters of the Alaskan Gulf. WINSTON (1955) pursued this suggestion in a fascinating case study. He used a violent development on February 1–4, 1950, to assess the role of sea–air interaction in cyclogenesis.

The broad-scale circulation changes associated with this cyclone development were well portrayed by the five-day mean 700 mb charts (not shown). The new Gulf of Alaska trough developed in conjunction with the westward retrogression of a large ridge originally in the Eastern Aleutians. This resulted in a northerly flow bringing cold air over the Gulf of Alaska where it was exposed to rapid heating, as we shall examine later.

The trough formation in the Gulf of Alaska abruptly shortened the downstream half wave length of the planetary waves in the westerly belt, with drastic consequences to the North American and Atlantic flow patterns. Prior to the development, a broad cyclonic flow dominated the Western and Central sections of the United States with attendant storminess and cold weather in the west. With the establishment of the new trough in the Gulf of Alaska and southward, heights rose rapidly over the

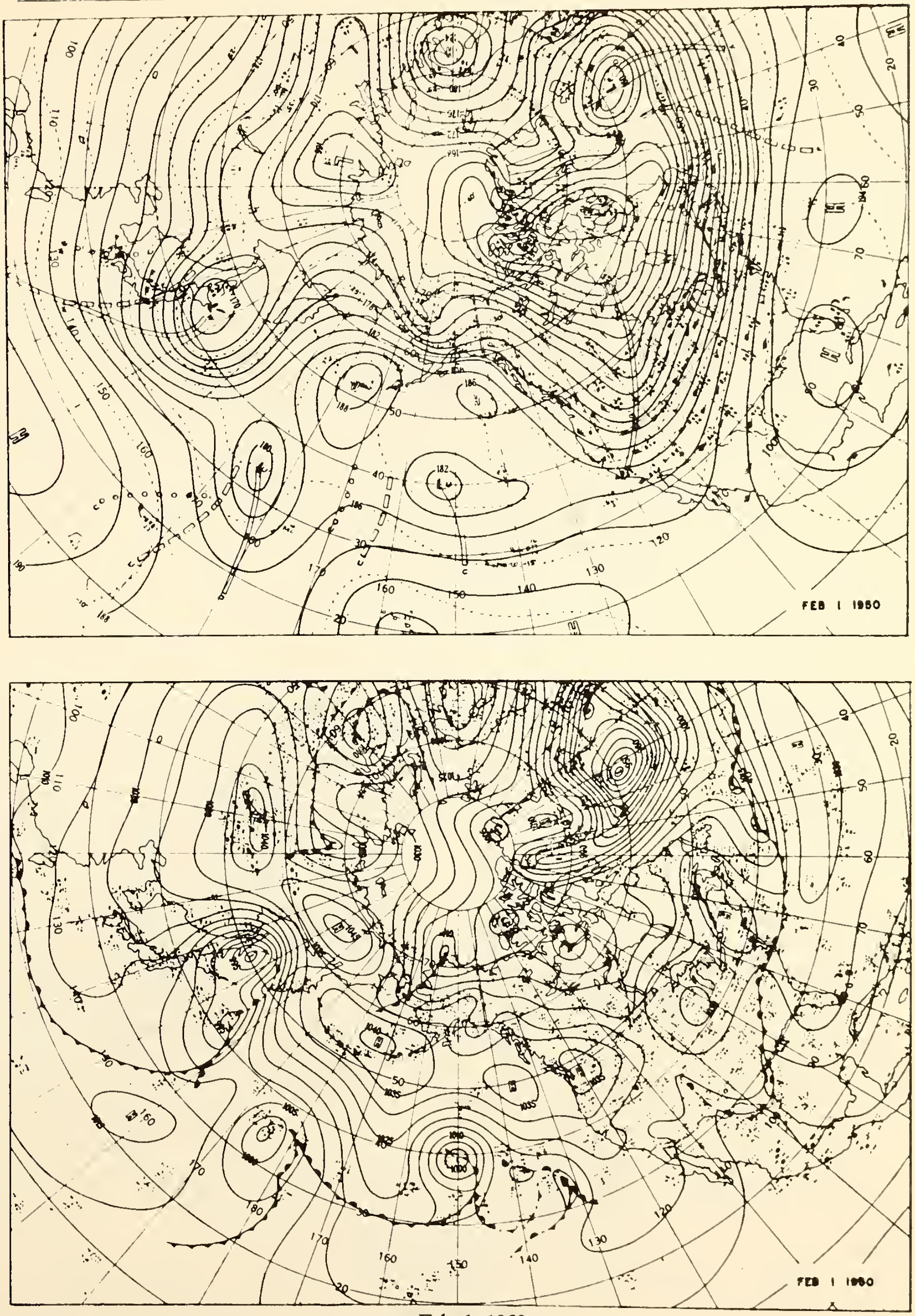

a. Feb. 1, 1950

Fig. 10. (After WINSTON, 1955). Sequence of daily maps for 500 mb (upper) and sea level (lower) portraying details of cyclonic development in Gulf of Alaska. Maps are reproductions from Daily Series Synoptic Weather Maps published by the U.S. Weather Bureau. 500 mb charts are for 1500 GMT and sea-level charts for 1230 GMT.

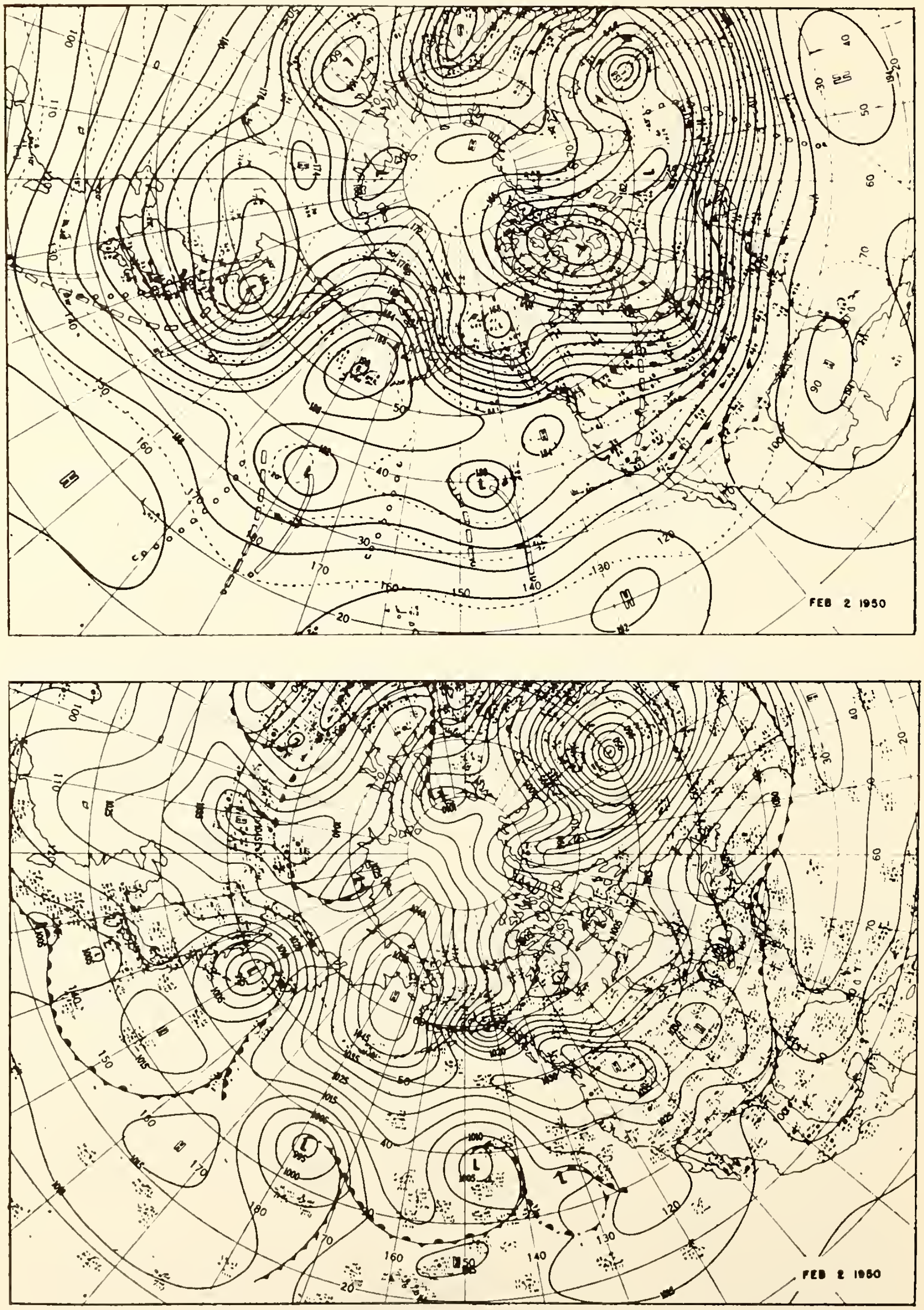

Fig. 10b. Feb. 2, 1950

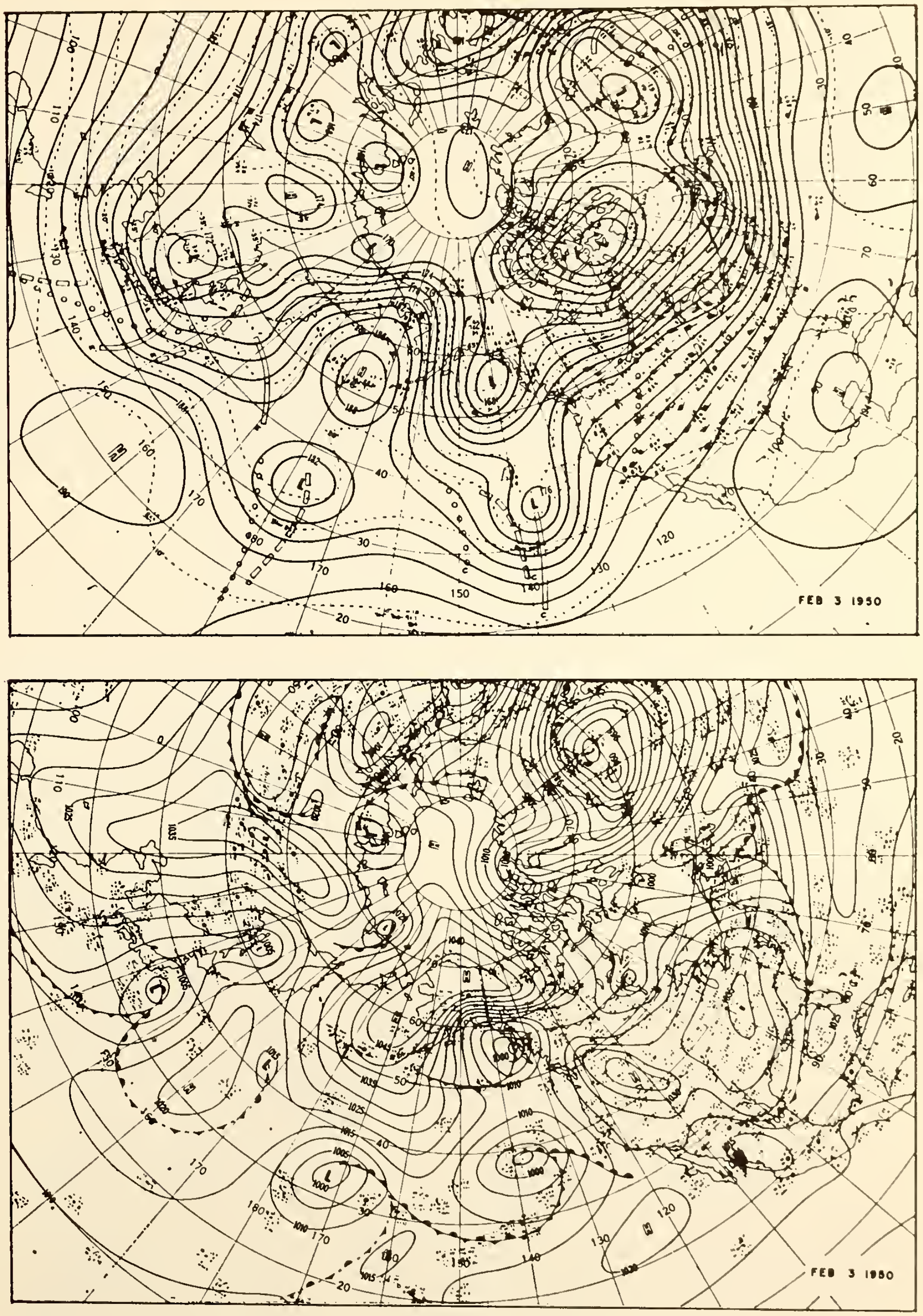

Fig. 10c. Feb. 3, 1950

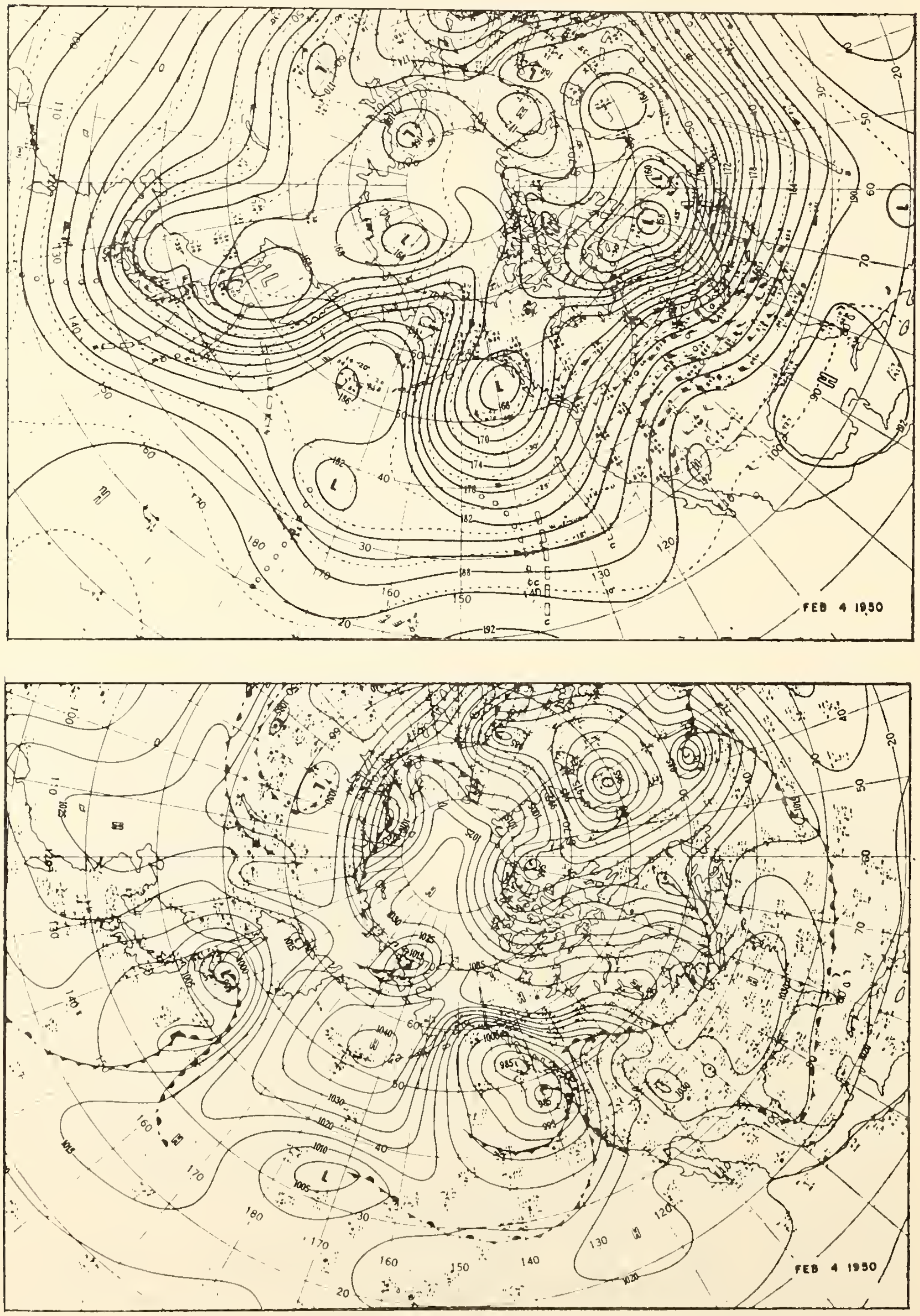

Fig. 10d. Feb. 4, 1950

Western United States, anticyclonic circulation developed and consequently improved weather set in. Such major adjustments in the large-scale flow over North America are typical following cyclogenesis in the Alaskan Gulf.

The cyclone growth is viewed in Fig. 10. At the surface the individual perturbation which triggered the development was a left-over occlusion which moved from the Bering Straits on February 1 (Fig. 10a) through Alaska and into the northern Gulf by February 2 (Fig. 10b). In this interval the occlusion transformed into a cold front with an icy Arctic air mass behind it. This front had just reached the Gulf by map time of February 2. The intensifying cyclone at sea level formed on this front and was not the same low which was in Northwestern Alaska in Fig. 10a. This new cyclone deepened to extremely low central pressure (985 mb) in the next two days (Figs. 10c and d).

Aloft, the development of a new trough in this vicinity was qualitatively inferrable from the initial setup for vorticity advection. Winston's first step was to determine quantitatively how much of the development was accountable to this mechanism. Therefore equation (1) was tried out with the right side equal to zero, namely

$$\frac{d\eta}{dt} = 0 \text{ or } \frac{\partial\zeta}{\partial t} = -\mathbf{V}\cdot\nabla\eta \tag{11}$$

where the vertical advection of vorticity $\omega\,\partial\eta/\partial p$ has also been ignored.

With the quasi-geostrophic approximation, (11) is expressed in terms of heights and height tendencies and the well-known methods of numerical forecasting with the barotropic model are utilized. The barotropic technique was applied at 700 mb to a large region surrounding the Alaskan Gulf.

In the early period of development (Feb. 1–Feb. 2, 0300 GMT) the agreement between the barotropic forecast and the observed development was excellent, both in the magnitude of the height changes and in the location of the centers of maximum falls. In the period of most rapid deepening, the barotropic prediction failed most badly. At 1500 GMT February 2, the maximum computed twelve-hourly height fall of − 340 ft was found along the Southeastern Alaskan coast, while the observed peak height fall of − 530 ft was located farther west near the middle of the Gulf of Alaska. This was just the time when cold Arctic air had begun streaming out over the Gulf, thereby abruptly introducing a large heat source into the atmospheric circulation.

By 0300 GMT February 3 a deep closed low had become established over the Gulf of Alaska at 700 mb. Barotropic computations from this flow pattern now indicated large height falls over the extreme Western Gulf of Alaska, whereas the observed fall center was farther east and weaker. This latter type of error in the barotropic computation persisted to the end of the period on February 4.

The important results of this very interesting experiment are twofold:

(1) Horizontal advection of absolute vorticity was responsible for much of the cyclone development in the Gulf of Alaska, particularly in the initial stages.

(2) Pure advection could *not* explain the rapidity and exact location of the intense development. At the time of most rapid deepening, computed height falls were east of and weaker than the observed falls, whereas following the establishment of the deep closed low, the computed falls were to the west of and stronger than the observed falls.

Winston attributed the main errors of the barotropic computation to the neglect of the divergence term in the vorticity equation. He suggested that the oceanic heat source produced an ageostrophic thermal circulation, with inflow at low levels, ascent and outflow aloft. A negative divergence in equation (1) would create cyclonic vorticity adding to that advected and obviously acting qualitiatively to correct the errors in the barotropic computation. It is noteworthy that the vorticity creation is greatest at the time and place where the cold air first reaches the warm waters of the Gulf.

MANABE (1957) made a now classic study of cold air outbreaks over the Japan Sea. He found, among other things, convergence in the cloud layer of the polar air after travel over the warm waters. Fortified with this result and with Petterssen's weather patterns relative to heating in oceanic cyclones (Figs. 3–6), we suggest the role of deep convection in producing this convergent circulation, as it so often does in tropical developments. Most significant is the fact that cyclonic vorticity already existed over the Gulf of Alaska when the cold air outbreak began (cf. Fig. 10b). Thus a heat source was imposed upon a troposphere favorable to penetrative convection.

WINSTON forged the first links in documenting this chain of reasoning by his vertical velocity and heating calculations. He computed the vertical velocities directly from equation (1) without further neglections, expanding it in the form

$$\frac{\partial \zeta}{\partial t} = - \mathbf{V} \cdot \nabla \eta - \omega \frac{\partial \eta}{\partial p} + \eta \frac{\partial \omega}{\partial p}. \qquad (12)$$

Here the divergence D on the pressure surface is written as $- \partial \omega / \partial p$.

Rearranging this equation, we have

$$\frac{\partial}{\partial p}\left(\frac{\omega}{\eta}\right) = \frac{\dfrac{\partial \zeta}{\partial t} + \mathbf{V} \cdot \nabla \eta}{\eta^2} \qquad (13)$$

which upon integration becomes

$$\left(\frac{\omega}{\eta}\right)_{p_1} = \left(\frac{\omega}{\eta}\right)_{p_0} - \int\limits_{p_1}^{p_0} \frac{\dfrac{\partial \zeta}{\partial t} + \mathbf{V} \cdot \nabla \eta}{\eta^2} \mathrm{d}p \qquad (14)$$

where p_1 and p_0 are arbitrary pressure surfaces. Winston used the surface chart and those for 700 and 500 mb for computing the integrand.

Before the cold air outbreak reached the ocean, a broad area of ascent was found in and east of the developing trough. In the northwesterly flow to its rear (over Alaska and Bering Straits) pronounced sinking was computed. Twelve hours later when the heat source had just set in, upward motion increased over most of the Gulf of Alaska. Also now the ascent extended well back into the northwesterly flow behind the developing trough at both 700 and 500 mb. The peaks of upward motion were now located in the cold air behind the front. These were found over the middle of the Gulf of Alaska to the southwest of earlier maxima, even though the trough had moved eastward.

Later, the vertical motion field once more took on a relation to the trough more familiar to continental situations. Generally pronounced downward motion developed west of the trough and upward motion was now restricted to the area east of the trough. Apparently the usual effects of subsidence and horizontal divergence of the cold air mass in its southward drift and lifting (with horizontal convergence) in the warm air east of the trough again dominated, although a pronounced heat source still operated as the cold air continued to stream out over the Gulf.

Thus a main result of Winston's work is that the heating was most influential in this development for a short 12–24 hr period following the initial impact of the heat source. After the cold dome moved out over the ocean in greater depth, the more powerful effects of sinking and spreading of the cold air killed or overcame the convergence produced by the oceanic warming. This fits in beautifully with what we have learned from the studies of Manabe, Petterssen and Bunker; here the heat source lost its ability to create convergence because the convection was suppressed by the subsidence linked with planetary divergence.

This inference is supported by WINSTON'S heating calculations. He computed the net heat added to the air in twelve-hour intervals by the same trajectory method employed by MANABE (1957). The results are shown in Table 1, broken down into two layers.

Table 1. *Heating of air associated with Gulf of Alaska cyclogenesis, Feb.* 2–4, 1950 (*after* WINSTON, 1955)

12–*hr period beginning*	dQ/dt 10–5	dQ/dt 10–7	dQ/dt 7–5
1500 GMT, Feb. 2	+2210	+1270	+940
0300 GMT, Feb. 3	+1430	+1020	+410
1500 GMT, Feb. 3	+1090	+ 850	+240
0300 GMT, Feb. 4	+ 520	+ 700	−180
1500 GMT, Feb. 4	+ 400	+ 500	−100

Subscripts 10–5, 10–7, and 7–5 refer to layers 1000–500, 1000–700, and 700–500 mb respectively. Units : cal/cm^2 per day.

It is interesting to compare Table 1 with Manabe's case. Presumably the radiational heat losses in the air columns should be nearly the same. If we also carry over Manabe's near balance between radiation loss and precipitation gain, the sensible heat supply from sea to air in the Gulf of Alaska must have reached about 2000 cal cm^{-2} per day in the peak twelve-hour period starting at 1500 GMT, February 2. The average oceanic sensible heating for the outbreak period of Table 1 would be about 1000 cal cm^{-2} per day, in good agreement with Manabe and confirming the results of both studies.

Even more interesting is the vertical distribution of heating and its time sequence. In the first twelve-hour period (just after the cold air hits the Gulf) the upper air layer is warmed nearly as much as the lower layer. Subsequently the heating becomes more and more concentrated at low levels, until in the last two periods we find cooling between 700 and 500 mb. The oceanic heat source was still at work, but its effects just were not being propagated upward. Concomitantly, convergence was no longer creating vorticity to enhance the deepening process.

The evidence points to penetrative cumuli as the linking mechanism between thermal and dynamic transformations here. We suggest convection as the means by which sea–air interaction can—in favorable (i.e. initially cyclonic) circumstances—act to aid marine cyclonic development, perhaps crucially in some cases. This would indeed be a very subtle feedback mechanism between sea and air, involving the large-scale planetary vorticity patterns.

The linkage between exchange, convection and storm deepening was explored further in the Gulf of Alaska case by PYKE (1965), as far as the pitifully sparse data permitted. The only ocean station in the Gulf is Ship P at 50°N, 145°W. The front is just passing the ship in Fig. 10c (1230 GCT, February 3). Figure 11 shows the calculated " before and after " picture of sea-air exchange at the ship, related to several weather parameters. An overall temporal connection between pressure fall, increased exchange and convective weather is obvious at first glance.

Looking more closely, one can observe the approach and intensification of the storm quite easily by noting the relationships between the plotted variables. A sudden increase in τ_0 began at 1800 GCT, 2 February. Increased stress was accompanied by showers and by an acceleration of the pressure fall and followed by a marked increase in $T_0 - T_a$. It is at this time that the edge of the strong pressure gradient surrounding the deepening cyclone (visible on the surface map for 2 February in Fig. 10b) must have reached the ship. The *mP* air that had been over and east of the ship is replaced by the cooler *mP* air coming from the large high pressure area building over the Aleutian Islands. Between 0900 and 1800 GCT on 3 February there was another sharp increase in $T_0 - T_a$, a further shift in wind, and an increase in convective precipitation associated with the actual cold front passage. Throughout the period, the sea temperature T_0 remained nearly constant (within 1°C) so that the increase in $T_0 - T_a$ is mainly a reflection of the drop in the air temperature as colder air is advected into the region.

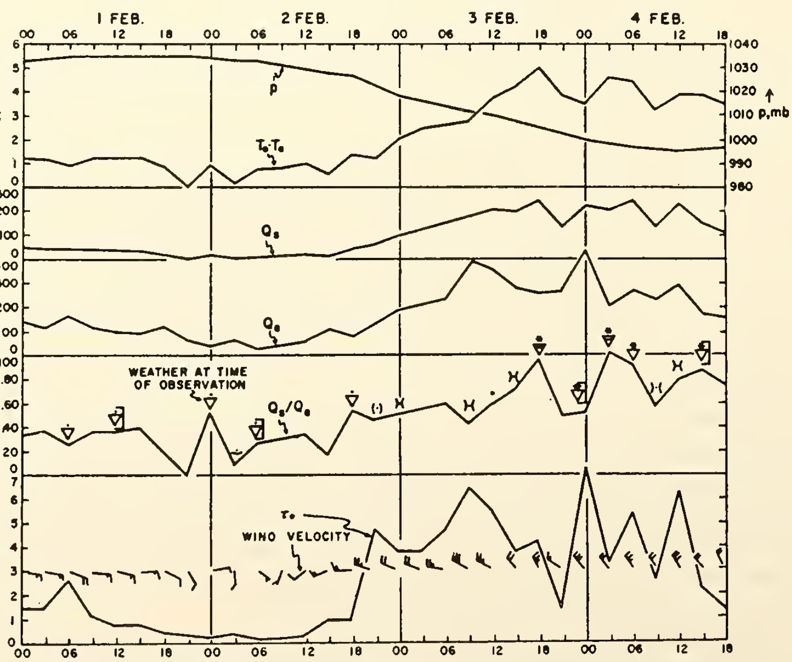

Fig. 11. (After PYKE, 1965). Computed sea-air energy exchanges, Q_s (sensible heat) and Q_e (latent heat) at Ship P (50°N; 145°W) for a period 0000 GCT, 1 February through 1800 GCT, 4 February 1950, plotted with sea-level pressure (p), air–sea temperature difference ($T_o - T_a$) eddy shearing stress (τ_o), observed weather and wind veolcity

Both latent and sensible heat exchange also rose by nearly an order of magnitude during the deepening of the cyclone. The increase is a joint consequence of the higher winds and the increased sea–air property difference as the cold, drier air moved in from the north. The maximum values of Q_e computed at Ship P for this period are on the order of 400×10^{-5} cal cm^{-2} sec^{-1}, with peak Q_s running at about 250×10^{-5} cal cm^{-2} sec^{-1}. Climatological mean values are about 70×10^{-5} cal cm^{-2} sec^{-1} for Q_e and about 20–30 $\times 10^{-5}$ cal cm^{-2} sec^{-1} for Q_s. Clearly, the first four days of February 1950 were a period of much greater than normal sea–air exchange by about an order of magnitude. The peak exchange values obtained here, however, still fall far short of the maximum values that occurred in the Gulf of Alaska during this storm. Ship P is far to the south of the initial point of contact of the arctic air with the sea (Fig. 10b). At the point where the continental air first hit the warm sea, there was a far larger exchange than was experienced at P, as indicated by calculations from Table 1.

The dissipation of atmospheric kinetic energy, which can be computed from windspeed and τ_0, had a maximum value of 27×10^{-5} cal cm^{-2} sec^{-1}, only an order of magnitude lower than the maximum value of Q_s. This is in good agreement with the model of Petterson, Bradbury and Pedersen for the deep occluded cyclone (Fig. 6) and much higher than mean or undisturbed values.

The onset of heavy shower symbols in Fig. 11 beginning at the cold front passage suggests an association between high exchange, convection and cyclonic vorticity. The drastic accompanying change in the ship's upper air sounding hammers home the association even more vividly (Fig. 12).

The first sounding (Fig. 12a) shows as yet no effects of the cold outbreak. A well-mixed layer extends up to 900 mb, capped by a sharp inversion and dry layer aloft. The sea–air temperature difference is very small. The second sounding (Fig. 12b)

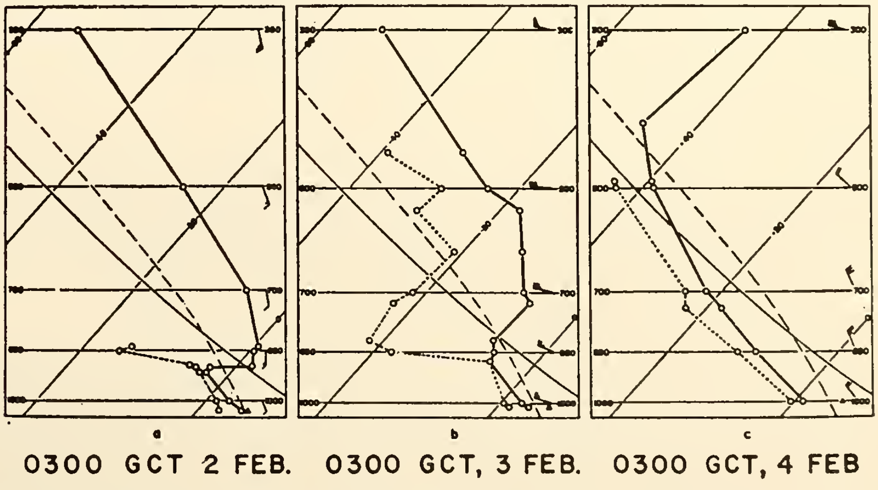

Fig. 12. (After PYKE, 1965). Upper air soundings at Ship P, surface to 300 mb and winds aloft, plotted on U.S. Air Force Skew-T, log p diagram. Solid lines are temperatures; dewpoint curves are dashed heavy lines. Sea surface temperatures are plotted in triangular symbols. The thin solid lines are dry adiabats; the thin broken lines are saturated adiabats.

a. 0300 GCT, Feb. 2, 1950 b. 0300 Feb. 3, 1950
c. 0300 Feb. 4, 1950

shows the first influence of the storm system on the weather at the ship. The winds have shifted considerably; there is an influx of moisture at high levels. Destruction of the marine inversion is beginning and the sea–air temperature difference is increasing as the cooler air from the northwest reaches the ship.

The third sounding (Fig. 12c) depicts a complete air mass transformation; it is a typical deep convective sounding. A well-mixed moist layer of air now extends to great heights. The winds (especially in the lower levels) have veered to north-northwest and the tropopause has lowered to 406 mb. It had been above 300 mb on the two previous soundings. The sea–air temperature difference is now very large, with conditionally unstable air throughout most of the troposphere. Thus the oceanic heating extends its influence, via convection, to great heights. A saturated moist-adiabatic parcel starting with the temperature of the sea surface would penetrate above the tropopause before losing its buoyancy. Intense convective activity is in fact well documented by the fact that heavy cumulus (Low Cloud Code 2) prevailed at every observation after 1500 GCT, 3 February. Showers dominated the past weather in every observation from 1200 GCT, 3 February until the end of the period.

The sharp contrast between this explosive development case and the nondeveloping wave examined earlier emphasizes the role of convection (and conditions favoring it) as necessary to implement sea–air exchange in marine storm growth. The ways that circulation growth may be affected by convection is best illustrated using the vorticity equation in rectilinear coordinates with altitude as the vertical coordinate, namely

$$\frac{d\zeta}{dt} = \underbrace{-(f+\zeta)\,D}_{\text{div.}} - \underbrace{\left[\frac{\partial\alpha}{\partial x}\frac{\partial p}{\partial y} - \frac{\partial\alpha}{\partial y}\frac{\partial p}{\partial x}\right]}_{\text{solenoid}} - \underbrace{\left[\frac{\partial w}{\partial x}\frac{\partial v}{\partial z} - \frac{\partial w}{\partial y}\frac{\partial u}{\partial z}\right]}_{\text{twisting}} + \underbrace{\left[\frac{\partial F_x}{\partial x} - \frac{\partial F_y}{\partial y}\right]}_{\text{friction}} \tag{15}$$

Here α is specific volume; u, v and w are rectilinear velocity components, and F_x and F_y are frictional forces per unit mass.

Physically, convection may influence disturbance growth in two ways, thermal and dynamic. Its thermal role is carried out by the effect of its heat release upon the mass field (density or specific volume). In the vorticity equation, this heat release alters or creates the solenoid term. The dynamic effects of convection arise from the fact that the convection changes the motion field. In the vorticity equation, these changes can enter via the divergence, twisting or even the friction term.

The thermal role of convection in the tropical hurricane is well known. The cloud towers pump up the water vapor fuel and convert it into sensible heat, thus creating the density and pressure gradients that maintain the storm. In vorticity terms, the precipitation warming leads to a specific volume increase toward storm center, creating a positive solenoid term which acts to increase the vorticity. The dynamic effects of convection are less well understood and will be much more difficult to formulate. In particular, the causal chain between deep convection and the growth of low-level convergence with upper outflow cannot be stated quantitatively or even sequentially. The Gulf of Alaska evidence hints that the development of deep convection can be instigated by increased sea–air exchange, *when conditions are favorable.*

The convection then presumably produces increased low-level convergence and outflow aloft, contributing to the increase of cyclonic vorticity, and so forth.

In tropical hurricanes, the twisting term and the friction term may also be controlled by convection in a manner that implements deepening. GRAY (1967) suggests that the vertical momentum transports by the huge cloud towers are essential to generate and maintain the high-level outflow, without which the storm could not remain viable. There is no reason why these effects should not operate in mid-latitudes. The dynamic interactions of convection with larger-scale circulations is an almost unbroken and probably crucial frontier in meteorology. Mechanistic understanding of tropical storms and some aspects of how convection operates in them has been advanced by meticulous case studies using instrumented aircraft. A similar approach is advocated for higher-latitude oceanic cyclones, supplemented by the powerful new tools of satellites and instrumented buoys. Although it may appear difficult to catch and measure adequately a fast-deepening cyclone with current aircraft capabilities, a great advantage is provided to these endeavors by the highly sophisticated numerical models available to predict mid-latitude circulation features.

6. NUMERICAL MODELS

SPAR (1962) pioneered in designing a numerical model specifically to investigate the role of sea–air interaction in cyclogenesis. It was quasigeostrophic, vertically integrated and baroclinic (thermotropic). Dynamically, the model used the complete frictionless vorticity equation. The energy equation contained terms representing the effects of latent heat of condensation and heat flux from sea to air. The heat of condensation was computed from the derived vertical velocity ω and humidity soundings. The oceanic heating was put in from a Jacobs-type formula, with an empirically determined proportionality constant. This constant was determined from calculated heating along trajectories during actual cold air outbreaks and thus allows for some other diabatic effects in addition to turbulent transfer from the sea. The computation program permitted four sets of predictions to be made for each case studied:

(1) a barotropic forecast;
(2) a baroclinic prediction in which water vapor is neglected (dry baroclinic);
(3) a baroclinic prediction including water vapor and latent heat of condensation, but without flux of heat or water vapor from the ocean (no flux), and
(4) a " complete " baroclinic prediction including all the above effects.

Results of twelve-hour forecasts for two Atlantic cases are reported by SPAR, GERRITY and COHEN (1961) and several more unpublished cases have been discussed informally. The major conclusions from Spar's work are that the direct effects of oceanic heating upon cyclogenesis are virtually negligible and that the indirect effects lie (1) in creating atmospheric baroclinity particularly at coast lines and (2) in instigating and driving convection. In the case studies Spar found that the main improvement in forecast occurred in progressing from a barotropic to a baroclinic model. In " wet " cyclones, a further improvement was gained by including latent heat release. Virtually no improvement was gained by progressing to the " complete " model with oceanic fluxes included. For our purposes, the main deficiency in Spar's model is that it is quasi-geostrophic. Its consequent inability to treat the divergence term in (15) excludes the possibly important dynamic effects of convection. Additionally, bad truncation errors forced the forecasts to terminate after twelve hours.

A hierarchy of nine-level hemispheric primitive-equation models have been developed by the staff of the Geophysical Fluid Dynamics Laboratory (G.F.D.L.) of the Environmental Science Services Administration (SMAGORINSKY, MANABE and HOLLOWAY, 1965; MANABE, SMAGORINSKY and STRICKLER, 1965; MANABE and SMAGORINSKY, 1967). These models can be either moist or dry and can include or exclude parameterized sea–air fluxes of heat, moisture and momentum. Particularly clever is their manner of treating cumulus precipitation by a method called "convective adjustment." When the lapse rate exceeds moist adiabatic and the relative humidity reaches a certain threshold (80 or 100%), the lapse rate is adjusted to moist adiabatic and the released heat is supplied to the air. Thus in this model heating from the ocean can play its role in sustaining convection through maintenance of an unstable lapse rate. The only aspects of convection wholly lost are its more subtle mesoscale dynamic effects and its vertical transports of momentum. The latter are being parameterized in a still unfinished stage of the model.

The G.F.D.L. models have been tested for two two-week winter periods (MIYAKODA, SMAGORINSKY, STRICKER and HEMBREE, 1969). Predicted circulations showed good resemblance to observed throughout the test. Each case was run with a three-tiered model hierarchy: Experiment 1 was without sea–air exchange; Experiment 2 had exchange and a 100% condensation criterion; and Experiment 3 had exchange and an 80% condensation criterion.* Experiments 2 and 3 gave better results than Experiment 1, particularly for oceanic cyclogenesis. In these two experiments, three generations of Atlantic cyclones were identifiable corresponding almost one-to-one with observed cyclones. Hence we infer that marine deepening is at least fairly well predicted. Experiment 3 gave better results than Experiment 2, simulating an eighth day cyclone missed by Experiment 2. However, the results between the three experiments differed less than had been expected, possibly suggesting the dominant role of baroclinity in most developments.

The foregoing series of computations was run using climatological mean sea surface temperatures. Later, an experiment was run by MIYAKODA† using the actually measured sea temperatures during the period, which in the Western Atlantic happened to be anomalously warm by about 5°C. The latter prediction, after ten days, was much better than those of the previous experiments. The improvement was apparently due to the growth of a single deep cyclone which, while originating in the warm ocean area, disrupted the planetary flow as far away as Siberia! This result has instigated a series of experiments introducing assumed sea temperature anomalies and examining their consequences on air circulations. Such calculations provide, at least, a quantitative start in testing the brilliant but previously qualitative hypotheses of NAMIAS (1959; 1963; 1965a; 1965b) and BJERKNES (1959; 1962; 1964) on the role of sea–air interaction in climatic change.

To date, a case of explosive marine cyclogenesis has not been specifically selected and post-analyzed with the G.F.D.L. model hierarchy. A deterrent is the several

*Other factors were also varied between experiments so they are not a strict test of the role of exchange.

†Work not yet completed for publication. Kindly discussed with the writer by Dr. MIYAKODA of G.F.D.L., ESSA.

man-years required to set up each experiment and then to interpret the results. Notwithstanding, the expense and labor is still smaller than that of a medium-scope observational program and is, in fact, a necessary prerequisite for the proper and well-guided use of future observations in unravelling a problem that is critical to both sea and air.

Acknowledgments—The writer is deeply grateful for the generous help of her colleagues in the Geophysical Fluid Dynamics Laboratory of the Environmental Science Services Administration, upon whose work the last section of this paper is largely based. Particularly stimulating conversations were held with Drs. J. SMAGORINSKY, K. BRYAN, S. MANABE and K. MIYAKODA.

Much gratitude is also due to Professor J. SPAR of New York University for generous help in interpreting his own work and other aspects of sea–air interaction.

REFERENCES

BJERKNES J. (1918) On the structure of the moving cyclone. *Geofys. Publn*, **1**, 8 pp.

BJERKNES J. (1959) The recent warming of the North Atlantic. In: *The Atmosphere and the sea in motion*, Rockefeller Inst., Oxford Univ. Press, London, 65–73.

BJERKNES J. (1962) Synoptic survey of the interaction of sea and atmosphere in the North Atlantic. *Geofys. Publn*, **24**, 115–145.

BJERKNES J. (1964) Atlantic air-sea interaction. *Adv. Geophys.*, **10**, 1–82.

BJERKNES J. and H. SOLBERG (1922) Life cycles of cyclones and the polar front theory of atmospheric circulation. *Geofys. Publn*, 3, 18 pp.

BJERKNES V., J. BJERKNES, H. SOLBERG and T. BERGERON (1933) *Physikalische Hydrodynamik*. Springer-Verlag. OHG, Berlin.

BUNKER A. F. (1957) Turbulence measurements in a young cyclone over the ocean. *Bull. Am. Met. Soc.*, **38**, 13–16.

GODBOLE R. V. (1961) A preliminary investigation of radiative heat exchange between ocean and atmosphere. Unpublished manuscript on file at the Geophysical Sci. Dept., Univ. of Chicago.

GRAY W. M. (1967) The mutual variation of wind, shear and baroclinity in the cumulus convective atmosphere of the hurricane. *Mon. Weath. Rev.*, **95**, 55–74.

MALKUS J. S. (1962) Large-scale interactions. *The Sea: Ideas and Observations*, M. N. HILL, editor, Interscience Publishers, 88–294.

MALKUS J. S. and H. RIEHL (1964) *Cloud Structure and Distributions over the Tropical Pacific Ocean*. Univ. Calif. Press, 229 pp.

MANABE S. (1957) On the modification of air-mass over the Japan Sea when the outburst of cold air predominates. *J. Met. Soc. Japan*, **35**, 311–326.

MANABE S., J. SMAGORINSKY and R. F. STRICKLER (1965) Simulated climatology of a general circulation model with a hydrologic cycle. *Mon. Weath. Rev.*, **93**, 769–798.

MANABE S. and J. SMAGORINSKY (1967) Simulated climatology of a general circulation model with a hydrologic cycle. II: Analysis of the Tropical Atmosphere. *Mon.Weath. Rev.*, **95**, 155–169.

MIYAKODA K., J. SMAGORINSKY, R. F. STRICKLER and G. D. HEMBREE (1969) Experimental extended predictions with a nine level hemispheric model. *Mon. Weath. Rev.*, 91, 1-76.

NAMIAS J. (1959) Recent seasonal interactions between North Pacific waters and the overlying atmospheric circulation. *J. geophys. Res.*, **64**, 631–646.

NAMIAS J (1963) Large-scale air-sea interactions over the North Pacific from summer 1962 through the subsequent winter. *J. geophys. Res.*, **68**, 6171–6186

NAMIAS J. (1965a) Short-period climatic fluctuations. *Science*, **147**, 696–706.

NAMIAS J., 1965b : Macroscopic association between mean monthly sea-surface temperature and the overlying winds. *J. geophys. Res.*, 70, 2307–2318.

NAMIAS J. and P. F. CLAPP (1944) Studies of the motion and development of long waves in the westerlies. *J. Meteor.*, **1**, 57–77.

PETTERSSEN S. (1955) A general survey of factors influencing development at sea level. *J. Meteor.*, **12**, 36–42.

PETTERSSEN S. (1956) *Weather analysis and forcasting*. Vol. 1, Second Edn. McGraw-Hill, New York.

PETTERSSEN S. and P. A. CALABRESE (1959) On some weather influences due to warming of the air by the Great Lakes in winter. *J. Meteor.*, **16**, 646–652.

Petterssen S., D. L. Bradbury and K. Pedersen (1962) The Norwegian cyclone models in relation to heat and cold sources. *Geofys. Publn*, **24,** 243–280.

Priestley C. H. B. (1954) Vertical heat transfer from impressed turbulent fluctuations. *Austral. J. Phys.*, **9,** 133–143.

Pyke C. B. (1965) On the role of sea-air interaction in the development of cyclones. *Bull. Am. Meteor. Soc.*, **46,** 4–15.

Smagorinsky J., S. Manabe and J. L. Holloway, Jr. (1965) Numerical results from a nine-level general circulation model of the atmosphere. *Mon. Weath. Rev.*, **93,** 727–768.

Spar J. (1962) A vertically integrated wet, diabatic model for the study of cyclogenesis. *Proc. Int. Symp. Numerical Weather Prediction, Tokyo* **1960**, *Met. Soc. Japan*, 185–204.

Spar J., J. P. Gerrity, Jr. and L. A. Cohen (1961) Some results of experiments with an integrated, wet, diabatic weather prediction model. *New York Univ., Sci. Report No.* 2, *Contract Nonr*-285 (09), *Dept. Meteorol. and Oceanography*, 28 pp.(Unpublished manuscript).

Sutcliffe R. C. and A. G. Forsdyke (1950) The theory and use of upper air thickness patterns in forecasting. *Q. J. R. Met. Soc.*, **76,** 189–217.

Thompson P. D. (1961) *Numerical Weather Analysis and Prediction*. MacMillan Co. New York.

Winston J. S. (1955) Physical aspects of rapid cyclogenesis in the Gulf of Alaska. *Tellus*, **7,** 481–500.

Yanai M. (1961) A detailed analysis of typhoon formation. *J. Met. Soc. Japan*, (2), **39,** 187–213.

Reprinted from MONTHLY WEATHER REVIEW, Vol. 97, No. 7, July 1969, pp. 471-489.

UDC 551.576.11:551.577.11:551.574.1:551.509.617

MODELS OF PRECIPITATING CUMULUS TOWERS

JOANNE SIMPSON and VICTOR WIGGERT

Atmospheric Physics and Chemistry Laboratory, ESSA, Miami, Fla.

ABSTRACT

This paper presents a model of the growth of cumulus clouds. The water content and maximum height of rising towers are calculated using a buoyancy equation with consideration of effects of entrainment and water load. The latter is subject to effects of modeled microphysical effects. Precipitation growth is parameterized in terms of an autoconversion equation and a collection equation. A precipitation fallout scheme is devised that depends on water content, drop spectrum, and the vertical rise rate of the tower.

Then "freezing subroutines" are devised to model the effects of silver-iodide seeding. A hierarchy of seeding routines, using different ice collection efficiencies and terminal velocities, is partially tested against the data of the Stormfury 1965 tropical cumulus-seeding experiment.

Some preliminary numerical experiments on warm clouds are performed, assuming changes in drop spectra from hygroscopic seeding.

1. INTRODUCTION

This paper reports a first step toward a long-standing goal, namely the joint dynamical-physical modeling of a cumulus cloud. The growth and fallout of precipitation interacts with the updraft, which in turn controls the amount and development of hydrometeors. The most sophisticated models of precipitation growth (e.g., Telford, 1955; Twomey, 1964; Berry, 1967) have assumed a fixed water content and invariant or zero motion field. Few dynamical models have yet considered the effects of variable fallout upon either the ascent rates or subsequent particle growth.

Kessler (1959, 1961, 1963) pioneered in introducing the effect of varying updraft into cloud physics. He evolved parameterized equations for precipitation growth. He used these equations in combination with assumed vertical motion profiles and an assumed water generation function, set to approximate adiabatic condensation. We adopt his physical approach, introduced into a simplified model predicting dynamical variables as a function of environment and cloud-base conditions.

This model is a direct outgrowth of model EMB 65 (Experimental Meteorology Branch, 1965) of an entraining cumulus tower, discussed by Simpson et al. (1965). That treatment bypassed the cloud physics by arbitrarily dropping out one-half of the liquid water condensed, regardless of updraft speed or particle spectrum. Here, we introduce the basic concepts of Kessler regarding precipitation growth, summarized by him in a recent memorandum (1967). All water is initially condensed in small cloud particles which rise with the ascending air. A process called autoconversion creates some precipitation-sized particles, which then continue to grow by collecting small cloud particles. Precipitation-sized particles have a specified terminal volocity and continually fall out of the cloud tower. The fallout relieves some of the liquid water reduction of buoyancy and acts to slow down subsequent coalescence. Our cloud physics thus consists of an autoconversion equation, a collection or coalescence equation, a terminal velocity law, and a fallout scheme.

At all stages, the model development has been tested against field measurements on both natural and artificially modified clouds. Silver-iodide seeding experiments have been particularly useful tests of cumulus models; the 1965 Stormfury series is particularly emphasized here (Simpson, Simpson, Stinson, and Kidd, 1966; Simpson, Brier, and Simpson, 1967). This modeling effort is designed to parameterize complex processes in such a way as to give realistic predictions of measurables, such as vertical tower growth, buoyancy, hydrometeor distribution, radar reflectivity, etc., in both seeded and unseeded cumulus towers.

A contrasting approach is exemplified by the brave attempts at much more sophisticated models (e.g., Ogura, 1963; Murray and Hollinden, 1966; Arnason, Greenfield, and Newburg, 1968) which integrate the full hydrodynamic equations of motion on a space grid in a series of time steps. So far, none of these have achieved sufficiently realistic relationships between vertical growth, buoyancy, size, velocity, and temperature for useful prediction in modification experiments. Among the major problems are the intractability of formulating turbulent entrainment, the limitations imposed by working within confined boundaries, errors and fictitious results introduced by finite-differencing schemes, and the restriction to two-dimensional or axisymmetric coordinates. All these difficulties have been bypassed in the EMB series by observationally guided parameterizations so that the models give realistic and useful results despite their obvious crudities. We hope that the full hydrodynamic models can build upon the more successful of our parameterizations as the recent work by Arnason et al. (1968) has built upon those of Kessler.

2. DYNAMIC ASPECTS OF THE MODEL

The development of the numerical model, up to the EMB–65 version, is described in detail by Simpson et al. (1965). It involves integrating a differential equation for the vertical acceleration of a cumulus tower, where the acceleration is formulated as the difference between a buoyancy term and a drag term. Turner (1962) showed that the same form of the equation is applicable whether a cloud tower is idealized as a jet, a buoyant rising plume, or a "thermal" with vortical internal circulation. With the basic postulate that the internal circulation takes one, or a hybrid, of these forms, the differential equation for the rate of rise w is as follows:

$$\frac{dw}{dt}=w\frac{dw}{dz}=\frac{d}{dz}\left(\frac{w^2}{2}\right)=\frac{gB}{1+\gamma}-\frac{3}{8}\left(\frac{3}{4}K_2+C_D\right)\frac{w^2}{R} \quad (1)$$

where z is height and t is time; gB is the buoyancy force per unit mass; γ is the virtual mass coefficient; K_2 is the entrainment coefficient; C_D is an aerodynamic drag coefficient; and R is the radius or horizontal half-width of the cumulus tower.

The derivation of this equation is discussed by Simpson et al. (1965), and in more detail in a thesis by Levine (1965). Here, we will emphasize the physical foundations. It is important to keep in mind that we are using a quasi-Lagrangian framework in tracing the rise of a single cloud tower and that the coordinate system follows the circulation center of the tower. Thus, the plots of w and other variables versus z represent properties of the tower as it rises through that level. The results can only be considered cloud "profiles" in the roughest sense, during the interval that a steady-state condition might be expected to prevail. This interval may be different for the thermaldynamic properties in comparison with the hydrometeors. In the cloud physics discussion to follow, we are treating the precipitation growth and fallout within and from a single vertically circulating tower, with a roughly spherical shape and radius R. We are not able to treat precipitation growth within the whole body of the cloud, nor the ultimate rainout from its base.

The cornerstone of the dynamic modeling lies in the entrainment relation hypothesized, namely:

$$\frac{1}{M}\frac{dM}{dz}\simeq\frac{0.2}{R} \text{ (laboratory result)} \quad (2a)$$

and

$$\frac{1}{M}\frac{dM}{dz}=\frac{9}{32}\frac{K_2}{R} \text{ (theoretical result)}. \quad (2b)$$

The fractional entrainment rate per unit height is $(1/M)dM/dz$ where M is the mass in the rising tower. The important point is that the entrainment or dilution is inversely related to dimension, a relationship derived in laboratory experiments on convection. Although airborne measurements are still too crude to test this relationship definitively, it was supported by a series of unpublished temperature and liquid water records made by aircraft measurements of the Woods Hole Oceanographic Institution. Deductions from other aircraft measurements are apparently in conflict (Sloss, 1967).

The proportionality constant in (2a) was found by Turner (1962) for laboratory plumes while (2b) was derived by Levine (1959) for a buoyant spherical vortex. The quantity K_2 is evaluated from equation (2b) as 0.71; if necessary, this value can be adjusted from observational tests. The radius R of the cloud tower is determined empirically, from photogrammetry or aircraft penetrations. Together with an environment sounding and conditions at cloud base, this completes the input to the numerical calculation. Over the oceans, cloud-base conditions are assumed to be saturation at environment temperature at the observed cloud base when available, or otherwise at the lifting condensation level. Over land, cloud-base temperature excesses must be known, since results are sensitive to as little as 0.5°C variation. On the other hand, the predictions are highly insensitive to the input ascent rate w at cloud base (Andrews, 1964), which is taken as 1 m sec^{-1} throughout this work.

Thus for the oceanic cases considered here, the entire calculation could be made when the sounding becomes available, without reference to the actual clouds, with the exception of the tower radius R. The necessity for measuring R on the experimental clouds is a major shortcoming of this approach, since, so far, meteorologists have no way of predicting the cloud dimensions that a given situation will produce. Nor have the more sophisticated hydrodynamic models successfully faced this problem; an input initial dimension is still required. Here, we try to pick a characteristic active tower size for each cloud. As seen in equation (2), this size selection is merely a device to determine the entrainment rate.

To date, a constant R with elevation has proved adequate. Above about 400 mb in the Tropics, entrainment becomes a less important brake on cumuli, due to lower saturation compared to actual mixing ratios. Hence, changes in R become decreasingly important with height.

The buoyancy term is evaluated as follows:

$$\text{buoyancy}=gB=\frac{g[\Delta T_v-\Delta T_v\text{ (LWC)}]}{T_v\text{ (env)}} \quad (3)$$

where ΔT_v is the virtual temperature difference between tower and surroundings and ΔT_v(LWC) is the reduction due to the weight of suspended liquid water, as formulated by Saunders (1957), namely,

$$\Delta T_v\text{ (LWC)}=T_v\cdot\text{LWC} \quad (4)$$

TABLE 1.—*Parameters of the EMB cumulus models*

Parameter	Meaning	EMB 65	EMB 68	Remarks
K_2	Entrainment	0.55	0.65	Lab. value 0.71
C_D	Aerodynamic drag coefficient	0.506	0	Solid-sphere value=1.125
γ	Virtual mass coefficient	0	0.5	Lab. value 0.5
LWC	Liquid water retained	½ condensate	Falloutscheme	Much improved in EMB 68

where T_v is the cloud virtual temperature and LWC is its liquid or solid water content in grams per gram.

Ideally, mixing and condensation should be calculated at each height step, followed directly by the buoyancy determination and integration of equation (1). The cost and complexity of this procedure has led us, however, to the simpler method involving an entrainment calculation following the method of Stommel (1947) which is independent of (1). First, the entrainment calculation is performed on the computer, proceeding from cloud base upward between sounding points and assuming in-cloud saturation with respect to either water or ice. Output variables are cloud temperature, specific humidity, and liquid water condensed. These cloud properties are then available to calculate buoyancies at any interpolated vertical intervals in order to integrate equation (1) in ascending steps. To complete gB and undertake the integration, it remains only to specify γ, C_D and a fallout scheme for the condensation products. The maximum top height achieved by the cloud is defined to be that level where w goes to zero.

Table 1 shows the specification of dynamic parameters in the EMB–65 version of the model, which was prescribed in advance of the 1965 Stormfury cumulus-seeding experiments, and the modifications made in the current EMB 68.

A major weakness in EMB 65 was the arbitrary assumption that one-half the liquid water condensed in the entrainment calculation has fallen out of the tower at each level. A fixed fractional fallout precludes any feedback between the model's physical and dynamical processes and prevents the model from even a crude prediction of precipitation growth.

With this limitation, K_2 was prescribed in the range 0. 55–0. 65 by numerous in-cloud temperature measurements, up to and including those from the Stormfury 1963 seeding experiments. A small value of C_D was introduced to allow for the apparently greater vertical-momentum reduction than that due to entrainment. Turner (1964) suggested that a virtual mass coefficient would have achieved this end more realistically. However, since EMB 65 so mishandled the water retention, it did not appear worthwhile to refine the momentum relationships further until this weakness was ameliorated. It is clear that a smaller entrainment rate and a larger fractional retention of liquid water would have equally satisfied the momentum relations, but reducing the entrainment would have given in-cloud temperature excesses higher than those observed, and so was precluded.

Despite its oversimplifications, EMB 65 gave an excellent prediction of the maximum cloud-top heights of the Stormfury 1965 seeding experiment and the growth or nongrowth of the seeded clouds (Simpson et al., 1967). The average absolute error in height prediction was only 166 m for unseeded clouds and 336 m for seeded coluds. These "errors" are within the accuracy to which top heights could be measured. Since cloud-top heights varied widely, often on the same day, this result supports the $1/R$ entrainment relation as a useful first approximation. The model was also used by McCarthy (1968) to predict seedability distributions for Project Whitetop clouds in Missouri.

3. CLOUD PHYSICS ASPECTS OF THE MODEL

Since the 1965 experiments, an improved version of the model has been developed, using parameterized equations for the growth and fallout of precipitation. This model series is called EMB 68. An intermediate model called EMB 67 was discussed by Simpson et al. (1968). It contained an error in logic in water budgeting, leading to the exhaustion of cloud water in some seeded clouds and hence will not be included here. The only important change in the dynamics from EMB 65 just described lies in the introduction of a virtual mass coefficient of $\gamma = 0.5$ and the dropping of the aerodynamic drag C_D (table 1). This change was made for two reasons. First, Turner's (1963) laboratory results suggested both that the turbulent boundary layer was continually swallowed by the rising convection element so that C_D should be zero and that a virtual mass effect arose from the pushing of outside air around the rising plume. Turner measured a laboratory value of γ of about 0. 5. Second, EMB 65 predicted too high ascent rates for the towers, at least in comparison with our somewhat fragmentary photogrammetric measurements. Use of virtual mass instead of C_D reduces rise rates while giving slightly higher cloud-top heights for the same bouyancy so that we could raise K_2 to 0.65 in the EMB–68 series. The latter figure is still consistent with the in-cloud temperature measurements and is now within 10 percent of the laboratory value of 0. 71. The figures in section 8 show that all EMB–68 cases have considerably lower and more realistic ascent rates than did the corresponding calculations in EMB 65.

The main improvement in EMB 68 is that precipitation growth is predicted, and its fallout interacts with the vertical motions. All water is first condensed as cloud water, with small drop size (roughly 5–30μ) and negligible terminal velocity. Then a process called autoconversion begins. This involves the formation of precipitation particles either by the aggregation of several cloud particles or by the action of giant salt nuclei, or similar processes. We reconsider autoconversion in relation to ice growth by vapor diffusion (Bergeron effect) later in section 6. We have used two different autoconversion equations in most of the EMB-68 cases, namely:

$$\frac{dM}{dt}\text{(autoconversion)}=K_1(m-a) \qquad \text{gm m}^{-3}\text{ sec}^{-1}\ (m>a) \qquad (5)$$

or

$$\frac{dM}{dt}\text{(autoconversion)}=\frac{m^2}{60\left(5+\frac{.0366}{m}\frac{N_b}{D_b}\right)} \qquad \text{gm m}^{-3}\text{ sec}^{-1} \qquad (6)$$

where equation (5) is due to Kessler (1965) and equation (6) is due to Berry (1968*a*). In both equations dM/dt is the rate of growth of the precipitation water content M in gm m^{-3} and m is the cloud water content in gm m^{-3}. Kessler's linear equation was obtained intuitively. The parameter K_1 is the reciprocal of the $1/e$ "conversion time" of the cloud water. Kessler chose K_1 as 10^{-3} sec^{-1} to be consistent with a cloud lifetime of about 1000 sec. Existing cloud data probably preclude values one order of magnitude higher or lower. The "a" is a threshold cloud water content at which conversion is hypothesized to begin; we have followed Kessler in taking $a=0.5$ gm m^{-3}.

Berry's equation (6) is developed theoretically from a model of initial cloud growth by condensation and coalescence of cloud-sized particles with each other. The early droplet spectrum near cloud base has a number concentration of N_b drops per cm^3 and a relative dispersion D_b due to the condensation spectrum. The relative dispersion D_b is defined as:

$$D_b=\frac{\text{standard deviation of droplet radii}}{\text{mean droplet radius}}. \qquad (7)$$

The derivation of Berry (1968*a*) used the collection efficiencies of Shafrir and Neiburger (1963). Subsequently, Berry (1968*b*) has redone the calculation for the Davis and Sartor (1967) collection efficiencies and, at our request, has modified his parameterization formula to suit a boundary of 200-μ diameter between cloud and precipitation particles. His thus modified values are given in equation (6). The choice of the 200-μ boundary between cloud and precipitation was made for three reasons: 1) a drop with 200-μ diameter has a terminal velocity of 1–2 m sec^{-1} and is thus beginning to fall at a speed comparable to cumulus updrafts, 2) our aircraft foil precipitation sampler fails to size reliably drops much smaller than this, and 3) most 10-cm radars begin to show an echo of a cloud when numerous drops of about this size are present.

An important feature of Berry's equation is that a different autoconversion rate is predicted for maritime and for continental clouds. For maritime clouds we have chosen a drop concentration of 50 cm^{-3} at cloud base and a relative dispersion of 0.366. For extreme continental clouds we later use a drop concentration of 2000 cm^{-3} and the smaller spectral dispersion of $D_b=0.146$. These numbers are consistent with measurements by Squires (1958), Battan and Reitan (1957), and MacCready and Takeuchi (1965, 1968).

For the main comparison with the 1965 seeding data, only the maritime formulation is used. Although Kessler's equation is linear and Berry's approximately cubic, the predicted physics and dynamics of the clouds differ little enough that observational selection between them is difficult with existing data. By and large, it appears that the models using Berry's autoconversion formula give somewhat better height predictions and more reasonable liquid water distributions, although observational tests of the latter are inadequate to date.

Twomey (1959), Braham (1968*a*), and others have postulated that the entire history of coalescence precipitation growth in a cumulus is largely controlled by the initial droplet spectrum at cloud base. Use of equation (6) in our physical-dynamical model permits a fascinating test of this hypothesis in section 10.

The coalescence or collection rate is that derived by Kessler (1965, 1967) with the assumption that the precipitation spectrum follows that of Marshall and Palmer (1948). The Marshall-Palmer spectrum is defined by a single parameter n_0, namely:

$$n_D=n_0e^{-\lambda D} \qquad (8)$$

where D is the diameter, $n_D\delta D$ is the number of drops with diameter in the range between D and $D+\delta D$ in unit volume of space, and n_0 is the value of n_D for $D=0$. The exponent λ is related to the precipitation water content by integrating over all diameters to obtain

$$\lambda=42.1n_0^{0.25}\,M^{-0.25} \qquad (9)$$

or

$$\lambda=\frac{3.67}{D_0}$$

in the gram-meter-second system of units. D_0 is the median volume drop diameter or the diameter which divides the distribution into parts of equal water content.

We use the following equation for terminal velocity of raindrops, namely:

$$V=-130D^{1/2}\quad \text{m sec}^{-1}\quad (D\text{ in meters}). \qquad (10)$$

This equation was developed by Kessler (1965) from Gunn and Kinzer's (1949) data in the "Smithsonian Meteorological Tables" by List (1951). It gives slightly different values from those in the empirical table by Mason (1957). Both were used alternatively in the trial stages of our model with undetectably different results.

Using equations (8) through (10) and physical reasoning, Kessler obtains a collection equation, namely:

$$\frac{dM}{dt}\text{(collection)}=6.96\times10^{-4}En_0^{0.125}mM^{0.875} \quad \text{gm m}^{-3}\text{ sec}^{-1} \qquad (11)$$

where E is the collection efficiency of precipitation particles for cloud particles, with a value near unity for liquid clouds. Thus the collection rate depends on the cloud water content m, precipitation water content M, and two parameters n_0 and E.

From the Marshall-Palmer spectrum, a terminal velocity V_0 as a function of M is derivable as follows:

$$V_0 = -38.3 n_0^{-0.125} M^{0.125} \quad \text{m sec}^{-1}. \tag{12}$$

Physically, V_0 is the terminal velocity of the median volume drop size D_0. We also compute and print out the median volume diameter of the precipitation particles from

$$D_0 = \frac{V_0^2}{130^2} \quad \text{meters} \tag{13}$$

or

$$D_0 = .087\ n_0^{-0.25} M^{0.25} \quad \text{meters}$$

for comparison with aircraft measurements.

The fallout scheme is now simple to design. We consider the average precipitation particle to be located at the tower center and to fall with terminal velocity V_0. It leaves the vortically circulating portion of the tower after falling through a height interval R. The fractional fallout of precipitation M in each height interval is therefore the ratio of the time for the tower to rise through the vertical height step over which the integration is being made (50 m) to the time for the volume median diameter drop to fall through one radius. Clearly, the larger the drops and the weaker the rise rate, the greater the fallout per unit height. Several other fallout schemes were attempted; but so far, only this one has given both consistent and realistic results.

From this point, the water-budgeting is straight forward. All water condensed in the Stommel entrainment calculation in each vertical interval $(z_2 - z_1) = dz$ is first put into cloud water m. Then autoconversion and collection calculations are applied to obtain ΔM in the interval where $dt = dz/w_1$. Then ΔM is added to M and subtracted from m. Finally, a fallout calculation is applied to obtain ΔM fallout, which is subtracted from M. The fallout is summed with height in a separate column to give later the total rainout from the tower. The final sum of $m+M$ after conversion, collection, and fallout is used in the buoyancy correction to calculate w_2, and this same sum is then exported upward to repeat the water budget in the next height interval.

The basic assumption in the cloud physics modeling is that the Marshall-Palmer (1948) spectrum, or some similarly tractable distribution, prevails for precipitation continuously during the active life of the tower. If true, this implies that the cloud processes are always restoring this spectrum in the face of the continuous fallout of the larger drops.

4. AIRCRAFT DETERMINATION OF MODELING PARAMETERS

A cooperative five-aircraft cumulus program was carried out in the vicinity of Puerto Rico in July 1967. Participants were from ESSA, the Naval Research Laboratory, and Meteorology Research, Incorporated, with dropsonde support provided by the U.S. Air Force.

The main purposes of the program were investigation of natural glaciation in tropical cumuli and measurement of the cloud-physics properties of actively rising towers. Droplet spectra were measured on the M.R.I. Piper Aztec using a foil sampler (MacCready and Takeuchi, 1967), and liquid water contents were determined by joint use of several instrument systems.

A major pertinent result was the testing of the Marshall-Palmer spectrum. Roughly, a dozen excellent penetrations through actively rising oceanic towers were obtained. The Marshall-Palmer spectrum verified to a good first-order approximation, as it also has verified in similar measurements in Project Whitetop clouds in Missouri (Braham, 1968*b*). In all cases, n_0 was 10^7 m^{-4} or slightly less; in no case would a larger value have been realistic.

With n_0 specified as 10^7 m^{-4}, sets of trial model runs were made on some of the July 1967 clouds and on the unseeded and preseeded clouds of the 1965 experiment and compared with all pertinent observations. A K_2 of no larger than 0.65 was confirmed; at least half the clouds would not reach observed levels with a higher value. The collection efficiency E in equation (11) is chosen as 1, following Kessler. Present modeling and observational deficiencies are such that adjusting it for unfrozen clouds would not be meaningful. The values of the cloud physics parameters used for all EMB–68 liquid clouds are shown in table 2.

TABLE 2.—*Cloud physics parameters for liquid clouds*

Parameter	Meaning	Value	Remarks
K_1	Autoconversion parameter	10^{-3} sec^{-1}	Kessler value
a	Autoconversion threshold	0.5 gm m^{-3}	Kessler value
D_b	Spectrum dispersion	0.366 maritime, 0.146 continental	Berry values
N_b	Particle concentration at cloud base	50 cm^{-3} maritime, 2000 cm^{-3} continental	Observed (see text)
n_0	Marshall-Palmer intercept	10^7 m^{-4}	Observed
E	Collection efficiency precipitation for cloud	1	Kessler value

5. RADAR ECHO PREDICTION AND PRELIMINARY TEST OF MODEL

Once the precipitation water content and spectrum are defined, the radar reflectivity

$$Z = \Sigma n_D D^6 \delta D \tag{14}$$

is readily predicted, namely:

$$Z = 3.2 \times 10^{-9}\ n_0^{-0.75} M^{1.75} \quad (\text{meters}^3) \tag{15}$$

or

$$Z = 3.2 \times 10^9\ n_0^{-0.75} M^{1.75} \quad (\text{mm}^6\ \text{m}^{-3})$$

and when $n_0 = 10^7$ m^{-4}

$$\boxed{Z = 1.8 \times 10^4\ M^{1.75} \quad \text{mm}^6\ \text{m}^{-3}.} \tag{16}$$

In EMB 68, we have also used the empirical relations between the rainfall rate R (mm hr^{-1}) and radar reflectivity Z that have been found useful in tropical areas (Gerrish and Hiser, 1964), namely:

$$R=\left(\frac{1}{68}M\right)^{1.136} \qquad (M \text{ in mg m}^{-3}) \tag{17}$$

and with

$$Z=320\ R^{1.44} \qquad (Z \text{ in mm}^6\text{ m}^{-3}) \tag{18}$$

as found by Wexler (1947), we get

$$Z=0.322\ M^{1.6358} \qquad (M \text{ in mg m}^{-3})$$

or

$$\boxed{Z=2.6\times10^4\ M^{1.6358} \qquad (M \text{ in gm m}^{-3}).} \tag{19}$$

The first test of EMB 68 was made using data from a fine radar study of tropical clouds by Saunders (1965). Saunders measured radar echo intensities with a calibrated M–33 ground radar on more than a dozen warm clouds topping between 10,000–15,000 ft over the ocean near Barbados, West Indies. He also measured photographically the base and top heights of the clouds and their tower dimensions, using the radar range to establish his distance scale.

With the values in tables 1 and 2, our cloud height predictions agreed within the margin-of-measurement errors with Saunders' values, although there was a systematic overprediction averaging about 600 m or roughly 17 percent. Calculated radar echoes with equation (16) agreed very closely with Saunders' values, their average departing from his by less than 1 db. Calculated radar echoes with equation (19) averaged about 1 db higher, or not differing from the theoretical result enough to be differentiated by the average calibrated radar. Hence, we have used equation (16) throughout this paper.

6. PROBLEMS IN DESIGN OF SUPERCOOLED SEEDING ROUTINES

Design of the supercooled seeding subroutine for use with model EMB 65 was relatively simple and successful from the outset. The latent heat from one-half the condensed water was released linearly between the levels of −4°C and −8°C in the seeded cloud. The seeded cloud also proceeded from water to ice saturation in this interval.

With the physical processes introduced as in EMB 68, the design becomes more complex and difficult, with many more degrees of freedom. Furthermore, successful results are far more sensitive to the choice of parameters. The latter difficulty is more of a longrun benefit than disadvantage, since it means that seeding experiments become a sensitive tool to evaluate cloud physics processes and parameters that are very difficult to measure directly.

Conferences were held with numerous experts to consider what values should be assigned to the constants in table 2 during and after seeding. Knowledge was both scanty and conflicting; measurements at heights above the −10°C level are particularly rare, and the few sets that do exist do not include enough simultaneously measured variables to test a model. Even the forms or habits of the ice particles are not well documented. Columns and large graupellike mixtures, together with junk ice, appear to be common near −4°C (Braham, 1964; Ruskin, 1967) while columns may be replaced by some hexagonal plates between −9°C and −13°C (Todd, 1965). In tropical clouds no measurements exist to tell us whether true snow crystals appear at higher levels.

Due to the uncertainties described, we have tried a hierarchy of 24 seeded cloud models, designated as models EMB 68A through EMB 68M, with subscript K for Kessler autoconversion and B for Berry autoconversion. The models and their results are summarized in table 3, to be discussed in the following. Each combination of the physical parameters is based on a reasonable hypothesis about the structure and processes in seeded clouds. The hypotheses are tested by comparing the model results with each other and with observations.

Kessler's (1967) calculations and our own demonstrate that when collection has become active in a cloud, autoconversion may be neglected as a precipitation-forming process. Hence, in models A through K we do not modify the autoconversion equations in a glaciated cloud. In these models we do not explicitly include the Bergeron process, although this process could be physically very important in early particle growth. According to Byers (1965), diffusion growth is important only as an initiating mechanism. Once a size is attained representing an appreciable terminal velocity, coalescence becomes the predominating mechanism. Hence in models A through K, we implicitly assume that the Bergeron process could be altering our cloud spectrum m in such a way as to increase collection efficiency E in equation (11); but aside from that, we concern ourselves mainly with the input to the collection equation (11) and with the terminal velocities of ice particles.

Kessler's autoconversion equation (5), however, is suitable for modeling the faster conversion that might result from ice diffusion. Hence, in models L and M we model the Bergeron effect explicitly with a K_1 of 4×10^{-3} sec^{-1} or a $1/e$ conversion time of 250 sec or about 4 min. Observations (Bethwaite et al., 1966) indicate indirectly that this may be an extreme value, so that a higher K_1 appears implausible at present.

We retain the Marshall-Palmer spectrum for the frozen precipitation. This assumption is weaker and less justified than it is in the case of liquid clouds. Nevertheless, preliminary calculations suggest that our model results are insensitive to the exact spectrum shape provided it has the general form of a rapid decrease in number with increasing size, which surely is the case.

Conflicting evidence prevailed on collection efficiencies of ice precipitation. Laboratory results of Hosler and Hallgren (1960) suggest that it may be much less than for water precipitation, while Weickmann (1957) shows evidence that the protuberances on snow particles may enhance their collection efficiencies above that of water particles containing the same mass. Ice collection efficiency probably depends on the forms, shapes, and wetness of the ice particles, all virtually unknown. Hence, we have run a hierarchy of ice collection efficiencies ranging from 0.1–2.0 in the EMB–68 model series. Most of our dynamical and physical results are quite insensitive to this very large variation, which retrospectively justifies our rather crude parameterization of precipitation growth in an ice cloud.

The model predictions are actually much more sensitive to the ice terminal fall velocity, which exerts a stronger control on the hydrometeor retention in the cloud. We have tried terminal velocities of 20, 50, and 100 percent relative to water particles of the same mass. The 20-percent value is hypothesized roughly to represent snow crystals and flakes (Weickmann, 1957); the 100-percent value represents frozen drops, junk ice, and possibly graupel (Braham, 1964). The 50-percent cases are supposed to typify some mixture of these forms.

In our physical modeling of a frozen cloud, we use equations (10)–(12) exactly as in a liquid cloud, adjusting E and V_0, as stated above, to be characteristic of ice. In the Marshall-Palmer spectrum, D is now the "equivalent water diameter" or diameter of an equivalent mass water drop. The particle number is thus obtained, with D and D_0 merely artifacts to calculate V_0. The quantity V_0 is then reduced by any factor desired to approximate roughly the fall rate appropriate to the ice shape present.

7. THE EMB–68 SEEDING SUBROUTINES AND THEIR STATISTICAL TESTING

In all seeding subroutines, two in-cloud temperatures specify the levels flanking the tower's all-water to all-ice transformation; this "slush region" is here defined between $-4°C$ and $-8°C$. Cloud water to ice changes proceed linearly with height in this interval, which is usually traversed in 3–5 min. In all seeding subroutines 60–100 percent of the total H_2O content at $-4°C$ was eventually frozen, with the corresponding latent heat of fusion released linearly. The cloud also proceeds linearly from water to ice saturation in this region.

The reduced percentage of water frozen was considered for two reasons: 1) to allow for fallout within the slush region and 2) to allow for some natural freezing in the cloud before seeding (Ruskin, 1967; Sax, 1969). A posteriori calculations of fallout in the slush region showed that at $-8°C$ most seeded clouds retained about 90 percent or more of their total H_2O content at $-4°C$.

We have made no change in equation (16) for the radar-reflectivity versus precipitation relationship for the seeded clouds. According to Austin (1963), for ice and snow we may use

$$Z\ (\text{ice}) = 1000\ R^{1.6} \qquad (R \text{ in mm hr}^{-1}), \quad (20)$$

while from Gunn and Marshall (1958) we find that in ice clouds

$$M = 250\ R^{0.90} \qquad (M \text{ in mg m}^{-3}) \quad (21)$$

has proved satisfactory. Combining (20) and (21) we get

$$Z\ (\text{ice}) = 0.0546\ M^{1.778} \qquad (M \text{ in mg m}^{-3}) \quad (22)$$

or

$$Z\ (\text{ice}) = 1.18 \times 10^4\ M^{1.778} \qquad (M \text{ in gm m}^{-3}).$$

Computations of Z were made and compared from (16) and (22) for numerous values of M in the range 0.5–3.0 gm m^{-3}, which corresponds to the range in our clouds. Equation (16) gives values less than 2 decibels (dB) higher than equation (22). We believe that the uncertainty in particle size and spectrum exceeds this margin, as do the calibration errors in most radars. Hence, we continue to use (16) for the seeded clouds, with the reservation that the predicted radar reflectivities for glaciated conditions should be regarded with skepticism until further measurements are available.

Table 3 describes the hierarchy of models and the statistical evaluation of each with the 1965 Stormfury cumulus data. It is important to note that so far the seeding model tests have been made (from necessity) almost entirely with dynamic properties of the clouds, using top heights in particular. In general, those models which failed badly to predict top heights also gave ridiculous water contents. Only one clearly unsuccessful model (E) is shown in table 3.

In table 3, column 1 gives the designation of the model; the subscript K or B denotes whether Kessler's or Berry's autoconversion was used. Column 2 gives the percent of the water content at $-4°C$ assumed frozen by the seeding. Column 3 gives the ice collection efficiency E_I used in equation (11). Column 4 gives the terminal velocity V_{TI} in terms of the percent of the terminal velocity computed from equation (12). Column 5 gives the average absolute error in top height prediction for all seeded clouds, while column 6 gives the average algebraic error.

It is immediately clear that model E, with no precipitation fallout, gives preposterous results, which will be analyzed later. Of the remaining models, those with 20-percent V_{TI} clearly give better results than those with 50 or 100 percent. Regardless of the shortcomings of the models or of the exact particle spectra, it is clearly necessary that relatively more water be retained in the clouds after seeding than before, in order to prevent overpredicted cloud tops. This conclusion is clarified by the waning effectiveness of entrainment in reducing buoyancy and hence vertical ascent in the upper levels of the clouds.

TABLE 3.—*Hierarchy of models and statistical evaluation of each with the 1965 Stormfury data. See text for details.*

1 Model	2 TLWC (%)	3 E_I	4 V_{TI} (%)	5 $\|\bar{l}\|$ (meters)	6 $\bar{l}$ (meters)	7 $R_{S.EF}$	8 m	9 b (kilometers)	10 $\overline{\Delta R/R}$ (%)	11 $R_{P_s.\Delta R}$	12 $R_{EF.\Delta R}$
68 A_K	100	0.1	20	570	−50	0.93	0.78	+0.44	−7	−0.92	+0.79
68 A_B				520	+33	0.93	0.82	+0.24	−8	−0.92	+0.75
68 B_K	60	0.1	20	480	−380	0.95	0.86	+0.55	−7	−0.90	+0.83
68 B_B				450	−330	0.94	0.92	+0.38	−9	−0.90	+0.78
68 C_K	80	0.1	20	490	−230	0.94	0.82	+0.50	−7	−0.91	+0.81
68 C_B				440	−160	0.94	0.87	+0.30	−8	−0.91	+0.77
68 D_K	90	0.1	20	480	−150	0.94	0.80	+0.46	−8	−0.92	+0.80
68 D_B				460	−60	0.94	0.84	+0.28	−9	−0.91	+0.76
68 E_K	100	0.1	None	1140	−1060	0.24	0.28	+2.48	No fallout		
68 E_B				1590	−1510	0.23	0.28	+2.46			
68 F_K	100	1.0	100	980	+510	0.90	0.65	+0.35	+22	−0.57	+0.97
68 F_B				900	+750	0.94	0.72	−0.03	+22	−0.69	+0.63
68 G_K	100	0.1	100	730	+230	0.91	0.71	+0.39	+7	−0.85	+0.86
68 G_B				730	+390	0.92	0.73	+0.16	+11	−0.81	+0.83
68 H_K	80	1.0	100	810	+310	0.91	0.68	+0.39	+20	−0.49	+0.98
68 H_B				760	+375	0.92	0.72	+0.20	+17	−0.57	+0.97
68 I_K	100	2.0	50	940	+460	0.92	0.66	+0.37	+19	−0.56	+0.96
68 I_B				820	+470	0.92	0.70	+0.17	+14	−0.68	+0.92
68 J_K	80	1.0	50	680	+160	0.93	0.71	+0.43	+13	−0.57	+0.97
68 J_B				610	+210	0.93	0.76	+0.24	+9	−0.65	+0.94
68 K_K	80	1.0	20	480	−90	0.94	0.77	+0.48	+1	−0.83	+0.89
68 K_B				430	−50	0.94	0.84	+0.29	−4	−0.86	+0.82
68 L_K^*	80	0.1	20	480	−180	0.94	0.80	+0.49	−4	−0.89	+0.84
68 M_K^*	80	1.0	20	480	−90	0.94	0.77	+0.48	+1	−0.84	+0.89

*Fast autoconversion (Bergeron effect)

Aloft, increased water retention becomes the sole way to restrict the vertical momentum. Logically, more water retention means less fallout, which works against increased precipitation by seeding (discussed in section 8).

Columns 7–9 in table 3 relate to statistical evaluation of results, similar to that performed by Simpson, Brier, and Simpson (1967) with EMB 65 and the same data. Two quantities, seedability S and seeding effect EF, are defined. Seedability is the difference in predicted top heights between seeded and unseeded clouds. Seeding effect is the difference between the observed maximum top height and the predicted unseeded top height. Column 7, $R_{S.EF}$ is the correlation coefficient between seedability and seeding effect for all 1965 seeded clouds.

If our models and data were perfect, the correlation $R_{S.EF}$ would be 1.0 for seeded clouds, since their observed growth above the unseeded predicted top should equal their seedability. For unseeded clouds, the correlation $R_{S.EF}$ should be zero. Note that in all models (except E) the seeded correlation exceeds 0.90, which is significant to better than 1 percent. Figure 1 shows the EF versus S diagrams for models EMB 68, C_B and K_B. Graphs with similar appearance resulted from all other models except E. Seeded and unseeded clouds formed different populations, with different means and regressions. (Unseeded computations were identical for all EMB–68 models A–M, except E, no fallout. With the exception of E, the only difference between models lies in seeded parameters.) Essentially no correlation between S and EF resulted for the unseeded cases. The slightly better correlation found with EMB 65 is accounted for by clouds 7 and 12 which actually failed to grow after seeding. The EMB–68 model series underpredicted the unseeded tops of both these clouds but correctly predicted the seeded tops leading to a finite (incorrect) EF.

The high correlation $R_{S.EF}$ demonstrates a linear relationship between S and EF. Columns 8 and 9 in table 3 give the slope and intercept, respectively, of the best fit straight line to the circled points in the diagrams exemplified in figure 1. Again, perfect modeling and data would give $m=1.0$ and $b=0$. The degree to which m and b approach these values is a measure of the adequacy of the models.

Using all the measures in columns 5–9, models A–D and K–M give the best results. These are the models with ice terminal velocity only 20 percent that of equivalent mass

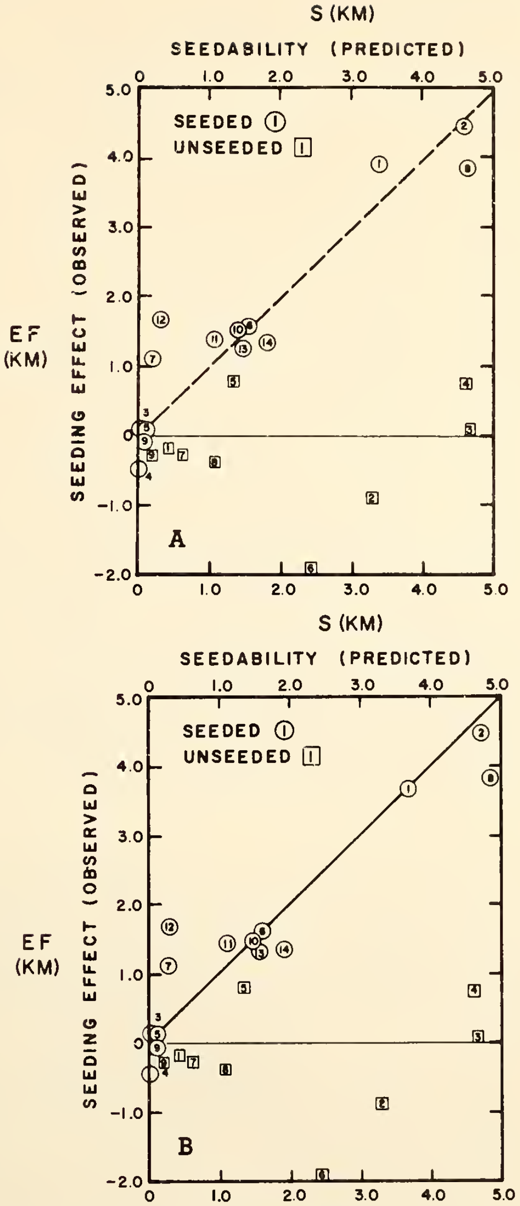

FIGURE 1.—Seeding effect *EF* versus seedability *S* (both in kilometers) for two versions of the EMB–68 model, (A) EMB 68 C_B and (B) EMB 68 K_B (see table 3 for both models). The dashed line is the theoretical curve for seeded clouds; the solid line is the theoretical curve for control clouds.

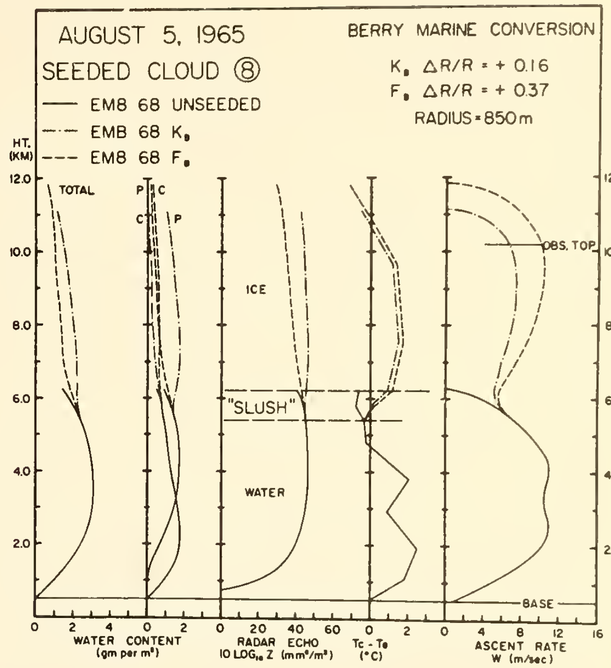

FIGURE 2.—Comparison of results for models EMB 68 K_B versus F_B for cloud of Aug. 5, 1965. The main difference between models is that F eventually freezes 100 percent of the water contained in the cloud at $-4°C$, while K freezes 80 percent. In F, ice particles have the same terminal velocities as water particles, while ice terminal velocity is greatly reduced in model K. The graphs give properties of the rising tower as functions of height. P stands for precipitation water content (*M* in text); C stands for cloud water content (*m* in text). ΔR is the seeded minus the unseeded fallout; *R* is the unseeded fallout. The heights are for the center of the cloud tower. Hence, the observed tops have been corrected by subtracting the tower radius.

liquid drops. Figure 2 compares, for a typical seeded cloud, results using models 68K and F. The much higher sustained water content in the more successful seeded models is evident. The difference in total H_2O content is of the order of 1 gm m^{-3}. This difference would be detectable with present instrumentation, such as the Lyman-α system with evaporator, if it could be flown into seeded cumuli at levels of 7–9 km.

In the two fast autoconversion (strong Bergeron effect) models, L_K is the same as C_K except for fourfold more rapid conversion, while M_K is the fast conversion version of K_K. The results of M_K and K_K are so nearly identical that the plotted curves and all other features are indistinguishable. The result shows that when the ice collection efficiency is 1.0 or more, even a strong Bergeron effect on conversion makes no difference and may be neglected for our present purposes. Figure 3 compares a sample case for C_K and L_K. The dynamics of the two clouds are virtually identical, hence only the physical parameters are shown. We see about 0.3 gm m^{-3} more precipitation in the L case. In large part, faster conversion compensates for reduced ice collection efficiency in seeded clouds. For this and other reasons, models A–D are probably less realistic since they reduce ice collection without allowing for the compensation by the Bergeron effect.

However, models A–D do make the important point that, within wide limits, the amount of liquid water frozen by seeding does not matter much. Model B, with 60 percent, produces as good results as model A with 100

352-162 O - 69 - 2

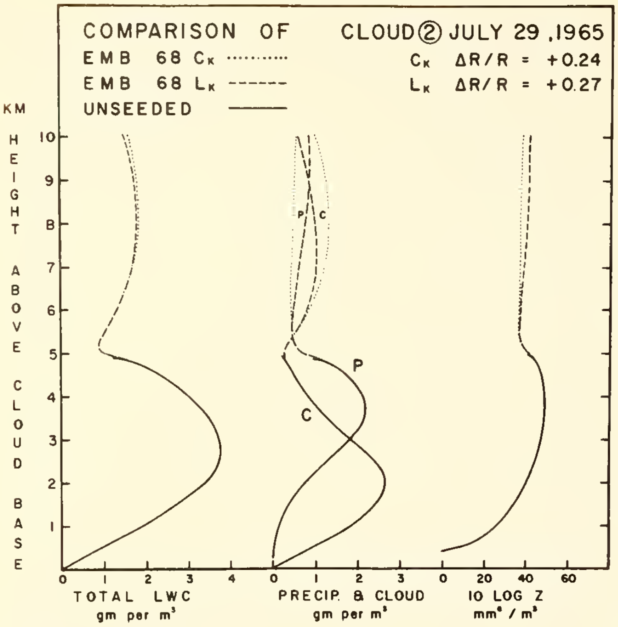

FIGURE 3.—Comparison of physical predictions by models C_K and L_K on expanded horizontal scale. Model C_K has same autoconversion rate in seeded as unseeded cloud and a 0.1 collection efficiency of ice for ice. Model L_K has the same low ice-collection efficiency but a four times faster autoconversion rate in the seeded cloud, to simulate a strong Bergeron effect. Other notation same as figure 2. Note little difference in fractional precipitation increase.

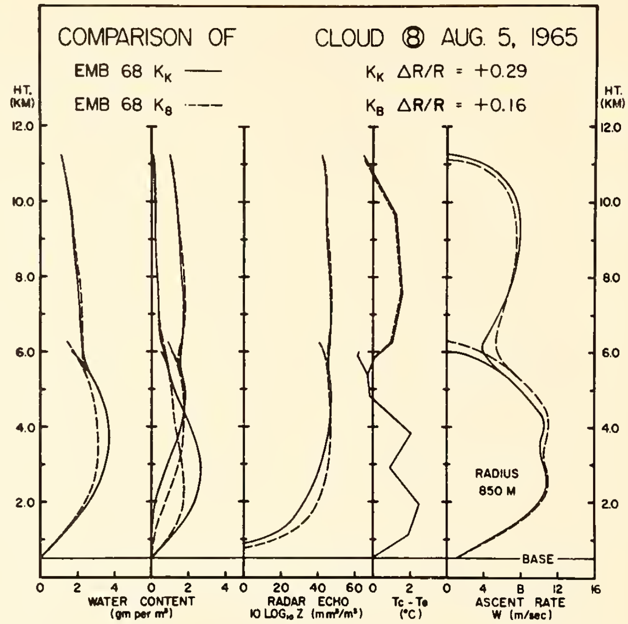

FIGURE 4.—Comparison of model results using Kessler's autoconversion (solid) versus that of Berry marine (dashed). Comparison made with model EMB 68K for the seeded cloud of Aug. 5, 1965. Note the similar end products despite faster early precipitation growth using Berry's formulation. With parameters characteristic of continental clouds (not shown), Berry's formulation leads to slower precipitation growth than Kessler's.

percent. Allowing for 10 percent fallout in the slush region, this means that as much as 30 percent of the water in the cloud updraft could be naturally frozen without much reducing the growth increases expected from seeding. Our field results (Ruskin, 1967; Mee and Takeuchi, 1968) suggest that 10–20 percent is nearer the amount of natural freezing in active updrafts between $-4°C$ and $-8°C$. Hence, we choose the models eventually realizing the latent heat from 80 percent of the water contained at $-4°C$.

Overall, model K appears to verify best, particularly the version with Berry's autoconversion. Figure 4 shows a typical comparison of results with the two autoconversion schemes, using seeded cloud 8 on Aug. 5, 1965. While the upper portions of the tower are nearly identical in all properties, between 2–4 km the proportions of precipitation versus cloud water differ. Berry's formulation leads to earlier growth of precipitation in the rising tower than does Kessler's.

At present, we do not regard the use of an ice collection efficiency of 1.0 as implying that the ice collection process is unaltered from that of water, but rather that opposing effects possibly compensate. It is likely that reduced collection by the hardened ice surfaces is compensated both by the branches or protuberances on the ice particles and by the Bergeron effect. In any case, results are quite insensitive to reasonable variations in E_I. The greater success of the lower V_{TI} models strongly suggests the dominance of the more slowly falling crystalline forms following seeding, whether they are snowflakes, columns, or plates. Much more particle sampling needs to be undertaken in seeded clouds and at higher levels than has so far been possible.

Table 4 compares, cloud by cloud, the predicted liquid water contents at $-4°C$ in all EMB–68 models except E (predicted unseeded water contents are identical for all models except E) with those measured by the ESSA DC–6 flying at 19,000 ft, where ambient temperatures were about $-6°C$ to $-8°C$. The measuring equipment used was that described by Levine (1965).

A correlation between water content at $-4°C$ and seeding effect was run. The correlation was -0.25, which is not statistically significant.

The complete failure of model E requires some discussion. In this model, zero fallout of precipitation was assumed from both the unseeded and the seeded towers. Cloud water was converted to precipitation using equations (5) or (6) and (11), but no water was dropped out of the tower. With this model, nearly half of the seeded clouds failed to reach the $-4°C$ level, in contradiction to observed heights at seeding. For those that were predicted to reach the seeding level, table 3 shows that the predictions were hopelessly poor, and no significant correlation between

TABLE 4.—*Predicted and observed water contents at −4°C in 1965 seeded clouds*

Cloud	Model (gm/m³)	Obs. (gm/m³)	Remarks
(1) K B	2.17 1.75	1.6–2.0..........	Several towers—average
(3) K B	1.95 2.10	1.6–1.8..........	Average for seeded tower
(5) K B	2.12 2.0	Missing.......	Aircraft passed over top.
(6) K B	3.92 3.30	0.6.............	Aircraft missed tower. Aircraft at 10,000 ft measured 3.5 gm/m³.
(7) K B	.... 2.08	Missing.......	Aircraft passed over top.
(8) K B	2.64 2.35	1.6–2.4..........	See Ruskin (1967).
(9) K B	2.70 2.33	Missing.......	Cloud did not reach aircraft level.
(10) K B	2.82 2.52	Missing.......	No before-seeding penetration
(11) K B	2.38 2.09	Missing.......	No before-seeding penetration
(12) K B	2.46 2.39	Missing.......	No before-seeding penetration
(13) K B	2.82 2.61	Missing.......	No data
(14) K B	3.36 3.11	~1.8–2.1.......	Two towers

Note: Clouds (2) and (4) were seeded at temperatures above 0°C and did not reach the −4°C level.

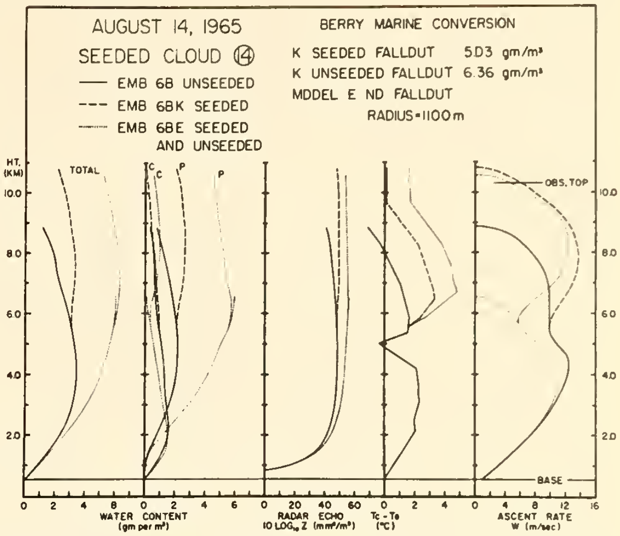

FIGURE 5.—Comparison of predictions by models EMB 68 E_B (dotted) and 68 K_B (unseeded, solid; seeded, dashed). Model E has no fallout. Note unrealistically large precipitation water and total water contents predicted by model E. The higher predicted seeded cloud temperature excess in model E is due to the higher water content and the fact that 100 percent of the water in the cloud at −4°C is eventually frozen.

seeding effect and seedability was obtained. Since no fallout of large drops occurs, the precipitation spectrum tends to larger and larger mean drop sizes and unrealistically rapid growth. From equation (11), we see that if M is too large, dM/dt will also be too large; and the error will build up with time or elevation.

Figure 5 shows a sample comparison between models E and K for the Aug. 10, 1965, case. The water content in E is nearly 6 gm m^{-3} in the slush region, compared to about 3 gm m^{-3} for model K, which was higher than the measured amount (table 4). In E, about 5 gm m^{-3} or 92 percent of the water is in precipitation. The radar echo exceeds 56 dB, and the volume median drop diameter for precipitation is 2.4 mm. In K, the corresponding values for the slush region are 3.2 gm m^{-3}, with 2.3 gm m^{-3} or 74 percent in precipitation; D_0 is 1.9 mm. The latter values are more consistent with Saunders' (1965) figures and with our own water and spectral measurements (Mee and Takeuchi, 1968).

Weinstein and Davis (1968) have used a model, in ome respects similar to E, with apparent success in predictions relating to Arizona clouds. In their model, no fallout is assumed for the cloud physics calculations of equations (10)–(16). However, for the dynamic calculation from equation (1), all water is dropped, in each height interval, that has a terminal fall speed greater than w. It is readily shown that this implies negligible fallout when w exceeds about 6 m sec^{-1}. The colder cloud base (~0°C) and continental character of Arizona clouds, however, favor smaller entrainment and higher relative water contents (Woodley, 1966). Sax (1969) has used the Weinstein-Davis model on the Stormfury 1965 cases with successful height predictions for all but cloud 1. Omitting cloud 1, the correlation $R_{S,EP}$ came out 0.92.

Closer examination, however, reveals that radii 50–400 percent larger than our values were used. For that model, R is supposed to comprise the entire cloud body. Since a comparable K_2 was used, radii this large reduce entrainment to a negligible braking effect. Thus, their height predictions are successful because of the large weights of water carried. No observational comparison of predicted in-cloud temperature excesses or water contents were made. Our earlier results (Simpson et al., 1965; Simpson, Brier, and Simpson, 1967) suggest that in-cloud temperatures would be at least 1–2°C too high if the radii are increased by 50–400 percent. Figure 5 shows that the no fallout water content is too large by a factor of about two with the correct radius; it would be still larger with a wider radius and the concomitant near-adiabatic condensation rate.

We conclude that models without fallout cannot treat precipitation growth nor cloud physical-dynamical interactions realistically enough to be useful, particularly in the case of maritime tropical clouds.

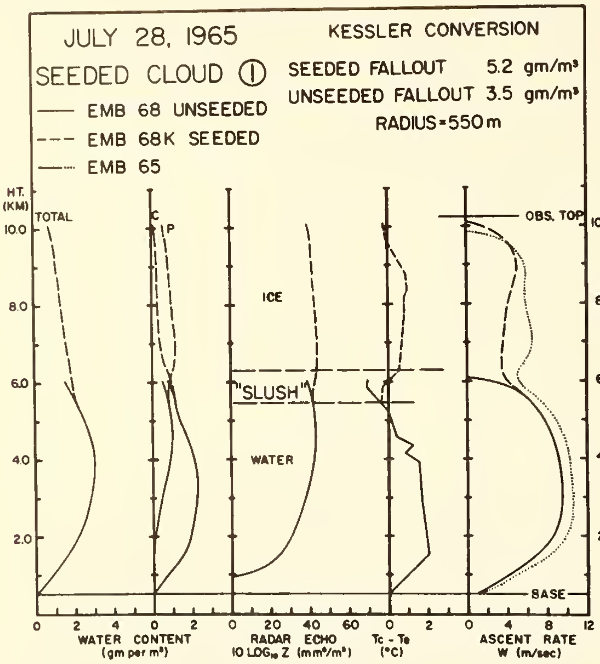

Figure 6.—Predicted properties of seeded cloud 1, July 28, 1965, using model EMB 68 K_K. The observed cloud (see figs. 9 and 12) grew explosively following seeding.

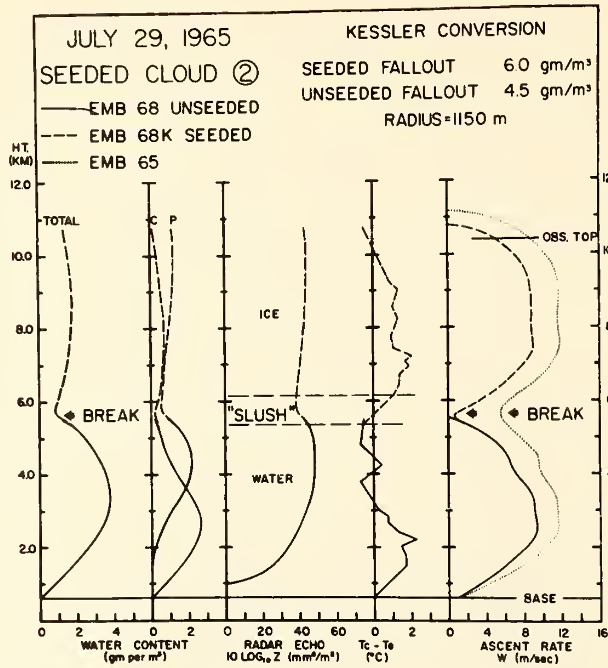

Figure 7.—Predicted properties of seeded cloud 2, July 29, 1965, using model EMB 68 K_K. The observed seeded cloud tower (see figs. 10 and 13) grew vertically following seeding, cutting off from the main cloud body which dissipated.

8. PRECIPITATION CHANGES FOLLOWING SEEDING AND PHYSICAL-DYNAMICAL INTERACTIONS

Columns 10–12 of table 3 deal with calculated precipitation changes between seeded and unseeded clouds. The quantity ΔR is defined as the difference in the summed fallout between the seeded and the unseeded tower, while $\Delta R/R$ is the ratio of this difference to the unseeded fallout or the fractional change in precipitation fallout due to seeding. The number appearing in column 10 is the average percentage change in fallout for all seeded clouds (except 3 and 4, which were seeded above 0° C).

The average $\overline{\Delta R/R}$ does not mean much in itself since it is composed of large increases versus large decreases, with roughly the same number of clouds showing predicted increases as decreases. Figures 6–8 illustrate this point with model K. Figures 6 and 7 show results for seeded clouds 1 and 2. In all models, these clouds showed the largest positive values of $\Delta R/R$. For example, cloud 1 (Kessler) showed a 19-percent increase in model A and a 51-percent increase in model F, the extreme cases. Figure 8 shows the results for seeded cloud 6, which showed the largest precipitation decrease. The correspond-

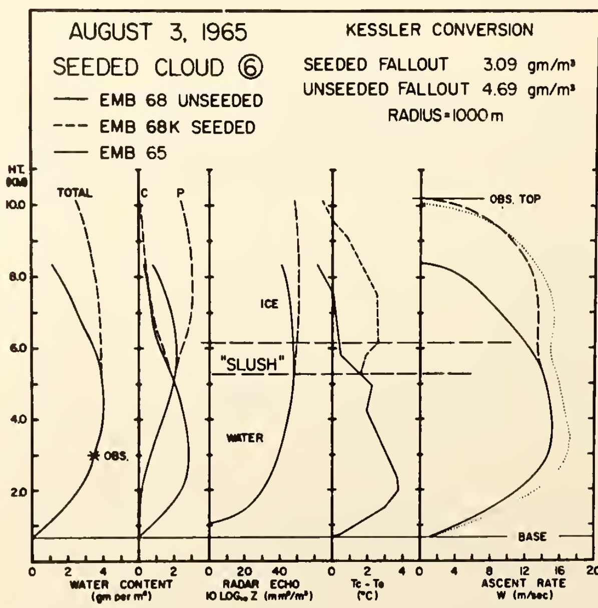

Figure 8.—Predicted properties of seeded cloud 6, Aug. 3, 1965, using model EMB 68 K_K. Note the relatively large top height predicted for the unseeded cloud and the smaller fallout predicted for the seeded cloud. The observed cloud (figs. 11 and 14) grew explosively following seeding.

ing range in its $\Delta R/R$ (Kessler) is from -44 percent in model A to $+12$ percent in model F. Thus, the average values should be interpreted in this light. When the average is negative for a model, it simply means smaller pluses, one or two fewer clouds with increases, and larger decreases.

Those clouds that showed large predicted precipitation increases from seeding in all models were those with low unseeded tops and large seeding effect EF, while those with large precipitation decreases were those with tall unseeded tops and a smaller value of EF. The two clouds that failed to grow (5 and 9) after seeding showed negligible precipitation change; these two are omitted from the correlations shown in columns 11 and 12. The inverse correlation between unseeded top heights and ΔR is, in nearly all models, significant at better than the 5-percent level. The positive correlation between seeding effect and ΔR is significant in all cases. Physically, this result means that if an unseeded cloud will grow naturally to heights of 8–10 km, seeding will probably decrease precipitation fallout by "hanging up" the precipitation particles in the ice phase. Little is gained by further growth above these levels since the condensation rate falls off to very small values at cold temperatures. The most promising cases for increased fallout from seeding are those clouds whose natural growth does not exceed 6–7 km and where a big seeding effect is predictable from the model.

Since ΔR denotes only the fallout difference between seeded and unseeded towers, similar calculations to those in columns 10–12 were run for total precipitation production by the towers. The results were so nearly similar to the foregoing that they are not shown.

The changes in precipitation fallout are on the order of 20–30 percent and generally in the range of about 1 gm m^{-3}. This is about half an inch over 2 sq mi, or more than 50 acre-feet. This amount is of course not much, but we are considering only the rising period of a single tower. In an explosive growth case, many towers succeed each other over a greatly prolonged lifetime, so that conceivably we could obtain the half inch over as much as three times the area, or a total of perhaps about 160 acre-feet, which is not negligible. By the same argument, of course, an explosive growth could overcome the calculated negative fallout difference computed only for the first tower in comparison with its unseeded fallout.

It should be emphasized that we are not able to compute how much of the cloud fallout reaches the ground as precipitation. This potentiality will depend upon how much of the tower fallout descends through the cloud body and how much through the drier environment, hence upon environmental circumstances such as humidity, wind shear, and cloud-base height. Nevertheless, we hypothesize a proportionality between our calculated fallouts and potential rainfall production by seeding. In other words, circumstances of explosive growths of towers which are predicted not to grow high without seeding are most favorable, while cut-off growths are less so. Clouds which are predicted to grow to the cumulonimbus or near-cumulonimbus stage, unseeded, should show the smallest gains or even rainfall losses from seeding. We plan to test this hypothesis with the results of a 1968 Florida seeding program in which the precipitation at numerous levels, from cloud base upward will be evaluated with calibrated ground radars.

Meanwhile, comparison of the clouds modeled in figures 6–8 illustrates very well the interactions between physical and dynamical features and perhaps explains some aspects of the difference between explosive growth and cut-off tower growth. Clouds 1 and 6 were observed to grow explosively following seeding, while cloud 2 exhibited the cut-off tower regime. Figures 9–11 are photographs of these clouds; figures 12–14 show their scale outlines, reconstructed photogrammetrically. Two features distinguish the cut off from the explosive cases. The first is the wider measured cloud body of clouds 1 and 6 compared to cloud 2. The second distinguishing feature lies in the calculated velocity, water, and temperature profiles. Note in figure 7 that the vertical ascent rate goes virtually to zero at 6 km, while it increases rapidly to above 8 m sec^{-1} between 7 and 8 km. The diminution of ascent rate causes a "dumping" of hydrometeors at 6 km, the level at which the break appears. The unloading of the tower permits it to accelerate rapidly, while the rather narrow cloud body below is apparently killed (fig. 10B) by the "fall-through" of the precipitation. A stable dry layer in the environment of cloud 2 gives rise to a strong negative buoyancy from just above 4 km to nearly 6 km.

9. MARITIME VERSUS CONTINENTAL CLOUDS AND WARM CLOUD EXPERIMENTS

Figure 15 shows a typical maritime tropical cumulus and its extreme continental counterpart. The same sounding and radius are used for both clouds, as is the Berry conversion equation (6). For the maritime cloud, $N_b=50$ cm^{-3} and $D_b=0.366$. For the continental cloud, $N_b=2000$ cm^{-3} and $D_b=0.146$. The dynamics of the resulting clouds are virtually identical, although the continental cloud terminates about 100 m lower due to the 1 gm m^{-3} higher water content near its top. The physical properties and radar echoes of the clouds are utterly different. The precipitation fallout is nearly eight times as much from the maritime cloud as from the continental cloud!

The vast predicted difference, particularly in precipitation, between maritime and continental clouds encourages experimentation on converting one type of cloud into the other, particularly by seeding with hygroscopic particles. Could a maritime cloud be inhibited from raining by the addition of very many small hygroscopic particles? More importantly, could a continental cloud be caused to rain more by broadening its cloud base spectrum? Figures 16 and 17 are preliminary numerical tests of these ideas.

FIGURE 9.—Photograph of seeded cloud 1, July 28, 1965, at seeding time (2217:30 GMT). Right-hand portion seeded.

In experiment 1 (fig. 16), we hypothesize adding enough small hygroscopic particles to reach the continental concentration, but since we cannot remove the giant oceanic nuclei, we leave the relative dispersion unchanged. The results are striking. We predict a large (nearly 100 percent) increase in cloud water content and a 72-percent decrease in precipitation fallout.

In experiment 2, we try to make a continental cloud more maritime and to increase precipitation by a hypothetical introduction of enough large hygroscopic particles to widen the relative dispersion to 0.488 while leaving the droplet concentration unchanged from 2000 per cm^3. The results are successful, although less so than in experiment 1. We predict an increased precipitation fallout of 150 percent per tower which, however, amounts to only 0.29 gm m^{-3} or at most about 15 acre-feet.

Thus, while hygroscopic seeding appears the most promising technique for rain increase under drought conditions, when only warm clouds are present, it is not as drastic nor as powerful a cloud modification technique as silver-iodide seeding, since it only affects the physics of the seeded tower itself, while silver-iodide seeding can affect the dynamics of the entire convective system over numerous life cycles of an individual tower.

10. CONCLUDING REMARKS

A final supercooled seeding experiment was tried numerically, designed to test the Bergeron effect alone. Dynamic effects via latent heat release were assumed to be zero, and the only seeding effect was hypothesized to be increased autoconversion beginning at −4°C in the seeded clouds. These experiments were performed with the Kessler formulation only. Values of K_1, 4 times and 10 times the value (10^{-3} sec^{-1}) used for liquid clouds, were taken. The tiny increases in precipitation and fallout were too small to affect any of the significant figures in the predictions. This result confirms an earlier

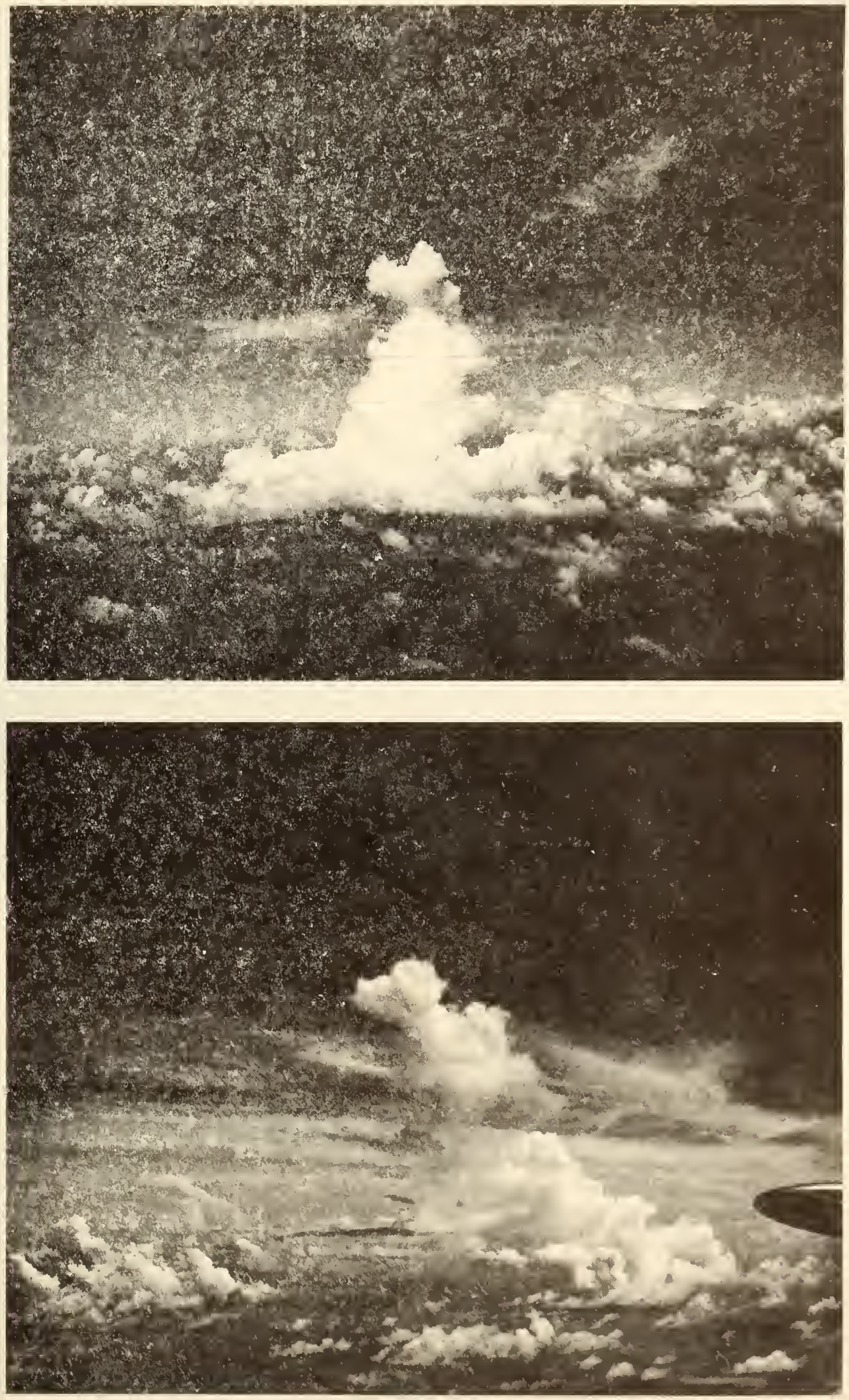

FIGURE 10.—Photographs of seeded cloud 2, July 29, 1965; (A) at 1½ min after seeding (1812 GMT); (B) at 15½ min after seeding (1826 GMT). Note that seeded tower has cut off and is showering into main cloud body below, which is dissipating.

FIGURE 11.—Photograph of seeded cloud 6, Aug. 3, 1965, at 11½ min before seeding (2147 GMT).

conclusion by Kessler (1967) that large changes in autoconversion do not affect precipitation growth after collection has become important in a cloud.

Therefore, the main conclusion of this paper is that the main effect of seeding supercooled tropical cumuli is through the alteration of the cloud dynamics, which in turn alters the water carried and precipitated. The feedback of the physics to the dynamics only changes the motion field critically in certain marginal situations, for example the cut-off case of figure 6.

A hierarchy of quite different physical models, with widely different ice collection efficiencies and ice fall speeds gives results dynamically very similar to each other. Furthermore, the results with the new EMB-68 series are qualitatively the same as with the simpler EMB-65 model—the clouds that grew significantly following seeding could not be made to fail to grow (and vice versa) with any reasonable permutations of the seeding subroutine nor of the ice regime. However, some selection among the physical models was possible with available measurements, suggesting a reduction of ice terminal velocity relative to that of water particles.

The best EMB-68 models give reasonable predictions of precipitation growth, fallout, and radar echo intensity, which stand to be tested with results of the next observational program. Both positive and negative precipitation changes of the order of 20–30 percent are predicted. These are equivalent to water amounts of 100–200 acre-feet per cloud of these dimensions, if precipitation falling from the tower reaches the ground. In any case, it

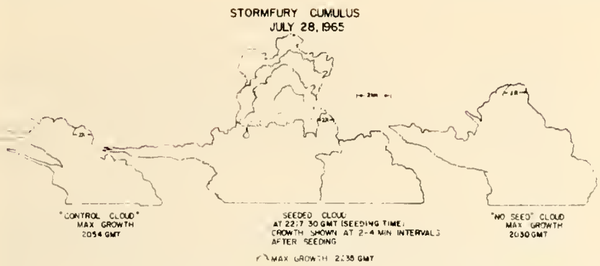

FIGURE 12.—Scale outlines of seeded and control clouds on July 28, 1965, constructed using photogrammetry as described by Simpson (1967).

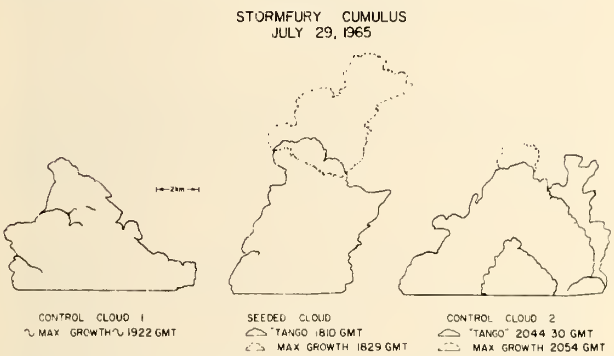

FIGURE 13.—Scale outlines of seeded and control clouds on July 29, 1965, constructed in the same manner as figure 12.

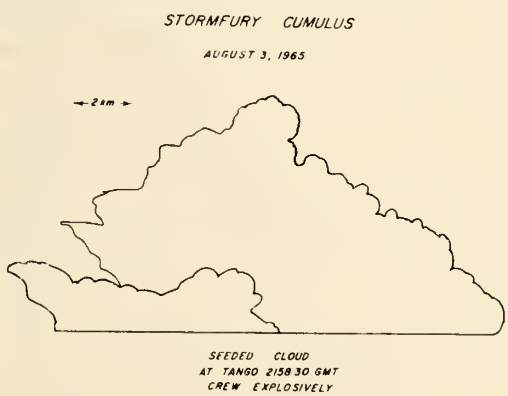

FIGURE 14.—Scale outline of seeded cloud 6, Aug. 3, 1965, at time of seeding. Due to aircraft radar failure, no photogrammetry was possible after seeding.

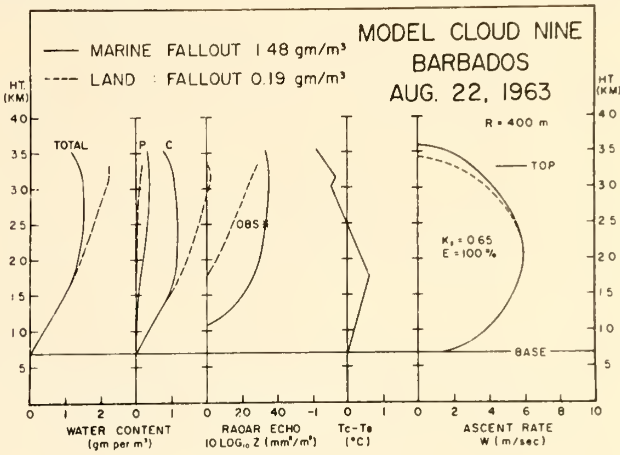

FIGURE 15.—Model cloud 9 for Barbados, Aug. 22, 1963. Model used was EMB 68K, with Berry marine (solid) and Berry land (dashed) autoconversion. Radius data, observed radar echo, and top heights obtained from original records of Saunders (1965). The Barbados radiosonde for 1823 GMT was used. The tower was followed by Saunders between 1802–1817 GMT.

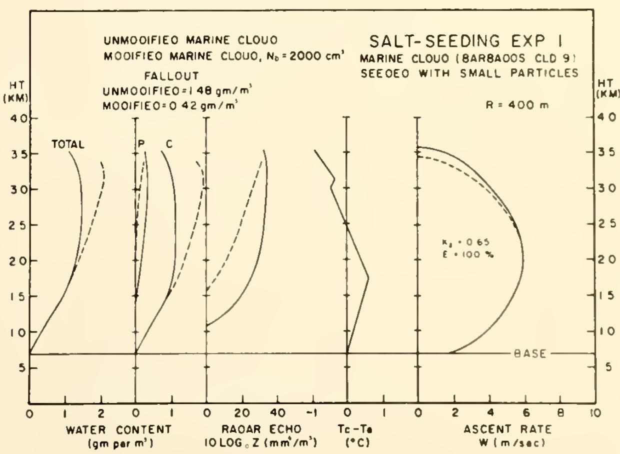

FIGURE 16.—Hypothetical salt seeding experiment 1. Solid lines denote unmodified cloud. Dashed lines denote modified cloud. Attempt to convert maritime toward continental cloud by addition of small particles to make $N_b = 2000$ per cm³. Relative dispersion unchanged from 0.366. Note reduced precipitation production and fallout.

is possible to predict with this model favorable and unfavorable situations for silver-iodide seeding. The favorable situations are those of large vertical growth following seeding or large seeding effect, particularly if explosive growth occurs. The difference between explosive and cut-off tower growth can now be foretold in part, at least, from the model. The less favorable or unfavorable situations for seeding are those with high natural cloud growth and small seedability.

Hygroscopic seeding of warm clouds appears to be an interesting and promising experimental series to test in the field on individual clouds. Several groups, particularly Howell and Lopez (1968), have such experiments underway. However, from both the cloud study and large-scale viewpoint, silver-iodide experiments on supercooled clouds probably have more to offer, in that the dynamics of single clouds and probably of whole cloud groups can be

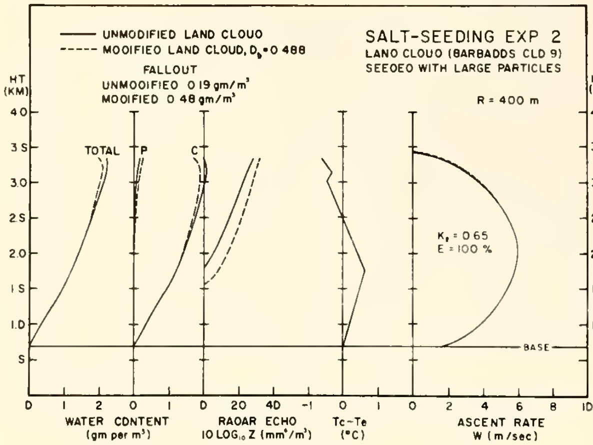

FIGURE 17.—Hypothetical salt seeding experiment 2. Attempt to convert continental toward maritime cloud by addition of large particles. Relative dispersion is increased from 0.146 to 0.488, while N_b remains 2000 per cm³. Note small but percentually significant increase in precipitation production and fallout.

drastically altered; this quite possibly can trigger persistent alterations in the physical cloud processes, such as precipitation structure and fallout.

Note added in proof—Some observational evidence on the hydrometeor spectrum in the ice phase has become available since completion of this paper. During a Florida cumulus seeding experiment in May 1968, it was found that while the slope of the ice particle spectrum did not differ much from the Marshall-Palmer relation used herein, the intercept n_0 (Takeuchi, 1969) was about one order of magnitude higher than that given in table 2.

In our model, n_0 appears to the 0.125 power in the collection equation (11) and the terminal velocity equation (12). An order of magnitude increase in n_0 would, therefore, lead to a collection rate multiplied by a factor of 1.33 and a particle terminal velocity divided by this factor, other parameters and variables being equal.

Let us consider the effect of the higher n_0 on model EMB 68K, which gave the best fit with observations. In this version of the model, the ice collection efficiency E was one, while the ice terminal velocity was reduced to 20 percent of the corresponding values for water. With n_0 increased by the 10 factor, we would obtain the same results as in 68K if we reduce the ice collection efficiency to two-thirds the water value and take the terminal velocities for ice to be 30 percent of those for water particles the same size. These changes appear quite reasonable. Unfortunately, no adequate measurements of either ice collection efficiencies or terminal velocities yet exist to test these inferences.

ACKNOWLEDGMENTS

The authors gratefully acknowledge the valuable help of their colleagues Roscoe Braham, Robert Ruskin, and Helmut Weickmann. They are particularly grateful to Edwin Kessler, upon whose fine work much of this approach is based and to Edwin X. Berry who worked closely with us on autoconversion. Mr. Robert Powell ably drafted the figures, and Mrs. Peggy Lewis prepared the numerous versions of the manuscript.

The work on warm cloud experiments has been kindly supported by the Bureau of Reclamation, U.S. Department of the Interior.

REFERENCES

Andrews, D. A., "Some Effects of Cloud Seeding in Cumulus Dynamics," M. A. thesis, Department of Meteorology, University of California, Los Angeles, **1964**, 139 pp.

Arnason, G., Greenfield, R. S., and Newburg, E. A., "A Numerical Experiment in Dry and Moist Convection Including the Rain Stage," *Journal of the Atmospheric Sciences*, Vol. 25, No. 3, May **1968**, pp. 404–415.

Austin, P. M., "Radar Measurements of the Distribution of Precipitation in New England Storms," *Proceedings of the 10th Weather Radar Conference, Washington, D.C., April 22–25, 1963*, American Meteorological Society, Apr. **1963**, pp. 247–254.

Battan, L. J., and Reitan, C. H., "Droplet Size Measurements in Convective Clouds," *Artificial Stimulation of Rain, Proceedings of the First Conference on the Physics of Cloud and Precipitation Particles, Woods Hole Oceanographic Institution, Woods Hole, Massachusetts, September 7–10, 1955*, Pergamon Press, New York, **1957**, pp. 184–191.

Berry, E. X., "Cloud Droplet Growth by Collection," *Journal of the Atmospheric Sciences*, Vol. 24, No. 6, Nov. **1967**, pp. 688–701.

Berry, E. X., "Modification of the Warm Rain Process," *Proceedings of the First National Conference on Weather Modification, Albany, New York, April 28–May 1, 1968*, American Meteorological Society, State University of New York, Albany, **1968*a***, pp. 81–85.

Berry, E. X., Desert Research Institute, University of Nevada, Reno, **1968*b***, (personal conversation).

Bethwaite, F. D., Smith, E. J., Warburton, J. A., and Heffernan, K. J., "Effects of Seeding Isolated Cumulus Clouds With Silver Iodide," *Journal of Applied Meteorology*, Vol. 5, No. 4, Aug. **1966**, pp. 513–520.

Braham, R. R., Jr., "What is the Role of Ice in Summer Rain-Showers?," *Journal of Atmospheric Sciences*, Vol. 21, No. 6, Nov. **1964**, pp. 640–645.

Braham, R. R., Jr., "Meteorological Bases for Precipitation Development," *Bulletin of the American Meteorological Society*, Vol. 49, No. 4, Apr. **1968*a***, pp. 343–353.

Braham, R. R., Jr., Department of Geophysical Sciences, University of Chicago, **1968*b***, (personal conversation).

Byers, H. R., *Elements of Cloud Physics*, University of Chicago Press, **1965**, 191 pp.

Davis, M. H., and Sartor, J. D., "Theoretical Collision Efficiencies for Small Cloud Droplets in Stokes Flow," *Nature*, Vol. 215, No. 5108, MacMillan (Journals) Ltd., London, Sept. **1967**, pp. 1371–1372.

Gerrish, H. P., and Hiser, H. W., "Mesoscale Studies of Instability Patterns and Winds in the Tropics," *Report* No. 5, Contract No. DA-36-039 SC-89111, University of Miami, Coral Gables, Fla., July **1964**, 55 pp.

Gunn, K. L. S., and Marshall, J. S., "The Distribution With Size of Aggregate Snowflakes," *Journal of Meteorology*, Vol. 15, No. 5, Oct. **1958**, pp. 452–461.

Gunn, R., and Kinzer, G. D., "The Terminal Velocity of Fall for Water Droplets in Stagnant Air," *Journal of Meteorology*, Vol. 6, No. 4, Aug. **1949**, pp. 243–248.

Hosler, C. L., and Hallgren, R. E., "The Aggregation of Small Ice Crystals," *The Physical Chemistry of Aerosols, Discussions of the Faraday Society*, No. 30, The Aberdeen University Press Ltd., Scotland, **1960**, pp. 1–8.

Howell, W. E., and Lopez, M., "Project Rainstart," *Interim Report*, Contract No. NSF-C453, E. Bollay Assoc., Inc., Goleta, Calif., July **1968**, 66 pp.

Kessler, E., III, "Kinematic Relations Between Wind and Precipitation Distributions, I," *Journal of Meteorology*, Vol. 16, No. 6, Dec. **1959**, pp. 630–637.

Kessler, E., III ,"Kinematic Relations Between Wind and Precipitation Distributions, II" *Journal of Meteorology*, Vol. 18, No. 4, Aug. **1961**, pp. 510–525.

Kessler, E., III, "Elementary Theory of Associations Between Atmospheric Motions and Distributions of Water Content," *Monthly Weather Review*, Vol. 91, No. 1, Jan. **1963**, pp. 13–27.

Kessler, E., III, "Microphysical Parameters in Relation to Tropical Cloud and Precipitation Distributions and Their Modification," *Geofisica International*, Vol. 5, No. 3, July **1965**, pp. 79–88.

Kessler, E., III, "On the Continuity of Water Substance," *ESSA Technical Memorandum* IERTM-NSSL 33, U.S. Department of Commerce, Washington, D.C., **1967**, 125 pp.

Levine, J., "Spherical Vortex Theory of Bubble-Like Motion in Cumulus Clouds," *Journal of Meteorology*, Vol. 16, No. 6, Dec. **1959**, pp. 653–662.

Levine, J., "The Dynamics of Cumulus Convection in the Trades: A Combined Observational and Theoretical Study," *Ref.* No. 65-43, Woods Hole Oceanographic Institution, Mass., **1965**, 129 pp.

List, R. J., "Smithsonian Meteorological Tables," *Publication* **4014**, Smithsonian Institution, Washington, D.C., 6th Rev. Ed., **1951**, 527 pp.

MacCready, P. B., Jr., and Takeuchi, D. M., "Precipitation Mechanisms and Droplet Spectra of Some Convective Clouds," *Analysis of Flagstaff Data, Report* No. 2, Contract No. DA 28-043-AMC-00406(E), Meteorology Research, Inc., Altadena, Calif., **1965**, pp. 3–33.

MacCready, P. B., Jr., and Takeuchi, D. M., "Aircraft Probing of Natural and Seeded Clouds for Project Skyfire," *Final Report*, Meteorology Research, Inc., Altadena, Calif., **1967**, 42 pp.

MacCready, P. B., Jr., and Takeuchi, D. M., "Precipitation Initiation Mechanisms and Droplet Characteristics of Some Convective Cloud Cores," *Journal of Applied Meteorology*, Vol. **7**, No. 4, Aug. **1968**, pp. 591–602.

Marshall, J. S., and Palmer, W. McK., "The Distribution of Raindrops With Size," *Journal of Meteorology*, Vol. 5, No. 4, Aug. **1948**, pp. 165–166.

Mason, B. J., "The Physics of Clouds," *Oxford Monographs on Meteorology*, Oxford University Press, London, **1957**, 421 pp.

McCarthy, J., "Computer Model Comparisons of Seeded and Not-Seeded Convective Cloud Depth Using Project Whitetop Data," *Proceedings of the First National Conference on Weather Modification, Albany, New York, April 28–May 1, 1968*, American Meteorological Society, State University of New York, Albany, **1968**, pp. 270–279.

Mee, T. R., and Takeuchi, D. M., "Natural Glaciation and Particle Size Distribution in Marine Tropical Cumuli," *Final Report* Contract No. E22-30-68(N), Meteorological Research, Inc., Altadena, Calif., Aug. **1968**, 71 pp.

Murray, F. W., and Hollinden, A. B., "The Evolution of Cumulus Clouds: A Numerical Simulation and Its Comparison Against Observations," *Final Report*, Contract Nonr-4715(00), Douglas Aircraft Co., Inc., Santa Monica, Calif., Mar. **1966**, 149 pp.

Ogura, Y., "The Evolution of a Moist Convective Element in a Shallow, Conditionally Unstable Atomsphere: A Numerical Calculation," *Journal of Atmospheric Sciences*, Vol. 20, No. 5, Sept. **1963**, pp. 407–424.

Ruskin, R. E., "Measurements of Water-Ice Budget Changes at −5C in AgI-Seeded Tropical Cumulus," *Journal of Applied Meteorology*, Vol. 6, No. 1, Feb. **1967**, pp. 72–81.

Saunders, P. M., "The Thermodynamics of Saturated Air: A Contribution to the Classical Theory," *Quarterly Journal of the Royal Meteorological Society*, Vol. 83, No. 357, July **1957**, pp. 342–350.

Saunders, P. M., "Some Characteristics of Tropical Marine Showers," *Journal of Atmospheric Sciences*, Vol. 22, No. 2, Mar. **1965**, pp. 167–175.

Sax, R. I., "The Importance of Natural Glaciation on the Modification of Tropical Maritime Cumuli by Silver Iodide Seeding," *Journal of Applied Meteorology*, Vol. 8, No. 1, Feb. **1969**, pp. 92–104.

Shafrir, U., and Neiburger, M., "Collision Efficiencies of Two Spheres Falling in a Viscous Medium," *Journal of Geophysical Research*, Vol. 68, No. 13, July 1, **1963**, pp. 4141–4148.

Simpson, J., "Photographic and Radar Study of the Stormfury 5 August 1965 Seeded Cloud," *Journal of Applied Meteorology*, Vol. 6, No. 1, Feb. **1967**, pp. 82–87.

Simpson, J., Brier, G. W., and Simpson, R. H., "Stormfury Cumulus Seeding Experiment 1965: Statistical Analysis and Main Results," *Journal of Atmospheric Sciences*, Vol. 24, No. 5, Sept. **1967**, pp. 508–521.

Simpson, J., Simpson, R. H., Andrews, D. A., and Eaton, M .A., "Experimental Cumulus Dynamics," *Reviews of Geophysics*, Vol. 3, No. 3, Aug. **1965**, pp. 387–431.

Simpson, J., Simpson, R. H., Stinson, J. R., and Kidd, J. W., "Stormfury Cumulus Experiments: Preliminary Results 1965," *Journal of Applied Meteorology*, Vol. 5, No. 4, Aug. **1966**, pp. 521–525.

Simpson, J., Wiggert, V., and Mee, T. R., "Models of Seeding Experiments on Supercooled and Warm Cumulus Clouds," *Proceedings of the First National Conference on Weather Modification, Albany, New York, April 28–May 1, 1968*, American Meteorological Society, State University, Albany, **1968**, pp. 251–269.

Sloss, P. W., "An Empirical Examination of Cumulus Entrainment," *Journal of Applied Meteorology*, Vol. 6, No. 5, Oct. **1967**, pp. 878–881.

Squires, P., "The Microstructure and Colloidal Stability of Warm Clouds: Pt. 1. The Relation Between Structure and Stability, Pt. 2. The Causes of the Variations in Microstructure," *Tellus*, Vol. 10, No. 2, May **1958**, pp. 256–271.

Stommel, H., "Entrainment of Air Into a Cumulus Cloud," *Journal of Meteorology*, Vol. 4, No. 3, June **1947**, pp. 91–94.

Takeuchi, D. M., "Analyses of Hydrometeor Sampler Data for ESSA Cumulus Experiments, Miami, Florida, May 1968," *Final Report*, Contract E22-28-69(N), Meteorology Research, Inc., Altadena, Calif., **1969**.

Telford, J. W., "A New Aspect of Coalescence Theory," *Journal of Meteorology*, Vol. 12, No. 5, Oct. **1955**, pp. 436–444.

Todd, C. J., "Ice Crystal Development in a Seeded Cumulus Cloud," *Journal of Atmospheric Sciences*, Vol. 22, No. 1, Jan. **1965**, pp. 70–78.

Turner, J. S., "The 'Starting Plume' in Neutral Surroundings," *Journal of Fluid Mechanics*, Vol. 13, No. 3, July **1962**, pp. 356–368.

Turner, J. S., "The Motion of Buoyant Elements in Turbulent Surroundings," *Journal of Fluid Mechanics*, Vol. 16, No. 1, May **1963**, pp. 1–16.

Turner, J. S., Department of Applied Mathematics and Theoretical Physics, Kings College, Cambridge, England, **1964**, (personal conversation).

Twomey, S., "The Nuclei of Natural Cloud Formation: Pt. 2. The Supersaturation in Natural Clouds and the Variation of Cloud Droplet Concentration," *Geofisica Pura e Applicata*, Vol. 43, May/Aug. **1959**, pp. 243–249.

Twomey, S., "Statistical Effects in the Evolution of a Distribution of Cloud Droplets by Coalescence," *Journal of Atmospheric Sciences*, Vol. 21, No. 5, Sept. **1964**, pp. 553–557.

Weickmann, H. K., "A Nomogram for the Calculation of Collision Efficiencies," *Artificial Stimulation of Rain, Proceedings of the First Conference on the Physics of Cloud and Precipitation Particles, Woods Hole Oceanographic Institution, Woods Hole, Massachusetts. September 7–10, 1955*, Pergamon Press, New York, **1957**, pp, 161–166.

Weinstein, A. I., and Davis, L. G., "A Parameterized Numerical Model of Cumulus Convection," *Report* No. 11, Contract No. NSF GA-777, The Pennsylvania State University, University Park, May **1968**, 44 pp.

Wexler, R., "Radar Detection of a Frontal Storm 18 June 1946," *Journal of Meteorology*, Vol. 4, No. 1, Feb. **1947**, pp. 38–44.

Woodley, W. L., "Computations on Cloud Growth Related to the Seeding of Tropical Cumuli," *Bulletin of the American Meteorological Society*, Vol. 47, No. 5, May **1966**, pp. 384–392.

[Received October 31, 1968; revised January 6, 1969]

U.S. DEPARTMENT OF COMMERCE
Environmental Science Services Administration
Research Laboratories

ESSA Technical Memorandum ERLTM-APCL 8

INTENSIVE STUDY OF THREE SEEDED CLOUDS ON MAY 16, 1968

Joanne Simpson
William L. Woodley

Experimental Meteorology Branch
Coral Gables, Florida

Atmospheric Physics and Chemistry Laboratory
Boulder, Colorado
May 1969

TABLE OF CONTENTS

ABSTRACT

Three cumulus clouds were seeded over the south Florida peninsula on a day ideally suited for a cloud modification experiment. Following seeding, one of these clouds dissipated without growth, while the other two grew explosively. Of these two, the first exhibited rapid growth of the tower that was tallest at the seeding time, the second underwent "hesitation" growth of a later tower, with dissipation of the tower that was tallest at seeding time. This paper analyzes the history of each cloud with aircraft and ground radar observations and with a parameterized numerical model.

Cloud measurements were made by four aircraft. Observations from the ESSA DC-6 and B-57 are described here. These consisted of quantitative photography and of in-cloud records of temperature, humidity, and water content. Photogrammetry with the airborne cameras was performed to obtain the heights and sizes of the clouds as a function of time.

The numerical model predicts the rise rate, cloud and precipitation water contents, and radar echo intensity of a rising cloud tower. The calibrated ground radars were used in conjunction with the aircraft penetrations to test the model predictions. The model was found to predict all parameters effectively in the case of liquid clouds. Complete data for a similar test for frozen clouds are still lacking.

The model results showed that the first cloud that failed to grow had (due to narrow width) zero seedability or growth potential. The second cloud was shown able to grow with little tower expansion, while the third cloud required significant tower expansion to reach observed heights, thus explaining the "hesitation" growth.

INTENSIVE STUDY OF THREE SEEDED CLOUDS ON MAY 16, 1968

Joanne Simpson and William L. Woodley

1. INTRODUCTION

During the period May 15 to June 1, 1968, the Experimental Meteorology Branch (EMB) and Research Flight Facility (RFF) of ESSA and the Naval Research Laboratory (NRL) conducted a supercooled cloud seeding project in south Florida. A description of the seeding system, experimental procedures, and a summary of results to date are reported elsewhere (Simpson et al., 1969). The results of the May 1968 Florida program left little doubt that seeding was effective in inducing explosive cloud growth. These results are consistent with past experimentation on tropical cumuli conducted in the Caribbean (Malkus and Simpson, 1964; Simpson et al., 1967). The summary figures of the effect of silver iodide seeding on tropical cumuli are certainly of interest. However, it is the case study that provides the best insight into the response of clouds to airborne silver iodide seeding. This paper is such a study.

Three clouds were selected for experimentation on May 16, 1968, with the randomized seeding instructions dictating that all clouds be seeded. The first experimental cloud on May 16 collapsed completely following seeding, while the second and third experimental clouds grew explosively following seeding. These clouds received careful scrutiny based on aerial time-lapse photography, detailed cloud pass observations, iso-echo radar data, and EMB numerical model predictions. Radar and photographic documentation of general convective developments over south Florida on May 16, 1968, have already been provided by Woodley and Partagas (1969).

Photogrammetric documentation of seeded cloud behavior was provided by 16 and 35 mm aerial time-lapse photography. The

35 mm cameras were mounted on the left and right sides of the RFF DC-6, while the 16 mm cameras were mounted on the noses of the RFF DC-6 and B-57 aircraft. The photogrammetric calculations of cloud tower diameter and rise rate were made from the time-lapse photography based on a system described in a report by Herrera-Cantilo (1969).

Briefly, the values of aircraft pitch and roll provided by the APN-81 Doppler on the DC-6 were used, along with a scaled plot of the aircraft track and a series of grid overlays to read horizontal and vertical angles to prominent cloud features at various points along the flight track. The azimuths to important cloud features read from the pictures were then plotted on the scaled flight track. The common intersection (generally only approximate to within a mile or so) of the azimuthal lines provided range of the aircraft to a particular cloud feature. The range values plus the readings of vertical and horizontal angles permitted a calculation of cloud tower height and diameter.

The radar measurements were obtained from the ground-based UM/10 cm radar of the Radar Meteorological Laboratory of the University of Miami operated with the iso-echo system described by Senn and Andrews (1968). This system provided four contours of echo return corresponding to ~~-190~~ -109, -86, -76, and -64 dbm as verified by the calibration scheme of Senn and Courtright (1968).

The detailed cloud pass measurements included temperature, relative humidity, liquid water, and inferences of cloud draft structure. In addition, samples of cloud and precipitation size particles were obtained with a continuous cloud particle sampler (MacCready and Todd, 1964).

The final phase of this study is a comparison of cloud behavior with that predicted by the latest version of the EMB cumulus model (Simpson and Wiggert, 1969). Maximum cloud top heights and cloud rainfalls computed with the radar data are compared with model predictions.

2. RADAR AND PHOTOGRAPHIC OBSERVATIONS OF THE SEEDED CLOUDS

The behavior of experimental clouds 5, 6, and 8 on May 16 is documented in figures 1 through 4. The time of each photograph and the aircraft from which it was taken are indicated under each picture. Important cloud features are lettered for easy identification and to facilitate discussion. Aircraft position and heading at the time of each photograph are indicated on the contoured 10 cm radar depiction of the subject cloud. The time of the radar depiction appears below each panel. The radar beam was centered at the flight level of the DC-6 ($\sim$ 20,000 ft) in all radar depictions. True north is at the top of each panel.

2.1 Cloud 5

The first view of cloud 5 is found in the right foreground of picture 1 in figure 1, 2 min after the RFF DC-6 had flown just over the cloud at A. The towering cloud in the background was the first to reach cumulonimbus stature over south Florida on this day. Cloud 5 had a double structure on radar at 1750Z. This cloud reached its reflectivity maximum at this time.

The view of the cloud from the nose camera of the B-57 during the first seeding run is shown in picture 2 (fig. 1). The cloud had dissipated considerably both visually and on radar since the first DC-6 cloud pass. Cloud 5 collapsed completely 6 min after commencement of the first seeding run (picture 3, fig. 1). It was the only cloud during the May program that failed to respond to seeding. No detailed photogrammetric calculations were made on this cloud because it did not grow following seeding. Cloud 5 had a maximum top of 20,000 ft, which coincided with the time of the first DC-6 pass. No detailed cloud pass information was obtained by the RFF DC-6 because the cloud was below the aircraft flight altitude at all times.

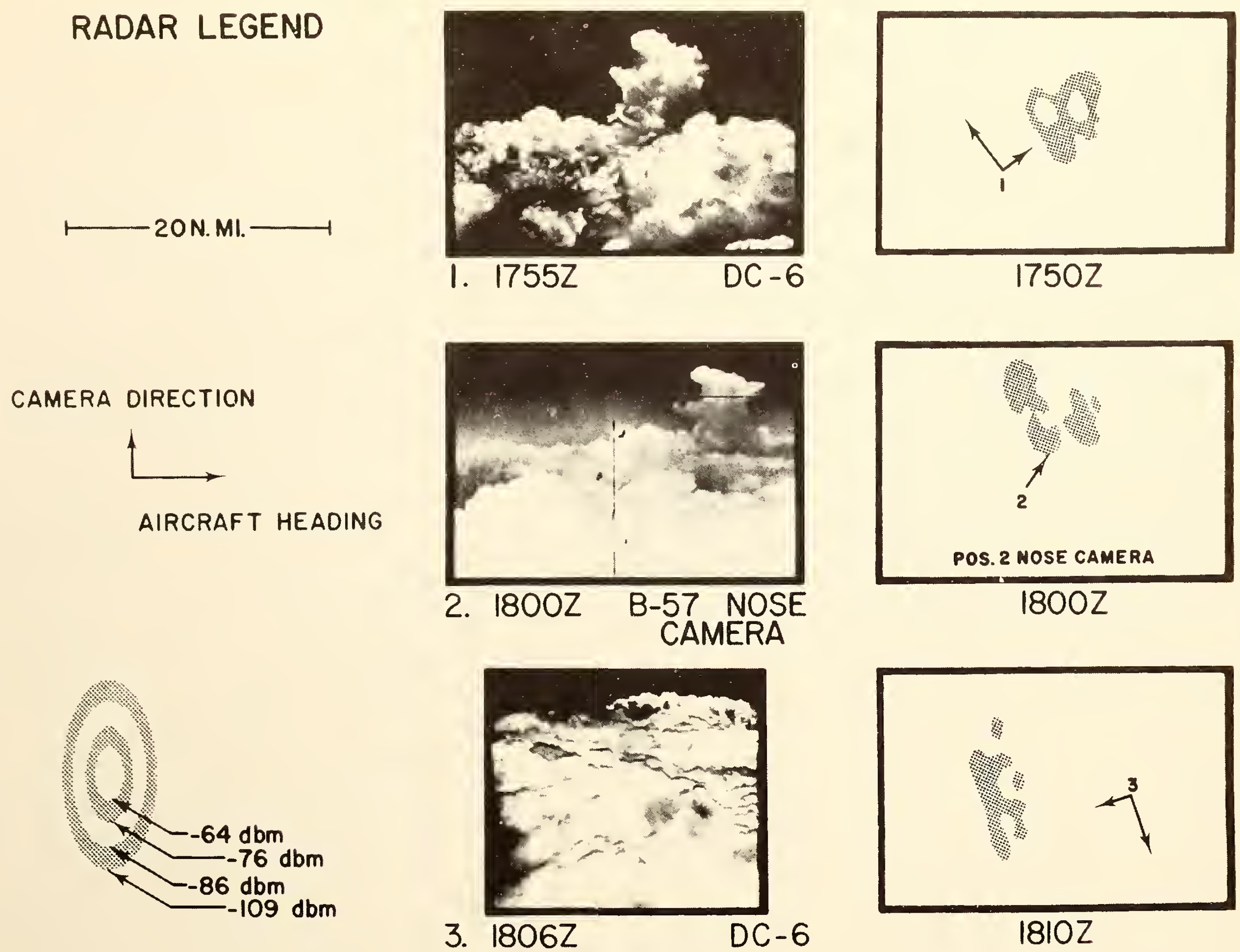

Figure 1. Selected photographs and 10 cm iso-echo radar observations of cloud 5, May 16, 1968. Aircraft position and heading at the time of each photograph are indicated on the contoured radar depiction.

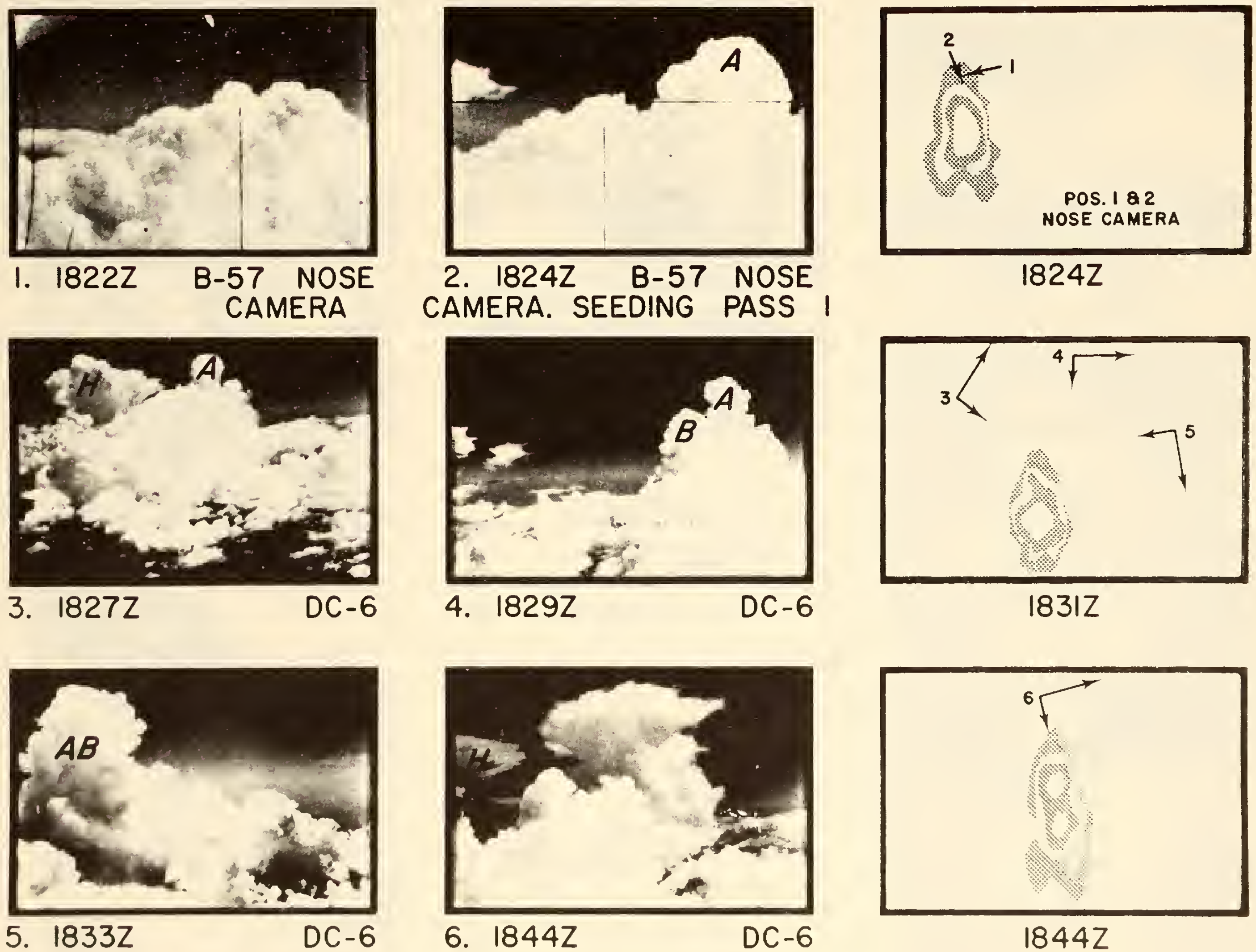

Figure 2. Selected photographs and 10 cm iso-echo radar observations of cloud 6, May 16, 1968. Aircraft position and heading at the time of each photograph are indicated on the contoured radar depiction.

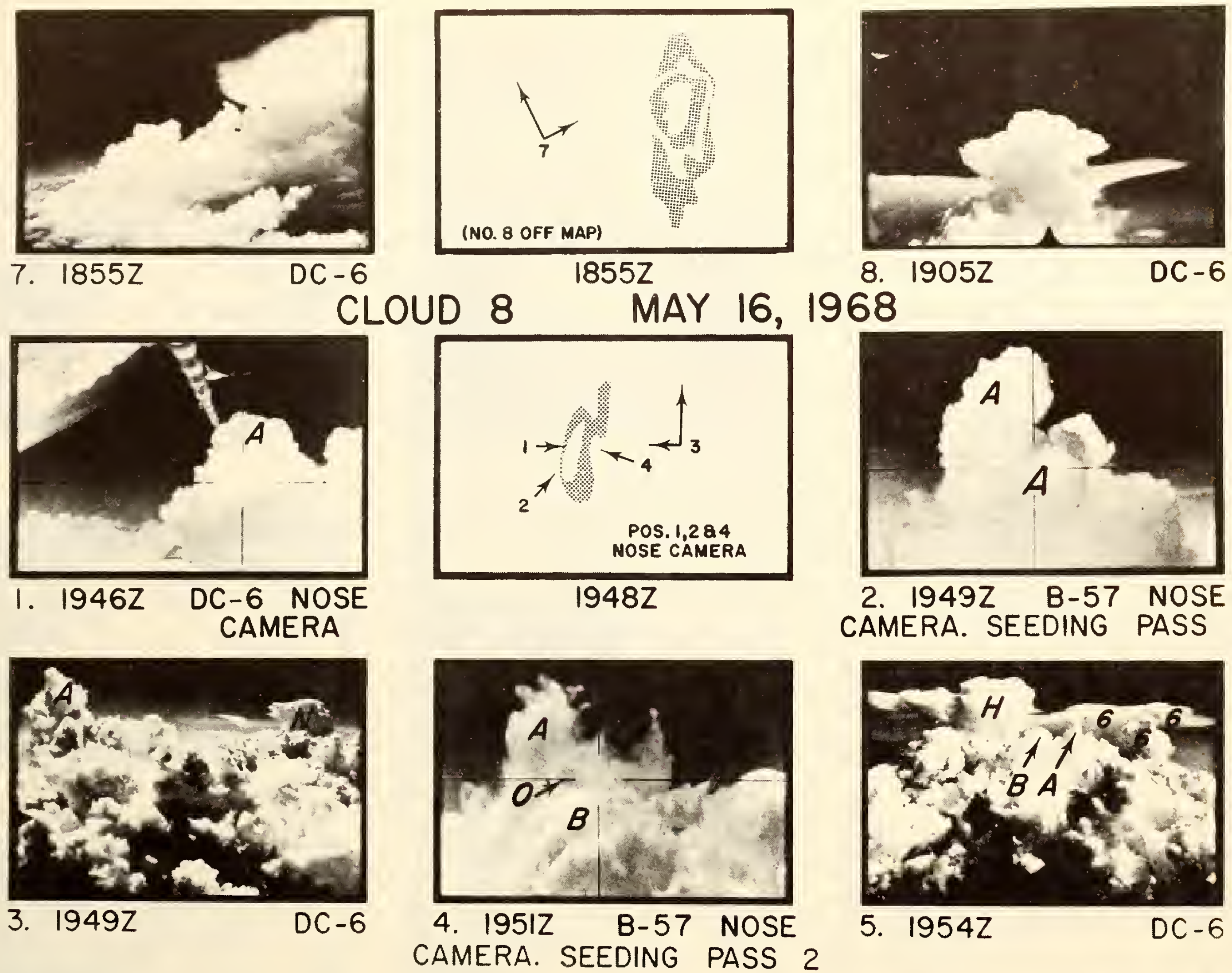

Figure 3. Selected photographs and 10 cm iso-echo radar observations of clouds 6 and 8, May 16, 1968. Top row pertains to cloud 6, second two rows to cloud 8. Aircraft position and heading at the time of each photograph are indicated on the contoured radar depiction.

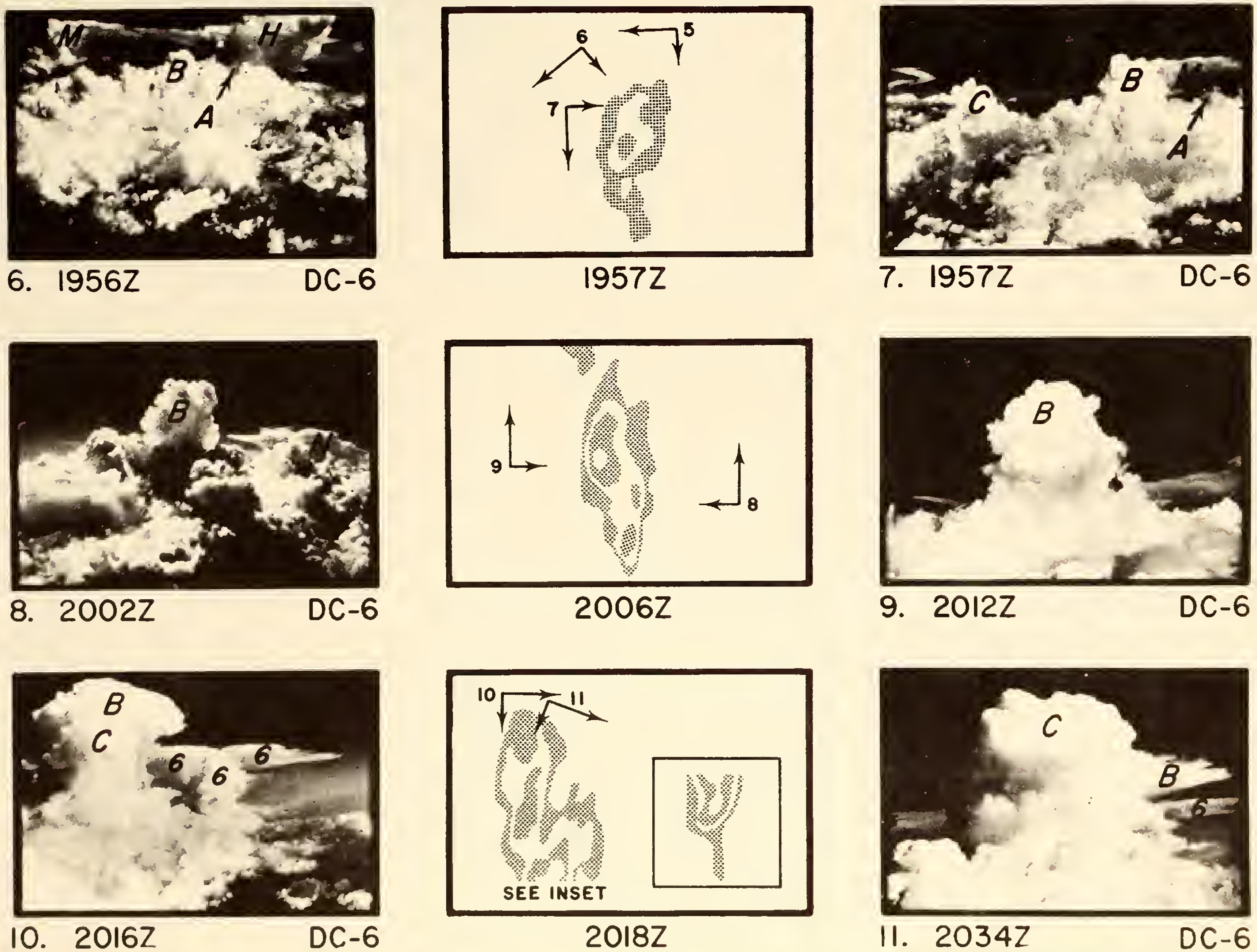

Figure 4. Selected photographs and 10 cm iso-echo radar observations of cloud 8, May 16, 1968. Aircraft position and heading at the time of each photograph is indicated on the contoured radar depiction.

2.2 Clouds 6 and 8

Photographic documentation of clouds 6 and 8 (figs. 2 through 4) is similar to that presented for cloud 5. Because these clouds reacted so spectacularly to seeding, scale outlines (fig. 5) and photogrammetric calculations were made for those clouds. Cloud top heights and tower radii calculated for clouds 6 and 8 appear in figures 6 and 7. The numbers appearing along the curves correspond to the numbers of the photographs in figures 2 through 4. Cloud top height and tower radius at the time of any picture is easily read from these curves. Prominent cloud towers are lettered, while the subscripts refer to short-lived turrets or bubbles on the towers. In figure 6, we see that the aircraft-measured maximum top of tower AB is nearly 6000 ft higher than the highest top seen photogrammetrically. This recurring discrepancy has been explained by Woodley (1969), and the explanation is illustrated in figure 8. The aircraft was flying at a distance of only 9 mi from cloud 6. Simple trigonometry shows that a tower 3 mi farther (the distance of the strongest echo) and 7000 ft higher than that measured would not have been visible on the photograph. Rather small distances from aircraft to cloud were necessary in order to obtain penetrations every 10 to 15 min.

Cloud 6 was photographed at 1822Z by the nose camera of the B-57 seeder aircraft while in formation to the right of the RFF DC-6 (picture 1, fig. 1). At this time, cloud 6 had several towers, none with special prominence. The B-57 then made a 90° right turn and a 180° left turn to position itself for the first seeding run, while the DC-6 continued on the same heading for its first penetration of cloud 6.

The photograph from the B-57 at 1824Z (picture 2, fig. 2) shows cloud 6 seconds before 10 silver iodide flares were ejected into tower A, which was the most prominent cloud feature. The photogrammetric calculations for this cloud (fig. 6) revealed

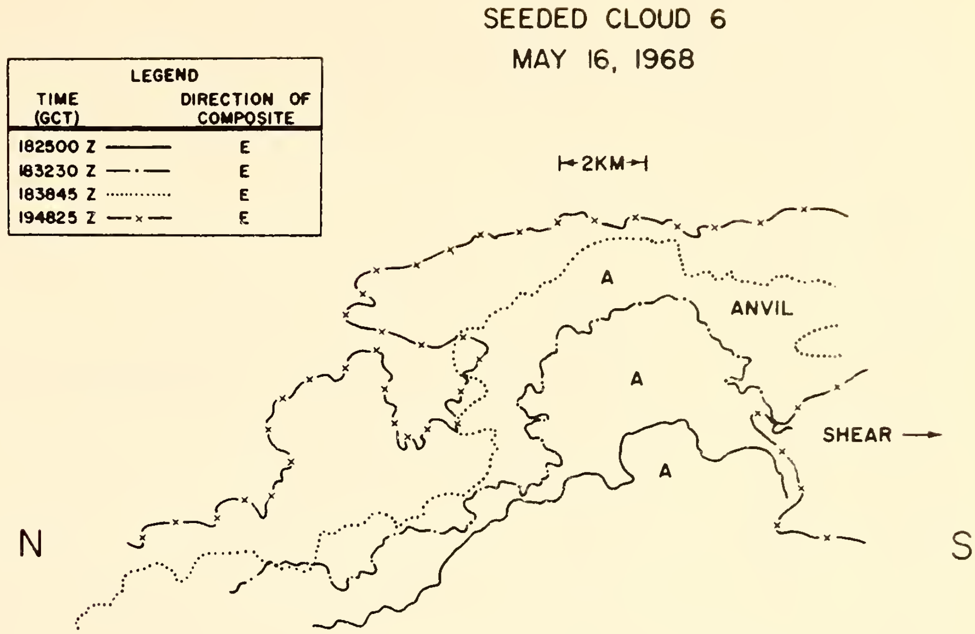

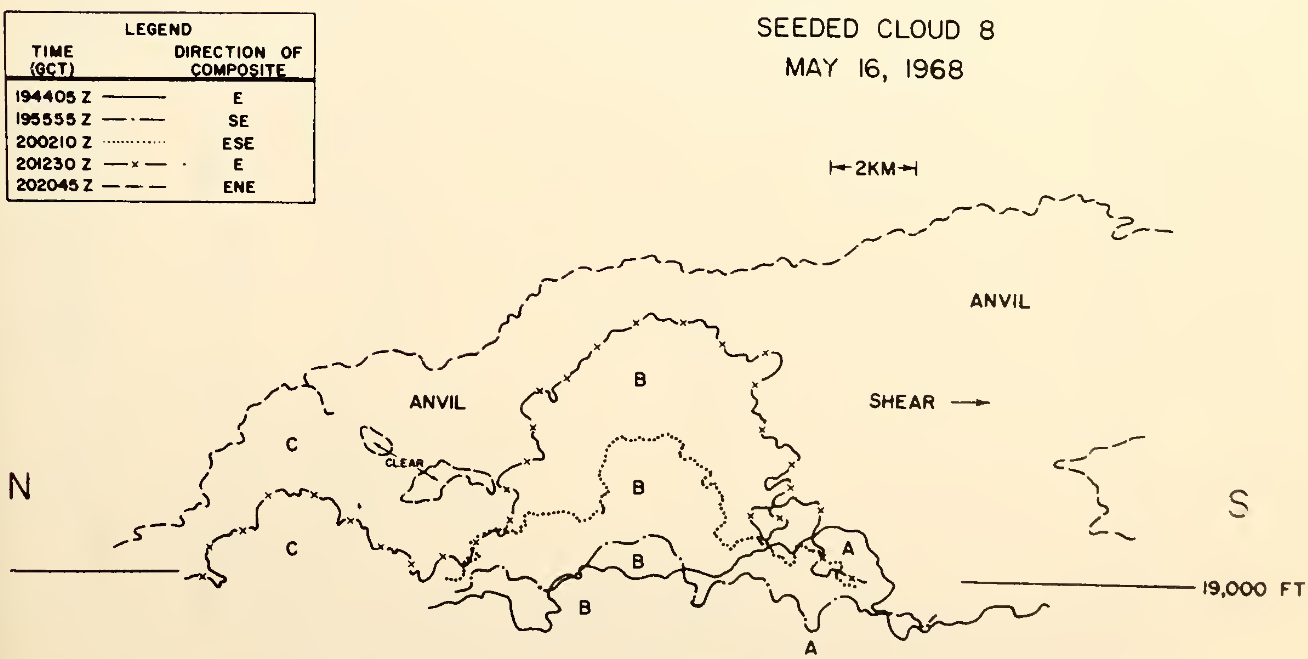

Figure 5. Scale outlines of clouds 6 and 8 at selected times.

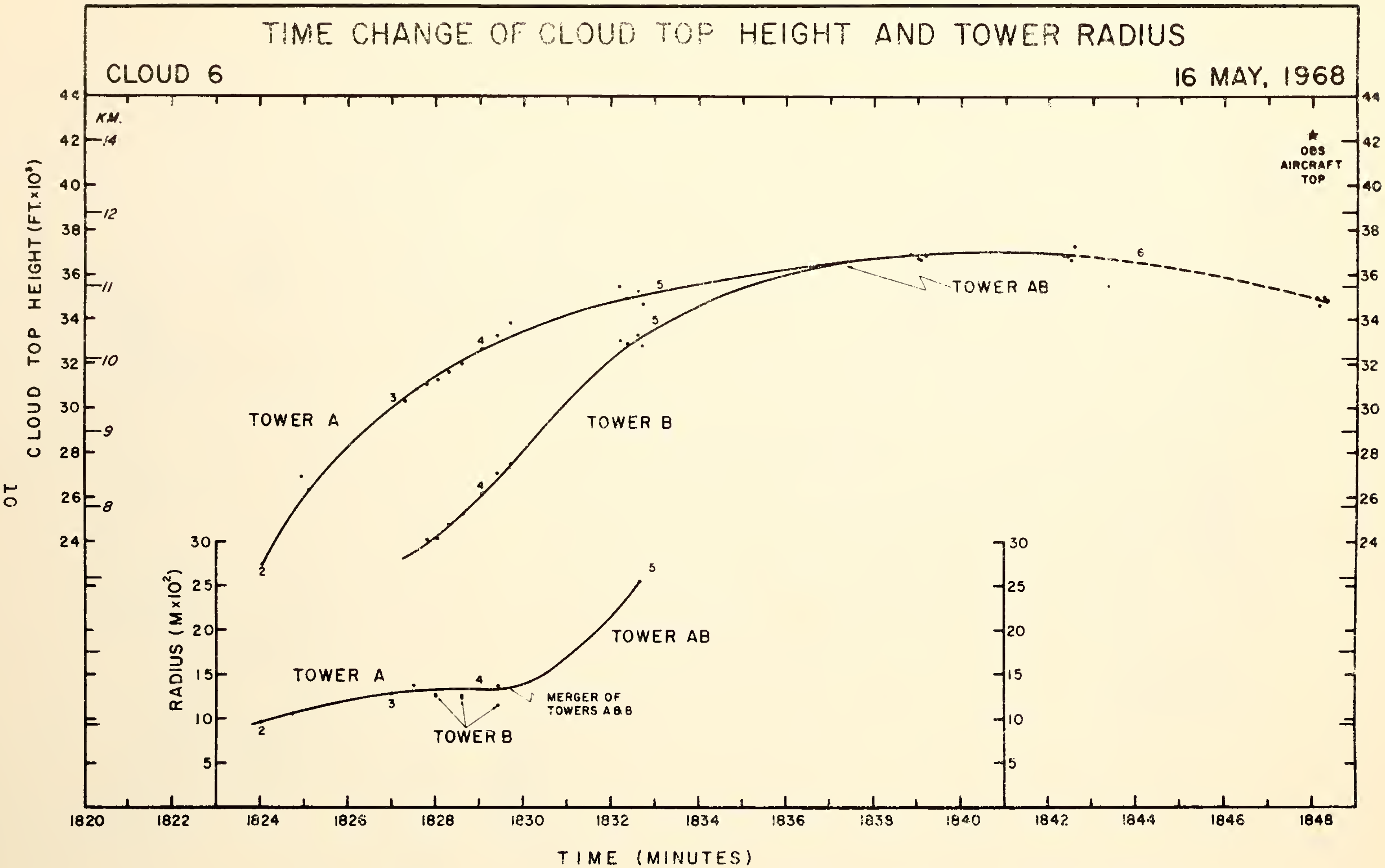

Figure 6. Photogrammetric calculations of the top heights and tower radii of cloud 6, May 16, 1968. The numbers along the curves correspond to the numbers of the photographs in figs. 2 and 3.

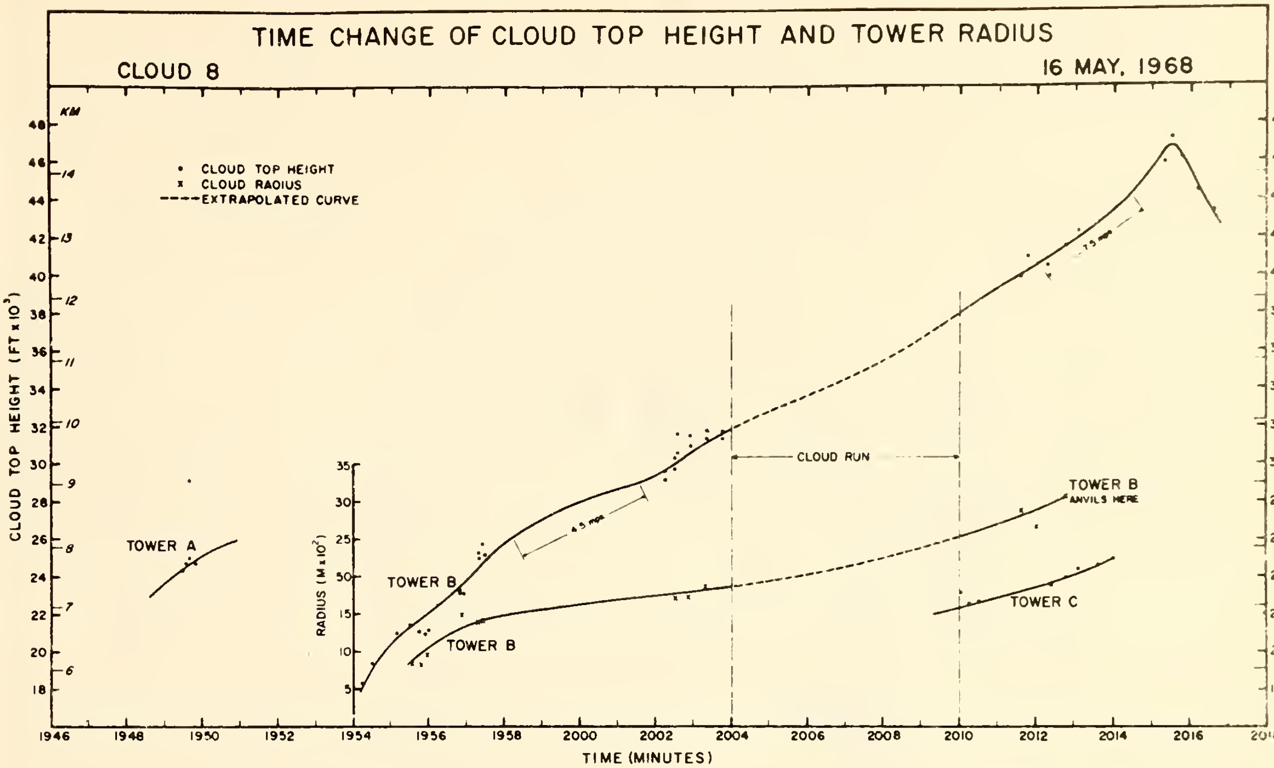

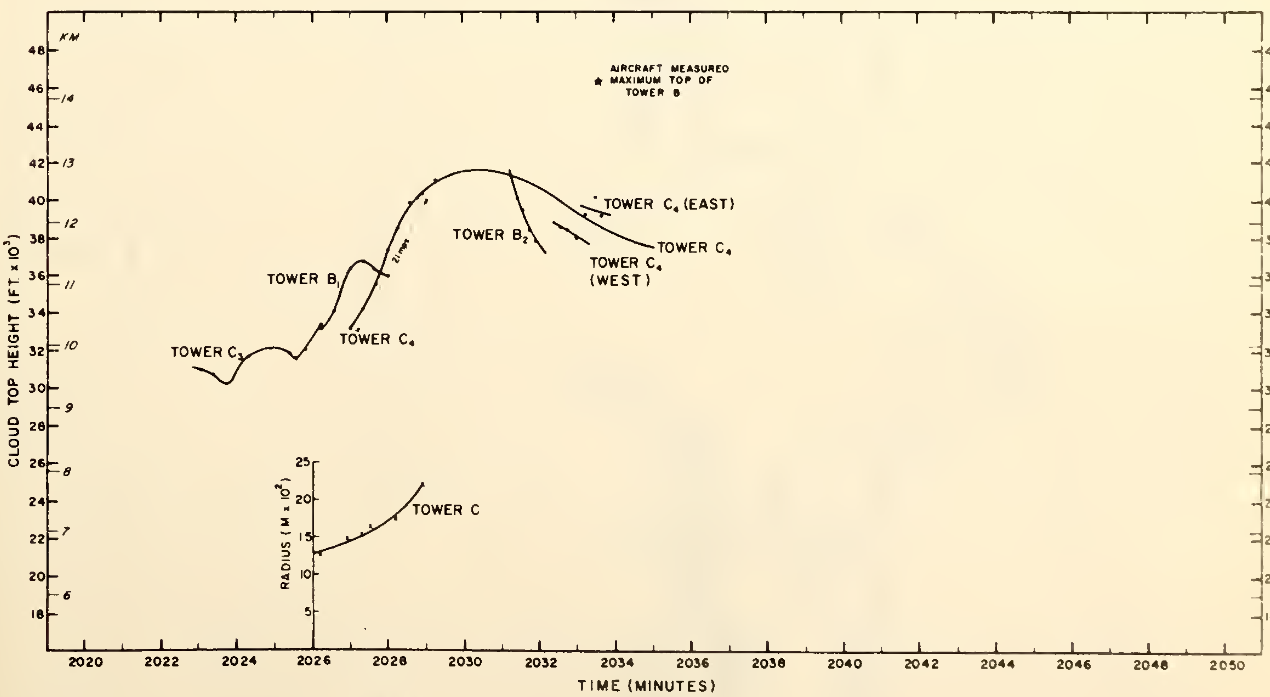

Figure 7. Photogrammetric calculations of the top heights and tower radii of cloud 8, May 16, 1968. The numbers along the curves correspond to the numbers of the photographs in figs. 3 and 4.

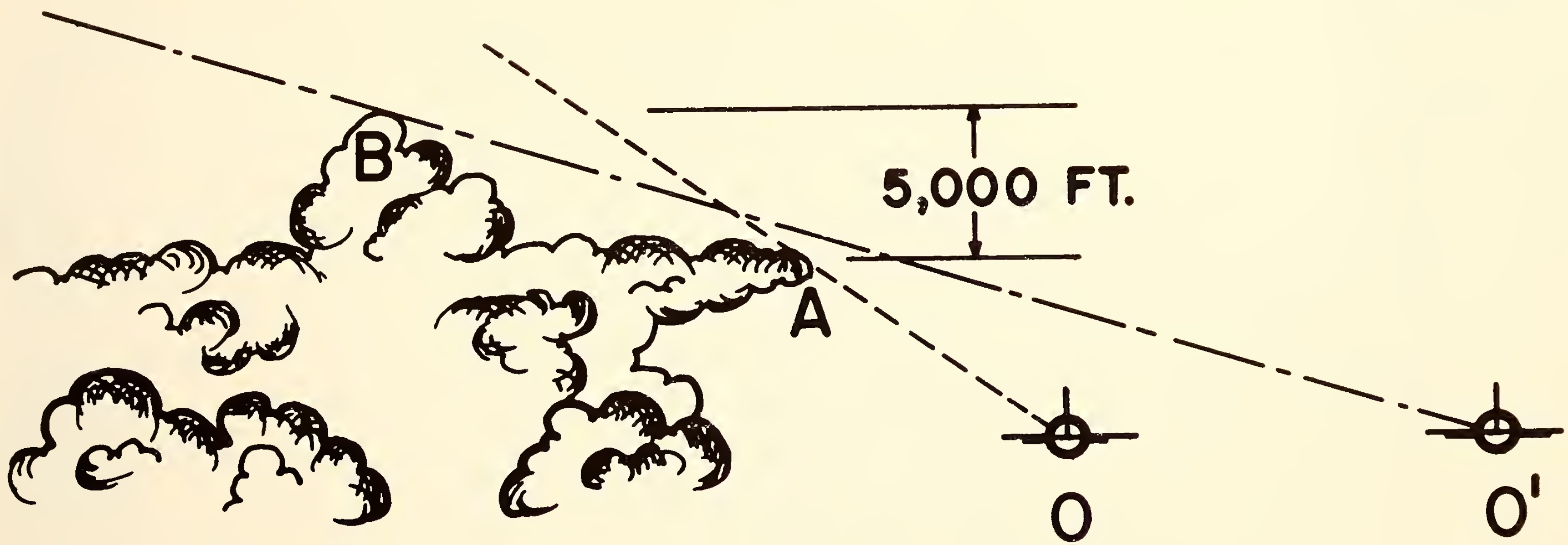

A: Fictitious maximum top height seen from position O.

B: True maximum top height seen from position O'.

Figure 8. Photographic detection of cloud top as a function range.

that tower A had a top height of 22,500 ft and a radius of 1000 m at the time of the first seeding run. Cloud 6 was contouring strongly on the 20,000 ft scan of the radar, indicating that it contained substantial amounts of water. (This is discussed in more detail in sec. 3.)

The views of cloud 6 from the DC-6 while the B-57 was making its second seeding run appear in pictures 3 and 4 (fig. 2). Tower A continued to grow, while secondary tower B paced it on its northeast flank. The natural cumulonimbus marked H, in the background of picture 3, was named the "Homestead cloud" by Woodley and Partagas (1969) in their discussion of convective developments over south Florida on this day. The Homestead cloud was the first cumulonimbus, natural or artificial, over the southern portion of the Florida peninsula on May 16, 1968.

Towers A and B of cloud 6 merged by 1833Z (picture 5, fig. 2), attaining cumulonimbus stature (picture 6, fig. 2) shortly after this time. The 20,000 ft 10 cm radar echo had developed two cores by 1844Z. The main seeded portion (tower AB) of cloud 6 reached maturity by 1855Z, with new growth on the upshear flank to the north (picture 7, fig. 3). The new growth was especially impressive at 1905Z (picture 8, fig. 3). This pattern of growth continued throughout much of the afternoon until dissipation and disappearance from radar at approximately 2100Z, 2½ hours after seeding.

Cloud 8 behaved differently from cloud 6 following seeding, although the final result was the same. Tower A of cloud 8 appears in picture 1 and again in picture 2 (fig. 3) 3 min later during the first B-57 seeding run. Photogrammetric calculations indicate that the top of tower A was at 25,000 ft at this time. Another view of cloud 8 during the first seeding run was obtained from the DC-6 (picture 3, fig. 3).

The radar information for cloud 8 is not as reliable as that for cloud 6. Unfortunately, cloud 8 was on the precise azimuth of the partially blind cone (267° to 273°) of the 10 cm radar of the Radar Meteorological Laboratory. This cone is caused by the University of Miami Library and the large WSR-57 radome mounted to the top of this building. This problem is worse when the 10 cm antenna is at a small elevation angle. For this reason, the contoured radar observations for cloud 8 may be used for intracomparison, but they should not be used to contrast with those of cloud 6.

Tower A of cloud 8 had dissipated at the beginning of the second seeding run (picture 4, fig. 3); in fact, there was a hole in this tower at 0, which was probably made by the seeder aircraft during the first seeding run. Towers A and B of cloud 8 received silver iodide flares during the second seeding run to the west. The sequence of pictures from 1954 to 1957Z shows both towers. Tower A continued to dissipate, while tower B began to grow. Cloud 6 and the Homestead cloud can be seen arrayed behind cloud 8 in picture 5.

Tower B became the dominate feature of cloud 8 by 2002Z (picture 8, fig. 4), attaining a top height of 37,000 ft at 2012Z (picture 9, fig. 4) and 43,000 ft at 2016Z (picture 10, fig. 4). The contoured echo of cloud 8 expanded and intensified with the growth of tower B.

When tower B of cloud 8 reached maturity, new growth (tower C) began on the northwest flank,as was the case with cloud 6. Tower C, upshear of tower B, grew markedly between 2016 and 2034Z (fig. 7), almost obscuring tower B from view at 2034Z when looking south-southwest from a position north of cloud 8 (picture 10, fig. 4). While not seeded directly with silver iodide, tower C showed the greatest rise rate (21 m/sec) yet measured in the program.

Cloud 8 became a large cumulonimbus complex and continued on radar past 2200Z, eventually merging with the Homestead cumulonimbus.

3. DETAILED CLOUD PASS OBSERVATIONS

Measurements of internal structures of seeded clouds 6 and 8 (figs. 9 to 17) provide further insight into the response of these clouds to seeding. The internal measurements include: pressure altitude, relative humidity measured by an infrared hygrometer, temperature obtained by a vortex thermometer, and liquid water as measured by the Johnson-Williams (solid curve) and Levine instrumentation (dashed curve). Inferences of cloud draft structure were made from the output of an integrating accelerometer. The technique suggested by Byers (1968) for inferring cloud draft structure was not compatible with the flight data obtained by the DC-6. The wind observations were made by the RFF Doppler navigation system.

The first DC-6 pass through cloud 6 at 19,000 ft pressure altitude revealed that the tower had an average total liquid water content (dashed curve) of 2.2 g m^{-3} and a virtual temperature lower than that of the environment (fig. 9). Two minutes later the B-57 seeded this tower.

The internal structure of cloud 6, 10 min after seeding changed considerably (fig. 10). The temperature and humidity profiles had a double structure that is representative of towers A and B discussed earlier. Cloud virtual temperature exceeded that of the environment by 0.5°C, with a temperature deficit (wet bulb effect) between the two towers. Very little liquid water was measured during this penetration.

The final DC-6 pass through cloud 6 detected negligible amounts of liquid water, a cloud virtual temperature excess of 0.7°C, and relative humidity values less than 100 percent (fig. 11). (The pass observations are discussed in more detail in sec. 4.)

The cloud pass observations obtained in cloud 8 are of considerable interest. Both passes 1 and 2 (figs. 12 and 13) were preseeding passes, with pass 2 through tower A. The cloud

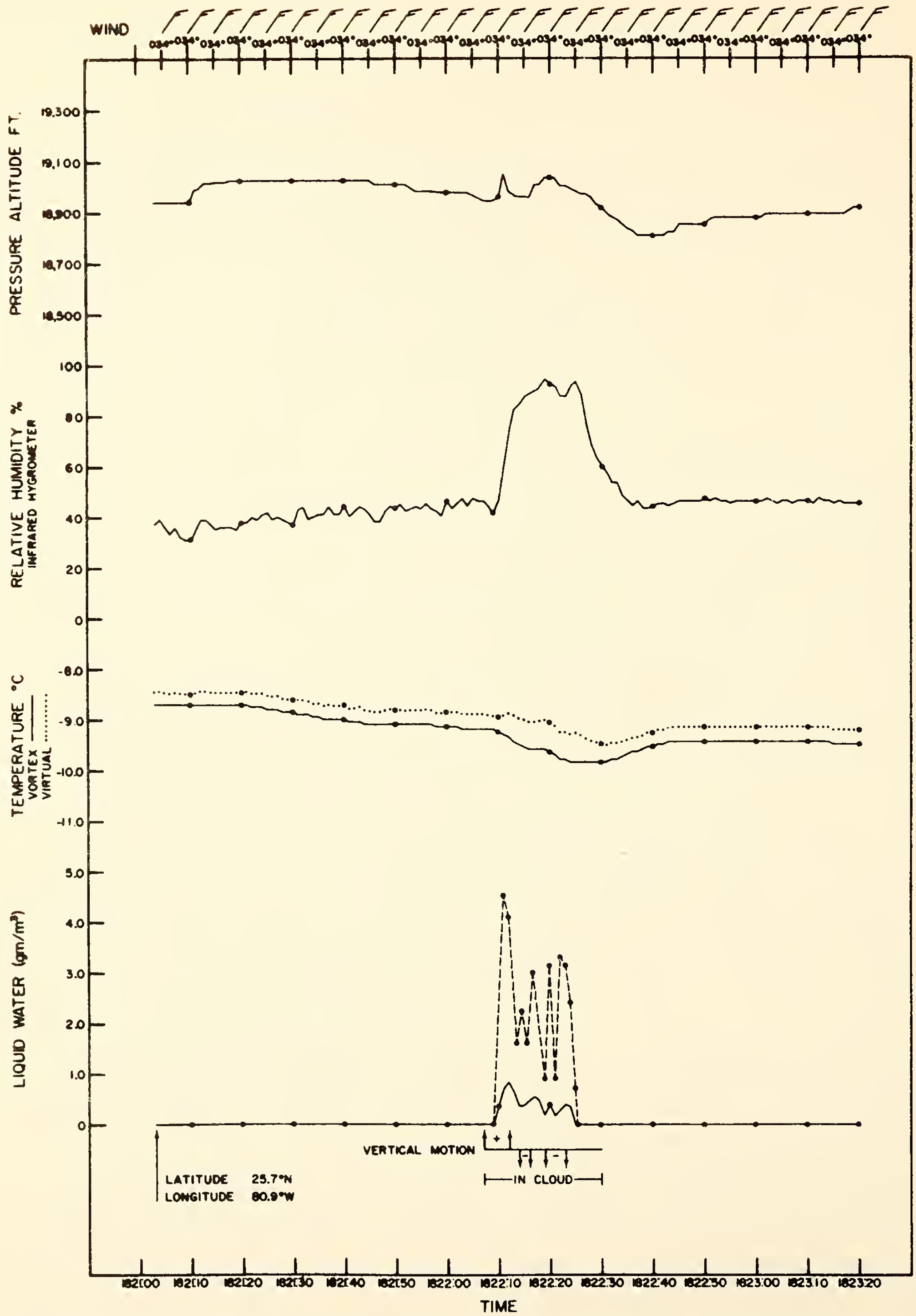

Figure 9. Internal measurements at 19,000 ft (pressure altitude) in cloud 6, pass 1, on May 16, 1968, made by instrumentation in the RFF DC-6. The temperature and humidity measurements were made with an infrared hygrometer and a vortex thermometer, respectively. Total liquid water (dashed curve) was measured with Levine instrumentation, while cloud water (in drops with diameter $\leq$ 40μ) was measured with a Johnson-Williams hot wire instrument. Cloud drafts were inferred from the output of an integrating accelerometer. The wind observations were made with the Doppler navigation system. The true aircraft heading on this pass was 250°.

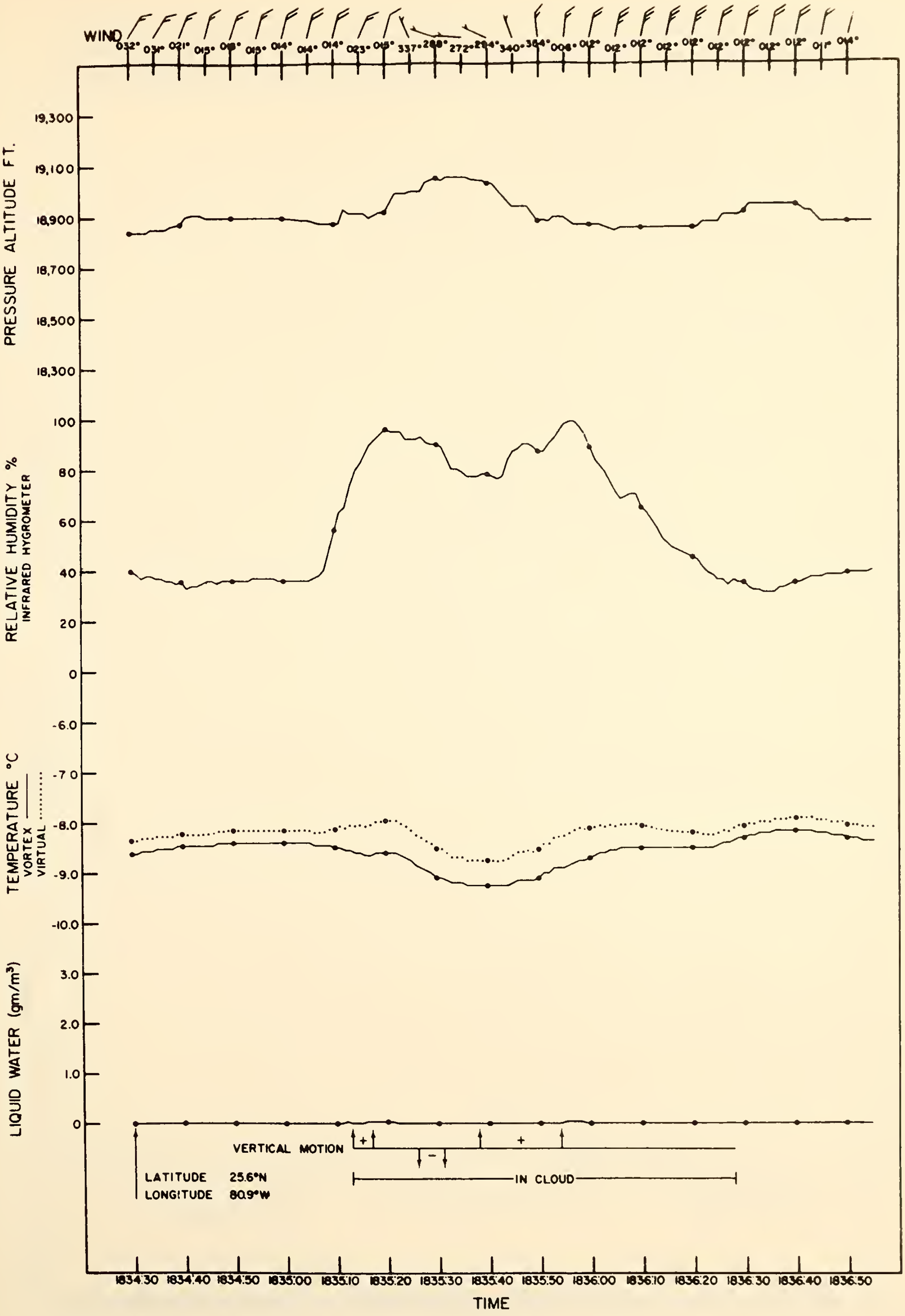

Figure 10. Cloud 6, pass 2, May 16, 1968. True heading 260°. Records same as fig. 9.

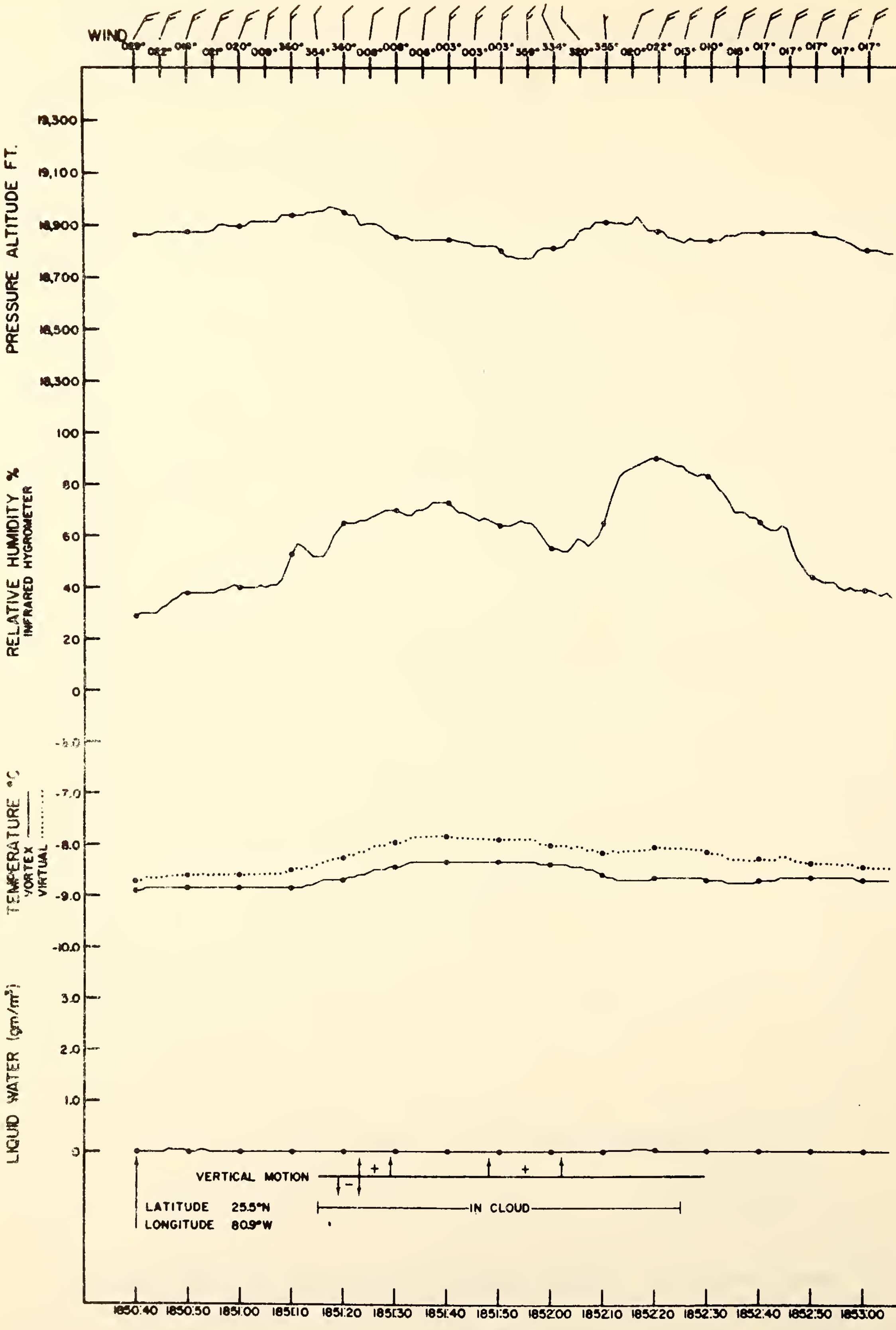

Figure 11. Cloud 6, pass 3, May 16, 1968. True heading 251°. Records same as fig. 9.

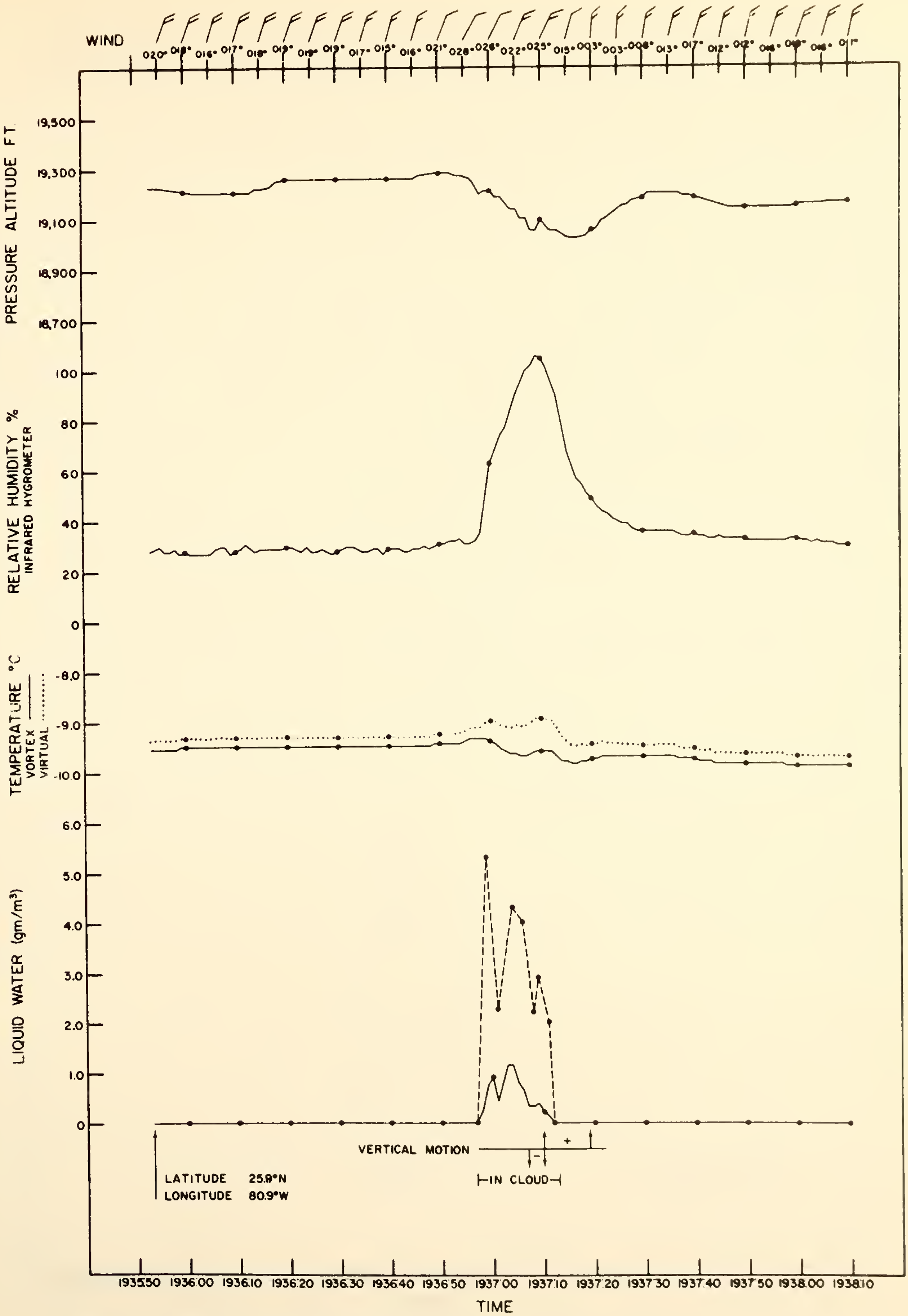

Figure 12. Cloud 8, pass 1, May 16, 1968. True heading 272°. Records same as fig. 9.

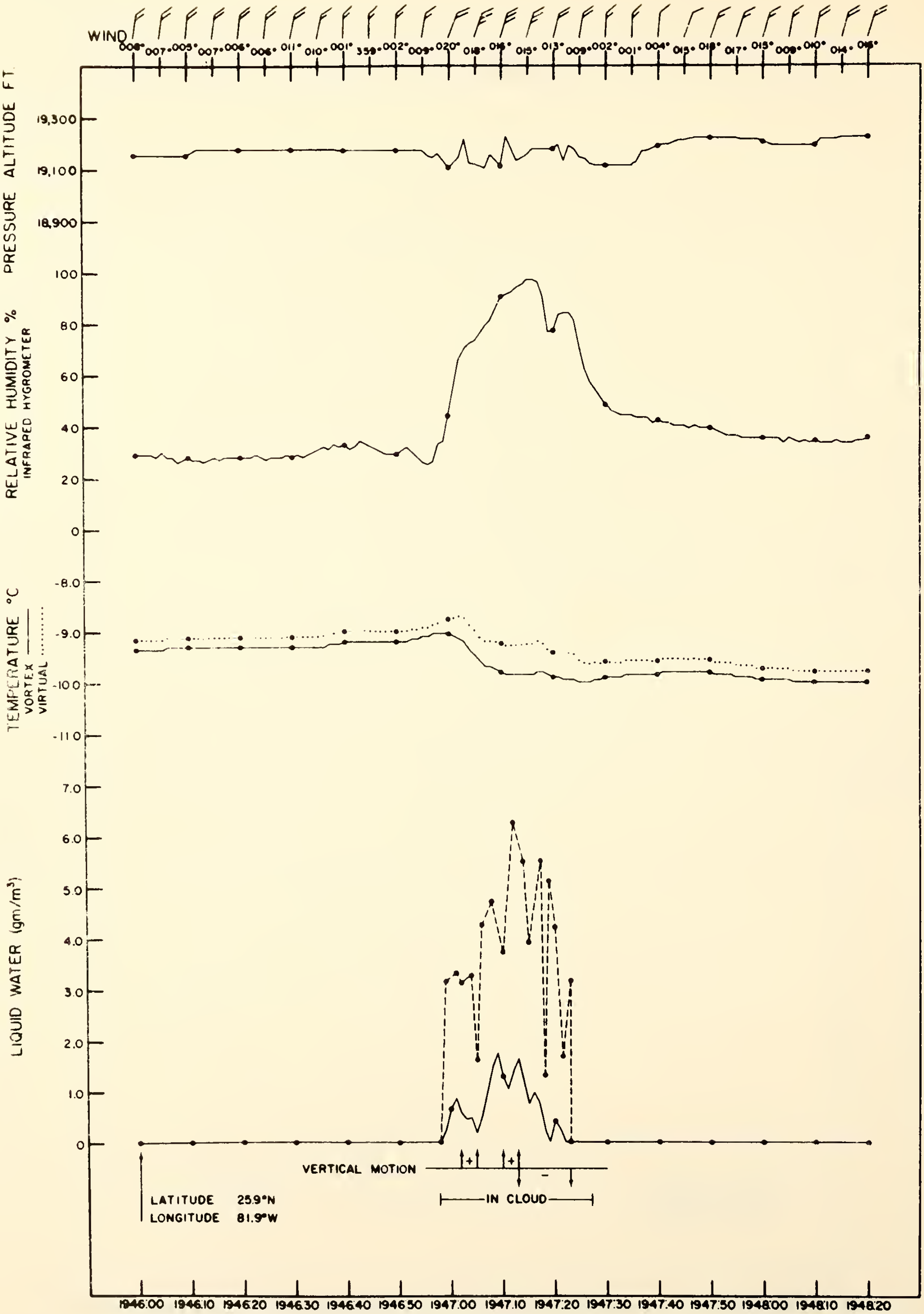

Figure 13. Cloud 8, pass 2, May 16, 1968. True heading 087°. Records same as fig. 9.

virtual temperature excesses ($T_{vc} - T_{ve}$) were small in both passes (0.3°C), but the average water contents were 3 and 3.5 g m^{-3} in passes 1 and 2 respectively. Pass 2 through cloud 8 is further evidence that the 10 cm radar underestimated the water in cloud 8 because of the obstructions on the University of Miami campus. Cloud 8 had more average liquid water than cloud 6 during the preseeding pass, yet the radar return is considerably greater for cloud 6 (fig. 2, panel 3 vs. fig. 3, panel 5). (For further detail, see sec. 4.)

Pass 3, the first postseeding pass through tower A of cloud 8, corroborates the dissipation evident in the photographs (fig. 14). There was still a temperature excess of 0.3°C, with a wet bulb cooling upon exit from the cloud, but the average liquid water had decreased to 1 g m^{-3}.

The first pass (pass 4) through the growing seeded tower (tower B) of cloud 8 indicated that it was a very vigorous tower (fig. 15). The cloud virtual temperature excess was 2.3°C, with a strong wet bulb cooling upon exit from the cloud. Total liquid water values were not available for this pass, but the Johnson-Williams readings which are indicative of cloud drops (diameter <40 μ) exceeded 2 g m^{-3} at two points in the cloud. The relative humidity values exceeding 100 percent are not errors, but are the result of evaporation of precipitation water.

Pass 5 (fig. 16) through cloud 8 includes observations obtained in towers C and B (see picture 10, fig. 4). The first group of water values are those of tower C, with average total water of 3 g m^{-3} and a peak value of 5.8 g m^{-3}. The water values beginning at about 2019:15Z are those of tower B. The average total water in this tower was 2.5 g m^{-3}. The virtual temperature rise commencing in the active portion of tower B and extending downwind reached a peak exceeding 6°C. The first impulse was to ascribe this warming to fusion heat release

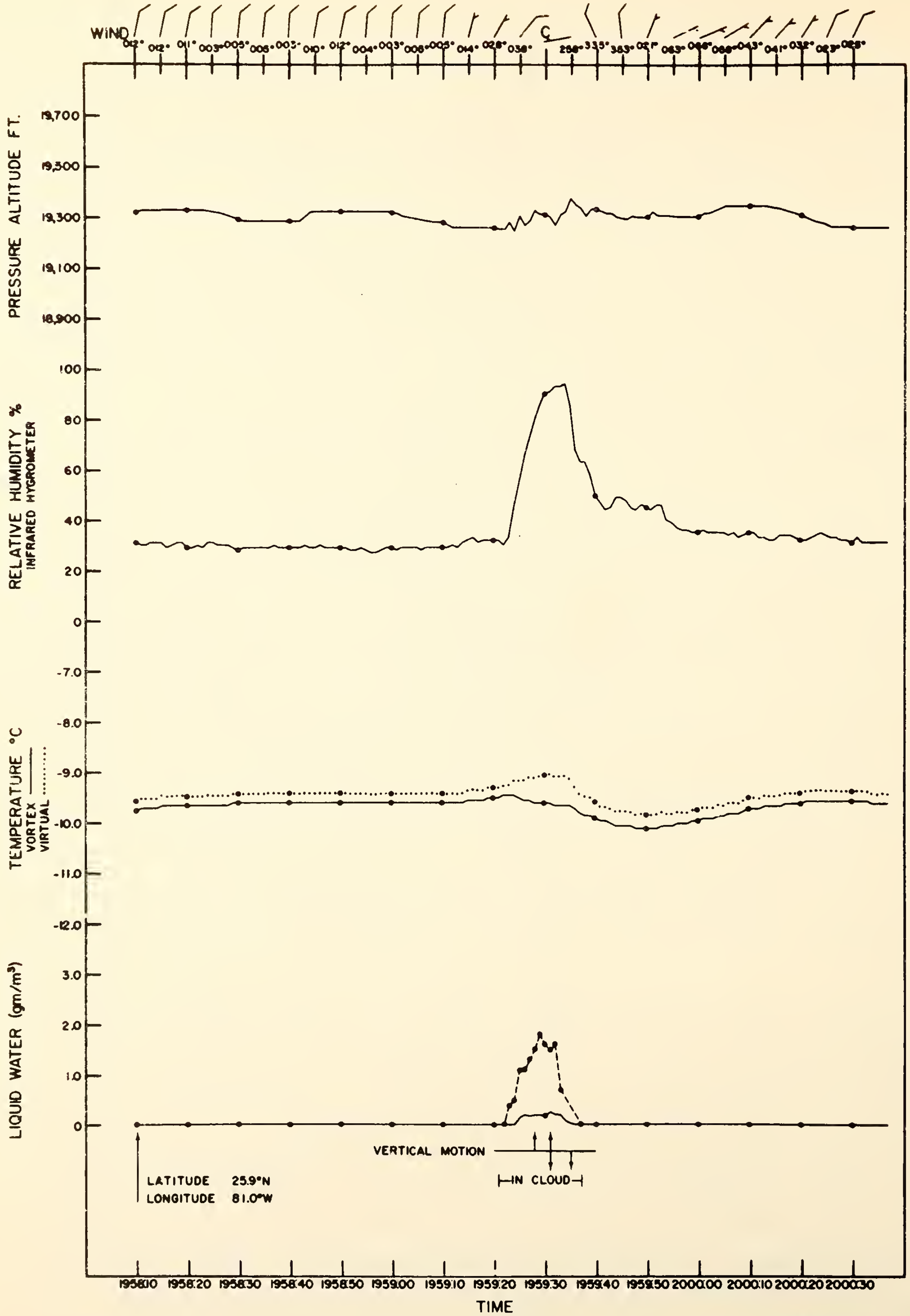

Figure 14. Cloud 8, pass 3, May 16, 1968. True heading 101°
Records same as fig. 9.

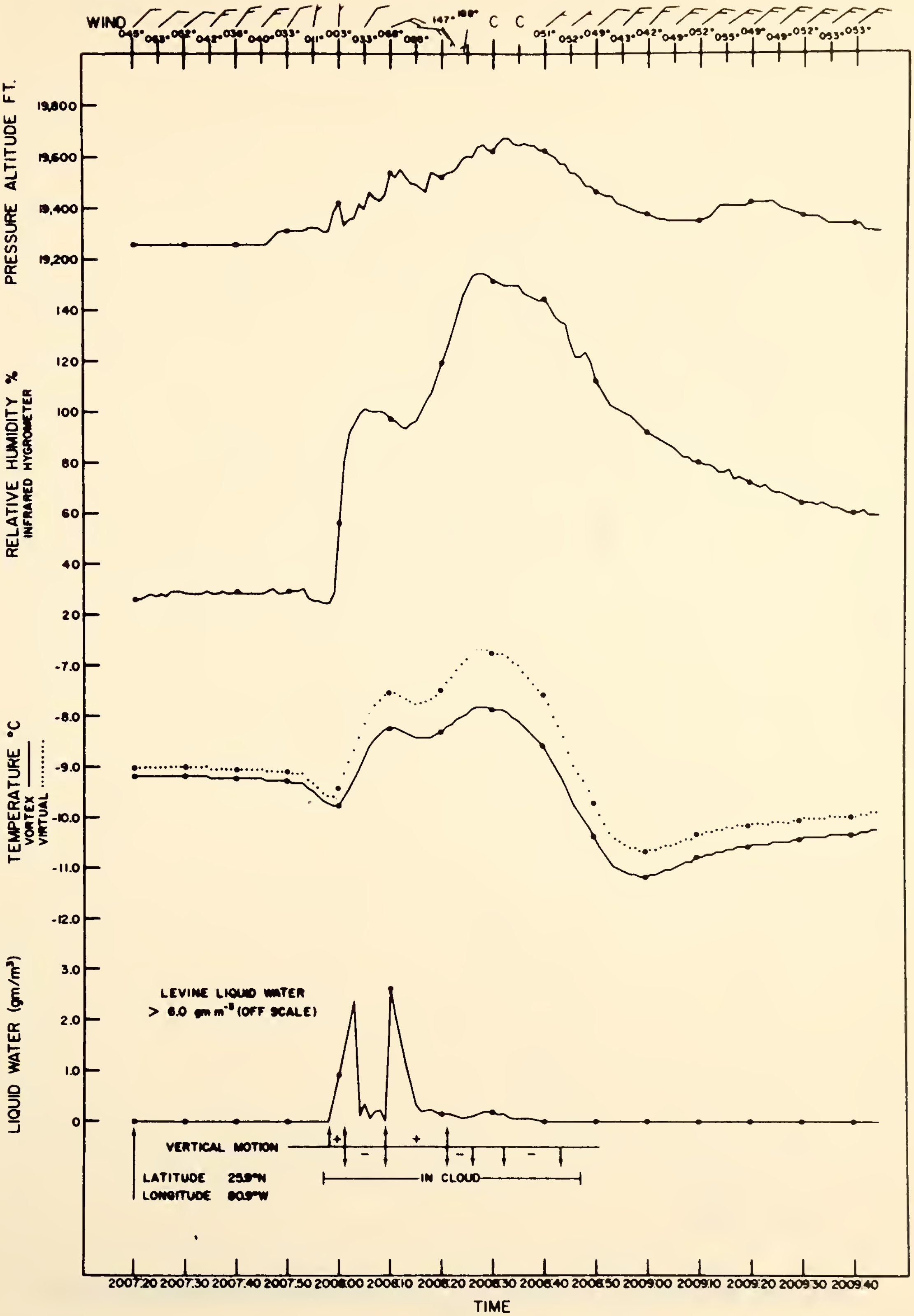

Figure 15. Cloud 8, pass 4, May 16, 1968. True heading 222°.
Records same as fig. 9.

Figure 16. Cloud 8, pass 5, May 16, 1968. True heading 177°
Records same as fig. 9.

provided by icing of the temperature probe. However, this rise was substantiated by a Rosemount probe and a thermocouple vortex thermometer at other locations on the aircraft and by the temperature observations made during pass 6.

Pass 6 (fig. 17) was made at approximately the same altitude as the previous passes, yet the temperatures in the cloud and the environment averaged 3°C warmer than before. It is very unlikely that any ice obtained during pass 5 could have persisted until pass 6, especially in an environment with an average relative humidity of 30 percent. An examination of the Miami soundings showed that the temperatures at the flight altitude of the DC-6 were -9.5°C at 1800Z and -10.5°C at 0000Z on May 17, 1968. One is led to the tentative conclusion that this large cumulonimbus complex had warmed its immediate environment. The average total liquid water measured in tower C exceeded 6 g m^{-3}, while the average total liquid water averaged approximately 1.7 g m^{-3} in the first half of tower B. It is not known why only 65 percent relative humidity was measured in tower C in spite of the high liquid water content.

4. NUMERICAL MODEL STUDIES OF THE MAY 16, 1968, CLOUDS

The EMB numerical cumulus model was used in two distinct ways in the 1968 experiment. The first way was the real time usage to predict seedability in advance of each day's operation. For this purpose the 0800 LDT (1200Z) Miami radiosonde was run with the model, with the use of a hierarchy of cloud radii. The results for May 16, 1968, have been discussed by Woodley and Partagas (1969). Good seedability, or vertical growth due to seeding, was predicted for initial radii in the range of 750 to 1250 m. Clouds with radii smaller than 750 m were predicted not to grow when seeded, while those with radii much above 1250 m were predicted to grow naturally almost as well as seeded clouds, provided the available fusion heat were released linearly between the -15°C and -40°C level.

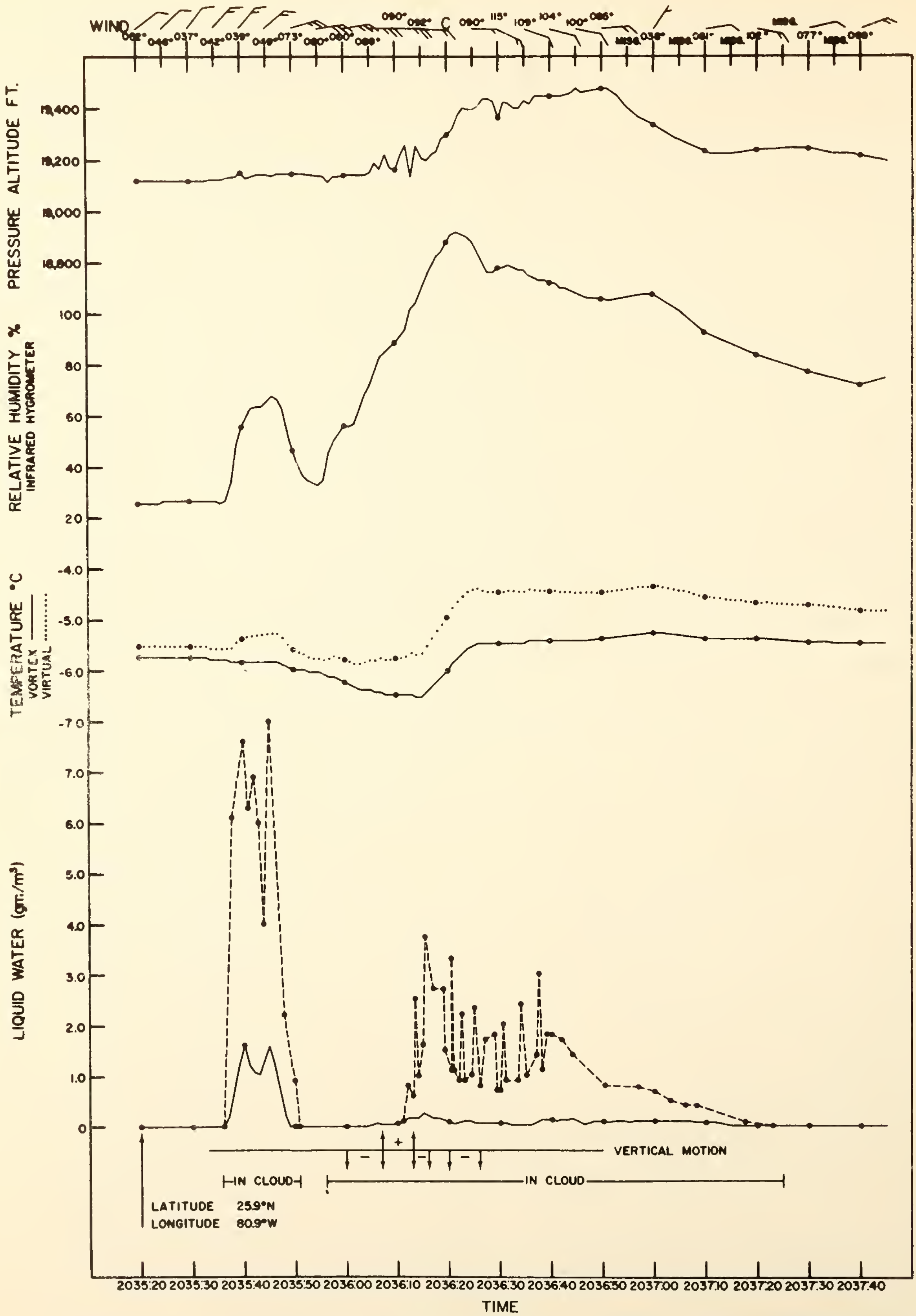

Figure 17. Cloud 8, pass 6, May 16, 1968. True heading 185°. Records same as fig. 9.

The second and most intensive use of the model lay in the data analysis, with the actually measured cloud radii and the sounding nearest the clouds in space and time constituting the input information for the model. It is this use of the model that will be described here.

In the postanalysis, a slightly improved version of the model was used. The real time version of the model was called EMB $68A_K$. In this model, Kessler's (1965) autoconversion equation was used, 100 percent of the liquid water present in the cloud at $-4^{\circ}C$ was frozen, the collection efficiency of ice for ice was 0.1, and the ice terminal velocity was 20 percent of that for droplets of equivalent mass.

The postanalysis version of the model is called EMB $68K_B$. In this version, Berry's (1968) autoconversion equation is used, 80 percent of the liquid water present in the cloud at $-4^{\circ}C$ is frozen, the collection efficiency of ice for ice is 100 percent, and the ice terminal velocity is the same as in EMB 68 A_K. A hierarchy of EMB models with precipitation growth and different seeding subroutines have been discussed by Simpson and Wiggert (1969). Each model is used to predict heights of the seeded and control clouds of the Stormfury 1965 cumulus program, and the results are compared with each other and with the field observations. Model K gave very slightly better height predictions than model A and hence is used here. Berry's autoconversion formula generally gave slightly better results than Kessler's and permits introduction of the droplet number and relative spectral dispersion at cloud base. In the calculations to be discussed here we took a cloud base particle concentration of 500 per cm^3, which was a good average of the measured nuclei counts in the operational area. The relative spectral dispersion was assumed to be 0.146, an average figure for continental clouds.

Clouds 5, 6 and 8 were seeded on May 16. Woodley and Partagas (1969) give the locations of these clouds. All were over land about 40 n mi from Coral Gables, in directions ranging from due west to west-southwest. Cloud 5 was seeded at 1800Z, cloud 6 at 1824Z, and cloud 8 at 1849Z. Since no dropsondes were available on May 16, the 1800Z Miami radiosonde is the closest sounding in space and time. This sounding, in comparison with the morning sounding (1200Z), is shown in figure 18. Aircraft also measured temperatures and humidities in the immediate vicinity of the experimental clouds, and some of their measurements are indicated on the tephigram. With the exception of a more moist layer between 800 to 900 mb, the aircraft values are close to, and mostly lie between, the two radiosondes. Model calculations with both radiosonde observations were made, and, since the results were quite similar, only those obtained with the closest (1800Z) sounding will be discussed. The cloud base heights were measured by the Navy S-2D, and the measured values were used in the calculations. The radius of each tower was measured by photogrammetry, as discussed, and the results have been shown in figures 6 and 7.

The main results of the model calculations for May 16 are shown in figures 19 and 20. In comparing heights in figures 6 and 7 with figures 19 and 20, it should be recalled that figures 19 and 20 give height of tower center above cloud base. Hence to go from this number to absolute height of cloud top it is necessary to add cloud radius and cloud base. Two points are immediately clear. First, cloud 5 had virtually no seedability, being too narrow a tower for growth. The measured tower radius was about 650 m. Thus its dissipation following seeding is explained. Second, the great vertical growth of cloud 6 and especially that of tower B of cloud 8 is not well predicted unless the measured tower expansion is included in the model calculation. In the case of cloud 6, the expansion was only about 30 percent, and the unexpanded tower would have

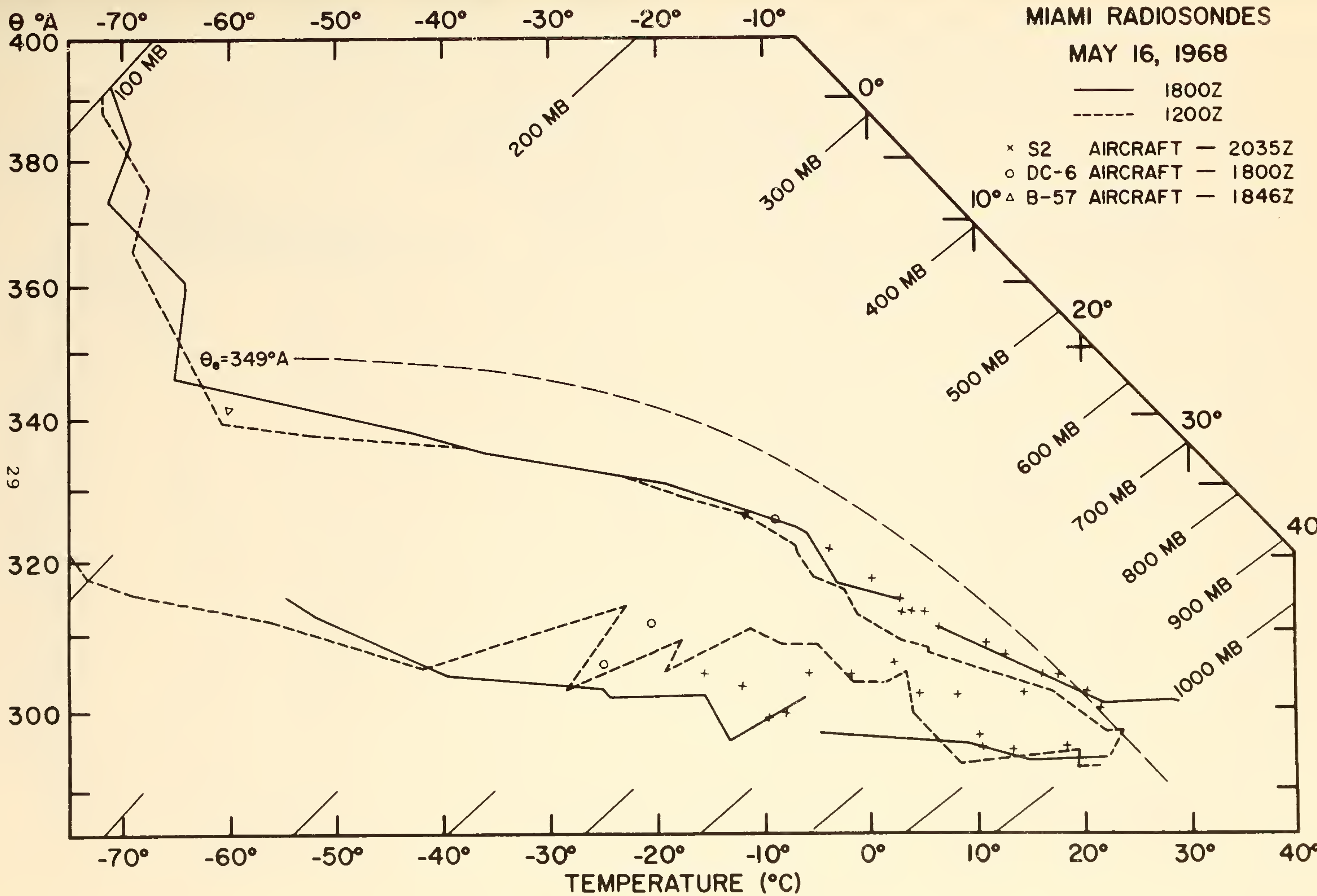

Figure 18. Miami radiosondes for May 16, 1968, plotted on a tephigram. Aircraft values for three aircraft flying close to the experimental clouds are shown for comparison.

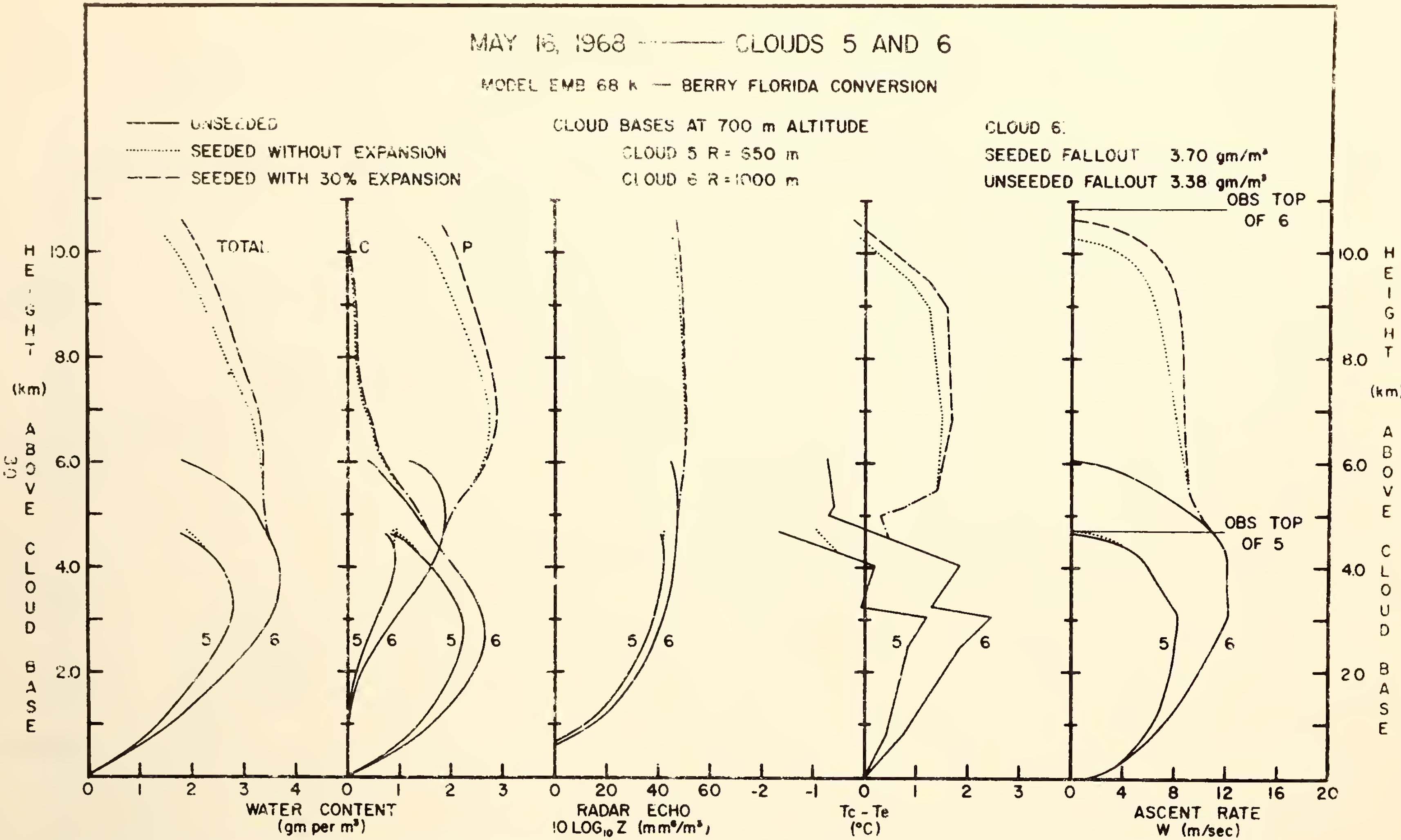

Figure 19. Model results for clouds 5 and 6, May 16, 1968. Cloud base was at 700 m. To convert top heights to compare with figs. 6 and 7, the cloud base height and tower radius must be added to the model values. To compare the predicted radar echoes with observations, only the cloud base is added, since the model discusses properties of the tower center. The predicted water contents are on the left. The leftmost panel shows total water content, while the next shows the breakdown into cloud water C (diameter < 200μ) and precipitation water P (diameter < 200μ).

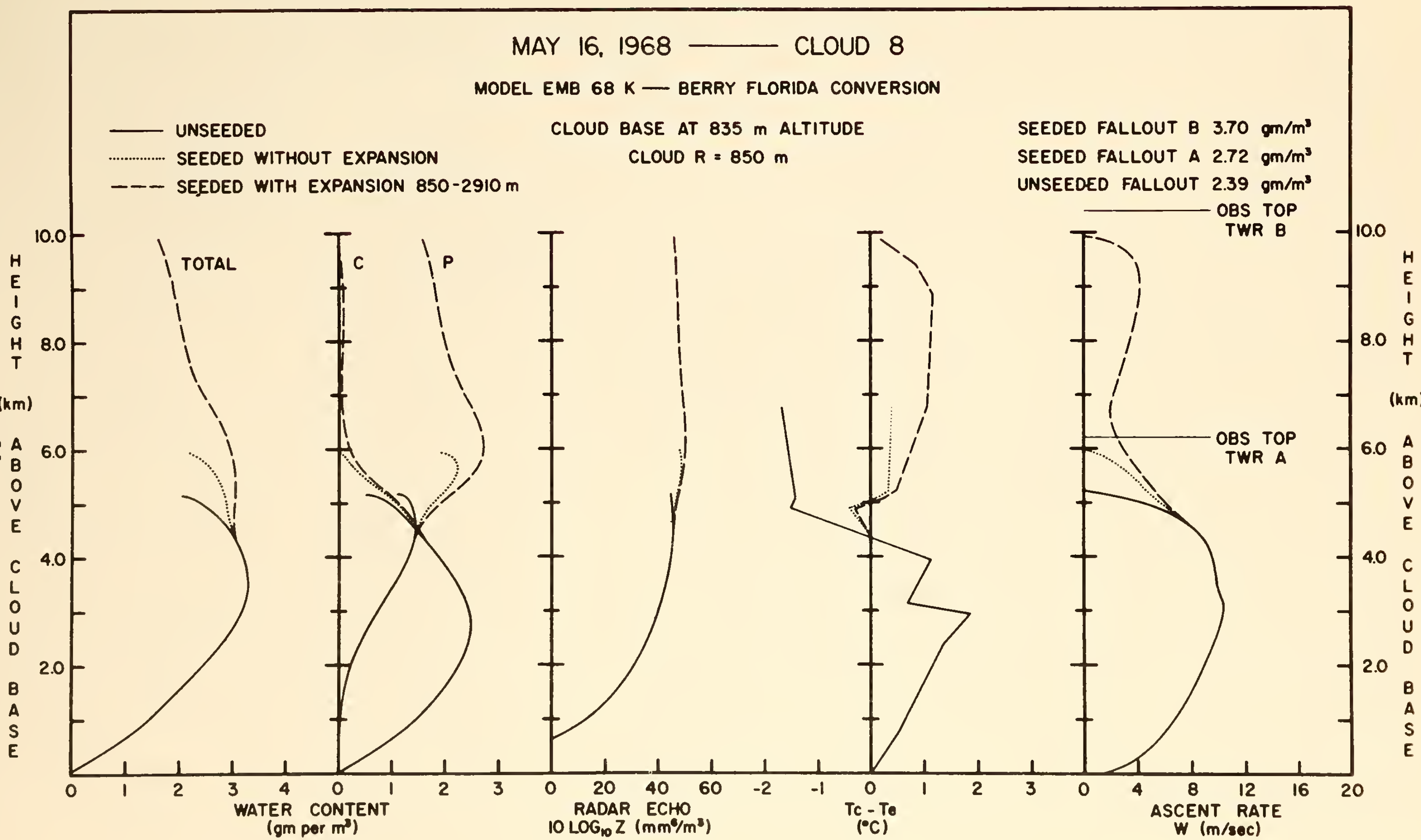

Figure 20. Model results for cloud 8, May 16, 1968. Cloud base at 835 m. Explanation same as fig. 18.

attained a level only 350 m short of the expanded tower. But in the case of cloud 8, tower A, which did not expand, terminated about 5 km lower than tower B, which was measured to expand by from 850 to about 3000 m following seeding.

This result points up a long-known weakness in the current EMB models, but also teaches us something about seeding effects. Our new method of seeding with many pyrotechnics on two mutually perpendicular passes (Simpson et al., 1969) permits such a good distribution of silver iodide smoke through a cloud body that not only an originally protuberant tower is seeded, but also fresh towers forming within or at the edge of the cloud at lower levels receive silver iodide. The fresher, lower towers can apparently draw upon their saturated cloudy environment to expand and attain greater heights than they could have without expansion. We hypothesize that this fresh tower seeding may be a main reason for the higher proportion of explosive growths in the 1968 experiment compared with that in 1965. This phenomenon is well illustrated by comparing towers A and B of cloud 8. Tower A was exposed to a dry environment (fig. 3) at seeding time, while, when tower B received silver iodide it was a recognizable part of the moist cloud body and thus able to expand in size. We plan later to try to model this type of growth with a "field of motion" type model developed by Murray (1968).

When the measured expansions are included, the observed top heights of all seeded towers are predicted fairly well. The rates of rise for cloud 6 check well against the values found from photogrammetry, as illustrated in table 1.

Table 1. Rise Rates of Tower Top

Height Interval (abs. altitude km)	Model Calc. m/sec	Measured Rise Rate m/sec
7-8	8.0	6.1
8-9	9.0	12.0
9-10	8.8	9.7
10-11	8.5	6.0
Average	8.6	8.5

In the case of cloud 8, tower A was modelled as an 850 m tower that rose without expansion, as observed. Its predicted top height agrees well with measurements, as illustrated by the dotted curves in figure 20. In the case of tower B, the observed expansion curve was approximated in the model by two linear segments. Even so, model results are only fair. The extreme growth is underpredicted by 400 m, and the rise rates are more seriously underpredicted. The average measured rise rate from seeding to maximum top is 6.8 m sec^{-1}, while the value given by the model is about 4.4 m sec^{-1}. At 6 to 7 km above cloud base, the measured rise rate was 4.5 m sec^{-1}, in good agreement with a model value of 4.2 m sec^{-1}, but at higher altitude the departures are worse. At 9 to 10 km above cloud base, the measured rise rate is 7.5 m sec^{-1}, while the model gives only 3.4 m sec^{-1}. This problem and the underpredicted top could have arisen from an environment sounding less stable in the upper troposphere than the Miami sounding. This hypothesis is supported by the fact that the local B-57 temperature at 200 mb is about 1.5^{o}C colder than that of the radiosonde (fig. 18).

Tower C, which began growing on the northwest flank of cloud 8 about 11 min after tower B had achieved maximum height, was 6 mi away from the seeded region (see figs. 4 and 5). Since it was located upshear of tower B, it is virtually impossible that C was seeded by silver iodide and not likely that it was seeded by ice particles falling from tower B's anvil.

Model calculations were undertaken on tower C to determine whether the very high rise rate could be explained. With the observed expansion, top height was well predicted when the fusion heat was released linearly between temperatures of -15° and $-40^{\circ}C$. However, the maximum predicted rise rate was only about 7 m sec^{-1} above 8 km. It seems that the high measured rise rate could only be explained by a marked steepening of the ambient lapse rate or by some dynamic effect of the large nearby cumulonimbus. Successive B-57 ascents between the time of tower B and tower C showed about a 6 percent steeper lapse rate at the appropriate levels, not enough to account for the increased ascent speed.

The removal of all drag from expanding tower C gave a maximum rise rate of only 8 m sec^{-1} - still far smaller than measured. In fact, only if tower C were seeded between $-4^{\circ}C$ to $-8^{\circ}C$ do we obtain rise rates approaching those observed near 10 km, and under these conditions the predicted top height is more than 2 km higher than that measured. Hence we must deduce that some dynamic interactions, such as a strong convergent flow, for example, took place with the nearby cumulonimbus (tower B) which cannot be incorporated in this model. It is noteworthy that several other cases were observed during the program of spectacular growth of a tower quite far on the upshear flank of a seeded cloud. These growths of outlying towers are very important to examine when we wish to extend our study from seeding effects on single clouds to the effects of this type of seeding on the cloud and rainfall patterns over a whole area. This latter type of study will be an essential prerequisite to any operational program undertaken with the purpose of altering rainfall.

A comparison that is possible for the EMB 68 model, but was not possible for earlier EMB models, is radar echo intensity. The model follows the rising active tower, and hence the most meaningful comparison is the computed maximum radar echo of the unseeded cloud versus the observed radar echo at a comparable level and time. In figure 19 we see that for cloud 6 the maximum echo intensity is about 47 db at a model height of 5 km, or an absolute height of about 19,000 ft. Figure 21 shows the radar echo distribution in cloud 6 at seeding time. Note that the maximum echo observed was 53 db at 16,000 ft.

Hamilton (1966) has presented a graph relating the height of maximum radar echo to the mean updraft in a thunderstorm. He found that these properties are inversely related. Using his graph, we find that a maximum echo at 16,000 ft corresponds to an average updraft of 5 m sec^{-1} in our cloud body at this time.

The inset graph in figure 21 shows the 20,000 ft scan of the University of Miami 10 cm radar. At the 40 mi range, this scan covers a cloud depth between 16,000 ft and 25,000 ft. The dark central region is surrounded by the 50 db contour. An average value for the cloud of 47 db seems about right.

Another check is provided by the DC-6 before seeding penetration shown in figure 9. Photogrammetry shows that the DC-6 at 19,000 ft (pressure altitude) penetrated the cloud tower about 700 m below its top. This and the penetration width of 1900 m demonstrates that the aircraft probed the heart of the active tower. We assume, for a rough computation, that the difference between the total liquid water and that measured by the Johnson-Williams hot wire is the precipitation content. The average precipitation content is then about 1.9 g m^{-3}. Using the Z, M relation derived by Kessler (1967) from theory, namely,

$$Z = 1.8 \times 10^4 \quad (M)^{1.75} \quad mm^6 \ m^{-3}, \qquad (1)$$

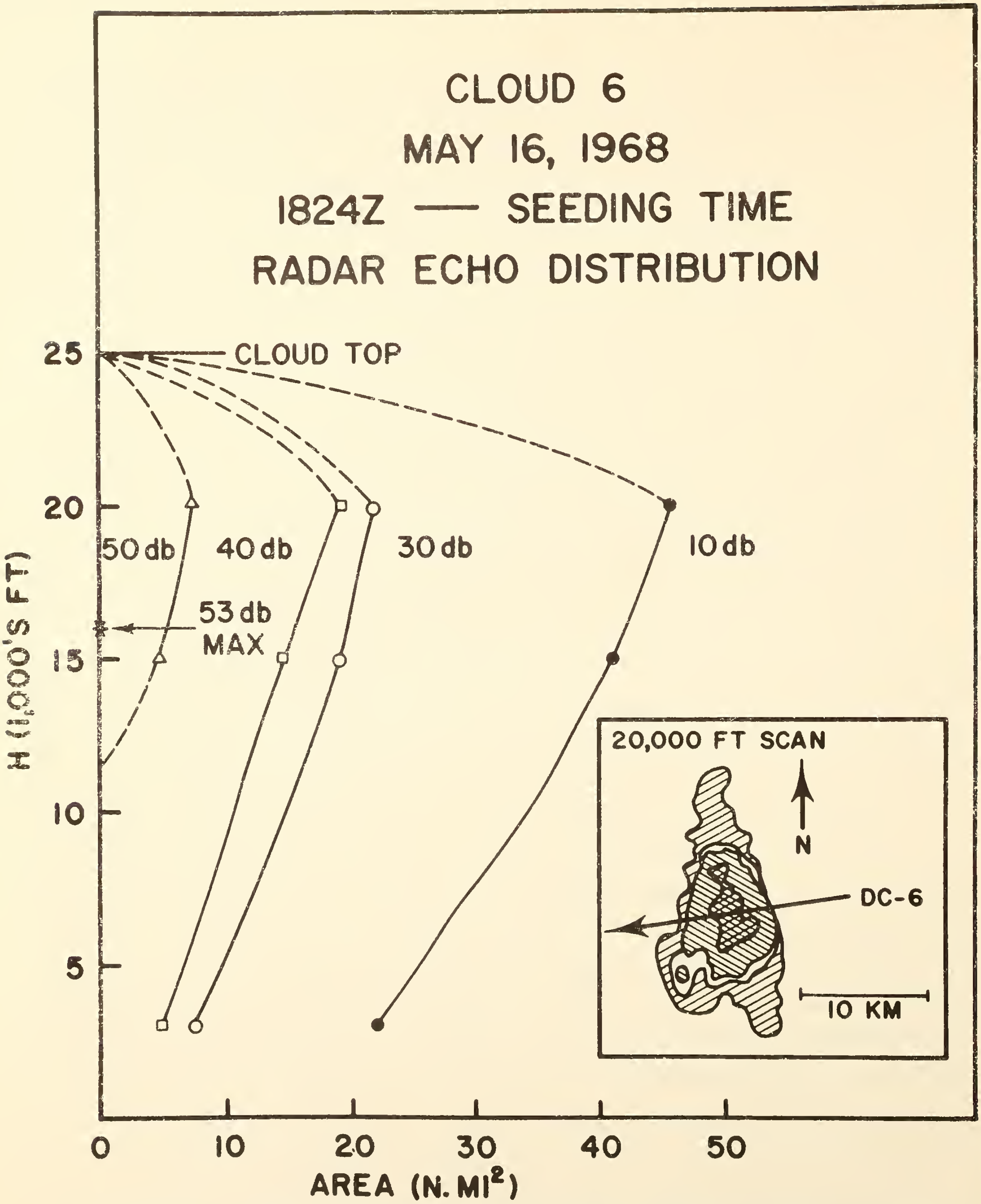

Figure 21. Area covered by radar echoes of given intensity at seeding time for cloud 6 (1824Z). The maximum intensity was 53 db at 16,000 ft. Inset diagram shows tracing of radar scope (20,000 ft scan) with same contours. DC-6 track indicated. Echo is wider than aircraft penetration because radar is integrating layer from 16,000 to 25,000 ft.

when M is in g m^{-3}, we get a Z of 47 db, in too good agreement with the model prediction!

A further test compares the total liquid water prediction of the model with that observed. The peak total water in the cloud from the DC-6 at 19,000 ft is 4.5 g m^{-3}, while the average value is about 2.5 g m^{-3}. The model value is 3.3 g m^{-3}, somewhere between the peak and mean value.

For cloud 8, a satisfactory comparison of model, aircraft pass, and radar observation is not feasible. First, the radar beam was obscured by the University library building. The maximum contour appearing on the 20,000 ft scan was only 30 db at seeding time (fig. 3). Using the liquid water contents in figure 12 with (1), we find an average difference of 3.0 g m^{-3} between total water and cloud water measured by the Johnson-Williams hot wire. This value gives a radar echo intensity of 51 db. Even if only half this liquid water were in true precipitation sizes, an echo of 46 db should have been measured as a minimum.

In addition, the penetration measurements in figure 13 cannot be used as a good test of the model prediction for cloud 8. The middle left photograph in figure 3 shows that the aircraft entered the cloud well below the central portion of the rounded tower, as is confirmed by the great length of the penetration (about 3500 m). The peak total water content was 6.2 g m^{-3}, while the average value was 3.5 g m^{-3}. The model value of 2.0 g m^{-3} should have been more characteristic of the cloud tower above the aircraft.

Finally, the model makes a prediction about the precipitation fallout from a single tower, seeded and unseeded. For a cloud 6 tower, the seeded fallout is predicted at 3.70 g m^{-3}, while the unseeded value is 3.38 g m^{-3}, an increase of less than 10 percent. For comparison with the radar results, we multiply 3.70 g m^{-3} by the volume of the cloud tower and convert to acre-feet. A single seeded tower, in the model, would have a fall-out of about 26.5 acre-feet of water. The radar observations showed that cloud 6 produced about 185 acre-feet of rainfall in the first 10 min following seeding. This is more rainfall by a factor of seven than has fallen from the model tower when it reaches its maximum height.

The real exploded cloud differs from the model in two main respects: (1) The real exploded cloud is a succession of towers, but the model is not, and (2) the fallout from each descends mainly through cloud body where it can collect smaller droplets and thus augment itself on the descent. If, in fact, two or three towers contributed to the measured 10 min precipitation and if the rain falling from each augmented itself by a factor of 2 to 3 by accretion during descent, the 185 acre-feet in 10 min is readily accounted for. Figure 2 shows that cloud 6 at 10 min after seeding consisted of at least two amalgamated towers (A and B).

A rough calculation shows that the falling precipitation from the tower can easily be doubled or tripled during descent. For this, we use an equation for drop growth by coalescence from Johnson (1954), namely,

$$d_2 - d_1 = \frac{\bar{E}\bar{m}}{2\rho} (z_2 - z_1) , \tag{2}$$

where d_2 is the final raindrop diameter in cm, d_1 is the initial raindrop diameter in cm, $\bar{E}$ is the average collection efficiency of raindrops for cloud drops, assumed unity, $\bar{m}$ is the average cloud water content in grams per gram, ρ is the density of water, and $z_2 - z_1$ is the height fallen in cm. The model gives the values of d_1 as about 1.75 mm when we define d_1 as the median volume diameter at the tower center when it has reached its maximum height. If this particle falls through a cloud water content of 0.5 g m^{-3} for 2 km, (2) shows it will double its mass, while the mass will increase by five times if the fall distance in cloud is 5 km. This result indicates that our accretion hypothesis is conservative. Because of the large expected accretion, the current model can probably not predict the final precipitation to a useful approximation. Since the distances required for doubling are so short, it should not affect this argument that the collecting particles are ice for the first few kilometers of fall.

The accretion hypothesis is further supported by the fact that the aircraft at 19,000 and 17,000 ft often measured higher than adiabatic water contents after seeding. An example is cloud 8, in which a peak total water content exceeding 7.0 g m^{-3} was recorded on pass 6 (fig. 17). Since the Johnson-Williams recorded only a little more than 1.0 g m^{-3} on this pass, most of the water must have been in precipitation.

5. CONCLUDING REMARKS

May 16 offered a rather complete study of three seeded clouds by means of photogrammetry, aircraft penetrations, calibrated radar, and a numerical model. These components fit rather beautifully together to document the behavior and structure of the clouds. One cloud (5) showed no computed seedability and failed to grow. The two other clouds (6 and 8) grew explosively following seeding. The model calculations suggest that cloud 6 would have grown without tower expansion, but cloud 8 required the tower size to more than double in order to account for the observed explosion. A main factor in this growth is believed to be the repetitive seeding with many small pyrotechnics, which seeds fresh towers growing within the main cloud body. A weakness of the EMB 68 model is that it does not predict expansion, which must be entered as input from observation. A more sophisticated model is being adapted for use with these experiments, which hopefully may predict expansion.

An excellent comparison was obtained for cloud 6 for the model's predicted (unseeded) radar echo with the echo observed on the University of Miami radar and with that computed from the water measurements made during the DC-6 penetration. This indicates that the model is handling the growth of precipitation in liquid clouds effectively.

From comparing model-predicted precipitation fallout with measured radar rainfall at cloud base, a hypothesis relating the dynamics and precipitation from an exploded cloud was advanced. This involves several towers contributing precipitation, which is augmented within cloud on descent. This hypothesis will be tested in further case studies from 1968, based on the airborne foil and Formvar particle samplers together with the measurement tools discussed here. Unfortunately, the DC-6 foil sampler was inoperative on May 16, although a similar sampler operated at cloud base. Results from the other two penetrating aircraft will be incorporated in this case study later.

We conclude that the focusing of these four tools (aircraft, radar, photography, and model) provide a uniquely productive method of analyzing both cloud physics and dynamics in general and seeding effects in particular.

6. ACKNOWLEDGEMENTS

The writers dedicate this effort to Dr. Helmut K. Weickmann, Director of the ESSA Atmospheric Physics and Chemistry Laboratory, for his persistent support of this program and for valuable discussions of every phase of the work.

We are much indebted to the personnel of the University of Miami Radar Laboratory for their valuable contribution of talent and facilities, which were key parts of this research.

Sincere appreciation is also due the Southern Region, U.S. Weather Bureau; the Director and staff of the National Hurricane Center, Miami, Florida, for making the extra radiosonde observation at 1800Z that was indispensable to the cloud modelling; Dr. Gerald Conrad and Mr. Lloyd Devol of RFF, ESSA, for providing and analyzing the Levine water content measurements; Mr. Robert L. Daniels of RFF and his staff for their valuable roles in instrument performance; and Mr. Merle Ahrens of RFF for the computer reduction and plotting of the DC-6 records.

7. REFERENCES

Berry, E.X. (1968), Modification of the warm rain process, Proc. First Natl. Conf. Weather Modification, Albany, N.Y., April 28-May 1, 1968, 81-85.

Byers, H.R. (1968), Cumulus cloud structure and dynamics from aircraft observations, Proc. Intern. Conf. on Cloud Physics, Toronto, Canada, August 26-30, 1968, 544-548.

Hamilton, P.M. (1966), Vertical profiles of total precipitation in shower situations, Quart. J. Roy. Meteorol. Soc. 92, 346-362.

Herrera-Cantilo, L. M. (1969), Cloud aerial photogrammetry based on Doppler navigation, Report on work performed under Contract No. 22-2-68(N) between ESSA and the Univ. of Miami.

Johnson, J.C. (1954), Physical Meteorology, 229-231 (Wiley Technology Press, New York, N.Y.).

Kessler, E. (1965), Microphysical parameters in relation to tropical clouds and precipitation distributions and their modification, Geofisica Intern. 5, No. 3, 79-86.

Kessler, E. (1967), On the continuity of water substance, ESSA Tech. Memo. IERTM-NSSL 33 (in press as Meteorological Monograph).

MacCready, P.B., Jr., and C.J. Todd (1964), Continuous particle sampler, J. Appl. Meteorol. 3, 450-460.

Malkus, J.S., and R.H. Simpson (1964), Modification experiments on tropical cumulus clouds, Science 145 (3632), 541-548.

Murray, F.W. (1968), Numerical models of a tropical cumulus cloud with bilateral and axial symmetry, Rand Memo. RM-5870-ESSA, The Rand Corporation, Santa Monica, Calif., 31 pp.

Senn, H.V., and C. L. Courtright (1968), Radar hurricane research, Inst. of Marine Sciences, Univ. of Miami, Miami, Fla., Final Rept. Contract No. E22-62-68(N), 31 pp.

Senn, H.V., and G.F. Andrews (1968), A new, low-cost, multi-level iso-echo-contour for weather-radar use, J. Geophys. Res. 73, 1201-1207.

Simpson, J., and V. Wiggert (1969), Models of precipitating cumulus towers, Monthly Weather Rev. (in press).

Simpson, J., G.W. Brier, and R. H. Simpson (1967), Stormfury cumulus seeding experiment 1965: Statistical analysis and main results, J. Atmospheric Sci. 24, 508-521.

Simpson, J., W. L. Woodley, H. A. Friedman, T. W. Slusher, R. S. Scheffee, and R. L. Steele (1969), An airborne pyrotechnic cloud seeding system and its use, ESSA Tech. Memo. ERLTM-APCL 5, 44 pp.

Woodley, W. L. (1969), The effect of airborne silver iodide pyrotechnic seeding on the dynamics and precipitation of supercooled tropical cumulus clouds, A dissertation submitted to the Graduate School of Florida State Univ. in partial fulfillment of the requirements for the degree of Doctor of Philosophy, 139 pp.

Woodley, W. L., and J. F. Partagas (1969), Radar and photographic documentation of convective developments on May 16, 1968, ESSA Tech. Memo. ERLTM-APCL 7, 16 pp.

U.S. DEPARTMENT OF COMMERCE
Environmental Science Services Administration
Research Laboratories

ESSA Technical Memorandum ERLTM-APCL 5

AN AIRBORNE PYROTECHNIC CLOUD SEEDING SYSTEM AND ITS USE

Joanne Simpson and William L. Woodley
Experimental Meteorology Branch, ESSA

Howard A. Friedman
Research Flight Facility, ESSA

Thomas W. Slusher
Olin Mathieson Corporation

R. S. Scheffee
Atlantic Research Corporation

Roger L. Steele
Colorado State University

Atmospheric Physics and Chemistry Laboratory
Boulder, Colorado
February 1969

TABLE OF CONTENTS

ABSTRACT

The development, testing, and use of an airborne pyrotechnic cloud seeding system is described. Pyrotechnic flares producing 50 g of silver iodide smoke each were developed by two industrial corporations and laboratory tested for nucleation effectiveness in the Colorado State University cloud chamber. A delivery rack and firing system were developed, under ESSA supervision, and installed on its B-57 jet aircraft. Night flight tests were made of reliability, burn time and flare trajectory.

The flare system was used in a Florida cumulus seeding experiment in May 1968 conducted jointly by ESSA and the Naval Research Laboratory, with the participation of the U. S. Air Force, the University of Miami Radar Laboratory and Meteorology Research, Incorporated. A randomized seeding scheme was used on 19 supercooled cumuli, of which 14 were seeded and 5 were studied identically as controls. Of the 14 seeded clouds, 13 grew explosively. Seeded clouds grew 10,900 ft higher than the controls, with the difference significant at better than the 1/2 percent level. Rainfall from seeded and control clouds was compared by means of calibrated ground radars. Large increases in rainfall were found from seeded clouds, but unfortunately not at a satisfactory significance level. A single successful repeat of the experiment could result in rainfall differences significant at the 3 percent level.

AN AIRBORNE PYROTECHNIC CLOUD SEEDING SYSTEM AND ITS USE

Joanne Simpson and William L. Woodley
Experimental Meteorology Branch, ESSA

Howard A. Friedman
Research Flight Facility, ESSA

Thomas W. Slusher
Olin Mathieson Corporation

R.S. Scheffee
Atlantic Research Corporation

Roger L. Steele
Colorado State University

1. INTRODUCTION

A silver iodide cloud seeding system was desired for a modification experiment upon individual cumulus clouds growing over and near the Florida peninsula in May 1968. This experiment, conducted jointly by ESSA and the Naval Research Laboratory with the participation of the U. S. Air Force, the University of Miami Radar Laboratory and Meteorology Research, Incorporated, was the sequel to the Stormfury cumulus seeding experiment conducted in the Caribbean in 1965 (Simpson et al. 1966, 1967; Simpson, 1967; Ruskin, 1967).

The seeding was intended to release as rapidly as possible all the latent heat of fusion in selected supercooled cumuli. The size of the subject clouds was about 1.5 to 3.0 km in tower diameter and 6 to 8 km in height, cloud base was at about 500 to 1000 m, and the freezing level was at roughly 4 km at this location and season.

The purpose of the experiment was to study with aircraft and calibrated ground radars the induced dynamic and physical changes in the seeded clouds and to compare these with unseeded control clouds, both chosen on a statistically randomized basis.

Some previous randomized seeding experiments are summarized in table 1, including the first results of the May 1968 Florida experimentation. The amount of silver iodide introduced per cloud is seen to vary widely, the only very high concentrations being achieved with pyrotechnics. Since complete and rapid latent heat release was desired, the aim was to introduce not less than about 100 nuclei per liter into the supercooled portion of the clouds. This figure is based on a calculation by MacCready (1959). To achieve this concentration in clouds of the size mentioned requires that about 10^{15} nuclei be introduced and distributed through the cloud in a few minutes. This could be done with 1000 g of silver iodide smoke if the nucleation efficiency is 10^{12} active particles per gram, which is within the capacity of pyrotechnics (Davis and Steele, 1968). Most airborne generators would require about 1 hour to produce the necessary quantity of silver iodide particles at these warm temperatures. This and the distribution problem precluded their use in our experiments.

2. THE PYROTECHNICS

Pyrotechnic flares were desired that could be dropped from the ESSA Research Flight Facility B-57 jet aircraft. For optimum distribution, it was planned to drop twenty (20) 50 g flares into each cloud top at approximately 100 m horizontal intervals. The flares were to be ejected on two successive seeding passes, made at right angles to each other about 3 min

Table 1. Randomized Supercooled Cumulus Seeding Experiments by Aircraft

Name	Method	Randomized	No. of Clouds in Sample	Amt. Per Cloud (Est.) Kg	Nuclei per Liter at -10°C (Est.)	Result	How Measured	Average Change Magnitude	Average Change Percent	Significant to 5% Level
Braham et al. Central U. S. (1957)*	Dry ice	Yes	53	8-14	$\sim 10^4$	Inconclusive	Radar	-	-	No
Bethwaite et al. Australia (1966)	AGI generator (single cloud)	Yes	28	2×10^{-2}	1 - 5	Incr. precip. (cloud tops <-10°C)	Airborne hydrometeor sampler	210 acre-ft	650	Yes
Bethwaite et al. Australia (1966)	AGI generator (single cloud)	Yes	25	2×10^{-4}	.01 - .05	Inconclusive (cloud tops <-10°C)	Airborne hydrometeor sampler	-	-	No
Battan Arizona (1966, 1967)	AGI generator (area)	Yes		2×10^{-2}	1 - 5	Incr. radar echoes, no change in precip.	Radar rain gages	-	-	No
Simpson et al. Caribbean (1967)	AGI pyrotechnics (single cloud)	Yes	23	10-20	2×10^3 - 2×10^4	Incr. cloud growth	Photogrammetry and aircraft	1.6 km		Yes
Neumann et al. Israel (1967)	AGI generator (area)	Yes		2×10^{-3} - 2×10^{-2}	0.1 - 5	Incr. precip.	Rain gages		18-19	Yes
Davis et al. Arizona (1968)	AGI generator (single cloud)	Yes	18	1.6×10^{-1} - 3×10^{-1}	5×10^2	Incr. cloud growth	Radar and visually	1.8 km	23	Yes
						Incr. precip.	Radar	3 mm (~ 5 acre-ft per cloud)	186	Yes
						Incr. cloud duration	Radar	11 min		Yes
Flueck Missouri (1968)	AGI pyrotechnics (area)	Yes		-	-	Inconclusive	Rain gages			No

Table 1. (Continued)

Name	Method	Randomized	No. of Clouds in Sample	Amt. Per Cloud (Est.) Kg	Nuclei per Liter at -10°C (Est.)	Result	How Measured	Average Change Magnitude	Average Change Percent	Significant to 5% Level
Korienko et al. Russia (1968)	Dry ice (single cloud)	Yes?	162	-	-	Incr. precip.	Airborne water collector	5×10^3 tons (~3.5 acre-ft per cloud)	240	Yes
Simpson et al. Florida (1969)**	AGI pyrotechnics (single cloud)	Yes	19	5×10^{-1} - 1	10^2 - 10^3	Incr. cloud growth	Aircraft	3 km	346	Yes
						Incr. precip.	Radar	100-150 acre-ft (By 40 min after seeding)	140	No

* Dates in parenthesis refer to publications as listed under references.

** Florida experiment described in this report.

\- Information not available

apart. The flares were to burn at ambient pressure for about 60 sec and to fall about 3 km vertically before burning out. Complete burnout was required for safety in use over land areas. Design goals were established in terms of laboratory tests of the efficiency and flight tests of the ignition reliability. The efficiency goal was 10^{10} active nuclei per gram at -5°C and 10^{12} active nuclei per gram at -10°C, with equal or better efficiency at lower temperatures. The tests of efficiency and related matters were to be undertaken in the isothermal cloud chamber at the Colorado State University according to prescribed procedures (Steele, 1968). The flight goal was that 80 percent of the flares should ignite and remain ignited until burnout when dropped from 20,000 ft.

The Olin Mathieson Company and the Atlantic Research Corporation undertook the development of suitable pyrotechnic mixes producing the silver iodide. The former company worked on its own initiative, the latter under contract with ESSA. Altogether more than 50 mixes were developed and tested. Preliminary tests were run at the company laboratories for such vital properties as safety, shelf life and burn characteristics, and the most promising mixes were then sent to Colorado State University (CSU) for efficiency tests in the cloud chamber. The work by the Atlantic Research Corporation is described in detail in a report by Scheffee et al. (1967). In a systematic program of research carried out to develop, test, and evaluate pyrotechnics for dissemination of AgI in a form suitable for cloud seeding, a large number of pyrotechnic compositions containing either powdered AgI or $AgIO_3$ as the source of AgI particles in the smoke were developed and found to be safe and reliable in terms of ballistic and physical properties and shelf life.

Results of the program indicated that the most promising mixes containing AgI were composed of $KClO_4$ and thiourea as the oxidizer and fuel, respectively, while those containing $AgIO_3$ were composed of $KClO_4$, magnesium and nitrocellulose plastecized with triacetin. These compositions were found to be safe to manufacture and use and to have acceptable physical properties and shelf life. Better combustion characteristics were found for compositions containing $AgIO_3$ and magnesium than for AgI-$KClO_4$-thiourea in terms of ease and uniformity of combustion at simulated altitudes up to 40,000 ft.

Of the several dozen mixes tested at CSU, those most efficient in the -5° to -15°C temperature range had two properties in common. The first was high percentages of metallic condensed species in the output, and the second was a high flame temperature ($\sim$ 2000°K or more). With the high flame temperature, the silver iodate is reduced, and the products are vaporized and react to form condensed silver iodide during the quenching process. The high burn temperatures should favor nucleation efficiency, by shifting the particle size distribution in the smoke toward smaller particles.

The metallic species consisted of high percentages of aluminum and magnesium oxides (roughly 20-30%) and smaller percentages of alkali chlorides and iodides. Aluminum and magnesium oxides are active freezing nuclei, starting at -6.5°C and -9.3°C, respectively (Fukuta, 1958). In the case of the alkali chlorides and iodides, a possible explanation has been given by St. Amand et al. (1969). They suggest that in the warm range of supercooled cloud temperatures nucleation may take place predominantly by contact and condensation, rather than by sublimation and diffusion as at lower temperatures. With only pure AgI, it is unlikely that condensation will occur at all in the regimes of saturation pressures found in nature, and particles greater than 1 μ are required. With supersaturations of about 3 percent, particles as small as 0.01 μ become effective as condensation nuclei. St. Amand et al. (1969) state that the process of condensation can be made vastly more effective by treating the AgI with alkali iodides and chlorides, which should reduce the vapor pressure of water over the surface of the material by much more than 3 percent locally. Experimental evidence supporting this hypothesis is presented by Mossop (1968) and Jiusto and Kochmond (1968).

The chemical compositions of Atlantic Research formulation 1-20M-45A and Olin Mathieson formulation X1055 chosen for the field experiment are given in tables 2 and 3.

Table 2. Composition, Atlantic Research Corporation Formulation 1-20M-45A

Material	Percent by Weight
Silver iodate	45.0
Potassium perchlorate	27.0
Magnesium	20.0
Nitrocellulose	4.0
Triacetin	4.0

Table 3. Composition, Olin Mathieson Company Formulation X1055

Material	Percent by Weight
Silver iodate	53.0
Potassium iodate	8.0
Magnesium	5.6
Aluminum	12.9
Strontium nitrate	10.5
Polyester binder	10.0

The reaction of AgI with likely combustion products is an important consideration in the design of pyrotechnic compositions. Since the computation of equilibrium mixtures is arithmetically complex and laborious, equilibrium calculations of mixtures of compounds at an assigned temperature and pressure were carried out at both the Atlantic Research Corporation and the Olin Mathieson Company by means of digital computer programs. These programs are used on a routine basis primarily for the computation of rocket propellent specific impulse and associated interior ballistics parameters in which it is assumed that combustion at an assigned pressure is adiabatic, that expansion of the combustion products to an assigned exhaust pressure is isentropic, and that thermodynamic equilibrium exists between the combustion products at both combustion and exhaust pressures. Based on available variations of this program, equilibrium values of the flame temperature and combustion product composition of ARC formulation 1-20M-45A and Olin formulation X1055 were computed and are given in tables 4 and 5. These results may or may not be representative of the actual species in the products but plume sampling by ARC does verify some of the predicted outputs.

Table 4. Equilibrium Composition of the Combustion Products of Composition 1-20M-45A for Adiabatic Combustion at 1 Atmosphere

Flame Temperature = 3082°K

Total Mols of Gas = 1.4208 g mol/100 g

Combustion Product Composition g mol/100 g

Specie	Amount	Specie	Amount
Ag(g)	0.1466	K(g)	0.0359
Ag(l)	0	KCl(g)	0.1315
AgCl(g)	0.0020	KCl(l)	0
AgH(g)	0.0002	KCl(s)	0
AgI(g)	0.0100	KI(g)	0.0216
AgI(l)	0	KI(l)	0
AgO(g)	0	K_2I_2(g)	0
Ag_2(g)	0.0002	KO(g)	0.0011
		KOH(g)	0.0048
C(g)	0	KOH(l)	0
C(s)	0		
CO(g)	0.1548	Mg(g)	0.0865
CO_2(g)	0.0983	MgCl(g)	0.0071
		$MgCl_2$(g)	0.0024
Cl(g)	0.0266	$MgCl_2$(l)	0
Cl_2(g)	0	MgI(g)	0.0054
ClO(g)	0.0001	MgI_2(g)	0
		MgO(g)	0.1278
I(g)	0.1207	MgO(l)	0
I_2(g)	0	MgO(s)	0.5721
ICl(g)	0	MgOH(g)	0.0201
		$Mg(OH)_2$(g)	0.0011
NO(g)	0.0054		
NOI(g)	0	O(g)	0.0584
N_2(g)	0.0153	O_2(g)	0.1098
		OH(g)	0.0564
H(g)	0.0337	H_2O(g)	0.0930
HCl(g)	0.0230		
HI(g)	0.0014		
H_2(g)	0.0199		

Table 5. Equilibrium Composition of the Combustion Products of Composition X1055 for Adiabatic Combustion at 1 Atmosphere

Flame Temperature = 2296°K

Total Mols of Gas = 1.5589 g mol/100 g

Combustion Product Composition, g mol/100 g

Specie	Amount	Specie	Amount
Ag(g)	0.1011	I(g)	0.0311
AgH(g)	0.0007		
AgI(g)	0.0841	K(g)	0.0030
AgI(1)	0	KCN(g)	0.0001
Ag_2(g)	0.0008	KCN(1)	0
		KI(g)	0.0343
Al(g)	0.0350	KI(1)	0
Al(1)	0	KH(g)	0
AlH(g)	0.0021	K_2(g)	0
AlOH(g)	0.0002	K_2I_2(g)	0
Al_2O(g)	0.0429		
AlN(g)	0	Mg(g)	0.1584
AlN(s)	0.0357	MgH(g)	0.0013
Al_2O_3(s)	0.1597	MgI(g)	0.0700
Al_2O_3(1)	0	MgI_2(g)	0.0005
		MgO(g)	0
C(g)	0	MgO(s)	0
C(s)	0	MgN(g)	0
CO(g)	0.5905		
CO_2(g)	0	N_2(g)	0.03122
CH_2(g)	0	NH(g)	0
CH_4(g)	0	NH_2(g)	0
C_2H(g)	0	NH_3(g)	0
C_2H_2(g)	0.0001		
CN(g)	0	Sr(g)	0.0495
		SrH(g)	0.0001
H(g)	0.0066	SrO(g)	0
HCN(g)	0.0010	SrO(s)	0
HI(g)	0.0044	SrOH(g)	0
H_2(g)	0.3101		
H_2O(g)	0		

Tables 4 and 5 show a considerable degree of dissociation of silver iodide gas into atomic species. The degree of dissociation increases with the flame temperature. Recombination will occur as the combustion products cool. The calculations also show that in the case of the composition containing potassium perchlorate, potassium chloride and silver iodide are the major stable products rather than potassium iodide and silver chloride. This was confirmed by X-ray analysis of samples collected in the smoke plume, where the latter products could not be detected at the 5 percent level.

Tables 6 and 7 give the expected combustion products when the smoke is cooled to ambient temperature, if one assumes recombination of dissociated species and, in the case of formulation X1055, oxidization of excess fuel with atmospheric oxygen.

Table 6. Expected Exhaust Products at Ambient Temperature Formulation 1-20M-45A

Compound	Grams per 100 g mix
Silver iodide	37.4
Potassium chloride	14.5
Magnesium oxide	33.2
Carbon dioxide	11.1
Water	3.3
Nitrogen	0.5

Table 7. Expected Exhaust Products at Ambient Temperature Formulation X1055

Compound	Grams per 100 g mix*
Silver iodide	44.0
Potassium iodide	6.1
Magnesium oxide	9.5
Aluminum oxide	24.1
Strontium oxide	7.2
Nitrogen	1.4
Carbon dioxide, water etc.	31.7

* Total adds up to more than 100, since some oxygen to burn the metal fuels is incorporated from the surrounding atmosphere.

The flame temperatures (estimated by calculation) were 3082°K for the 1-20M-45A mix and 2296°K for the X1055 mix. Attempts are currently underway to measure the flame temperatures.

3. LABORATORY TESTS

A facility has been constructed at Colorado State University (CSU) for testing and comparing silver iodide generators and other devices for weather modification experiments. The test facility has been described in detail by Steele (1968).

One of the main objectives of the laboratory tests is to determine how many active freezing nuclei are produced per gram of silver iodide in the smoke. This is done by burning the flares in a wind tunnel, collecting a smoke sample in a syringe, diluting it a known amount, and finally introducing the dilute smoke into a temperature-controlled chamber in which a supercooled cloud is maintained. The number of ice crystals in a fixed portion of the chamber are counted and related to the mass of silver iodide burned.

The intention in the tests is to burn the flares and nucleate the cloud under as realistic conditions as possible. The results reported here and the inferences drawn from them are only preliminary because of limitations in simulating a pyrotechnic in free fall and in simulating real clouds. The wind tunnel used to produce the results reported here had a test section approximately 0.5 m in diameter and produced a flow of only 130 m^3 min^{-1}. The small diameter produced adverse wall effects. It was also far from representative of the ventilation past the unit at its normal fall speed.

Free fall is currently being simulated in a new vertical wind tunnel in which actual free fall velocities can be simulated by La Grangian techniques. Wall effects are minimized, since the new tunnel has a test section 1.15 m, which results in an area 6.25 times greater than the old tunnel.

Flows of 3100 m^3 min^{-1} are possible at velocities up to 62 m sec^{-1}. Recent results show that the measured nucleation efficiency depends strongly on ventilation past the pyrotechnic.

In the cloud chamber, ice crystal counts have been made so far with a cloud liquid water content of about 0.8 g m^{-3}. Recent addition of improved cloud chamber instrumentation shows that measured nucleation efficiencies depend markedly upon the cloud liquid water content, as described below.

With these reservations, test results from the old CSU facility are shown for the two mixes in figure 1. Note that the apparent greater efficiency of the 1-20M-45A flares is due to sample size and is not representative. The full X-1055 flare was burned in the tunnel with a burn rate of 45 g min^{-1}, while only a 2 g sample of the 1-20M-45A mix was burned, with a burn rate of 4.5 g min^{-1}. As shown by Davis and Steele (1968) and by Scheffee and Steele (1968), coagulation of the smoke particles was a major problem in the old slow-speed wind tunnel. In their study of effectiveness as a function of burn rate Davis and Steele (1968) showed that increasing the sample size of the 1-20M-45A mix to that of the full flare would reduce its measured effectiveness (in the old tunnel) to values very close to that of the X-1055 flares.

Since these preliminary tests, others have begun with the new vertical wind tunnel described above. Results for a very similar Navy[1] flare are shown in figure 2. A tunnel flow of 3100 m^3 min^{-1} corresponds to about 62 m sec^{-1}, or about 200 ft sec^{-1}. At most temperatures, about one order of magnitude greater effectiveness is measured at these more realistic air flow

---

[1] Naval Weapons Center (China Lake, California), Pyrotechnic LW-83. Information kindly furnished the authors by Dr. Pierre St. Amand.

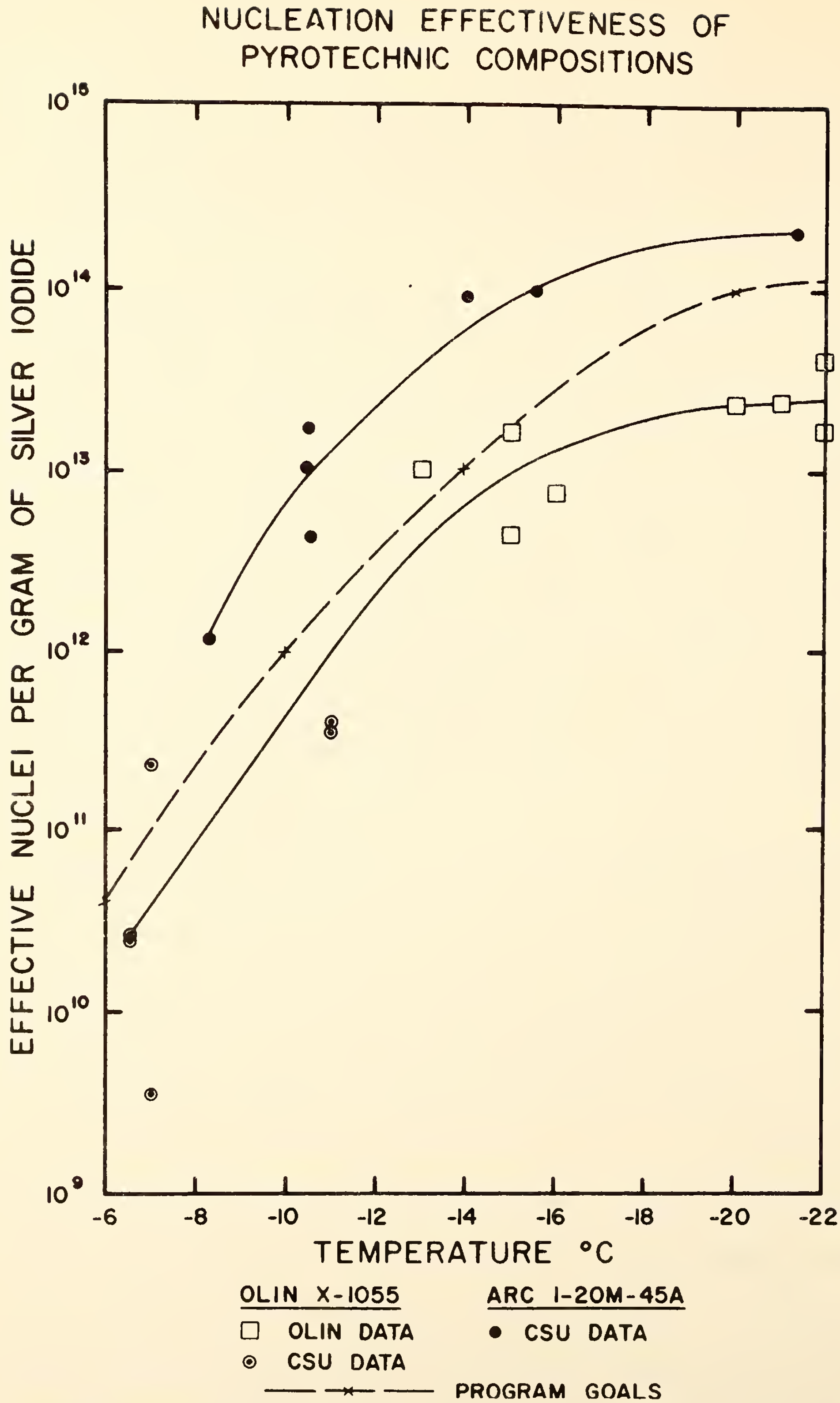

Figure 1. Nucleation effectiveness of the two pyrotechnic compositions used in 1968 Florida experiment. Higher solid line (with heavy circles) shows effectiveness as function of temperature for mix 1-20M-45A, with the burn rate of 4.5 g min^{-1}. Lower solid line (with squares and double circles) shows effectiveness as function of temperature of mix X-1055 with the burn rate of 45 g min^{-1}. Dashed line denotes desired program goal.

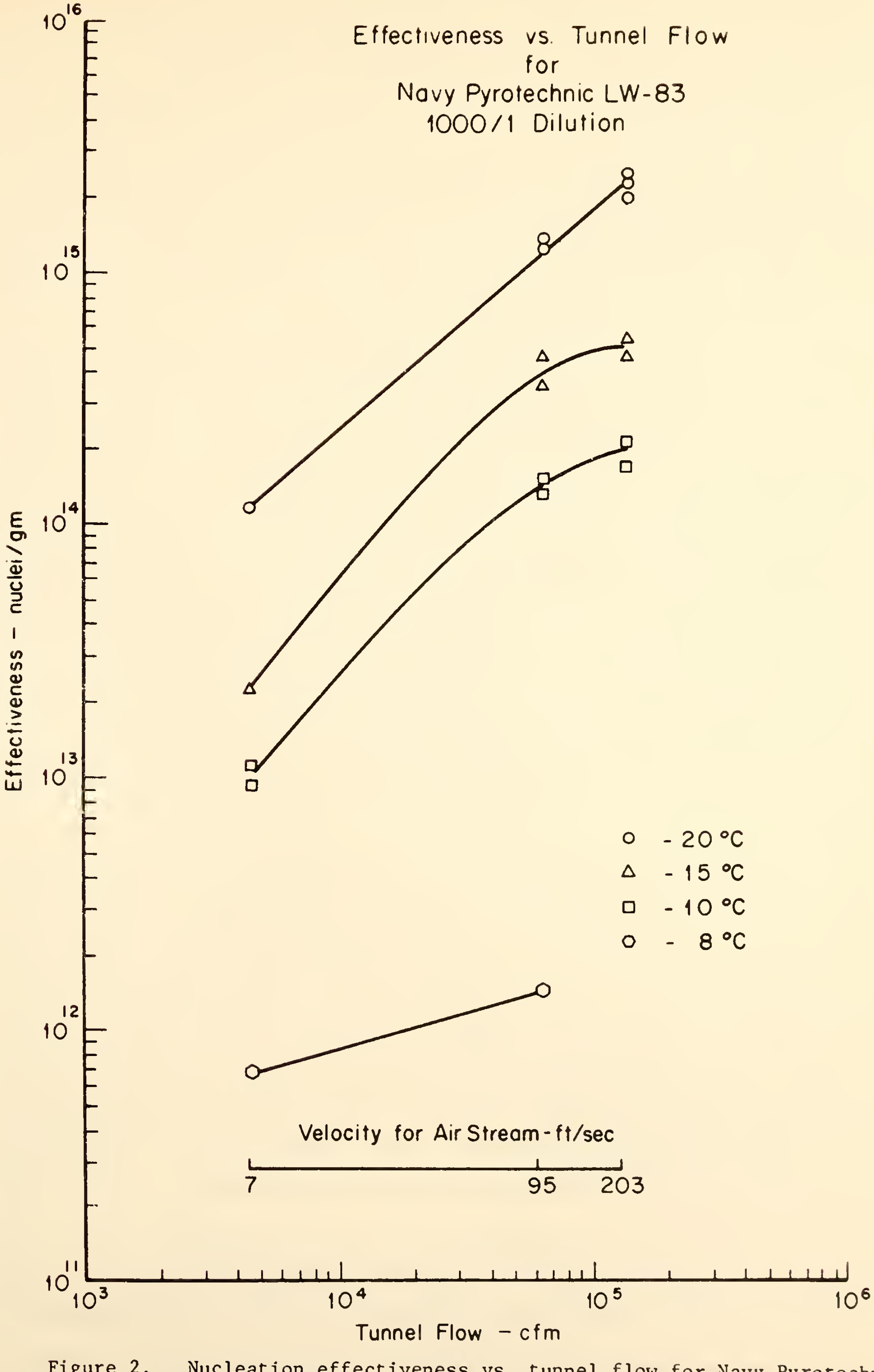

Figure 2. Nucleation effectiveness vs. tunnel flow for Navy Pyrotechnic LW-83 (a mix similar to X-1055). A flow rate of 10^5 cfm corresponds roughly to 150 ft sec^{-1}, the fall speed of the pyrotechnics.

speeds than was measured in the old tunnel. Applying a corresponding correction to the lower curve in figure 1, we have easily an effectiveness of 10^{12} particles per gram at -10°C. It is also significant that the new facility will permit effectiveness measurements at -5°C, which were awkward if not impossible with the old facility.

Finally, the effect of varying cloud liquid water content upon the measured effectiveness was evaluated, and figure 3 shows a typical result for a low output, steady state, silver iodide generator. In the range just above 1 g m^{-3}, increasing the cloud water content by only 50 percent increases measured nucleation efficiency by a factor of 100 at temperatures in the range of -12°C (Steele and Davis, 1969). Since our experimental clouds rarely exhibited water contents of less than 1 g m^{-3} and often had water contents of 2-3 g m^{-3} at seeding times and levels, we conclude that 10^{12} nuclei per gram of silver iodide smoke at -10°C is probably a very conservative figure.

Detailed measurements in the new CSU facility are now being performed with both Olin and ARC pyrotechnic flare mixes, at varying flow speeds (fall velocities) and with liquid water contents in the range simulating natural cloud conditions. Until these results are available, we conclude tentatively that at -5°C and -10°C respectively, 10^{10} and 10^{12} active nuclei per gram of silver iodide are reasonable but probably considerable underestimates for the flares used in our May 1968 Florida cumulus experiments.

4. FLARE CONFIGURATIONS AND DELIVERY SYSTEM

The standard aircraft signal flare case was found to be of sufficient size to meet the 50 g AgI output requirement. The unique feature of the

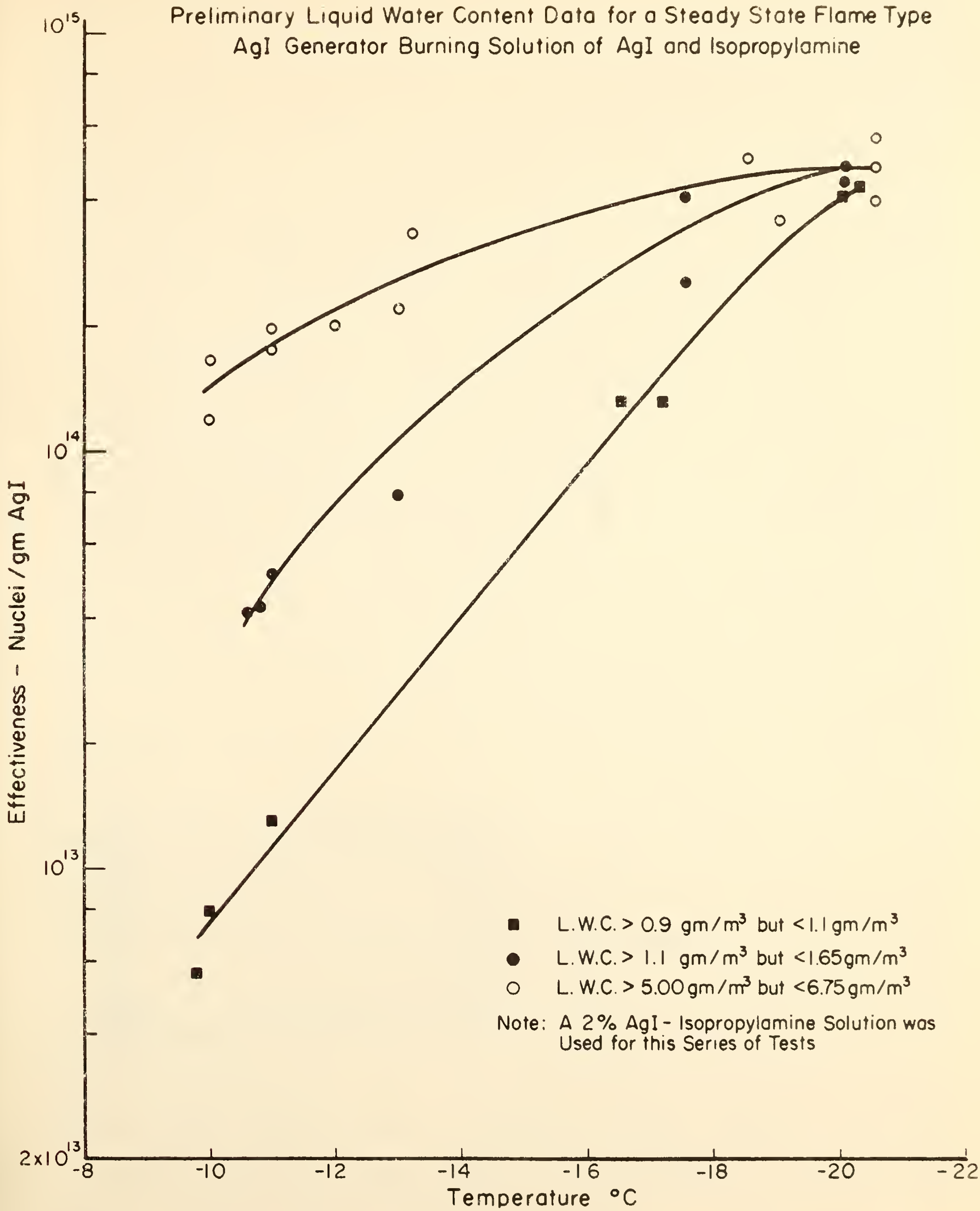

Figure 3. Silver iodide generator effectiveness as a function of cold chamber liquid water contents and temperature.

signal flare cartridge as adapted to this application was an electric squib for initiation. A sketch of this 40 mm outside diameter by 96 mm long device is shown in figure 4 and a photograph in figure 5. The flare cartridge was designed to use the exhaust gas pressure to expel the candle to assure positive ignition while providing mild fail-safe expulsion. The flares weigh a total of 120 g and cost about $14.00 each.

The firing control for the dispensing system is provided by an AN/ALE-20 flare ejector set. The ESSA Research Flight Facility (RFF) installation is a slightly modified version of the set originally manufactured by the Dynalectron Corporation for military applications. The AN/ALE-20 flare ejector consists of the following components: (1) control panel (fig. 6), (2) junction box, (3) stepping switch assembly, and (4) in the present RFF configuration, flare mounting racks. Figure 7 is a functional diagram of the overall flare-dispensing system.

The RFF B-57 aircraft carries two flare-mounting racks, each housing 56 flares. The mounting location of the rack was suggested by the RFF, the Olin Mathieson Company designed and manufactured the rack, and the RFF designed the mating hardware and electronics. Currently, the system is limited to the B-57 aircraft, but it could readily be installed on almost any other type of aircraft.

The racks themselves are 18 in. long (parallel to the longitudinal axis of the aircraft), 16 in. wide, 4 1/2 in. deep, and weigh approximately 50 lb each unloaded. Each rack contains 56 steel cylinders, which house the flare canisters arranged in an 8 x 7 matrix, which are fired in a fixed sequence. The racks are installed on the left and right undersides of the

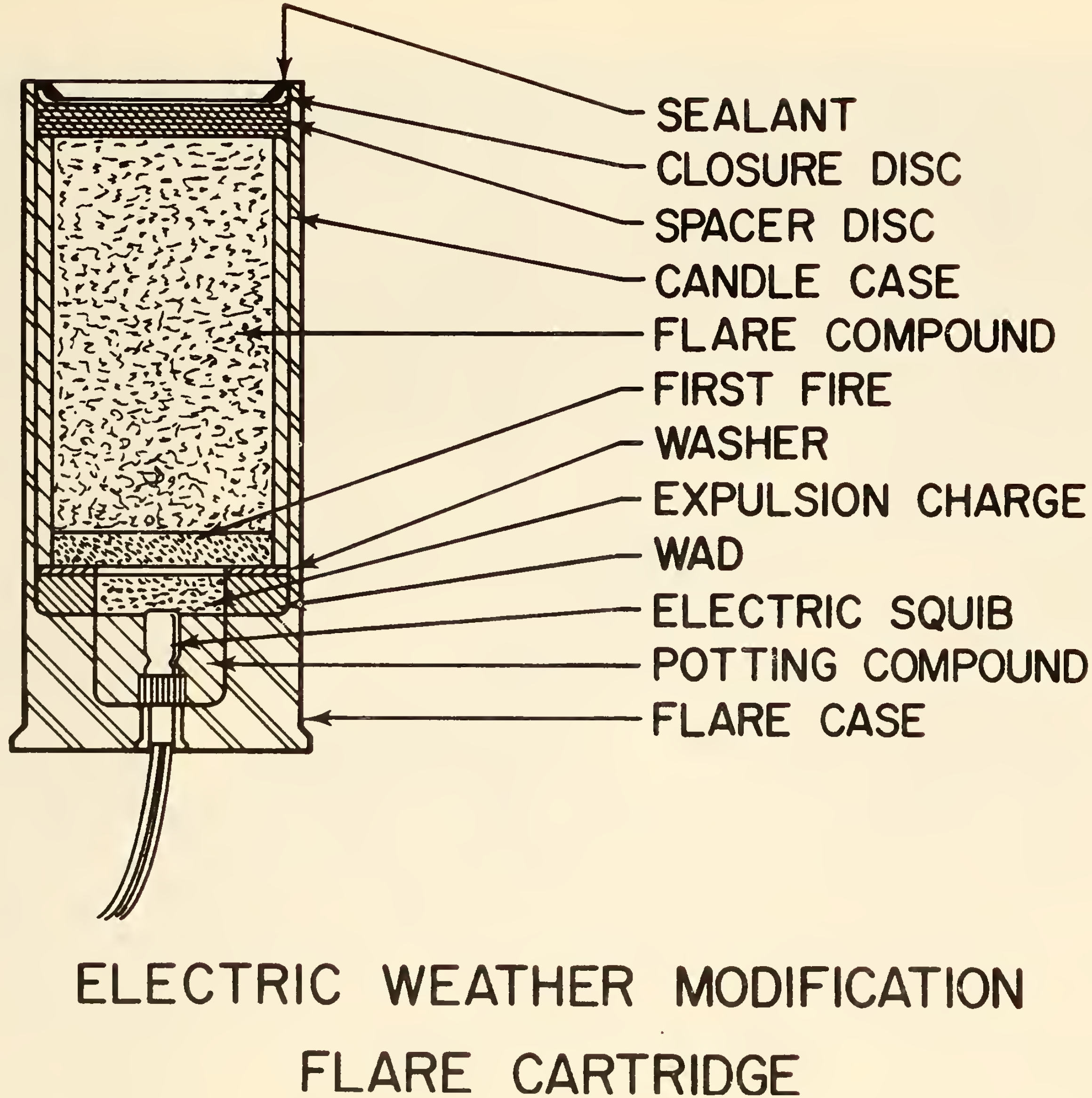

Figure 4. Diagram of flare cartridge used with mix X-1055 in 1968 Florida program; 1-20M-45A cartridges had the same case and were similar in construction.

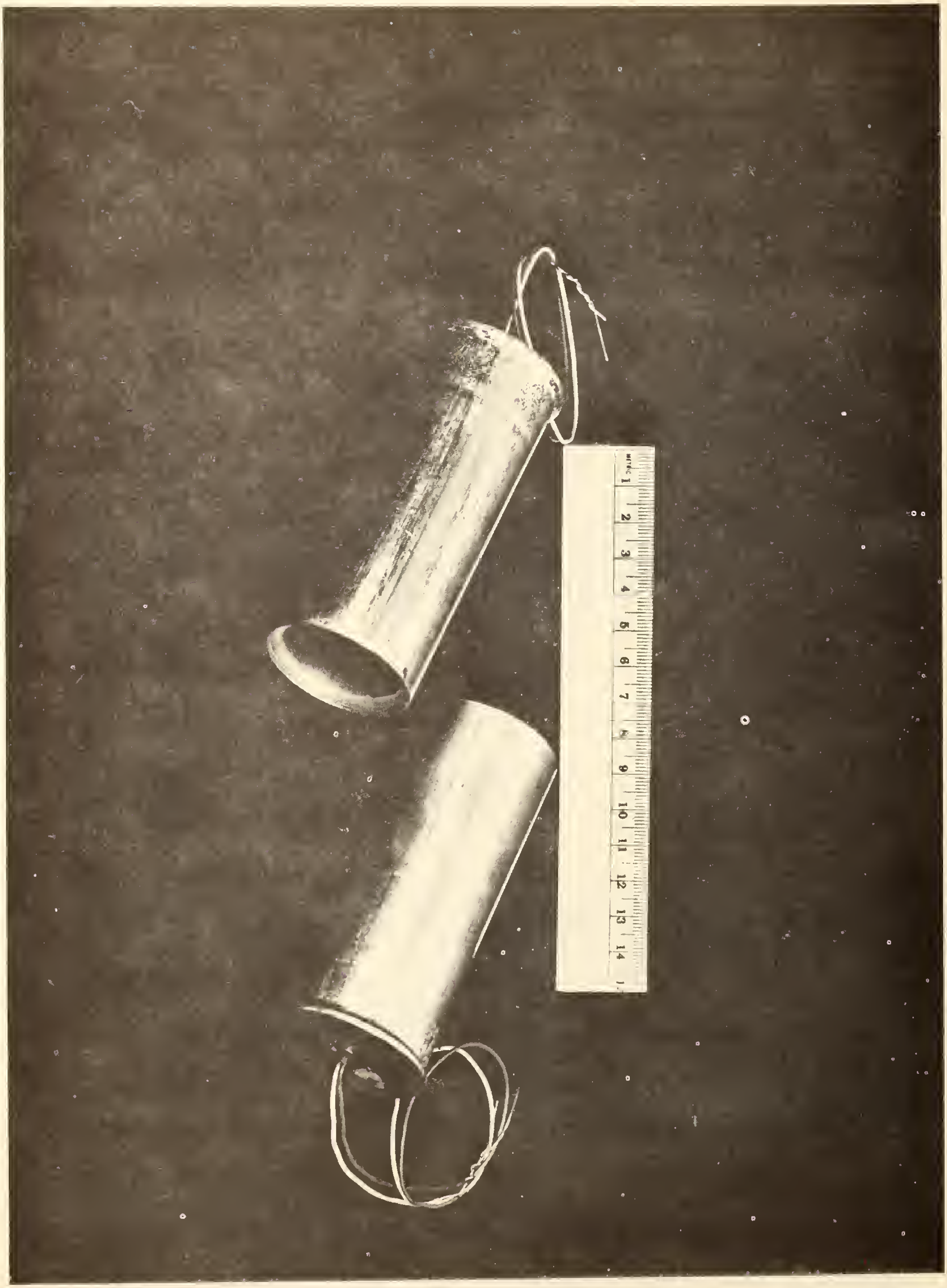

Figure 5. Photograph of two flares used in Florida 1968 experiment; centimeter scale.

Figure 6. Control panel of AN/ALE-20 flare ejector delivery system.

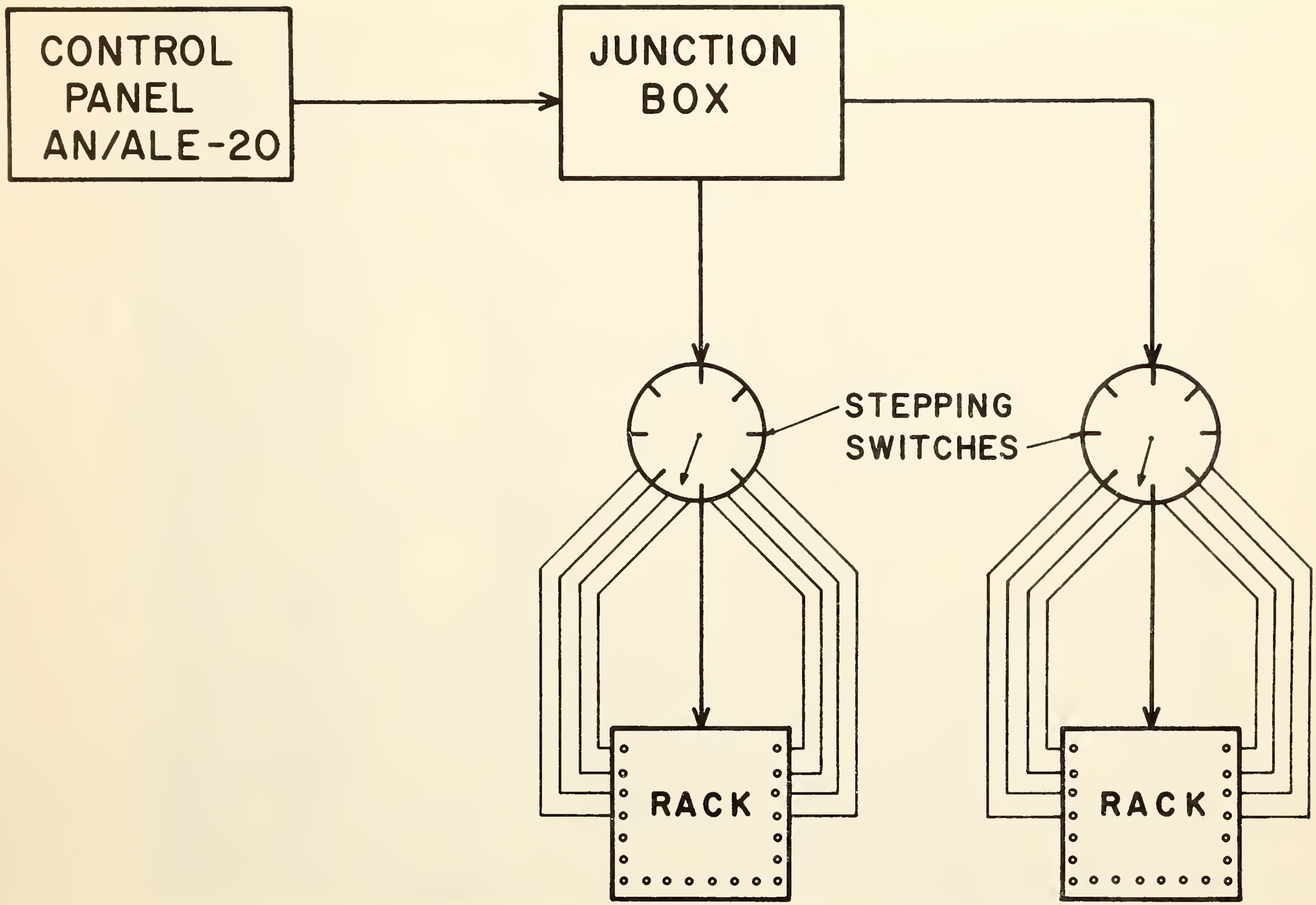

Figure 7. Functional diagram of overall flare-dispensing system.

aircraft wing, with the output end of the tubes mounted flush with the exterior surface. The flares are ejected downward into the slipstream during flight.

To eject and ignite the flare, a 28VDC, 1 A (approximately) pulse of 35-ms duration is supplied by the AN/ALE-20 flare ejector system to the selected flare (or flares). The pulse ignites the firing of the electric squib that is bonded to the back of the pyrotechnic material within each canister (fig. 4), causing the AgI flare to be ejected and the first fire or match mixture to be ignited.

The control panel (fig. 6) is located within the B-57 aircraft at the flight meteorologist's position. The setting of the controls on this component of the AN/ALE-20 system determines the number of flares ejected and the interval between flare ejections. Flare ejection can be initiated manually with the "release" button or automatically by establishing a firing program with other control panel settings (i.e., "interval selector" and "burst selector"), the selection of the number of flares per burst, and then initiating the firing program through the "release" button. The "release" button thus serves to initiate the firing program established by the other control panel settings.

Available options permit the selection of from one to three flares per burst. Under our operating conditions in 1968, this switch was set in the "1" position, which would indicate that only one flare per burst was fired. Automatic firing interval selection from 2 to 20 sec is provided. In our 1968 program the flares were ejected manually to insure an even distribution throughout the active portion of the cloud. On bombing runs, the B-57 was flown at a true airspeed of approximately 150 m sec^{-1}, and the flight meteorologist therefore pressed the "release" button approximately three times every 2 sec in order to deliver roughly one flare per 100 m of active cloud.

There are several safety items in the AN/ALE-20 flare ejector system. Radio noise filters are incorporated to prevent AC voltages in the 240 to 1000 MHz frequency range from causing erratic operation of the unit and/or accidental initiation of flare firing. There are also means of rapidly ejecting all flares in flight by a "fast train switch," which serves to salvo (simultaneously discharge) all flares from both racks in succession at a rate of one flare every 65 ms.

While the flares do have to be carefully handled and stored, they do not require specially trained pyrotechnic experts for loading. Normal loading is approximately 1 1/2 man hours per rack. Figures 8 and 9 show a side and front view of the rack in the "down" or loading position. The delivery system costs about $20,000, including installation. Details of its operation and use are described in a manual by Friedman et al. (1969).

5. FLIGHT TESTS

The major consideration in the development of this system was performance under actual flight conditions. Several configurations of units with various amounts and types of expulsion and first fire materials were evaluated in flight. The first series of tests was conducted in daylight, with observers on the ESSA DC-6 following the B-57 seeder aircraft. These tests were adequate for tailoring the types of ignition materials, but the full fall of the flares was hard to observe for measurement of burn characteristics and trajectory.

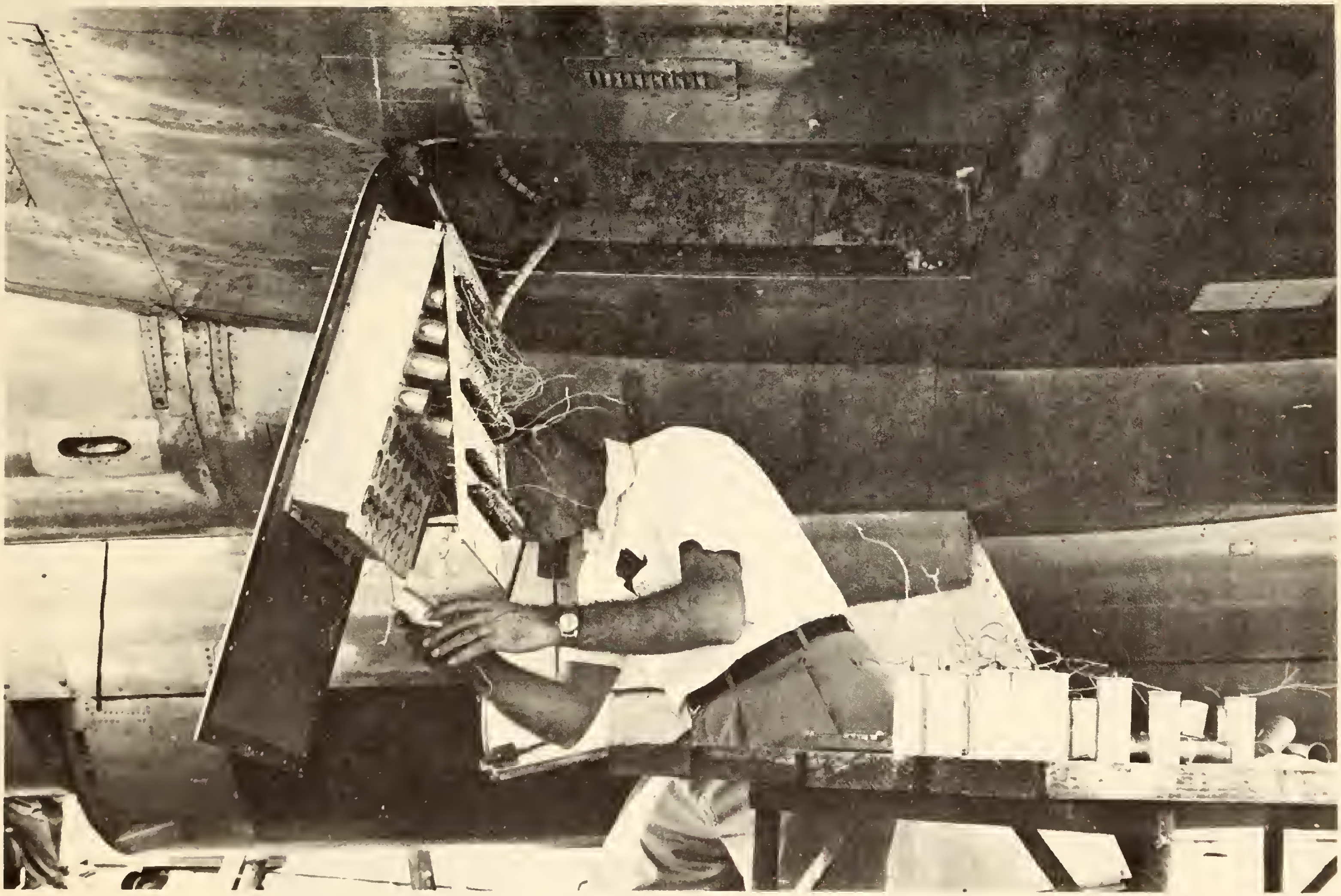

Figure 8. Side view of loading flare rack on ESSA B-57 aircraft, showing connecting circuitry from stepping siwtch (inside aircraft) to individual flares via the rack terminal strips. Nose of aircraft is on left.

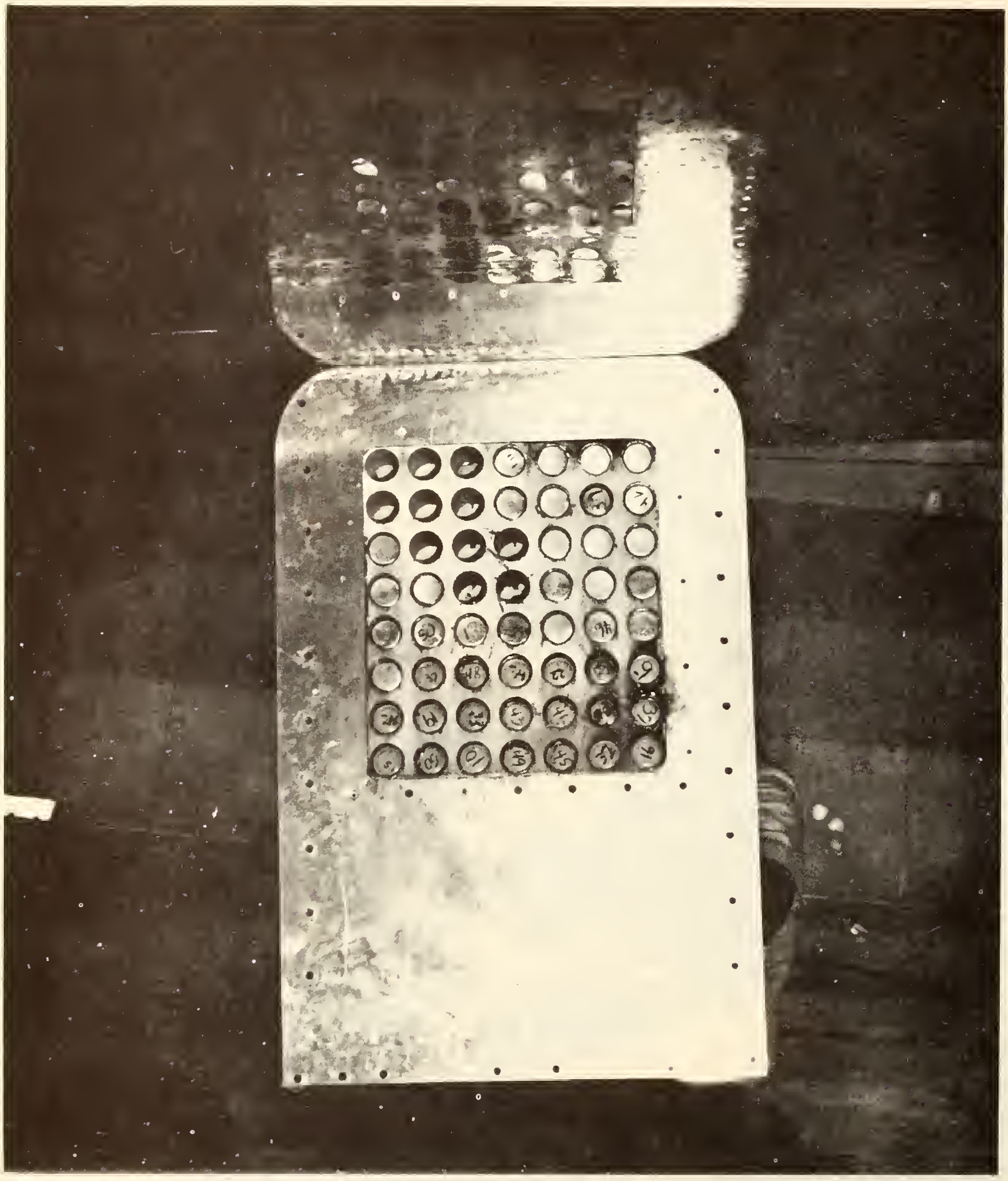

Figure 9. Front view of flare rack (in "down" position) on ESSA B-57 aircraft, looking toward tail of aircraft. Numbers on flares indicate firing sequence.

A subsequent series of nighttime flight tests was undertaken at Cape Florida State Park, located at the southern end of Key Biscayne or about 7 mi south-southeast of downtown Miami. The B-57 flights were made parallel to the beach. The flare drops were monitored by observers on the beach who were in radio communication with the aircraft. Time exposures were taken of all drops, providing information on flare reliability, burn time, and trajectory. Representative photographs of an ARC and Olin flare test are shown in figures 10 and 11, respectively. The aircraft was flown at 400 ft sec^{-1}, and the landing light was turned on for 10 sec simultaneously with the first release. The light streak is thus 4000 ft long and provides a distance scale. Both groups of flares followed similar trajectories, moving forward only about 1500 ft from the ejection point. This feature insures accurate bombing when the flares are released within the desired portion of the cloud tower; little chance exists of missing the cloud or of dropping flares into the wrong tower or into clear air.

When dropped from 20,000 ft, the Atlantic Research flares had a burn time of 30 sec and burned out in 4500 ft of fall. The Olin flares had a burn time of 80 sec and burned through about 12,000 ft. Both sets of flares thus had a terminal fall speed of about 150 ft sec^{-1}.

The Olin flares were tested with units having both 10 g and 20 g of first fire material. Twenty-five of 25 units with 20 g first fire burned completely. Only 9 of 25 units with 10 g of first fire burned completely. The other units went out after the first fire was consumed because of the high velocity and tumbling rate during the first few seconds after ejection. Twenty grams of first fire sustained burning during deceleration to a velocity where the X1055 would remain ignited.

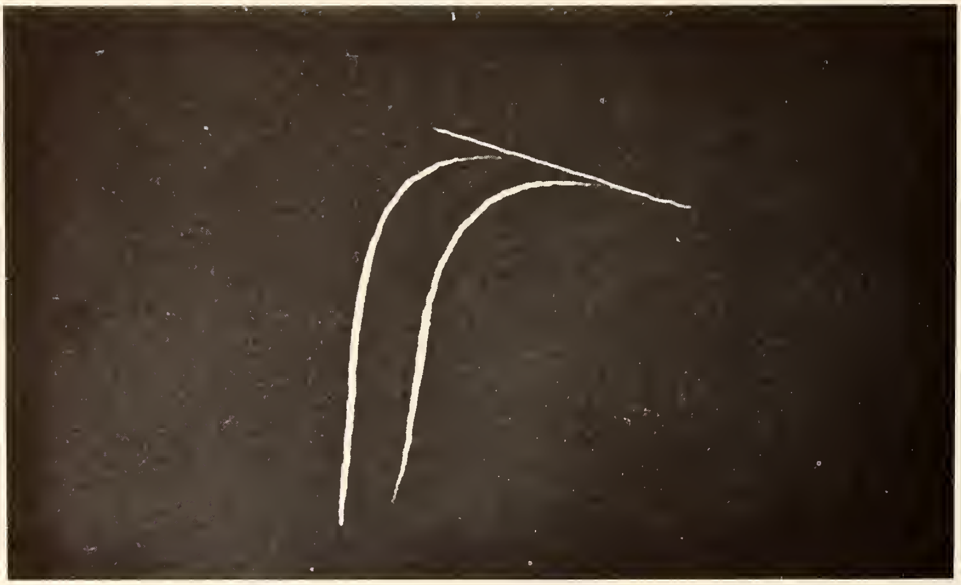

Figure 10. Time exposure photograph of nighttime release of two flares ejected at 20,000 ft.

Figure 11. Time exposure photograph of nighttime release of five flares ejected at 20,000 ft. Streak on top is aircraft's landing light, on for exactly 10 sec. Aircraft's true airspeed is 400 ft sec^{-1}.

A breakdown of the tests with 20 g of first fire is as follows:

Altitude (ft)	Successful Tests
20,000	15 of 15
15,000	2 of 2
12,000	2 of 2
11,000	3 of 3
10,000	3 of 3

The low altitude tests were conducted (over water) to check the calculated vertical fall distance during burning. This was 10,000 ft when the drops were made at 10,000 ft. When drops are made from 20,000 ft, the lower ambient air density permits the 20 percent greater fall distance.

Unfortunately, the 1-20M-45A flares had both ejection and ignition problems due to poor squibs at this stage of development. Only 50 percent of the 30 flares tested ejected, and of these only 76 percent burned completely. A slightly better ejection record was obtained in the field.

On the first 2 days of the program, 1-20M-45A flares were used with a correspondingly larger number ejected to compensate for unreliability. Then the switch was made to the more reliable X-1055 flares. Unfortunately, some with the 10 g first fire mix were inadvertently used on the last 5 days of the program. Careful post-operational checks of the flare loading showed that only one seeded cloud (the first one) could have received as little as 400 g of silver iodide, while the remaining ones almost surely received 650 g or more.

6. DESIGN OF THE 1968 FLORIDA EXPERIMENT

The field phase of the 1968 Florida cumulus seeding program encompassed the period May 15 through June 1, during which time there were 13 days of successful flight operation. Participating in the program were the Experimental Meteorology Branch (EMB) and the Research Flight Facility (RFF) of the Environmental Science Services Administration (ESSA), the Naval Research Laboratory (NRL), the Radar Meteorology Laboratory of the University of Miami, the U. S. Air Force, and Meteorology Research, Inc. (MRI) of Altadena, California.

Aircraft altitudes and tracks flown are shown in figure 12. The RFF supplied two aircraft, a DC-6 for command control, cloud physics measurements, and photogrammetry at 19,000 ft ($\sim -9°C$), and a B-57 for seeding and monitoring cloud top. The NRL supplied two aircraft, a WC-121 Super Constellation for cloud physics measurements at 17,000 ft ($\sim -5°C$) and a S-2D for measurement of rainfall and other parameters at cloud base. The Air Force provided a C-130 for dropsondes at 90 min intervals on experimental days. The Radar Laboratory contributed its calibrated 5 and 10 cm ground radars, which were used to infer rainfall from cloud base. These radars and their use will be discussed fully in a subsequent paper. MRI installed and operated a condensation nucleus counter, a continuous cloud replicator and a hydrometeor foil sampler on the ESSA DC-6 and installed a foil sampler on the Navy S-2D.

The numerical cumulus model developed by Simpson and Wiggert (1969) was run on the Miami 1200 GMT radiosonde each possible operational day. If the model predicted that all horizontal tower sizes would either grow naturally or would fail to grow even if seeded, no operation was scheduled.

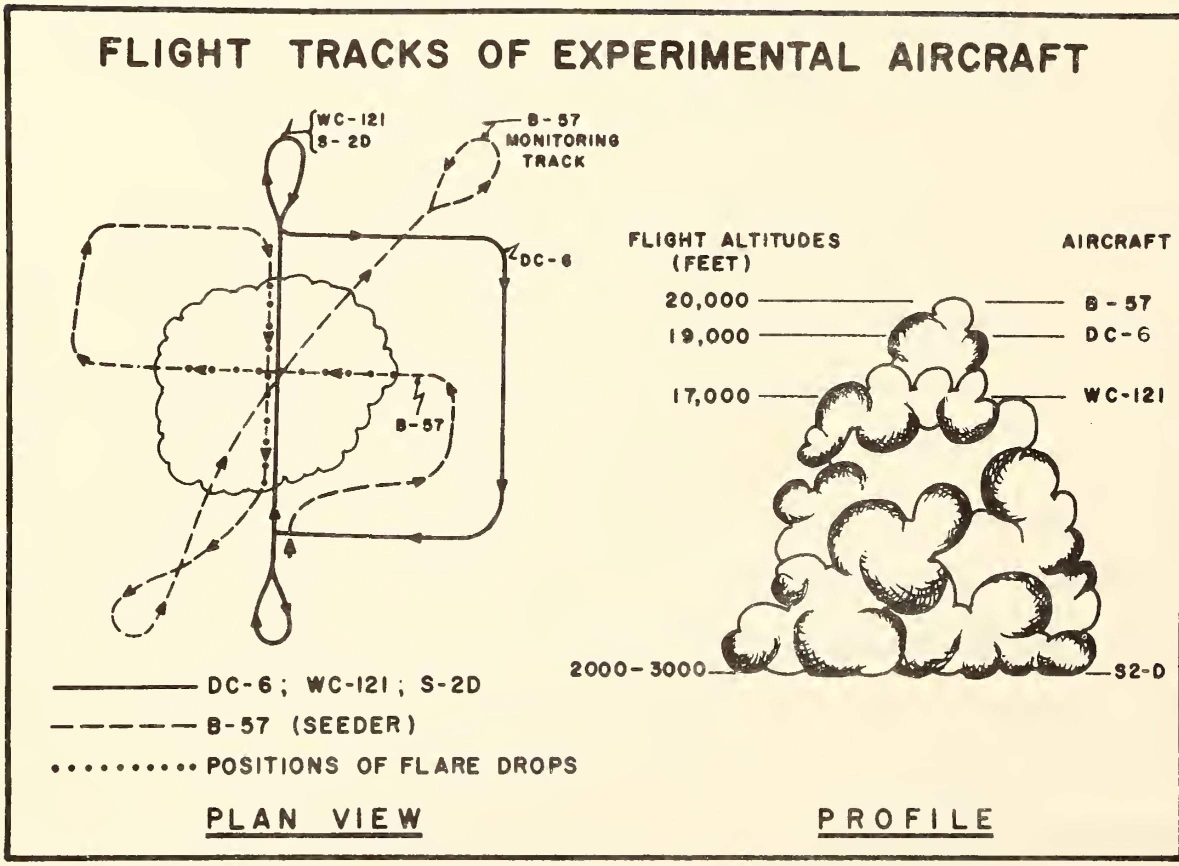

Figure 12. Plan view (left) and profile view (right) of aircraft tracks in Florida 1968 cumulus experiment.

If it predicted good seedability or potential growth from seeding (see Simpson et al. 1967), the command DC-6, the WC-121 and Air Force C-130 were launched for a day's operation. After rendezvous at a predesignated point, these aircraft surveyed the experimental area for clouds that might meet the selection criteria. These were supercooled clouds that must be relatively isolated, with tops in the 19-26,000 ft range.

If suitable clouds were found, or expected within an hour, the shorter range seeder and cloud base aircraft were launched. When all project aircraft were joined together (by radar and/or visually) a cloud was selected for experimentation by one of the first two authors. The monitoring aircraft (DC-6, WC-121, and S-2D) made an initial penetration of the cloud while the seeder aircraft broke from a position slightly above and to the right of the command aircraft to set up for a seeding run (fig. 12).

If the cloud chosen neither died nor grew above about 26,000 ft, the final go-ahead was radioed to the seeder pilot; he opened one envelope from his randomized set of instructions for a decision whether or not to seed. Regardless of which decision was made, the flight pattern was exactly the same: one pass through cloud top, followed by a pass at right angles to the first approximately 2-3 min later. If he had received a seed instruction, 10 silver iodide flares[1] were dropped at about 100 m intervals on each pass. Following the seeding run, the B-57 aircraft monitored the cloud top, following it up as it grew. In addition to frequent top height reports, the pilot obtained valuable nose camera motion pictures and a sounding of the air near the cloud.

[1] When 1-20M-45A flares were used, 15 per pass were dropped to compensate for unreliable ignition.

The Air Force C-130 remained over water but as close as possible to experimental clouds, ejecting dropsondes from 30,000 ft and recording winds and temperatures at that level. At the time of cloud selection, the scientists at the University of Miami Radar Laboratory were informed of cloud location. They immediately began monitoring the cloud in a set sequence to be described elsewhere.

All aircraft monitored the experimental cloud for as long as practicable (sometimes 1 hour) after the seeding pass. The NRL aircraft made repeated penetrations of the cloud, while the DC-6 flew a compromise pattern, a rectangle with the cloud centered on one of the long sides of the rectangle (fig. 12). Three of the legs provided cloud photogrammetry (see Simpson, 1967), while the last leg served as a cloud penetration run.

The randomization scheme adopted for the May 1968 program was similar to that used in the 1965 Stormfury experiments (Simpson et al., 1967). Two hundred envelopes in sets of 10 were prepared by Mr. J. Cotton of the Meteorological Statistics Group of ESSA. The instructions were weighted 0.65 versus 0.35 in favor of the seed instruction. There were not more than two consecutive "no seed" and not more than three consecutive "seed" instructions. The details of the series were not known to anyone involved in the project, nor did the experimenters know of the actual decision in each case until the aircraft landed on completion of a day's work. A new set of 10 envelopes was begun on each day.

7. FIRST RESULTS OF THE FLORIDA 1968 SEEDING PROGRAM

A total of 19 experimental clouds was selected from the command control aircraft. Fourteen were seeded and five were used as controls.

The dates and locations of all experimental clouds are shown in figure 13. A cloud summary, for each cloud is given in table 8. The cloud top heights were first measured by the B-57 and then checked by photogrammetry. Heights are given in pressure altitude.

The average growth following the seeding run was 12,000 ft for the 14 seeded clouds and 1,100 ft for the five control clouds. The difference is 10,900 ft, which is signficant to better than 1/2 percent based on a two-sided "t" test. The average maximum top of the seeded clouds was 35,300 ft (pressure altitude), and the corresponding figure for the controls was 25,800 ft. Thirteen of the 14 seeded clouds underwent explosive growth; one died without growth. Of the 13 explosive growths, 10 occurred soon after seeding and involved the actual tower seeded, while three were delayed or "hesitation" growths, where a newer tower than the one originally selected for seeding appeared and grew.

8. CONCLUSIONS AND FUTURE WORK

In terms of cloud growth, the 1968 Florida program was much more successful than the 1965 Stormfury Caribbean program. In 1968, both a larger fraction of the seeded clouds grew (93% vs. 66%) following seeding, and the average seeded cloud grew more than twice as much (10,900 ft vs. 5,200 ft). The main reason was the use of the computer program in real time so that all but one case of predicted poor seedability were excluded. In 1965 it was found only *a posteriori* that the one-third of the seeded clouds that failed to grow were seeded under conditions of poor seedability.

Other reasons for the better results in 1968 are probably a more effective seeding technique and the more continental character of the clouds.

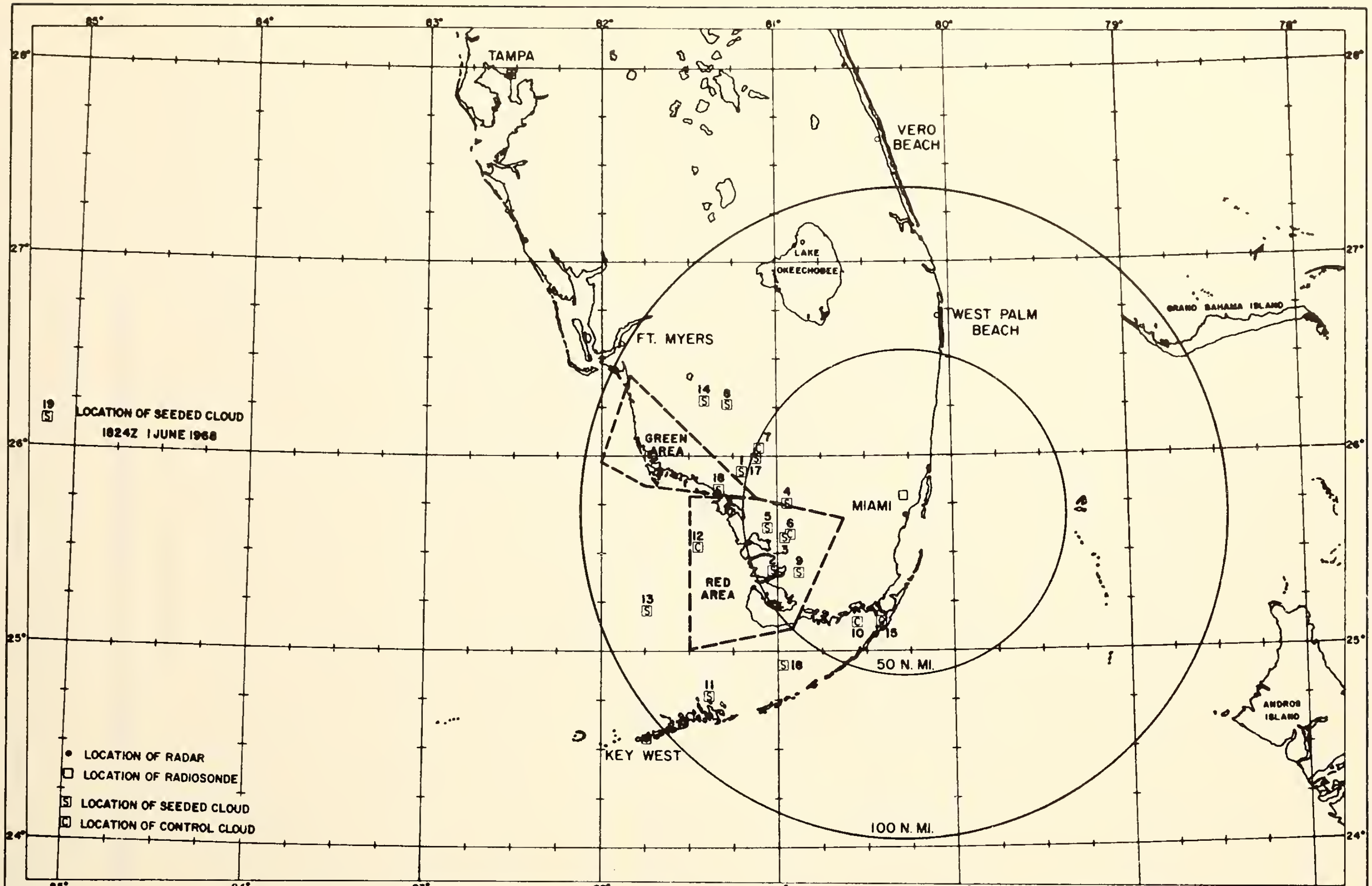

RED AND GREEN AREAS, PRIMARY SEEDING AREAS FOR FLORIDA CLOUD SEEDING PROJECT. MAY 1968

DATES AND TIMES FOR NUMBERED SEEDED AND CONTROL CLOUDS

1. 1930Z 15 MAY	4. 1937Z 16 MAY	7. 1748Z 20 MAY	10. 1738Z 26 MAY	13. 1618Z 27 MAY	16. 1750Z 30 MAY
2. 1753Z 16 MAY	5. 1755Z 19 MAY	8. 1908Z 20 MAY	11. 1823Z 26 MAY	14. 1640Z 28 MAY	17. 1842Z 30 MAY
3. 1822Z 16 MAY	6. 2006Z 19 MAY	9. 2034Z 21 MAY	12. 1529Z 27 MAY	15. 1659Z 30 MAY	18. 1942Z 30 MAY

Figure 13. Location of seeded (S) and control (C) clouds in Florida 1968 cumulus experiment. Dash-outlined areas are so-called "red" and "green" areas, set aside by the Federal Aviation Administration as the main land areas to be used in the experiment.

Table 8. Cloud Summary Data From 1968 Florida Cumulus Program

DATE	EXPERIMENTAL CLOUD NUMBER	DAILY CLOUD NUMBER	TIME OF FIRST DC-6 PASS (GMT)	TIME OF SEEDING RUN (GMT)	DURATION MIN	DURATION SEC	ACTION	SEEDING ALTITUDE (WITHIN 100 FT.) *	ESTIMATED TOP TEMP. AT SEEDING (TO NEAREST °C)	TOP AT SEEDING (FEET)*	MAX TOP AFTER SEEDING (FEET) *	TOP GROWTH AFTER SEEDING RUN
MAY/15/68	1	5	1930	193859 - 194324	4	25	S	19,100	-35.0	30,000	35,000	5000
MAY/16/68	2	5	1753	180050 - 180450	4	20	S	20,200	-10.0	19,000	19,000	0
MAY/16/68	3	6	1822	182409 - 182901	4	52	S	20,200	-16 0	22,000	40,500	18,500
MAY/16/68	4	8	1937	194855 - 195222	3	27	S	20,200	-18.0	23,000	45,000	22,000
MAY/19/68	5	1	1755	175520 - 175853	3	33	S	20,300	-15 0	22,000	34,000	12,000
MAY/19/68	6	4	2006	201035 - 201232	1	57	NS	20,000	-13.0	21,500	21,500	0
MAY/20/68	7	1	1748	175757 - 180051	2	54	NS	20,300	-17 0	23,000	23,000	0
MAY/20/68	8	5	1908	190945 - 191230	2	45	S	18,500	-12.0	20,000	36,000	16,000
MAY/21/68	9	2	2034	203555 - 203825	2	30	S	19,200	-16 0	23,000	40,000	17,000
MAY/26/68	10	9	1738	174138 - 174440	3	02	NS	20,000	-13 0	21,000	21,000	0
MAY/26/68	11	11	1823	182455 - 182800	3	05	S	19,300	-24.0	25,000	36,000	10,000
MAY/27/68	12	1	1529	153230 - 153504	2	34	NS	20,200	-34 0	29,500	31,500	2,000
MAY/27/68	13	2	1618	162600 - 162855	2	55	S	20,250	-27.0	26,000	37,000	11,000
MAY/28/68	14	5	1635	163850 - 164137	2	47	S	18,700	-12.0	19,500	32,500	13,000
MAY/30/68	15	6	1659	170137 - 170440	3	03	NS	20,300	-31.0	28,500	32,000	3,500
MAY/30/68	16	7	1750	175147 - 175437	2	50	S	21,000	-22.0	25,000	33,000	8,000
MAY/30/68	17	8	1842	184845 - 185141	2	56	S	20,400	-31 0	28,500	37,000	8,500
MAY/30/68	18	10	1942	193650 - 193856	2	06	S	20,000	-16 0	21,000	38,000	17,000
JUNE/1/68	19	8	1824	182817 - 183059	2	42	S	20,200	-15.0	21,000	31,000	10,000

* HEIGHTS IN PRESSURE ALTITUDE

More and smaller pyrotechnics ejected on two successive passes at right angles not only give better distribution within a cloud but enable fresh towers to receive seeding material. Continental clouds quite likely have a greater tendency than maritime clouds for repeated tower generation in or near the same spot. Additional effects of continentality, such as higher water contents distributed in more, smaller drops, are also being investigated.

Further work with the data from this program falls into five main categories:

1) Quantitative analysis of the rainfall data on all "go" clouds and numerous others. The primary analysis tool is the calibrated ground radars, supplemented by the S-2D aircraft foil sampler records and rain gage measurements.

2) Numerical model studies of all "go" clouds based on the actual sounding nearest the cloud in space and time.

3) Analysis of each cloud with the penetration data obtained on the monitoring aircraft to study the dynamics and physics of each cloud and the changes following seeding.

4) Photogrammetric study of each cloud based on the aircraft time-lapse cameras and on the flight tracks determined by Doppler navigation.

5) Satellite, synoptic, and aircraft study of the weather and cloud conditions over and near the Florida peninsula on each operational day to determine the context of the experiment and to delineate conditions favorable for seeding both individual cumuli and groups of cumuli. An attempt will be made to determine whether seeding individual clouds had mesoscale or larger scale effects on cloud patterns.

Preliminary results of the radar rainfall study indicate that the precipitation from seeded clouds averaged about double that from control clouds. These results also suggest that the rain increases were on the order of 100 to 150 acre-feet per cloud, which could be important. Unfortunately, the small sample and large cloud-to-cloud variability in precipitation reduces the statistical significance of the rainfall results to the 25 percent level when a two-sided "t" test is used. Calculations show that if the experiment was repeated one more time with identical outcome, and the results of both experiments combined, the rainfall increases would be significant to better than 3 percent. Hence it is imperative to repeat this experiment at least once.

9. ACKNOWLEDGMENTS

The writers are deeply indebted to many persons and organizations who helped with the planning and execution of this experiment and in the design and fabrication of the necessary technology.

We dedicate this effort to Dr. Robert M. White, Administrator of ESSA, who first suggested this program and supported it through many vicissitudes.

We are deeply grateful to the ESSA Research Flight Facility and its director, Mr. Howard J. Mason, Jr. The whole of RFF went far beyond the call of duty in the implementation of this program. Particularly noteworthy contributions were made by RFF's Marshall Hatch and Harlan Davis, flight meteorologists' on the B-57 and DC-6, respectively; Jack Lubin, Chief Controller; and Paul Connor for operation, installation and information on the flare delivery system. Richard Decker and Frank Norimoto capably carried out the photography.

We also thank the Federal Aviation Administration for handling this difficult operation in an area with heavy air traffic and for the fine cooperation of their Miami staff at both the planning and execution stages of the work; the senior staff of the Naval Weapons Center, China Lake, California, for many useful discussions on the physics, design and use of pyrotechnics in relation to cloud seeding; and the Naval Air Systems Command, who, through Mr. Robert Ruskin of the Naval Research Laboratory, purchased and provided the X-1055 flares used in the experiment.

10. REFERENCES

Battan, L. J., (1966), Silver-iodide seeding and rainfall from convective clouds, J. Appl. Meteorol. 5, 669-683. See table 1.

Battan, L. J., (1967), Silver-iodide seeding and precipitation initiation in convective clouds, J. Appl. Meteorol. 6, 317-322. See table 1.

Bethwaite, F. D., E. J. Smith, J. A. Warburton and K. J. Heffernan (1966), Effects of seeding isolated cumulus clouds with silver-iodide, J. Appl. Meteorol. 5, 513-520. See table 1.

Braham, R. R., Jr., L. J. Battan and H. R. Byers, (1957), Artificial nucleation of cumulus clouds, Meteorol. Mongraphs 2, 47-85 (Am. Meteorol. Soc., Boston, Mass.). See table 1.

Davis, C. I. and R. L. Steele (1968), Performance characteristics of various artificial ice nuclei sources, J. Appl. Meteorol. 7, 667-673.

Davis, L. G., Kelley, J. I., Weinstein, A., and Nicholson, H., (1968), NSF Report #12A. Final Report NSF GA-777, The Pennsylvania State University, University Park, Pennsylvania, 128 pp. See table 1.

Flueck, J. A., (1968), A statistical analyses of Project Whitetop's precipitation data. Proc. First Natl. Conf. on Weather Modification, Albany, New York, 26-35. See table 1.

Friedman, H. A., G. Conrad, and P. Connor (1969), Research Flight Facility. Description of instrument systems. Part 3. ESSA Tech. Rept. (to be published).

Fukuta, N., 1958, Experimental investigations on the ice-forming ability of various chemical substances, J. Meteorol. 15, 17-26.

Jiusto, J. and W. C. Kochmond (1968), Condensation on non-hygroscopic particles, Journal de Recherches Atmosphériques 3, 19-24.

Korienko, E. E., B. N. Leskow and I. P. Polvina (1968), Results of seeding clouds with solid CO_2 aimed at the stimulation of precipitation over the Ukraine. Proc. Intern. Conf. on Cloud Physics, Toronto, Canada, 724-729. See table 1.

MacCready, P. B. (1959), The lightning mechanism and its relation to natural and artificial freezing nuclei, Recent Advances in Atmospheric Electricity, 369-381 (Pergamon Press, London).

Mossop, S. C. (1968), Silver iodide as nucleus for water condensation and crystallization, Journal de Recherches Atmospheriques 3, 185-190.

Neumann, J. K., R. Gabriel and A. Gagin (1967), Cloud seeding and cloud physics in Israel. Results and Problems, International Conference on Water for Peace, 53. See table 1.

Ruskin, R. E., 1967, Measurement of water-ice budget changes at -5°C in AgI-seeded tropical cumulus, J. Appl. Meteorol. 6, 72-81.

St. Amand, P., W. Finnegan, and F. K. Odencrantz (1969), Effects of the type of nucleant on modification of clouds for the stimulation of rainfall, Naval Weapons Center, China Lake, Calif. (to be published).

Scheffee, R. S., R. W. Evans, and C. Huggett (1967), Development of a pyrotechnic cloud seeding system. Part 1: Development of pyrotechnic compositions, Report by Atlantic Research Corporation to ESSA under Contract Cwb-11346, 42 pp.

Scheffee, R. S. and R. L. Steele (1968), Production of silver iodide smokes by pyrotechnics. Proc. First Natl. Conf. on Weather Modification Albany, New York.

Simpson, J. (1967), Photographic and radar study of the Stormfury 5 August 1965 seeded cloud, J. Appl. Meteorol. 6, 82-87.

Simpson, J., R. H. Simpson, J. R. Stinson, and J. W. Kidd (1966), Stormfury cumulus experiments: Preliminary results 1965, J. Appl. Meteorol. 5, 521-525.

Simpson, J., G. W. Brier, and R. H. Simpson (1967), Stormfury cumulus seeding experiment 1965: Statistical and main results, J. Atmospheric Sci. 24, 508-521.

Simpson, J. and V. Wiggert (1969), Models of precipitating cumulus towers, Monthly Weather Rev. (in press).

Steele, R. L. (1968), Evaluation of ice nuclei sources and their development, Production and Delivery of Cloud Nucleating Materials, Project Skywater Proceedings, Skywater Conference III, Office of Atmospheric Resources, Bureau of Reclamation, U. S. Dept. of Interior, Denver, Colorado, 51-92.

Steele, R. L. and C. I. Davis (1969), Variation of ice nuclei effectiveness with liquid water, J. Atmospheric Sci. 26 (in press).

U.S. DEPARTMENT OF COMMERCE
Environmental Science Services Administration
Research Laboratories

ESSA Technical Memorandum ERLTM-AOML 2

PRECIPITATION RESULTS FROM A PYROTECHNIC CUMULUS SEEDING EXPERIMENT

William L. Woodley

Experimental Meteorology Laboratory

Atlantic Oceanographic and Meteorological Laboratories
Miami, Florida
Augus 1969

TABLE OF CONTENTS

ABSTRACT

In an attempt to specify the changes in precipitation produced by alteration of cloud dynamics, airborne seeding with silver iodide pyrotechnics was carried out in South Florida during May 1968. Emphasis was placed on altering cloud dynamics and on increasing precipitation as a by-product of the dynamic alteration. Nineteen clouds were studied; 14 were seeded and 5 unseeded (controls) as dictated by the randomized seeding instructions. Each of the 14 clouds received approximately 1 kg of silver iodide smoke. Seeding was found to be effective in promoting increased cloud growth; the average growth difference between the seeded and control clouds was 11,400 ft, significant at the 1 percent level. The induced growths took many forms and in many cases were produced in clouds containing significant amounts of natural ice.

A 10-cm radar with iso-echo contouring was used to infer changes in precipitation. Analysis indicates that seeding increased rainfall an average of 100 to 150 acre-feet 40 min after the seeding pass, an increase of over 100 percent. The result is changed little by using an alternate analysis scheme or by including 5 additional control clouds selected after the program. The rainfall increases would probably have been greater if calculations had been possible for entire cloud lifetimes. Because of heavy natural rains during the program, the rainfall computations must be viewed with reservation. The significance of the rainfall results ranged between 5 and 20 percent based on two-sided statistical tests.

Comparison between radar and rain gage rainfall demonstrates that the rainfall calculations are probably underestimates by no more than 30 percent. The Z-R relation used in the rainfall calculations was equally valid for the seeded and control clouds. The amount of rain from the seeded clouds was positively correlated with the maximum top growth following seeding. The seeded rainfall increases were apparently the result of larger and more lasting clouds that were the by-product of the dynamic invigoration; there is no evidence that they were produced by improved efficiency of natural precipitation processes through disturbance of stability of supercooled drops. The natural glaciating behavior of the experimental clouds would appear to preclude the "colloidal stability" approach to rainfall augmentation from Florida cumuli.

PRECIPITATION RESULTS FROM A PYROTECHNIC CUMULUS SEEDING EXPERIMENT

William L. Woodley

1. INTRODUCTION

Since laboratory discoveries of the ice nucleating properties of dry ice (Schaefer, 1946) and silver iodide (Vonnegut, 1947), there have been numerous attempts to increase precipitation by seeding supercooled cumulus clouds with these materials. Most efforts have been predicated on the production of "colloidal instability" in a cloud containing supercooled drops. The theoretical principles for this type of seeding have been formulated for many years.

Seeding with silver iodide or dry ice induces ice particle formation in a supercooled cloud that has little ice because natural ice nuclei are lacking. The stability of such a cloud is disturbed by the ice particles, because the equilibrium vapor pressure for ice particles is lower than that for water drops at temperatures below 0° C. Because of this vapor pressure difference, the ice particles grow by diffusion at the expense of the cloud vapor and water drops. When they are large enough to fall relative to the cloud updraft, they grow further by accretion of other cloud hydrometeors. If conditions are right, the falling particles grow large enough to reach the ground before evaporating. Between one (McDonald, 1958) and 10 (Fletcher, 1962; Mason, 1962) artificial ice nuclei per 10 liters of cloud air are considered optimum for promoting precipitation growth. Massive seeding of cumulus clouds, producing many ice crystals, is avoided because the competition for cloud vapor reduces their chances of reaching precipitation size.

Seeding to produce"colloidal instability" is a passive approach to rainfall enhancement because its aim is to precipitate some fraction of the water in the cloud during seeding. The active approach would be the modification of the buoyancy forces and circulations that sustain the clouds, referred to here as dynamic modification. If it were possible to artificially increase cloud buoyancy and invigorate cloud circulations, a larger and more lasting cloud would result. Water in addition to that contained in the cloud at seeding would be processed, and precipitation increases would be the natural consequence.

It has long been recognized that seeding to transform a supercooled cumulus cloud to ice might increase cloud buoyancy. From the first law of thermodynamics, one can show that the fusion heat release and the conversion of the vapor excess over ice saturation following seeding might produce a warming of 0.5 to 1.0° C, even if only a fraction of the liquid water is artificially glaciated. Because clouds are rarely more than 1° C warmer than their environments, seeding might, under ideal circumstances, effectively double cloud buoyancy and lead to increased growth. One hundred ice nuclei per liter of cloud air is thought to be the minimum number for sudden and complete glaciation (McCready, 1959) -- a number that, interestingly enough, in the "colloidal instability" approach to rainfall enhancement is thought to represent overseeding.

Although there is a theoretical basis for dynamic modification, as late as 1960 serious doubts existed that man could significantly affect cloud dynamics (McDonald, 1958). Except for isolated cases (Kraus and Squires, 1947; Orr, Fraser, and Pettit, 1949; Vonnegut and Maynard, 1952), dynamic modification was not observed during seeding experiments before 1960. There are several reasons for this circumstance. The objective of most of the early experiments was to alter cloud precipitation processes directly, not cloud dynamics. Also, the quantities of seeding material required for dynamic alteration were rarely used, either because of a desire to avoid overseeding or because the technology for massive seeding was lacking.

Since 1960, more attention has been given to the possibility of modifying cloud buoyancy forces and circulations. Individual cumulus clouds have been seeded with silver iodide from an aircraft penetrating a cloud. (In such experiments there is greater certainty that the silver iodide reaches the right portions of the clouds in the intended concentrations at the right moment to be effective.) Notable examples are the Stormfury cumulus experiments over the Caribbean south of Puerto Rico in 1963 (Malkus and Simpson, 1964) and in 1965 (Simpson et al., 1967), in which impressive cloud growth after seeding occurred. In the 1965 experiment, 23 clouds were studied; 14 were seeded and 9 were controls as dictated by the randomized seeding instructions. Individual seeded clouds received up to 34 kg of silver iodide smoke. The average vertical growth difference between the seeded and control clouds was 1.6 km, which is significant at the 1 percent level. The top heights of unseeded and seeded clouds predicted by the Stormfury dynamic cumulus model agreed very well (correlation of 0.97, significant at the 1 percent level) with the observed top heights. The behavior of the seeded clouds could only be explained by incorporating the postulated effects of seeding (fusion heat release and establishment of saturation with respect to ice). This result demonstrated that the physical hypothesis behind dynamic modification has basis in fact and that man can alter cloud dynamics under specifiable conditions. No specification of the effects of dynamic invigoration on precipitation was obtained in these experiments.

Following the Stormfury experiments, seeding in Pennsylvania (Davis and Hosler, 1967) and Arizona (Davis et al., 1968) resulted in impressive cloud growth. In the Arizona experiments, nine pairs of clouds were the subject of randomized seeding and received up to 400 g of silver iodide, considerably less than the amount used in Project Stormfury. The average tops of the seeded clouds were 5900 ft higher than the corresponding controls, a difference that is significant at the 1 percent level. Seeded cloud behavior predicted by a dynamic cumulus model developed at Pennsylvania State University (Weinstein, 1969) agreed very well with the observations. A 10-cm radar, calibrated twice daily, was used to infer changes in precipitation following seeding. The average rainfall measured at cloud base from the "core" of the cloud was 4.52 mm for the seeded clouds compared with the 1.52 mm for the control clouds, an increase of 186 percent, which is significant at slightly less than 5 percent. Because of the high cloud bases and dry environment, it is questionable how much of the rainfall increase produced by seeding actually reached the ground.

There has been little study of the effect of dynamic changes on precipitation. Where attempts were made to measure the effect of dynamic modification on precipitation, no evidence was found of real precipitation increases on the ground.

2. BACKGROUND OF THE FLORIDA PROGRAM

Individual cumulus clouds growing over and near the Florida peninsula were seeded with silver iodide in May 1968. The experiment was conducted jointly by ESSA and the Naval Research Laboratory (NRL) with the participation of the Radar Meteorological Laboratory of the University of Miami, the U. S. Air Force, and Meteorology Research, Inc. (MRI) to study with aircraft and calibrated ground radars the induced dynamic and precipitation changes in the seeded clouds and to compare these with the unseeded control clouds, both chosen on a statistically randomized basis. Simpson et al. (1969) discuss the experiment, the pyrotechnic seeding system, and the first results. The seeding was designed to glaciate the supercooled portions of the clouds suddenly and completely to provide the impulsive fusion heat release necessary for dynamic invigoration and increased cloud growth. Precipitation changes were expected as the by-product of the dynamic alteration. The selection criteria for the experimental clouds were: (1) hard, cauliflower appearance with top between 19,000 and 26,000 ft, indicating a vigorous cloud with its top cooled below the activation threshold of silver iodide (-4° C) but not cold enough for complete natural glaciation, (2) minimum supercooled water content of 1 g m^{-3} as measured by Johnson-Williams instrumentation during cloud penetration, indicating the fusion heat potential necessary for dynamic changes, (3) cloud still vigorous after first penetration by the three monitoring aircraft, and (4) isolation from other convective activity, especially cumulonimbus where the risk of natural seeding is especially great.

If a cloud was accepted for experimentation, the final go-ahead was given to the seeder aircraft pilot, who then opened a sealed envelope for his instructions. No matter what the decision, his flight pattern was exactly the same: one penetration near top of the cloud, followed by a second penetration perpendicular to the first. If the pilot obtained a seed instruction, 10 silver iodide flares were dropped at about 100-m intervals during each penetration. The multiple pass technique was used to insure better distribution of the silver iodide. Following the seeding run, all aircraft flew patterns to monitor the cloud (fig. 1).

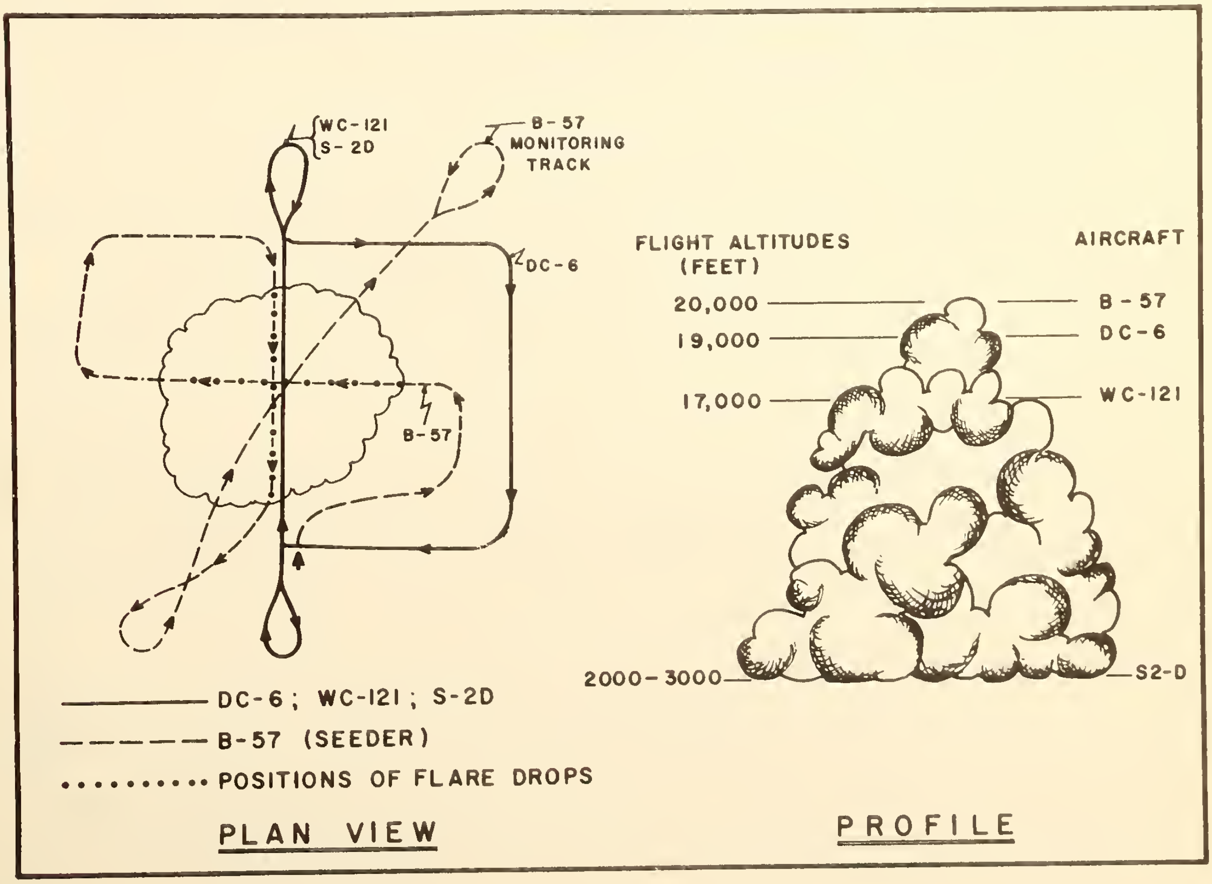

Figure 1. Flight tracks of experimental aircraft.

There were 19 experimental clouds during the Florida program; 14 were seeded and 5 were controls as dictated by the randomized seeding instructions. The seeded clouds grew an average of 11,400 ft more than the controls, a difference significant at the 1 percent level. This result is consistent with post-1960 experimentation over the Caribbean, Arizona, and Pennsylvania that demonstrated the feasibility of seeding to alter cloud dynamics. Woodley (1969) and Simpson and Woodley (1969) treat instances of dynamic alteration in some detail.

Because cloud dynamics and precipitation physics are intimately connected in cumulus cloud, alteration of one must affect the other. This effect is treated extensively in the next section.

3. RADAR SYSTEMS FOR STUDY OF PRECIPITATION

The modified UM/10-cm radar of the Radar Meteorological Laboratory, Institute of Marine Science, University of Miami, was the main tool for measuring precipitation from the experimental clouds. The characteristics and operation of this radar are treated in detail by Senn and Courtright (1968). The UM/10-cm radar has a 2° conical beam, a transmitter power of 5.5×10^5 W, a minimum detectable signal of 10^{-14} W, a pulse length of 2 μs, and a pulse repetition rate of 300 pulses/sec. Important features include special logarithmic and linear radar receiver systems and an RF range attenuation corrector (Hiser and Andrews, 1966). The UM/10-cm radar has an iso-echo contour (IEC) unit developed by Senn and Andrews (1968). Another "level" has been added to the unit by inverting signals again at a given level higher than the highest used in the basic device.

The effective antenna gain of the 12-ft reflector and radome of the UM/10-cm radar was calibrated by Andrews' (1966) solar method. A semi-automatic system was devised by Andrews and Senn (1968) to calibrate many features of the UM/10-cm radar system simultaneously. Briefly, it puts known signal levels on all scopes including those used for photography, so that the range attenuation correction, IEC, and all signal handling including degradations due to the photographic process are simultaneously calibrated on the final filmed data used by the analyst. This was done twice daily during the experiment. Table 1 presents the signal levels used and the radar reflectivities and approximate precipitation rates, all normalized to 100-n mi range. The IEC values are somewhat different from those requested because of the differences between the methods and video paths used in setting up values and those used in the data-gathering process.

The Z-R relationship used to obtain the values in table 1 is based on the work by Sims et al. (1963), who obtained the relation

$$Z = 286\ R^{1.43} \qquad (1)$$

by independently calculating reflectivity Z and rainfall rate R from raindrop photographs taken during showers in Miami, Florida. Equation (1) has been modified slightly to

$$Z = 300\ R^{1.4} \qquad (2)$$

by Gerrish and Hiser (1965), who averaged the Z-R relations derived by Sims et al. (1963) for air mass (wet season), easterly wave, cold trough, and overrunning situations, and for showers and thunderstorms for Miami, Florida.

The overall accuracy of any radar system is difficult to estimate. Senn and Courtright (1968) estimate the relative accuracy of the UM/10-cm

Table 1. UM/10-cm Signal Levels (Pr), Z Values, and Equivalent Precipitation Rates (R)

May 1968 Florida Program

DATE	CONTOUR	P_r (dbm)	$Z mm^6 m^{-3}$	R(IN/HR)	CONTOUR	P_r (dbm)	$Z mm^6 m^{-3}$	R(IN/HR)	CONTOUR	P_r (dbm)	$Z mm^6 m^{-3}$	R(IN/HR)	CONTOUR	P_r (dbm)	$Z mm^6 m^{-3}$	R(IN/HR)
MAY 15-20	1	-109	5	.002	2	-86	1.1×10^3	.09	3	-76	1.1×10^4	.45	4	-64	1.9×10^5	3.5
21	1	-109	5	.002	2	-86	1.1×10^3	.09	3	-77	$.9 \times 10^4$	.40	4	-64	1.9×10^5	3.5
23	1	-109	5	.002	2	-86	1.1×10^3	.09	3	-76	1.1×10^4	.45	4	-64	1.9×10^5	3.5
25	1	-109	5	.002	2	-85	1.5×10^3	.10	3	-74	1.8×10^4	.60	4	-64	1.9×10^5	3.5
26	1	-109	5	.002	2	-85	1.5×10^3	.10	3	-72	3×10^4	.80	4	-63	2.1×10^5	4.0
27	1	-106	11	.003	2	-86	1.1×10^3	.09	3	-74	1.8×10^4	.60	4	-63	2.1×10^5	4.0
28	1	-102	24	.006	2	-86	1.1×10^3	.09	3	-77	$.9 \times 10^4$	.40	4	-63	2.1×10^5	4.0
30	1	-100	40	.009	2	-86	1.1×10^3	.09	3	-75	1.4×10^4	.55	4	-63	2.1×10^5	4.0
REQUESTED VALUES	1	–	–	–	2	-85	1.1×10^3	.10	3	-73	2×10^4	.75	4	-67	$.9 \times 10^5$	2.30

radar at 1 to 2 db. Antenna elevation angles are probably accurate to ± 0.1°. Azimuth checks of known targets were made several times daily to determine error between the printed azimuth and PPI scan azimuth.

4. RADAR PROCEDURES

The meteorologists in the Radar Meteorological Laboratory were in continuous VHF radio contact with the scientists on the project aircraft, who were informed of their azimuth and range from an experimental cloud by the navigator on the command DC-6 aircraft. Positive identification of the experimental cloud by the ground radar was possible if it had a 10-cm radar echo (the usual case); if not, the azimuth and range of the cloud were monitored on the scope for appearance of an echo. It was often pos sible to see the experimental aircraft on radar and follow their patterns around the cloud echoes.

The UM/10-cm radar was used to collect precipitation rate data on film. During individual cloud experiments the operator raised the antenna to provide PPI scans of both the lowest levels (0.5° tilt) and the 14,000- and 20,000-ft levels through the experimental clouds. The radar scope was photographed once with each scan. The scan levels were chosen to get observations at, or close to,the flight levels of the experimental aircraft and to obtain precipitation rate data at low, bright-band middle, and slightly higher levels.

The locations of the experimental clouds with respect to the UM/10-cm radar are shown in figure 2, summary information on the experiment is given in table 2, and the distances of the experimental clouds from the

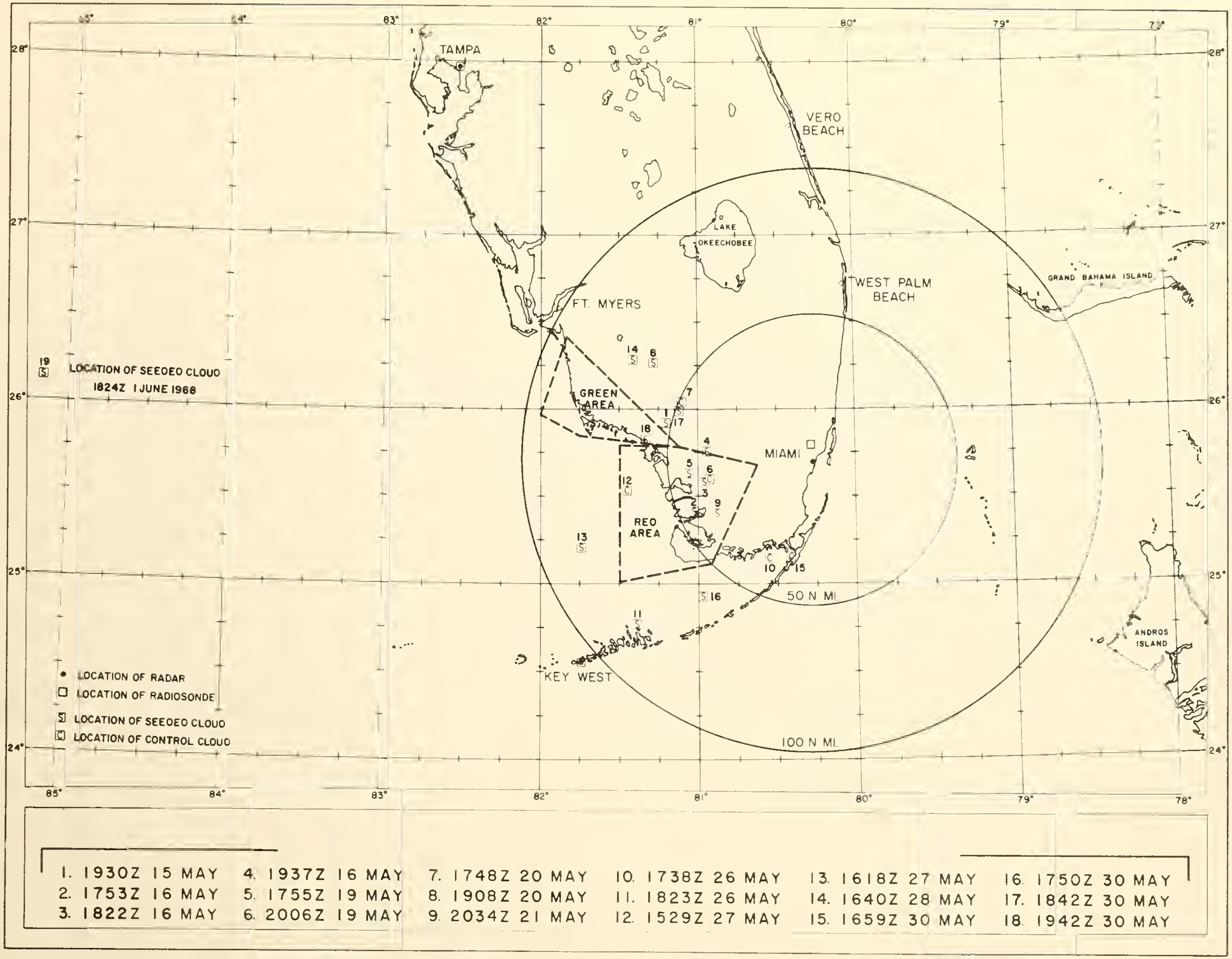

Figure 2. Red and green areas, primary seeding areas for Florida cloud seeding project, May 1968.

Table 2. Cloud Summary Data From 1968 Florida Cumulus Program

DATE	EXPERIMENTAL CLOUD NUMBER	DAILY CLOUD NUMBER	TIME OF FIRST DC-6 PASS (GMT)	TIME OF SEEDING RUN (GMT)	DURATION MIN	DURATION SEC	ACTION	SEEDING ALTITUDE (WITHIN 100 FT.) *	ESTIMATED TOP TEMP. AT SEEDING (TO NEAREST °C)	TOP AT SEEDING (FEET)*	MAX TOP AFTER SEEDING (FEET) *	TOP GROWTH AFTER SEEDING RUN
MAY/15/68	1	5	1930	193859-194324	4	25	S	19,100	-35.0	30,000	42,500	12,500
MAY/16/68	2	5	1753	180050-180450	4	20	S	20,200	-10.0	19,000	19,000	0
MAY/16/68	3	6	1822	182409-182901	4	52	S	20,200	-16.0	22,000	40,500	18,500
MAY/16/68	4	8	1937	194855-195222	3	27	S	20,200	-18.0	23,000	45,000	22,000
MAY/19/68	5	1	1755	175520-175853	3	33	S	20,300	-15.0	22,000	34,000	12,000
MAY/19/68	6	4	2006	201035-201232	1	57	NS	20,000	-13.0	21,500	21,500	0
MAY/20/68	7	1	1748	175757-180051	2	54	NS	20,300	-17.0	23,000	23,000	0
MAY/20/68	8	5	1908	190945-191230	2	45	S	18,500	-12.0	20,000	36,000	16,000
MAY/21/68	9	2	2034	203555-203825	2	30	S	19,200	-16.0	23,000	40,000	17,000
MAY/26/68	10	9	1738	174138-174440	3	02	NS	20,000	-13.0	21,000	21,000	0
MAY/26/68	11	11	1823	182455-182800	3	05	S	19,300	-24.0	26,000	36,000	10,000
MAY/27/68	12	1	1529	153230-153504	2	34	NS	20,200	-34.0	29,500	31,500	2,000
MAY/27/68	13	2	1618	162600-162855	2	55	S	20,250	-27.0	26,000	37,000	11,000
MAY/28/68	14	5	1635	163850-164137	2	47	S	18,700	-12.0	19,500	32,500	13,000
MAY/30/68	15	6	1659	170137-170440	3	03	NS	20,300	-31.0	28,500	32,000	3,500
MAY/30/68	16	7	1750	175147-175437	2	50	S	21,000	-22.0	25,000	33,000	8,000
MAY/30/68	17	8	1842	184845-185141	2	56	S	20,400	-31.0	28,500	37,000	8,500
MAY/30/68	18	10	1942	193650-193856	2	06	S	20,000	-16.0	21,000	38,000	17,000
JUNE/1/68	19	8	1824	182817-183059	2	42	S	20,200	-15.0	21,000	31,000	10,000

* HEIGHTS IN PRESSURE ALTITUDE

radar are summarized in table 3. All but one of the 19 experimental clouds were within 100 n mi of the UM/10-cm radar. The radar control clouds are discussed later.

5. ANALYSIS

The PPI radar return at the bases (0.5° tilt) of all but one of the experimental clouds was converted to rainfall. Seeded and control clouds were compared in terms of the radar-derived precipitation. The size of the cloud sample could be increased artificially by selecting control clouds from the aerial time-lapse photography. These clouds were not selected randomly and, in this sense, are not true controls. In an attempt to avoid bias in the cloud selection, an individual experienced in the study of cumulus clouds but unconnected with the project viewed the nose camera films taken by the seeder aircraft and selected clouds from the films that fulfilled the visual eligibility criteria for experimental clouds. These clouds were then located on the radar film. The time of selection was taken as the time of a simulated seeding pass, and the rest of the analysis was done in the same way as for the actual experimental clouds (described below). Five additional control clouds were selected by this procedure. These were clouds we might have selected for experimentation but did not, either because we were busy studying another cloud or because we found that they formed in air space restricted to our use.

The analysis procedure included (a) location of the experimental clouds on the photographs of the UM/10-cm radar scope, (b) tracings of the iso-echo contours as long as a cloud remained eligible for analysis, and (c) planimeter measurement of the areal coverage of the contours by

Table 3. Distance of Experimental Clouds From Radar

Seeded			Control		
Date	Time	Distance	Date	Time	Distance
May 15	1930 Z	52 n mi	May 19	2006 Z	35 n mi
May 16	1735 Z	45 n mi	May 20	1748 Z	50 n mi
May 16	1822 Z	38 n mi	May 26	1738 Z	36 n mi
May 16	1937 Z	36 n mi	May 27	1529 Z	65 n mi
May 19	1755 Z	43 n mi	May 30	1659 Z	33 n mi
May 20	1908 Z	55 n mi			
May 21	2034 Z	37 n mi		MEAN:	44 n mi
May 26	1823 Z	83 n mi		MEDIAN:	36 n mi
May 27	1618 Z	85 n mi	May 15	1916 Z	43 n mi
May 28	1640 Z	71 n mi	May 16	1738 Z	30 n mi
May 30	1750 Z	60 n mi	May 20	1553 Z	52 n mi
May 30	1842 Z	50 n mi	May 28	1608 Z	62 n mi
May 30	1942 Z	58 n mi	May 28	1637 Z	72 n mi
All Seeded Clouds	Mean :	55 n mi		Mean :	52 n mi
	Median:	52 n mi		Median:	52 n mi
			All Control Clouds	Mean :	48 n mi
				Median:	46 n mi

a person who did not know whether an echo was that of a seeded or unseeded (control) cloud. An example of the iso-echo contour tracings is shown in figure 3 for part of the life history of cloud 6 on May 16, 1968.

To be eligible for analysis, the echoes of the experimental clouds had to be separate from the echoes of neighboring clouds. When the echo of an experimental cloud expanded and merged with its neighbors, the analysis was discontinued. This criterion, while necessary for an objective analysis , led to a nonhomogeneous data sample. The number of clouds dropped from consideration increased with elapsed time after seeding.

The areal extent of the cloud base iso-echo contours were measured for all experimental clouds before and for as long as possible after the seeding pass. These area magnitudes were plotted on a time-area diagram with the time of the first seeding pass used as a reference as shown in figure 4. The ordinate of the diagram is area in $(\text{n mi})^2$, the abscissa is in minutes after the first seeding pass, and the three curves represent the time change of the areas contained within the specified contours. If the radar rainfall at cloud base had exceeded 3.50 in. hr^{-1}, the threshold for the next contour, a fourth curve would be shown in the graph.

The problem now is to calculate total rainfall from the cloud. The area covered by rainfall rates between 09 in. hr^{-1} and .45 in. hr^{-1} in the 10-min period after seeding is shown as the hatched region B. The rainfall contribution from this region is the area of region B having units $(\text{n mi})^2$ min, multiplied by a mean rainfall rate having units in.min^{-1}. By inserting an appropriate constant, the result is converted to acre-feet of water, which is merely a volumetric measurement and does not represent the

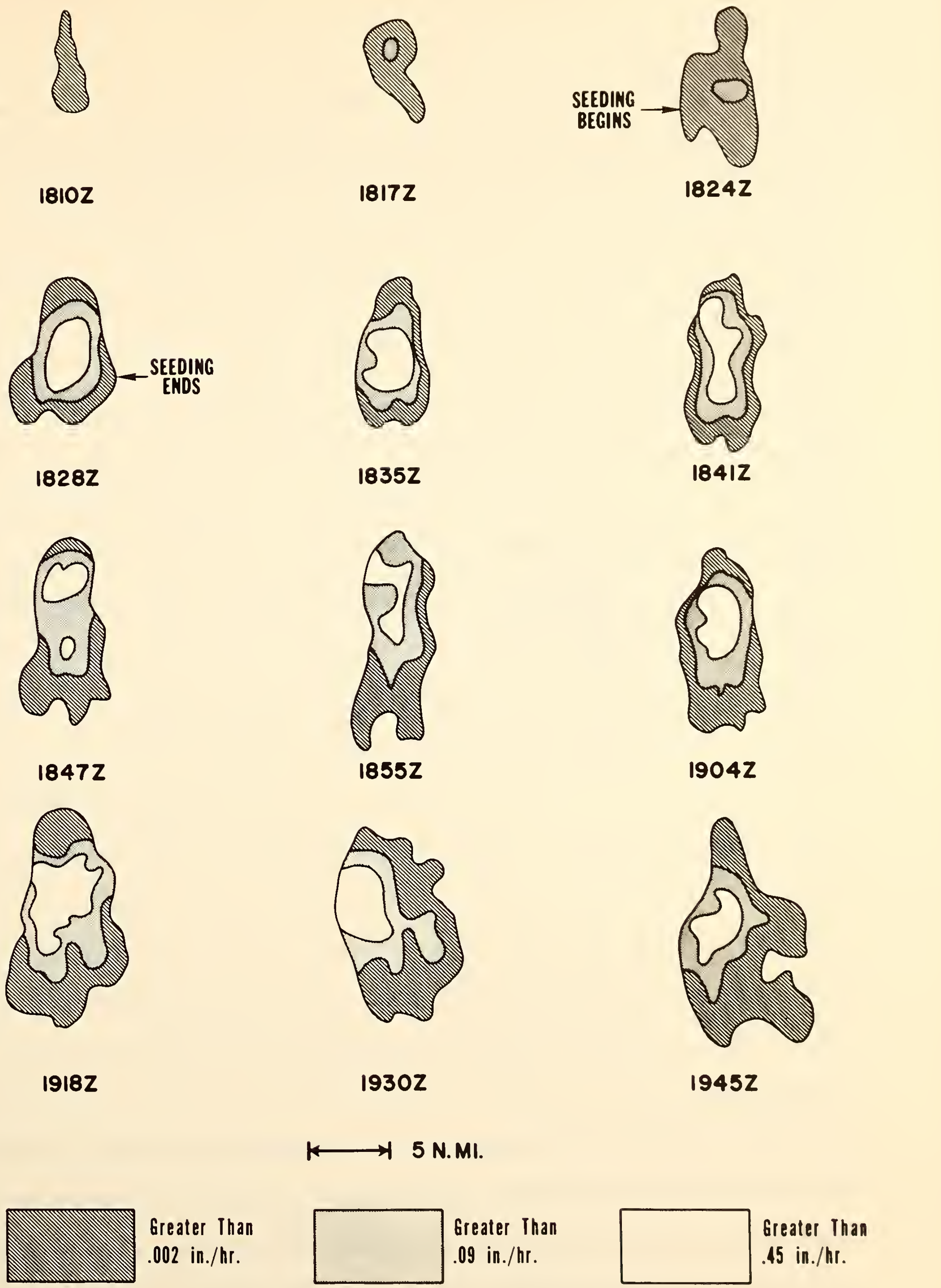

Figure 3. Example of cloud base iso-echo contouring for cloud 6, May 16, 1968.

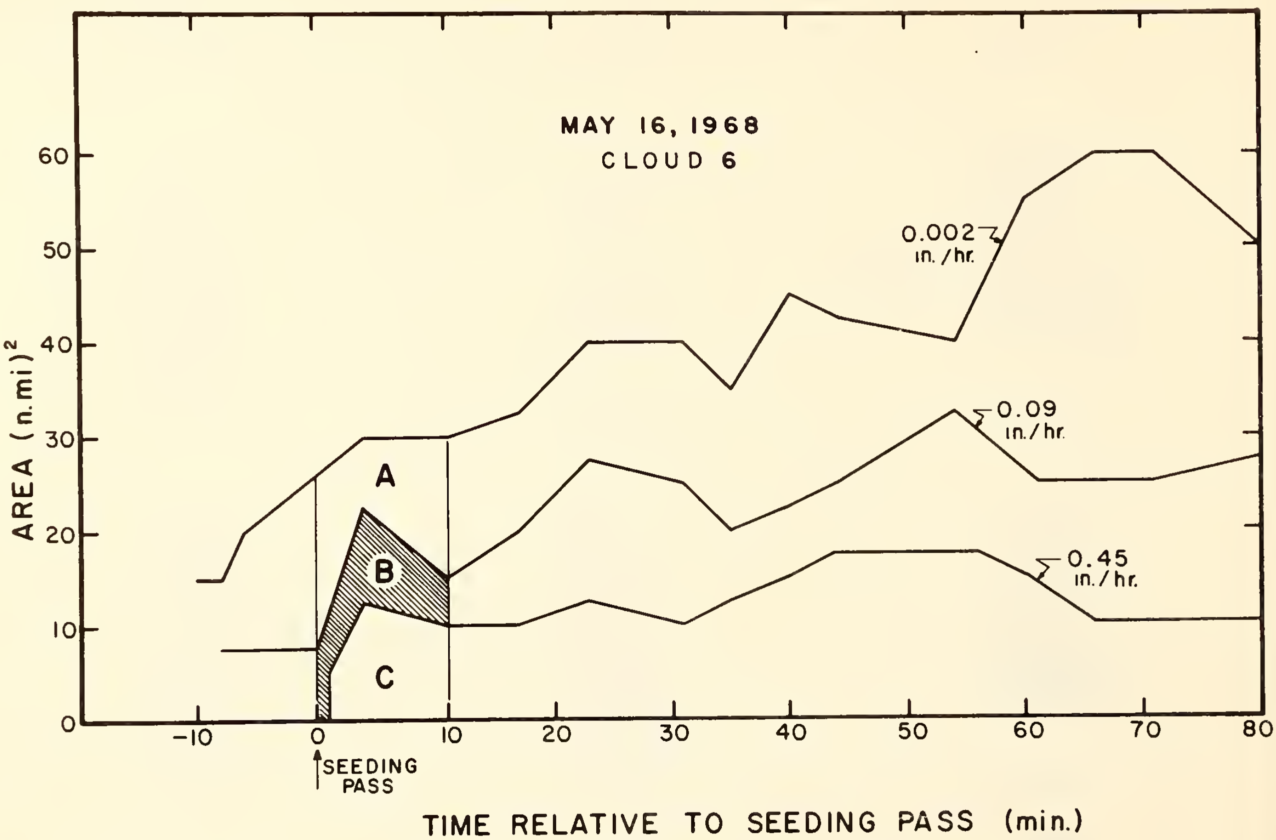

Figure 4. Graph of iso-echo area relative to time of seeding pass.

true distribution of water on the ground. When this procedure is extended to all contours for the lifetime of the cloud, an estimate of total rainfall is possible.

The selection of a mean rainfall rate for an area bounded by two known rates was an arbitrary one. The mean value selected was one-third the difference between the known rates plus the lower value. This decision was based on rainfall analyses, which often show that the isoheyts are concentrated near the higher values, implying that the increase in rainfall rate from the edge of a shower to the core is nonlinear. The mean rainfall rate for an area bounded by only one rainfall rate was obtained by taking one-third the difference between the boundary value and the next iso-echo contour permitted by the system plus the boundary value. The mean rainfall rate assigned to the area inside the last contour permitted by the system was one-tenth the boundary value plus the boundary value. Since rainfall rate at cloud base rarely approached the value corresponding to the fourth contour, this last mean was seldom used.

Other more elaborate schemes could be devised to arrive at mean rainfall rates, but they are not warranted because of the many other uncertainties. The same analysis was applied to seeded and control clouds, and the relative differences, seeded cloud rainfall minus control cloud rainfall, should still be valid. The accuracy of the rainfall calculations is discussed in section 8.

All rainfall derived was assumed equal to rainfall reaching the ground. However, at a constant antenna tilt the height of the scan is range dependent; as range increases the height of the scan increases. Therefore, the radar measurements at 0.5° elevation are not at the same heights in the experimental clouds. For clouds at ranges between 25 and 50 n mi, the center of the beam is within 1000 ft of cloud base, which averages approximately 2500 ft at this time of year (fig. 5). Evaporation of the rainfall in falling from the level of measurement has been assumed insignificant, especially in view of the other uncertainties in this procedure. A radar-rain gage comparison (sec. 9) shows that this is not a bad assumption.

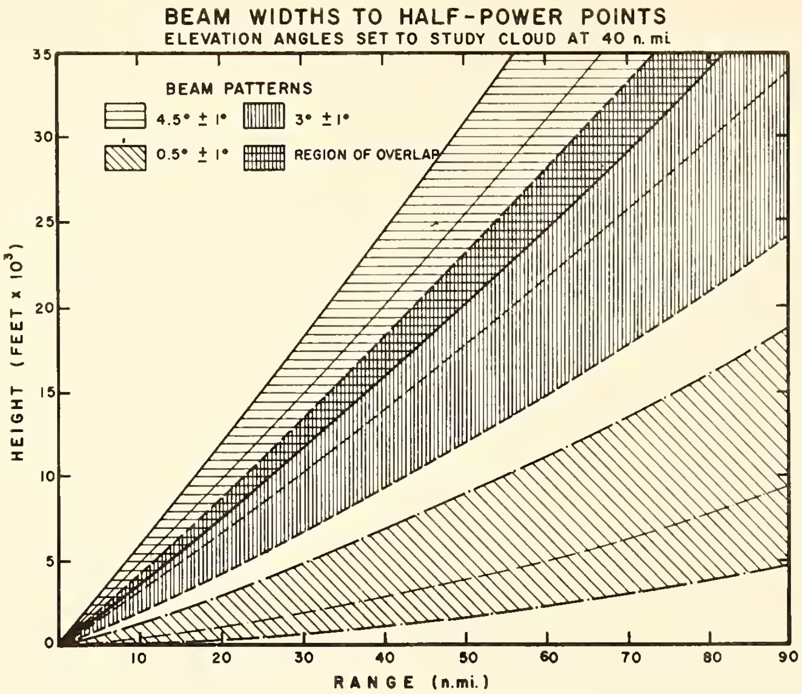

Figure 5. Beam dimensions for the UM/10-cm radar for the tilts that were used to study an echo at 40 n mi (after Senn and Courtright, 1968).

Two comparisons were made between seeded and control rainfalls. First, total radar rainfall from the seeded clouds in 10-min intervals (relative to the time of the first seeding pass) was compared with that from the controls. Second, the seeded and control clouds were compared among themselves and then with each other. The radar rainfall from a given cloud in the 10-min period before the seeding pass was taken as a standard, which was then subtracted from the radar rainfall produced by the cloud in the 10-min intervals after the seeding pass. If a cloud produced 10 acre-feet of water in the 10-min period before the seeding pass and 30 acre-feet afterward, the difference is 20 acre-feet. The cloud produced 20 acre-feet more water in the 10-min period after the seeding pass than it would have had the rainfall rate in the 10-min period prior to the seeding pass persisted through the 10 min after the seeding pass. Similar calculations were made in 10-min increments for the entire lifetime of the cloud.

The second comparison should be better than the first as a measure of the effects of seeding on rainfall. The first comparison of total, post-seeding pass rainfall weights the result toward the clouds with a head start, that is, those that already have a large echo at the time of seeding. The second scheme should be insensitive to the initial size of the echo.

It was not possible to calculate percentage changes in rainfall or to normalize the rainfall to that falling before seeding for all the experimental clouds. To have done so would have meant an infinite increase in rainfall for the five clouds that had no pre-seeding echoes on the 0.5° scan.

6. RESULTS OF RADAR RAINFALL ANALYSES

The most striking feature of the analysis was the high variability in rainfall from the experimental clouds, which occurred in rainfall from cloud-to-cloud and day-to-day, as shown by the rainfall figures in table 4 and by the bar graph plot of these values in figure 6. The solid portion of the bar in figure 6 indicates water relative to that produced by the cloud in the 10-min period before the seeding pass (see sec. 5). The entire bar represents the total water produced by the cloud in the interval specified; the cloud number and date corresponding to the numbers over the bars are shown. The number of experimental clouds in the sample decreased with elapsed time after the seeding pass because many of them merged with their neighbors. As seen in this figure, 40 min after the seeding pass, the rainfall observations represent a bias in favor of the smaller drier clouds.

Table 4. Radar Rainfall Data (acre-feet) Relative to the Time of Seeding Pass May 15-June 1, 1968

DATE	CLOUD	-10-0	0-10		10-20		20-30		30-40		40-50		50-60	
	NO.	W	ΔW	W	ΔW	W	ΔW	W	ΔW	W	ΔW	W	ΔW	W
SEEDED CLOUDS														
5/15/68	C5	36.3	18.1	54.4	-.3	36.0	-14.0	22.3	-28.4	7.9	-27.3	9.0	—	—
5/16/68	C5	15.3	-3.2	12.1	-3.7	11.6	-8.2	7.1	-14.7	0.6	-15.3	0.0	-15.3	0.0
5/16/68	C6	19.0	166.5	185.5	169.8	188.8	213.7	232.7	224.2	243.2	289.3	308.3	313.6	332.6
5/16/68	C8	0.0	2.4	2.4	11.7	11.7	53.8	53.8	159.2	159.2	—	—	—	—
5/19/68	C1	7.6	73.6	81.2	154.8	162.4	45.7	53.3	7.0	14.6	24.8	32.4	78.5	86.1
5/20/68	C5	11.2	91.6	102.8	88.6	99.8	89.0	100.2	—	—	—	—	—	—
5/21/68	C2	1.2	43.0	44.2	73.6	74.8	—	—	—	—	—	—	—	—
5/26/68	C11	2.4	1.7	4.1	—	—	—	—	—	—	—	—	—	—
5/27/68	C2	5.4	19.5	24.9	17.0	22.4	20.2	25.6	9.5	14.9	-0.8	4.6	—	—
5/28/68	C5	0.0	4.1	4.1	7.1	7.1	5.7	5.7	0.6	0.6	—	—	—	—
5/30/68	C7	30.7	64.1	98.8	40.8	71.5	-5.2	25.5	-25.8	4.9	-30.7	0.0	-30.7	0.0
5/30/68	C8	92.6	-21.8	70.8	-8.0	84.6	26.7	119.3	—	—	—	—	—	—
5/30/68	C10	6.2	10.6	16.8	16.7	22.9	27.6	33.8	—	—	—	—	—	—
AVERAGE		17.5		53.7		66.1		61.8		55.7		59.1		139.5
CONTROL CLOUDS														
5/19/68	C4	26.8	4.7	31.5	-9.9	16.9	2.6	29.4	-17.6	9.2	—	—	—	—
5/20/68	C1	7.1	12.8	19.9	68.0	75.1	—	—	—	—	—	—	—	—
5/26/68	C9	0.0	0.0	0.0	0.0	0.0	0.0	0.0	0.0	0.0	0.0	0.0	0.0	0.0
5/27/68	C1	5.0	0.6	5.6	2.9	7.9	-1.8	3.2	-4.4	0.6	—	—	—	—
5/30/68	C6	43.5	39.9	83.4	31.6	75.1	48.8	92.3	11.6	55.1	-28.2	15.3	—	—
5/16/68	RC	1.5	1.4	2.9	19.1	20.6	1.3	2.8	-1.5	0.0	-1.5	0.0	-1.5	0.0
5/20/68	RC	32.2	1.6	33.8	85.5	117.7	69.8	103.0	51.9	84.1	-1.0	31.2	-29.6	2.6
5/15/68	RC	2.4	18.9	21.3	2.4	4.8	-2.4	0.0	-2.4	0.0	-2.4	0.0	-2.4	0.0
5/28/68	RC	0.0	1.7	1.7	11.3	11.3	6.1	6.1	2.7	2.7	2.6	2.6	0.0	0.0
5/28/68	RC	0.0	4.6	4.6	6.8	6.8	0.1	0.1	0.0	0.0	0.0	0.0	0.0	0.0
AVERAGE		12.1		20.5		33.6		26.3		16.9		7.0		0.4

W = TOTAL RAINFALL IN INTERVAL SPECIFIED
ΔW = RAINFALL IN INTERVAL SPECIFIED RELATIVE TO 10 MINUTE INTERVAL BEFORE SEEDING PASS (SEE TEXT)
RC = RADAR CONTROL CLOUD
— = NO OBSERVATIONS AVAILABLE BECAUSE IT WAS IMPOSSIBLE TO DISTINGUISH THE ECHO OF THE EXPERIMENTAL CLOUD FROM THOSE OF SURROUDING CONVECTION

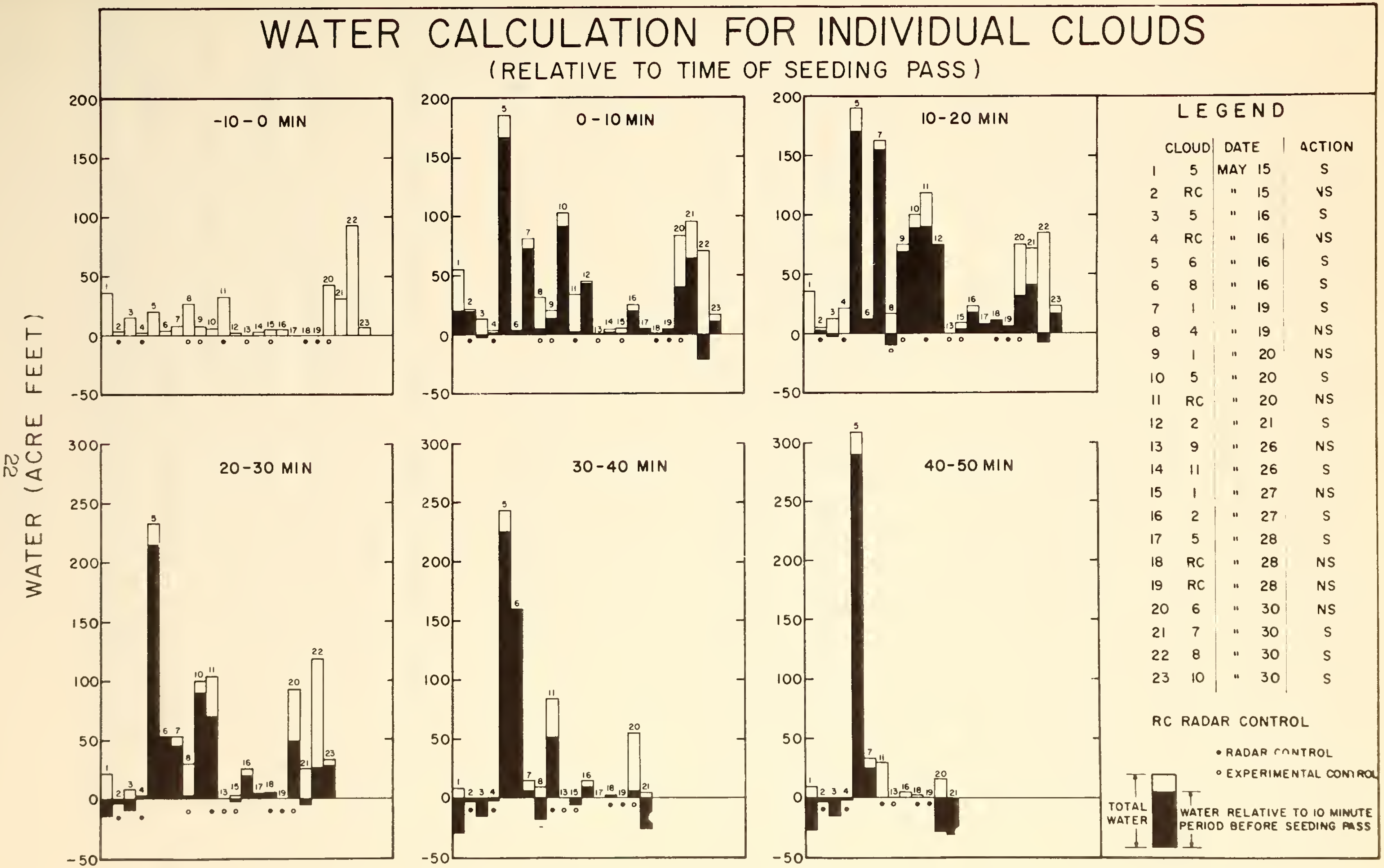

Figure 6. Bar graph of radar rainfall for the experimental clouds in 10-min increments relative to the time of the seeding pass. The solid portion of the bar indicates water relative to that produced by the cloud in the 10-min period before the seeding pass. The entire bar represents the total water produced by the cloud in the interval specified. The numbers above each bar correspond to the numbers in the legend.

The bar graph of rainfall (fig. 6) reveals that the sample is dominated by the few wet clouds, especially cloud 6 on May 16, 1968. Seeded cloud 8 on May 16, 1968, probably produced more rain than any in the sample. but because of its azimuth from the radar the rainfall estimates are grossly too low. Cloud 8 was at the azimuth of the partially blind cone, 267° and 273°, of the UM/10-cm radar which is due to interference by the University of Miami Library and the WSR-57 radome on its roof. The energy loss is worst when the 10-cm radar antenna is at a small elevation angle while scanning near cloud base.

The contention that the radar rainfall for cloud 8 is an underestimate is supported by Simpson and Woodley (1969), who compare measured reflectivities with those computed theoretically. Woodley (1969) calculates that the actual rainfall from this cloud is probably twice that computed.

Seeded clouds 1 on May 19 and 10 on May 30, and control cloud 4 on May 19 were also within the partially blind region at some time during their life histories. The estimates of rainfall from these clouds are probably also too low.

The amount of rain from the seeded clouds was positively correlated with the maximum top growth following seeding. Table 5 shows the correlations between maximum cloud top growth following seeding and the total water produced by the clouds in 10-min intervals after the first seeding pass. The correlation is positive in all intervals, increasing to a maximum with high statistical significance in the 30 to 40 min following seeding. This finding implies that the more a cloud grows following seeding,

Table 5. Correlation Between Maximum Growth and Total Water in 10-min Intervals After First Seeding Pass

TIME INTERVAL (MIN.)	0-10	10-20	20-30	30-40	40-50
NO. OF CLOUDS	13	12	11	8	6
CORRELATION COEFFICIENT	.20	.18	.54	.91	.79
SIGNIFICANCE	> 50 %	> 50 %	10 %	< 1 %	< 5 %

the more rain it is likely to produce. The high correlation between cloud growth and water production suggests that a dynamic cumulus model such as the one developed by Simpson and Wiggert (1969) that can predict cloud growth following seeding can also be used to infer the effect of seeding on precipitation.

The positive correlation between cloud growth and water production in Florida cumuli after seeding differs from the finding in Australia (Bethwaite et al., 1966) of large cloud-base increases in rainfall from seeded clouds without detectable changes in cloud top height.

The rainfall calculations indicate that precipitation decreases accompany the collapse or the cutoff tower growth of seeded clouds consisting of one primary tower. This is consistent with the conclusions reached above and is supported by the analysis of cloud 5 on May 16 and cloud 8 on May 30, 1968. The seeded tower of cloud 5 on May 16 collapsed completely following the seeding, and no new tower appeared. In successive 10-min intervals after seeding, this cloud produced increasingly less rainfall than it had in the 10-min period before seeding (fig. 6). There is no way of knowing whether these decreases would have been even larger had the cloud not been seeded. In seeded cloud 8 on May 30, discussed by Woodley (1969), a cutoff tower growth was followed by collapse and then regeneration of the cloud body and explosive growth. The rainfall calculations are consistent with this behavior. During the cutoff tower regime 0-10 and 10-20 min period after seeding, this cloud produced 22.8 and 8.0 acre-feet less water respectively than it had in the 10-min before seeding. During the 20-30 min after seeding, regeneration and intense growth began, with the cloud producing 26.7 acre-feet more water than it had in the 10-min before seeding. Subsequently, this cloud merged with its neighbors and was dropped from the sample.

The average rainfall statistics are of interest, provided one is aware of the small sample and of the effect of the few wet clouds on the averages. The average total water from the experimental clouds is presented in figure 7a. The number in parenthesis near each data point refers to the number of clouds contributing to the average. Rainfall values are presented only to 40 min after the seeding pass, because the sample is very small after this. Inclusion of the radar control clouds in the sample does not change the curves significantly. The average total water from the seeded clouds after the seeding pass exceeds that from the controls by at least a factor of two for each time interval.

The results of the analysis change little when the post-seeding pass rainfall is compared with that in the 10-min period before the seeding

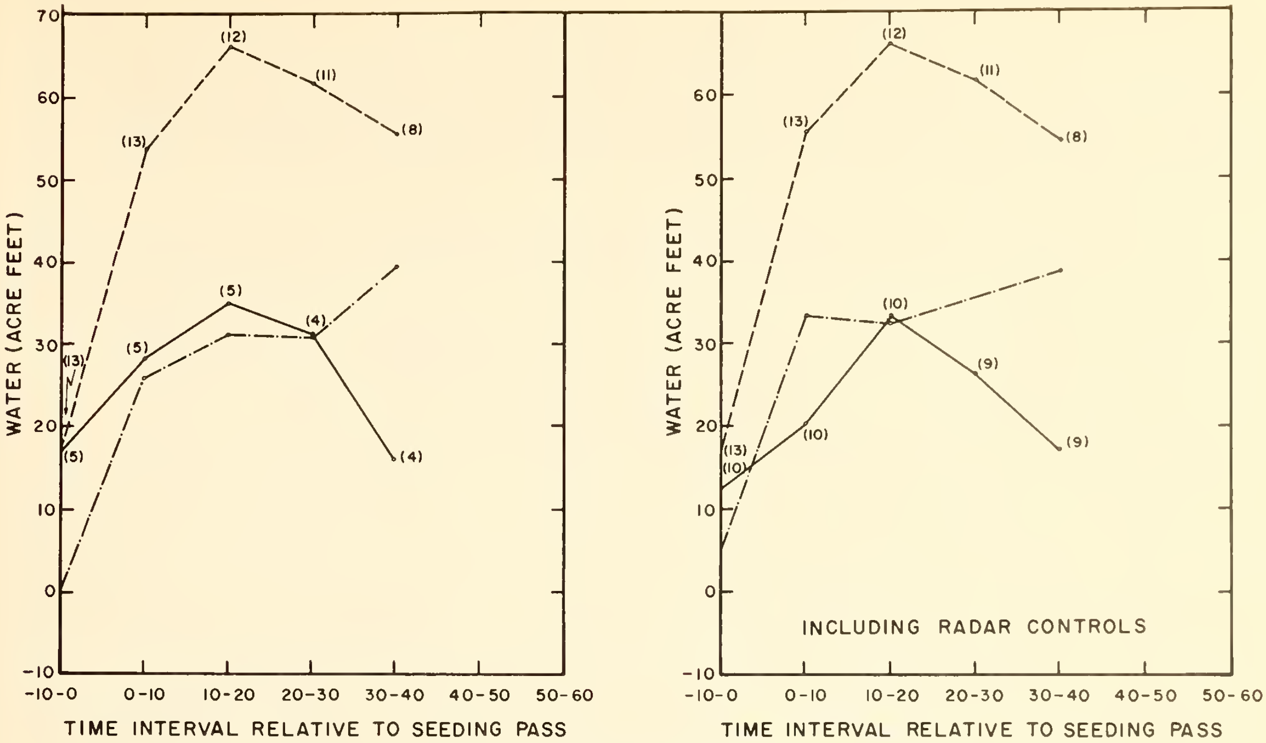

(a) Average total water from the experimental clouds in 10-min intervals relative to the time of the first seeding pass.

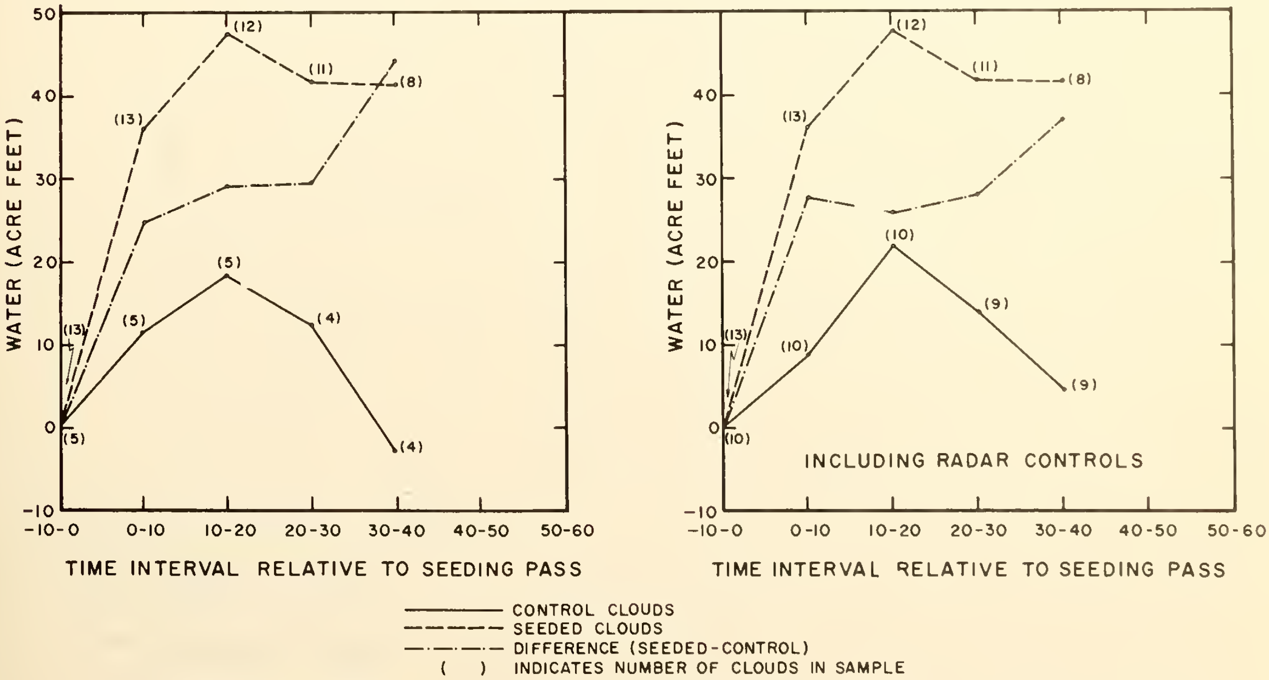

(b) Average water from the experimental clouds relative to the water produced in the 10-min period before the seeding pass. Time intervals are relative to the time of the first seeding pass.

Figure 7. Average rainfall from the experimental clouds. Inferred from $Z=300R^{1.4}$ The number in parenthesis near each data point refers to the number of clouds contributing to the average.

pass (fig. 7b). The average rainfall difference (seeded cloud rainfall minus control cloud rainfall) increases with time and is greater than the average rainfall from the controls.

A summary of the comparison of the average seeded cloud rainfall with that from the control clouds is presented in table 6. Forty min after the seeding pass, the average seeded cloud had produced 100 to 150 acre-feet more water than the average control cloud, an increase of more than 100 percent. This result is independent of the analysis scheme. The average total water difference between the seeded and control clouds might be increased by a factor of two if there were calculations for entire cloud lifetimes, and if a true rainfall representation were available for the clouds in the blind radar cone.

7. STATISTICAL TEST OF RAINFALL RESULTS

The difference in average total water for the seeded and control clouds 40 min after the seeding pass was tested for significance by three statistical tests: (1) a pooled Student $\underline{t}$ statistic with the variances assumed equal (a good assumption), (2) the Normal Scores test, and (3) the Wilcoxon-Mann-Whitney test. The Student $\underline{t}$ test is probably the most powerful if the data are normally distributed. However, the assumption of normality is not satisfactory for the rainfall data. The Normal Scores test is also based on the normal distribution, but it has been shown to be a powerful test when the distributions are non-normal (highly skewed and bimodal) (Neave and Granger, 1968). The Wilcoxon-Mann-Whitney nonparametric test makes no assumption about the shape of the population

Table 6. Comparison of Average Seeded and Control Cloud Rainfalls

40 Minutes After Seeding Pass	
Total Water Calculation:	
Without Radar Controls	
Seeded clouds	237 acre-feet
Control clouds	110 acre-feet
Difference	127 acre-feet
Percent difference	$\frac{237-110}{110}$ X 100 = 115%
With Radar Controls	
Seeded clouds	237 acre-feet
Control clouds	97 acre-feet
Difference	140 acre-feet
Percent difference	$\frac{237-97}{97}$ X 100 = 144%
Water Calculation Relative to 10-min Period Before Seeding Pass	
Without Radar Controls	
Seeded clouds	167 acre-feet
Control clouds	40 acre-feet
Difference	140 acre-feet
Percent difference	$\frac{167-40}{40}$ X 100 = 318%
With Radar Controls	
Seeded clouds	167 acre-feet
Control clouds	49 acre-feet
Difference	118 acre-feet
Percent difference	$\frac{167-49}{49}$ X 100 = 241%

distribution from which the samples are drawn; the disadvantage is that it is not as powerful as the former two tests when the data are drawn from a population having a normal distribution.

Table 7 shows the results of the statistical tests on rainfall. In the last category (radar controls plus the mergers), the clouds dropped from the May data sample because of mergers with surrounding echoes were assumed to persist in a steady state until 40 min after the seeding pass. The rainfalls produced by these clouds in the 10 min before being dropped were assumed to fall in 10-min intervals until the 40-min cutoff. This artifice permitted all clouds to be retained in the sample, which resulted in total population of 23 clouds (13 seeded and 10 controls).

Table 7. Statistical Test of Rainfall Results*

TYPE OF TEST	STUDENT t TEST	NORMAL SCORES TEST	WILCOXN-MANN -WHITNEY
	SIGNIFICANCE		
WITHOUT RC Ns = 8 Nns = 4	20 %	< 10 %	< 20 %
WITH RC Ns = 8 Nns = 9	< 10 %	< 5 %	< 10 %
WITH RC AND MERGERS Ns = 13 Nns = 10	< 10 %	< 5 %	< 10 %

* ALL TESTS TWO SIDED
RC: RADAR CONTROLS
Ns: SIZE OF SEEDED SAMPLE
Nns: SIZE OF NON-SEEDED SAMPLE

The test results indicate that their significance ranges between 20 percent and 5 percent, depending on the category and test chosen. Note that all the tests are two-sided, because no postulate concerning the direction of the changes in rainfall produced by seeding was made when the experiment was first planned (about 1966). If, at the outset, we had postulated that dynamic modification would increase rainfall, a right-sided test would have been appropriate. Then, all but two of the blocks in table 7 would show significance for the rainfall results at the 5 percent level. However, even the two-sided tests give strong statistical support to the hypothesis that dynamic cloud modification produces precipitation increases.

A rather different approach to the statistical analysis of the precipitation results strengthened the conclusions reached above. A fourth root transformation was applied to the seeded and control cloud total rainfalls in table 4. Such a transformation has been shown to make data better behaved in terms of sampling theory (Howell, 1960). In the rest of this discussion all rainfalls are to be interpreted as transformed (fourth root transformation) rainfalls. The control cloud rainfalls in the 10-min period before the seeding pass [$W_c^{1/4}(-10\text{-}0)$] were plotted on the abscissa versus the control cloud rainfalls in the 40-min period after the seeding pass $W_c^{1/4}(0\text{-}40)$ $W_c^{1/4}(0\text{-}40)$ on the ordinate. (The one control cloud that was dropped because of merger was not included in this analysis.) The scatter diagram plot of these values is shown in fig. 8. The correlation between $W_c^{1/4}(-10\text{-}0)$ and $W_c^{1/4}(0\text{-}40)$ is 0.83. Regression analysis provided the best fit line having an equation of the form

$$\hat{y} = 1.1878 + 1.0281x \,, \tag{3}$$

where $\hat{y} = W_c^{1/4}(0\text{-}40)$ and $x = W_c^{1/4}(-10\text{-}0)$.

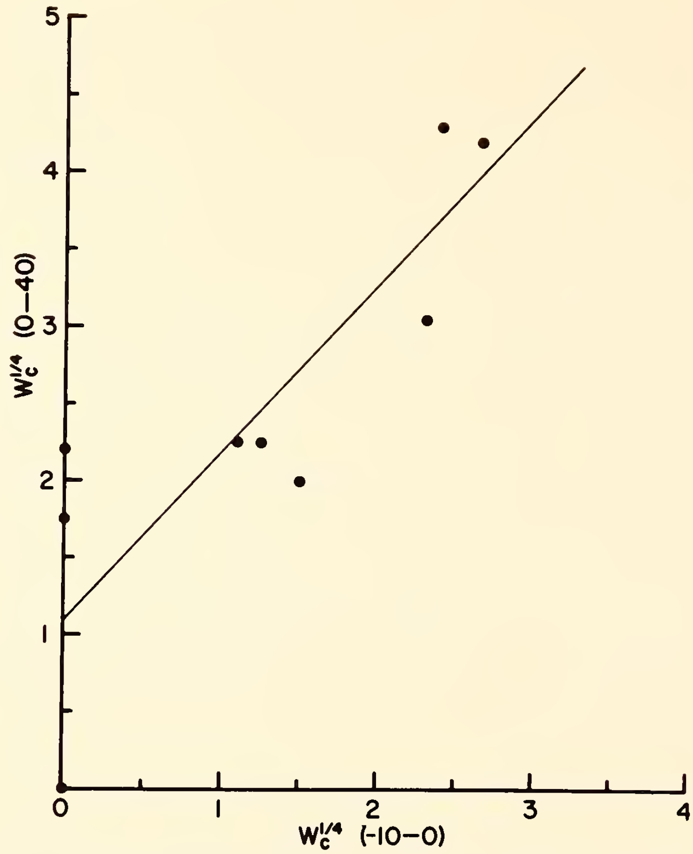

Figure 8. Scatter diagram plot of transformed control cloud rainfalls. Solid line is the best fit for the plotted points.

Equation (3) was used as a prediction equation for the seeded clouds. The seeded cloud rainfalls in the 10-min period before seeding were substituted for x in (3) and seeded cloud rainfalls in the 40 min after seeding ($\hat{y}$) were predicted. These generated values were then compared with the observed seeded cloud rainfalls in the 40 min after seeding (Table 8). All seeded clouds that were dropped because of merger were retained in this analysis, by substituting the average rainfall in the time period after seeding for the missing 10-min period or periods.

Table 8. Fourth Root of Seeded Cloud Rainfalls (observed vs. predicted)

$\hat{y}_o$ (observed)	$\hat{y}_p$ (predicted)	$\hat{y}_o - \hat{y}_p = d$
3.31	3.71	−.40
2.37	3.23	−.86
5.40	3.34	2.06
3.88	1.19	2.69
4.20	2.90	1.30
4.48	3.07	1.41
3.93	2.27	1.66
2.01	2.46	−.45
3.06	2.75	.31
2.05	1.19	.86
3.76	3.61	.15
4.37	4.38	−.01
3.14	2.81	.33

$\Sigma d = 9.05$ $\quad s_d^2 = 1.1402$ $\quad t^* = 2.35$

$\bar{d} = .6962$ $\quad s_{\bar{d}}^2 = .0877$ $\quad t_{12,.975} = 2.18$

If the seeded clouds produced more rainfall than the controls, it should be evident in the comparison between the observed and the predicted seeded rainfalls. The average difference ($\bar{d}$) between the actual and predicted rainfalls and its variance ($s_d{}^2$) were computed, and the variance of the mean difference ($s^2_{\bar{d}}$) was calculated using

$$s_{\bar{d}}^2 = \frac{s_d{}^2}{n} \tag{4}$$

The ratio

$$\frac{\bar{d}}{s_{\bar{d}}} = t^* \qquad (5)$$

has a sampling distribution approximated by Student's t distribution.

To test whether

$$\bar{d} = 0 \quad (H_1)$$

against the two-tailed alternative

$$\bar{d} \neq 0 \ (H_2),$$

reject if

$$t^* \begin{cases} < t_{n-1,.025} \\ \\ > t_{n-1,\ .975} \end{cases} ;$$

otherwise do not reject H_1. For the problem at hand, $t^* = 2.35$ and $t_{12,.975} = 2.179$ so reject H_1. This implies that the difference between the actual seeded rainfalls and those predicted, using the control cloud prediction equation, is significantly different at the 5 percent level. This says, in effect, that the seeded and control cloud rainfalls constitute distinctly different populations, which is the same conclusion reached earlier.

8. UNCERTAINTIES IN THE RAINFALL ANALYSIS

Because of the uncertainties in the radar observations and in the analysis, there is little likelihood that the calculations made from the radar data represent exact rainfall. Fortunately, many of the uncertainties are compensating. Even if the radar return is a poor representation of rainfall, the comparison of seeded and control cloud rainfalls should still be valid.

The sources of uncertainty in the radar rainfall study are analyzed in table 9. They are not listed in order of importance, because the author

Table 9. Uncertainties in Representing Rainfall From Seeded and Control Clouds During May 1968*

SOURCE OF UNCERTAINTY	UNDERESTIMATE OR OVERESTIMATE	IMPORTANCE
VALIDITY OF Z-R RELATION $Z=300\,R^{1.4}$	MAJOR UNKNOWN.	IMPORTANT FOR ABSOLUTE VALUES OF RAINFALL. RELATIVE VALUES (SEEDED vs. CONTROL) SHOULD STILL BE GOOD.
EFFECT OF SEEDING ON SEEDED CLOUD DROP SPECTRUM.	UNKNOWN.	IF SPECTRUM CHANGES ARE LARGE, $Z=300R^{1.4}$ MAY BE INVALID FOR SEEDED CLOUDS.
CHANGES IN RADAR SYSTEM DURING THE DAY.	UNKNOWN	SHOULD BE MINOR BECAUSE OF TWICE DAILY CALIBRATION.
OVERALL ACCURACY OF RADAR SYSTEMS.	ESTIMATED AT $\pm$ 1-2 db.	MAY BE IMPORTANT AT LARGE VALUES OF REFLECTIVITY.
RADAR BEAM NOT UNIFORMLY FILLED WITH PRECIPITATION	UNDERESTIMATE PRECIPITATION	IMPORTANT FOR SMALL CLOUDS AND CLOUDS BEYOND 60 N. Mi.
RANGE AND AZIMUTHAL STRETCHING.	OVERESTIMATE PRECIPITATION.	IMPORTANT FOR CLOUDS BEYOND 60 N. Mi.
INTERPOLATION SCHEME.	UNDERESTIMATE AT LOW AND MODERATE PRECIPITATION RATES BUT OVERESTIMATE AT HIGH PRECIPITATION RATES.	IMPORTANT FOR STRONG ECHOES
LOSS OF RADAR ENERGY TO GROUND	UNDERESTIMATE	MINOR
NEGLECT OF EVAPORATION	OVERESTIMATE	MINOR
PLANIMETER MEASUREMENTS	PROBABLY NOT SYSTEMATIC	MINOR
HUMAN BIAS	UNKNOWN	MINOR

* THE UNCERTAINTIES ARE NOT RANKED IN ORDER OF IMPORTANCE

has no preconception of their relative importance. Those considered small include analysis interpolation scheme, planimeter measurements, human bias, loss of radar energy to the ground when the beam is at 0.5° elevation (except on the azimuth of the University of Miami Library), and neglecting evaporation in relating cloud base echoes to rain on the ground. Uncertainties in the radar system are more important because the characteristics of any radar are subject to day-to-day changes, especially with respect to MDS, gain settings, and the recording of a signal of known intensity. However, the twice-daily calibrations of the radar systems should have minimized these uncertainties.

More significant are uncertainties associated with the beam width. An echo will be stretched in azimuth and range because of the characteristics of the radar beam. With a 2° conical beam and a pulse length of 600 m the range and azimuthal stretching of an echo at 60 n mi is 300 and 3900 m respectively. Targets at ranges exceeding 60 n mi will be considerably distorted in azimuth. The stretching of an echo in range is a constant, a function of radar pulse length. The distortion of the cloud echoes will lead to an overestimate of the precipitation volume which is compensated by the underestimate caused by nonuniformity of precipitation in the radar beam. At all ranges, the beam is integrating large vertical and horizontal slices that will probably not be uniformly filled with precipitation. At 40 n mi, an echo must be at least 1 to 2 miles in diameter to completely fill the radar beam (fig. 5). As range increases, an echo must be even larger to fill the beam.

Errors caused by beam-filling problems were probably greater than those caused by distortion of the radar targets. The net effect of uncertainties associated with the beam width is thought to be an underestimate of precipitation, especially for the seeded clouds that were at a slightly greater average distance from the UM/10-cm radar (table 3).

9. REPRESENTATIVENESS OF Z-R RELATION

The Z-R relation (2) used in the rainfall calculations is the foundation on which this research has been built. At the outset it was not known how well this relation would represent the convective rainfall on the ground during May 1968. If no one Z-R relation were to fit the convective showers during this month, the absolute magnitudes of the calculated rainfalls might be seriously in error.

The representativeness of the Z-R relation for convective rains during May 1968 was checked by 50 comparisons of rain-gage rainfall with radar rainfall. Woodley and Herndon (1969) treat this in another paper. Only total shower rainfalls were compared because the recording rain gage measurements were too coarse to permit rainfall rate comparisons.

Based on the rain gage as the standard, the radar underestimated the actual rainfall by an average of 8 percent. The average percentage difference is defined here as the average difference between the gage and radar rainfalls divided by the average gage rainfall, rather than the mean of the individual percentage differences, in order to avoid giving undue weight to the few comparisons showing small absolute differences but with large percentage differences. The correlation coefficient between the radar and gage rainfalls was 0.93, significant at the 1 percent level.

The interpolation scheme for calculating point rainfall (radar-rain gage comparison) differed from that used to calculate volume (total cloud) rainfall. In the calculation of point rainfall, the rainfall rate between two known contours was linearly interpolated, and the mean rainfall rate between two known contour values was assumed to lie half the distance between them and not two-thirds the distance to the higher contour as was done in computing volume rainfall. This simplification was necessary because it was very difficult to apply the original interpolation scheme to read rainfall rate at a point. In effect, the interpolation scheme used in the calculation of volume rainfall gives 16 percent less rainfall [(1/2 - 1/3) x 100] than the linear interpolation scheme. Since the radar underestimated point rainfall by about 8 percent, volume rainfall is probably underestimated by 20 to 30 percent of the actual, 8 percent being due to the shortcomings of the radar as revealed by the radar-rain gage comparison and 16 percent to the nonlinear interpolation scheme.

The analysis has revealed that the radar approximated unmodified showers rather well. The remaining uncertainty is whether the radar did as well for showers from the seeded clouds. Unfortunately, because none of the seeded clouds passed over rain gages during the operation of the UM/10-cm radar, a radar-rain gage comparison was not possible for the seeded clouds.

10. VALIDITY OF Z-R RELATION FOR THE SEEDED CLOUDS

The Z-R relation (2) used in the rainfall calculations was derived for unmodified Florida showers having characteristic droplet spectra. If seeding produced clouds with grossly different droplet structures, (2) might not be applicable to showers from these clouds. In studying the seeded cumuli of Flagstaff, Arizona, Jones et al. (1968) found that seeded rains had higher drop concentrations and smaller drops than unseeded rains. Because reflectivity Z is a linear function of the droplet concentration (N) and is proportional to the sixth power of the droplet diameter D ,

$$Z = \sum N_i D_i^6 , \tag{6}$$

these results imply that the same value of reflectivity does not represent the same rainfall rate from seeded and unseeded clouds. In Arizona, a Z-R relation different from the one used to represent unmodified showers might well be applicable to showers from seeded clouds. Seeding may have affected the Florida cumuli in a similar manner.

Precipitation size particles (diameters $>$ 180μ) were observed in the experimental clouds at cloud base and at 20,000 ft with MRI continuous hydrometeor samplers (Mee and Takeuchi, 1968) that had been installed on the RFF DC-6 and NRL S-2D aircraft. A sampler of this type is described in detail by Duncan (1966). A moving strip of soft aluminum foil approximately 3 in. wide was exposed to the ambient airflow through a 1.5 x 1.5-in. slot. Cloud particles with diameters larger than about 180μ striking the foil leave distinct impressions that can be measured and counted. With this information, and the speed of the foil moving by the slot, the true airspeed of the aircraft, and the ratios of imprint to particle size, determined at NRL (1968, private communication), one can then compute representative size distributions of the sampled particles, water contents in ice and water, radar reflectivity, and rainfall intensity. The foil calibration and data reduction and analysis procedures are discussed by Takeuchi (1969).

The individual sample calculations (sample volume $\sim$ 1 m^3) of reflectivity Z and rainfall rate R from the foil observations in the experimental clouds at 20,000 ft and at cloud base (1500 - 3000 ft) were used to derive Z-R relationships in the seeded and control clouds. Empirical relationships of the form

$$Z = AR^b \tag{7}$$

were determined by the method of least squares. Reflectivity was calculated from (6), and rainfall rate was derived from the water mass by size interval and the terminal fall velocities calculated by Gunn and Kinzer (1949) for water and by Weickmann (1953) for ice. The Z-R relationships derived are found in table 10 with 95 percent confidence intervals placed on the A's and b's. Rainfall rate R was the independent variable in the regression analysis.

Analysis of covariance (Li, 1961) showed no significant differences in the exponents b and coefficients A at the 5 percent level between the relationships for the seeded and control clouds. The sample calculations of the Z and R in the seeded and control clouds were then pooled to obtain the combined relationships.

Table 10. Z-R Relations Calculated From Hydrometeor Samples

	DATA SOURCE	n	r	s^2	A	b
DC-6*	SEEDED CLOUDS	110	.95	0.12677	132.04	1.5935
	UNSEEDED CLOUDS	29	.987	0.048897	105.21	1.4734
DC-6	(COMBINED SEEDED & CONTROL CLOUDS)	139	.95	0.11598	$109 \leq 128 \leq 149$	1.5583 ± 0.0760
NRL†	SEEDED CLOUDS	174	.968	0.095972	753.73	1.5179
	UNSEEDED CLOUDS	122	.96	0.10821	759.42	1.4768
NRL	(COMBINED SEEDED & CONTROL CLOUDS)	296	.97	0.10084	$653 \leq 757 \leq 865$	1.5025 ± 0.0449

Z = $mm^6\ m^{-3}$
R = $mm\ hr^{-1}$
n = SAMPLE SIZE
r = CORRELATION COEFFICIENT
s^2 = VARIANCE
ESSA Z = $\Sigma N_i D_i^6$
NRL Z = $\Sigma N_i D_i^6$

* DC-6 = HEIGHT 20,000
† NRL = CLOUD BASE

The Z-R analysis indicates no detectable difference in droplet spectra and the derived Z-R relationships in the seeded and control clouds. This means that (2) was equally valid for showers from seeded clouds and also implies that the rainfall increases from the seeded clouds calculated with (2) are real and not spurious because of an alteration of seeded cloud droplet spectra.

One might wonder why the pooled Z-R relation

$$Z = 757R^{1.5} \qquad (8)$$

that was derived from aircraft measurements at cloud base was not used in preference to (2) to represent rain reaching the ground, especially when one considers that the ground-based radar measurements were made as near cloud base as possible. Equations (2) and (8) are plotted in figure 8.

When plotted, (8) has a greater slope and a greater Z intercept (at R = 1.0 mm hr^{-1}) than (2). This means that for the same reflectivity the rainfall rate is higher for (2) than for (8). If (8) had been used to represent volume and point rainfall, the estimates would have been 50 percent greater underestimates compared with the rain gages than they were.

The reason (2) represents rainfall better than (8) is under intensive study, and attempts are also being made to explain the difference between the Z-R relation derived from droplet measurements at the ground (2) and that derived from aircraft measurements of droplet spectra at cloud base (8).

11. NATURAL GLACIATING BEHAVIOR OF FLORIDA CUMULI

A striking feature of the hydrometeor observations at 20,000 ft (temperature $\sim$-9° C) was the concentrations of natural ice (diameters $>$ 180μ) in the experimental clouds before the seeding pass. Virtually all clouds in which measurements were made had at least one ice particle per liter of cloud air before seeding. It is unlikely that contamination from seeding on other days can explain this ice.

A preliminary analysis of the MRI continuous particle sampler (MacCready and Todd, 1964) observations (particle diameters $<$ 180μ) made from the same aircraft in the same clouds (Takeuchi, 1969) indicate substantial amounts of liquid water in cloud droplets before the seeding pass concurrent with the predominance of ice in precipitation size particles. There was still enough fusion heat potential in the smaller supercooled drops to provide the impetus for dynamic changes induced by seeding. This

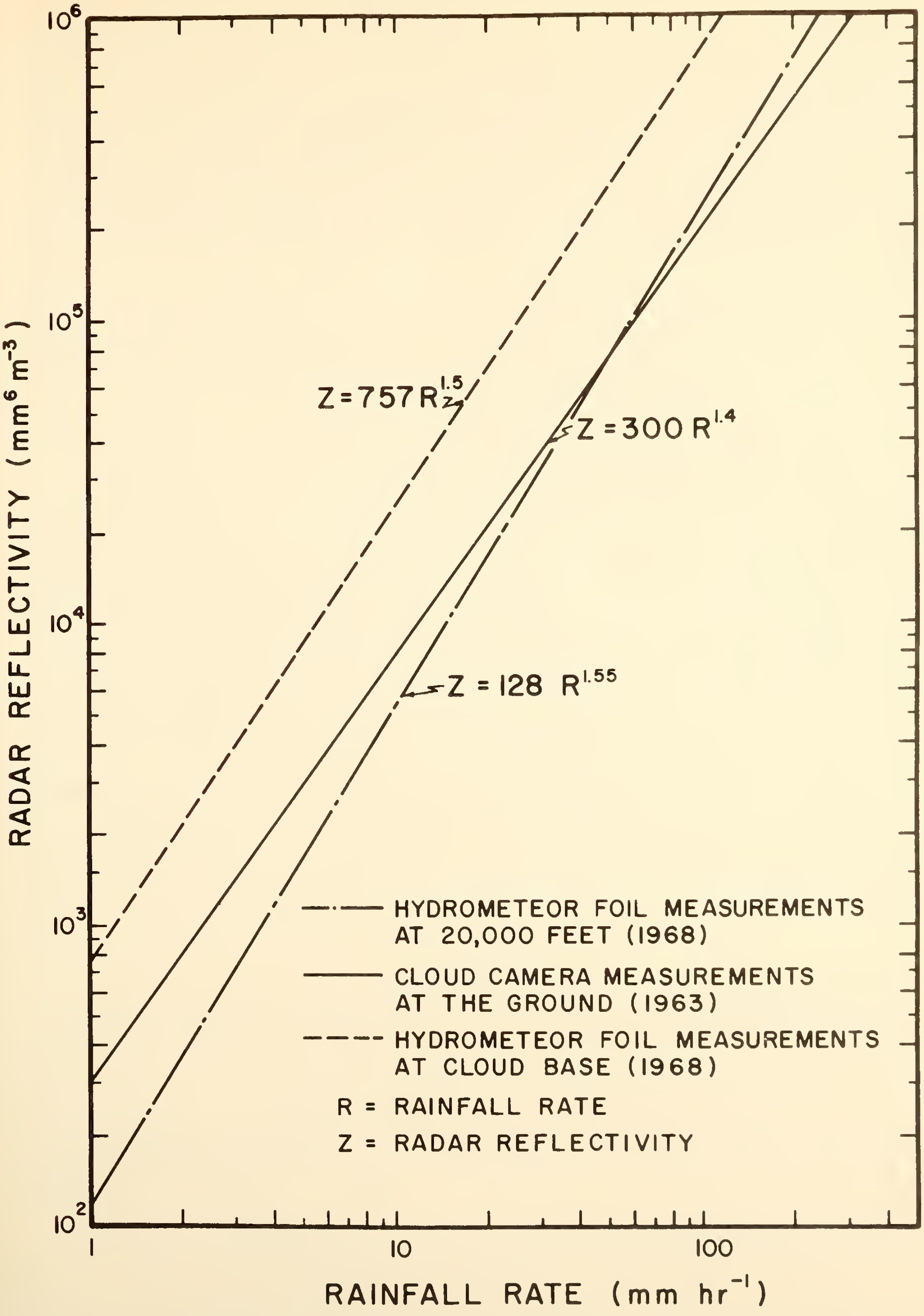

Figure 9. Z-R regression lines for Miami, Florida. The solid line is based on measurements of droplet spectra by Sims et al. (1963) with a droplet camera on the ground. The dash and dot-dash lines were obtained from droplet measurements at the bases and at 20,000 ft in selected experimental clouds. A continuous hydrometeor sampler was used to obtain the in-cloud measurements.

agrees with Sax (1969), who found that portions of the cumuli studied during the 1965 Stormfury cumulus experiments were partially glaciated at -5° C. However, he could explain the dynamical behavior of the clouds following seeding only if their updraft cores remained largely supercooled to -10° C or colder.

The presence of one ice particle per liter of cloud air in the experimental clouds before the seeding pass has several important implications. The "colloidal stability" approach to rainfall enhancement requires that seeding produce about one ice particle per liter of cloud air in clouds that are almost completely supercooled. Because Florida cumuli have this ice concentration naturally, the "colloidal stability" approach to increase rainfall does not seem to be applicable here. Braham (1964) has found natural concentrations of ice as high as 10 per liter in Missouri cumuli with top temperatures of -10° C and warmer. A partial explanation for the failure of the "colloidal stability" approach to produce rainfall increases from seeded Missouri cumuli (Flueck, 1968; Neyman et al., 1969) may be related to the natural ice concentrations in these clouds.

12. DISCUSSION

The increases in precipitation noted during May 1968 Florida program were the result of dynamical invigoration of the cloud and not the direct result of important alteration of cloud microphysics. This agrees quite well with the prediction by Simpson and Wiggert (1969) based on model calculations of seeded cloud behavior. Except for momentary increases in ice in the clouds after seeding, no important differences in cloud particle habit or spectra have been noted between the seeded and control clouds.

The seeded clouds were larger and more lasting and processed more moisture than their unseeded counterparts, which accounted for the increases in precipitation. Because dynamics and not microphysical processes control rain from cumuli in Florida, Missouri (Braham, 1964), and Arizona (Battan, 1963), the dynamic approach to rainfall enhancement from these clouds seems to be the most promising.

13. SUMMARY AND CONCLUSIONS

In analyzing the observations made during May 1968, Woodley (1969) and Simpson et al. (1969) showed clearly that silver iodide pyrotechnic seeding of supercooled Florida cumuli induced cloud growth. This phase of the research strongly suggests that seeding increased rainfall and that these increases were positively correlated with increased cloud growth. Precipitation increases were the result of dynamic alteration, not of direct alteration of cloud microphysics. Pyrotechnic silver iodide seeding apparently provides the impetus for increased cloud growth, following which prolonged and enhanced natural precipitation processes (especially in secondary unseeded towers) account for the increased rainfall.

The average rainfall difference between the seeded and control clouds was subjected to three different, two-tailed statistical tests and was found to be significant between the 5 and 20 percent levels, strongly supporting the hypothesis that invigoration of cloud dynamics increases rainfall.

Silver iodide pyrotechnic seeding had an important effect on cloud dynamics even when certain portions of the clouds contained significant amounts of natural ice. The remaining supercooled water was still adequate to provide the fusion heat necessary for dynamic alteration. This is an important finding, considering the natural glaciating behavior of cumulus clouds in Missouri, Florida, and elsewhere. The presence of pockets of ice at relatively warm temperatures (-5° C to -10° C) need not preclude silver iodide seeding to alter cloud dynamics and increase rainfall. However, the "colloidal stability" approach to rainfall enhancement is apparently not applicable to Florida cumuli -- whether it is to clouds of other seasons and locations must still be determined.

The calibrated 10-cm radar of the Radar Meteorological Laboratory was particularly effective in evaluating precipitation changes following seeding, not only relative precipitation differences between seeded and control clouds but, as indicated by the radar rainfall-rain gage rainfall comparison, the magnitude of the volume rainfall within 30 percent of the actual. This is probably the first time dynamic modification has been demonstrated to result in precipitation increases on the ground.

The efficacy of other silver iodide seeding systems in promoting dynamic changes and new growth had not been evaluated here. However, their effectiveness will probably depend on where and at what rate the silver iodide is released in the cloud. (A critical amount of silver iodide is undoubtedly necessary to affect cloud dynamics, but its distribution is probably of greater importance.) As this research indicates, as little as 500 g of silver iodide can induce growth if it is strategically placed in the active supercooled portion of a cloud.

To recommend routine use of pyrotechnic seeding of individual clouds for augmenting rainfall would be premature. Cloud and environmental conditions favoring large increases in rainfall must be better specified.

Model predictions, which indicate that large precipitation increases can be expected from clouds with large seedability, are a first step, but the optimum amount of silver iodide for the desired effect is still to be specified. The large-scale effect of pyrotechnic seeding is unknown. Invigoration of one cloud with subsequent increase of rainfall might represent only a reorganization of the rainfall over an area, not a net increase. The effect of seeding all suitable clouds over a large area, such as the South Florida peninsula, must still be investigated. Should it be possible to dynamically invigorate whole groups of areas of clouds with subsequent precipitation increases, this would be an important finding indeed.

14. ACKNOWLEDGMENTS

I am greatly indebted to Dr. Joanne Simpson, Chief of the Experimental Meteorology Laboratory, for her help throughout all phases of this research. Without her efforts, the seeding experiment would never have been possible and her advice and suggestions were invaluable in planning and in seeing this research to its completion.

I am also indebted to the following groups and individuals for their outstanding assistance: the Research Flight Facility (RFF) which, under its Director, Mr. Howard Mason, did its customary superb job in carrying out the May 1968 experiment; Dr. Gerry Conrad of RFF, who was particularly helpful in discussions and in helping reduce the liquid water data; the Radar Meteorological Laboratory, University of Miami, which provided radar observations of high quality; Professor Harry Senn whose discussion of the radar systems were most helpful; the Naval Research Laboratory and particularly Mr. Robert Ruskin of NRL, who made his observations available to me; the personnel of the Federal Aviation Agency in Miami for their spirit of cooperation during all phases of the seeding operation; Mr. Alan Herndon of the Experimental Meteorology Laboratory suffered with me through the many tedious calculations; Mr. Don Takeuchi of Meteorology Research, Inc., for helpful discussions and for his work with the hydrometeor observations; Mr. Glen Brier, Director of the Meteorological Statistics Group, Washington, D. C., and his associate Mr. Gerald Cotton provided guidance on the statistical analysis and compiled the randomized seeding instructions; Mr. John Brown for selecting the radar controls.

15. REFERENCES

Andrews, G. F. (1966), Solar radiation - A useful tool for radar antenna orientation, Tech. Rept. Southern Region, Federal Aviation Agency. (unpublished).

Andrews, G. F. , and H. V. Senn (1968), Semi-automatic calibration of receiver and video system characteristics for weather radars, Proc. 13th Radar Meteorol. Conf., Montreal, Canada, 20-23.

Battan, L. J. (1963), Relationship between cloud base and initial radar echo, J. Appl. Meteorol. 2, 333-336.

Bethwaite F. D., E. J. Smith, J. A. Warburton, and K. J. Heffernan (1966), Effects of seeding isolated cumulus clouds with silver-iodide, J. Appl. Meteorology 5, 513-520.

Braham, R. R., Jr. (1964), What is the role of ice in summer rainshowers?, J. Atmospheric Sci. 21, 640-645.

Davis, L. G., and C. L. Hosler (1967), The design, execution and evaluation of a weather modification experiment, Fifth Berkely Symp. Math. Statistics and Probability, 253 -270 (University of California Press, Berkeley, Calif.)

Davis, L. G., J. I. Kelley, A. Weinstein, and H. Nicholson (1968), Weather modification experiments in Arizona, Dept. Meteorol., Pennsylvania State University, State College, Penn. 128 pp.

Duncan, A. D. (1966), The measurement of shower rainfall using an airborne foil impactor, J. Appl. Meteorol. 5, 198-204.

Fletcher, N. H. (1963), The Physics of Rainclouds (Cambridge University Press, Cambridge, England), 386 pp.

Flueck, J. A. (1968), A statistical analysis of Project Whitetop's precipitation data, Proc. First Natl. Conf. Weather Modification, Albany, New York, 26-35.

Gerrish, R., and H. W. Hiser (1965), Meso-scale studies of instability patterns and winds in the tropics, Rept. 7, U. S. Army Electronics Laboratories, Fort Monmouth, New Jersey, 63 pp.

Gunn, R., and G. D. Kinzer (1949), The terminal velocity of fall for water droplets in stagnant air, J. Meteorol. 6, 243-248.

Hiser, H. W. and G. F. Andrews (1966), A new approach to range normalization and stepped attenuation for weather radars, Proc. 12th Conf. Radar Meteorol., Norman, Oklahoma, 62-66.

Howell, W. E. (1960), A comparison between two tranformations used in normalizing meteorological data. J. Meteorol. 17, 684.

Jones, D. M. A., G. E. Stout, and E. Mueller (1968), Raindrops spectra for seeded and unseeded showers, Proc. First Natl. Conf. Weather Modification, Albany, New York, 26-35.

Kraus, W. E. B., and P. Squires (1947), Experiments on the stimulation of clouds to produce rain, Nature 159, 489-491.

Li, J. C. R. (1961), Introduction to Statistical Inference (Edward Brothers, Inc., Ann Arbor, Michigan), 568 pp.

MacCready, P. B. (1959), The lightning mechanism and its relation to natural and artificial freezing nuclei, Recent Advances in Atmospheric Electricity, 369-381 (Pergamon Press, London, England).

MacCready, P. B., Jr., and C. J. Todd (1964), Continous particle sampler, J. Appl. Meteorol. 3, 450-460.

McDonald, J. E. (1958), The physics of cloud modification, Advances in Geophysics 5 (Academic Press, Inc., New York, N. Y.).

Malkus, J. S., and R. H. Simpson (1964), Modification experiments on tropical clouds, Science 145, 541-548.

Mason, B. J. (1962), Clouds, Rain and Rainmaking (Cambridge University Press, Cambridge, England), 145 pp.

Mee, T. R., and D.M. Takeuchi (1968), Natural glaciation and particle size distribution in marine tropical cumuli, Final Rept. by Meteorology Research, Inc. to Experimental Meteorology Laboratory, APCL, ESSA, Contract No. E22-30-68 (N), 71 pp.

Neave, H. R., and C. W. J. Granger (1968), A Monte Carlo study comparing various two sample tests for differences in mean, Technometrics 10, 509-522.

Neyman, J., E. Scott, and J. A. Smith (1969), Areal spread of the effect of cloud seeding at the Whitetop experiment, Science 163, 1445-1449.

Orr, J. L., D. Fraser, and K. G. Pettit (1949), Canadian experiments on artificially inducing precipitation, U. N. Conf. Conservation and Utilization of Resources, Water Resources 4.

Sax, R. I. (1969), The importance of natural glaciation on the modification of tropical maritime cumuli by silver iodide seeding, J. Appl. Meteorol. 8, 92-104.

Schaefer, V. J. (1946), The production of ice crystals in a cloud of supercooled water droplets, Science 104, 457-459.

Senn, H. V., and G. F. Andrews (1968), A new, low-cost multi-level iso-echo contour for weather-radar use, J. Geophys. Res. 73, 1201-1207.

Senn, H. V., and C. L. Courtright (1968), Radar hurricane research, Final Rept. by Institute of Marine Sciences, Univ. of Miami, Radar Meteorology Section to U. S. Weather Bureau, Contract No. E22-62-68(N), 31 pp.

Simpson, J., G. W. Brier, and R. H. Simpson (1967), Stormfury cumulus seeding experiment 1965: Statistical analysis and main results, J. Atmospheric Sci. 24, 508-521.

Simpson, J., and V. Wiggert (1969), Models of precipitating cumulus towers, Mon. Wea. Rev. 97(7), 471-489.

Simpson, J., and W. L. Woodley (1969), Intensive study of three seeded clouds on May 16, 1968, ESSA Tech. Memo. ERLTM-APCL 8.

Simpson, J., W. L. Woodley, H. A. Friedman, G. W. Slusher, R. S. Scheffee, and R. L. Steele (1969), A pyrotechnic cloud seeding system and its use, ESSA Tech. Memo ERLTM-APCL 5.

Sims, A. L., E. A. Mueller, and G. E. Stout (1963), Investigation of quantitative determination of point and areal precipitation by radar echo measurements, 8th Quart. Tech. Rept., 1 July 1963-30 September 1963, Meteorological Laboratory, Illinois State Water Survey, University of Illinois, Urbana, Ill., 27 pp.

Takeuchi, D. M. (1969), Analysis of hydrometeor sampler data for ESSA cumulus experiments, Miami, Florida, May 1968, Final Rept. by Meteorology Research, Inc. to Experimental Meteorology Branch, APCL, ESSA, Contract No. E22-28-69(N), 44 pp.

Vonnegut, B. (1947), The nucleation of ice formation by silver iodide, J. Appl. Phys. 18, 593-595.

Vonnegut, B., and K. Maynard (1952), Spray-nozzle type silver iodide smoke generator for airplane use, Bull. Am. Meteorol. Soc. 33, 420-428.

Weickmann, H. (1953), Observational data on the formation of precipitation in cumulonimbus clouds, Thunderstorm Electricity, 66-138 (University of Chicago Press, Chicago, Ill.).

Weinstein, A. I. (1969), A numerical model of cumulus dynamics and microphysics, Dept. Meteorol., Pennsylvania State University, State College, Penn., 75 pp.

Woodley, W. L. (1969), The effect of airborne silver iodide pyrotechnic seeding on the dynamics and precipitation of supercooled tropical cumulus clouds, A dissertation submitted to the Graduate School of Florida State University in partial fulfillment of the requirements for the degree of Doctor of Philosophy. 187 pp.

Woodley, W. L., and A. Herndon (1969), A rain gage evaluation of the Miami Z-R relation (to be published).

GPO 853-653

U.S. DEPARTMENT OF COMMERCE
Environmental Science Services Administration
Research Laboratories

ESSA Technical Memorandum ERLTM-AOML 3

A RAIN GAGE EVALUATION OF THE MIAMI REFLECTIVITY-RAINFALL RATE RELATION

William Woodley
Alan Herndon

Experimental Meteorology Laboratory

Atlantic Oceanographic and Meteorological Laboratories
Miami, Florida
September 1969

TABLE OF CONTENTS

ABSTRACT

To provide a foundation for other radar studies in the Miami area, fifty comparisons were made between shower rainfall recorded by rain gages and observed with radar to evaluate the reflectivity (Z) -- rainfall rate (R) relation, $Z = 300R^{1.4}$, referred to here as the Miami Z-R relation. Total shower rainfall measured by recording rain gages was compared with estimates derived from the Miami Z-R relation in conjunction with radar reflectivity measurements with iso-echo contouring and the analysis scheme described. The radar and rain gages estimates of shower rainfall were highly correlated (+0.93, significant at the 1 percent level) and differed an average between 8 and 30 percent. Stratification by shower amount revealed that radar estimate of gage-recorded rainfall was too high for small shower amounts (<0.25 in.) and too low for large shower amounts. In terms of percentage the comparison was best for the heavy showers. Stepwise regression analysis showed that consideration of the square of the range from gage to radar made a small (3 percent) but statistically significant (< 1 percent level) reduction in the variance and improved the correlation (0.93 to 0.944) between the gage and radar estimates of precipitation. It is concluded that the Miami Z-R relation, when used with the radar system described, is an effective tool in representing point and areal rainfall from South Florida convective showers.

A RAIN GAGE EVALUATION OF THE MIAMI REFLECTIVITY-RAINFALL RATE RELATION

William Woodley and Alan Herndon

1. INTRODUCTION

Over the last two decades radar has been used for quantitative measurements of rainfall, based on investigations relating rainfall rate, R, to reflectivity, Z. The Z-R relations computed directly by measuring radar reflectivity and rainfall amount or indirectly by measuring raindrop size spectra, have been derived for various locations, seasons, and storm types. Stout and Mueller (1968) give an excellent survey of these relations and a discussion of their accuracy when used for quantitative rainfall measurements.

The accuracy of Z-R relations is assuming greater importance because these relations are now being used in evaluating the results of seeding experiments designed to increase rainfall. Cloud seeding experiments in Arizona (Davis et al., 1968) and in Florida (Woodley, 1969) are but two recent examples. The Florida study showed that seeding increased rainfall an average of 100 to 150 acre-feet per cloud by 40 min after the seeding pass, representing an increase of over 100 percent. If these radar-derived precipitation results are to have credibility, it is important to demonstrate that the Z-R relation and radar system used in the analysis accurately represented rain reaching the ground during the period of experimentation.

The Miami Z-R relation is based on the work by Sims et al. (1963), who obtained the Z-R relation

$$Z = 286R^{1.43} \tag{1}$$

by independently calculating reflectivity (Z mm^6 m^{-3}) and rainfall rate (R, mm hr^{-1}) from raindrop photographs taken during showers in Miami, Florida. Equation (1) has been modified slightly to

$$Z = 300R^{1.4} \tag{2}$$

by Gerrish and Hiser (1965), who averaged the coefficients and exponents of the Z-R relations derived by Sims et al. (1963) for air mass (wet season), easterly wave, cold trough, and overrunning situations, and for showers and thunderstorms for Miami, Florida. Equation (2), referred to here as the Miami Z-R relation, is evaluated in this paper by comparing recording rain gage measurements with shower rainfall estimated from the same filmed radar observations used in studying the experimental clouds during May 1968. Only total shower rainfalls were compared, because the time scale on the recording rain gage trace was too compressed to permit rainfall rate comparisons. Gage-measured rainfall was the standard of comparison, although the accuracy might be questionable since no attempt was made to evaluate the condition and exposure of the rain gages used.

2. RADAR SYSTEMS

The modified UM/10-cm radar of the Radar Meteorological Laboratory, Institute of Marine Science, University of Miami, was used in the comparison. It has a 2° conical beam, a transmitter power of 5.5×10^5 W, a minimum detectable signal of 10^{-14} W, a pulse length of 2 μs, and a pulse repetition rate of 300 pulses/sec. Included are special logarithmic and linear radar receivers, an RF range attenuation corrector, and an iso-echo contour unit. The UM/10-cm radar was calibrated twice daily during the experiment. For more details on this radar unit, including a discussion of its calibration, the reader is referred to Senn and Courtright (1968) and Woodley (1969).

The comparisons between radar and rain gage rainfall observations were made in the annulus 20 to 50 n mi from the UM/10-cm radar. The antenna tilt was 0.5°, which means that the center of the radar beam was within 1500 ft of cloud base (∿2500 ft) for clouds within this annulus. All cloud echoes were contoured with the IEC unit built at the radar laboratory (Senn and Andrews, 1968). The Z values and equivalent precipitation rate for various contours are shown in table 1.

3. METHOD

The photographs of the UM/10-cm radarscope were projected frame by frame onto the rain gage map as shown in figure 1. The map projection represents true distances to within 50 ft. The ground targets on the map were aligned with the corresponding ground targets on the radar film. Several areas of contoured echoes are shown schematically on the rain gage map. Each contour corresponds to a reflectivity threshold and rainfall rate; the former was obtained with the calibration systems described by Andrews and Senn (1968), the latter from the Miami Z-R relation in (2).

Readings were made from the radar photographs taken at 1- to 2-min intervals at the location of a recording rain gage, plotted versus time, integrated with a planimeter to provide total shower rainfall, and then compared with the shower rainfall recorded by the rain gage. Evaporation of the rain drops in falling from the level of scan to the

Table 1. UM/10-cm Signal Levels, P_r, and Z R Values, May 1968 Florida Program.

DATE	CONTOUR	P_r (dbm)	$Zmm^6 m^{-3}$	R(IN/HR)	CONTOUR	P_r (dbm)	$Zmm^6 m^{-3}$	R(IN/HR)	CONTOUR	P_r (dbm)	$Zmm^6 m^{-3}$	R(IN/HR)	CONTOUR	P_r (dbm)	$Zmm^6 m^{-3}$	R(IN/HR)
MAY 15-20	1	-109	5	.002	2	-86	1.1×10^3	.09	3	-76	1.1×10^4	.45	4	-64	1.9×10^5	3.5
21	1	-109	5	.002	2	-86	1.1×10^3	.09	3	-77	$.9 \times 10^4$	.40	4	-64	1.9×10^5	3.5
23	1	-109	5	.002	2	-86	1.1×10^3	.09	3	-76	1.1×10^4	.45	4	-64	1.9×10^5	3.5
25	1	-109	5	.002	2	-85	1.5×10^3	.10	3	-74	1.8×10^4	.60	4	-64	1.9×10^5	3.5
26	1	-109	5	.002	2	-85	1.5×10^3	.10	3	-72	3×10^4	.80	4	-63	2.1×10^5	4.0
27	1	-106	11	.003	2	-86	1.1×10^3	.09	3	-74	1.8×10^4	.60	4	-63	2.1×10^5	4.0
28	1	-102	24	.006	2	-86	1.1×10^3	.09	3	-77	$.9 \times 10^4$	.40	4	-63	2.1×10^5	4.0
30	1	-100	40	.009	2	-86	1.1×10^3	.09	3	-75	1.4×10^4	.55	4	-63	2.1×10^5	4.0
REQUESTED VALUES	1	—	—	—	2	-85	1.1×10^3	.10	3	-73	2×10^4	.75	4	-67	$.9 \times 10^5$	2.30

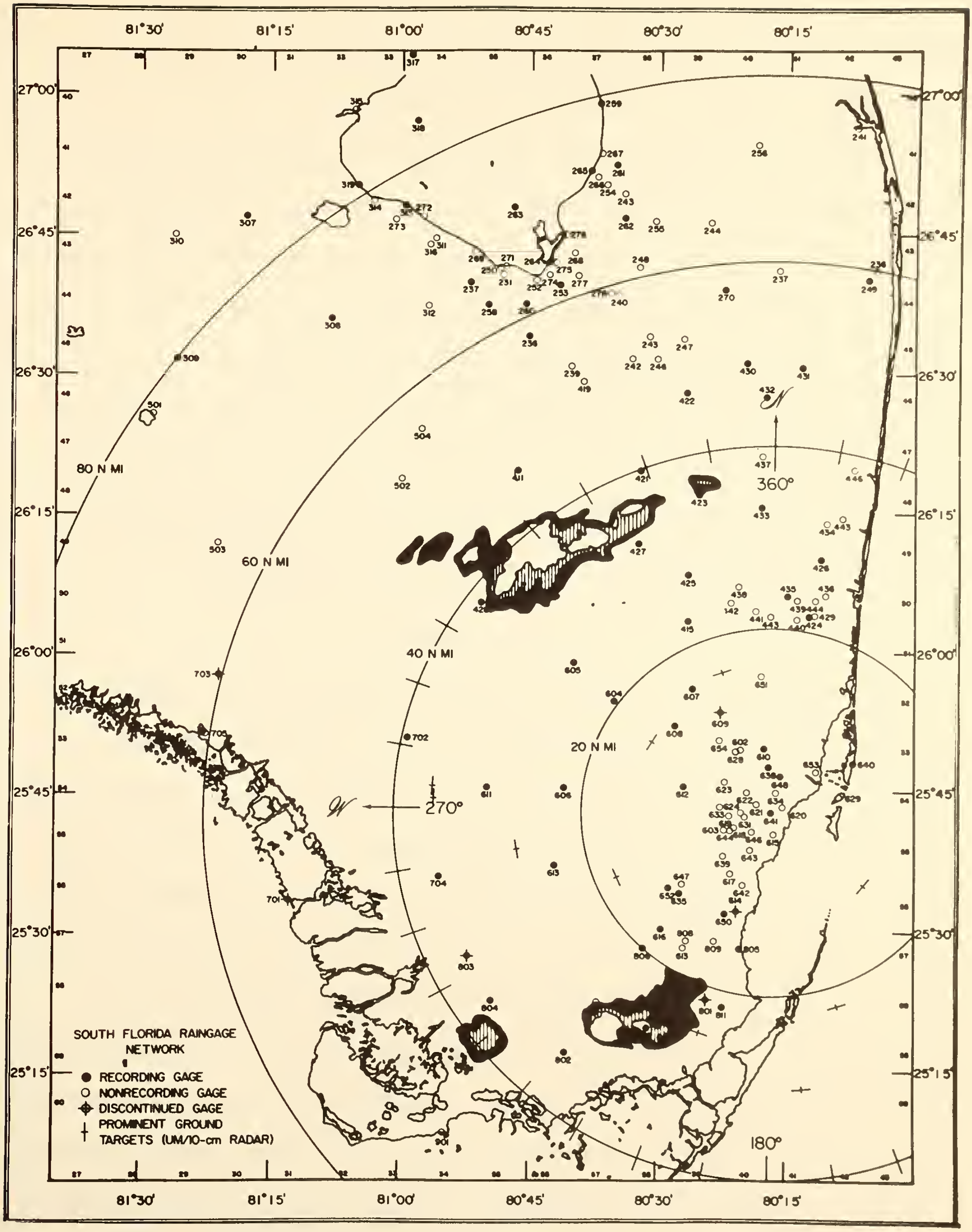

Figure 1. Example of contoured echoes superimposed on the South Florida rain gage network (network based on the work by Mr. Garold Gerrish, Radar Meteorological Laboratory, University of Miami). The first (boundary) contour corresponds to .006 in. hr^{-1}, the second to .09 in. hr^{-1}. Inside the white area the rainfall rate exceeds 0.40 in. hr^{-1}.

ground was neglected. The person reading rainfall rate from the film did not know the gage amount until after the reading.

A linear interpolation scheme was used to determine the radar rainfall rate at a gage location between two known contours. The rainfall rate for a point bounded by only one contour, A for example, was obtained by linearly interpolating between A and the next higher contour permitted by the system, which was assumed to exist as a point value at the center of the area contained by A. The rainfall rate for a point within the highest contour permitted by the system was linearly interpolated between the boundary value and rainfall rate of 6.00 in. hr^{-1}, which was assumed to exist as a point value at the center of the contoured area.

4. ANALYSIS PROBLEMS

Comparing a radar estimate of shower rainfall with a rain gage estimate is difficult. The vertical separation (1000 to 4000 ft) between the rain gage and the level of the radar scan and the drift of the precipitation while falling this distance are decided problems. Also degrading the comparison are the tremendous difference between the size of the radar and rain gage samples and the likelihood that the radar beam is not always uniformly filled with precipitation, but the most serious obstacles are the convective rains in Florida; the observation that it often rains heavily on one side of the street and not on the other is certainly true here. Unfortunately, the 10-cm radar does not have resolution to this distance scale, and even if it did the 1/2 n mi diameter of the dot representing the rain gage precludes accurate rainfall rate interpolation on a scale less than one half the dot's diameter. Because a gage might easily be placed too close or too far by 1/4 n mi with respect to an echo, there will be errors in representing rainfall with a radar at the location of a gage even if the Z-R relation, the map projection, and the rain gage locations on the map are perfect. However, the resulting error in estimating point rainfall should not be systematic.

5. RESULTS

The rain gage (G) and radar observations (R_a) permitted 50 comparisons, none of which involved seeded clouds. These comparisons are tabulated in table 2 and summarized in table 3. Using the rain gage results as the standard, the average error is an 8 percent underestimate by the radar when the differences are summed algebraically and about 30 percent if their values are summed. The average percentage difference is defined here as the average difference divided by the average gage-recorded rainfall, rather than the mean of the individual percentage differences, in order not to give undue weight to the few comparisons with the small absolute differences but large percentage differences. The correlation coefficient between G and R_a was found to be 0.93, significant at better than the 1 percent level.

A more meaningful analysis of the comparison between G and R_a is stratification of the observations by shower amount, as shown in table 4. The mean difference ($\overline{G - R_a}$) suggests that the radar overestimated the gage-recorded rainfall for shower amounts less than 0.25 in. and underestimated it for larger amounts. The radar did best for the heavy showers, as suggested by the ratio of the mean difference to the mean gage-recorded rainfall and the ratio of the standard error to the mean

Table 2. Comparison of Rainfall Recorded by Rain Gages and Rainfall Observed With the UM/10-cm Radar, May 1968.

DATE (MAY)	STN. NO.	RAIN GAGE MEASUREMENTS RAINFALL (G) (IN.)	RADAR MEASUREMENTS MAX RAINFALL RATE (IN HR^{-1})	SHOWER DURATION (MIN.)	RAINFALL (R_a) (IN.)	$G-R_a$ (IN.)	$G-G_p$ $G_p=-0.1488+1.1428R_a+.000153d^2$	DIST. OF GAGE FROM RADAR (N. MI.)
16	433	.00	.20	11	.01	-.01	-.03	33.3
16	423	.07	.45	37	.10	-.03	-.09	35.8
16	415	.05	.10	35	.03	.02	.05	27.5
19	422	1.22	3.40	52	.71	.51	.22	47.0
19	423	.22	2.00	44	.29	-.07	-.16	35.8
19	425	.15	.80	70	.22	-.07	-.07	27.4
19	430	.18	1.50	56	.37	-.19	-.18	23.0
19	415	.05	1.50	62	.18	-.13	-.12	27.5
19	425	.08	.60	30	.10	-.02	.00	27.4
19	424	.03	.20	29	.02	.01	.08	21.6
19	424	,20	1.00	34	.13	.07	.13	21.6
20	812	.78	1.50	62	.41	.37	.35	27.0
20	426	1.41	3.60	56	1.19	.22	.08	28.1
20	428	.10	.40	15	.03	.07	-.01	38.2
20	604	.21	4.00	35	.46	-.25	-.23	20.4
20	605	.19	2.00	22	.21	-.02	-.01	26.5
20	423	.11	.50	21	.09	.02	-.04	35.8
20	435	.39	3.50	28	.40	-.01	.00	23.5
20	807	.99	3.50	65	.92	.07	.01	22.5
20	613	.18	.60	48	.11	.07	.12	23.5
21	435	.10	1.00	35	.13	-.03	.02	23.5
21	605	.01	.50	16	.02	-.01	.03	26.5
25	807	.48	.65	88	.39	.09	.11	22.5
26	702	.20	1.50	32	.13	.07	-.03	38.7
26	433	1.06	3.00	35	.77	.29	.16	33.3
27	426	.11	1.50	18	.14	-.03	-.02	28.1
28	428	.30	.55	35	.18	.12	.02	38.2
28	812	.17	.50	50	.16	.01	.02	27.0
28	812	.47	.90	55	.33	.14	.13	27.0
28	811	.15	.50	48	.16	-.01	.14	22.1
28	432	.02	.40	22	.05	-.03	-.21	45.6
28	422	.43	.45	17	.06	.37	.17	47.0
28	807	.13	.45	50	.11	.02	.08	22.5
28	807	.03	.60	20	.06	-.03	.03	22.5
28	804	.15	.60	22	.07	.08	.02	36.1
30	613	.00	.40	14	.04	-.04	.02	23.5
30	423	.06	.60	28	.10	-.04	-.10	35.8
30	605	.68	4.00	64	.81	-.13	-.21	26.5
30	423	.90	4.00	60	.77	.13	-.03	35.8
30	423	.98	4.00	73	1.04	-.06	-.26	35.8
30	605	.22	5.00	17	.62	-.40	-.45	26.5
30	424	.38	5.00	32	.55	-.17	-.17	21.6
30	426	.18	1.00	21	.17	.01	.01	28.1
30	807	.22	2.45	21	.30	-.08	-.05	22.5
30	807	.60	2.00	38	.46	.14	-.15	22.5
30	811	.04	.55	26	.07	-.03	.03	22.1
30	812	.05	.60	20	.09	-.04	-.02	27.0
30	811	.48	3.55	30	.38	.10	.12	22.1
30	702	1.40	4.00	113	1.05	.35	.12	38.7
30	435	1.59	5.00	75	1.30	.29	.17	23.5

Table 3. Statistical Summary of Comparison Between Rainfall Recorded by Rain Gages (G) and Observed by Radar (R).

ΣG	$\bar{G}$	ΣR_a	$\bar{R}_a$	$\overline{G-R_a}$	$\frac{\overline{G-R_a}}{\bar{G}} \times 100$	$\overline{\lvert G-R_a \rvert}$	$\frac{\overline{\lvert G-R_a \rvert}}{\bar{G}} \times 100$	r_{G,R_a}	b	R_{a_o}
(in.)	(in.)	(in.)	(in.)	(in.)	(%)		(%)			
17.51	.36	16.58	.33	.03	8	.11	30	0.93	.80	+.06

r_{G,R_a} = correlation of G and R_a.

b = slope of least squares best fit line.

R_{a_o} = intercept on R_a axis of least squares best fit line.

difference. The better radar-rain gage agreement with increasing shower amount is a fortunate circumstance, because the heavy rainfall is the one of most concern.

Table 4. Stratification by Shower Amount of G and R_a Comparison.

Rainfall Category	n	G (in.)	$\overline{G - R_a}$ (in.)	$\dfrac{\overline{G - R_a}}{\overline{G}}$	σ	$\dfrac{\sigma}{\overline{G - R_a}}$
0 G .10	15	.046	-.023	-.49	.04	-1.74
.11 G .25	17	.175	-.046	-.27	.13	-2.83
.26 G .50	7	.418	.091	.22	.18	1.98
G .50	11	1.055	.200	.20	.20	1.00

$$\sigma = \left[\frac{\Sigma \left[(G - R_a)_i - \overline{(G - R_a)} \right]^2}{n - 2} \right]^{1/2}$$

In figure 2, G and R_a are plotted on a scatter diagram, where the solid line is a theoretical line of perfect agreement (slope 1, intercept 0) between the two measures of shower rainfall and the dashed line is the least squares best fit line (Guttman and Wilks, 1965) for the plotted points. Gage-recorded rainfall (G) was the independent variable in this analysis. The values of the slope and the R_a intercept of the best fit line are given in table 3.

The scatter of points about the best fit line (fig. 2) is probably the result of the nonsystematic, inexact placement of the rain gages with respect to the echoes, especially in regions of intense rainfall rate

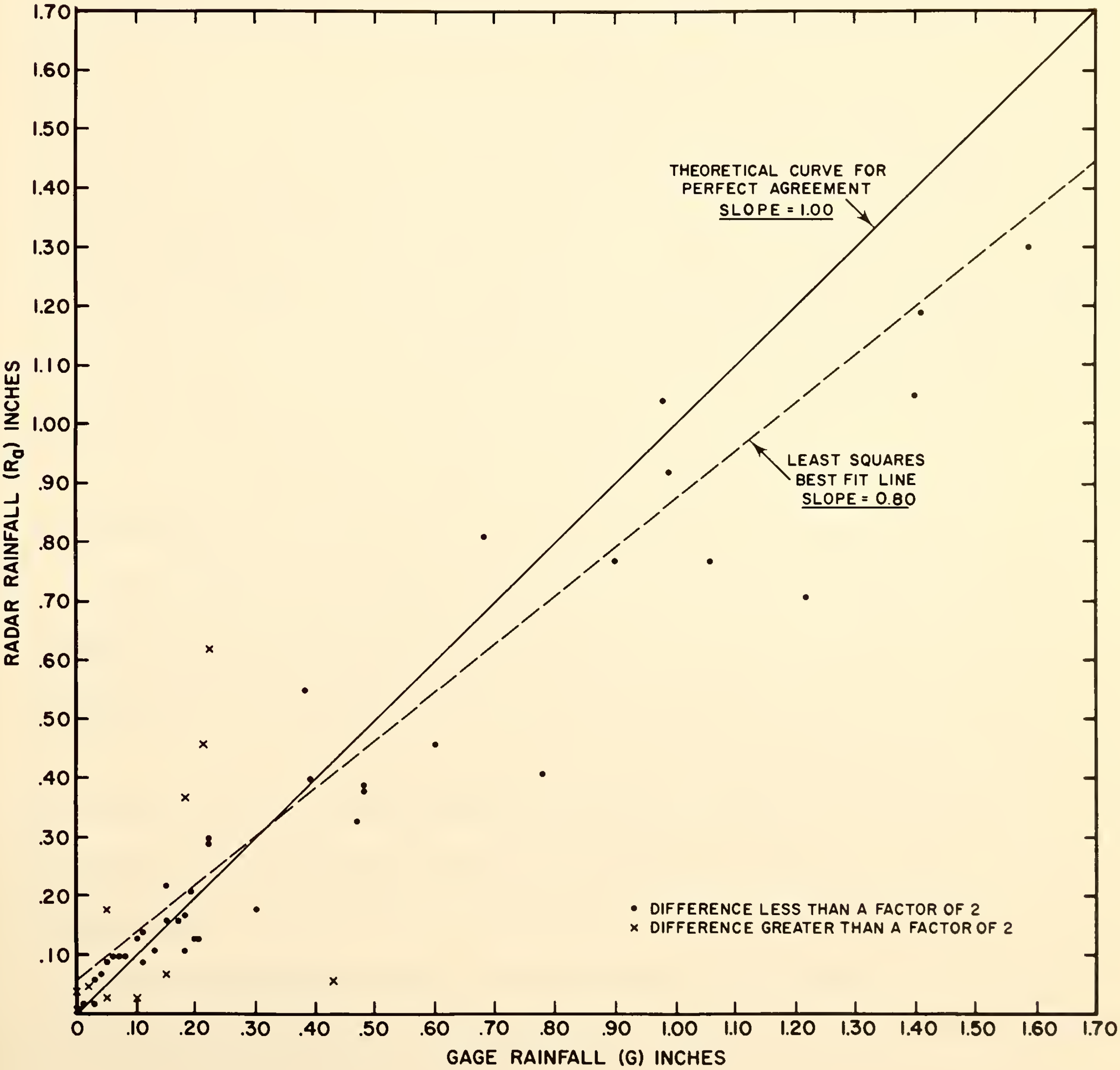

Figure 2. Comparison between G and R_a. The solid line is the line of perfect agreement, and the dashed line is the least squares best fit line for the plotted points.

gradient. The point scatter appears random, in contrast to the systematic error that would be generated by shortcomings in the Miami Z-R relation or the UM/10-cm radar system.

Regression analysis with G as the dependent variable was performed to derive a prediction equation that might then be used to estimate gage-recorded rainfall from rainfall measurements by radar. The best fit equation

$$G = -.0128 + 1.1424\ R_a \tag{3}$$

provides a better estimate of G than R_a itself.

Stepwise regression analysis revealed that consideration of the square of the distance (d^2) from the gage to the radar would improve the radar estimate of gage measurements. With R_a and d^2 as predictors and G as the predictand, stepwise regression gave the equation

$$G_p = -0.1488 + 1.1428\ R_a + .000153\ d^2. \tag{4}$$

The multiple correlation of R_a and d^2 with G is 0.944, and the variance between the estimated and actual gage-recorded rainfall is reduced by 3 percent over what it was with a simple linear regression between G and R_a, a reduction significant at the 1 percent level. The multiple correlation was higher with d^2 than with d itself.

Equation (4) was used as a prediction equation to provide a new estimate of the rain-gage rainfall, G_p; R_a and the ranges of the radar to the rain gages tabulated in table 2 were substituted into (4), and G_p was calculated. The gage-recorded rainfalls G were then differenced with the corresponding predicted rainfalls G_p and tabulated in column 8 of table 2.

Equation (4) generated estimates of G that are much improved over the original estimates, R_a. As examples, the average percentage error is 1 percent if the differences $(G - G_p)$ are summed algebraically and 10 percent if their absolute values are summed.

6. CONCLUSIONS

Based on the preceding discussion the following conclusions seem justified:

(1) The Miami Z-R relation in conjunction with the UM/10-cm radar system gave estimates of point rainfall that averaged within 30 percent of the values provided by rain gages.

(2) The radar tended to underestimate the gage-recorded rainfall with increasing shower amount and increasing distance of the gage from the radar.

(3) In terms of percentage, the radar did best for large shower amounts.

(4) Consideration of range effects made a small (3 percent) but statistically significant (1 percent) reduction in the variance between the gage and radar estimates of precipitation.

(5) The precipitation increases from Florida seeded clouds found by Woodley (1969), using the Miami Z-R relation, represent real increases on the ground, provided the Miami Z-R relation is equally valid for the seeded clouds.

(6) The UM/10-cm radar in conjunction with the Miami Z-R relation should represent areal rainfall better than point rainfall because in the former case the exact position of an echo with respect to a particular ground feature is not a critical consideration.

If one can extrapolate the above conclusions to other months during the South Florida wet season, this study has the following important implications:

(1) The UM/10-cm radar with iso-echo contouring is an effective tool in evaluating cumulus seeding experiments in South Florida, probably the best tool for clouds at ranges no greater than 100 n mi.

(2) Combined with the Miami Z-R relation, the radar should be of more use to hydrologists in South Florida than the current network of rain gages because the radar (a) generally comes within 30 percent of the rainfall measured by a gage and (b) provides the equivalent of a rain-gage network of infinite density when used to estimate areal rainfall. This is vitally important in South Florida, where a meaningful interpolation between rainfall measured by rain gages separated by more than a few miles is very difficult, if not impossible, to obtain.

If the Miami Z-R relation and the UM/10-cm radar systems are to be used in the future to estimate rainfall, it is important that the whole system be automated to circumvent the tedious analysis that was necessary in this study. Also, additional comparisons of this nature should be made in different months and under differing synoptic conditions to clarify the situation under which the Miami Z-R relation provides an accurate estimate of shower rainfall.

7. ACKNOWLEDGEMENTS

We are especially grateful to the Radar Meteorological Laboratory of the Institute of Marine Sciences, University of Miami, for the excellent quality of the radar observations. Professor Harry Senn was very helpful in providing technical information, and Mr. Harold Gerrish made available the South Florida rain gage network.

The Meteorological Statistics Group in Washington, D. C., especially Mr. Glenn Brier and his associates, Messrs. Gerald Cotton and Tom Carpenter, receive special thanks for advice and assistance with the statistical analysis.

Mr. Richard Schwartz played a vital role in working with the South Florida rain gage network. We also appreciate the cooperation of the many agencies in South Florida that made their rain gage observations available to us.

8. REFERENCES

Andrews, G. F., and H. V. Senn (1968), Semi-automatic calibration of receiver and video system characteristics for weather radars, Proc. published by 13th Radar Meteorology Conf Montreal, Canada, 20-23.

Davis, L. G., J. I. Kelley, A. Weinstein, and H. Nicholson (1968), NSF Rept. #12A, Final Rept. NSF GA-777, The Pennsylvania State University, University Park, Pennsylvania, 128 pp.

Gerrish, H. P., and H. W. Hiser (1965), Meso-scale studies of instability patterns and winds in the tropics, Rept. 7, U. S. Army Electronics Laboratories, Fort Monmouth, New Jersey, 63 pp.

Guttman, J., and S. S. Wilks (1965), Introductory Engineering Statistics (John Wiley and Sons, Inc, New York), 340 pp.

Senn, H. V., and G. F. Andrews (1968), A new low cost multi-level iso-echo contour for weather-radar use, J. Geophys. Res. 73, 1201-1207.

Senn, H. V., and C. L. Courtright (1968), Radar hurrricane research, Final Rept. by Institute of Marine Sciences, Univ. of Miami, Radar Meteorology Section to U. S. Weather Bureau, Contract # E22-62-68(N), 31 pp.

Sims, A. L., E. A. Mueller, and G. E. Stout (1963), Investigation of quantitative determination of point and areal precipitation by radar echo measurements, 8th Quart. Tech. Rept., 1 July 1963 -- 30 September

1963, Meteorological Laboratory, Illinois Water Survey, University of Illinois, Urbana, Ill., 27 pp.

Stout, G. E., and E. A. Mueller (1968), Survey of relationships between rainfall rate and radar reflectivity in the measurement of precipitation. J. Appl. Meteorol. 7, 465-473.

Woodley, W. L. (1969), Precipitation results from a pyrotechnic cumulus seeding experiment, ESSA Tech. Memo (to be published).

GPO 854-004

U.S. DEPARTMENT OF COMMERCE
Environmental Science Services Administration
Research Laboratories

ESSA Technical Memorandum ERLTM-AOML 5

LARGE-SCALE PRECIPITATION EFFECTS OF SINGLE CLOUD PYROTECHNIC SEEDING

W. L. Woodley
A. Herndon
R. Schwartz

Experimental Meteorology Laboratory

Atlantic Oceanographic and Meteorological Laboratories
Miami, Florida
November 1969

TABLE OF CONTENTS

ABSTRACT

The large-scale precipitation effects of single cloud pyrotechnic seeding in South Florida during May 1968 are investigated with a twofold approach:

(1) Rainfall over areas traversed by the silver iodide plume is compared with that over areas not affected by the plume, and

(2) "radar rainfall" over a circular grid centered on the core of the seeded clouds is compared with grid rainfall centered on the non-seeded experimental clouds.

Analysis techniques are described with their limitations and uncertainties. The results are not conclusive. In the plume analysis, the precipitation maxima on four of the nine experimental days might be explained by the passage of the seeded plume. In the grid analysis there was higher average grid rainfall within a 20-n mi radius of the seeded clouds than there was for the controls, but this result is not significant, even at the 20% level using a Wilcoxon-Mann-Whitney non-parametric test. Data limitations preclude a meaningful statement about the grid rainfall at greater radii from the experimental clouds.

Although single cloud silver iodide pyrotechnic seeding caused increased growth and precipitation from the seeded clouds during May 1968, the large scale precipitation effects during this period, while positive, were apparently too small to be significant. A more definitive statement must await a longer experimental period with a much larger sample of clouds.

LARGE-SCALE PRECIPITATION EFFECTS OF

SINGLE CLOUD PYROTECHNIC SEEDING

W. L. Woodley, A. Herndon, and R. Schwartz

1. INTRODUCTION

Silver iodide pyrotechnic seeding of individual supercooled cumulus clouds in South Florida is an effective technique in promoting growth, longer lifetime, and, as a consequence, increased precipitation from these clouds (Woodley, 1969). The effect of this seeding on clouds and precipitation on a scale one to two orders of magnitude larger than that of an individual cloud is not known.

The precipitation increases produced by single cloud seeding could represent a net increase, a decrease, or simply a redistribution of the precipitation over a large area encompassing the seeded cloud. Analysis of two other seeding experiments in which silver iodide was dispersed from airborne silver iodide generators into clear air upwind of the target clouds has revealed apparent decreases (not significant at 5% level) of the large-scale precipitation (Battan, 1966; Flueck, 1968; Neyman et al., 1969). Because the seeding technique and physical hypothesis behind these experiments differ considerably from that behind the Florida experimentation, it is not wise to extrapolate their results to cloud seeding studies in Florida. For this reason, we have embarked on a study of the large-scale precipitation effects of single cloud seeding in Florida.

The response of the South Florida supercooled cumulus clouds to pyrotechnic seeding during May 1968 was dramatic in almost all instances.

Thirteen of the fourteen seeded clouds attained cumulonimbus stature with an attendant increase in precipitation, while none of the five controls grew significantly. In some instances the seeding may have hastened natural cumulonimbus development; in others it may have induced cumulonimbus development when none would have occurred naturally. In either instance the seeded cumulonimbus clouds probably had some effect on cloud developments and precipitation in their environments.

A seeded cumulonimbus cloud might affect environmental cloud developments and precipitation in a number of ways. The silver iodide introduced into one cloud might remain active in a plume an order of magnitude longer than the lifetime of the seeded cloud, entering other clouds and affecting their precipitation processes (microphysics) in an unknown way. Dynamic effects of the seeded cumulonimbus cloud might be a precipitation-induced downdraft that might act as a meso-front, radiating away from the parent cloud, lifting sub-cloud moist air, resulting in other clouds and precipitation. Cloud developments tens of miles from a seeded cumulonimbus might be inhibited due to either the anvil cirrus canopy that cuts off insolation or to compensating subsidence around the vigorous seeded cloud.

Natural cumulonimbus clouds over South Florida undoubtedly have a profound effect on other cloud developments and precipitation in their environments, but few are concerned because little can be done about it. However, when man can induce cumulonimbus clouds that may act to reorganize and redistribute the rainfall or to increase or decrease it over large areas, everyone is concerned because any adverse effects can be eliminated by simply terminating the seeding.

2. APPROACH TO THE PROBLEM

There are many approaches one might take in the investigation of the large-scale effects of silver iodide seeding of individual cumulus clouds. Two are adopted here: (1) investigation of microphysical (i.e., on the scale of the individual cloud particles) effects and (2) investigation of any dynamic effects. With the microphysical approach, rainfall over areas traversed by the seeded plume is compared with the rainfall over areas unaffected by the seeded plume. With the dynamic approach "radar rainfall" is calculated over a circular grid of 120-n mi diameter, centered on the experimental clouds.

3. MICROPHYSICAL EFFECTS OF SINGLE CLOUD SEEDING ON AREAL PRECIPITATION

3.1 Superposition of Silver Iodide Plume on Rainfall Analyses

The silver iodide introduced into one cloud may have entered other clouds at a later time, affecting their precipitation processes. Our calculations indicate that the concentration of silver iodide active at -10°C decreased from 10^2 to 10^3 nuclei per liter in a typical seeded cloud with a 1-km radius and supercooled depth of 2 km to about one nucleus per liter in a triangular plume volume 37 km on a side and 2 km deep. Because about 100 nuclei per liter in the supercooled portion of a cloud is apparently necessary for important dynamic effects through fusion heat release (MacCready, 1959), the silver iodide concentration in a typical seeded plume was too low to induce dynamic changes. However, one ice nucleus per liter of cloud air has been considered optimum for inducing increased precipitation through alteration of cloud microphysics (McDonald, 1958; Fletcher, 1962; Mason, 1962). This phase of the research is approached with this in mind. Silver iodide plumes subsequent to seeding are constructed, and rainfall over areas traversed by the plume is compared with that over areas not affected by it.

3.2 Method

Horizontal projections of air trajectories at 8,000 and 20,000 ft were estimated from streamline analyses for an air parcel originating at the location of each of the experimental clouds at the time of the first seeding pass. The altitudes of the trajectories were chosen for two reasons: (1) the pyrotechnics were dropped at 20,000 ft MSL, and (2) tests have indicated (Simpson et al., 1969) that the pyrotechnics, when dropped from 20,000 ft, probably burn out before reaching 8,000 ft. Connection of the terminus of each trajectory after any time interval defines the largest possible volume in which the silver iodide might be distributed.

After construction, each seeded plume was superimposed on the rainfall analysis closest to it in time. Two different individuals did the plume and rainfall analyses, neither seeing the work of the other until it was completed. Comparisons were made between rainfall beneath the seeded plume with that over areas not traversed by the plume, with care taken to determine whether the rainfall fell before or after plume passage.

3.3 Problems and Uncertainties

The most serious problem with this phase of the study was obtaining a representative rainfall analysis. The South Florida rain gage network (fig. 1) is least dense at ranges exceeding 20 n mi west and northwest of Miami where most of the experimental clouds were located. Because interpolation of the rainfall between gages is of questionable value in instances of showery precipitation, a true representation of the rainfall was difficult to obtain. This problem could have been circumvented had there been continuous UM/10-cm radar observations. This radar with its iso-echo contouring unit, discussed later, has been shown to be an effective tool in accurately (within 30%) representing rain reaching the ground (Woodley and Herndon, 1969). If the radar observations had been available for extended periods, it would have been a simple matter to project the filmed radar observations on a gridded map of South Florida and then make radar rainfall readings at selected time intervals at the points on the grid. The rainfall rate readings could then have been time-integrated to provide total rainfall at each grid point. The isohyetal analyses resulting from this procedure certainly would have been more accurate than those used in this study.

With the observations made during the seeding program, there is no way of knowing exactly where the silver iodide went or how long it remained active after it was dropped into a single cumulus cloud. It is likely that much of it was either washed out with the precipitation or was carried away in ice crystals in the anvils of the large cumulonimbi that formed subsequent to seeding.

The scheme used to define the volume containing silver iodide, described earlier, is an approximation that probably maximizes the true plume volume, if anything. In instances where the wind did not change linearly between 8,000 and 20,000 ft, the true shape of the seeded plume differed from that provided by the analysis scheme.

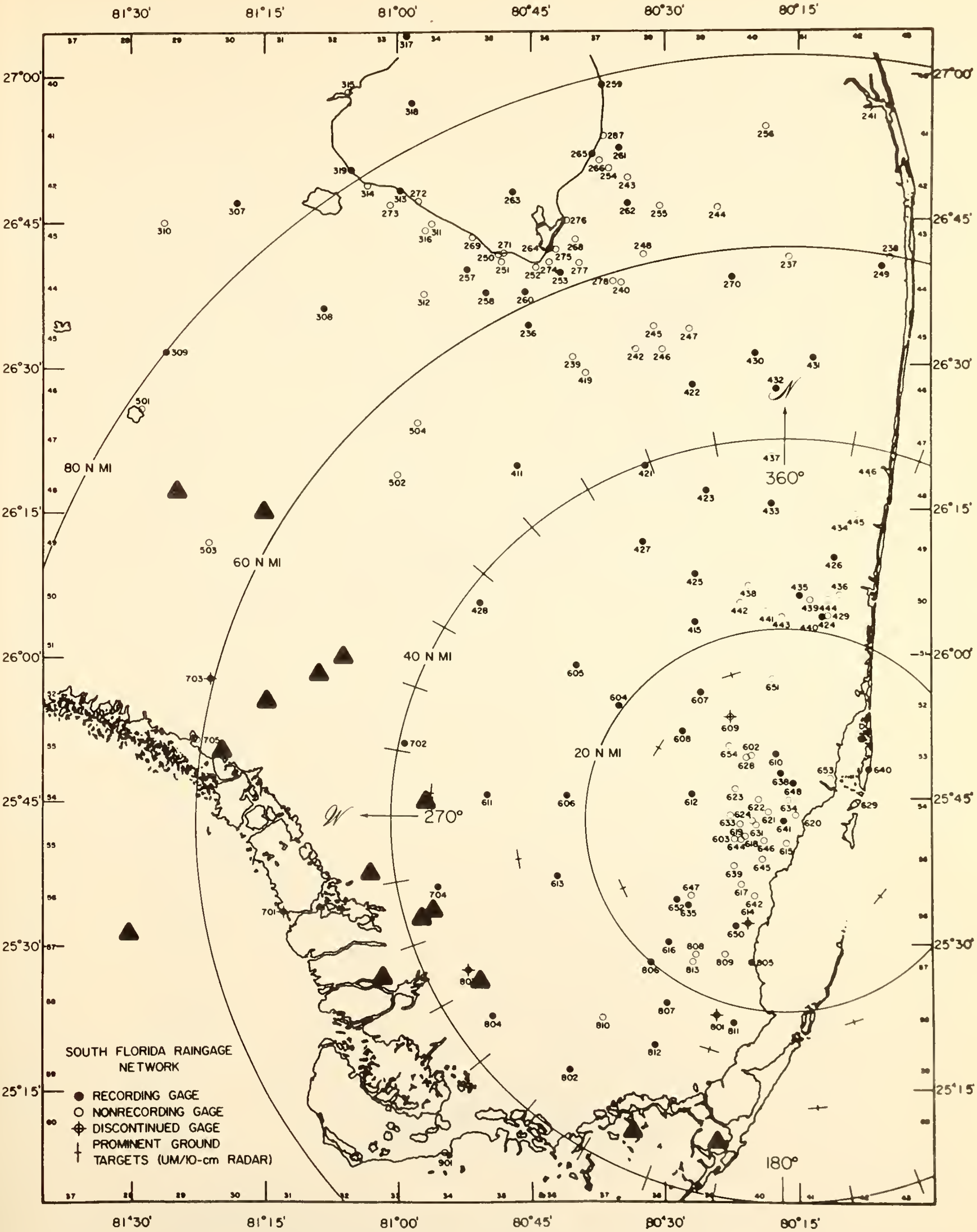

Figure 1. South Florida rain gage network(after Mr. Harold P. Gerrish of Radar Meteorological Laboratory,University of Miami) with positions of the experimental clouds denoted by ▲. Four clouds are off map.

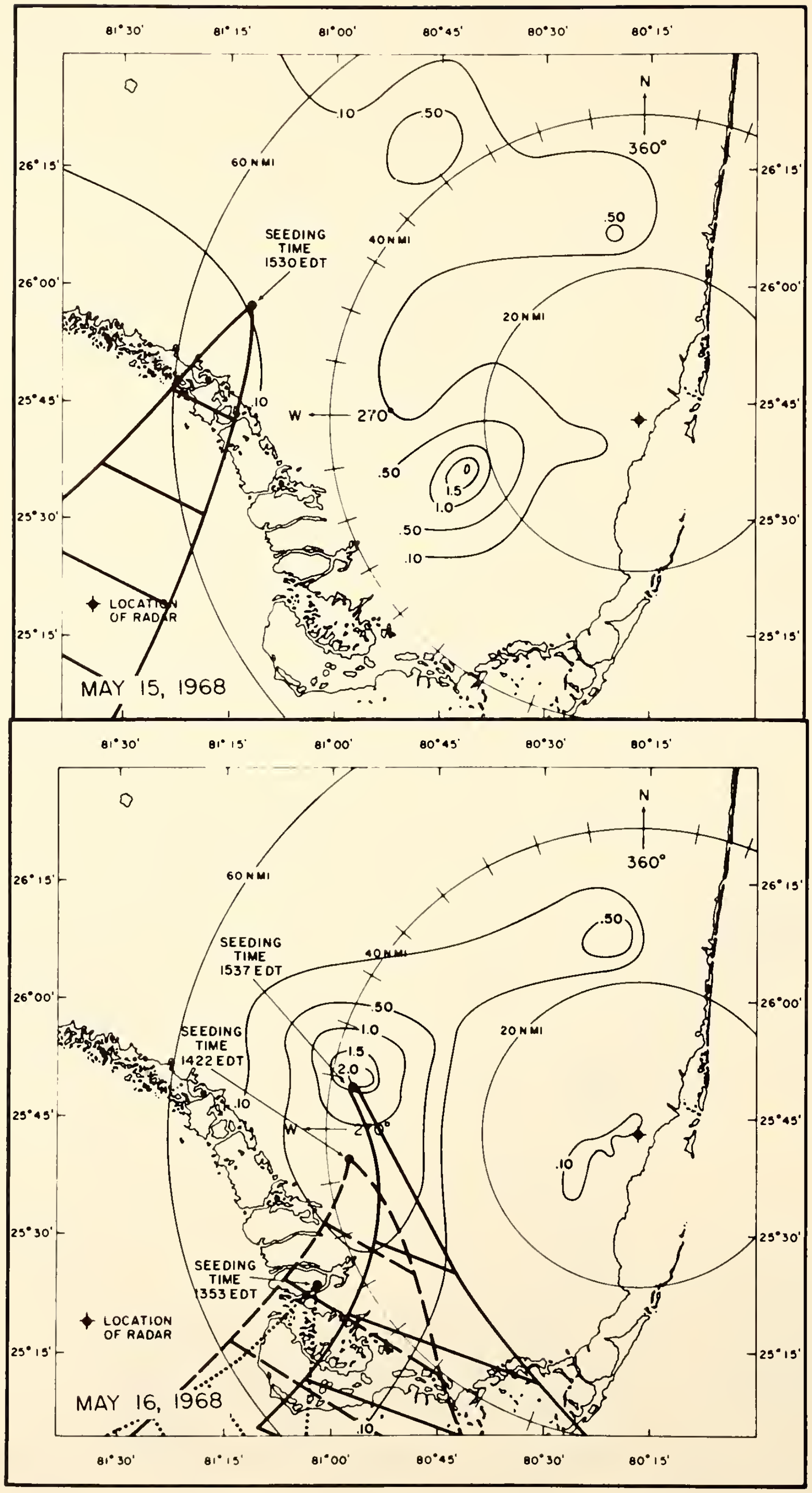

Figure 2. Superposition of silver iodide plume on observed rainfall pattern. May 15 and 16, 1968.

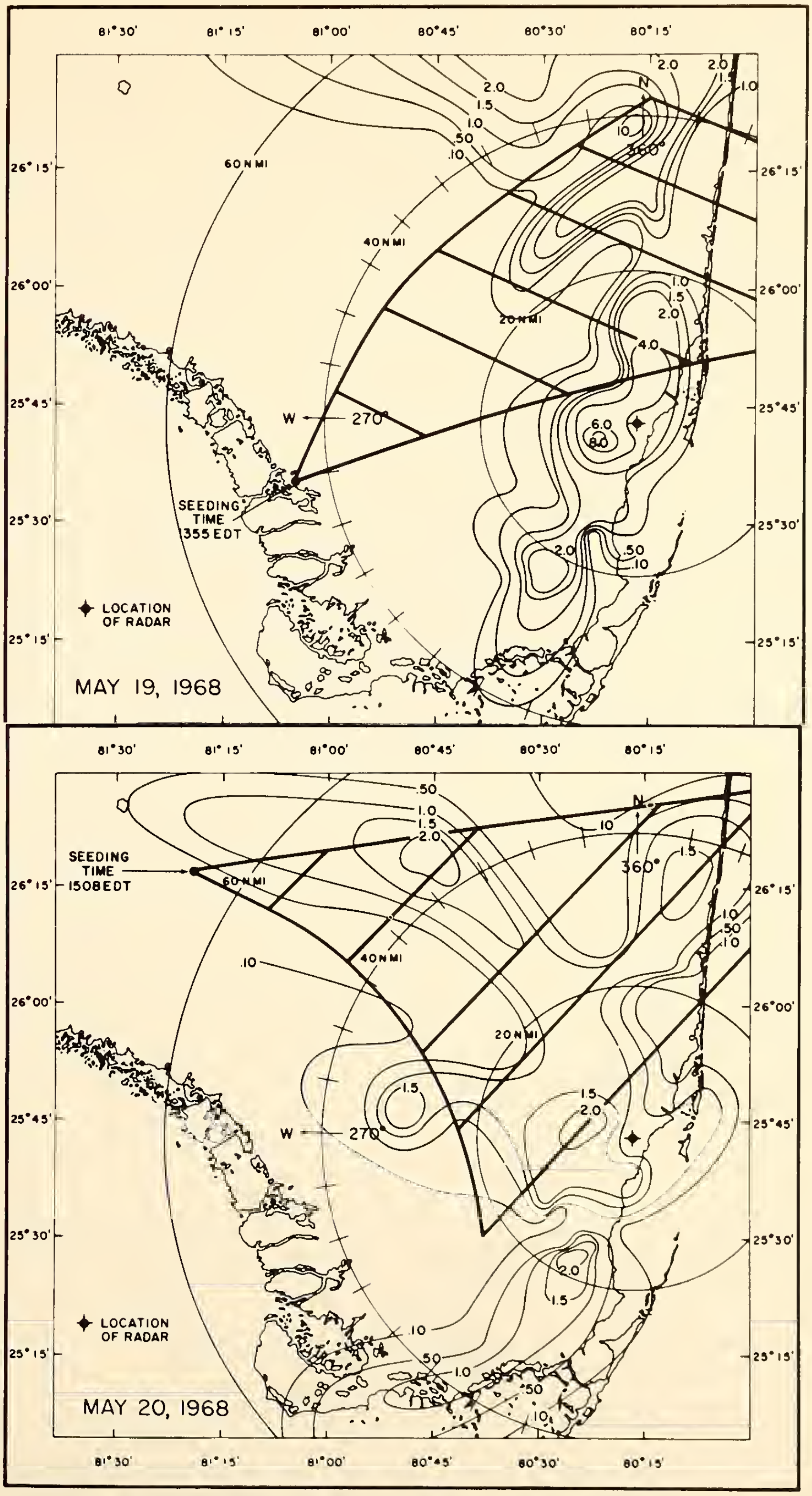

Figure 3. Superposition of silver iodide plume on observed rainfall pattern. May 19 and 20, 1968.

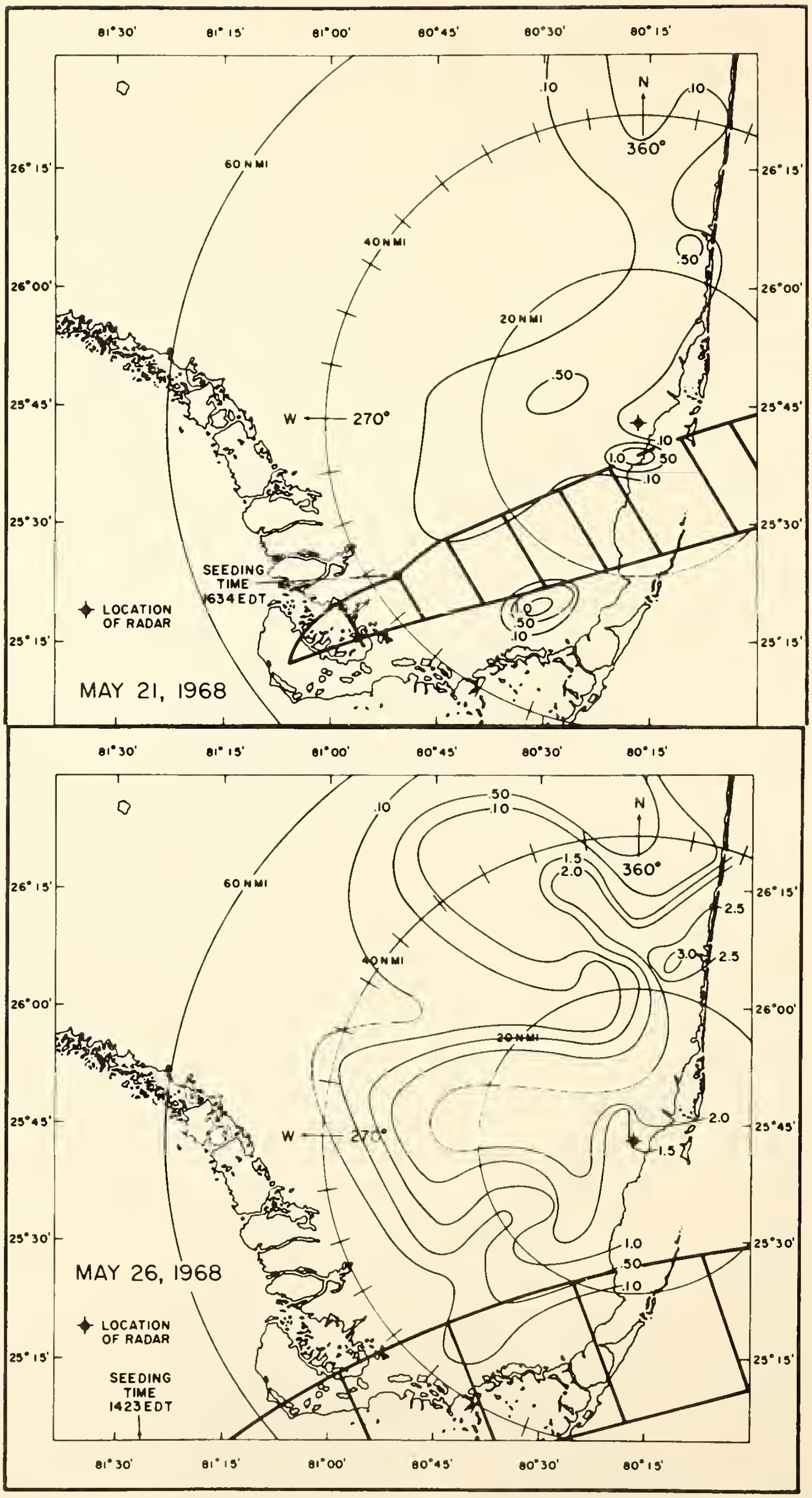

Figure 4. Superposition of silver iodide plume on observed rainfall pattern. May 21 and 26, 1968.

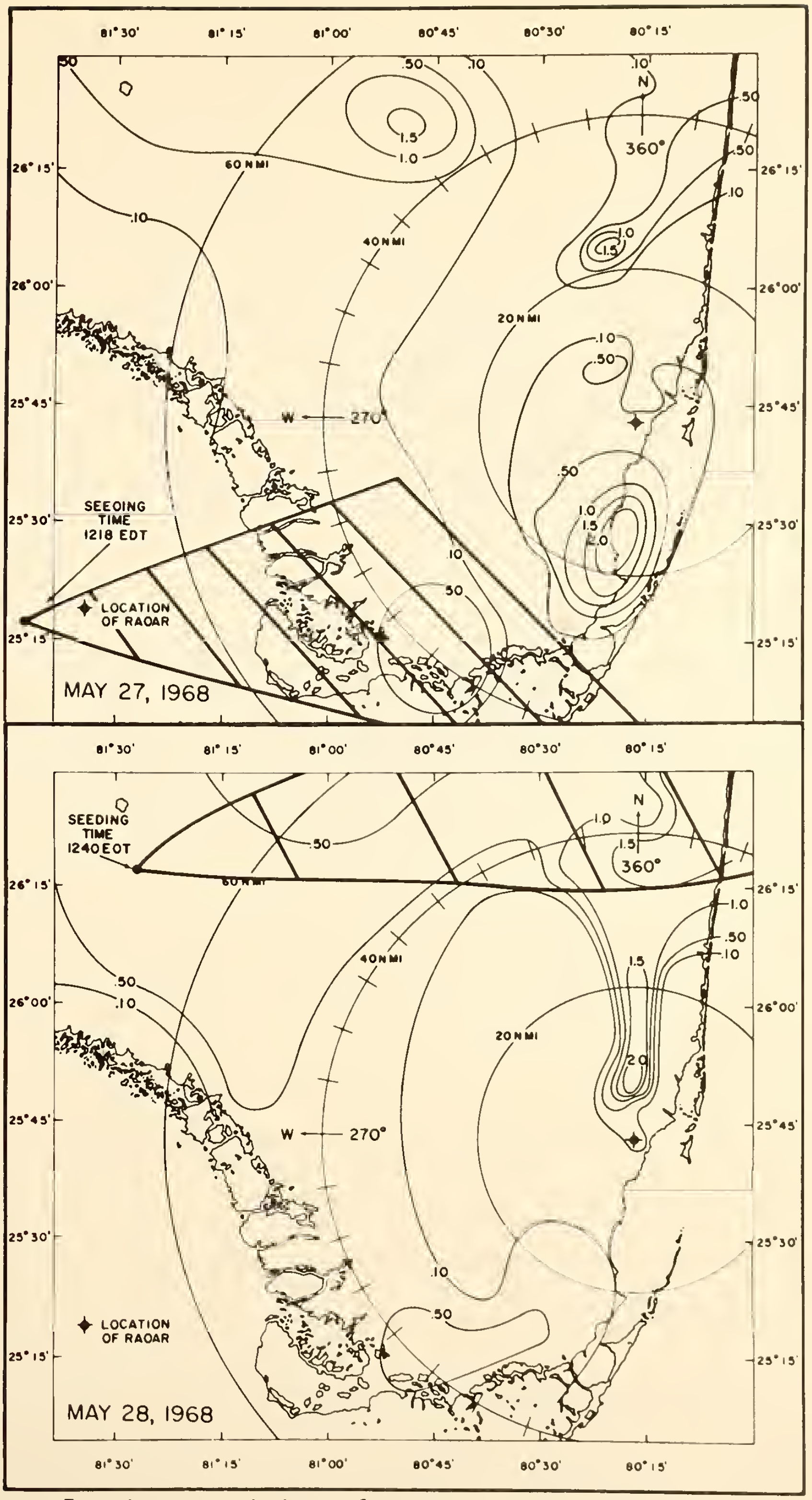

Figure 5. Superposition of silver iodide plume on observed rainfall pattern. May 27 and 28, 1969.

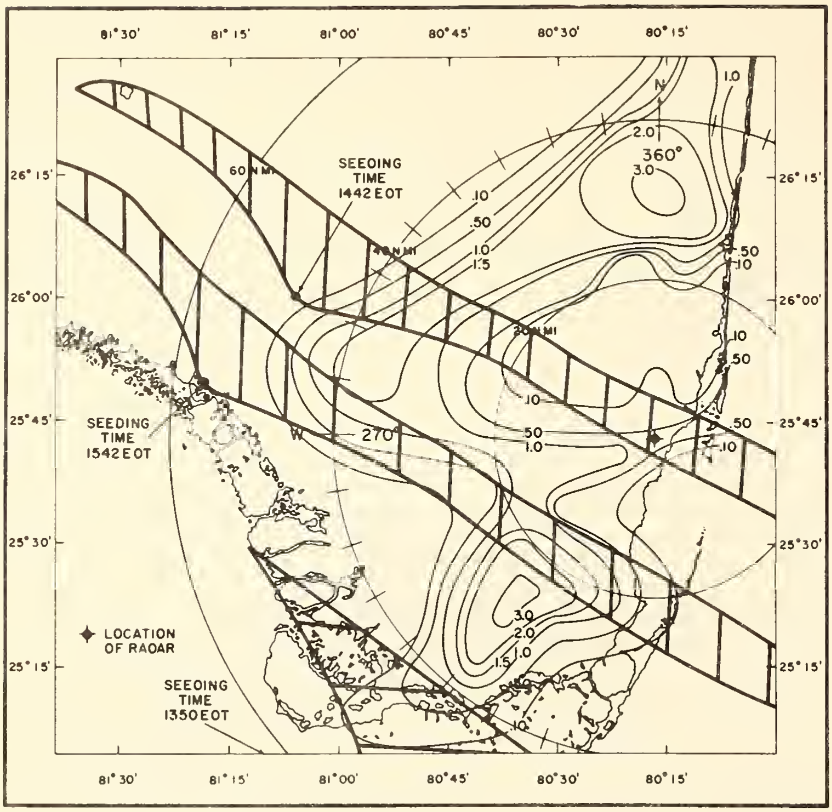

Figure 6. Superposition of silver iodide plume on observed rainfall pattern. May 30, 1968.

3.4 Results

The results of the superposition of the seeded plumes on the rainfall analyses are presented in figures 2 through 6. The important points to be gleaned from the individual analyses are summarized below:

May 15 - The seeded plume moved over the Gulf of Mexico and did not pass over the region of heavy rainfall centered 20 n mi west-southwest of Miami. However, the rainfall beneath the plume along the Florida west coast is a gross underestimate because of lack of rain gage observations.

An examination of the available radar observations suggests that over 1 in. of rain may have fallen in this region associated with the seeded cloud. There is no way of knowing whether the plume affected the precipitation processes of other clouds in its path.

May 16 - There is strong evidence that the rainfall maximum was directly associated with the three clouds that were seeded, especially the last two. There is no evidence that a significant portion of the rainfall fell from secondary clouds that may have entrained silver iodide from the plume.

May 19 - On this day the seeded cloud entered a squall line moving southeastward over South Florida and the squall system produced the heavy precipitation. It is not known whether the intensity of the precipitation was increased because of the presence of the silver iodide. The rainfall at the origin of the plume to within 20 n mi of Miami is an underestimate due to a lack of rain gage observations.

May 20 - The silver iodide plume passed over the regions of heavy rainfall after the rain had fallen. There is no evidence that the plume affected the rainfall on this day.

May 21 - The silver iodide plume passed over the regions of heavy rainfall at the time the rain was occurring and could have affected the precipitation in some way. The heaviest rainfall over South Florida fell near the path of the plume.

May 26 - The silver iodide plume originated over the Gulf of Mexico, 80 n mi south-southwest of Miami, and moved northeast, crossing the extreme southern portion of the Florida peninsula. The plume did not cross the regions of maximum rainfall.

May 27 - The silver iodide plume originated over the Gulf of Mexico, 85 n mi west-southwest of Miami and moved eastward over the Florida peninsula. It passed over the area of heaviest rainfall at least 6 hours after the rain had fallen.

May 28 - The silver iodide plume passed over a region of heavy rainfall at the time of the heavy precipitation. The radar observations indicate that the seeded cloud and plume were amalgamated into the group of clouds that produced the heavy precipitation. It is not known whether the rain was heavier because of the silver iodide.

May 30 - There were three seeded clouds on this day with very distorted plumes caused by highly diverging winds between 8,000 and 20,000 ft. Heavy precipitation was noted over most of South Florida, and there is no evidence that it was either increased or decreased because of the silver iodide plumes.

A summary of the results of the superposition of the seeded plumes on the rainfall analyses is presented in table 1; four of the nine calculations indicate that the seeded plume traversed a region of heavy rainfall at approximately the time the heavy precipitation was occurring, although the time and space superposition of the seeded plume and the heavy rainfall may have been merely fortuitous. In one instance (May 16) the rainfall maximum was produced by the seeded clouds and not by any others that may have ingested the silver iodide at a later time. In another (May 19) the seeded cloud entered a squall line moving southeastward over South Florida and the squall system produced the very heavy precipitation. It is not known whether the intensity of the precipitation was increased because of the

Table 1. Seeded Plume Rainfall Summary

Date	Number Seeded Clouds	Rainfall Maximum on Map (in.)	Rainfall Maximum Under Plume (in.)	Comments	Possible That Plume Increased Rainfall?
May 15	1	2.00	?	Plume moved over the the Gulf of Mexico	No
May 16	3	2.00	2.00	Maximum rainfall traversed by plume	Yes
May 19	1	8.00	4.00	Maximum rainfall 10 n mi south of plume. Squall line crossed region	Yes
May 20	1	2.00	2.00	Rain fell 2-3 hrs before passage of the plume	No
May 21	1	1.00	1.00	Plume traversed area of heaviest rainfall	Yes
May 26	1	3.00	?	Much of plume over water	No
May 27	1	2.00	2.00	Rain fell 6 hrs prior to passage of plume	No
May 28	1	2.00	1.50	Maximum rainfall south of plume	Yes
May 30	3	3.00	2.50	Distorted and elongated plumes. Chaotic rainfall pattern	No

silver iodide. In five of the nine cases the heavy rainfall over the peninsula could not be explained by the passage of the seeded plume because either the plumes remained mainly over water or the rainfall occurred before the passage of the plume.

The results of this phase of the study are hardly conclusive; there is no evidence that the seeded plume either increased or decreased the precipitation over areas not traversed by the originally seeded clouds.

3.5 Discussion

For the silver iodide plume to alter the precipitation processes of clouds in its path, some of it would have to be entrained through the sides of these clouds. Further, to produce precipitation increases these clouds would also have to be deficient in natural ice nuclei. Cloud seeding studies in Arizona (Battan, 1966) cast doubt on the efficacy of entrainment as an efficient mechanism for drawing silver iodide into the sides of a cloud, while study in Florida (Woodley, 1969) has indicated that from a microphysical standpoint, the clouds here are not deficient in natural ice nuclei. In view of these findings it is not surprising that superposition of the seeded plume on rainfall analyses produced inconclusive results.

The results of the first phase of this study imply that the seeding of a single cloud has no detectable effect on the microphysical processes of other clouds in its environment; the dynamics of the problem are yet to be examined. Changes in the wind field and patterns of insolation associated with the vigorous seeded cloud may well affect precipitation development in its environment. The next phase of this study is concerned with this problem.

4. DYNAMIC EFFECTS OF SINGLE CLOUD SEEDING ON AREAL PRECIPITATION

A second approach is adopted in the investigation of the large scale precipitation effects of silver iodide pyrotechnic seeding of individual cumulus clouds. Radar rainfall at selected time intervals is calculated over a circular grid, 120 n mi diameter, which is orientated along the 4,000 to 20,000 ft shear vector and centered on the core of each experimental cloud. Comparisons are made between seeded and non-seeded grid rainfall and, with the shear vector as a reference, the grid rainfall is examined for preferred regions of development.

4.1 Tools

The modified UM/10-cm radar of the Radar Meteorological Laboratory at the University of Miami was the main tool in this phase of the research. This radar has a 2° conical beam, a transmitter power of 5.5×10^{5}W, a minimum detectable signal of 10^{-14}W, a pulse length of $2\mu s$, and a pulse repetition rate of 300 pulses per second. Important features of this system include special logarithmic and linear receivers, an RF range attenuation corrector (Hiser and Andrews, 1966) and an iso-echo-contour (IEC) unit developed by Senn and Andrews (1968). This radar was calibrated twice daily during the experiment. For more details on this radar unit, including a discussion of its calibration, the reader is referred to the report by Senn and Courtright (1969).

All radar echoes within range during the period of study were contoured using the IEC unit. The reflectivity (Z) values and equivalent rainfall rates (R) for the various contours are shown in table 2. The Z values in this table were obtained using the calibration systems of Andrews and Senn (1968). The R values were then computed from the Miami Z-R relation, $Z=300R^{1.4}$, which has been shown by Woodley and Herndon (1969) to accurately represent South Florida showery precipitation when it is used with the modified UM/10-cm radar and a linear interpolation scheme.

Table 2. UM/10-cm Signal Levels (P_r), Z Values and Equivalent Precipitation Rates (R) May 1968 Florida Program

DATE	CONTOUR	P_r (dbm)	$Z\,mm^6\,m^{-3}$	R(IN/HR)	CONTOUR	P_r (dbm)	$Z\,mm^6\,m^{-3}$	R(IN/HR)
MAY 15-20	1	-109	5	.002	2	-86	1.1×10^3	.09
21	1	-109	5	.002	2	-86	1.1×10^3	.09
23	1	-109	5	.002	2	-86	1.1×10^3	.09
25	1	-109	5	.002	2	-85	1.5×10^3	.10
26	1	-109	5	.002	2	-85	1.5×10^3	.10
27	1	-106	11	.003	2	-86	1.1×10^3	.09
28	1	-102	24	.006	2	-86	1.1×10^3	.09
30	1	-100	40	.009	2	-86	1.1×10^3	.09
REQUESTED VALUES	1	—	—	—	2	-85	1.1×10^3	.10

DATE	CONTOUR	P_r (dbm)	$Z\,mm^6\,m^{-3}$	R(IN/HR)	CONTOUR	P_r (dbm)	$Z\,mm^6\,m^{-3}$	R(IN/HR)
MAY 15-20	3	-76	1.1×10^4	.45	4	-64	1.9×10^5	3.5
21	3	-77	$.9 \times 10^4$	.40	4	-64	1.9×10^5	3.5
23	3	-76	1.1×10^4	.45	4	-64	1.9×10^5	3.5
25	3	-74	1.8×10^4	.60	4	-64	1.9×10^5	3.5
26	3	-72	3×10^4	.80	4	-63	2.1×10^5	4.0
27	3	-74	1.8×10^4	.60	4	-63	2.1×10^5	4.0
28	3	-77	$.9 \times 10^4$	.40	4	-63	2.1×10^5	4.0
30	3	-75	1.4×10^4	.55	4	-63	2.1×10^5	4.0
REQUESTED VALUES	3	-73	2×10^4	.75	4	-67	$.9 \times 10^5$	2.30

4.2 Method

The experimental cloud echo and all surrounding echoes were traced onto a circular grid at 20-min intervals for as long as possible after the seeding pass[1]. At all times the grid was centered on the central core of the experimental cloud and orientated along the 4,000 to 20,000 ft shear

[1] This refers to the first pass of the seeder aircraft through the experimental cloud. There was no seeding during its pass through the control cloud.

vector, as shown in figure 5. The shear vectors for the days with experimental clouds are tabulated in table 3. The grid is composed of twelve annular sections each with a width of 20 n mi; the downshear sections are numbered 1-6 and the upshear sections are numbered 7-12.

The method of obtaining radar rainfall is analogous to that used by Woodley (1969) for a similar problem. All of the echoes in a section were integrated with a planimeter to provide the total area (in n mi^2) contained between the contours - each contour corresponding to a discrete rainfall rate. The areas contained between the contours were then multiplied by the

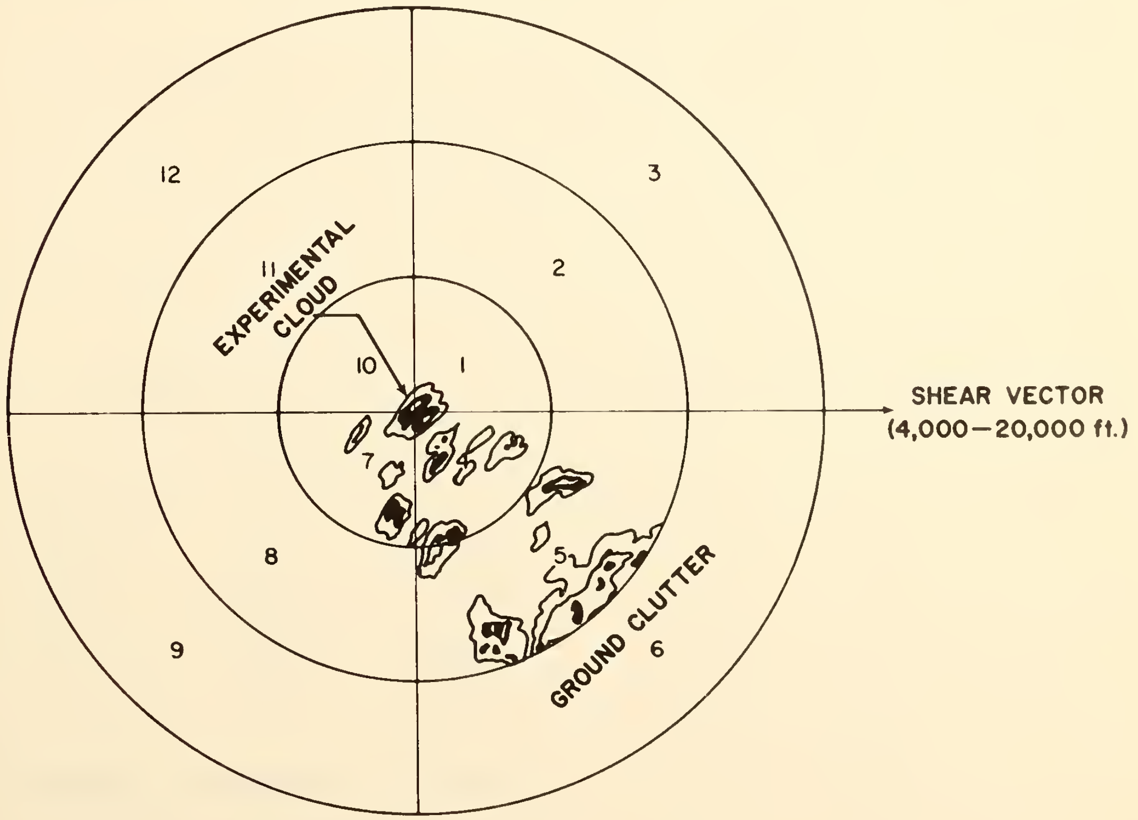

Figure 5. Analysis of grid superimposed on contoured cloud echoes. Each contour of an echo corresponds to a discrete rainfall rate.

appropriate mean rainfall rate and a constant to convert the result to acre-feet of water. Each echo was assumed to remain unchanged for 10 min so the final rainfall values represent 10-min contributions.

Total water values were not used in this study; rather the change in water (ΔW) relative to that at seeding was computed. The change of water in a section was defined as the total water in the section in a 10-min period after seeding minus the total water in the section in the 10-min period immediately before the seeding pass. The use of water change was desirable to eliminate the "head start" enjoyed by a section with strong echo development at seeding time.

The original intention was to include cloud conditions up to a 60-n mi radius from the experimental cloud for 2 hours after the seeding pass, but this was impossible. A sample large enough for statistical testing was obtained only for the annulus 20 n mi from the core of the experimental

Table 3. Vertical Shears (Degrees & Knots) on the Experimental Days During May 1968

Altitude (ft x 10^3)	4-8	8-12	12-16	16-20	4-20
Date		SHEARS			
May 15	070/08	325/05	230/04	0	010/05
May 16	345/08	085/05	325/03	255/05	330/10
May 19	130/04	265/13	305/04	070/02	270/11
May 20	245/03	230/03	280/12	020/05	255/21
May 21	0	0	250/05	255/18	255/23
May 26	230/04	325/03	320/03	070/01	290/06
May 27	325/02	310/04	300/04	320/04	315/14
May 28	315/03	0	0	335/07	330/10
May 30	155/11	295/08	005/08	245/03	270/05

cloud for a period of 1 hour. The sample could not be extended to the desired limits for the following reasons: early shutdown of the radar, ground clutter and anomolous propagation, the limited range of the scope used for analysis (100 n mi), and the overlap in time and space of the seeded and control clouds.

4.3 Results

The water calculations for the 12 sections of the grid with means for sections 1, 4, 7, and 10 are found in table 4. The calculations are segregated depending on whether the cloud at the center of the grid was seeded or unseeded. The first block of values are the total water values in the 10 min before the seeding pass. The values in all subsequent blocks represent the change in section rainfall in the specified 10-min interval over the section rainfall in the 10 min immediately before the seeding pass. The radar control clouds are control clouds selected after the seeding program from airborne, 16-mm time-lapse photography (see Woodley, 1969).

There are severe gaps in the data. Even the averages presented for section 1, 4, 7, and 10 can be misleading because of the great range of values and the small sample size. There are certain points of interest, however. In the 40-n mi diameter circle surrounding the experimental clouds, there were no important differences between the water values for the seeded and control clouds, with the exception of downshear section 1. In this section the seeded rainfall averaged 2 to 4 times that of the controls. This may be a real effect due to either new cloud development downshear to the left of the seeded cloud or to the seeded cloud itself streaming off downshear. It is not known why downshear section 4 (to the right of the shear vector) did not show a corresponding increase in rainfall. Section 4 is a section of minimum rainfall in most time intervals regardless of whether the cloud at the center of the grid is seeded or non-seeded.

The seeded grid rainfall for sections 1, 4, 7, and 10 was tested for significant differences against the non-seeded grid rainfall in the corresponding sections using the Wilcoxon-Mann-Whitney test (Guttman and Wilks, 1965), a test which is non-parametric and two-sided. No significant differences were found in the ΔW values between the seeded and unseeded sections at any time, not even at the 20 percent level. This is not surprising in view of the small rainfall differences and small sample size. The seeded rainfall in sections 1 and 4 were pooled and tested for differences against the pooled non-seeded rainfall in the corresponding sections (pooling has the effect of doubling the size of the seeded and non-seeded samples). Again, no significant differences were found at the 20-percent level.

Several other comparisons were made between seeded and non-seeded section rainfall. Seeded section rainfall differences along the shear vector ($\Delta W_{S1} - \Delta W_{S10}$ and $\Delta W_{S4} - \Delta W_{S7}$); perpendicular to the shear vector ($\Delta W_{S1} - \Delta W_{S4}$); and diagonally across the shear vector ($\Delta W_{S1} - \Delta W_{S7}$ and $\Delta W_{S4} - \Delta W_{S10}$) were tested for significant differences against the corresponding non-seeded section rainfall differences (first subscript refers to seeding action and the second to the section number). Again, no significant differences were found at the 20-percent level.

Table 4. Grid Rainfall Calculations (Acre-Feet)

W (-10 → 0)

	DATE		CLOUD NO. FOR GRID CENTER	SECTION 1	2	3	4	5	6	7	8	9	10	11	12
GRID CENTERED ON CONTROL CLOUDS	MAY	15	RC	6.4	0	8.8	2 0	–	–	3.3	–	–	11.0	–	–
		16	RC	16.5	–	–	.5	0	–	14.8	–	–	64.9	–	–
		20	1	31.8	–	–	4.4	–	–	40.4	47	–	14.3	–	–
		26	9	41.8	–	–	4	643.9	–	0	0	–	0	112.5	128.1
		27	1	1.0	0	–	.9	3.2	–	.6	0	–	2.1	0	20.7
		28	RC	2.0	316.2	–	6.0	8.1	59.8	19.0	11.7	–	0	0	–
		30	6	311.2	–	–	29.2	–	–	18.0	–	–	31.4	–	–
			Σ	410.7			42.4			95.1			123.7		
			n	7			7			7			7		
			MEAN	58.7			6.1			13.6			17.7		
GRID CENTERED ON SEEDED CLOUDS	MAY	15	5	54 2	8 9	–	23 6	–	–	23 5	–	–	41.3	329.1	–
		16	5	6.2	–	–	2.9	0	–	5.0	0	0	3 1	–	–
		16	6	425.4	–	–	36 8	0	–	45 8	0	0	63.1	–	–
		19	1	19 8	–	–	5.1	–	–	2 9	0	0	0	0	104.1
		20	5	16 1	–	–	297.0	1491.0	–	16.8	0	–	1.8	–	–
		21	2	1065.2	–	–	633.5	–	–	6 4	–	–	54 6	–	–
		26	11	83.6	480.9	–	3.3	0	0	1.1	0	–	6.2	30.7	17.0
		27	2	1.1	0	0	40.9	–	–	4 7	–	–	16.1	0	5.7
		29	5	6.6	929.4	–	13 2	0	15 8	0	–	–	1 8	–	–
		30	7	22 9	30 8	–	39 5	0	–	5 4	0	–	44 9	18 2	20 5
		30	8	6.7	798 0	–	0	–	–	12.2	6.8	0	40 0	0	–
		30	10	36.8	962 0	–	1.3	–	–	4.3	0	–	3 4	0	–
			Σ	1743 6			1097.3			128.1			275.3		
			n	12			12			12			12		
			MEAN	145 3			91.4			10.7			22 9		

ΔW ($W_{20 \to 30} - W_{-10 \to 0}$)

	DATE		CLOUD NO. FOR GRID CENTER	SECTION 1	2	3	4	5	6	7	8	9	10	11	12
GRID CENTERED ON CONTROL CLOUDS	MAY	15	RC	-4 1	0	-5.1	-2 0	–	–	62 1	–	–	2 9	–	–
		16	RC	133.5	–	–	1.7	0	–	51 4	0	0	23 0	–	–
		20	1	148 2	–	–	4.8	–	–	122 2	-1 2	–	37 6	–	–
		26	9	-41.8	–	–	57 7	-452 4	–	0	0	–	0	-112 6	-128 1
		27	1	0	0	–	4 4	-7	–	3 3	2	–	9	7 4	298 1
		28	RC	39.8	600.7	–	3 2	-5 9	-35 9	-9 9	-11 7	–	4 7	0	–
		30	6	-130.9	–	–	14 0	–	–	24 4	–	–	-28 1	–	–
			Σ	144.5			93 9			263 8			43 9		
			n	7			7			7			7		
			MEAN	20.6			12 0			39.2			6 3		
GRID CENTERED ON SEEDED CLOUDS	MAY	15	5	-6 1	5 7	–	-1 1	–	–	-5 4	–	–	-17 7	-143 4	–
		16	5	-3 4	–	–	1 8	0	–	-1 9	0	0	186.9	–	–
		16	6	379 0	–	–	46 6	0	–	-14 5	0	1 7	14 7	–	–
		19	1	33 5	–	–	17.2	–	–	21 7	0	0	49 9	0	-4 9
		20	5	49 5	–	–	-176 0	387 6	–	47 0	0	–	25 0	–	–
		21	2	356.8	–	–	90 2	2343.2	–	587 6	5	–	66.7	–	–
		26	11	-67.0	-178.8	–	-1.4	–	–	-.3	–	–	-4 1	-9.6	4
		27	2	.6	0	0	-16.8	–	–	-2.4	–	–	-1 3	0	29.1
		29	5	231 2	267 8	–	41 8	0	-15 8	98 5	–	–	79 5	–	–
		30	7	-8 2	76 6	–	-27 0	0	–	15 0	11 9	–	-19 9	47 2	-2 9
		30	8	182 4	681 5	–	16 9	–	–	5 9	25.1	0	-10 6	0	–
		30	10	161.5	642.7	–	7 3	–	–	3 2	0	–	5 4	0	–
			Σ	1309.8			5			754 4			363 2		
			n	12			12			12			12		
			MEAN	109 2			0 4			62 9			30 3		

ΔW ($W_{40\rightarrow50} - W_{-10\rightarrow0}$)

	DATE	CLOUD NO. FOR GRID CENTER	Section 1	2	3	4	5	6	7	8	9	10	11	12
GRID CENTERED ON CONTROL CLOUDS	MAY 15	RC	-6.4	0	—	-2.0	—	—	—	—	—	19.6	—	—
	16	RC	—	—	—	—	—	—	—	—	—	—	—	—
	20	1	293.3	—	—	13.2	—	—	202.0	15.1	—	51.2	—	—
	26	9	-40.4	—	—	18.9	-553.6	—	0	0	—	0	-112.5	-128.1
	27	1	24.4	0	—	14.8	7.4	—	19.1	3.4	—	43.1	73.2	1121.7
	28	RC	117.7	961.5	—	-3.8	-8.1	22.0	160.7	—	—	—	—	—
	30	6	-236.0	—	—	-18.2	—	—	29.3	—	—	-15.0	—	—
		Σ	152.6			22.9			411.1			98.9		
		n	6			6			5			5		
		MEAN	25.4			3.8			82.2			19.8		
GRID CENTERED ON SEEDED CLOUDS	MAY 15	5	-23.3	262.3	—	-19.8	—	—	-20.6	—	—	664.2	-49.4	—
	16	5	—	—	—	—	—	—	—	—	—	—	—	—
	16	6	-201.4	—	—	14.9	0	—	15.8	0	2.8	-3.3	—	—
	19	1	8.4	—	—	-.8	—	—	13.2	0	0	18.5	2.1	225.4
	20	5	356.8	—	—	90.2	2343.2	—	587.6	.5	—	55.7	—	—
	21	2	414.3	—	—	464.5	—	—	68.8	—	—	23.8	—	—
	26	11	-83.6	89.9	—	-3.3	—	—	10.9	—	—	-6.2	-28.8	53.7
	27	2	-.4	0	8.1	-3.8	—	—	-1.4	—	—	-11.3	0	78.7
	28	5	266.2	393.0	—	32.5	0	0	141.4	—	—	51.2	—	—
	30	7	32.7	99.4	—	-38.9	0	—	22.8	48.4	—	-41.7	171.2	-20.5
	30	8	334.1	394.6	—	105.4	—	—	238.8	42.8	0	48.1	0	—
	30	10	96.4	1100.2	—	8.7	—	—	14.2	0	—	10.7	0	—
		Σ	1200.2			649.6			1091.5			809.7		
		n	11			11			11			11		
		MEAN	109.1			59.1			99.2			73.6		

ΔW ($W_{60\rightarrow70} - W_{-10\rightarrow0}$)

	DATE	CLOUD NO. FOR GRID CENTER	Section 1	2	3	4	5	6	7	8	9	10	11	12
GRID CENTERED ON CONTROL CLOUDS	MAY 15	RC	—	—	—	—	—	—	—	—	—	—	—	—
	16	RC	—	—	—	—	—	—	—	—	—	—	—	—
	20	1	561.9	—	—	130.9	—	—	272.9	97.1	—	93.4	—	—
	26	9	-41.8	—	—	-.4	-633.0	—	0	0	—	0	-112.5	—
	27	1	-.1	0	—	-.9	—	—	0	—	—	-2.1	16.6	456.0
	28	RC	64.7	1089.2	—	-6.0	-8.1	-49.3	157.4	—	—	—	—	—
	30	6	-160.6	—	—	-26.7	—	—	40.1	—	—	-29.9	—	—
		Σ	424.1			96.9			470.4			61.4		
		n	5			5			5			4		
		MEAN	84.8			19.4			94.1			15.4		
GRID CENTERED ON SEEDED CLOUDS	MAY 15	5	-14.7	107.2	—	-22.1	—	—	-20.0	—	—	79.2	-77.5	—
	16	5	—	—	—	—	—	—	—	—	—	—	—	—
	16	6	-53.4	—	—	27.1	0	—	-37.5	0	18.6	53.8	—	—
	19	1	2.9	—	—	2.8	—	—	40.8	0	0	23.2	24.0	313.0
	20	5	369.0	—	—	-147.7	—	—	176.0	17.2	—	39.4	—	—
	21	2	—	—	—	—	—	—	—	—	—	—	—	—
	26	11	—	—	—	—	—	—	—	—	—	—	—	—
	27	2	-1.1	0	0	-27.5	—	—	13.5	—	—	-15.1	0	274.0
	28	5	597.5	—	—	-4.9	0	-15.6	333.3	—	—	62.8	—	—
	30	7	-21.2	106.3	—	-37.6	—	—	70.3	—	—	-19.1	-18.2	-20.8
	30	8	637.4	-89.6	—	152.8	—	—	137.4	—	—	281.4	0	—
	30	10	589.0	1085.5	—	17.7	—	—	1.5	0	—	6.4	0	—
		Σ	2105.4			-39.4			717.3			514.0		
		n	9			9			9			9		
		MEAN	233.9			-4.4			79.7			57.1		

W = WATER IN ACRE FEET

RC = RADAR CONTROL CLOUD

— = NO WATER CALCULATION POSSIBLE

Considering the results of this portion of the study, there is reasonable statistical justification for stating that the seeded clouds did not have a significant effect on the rainfall in a 40-n mi diameter circle centered on them up to 1 hour after the seeding pass. Because of the problems mentioned earlier, no statement can be made about the rainfall at ranges exceeding 20 n mi from the experimental clouds.

5. SUMMARY AND CONCLUSIONS

Although seeding had a profound effect on the growth and precipitation of the seeded clouds, it apparently did not significantly affect cloud developments in their environments. Neither plume nor grid rainfall comparisons detected significant differences between precipitation developments in the vicinity of the seeded and control clouds. Although both approaches suggested that the large scale effects of single cloud seeding were precipitation increases, these increases were small and not significant at the 20-percent level.

The analysis schemes used in this study are potentially very powerful techniques for detecting large scale precipitation changes near experimental clouds. There are several requirements if these techniques are to be of any use in future analyses:

(1) A larger cloud sample with a more complete time and space history is mandatory.

(2) Twenty-four hour operation of the UM/10-cm radar with the systems described is an absolute necessity.

(3) Overlap of the experimental clouds in time and space should be avoided by the scientists selecting them during future experiments.

(4) Finally, it is desirable to study clouds during a period with less developed natural convective activity. The heavy natural rainfall during May 1968 was an annoying source of noise throughout all phases of this analysis.

6. ACKNOWLEDGEMENTS

We are especially indebted to Mr. Jose Fernandez Partagas for making the silver iodide plume and shear calculations that were used in this paper. We also appreciate the following contributions: the radar observations from the Radar Meteorological Laboratory of the Institute of Marine and Atmospheric Sciences at the University of Miami and the map of the South Florida rain gage network from Mr. Harold Gerrish of the same organization; the rain gage measurements provided by many agencies in South Florida; and the advice and assistance afforded us by the staff of the Experimental Meteorology Laboratory.

7. REFERENCES

Andrews, G. F., and H. V. Senn (1968), Semi-automatic calibration of receiver and video system characteristics for weather radars, Proc. 13th Radar Meteorol. Conf., Montreal, Canada, 20-23.

Battan, L. J. (1966), Silver iodide seeding and rainfall from convective clouds, J. Appl. Meteorol. 6, 317-322.

Fletcher, N. H. (1962), The Physics of Rainclouds (Cambridge University Press, Cambridge, England), 386 pp.

Flueck, J. A. (1968), A statistical analysis of Project Whitetop's precipitation data, Proc. First Natl. Conf. Weather Modification, Albany, New York, 26-35.

Guttman, J., and S. S. Wilks (1965), Introductory Engineering Statistics (John Wiley and Sons, Inc., New York), 340 pp.

Hiser, H. W., and G. F. Andrews (1966), A new approach to range normalization and stepped attenuation for weather radars, Proc. 12th Radar Meteorol. Conf., Norman, Oklahoma, 62-66.

MacCready, P. B. (1959), The lightning mechanism and its relation to natural and artificial freezing nuclei, Recent Advances in Atmospheric Electricity (Pergamon Press, London, England), 369-381.

McDonald, J. E. (1958), The physics of cloud modification, Advances in Geophysics 5 (Academic Press, Inc., New York, N.Y.).

Mason, B. J. (1962), Clouds, Rain and Rainmaking (Cambridge University Press, Cambridge, England), 145 pp.

Neyman, J., E. Scott, and J. A. Smith (1969), Areal spread of the effect of cloud seeding at the Whitetop experiment, Science 163, 1445-1449.

Senn, H. V., and G. F. Andrews (1968), A new, low-cost multi-level iso-echo contour for weather-radar use, J. Geophys. Res. 73, 1201-1207.

Senn, H. V., and C. L. Courtright (1968), Radar hurricane research, Final Rept. by Institute of Marine Sciences, Univ. of Miami, Radar Meteorology Section to U.S. Weather Bureau, Contract No. E22-62-68(N), 31 pp.

Simpson, J., W. L. Woodley, H.A. Friedman, G. W. Slusher, R.S. Scheffee, and R. L. Steele (1969), A pyrotechnic cloud seeding system and its use, ESSA Tech. Memo ERLTM-APCL 5.

Woodley, W. L. (1969), Precipitation results from a pyrotechnic cumulus seeding experiment, ESSA Tech. Memo ERLTM-AOML 2.

Woodley, W. L., and A. Herndon (1969) A rain gage evaluation of the Miami Reflectivity-Rainfall Rate Relation. ESSA Tech. Memo ERLTM-AOML 3.

U.S. DEPARTMENT OF COMMERCE
Environmental Science Services Administration
Research Laboratories

ESSA Technical Memorandum ERLTM-APCL 7

RADAR AND PHOTOGRAPHIC DOCUMENTATION OF CONVECTIVE DEVELOPMENTS ON MAY 16, 1968

William Lee Woodley

Jose Fernandez Partagas

Experimental Meteorology Branch
Coral Gables, Florida

Atmospheric Physics and Chemistry Laboratory
Boulder, Colorado
April 1969

TABLE OF CONTENTS

ABSTRACT

The convective developments over South Florida on May 16, 1968, are documented to provide a basis for comparison for seeded cloud behavior on this day. Ground-based 10-cm radar observations, concurrent aerial time lapse photography, and an ESSA VI satellite picture are used in the documentation.

Large convective clouds developed in a band near a preexisting cloud line that stretched from the Gulf of Mexico to Miami. Four cumulonimbus clouds formed in this band; two were natural and the other two were apparently artificially induced. By late afternoon several other small cumulonimbus clouds were scattered over the southern portion of the peninsula.

Seeding probably induced two of the cumulonimbi studied, which, once formed, behaved like their natural counterparts. The natural and artificially induced cumulonimbi were similar in appearance and had comparable lifetimes and radar echoes. Detailed study based on the cumulus model developed by ESSA's Experimental Meteorology Branch is needed to clarify the effect of seeding on May 16, 1968.

RADAR AND PHOTOGRAPHIC DOCUMENTATION OF CONVECTIVE DEVELOPMENTS ON MAY 16, 1968

William Lee Woodley and Jose Fernandez Partagas

1. INTRODUCTION

From May 15 to June 1, 1968, a joint cloud seeding project was conducted over the South Florida peninsula. Participating in the program were the Experimental Meteorology Branch (EMB) and the Research Flight Facility (RFF) of ESSA, the Naval Research Laboratory, U. S. Air Force, and the Radar Meteorological Laboratory of the University of Miami. Nineteen clouds were selected randomly by a sealed envelope procedure; 14 were seeded and five were used as controls. The analysis to date indicates that silver iodide seeding was effective in inducing increased growth and precipitation from the seeded clouds. Details of the analysis will appear in a sequel to this report.

To correctly interpret seeded cloud behavior, it is important to study the behavior of unmodified convection close in space and time to the seeded clouds. Such a study was made for May 16, 1968, a day on which there were three seeded clouds, one that collapsed and two that showed explosive growth.

The important convective developments over South Florida were studied on the basis of radar data and aerial time lapse photography. The radar data were obtained by the AN/CPS-6B 10-cm radar of the Radar Meteorological

Laboratory of the University of Miami operating with the iso-echo system described by Senn and Andrews (1968). The photographic data were obtained by the 35-mm side cameras installed on the Research Flight Facility (RFF) DC-6.

2. SYNOPTIC SITUATION

The surface pressure pattern was very weak over the Gulf of Mexico, Florida and the western Bahamas at 1200Z on May 16, 1968 (fig. 1a). Just above the surface, the main feature of interest is a small high-pressure area west of Tampa producing a light north-northwest flow over the southern portion of the peninsula. The situation at 500 mb is just as indeterminate (fig. 1b), with a weak pressure field and light winds. The center of highest pressure is displaced westward into the central Gulf of Mexico with a large col region over central Cuba. The Miami 1200Z sounding (fig. 1c) shows moderately moist conditions up to 600 mb, with drying above this level.

3. MORNING FORECAST

The EMB cumulus model developed by Simpson and Wiggert (1969) of ESSA's Experimental Meteorology Branch was used for the first time in real time as a tool in forecasting seeding conditions. Based on the 1200Z Miami sounding and a spectrum of cloud radii as input, the model was used to predict the maximum top growth for seeded and unseeded clouds. The major unknown is the characteristic tower diameter that atmospheric conditions will produce on any given day. The May 16 predictions could be expected to be valid if cumulus clouds with tower radii comparable to those assumed developed during the day.

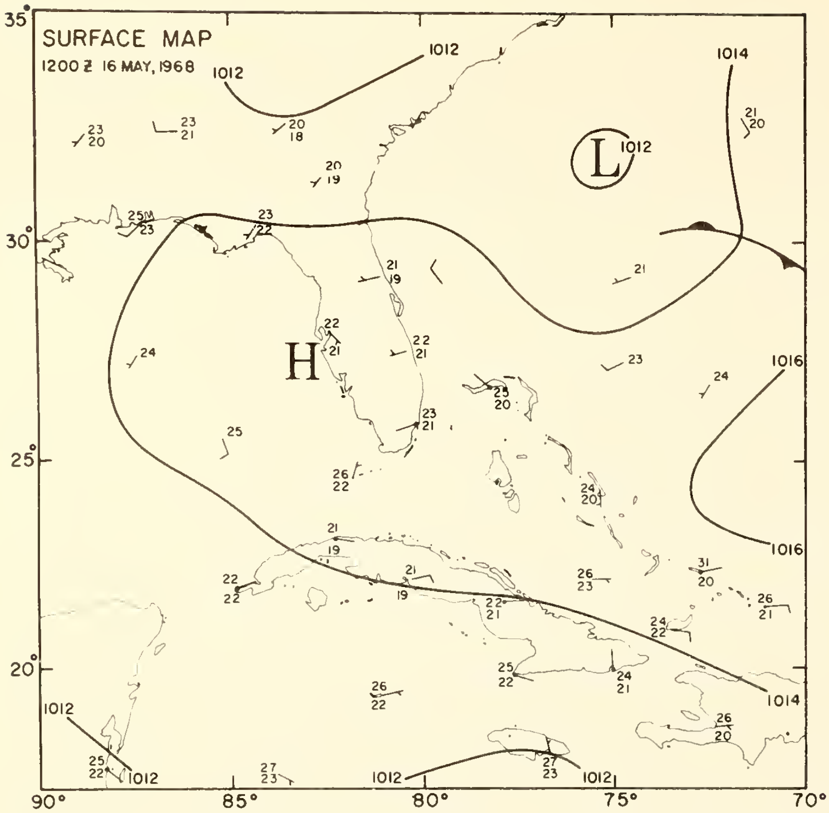

Figure 1a. Surface map for Florida and surrounding region, 1200Z, May 16, 1968.

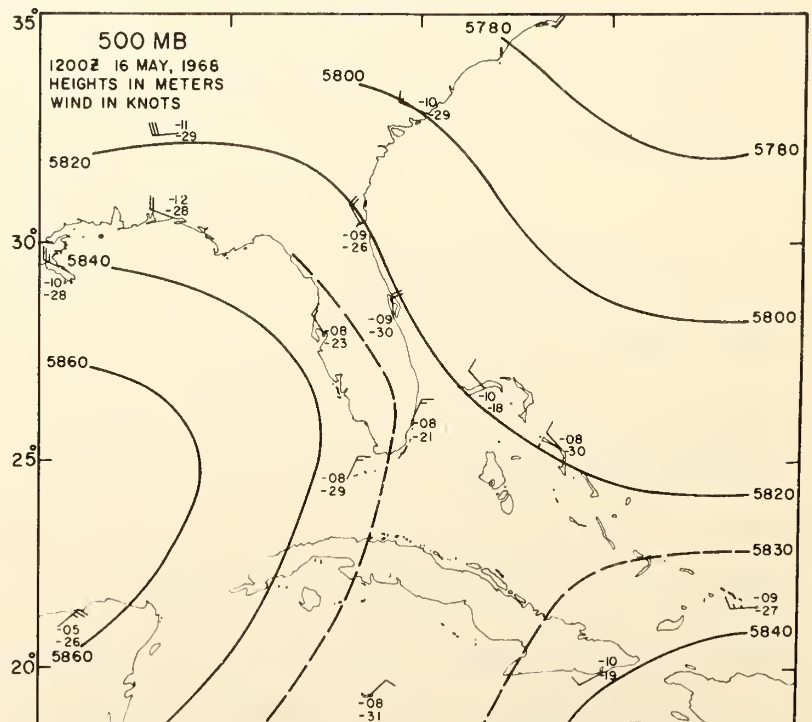

Figure 1b. 500-mb map for Florida and surrounding region, 1200Z, May 16, 1968.

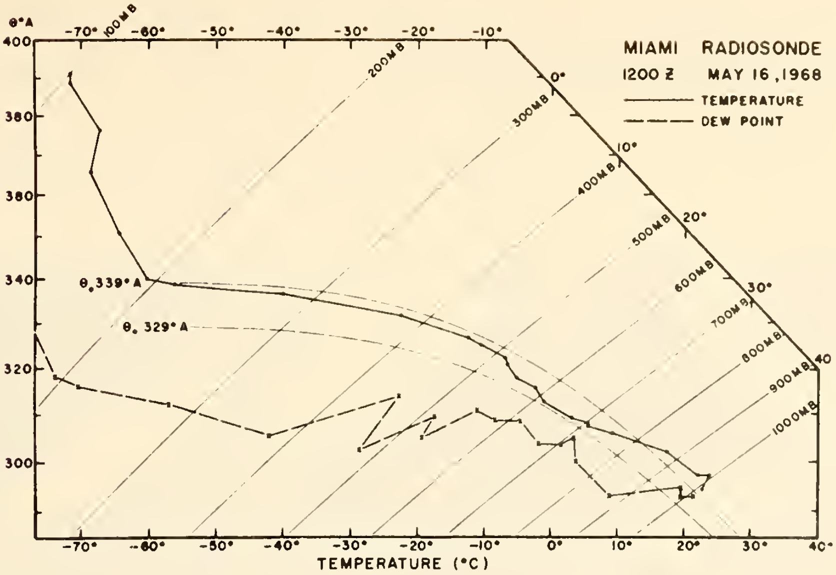

Figure 1c. Miami radiosonde, 1200Z, May 16, 1968.

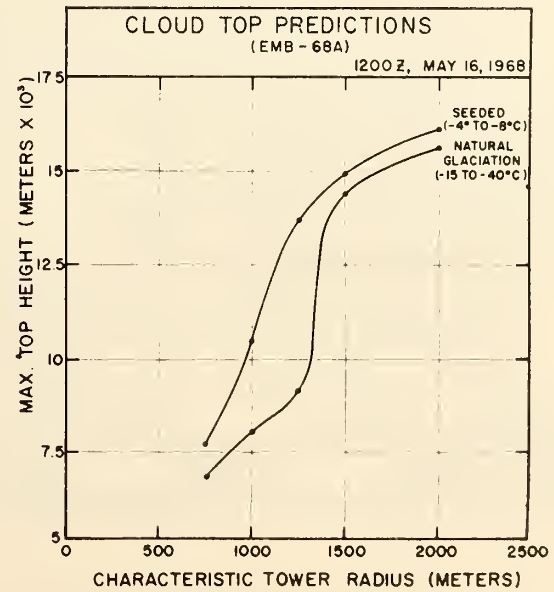

Figure 1d. Cloud top predictions based on the EMB cumulus model (EMB-68A), 1200Z, May 16, 1968.

The morning model predictions for May 16 indicated that cumulus clouds with tower radii greater than 750 m would penetrate the freezing level (13,500 ft), making them suitable for seeding (fig. 1d). The predictions indicated further that seeding would induce cloud growth that could not have occurred naturally, especially in clouds with tower radii of 1250 m. Clouds with tower radii greater than 1250 m were predicted to cumulonimbus heights (>40,000 ft) without seeding. Seeding was predicted to induce very little additional growth in such clouds . The model predictions indicated that there would be cumulus clouds that would be responsive to seeding and also some that would grow to cumulonimbus naturally.

4. LARGE-SCALE CLOUD COVER

The convective conditions during late morning over and near the Florida peninsula are shown on the 1521Z ESSA VI satellite picture, on which a 1200Z-ft streamline analysis has been superimposed (fig. 2). There is little convection anywhere except for a cloud line that extends from the Gulf of Mexico across the southwest Florida coast. This line of clouds is still evident on the aerial time lapse photographs during the afternoon. Note that it lies close to the line of confluence in the streamline analysis, which was made independently of the satellite picture and then superimposed. The analysis to follow shows that this line consists of small cumulus with the portion extending across the peninsula marking a preferred region of cloud development.

5. RADAR AND PHOTOGRAPHIC OBSERVATIONS

The radar and visual appearances of the subject clouds are compared in the analysis that follows. All clouds are lettered alphabetically

ESSA VI SATELITE PICTURE WITH 2000 FOOT STREAMLINE ANALYSIS

SATELLITE PICTURE: 1521 Z

STREAMLINE ANALYSIS: 1200 Z

Figure 2. ESSA VI satellite picture at 1521Z with 1200Z 2,000-ft streamline analysis superimposed; May 16, 1968.

(except the unnamed cloud) by order of appearance on the radar. The radar antenna is at 0.5° elevation angle in all the radar pictures. This means that the radar is depicting increasingly higher portions of the clouds as range increases. The echoes were contoured, but the contouring is not shown here because of difficulty in presenting it in the small diagrams. Only the outer boundary and cores are delineated. The position of the DC-6 aircraft, its heading, and the camera direction when the picture was taken are also shown on the radar plot. The camera data chamber has been included for easy reference.

Cumulus cloud development began over South Florida by midmorning, with the preferred region of convective activity lying in a band extending 10 mi on both sides of the cloud line southwest of the col point shown in fig. 2. Cloud bases were generally at 2,000 ft. The positions of the major cloud developments, including times of appearance and disappearance of their echoes from the 10-cm radar scope, appear in figure 3.

The initial clouds of interest are experimental cloud 5 and the Homestead cloud, having first echo times of 1647 and 1727Z respectively (fig. 4a). Cloud 5 attained its peak reflectivity at 1750Z and then decayed, although it was seeded at 1800Z. Seeding did not appear to interrupt the decay. The Homestead cloud, which was not seeded, attained cumulonimbus stature (characteristic anvil appearance) at about 1800Z, 33 min after its initial appearance on radar. Note the linear organization of the three echoes and the interesting line of small cumulus that extends well out into the Gulf of Mexico (picture from left-side camera). This is the same line of cumulus that appears in the satellite picture discussed earlier. This

INITIAL TIME AND POSITION OF IMPORTANT CONVECTIVE DEVELOPMENTS

MAY 16, 1968

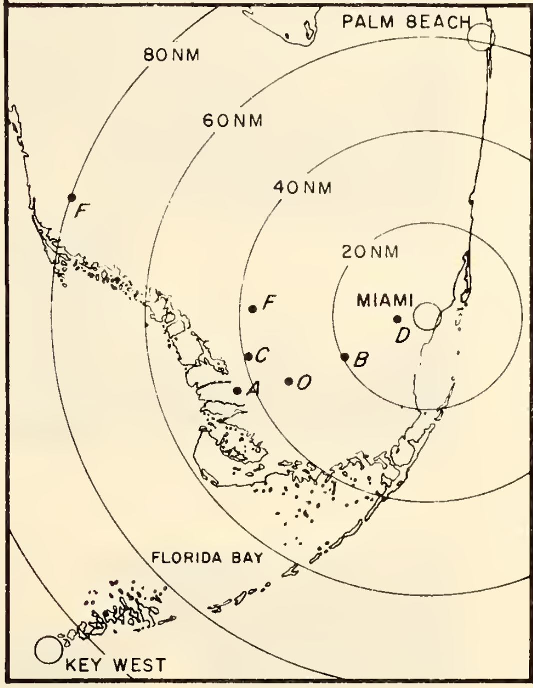

• POSITION OF INITIAL APPEARANCE OF CLOUD ON 10 cm RADAR

DESCRIPTION	DESIGNATION	TIME OF FIRST APPEARANCE ON 10 cm RADAR (GMT)	TIME OF DISAPPEARANCE FROM 10 cm. RADAR (GMT)
CLOUD 5	A	1647	1837
HOMESTEAD CLOUD	B	1727	> 2100
UNNAMED CLOUD	O	1733	1806
CLOUD 6	C	1804	~ 2100
MIAMI CLOUD	D	GROUND CLUTTER	GROUND CLUTTER
NAPLES CLOUD	E	1843	> 2100
CLOUD 8	F	1948	> 2100

Figure 3. Inital time and position of important convective developments as indicated by 10-cm radar.

RADAR AND PHOTOGRAPHIC DOCUMENTATION OF CONVECTIVE DEVELOPMENTS
MAY 16, 1968

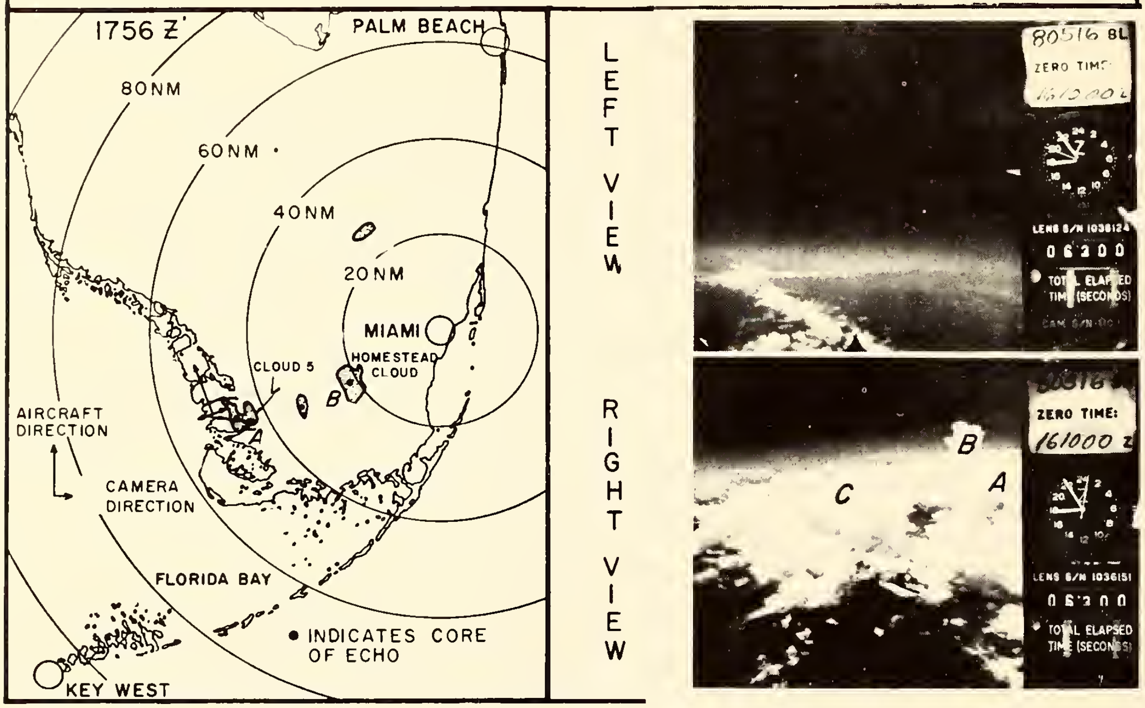

Figure 4a. Radar and photographic documentation of convective developments, 1756Z.

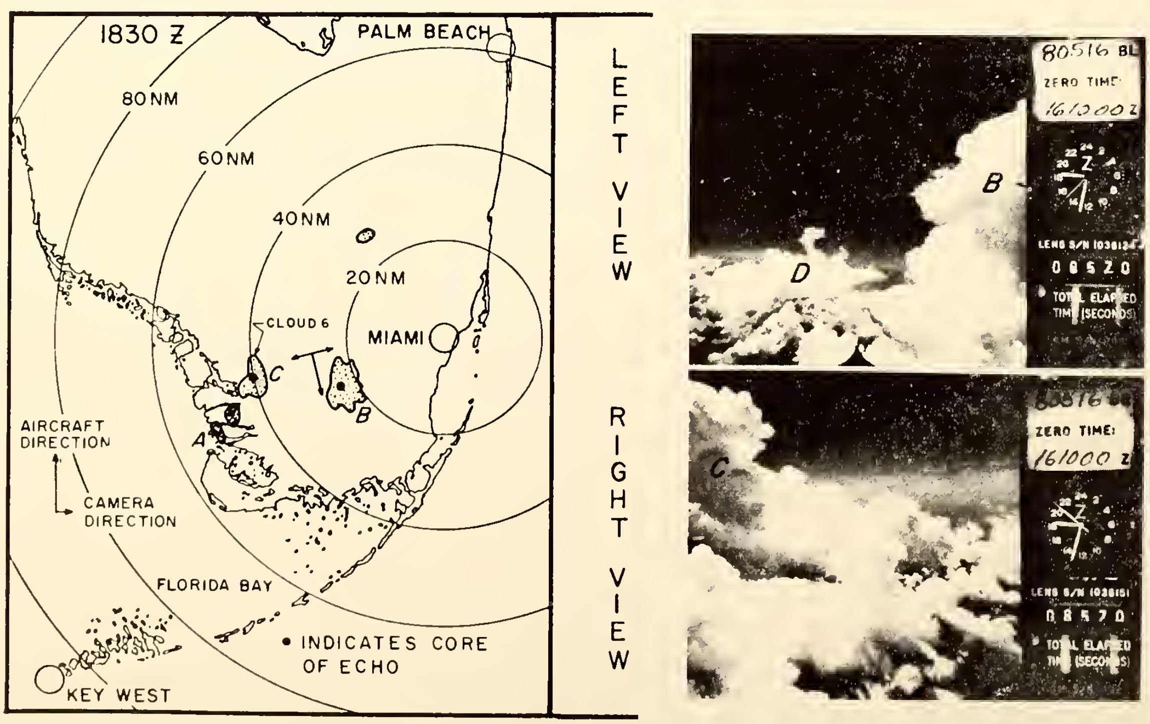

Figure 4b. Radar and photographic documentation of convective developments, 1830Z.

cloud line crosses the coast line, passes under the aircraft and then up into cloud region C, just north of cloud 5 (right-side camera). The cloud tower marked B is the Homestead cloud that attains cumulonimbus form 6 min later; it too lies in this convective zone. Cloud 6, seeded at 1824Z, will come from region C.

The mechanism that accounts for the convective line stretching from the Gulf of Mexico across the Florida peninsula is not fully understood, although the streamline analysis suggests that weak convergence is the primary factor. The portion of the line over the water consists of very small cumulus, but the portion over land has large cumulus that were undoubtedly influenced by solar heating of the ground.

The situation at 1830Z is shown in figure 4b. All echoes have drifted slowly west-southwest. The northern portion of experimental cloud 6 (marked C), seeded 6 min earlier, is shown on the picture of the right-side camera, while the Homestead (B) and Miami (D) clouds appear on the left. It is difficult to get an accurate position and tracing for the echo of the Miami cloud because it is well within the Miami ground clutter.

At 1900Z there are new echo developments 15 mi southeast of Lake Okeechobee, 10 mi east of Naples (the Naples cloud marked E) and a new echo just northwest of the Homestead cloud (fig. 5a). The picture of the right-side camera shows the cloud line crossing the coast and extending into cloud 6 (C), which has grown tremendously.

The situation is little changed at 1930Z, as shown by figure 5b. Here the nose camera of the DC-6 shows the Naples cloud at approximately the time it was rejected as an experimental cloud because it had grown too

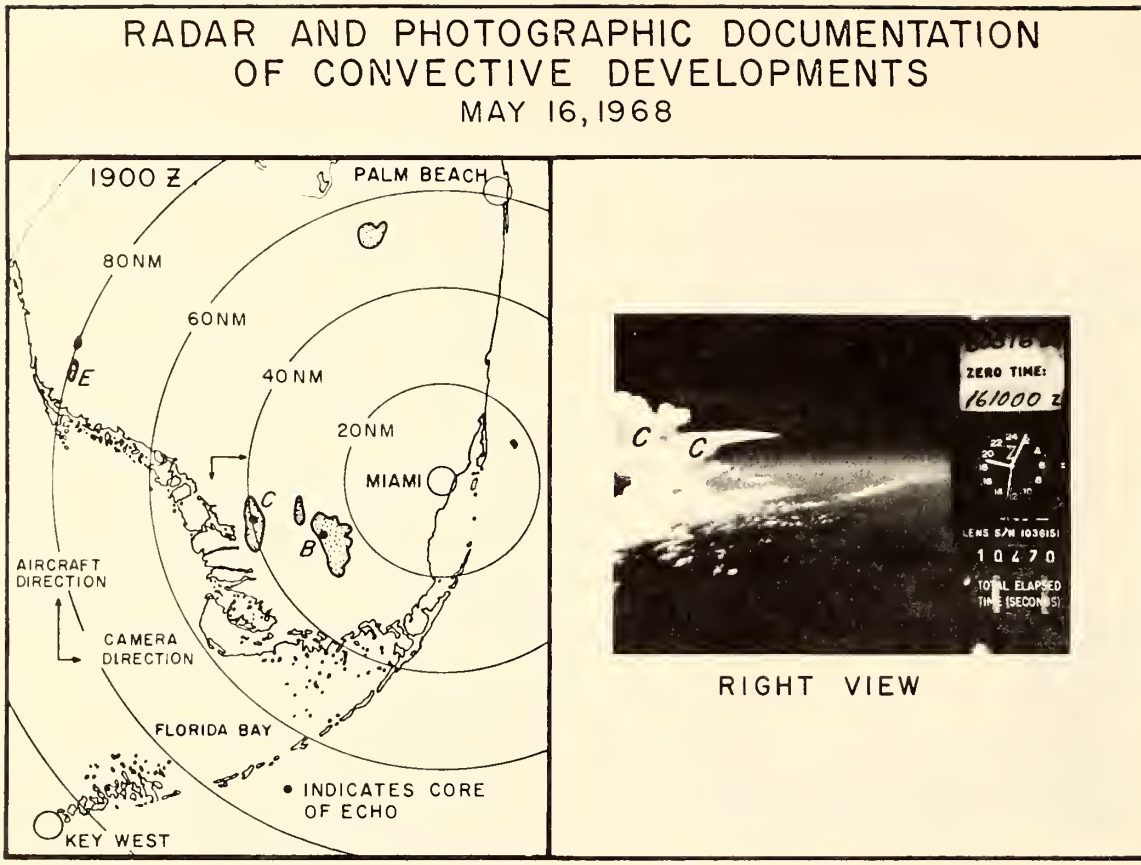

Figure 5a. Radar and photographic documentation of convective developments, 1930Z.

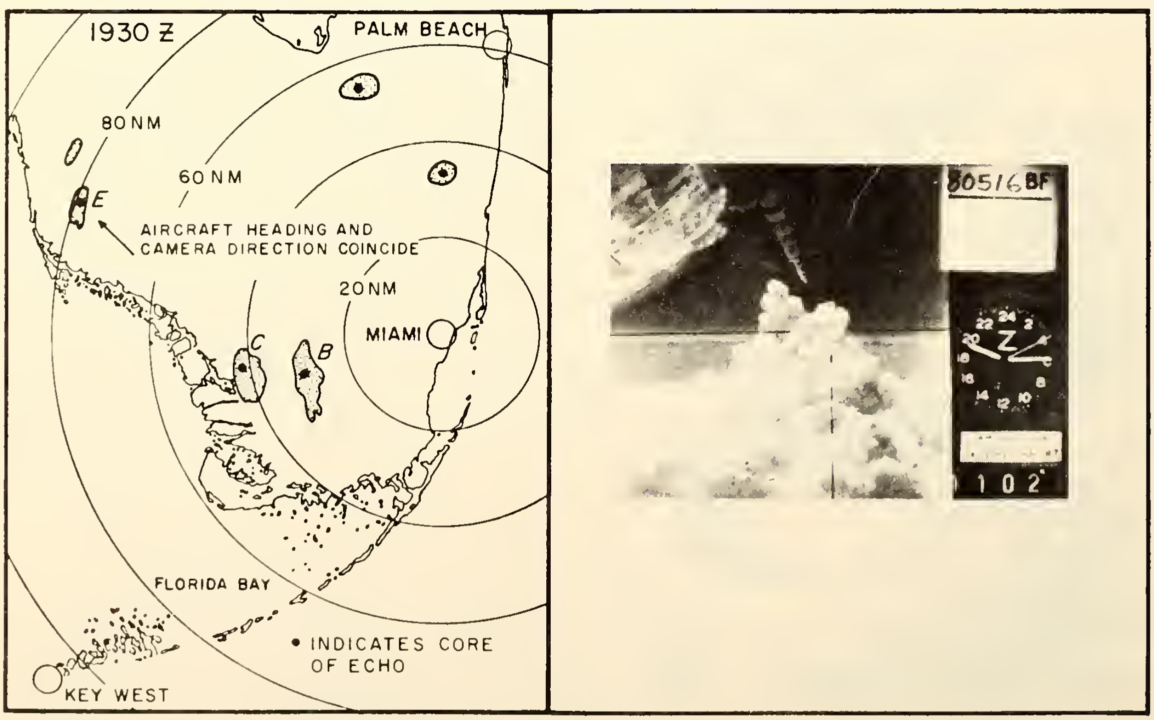

Figure 5b. Radar and photographic documentation of convective developments, 1900Z.

large. This picture is the only one in the series taken with this camera. The protrusions on the boom are the probes for the hot wire liquid water instrumentation.

There are several developments over the southern portion of the Florida peninsula at 2000Z (fig. 6a). The echo of cloud 8 (marked F) now appears on the scope, 6 min after seeding. The pictures of the side cameras show the cloud developments of interest very well. The growing tower of cloud 8 (F) can be seen with cloud 6 (C), the Homestead (B) and the Miami clouds (D) arrayed behind it. The picture 7 min later, again from the left side, shows the Naples cloud (E), now a cumulonimbus, 57 min after initial appearance on radar, and the growing tower of seeded cloud 8 (F). There are also two other small cumulonimbus developments between Miami and Lake Okeechobee.

Cloud 8 has grown significantly between 2000Z and 2030Z (fig. 6b) attaining cumulonimbus form 22 min after initial appearance on radar. At 2030Z this cloud has two cores marked on the radar display and on the side-camera photo. Tower F_2 is growing very rapidly as the picture is taken. Cloud 8 and the Homestead clouds merge shortly afterwards. Cloud 6 and the Miami cloud have diminished significantly. The picture from the left side at about 2040Z shows decaying cloud 6, the anvil overhang from cloud 8 (top of picture) and the persistent cumulus line in the Gulf that crosses the coast and feeds into the northern portion of Cloud 6.

Top-height information is available for several of the clouds examined here. Cumulonimbus tops were generally around 40,000 ft, with clouds 6 and 8 having aircraft-measured, maximum tops of 40,500 and 45,000

RADAR AND PHOTOGRAPHIC DOCUMENTATION
OF CONVECTIVE DEVELOPMENTS
MAY 16, 1968

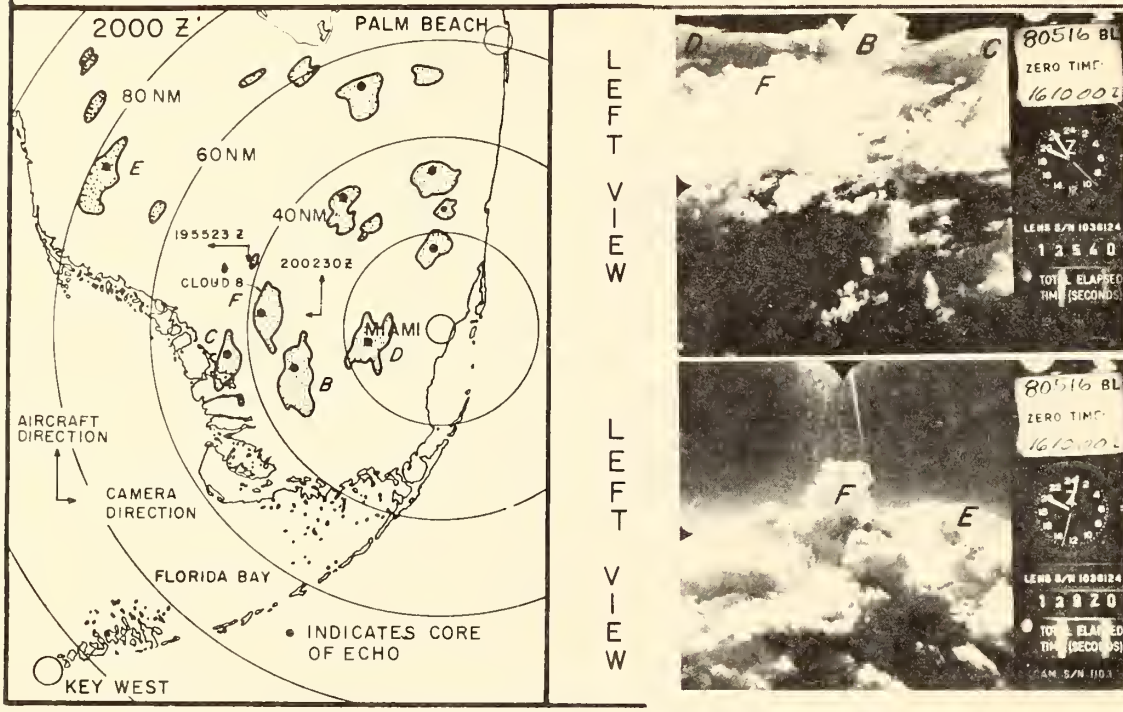

Figure 6a. Radar and photographic documentation of convective developments, 2030Z.

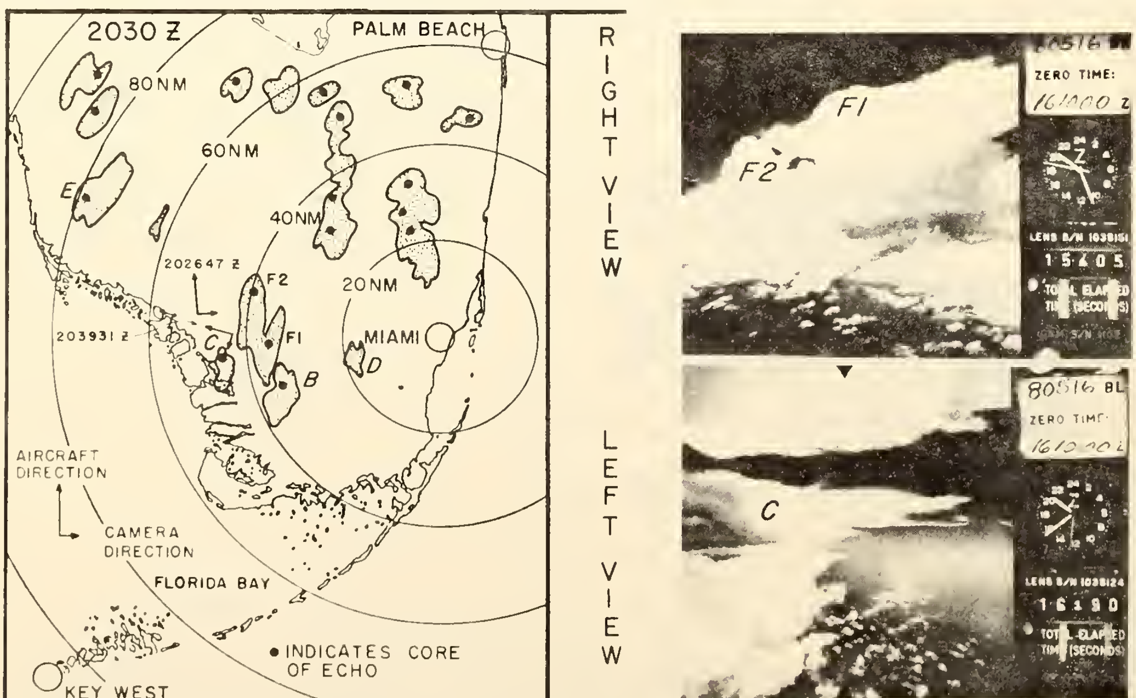

Figure 6b. Radar and photographic documentation of convective developments, 2000Z.

ft respectively, which is at or slightly above the tropopause height of 39,000-40,000 ft (196 mb). The Homestead cloud had a maximum radar top of at least 47,000 ft, while experimental cloud 5 had a maximum top of approximately 20,000 ft.

The pictures from the side cameras indicate that the shear was from the north, with new convective towers growing upshear. This is not unexpected and is qualitatively consistent with the shear diagram (fig. 7), which was estimated for the locations of clouds 5, 6, and 8 from the three-dimensional streamline analyses for 1200Z May 16 and 0000Z May 17.

Since flights ended after 2045Z, there are no photographs of developments after this time. However, examination of the radar film indicates that the basic pattern persisted into the early evening, with the Homestead-cloud 8 amalgamation and the Naples cloud disappearing from the scope between 2200 and 2300Z.

6. SUMMARY AND CONCLUSIONS

Cumulus cloud development occurred over all of the southern portion of the Florida peninsula on May 16, 1968, with the region of preferred development near a preexisting cloud line extending from the Gulf of Mexico across the peninsula to Miami. In the region 10 mi to either side of this line at a range exceeding 20 mi from Miami, there were six distinct separate echoes, three of which were those of clouds that eventually reached cumulonimbus proportions. One of the cumulonimbus was natural; the other two were apparently the result of seeding. There were also radar echoes one of which was that of a cumulonimbus within 20 mi of Miami, but little can be said of them because of ground clutter. Several smaller cumulonimbus developments

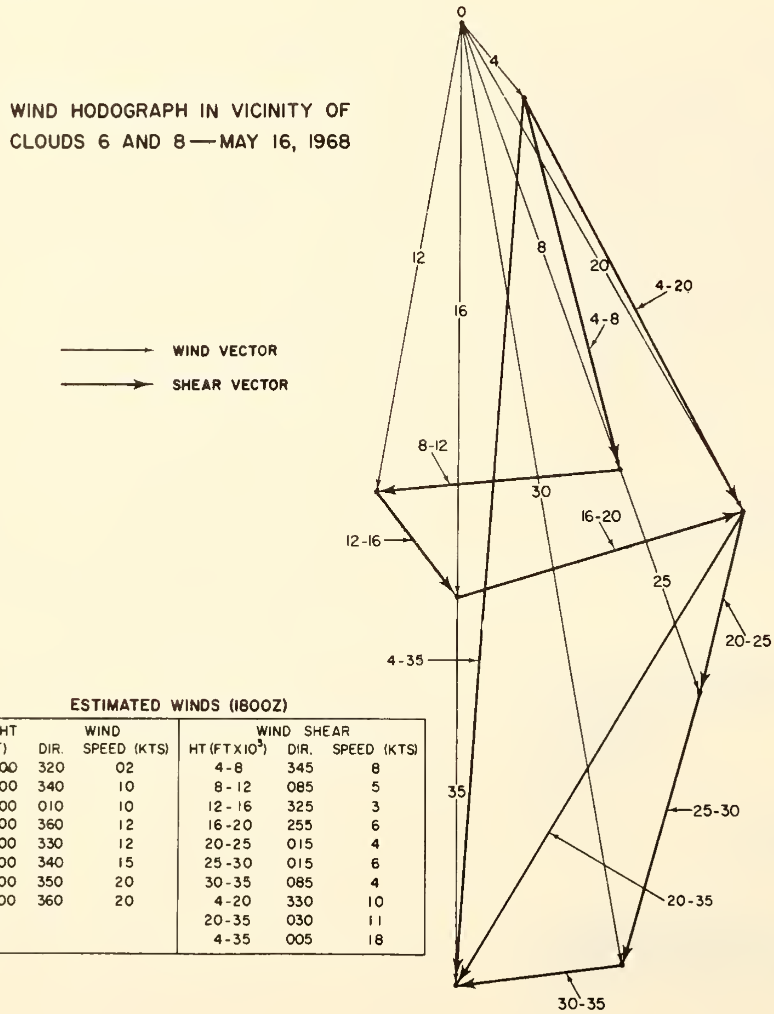

ESTIMATED WINDS (1800Z)

HEIGHT (FT)	WIND DIR.	WIND SPEED (KTS)	WIND SHEAR HT (FT X 10^3)	WIND SHEAR DIR.	WIND SHEAR SPEED (KTS)
4,000	320	02	4-8	345	8
8,000	340	10	8-12	085	5
12,000	010	10	12-16	325	3
16,000	360	12	16-20	255	6
20,000	330	12	20-25	015	4
25,000	340	15	25-30	015	6
30,000	350	20	30-35	085	4
35,000	360	20	4-20	330	10
			20-35	030	11
			4-35	005	18

Figure 7. Shear diagram estimated for the times and locations of clouds 6 and 8.

also appeared by late afternoon between Miami and the vicinity of Lake Okeechobee.

The visual and radar appearance of the seeded clouds did not differ noticeably from that of unseeded clouds of comparable size. Cloud lifetimes were also comparable. However, the average time from first appearance on radar to cumulonimbus form was less for the seeded clouds. This suggests that seeding is either inducing cumulonimbus stature that could not have developed naturally or inducing it prematurely. The possibility also exists that the dissipation of cloud 5 was hastened by seeding and the disruptive effects of the monitoring aircraft. Detailed study of individual clouds, including predictions of the EMB cumulus model, is necessary before a definite statement can be made about the effects of seeding on this day.

The occurrence of natural cumulonimbus during the seeding program emphasizes the importance of randomization in determining the seeding decision to avoid criticism that cloud developments attributed to seeding would have occurred naturally. Randomization does not eliminate this possibility, but it makes it much less likely.

7. ACKNOWLEDGEMENTS

The authors are especially indebted to the Research Flight Facility for the excellent photographic data and the superb way in which it carried out all phases of the seeding operation. The Radar Meteorological Laboratory of the University of Miami also receives our special thanks for the excellent quality of the radar data. Thanks are also due the members of EMB, particularly Dr. Joanne Simpson and Mr. Ronald Holle for helpful discussions, Messrs. Jorge Posada and Robert Powell for the drafting of the figures, and Mrs. Peggy M. Lewis who capably typed the manuscript.

8. REFERENCES

Senn, H. V., and G. F. Andrews (1968), A new low cost multi-level iso-echo-contour for weather-radar use, J. Geophys. Res. 73, 1201-1207.

Simpson, J., and V. Wiggert (1969), Models of precipitating cumulus towers, Monthly Weather Rev. 97 (to be published).

PREPRINT NO. 105-52

CLOUD PHOTOGRAMMETRY FROM AIRBORNE TIME-LAPSE PHOTOGRAPHY

by
Luis M. H. Cantilo and
William L. Woodley
Univ. of Miami Experimental
Meteorology Branch, ESSA

PRESENTED AT THE

105th TECHNICAL CONFERENCE

APRIL 20 – APRIL 25, 1969

SOCIETY OF MOTION PICTURE AND TELEVISION ENGINEERS

Measuring the growth of a cloud is a necessity in many current cloud studies. The ideal location for the observer who performs this task is aboard an airplane in continuous flight around the cloud. His record mainly consists of time-lapse photographs, and some means of locating the aircraft at the time each photograph was taken. The location of the aircraft in this case, was determined by means of its Doppler navigation equipment. The technique used to analyze the photographs, process the navigational information and obtain the desired measurements of the clouds is described. The various problems inherent in this method are considered, and results of its application are presented.

1. Introduction

Convective clouds, these all-important agents of energy transfer throughout the troposphere, are the seat of simultaneous and interacting physical phenomena of different kinds, such as the change of state of a population of droplets and the establishment or modification of a pattern of motion. For this reason, it is often desired to perform a running measurement of a cloud's dimensions, while carrying out other observations relevant, for instance, to its composition.

Chiefly, the aim of that measurement is a record, as a function of time, of the top height and the growth rate of a cloud; one may also wish to know its diameter, that of its main turrets, its motion at various levels (which may differ) and other such geometric parameters, generally as functions of time.

The extent of a young convective cloud is of the order of one or a few kilometers, horizontally and vertically. And while one wishes the inevitable errors small enough to be neglected in comparison, it is certainly meaningless to attempt to even define the size, or location, of a cloud to better than 10 meters, and usually good enough to measure them to the nearest 100 meters, which is tantamount to an accuracy of several units percent - by no means, at first sight, a frightening requirement.

Consider, however, that the measurements must be remote, in practice, optical, and that one does not know, at the beginning, the location of the cloud with respect to the observer; that the measurement must be carried out quickly and repeated, so that successive results may be correlated to the changing conditions under study; that a cloud rarely occurs by itself and that as a consequence, an unobstructed view of a cloud only exists in a limited region around it; that a cloud drifts, and will soon be out of an observer's range if he occupies a fixed position - or will present to him after a while an entirely different view, that he cannot compare to the previous. These and other similar annoyances, unimpressive though they seem, account for the unsuccess of such perfectly sound methods, in principle, as ground-based bistatic observations with theodolites or ground-based photography with stereo-cameras, which have been tried a number of times.

We present here another method, which we make no claim to be a cure-all. Perhaps its chief merit is in yeidling to nature: rather than a heavy restriction on the cloud sample (which is inherent in ground-based observations) we put heavy demands on the techniques of data acquisition and analysis. We depend on a well-instrumented aircraft, a computer, a digital plotter and, perforce, a lot of patience. However, the photographic stages of our work are done with simpler means and, characteristically, are the least troublesome.

2. Description of the Method.

Data are gathered by flying repeatedly around the selected cloud and photographing it at 5-second intervals; given the speed of the aircraft, usually around 200 kts., successive photographs are taken about 1500 ft. apart. The flight pattern consists mainly of nearly square boxes of appropriate size to keep a distance in the order of 10 n.m. to the cloud.

The photographic equipment includes, among others, two Automax G2 35-mm film cameras fitted with Angenieux wide-angle lenses of 14.8 mm. focal length. They are rigidly mounted in the rear section of the fuselage, looking out at right angles to it, i.e., along the pitch axis. They are triggered by the very accurate timing device that synchronizes all observations and records in the airplane. That device pulses once a second; the cameras shoot every fifth pulse. Their frame is divided into a square

picture frame and the rest of the format, which shows a data panel with the necessary identification and a digital second-counter, controlled by the general timer. The principal point of the image is at the center of the square. The half-angle of view is 32.5^{o} in all directions. Plus X 4231 Eastman panchromatic negative film is used, without any filters, and the exposure adjusted so as to give good contrast of clouds on the picture during daylight hours; ground detail is usually underexposed under these conditions.

So far, photographs of the subject cloud are automatically provided at sufficiently small time-intervals to be considered simultaneous. The next step is to ascertain the aircraft's position and attitude at the time of the photographs. This is achieved by means of the navigation equipment on board.

The airplanes used in our project are the CD-6 operated by the ESSA Research Flight Facility. These heavily instrumented birds navigate on the basis of an APN-82 system eomposed mainly of an APN-81 Doppler radar and an ASN-6 computer; complemented by an N-1 compass, a radio altimeter and other conventional instrumentation. Each second, a digital record is made on tape, of the output of most individual instruments, with the result that the navigation can be entirely re-computed after the flight, on an electronic machine more aceurate than the ASN-6.

This we do indeed, on the IBM 7040 available on campus, the output of our program being processed by a CALCOMP mod 563 plotter which then provides us with a plot of the positions of the aircraft at each "photo time" during the period of observations of a given cloud. A photogrammetric base may now be defined between two points of the flight track and, by reading the necessary angles from the two corresponding film frames, the subject cloud can be located and its dimensions determined. By repetition, the process describes the evolution of the cloud with time.

The film is then projected on a translucent screen, to a magnification set as accurately as possible to x 15. Vertical and horizontal angles of the desired object with respect to the principal point are read from each selected frame by means of a plastic overlay, which is pivoted at the principal point in order to afford the necessary compensation for changes in aircraft pitch. Because the optical axis tilts away from the horizontal according to aircraft roll, the isolines of horizontal angle change[1] and as a result a set of overlays must be used to cover the roll range of the aircraft.

Now, given two "stations" A and B on the flight track, if we call c the distance between them, w the orientation (with respect to true North) of the line of sight from B to the object, ρ the orientation of the base c, $\Delta\theta$ the change in aircraft heading from A to B and $\Delta\psi$ the change in object horizontal angle in the same time, it is easily shown that the range r from station A to the object is:

$$r = c\,\frac{\sin(w - \rho)}{\sin(\Delta\theta + \Delta\psi)}$$

Now, if ζ is the object vertical angle read from the film, R the aircraft roll and RA the radar altimeter reading, then the height of the object above the ground is given, in principle, by the expression:

$$z = r.\mathrm{tg}\,(\zeta \pm R)\cos\psi + RA$$

where the plus sign applies to the right-side camera, the minus to the left side camera.

---

[1] These lines are intersections of the image plane with a set of vertical planes whose axis passes through the perspective center.

This is the essence of our method, which has now been in use for some eight months in the analysis of experimental data gathered in recent field projects, (1,2). As an example, a case taken from the first reference follows.

3. The Analysis of Cloud 6 of May 16, 1968.

Cloud 6 was seeded with silver iodide flares and reacted spectacularly to the seeding. Accordingly, a photogrammetric study was made of it. Cloud-top heights and tower radii calculated in the process are shown in fig. 2, following the observations of the cloud by photography and radar, shown on fig. 1. The numbers appearing along the curves on fig. 2 correspond to the numbers of the photographs of fig. 1. Prominent cloud towers are lettered correspondingly in both.

In fig. 1, panels 1 and 2 are nose-camera photographs taken at 1822Z and 1824Z by the high-flying jet in charge of the seeding. They show a rather amorphous cloud, of which turret A is the prominent feature. It was seeded six seconds after the second picture. The following panel shows a contoured radar echo of the cloud at that time, and the directions from which the first two photos were taken.

Panels 3,4,5 and 6 on fig. 2 are side camera pictures taken from the DC-6 at the indicated times, from positions shown on the remaining panels with the radar echoes. These and other similar pictures are the ones analyzed in the photogrammetric process.

These pictures are not reproduced in their entirety, and as a result the data panel is not shown, nor do the upper and lower fiducial marks appear; the one on the left edge, however, is visible. These marks are used to align the projected frame when reading angles.

The photographs show the growth of the seeded turret A and its merger with turret B, whereupon the cloud reaches cumulonimbus stature (panel 6).

This is depicted quantitatively in fig. 2, where the upper curves show the altitude of towers A and B from their initial observation (22,500 ft. at 1824 for tower A) until a flat anvil formed around 1842, after which it is no longer possible to observe the true top from the relatively low-flying DC-6; thus, at 1848 the edge of the anvil is revealed at an altitude of 35,000 ft. by the photogrammetry, while the jet aircraft traverses the cloud top, some 3 miles behind the edge, just over 42,000 feet.

The lower curve on fig. 2 shows the increase of the radius of the main tower during the process. This can best be defined, and is most meaningful, before the cloud top glaciates, for which reason the curve is interrupted after 1833Z.

4. Experimental Error

Given the simplicity of the principle involved, the success of the method presented here is mainly a question of accuracy and operational ease.

The problem of experimental errors can be looked at in two ways. Ranges to the cloud can be plotted on the flight track, heights can be shown on diagrams as the one in fig. 2, and the scatter of the points around a "reasonable mean curve" will show the variance of the readings. Or one can write each measured value as a function of the variables that go into its definition and apply error propagation formulae to the observational errors, in order to determine the error in the end result.

Both are long processes as can be realized when it is noted that several aircraft attitude angles and navigational results are involved, and that a complete study therefore requires a careful look into the performance of the navigation gear, the gyro system and the compass.

In addition, there is a host of possible optical errors: distortion and irregularity in the positioning of the film in the camera, effects of the development process on the film dimensions, distortion in the projector, errors in the plastic grids and so on.

However, in the search of an assessment of the performance of the airplane's measuring and recording devices, several good samples of data were gathered, reading the vertical angle of the horizon, on the few occasions when it was clearly defined on the film. These were compared to the flight record, thus providing the answer to a number of important questions, for example:

1) The side cameras are not exactly collinear; there is an angle of 2.2^{o} between the optical axis of the right camera and the pitch axis, 0.9^{o} between the left camera's axis and the pitch axis. However, the pitch shown by both cameras agrees within 0.2^{o} with that recorded on the flight tape. These corrections are now entered into the height equation shown earlier.

2) Angles are read from the film with a variance of about 0.2^{o} - for the horizon. However, we conclude that cloud features, always more clear-cut, are read better, say to $\pm 0.1^{o}$.

3) The variance in the roll-record on the flight tape is about 0.55^{o}. This is the largest single source of error at this point.

In conclusion, the method is not affected by severe errors originating in the photographic process. We may mention, however, some annoying details for which we have not yet found a cure. Firstly, the image does not always appear in exactly the same place on the film, necessitating a frequent realignment of the projecting system. This includes, quite often, an adjustment in the magnification.

Secondly, we seem to have a good case for the modern plastic high-strength film bases. Our film is, unfortunately, destroyed by the projecting system in less time than we need to analyze it.

These are certainly minor problems. And there is no question that this photogrammetric technique is free from any important photographic problems. The only limit to its accuracy is, at present, the error in the aircraft's instrumentation. Even so, measurements of range are made to about 1/20 of a nautical mile, which is sufficient to measure cloud heights to about 500 feet. Far from a desideratum, but better than generally done before.

References:

1. William L. Woodley and Joanne Simpson, Intensive Study of Three Seeded Clouds on May 16, 1968, ESSA/ERL Report, 1969.

2. Luis M. Herrera Cantilo, A Method of Serial Cloud Photogrammetry Based on Doppler Navigation, ESSA Report under Contract 22-2-68(N).

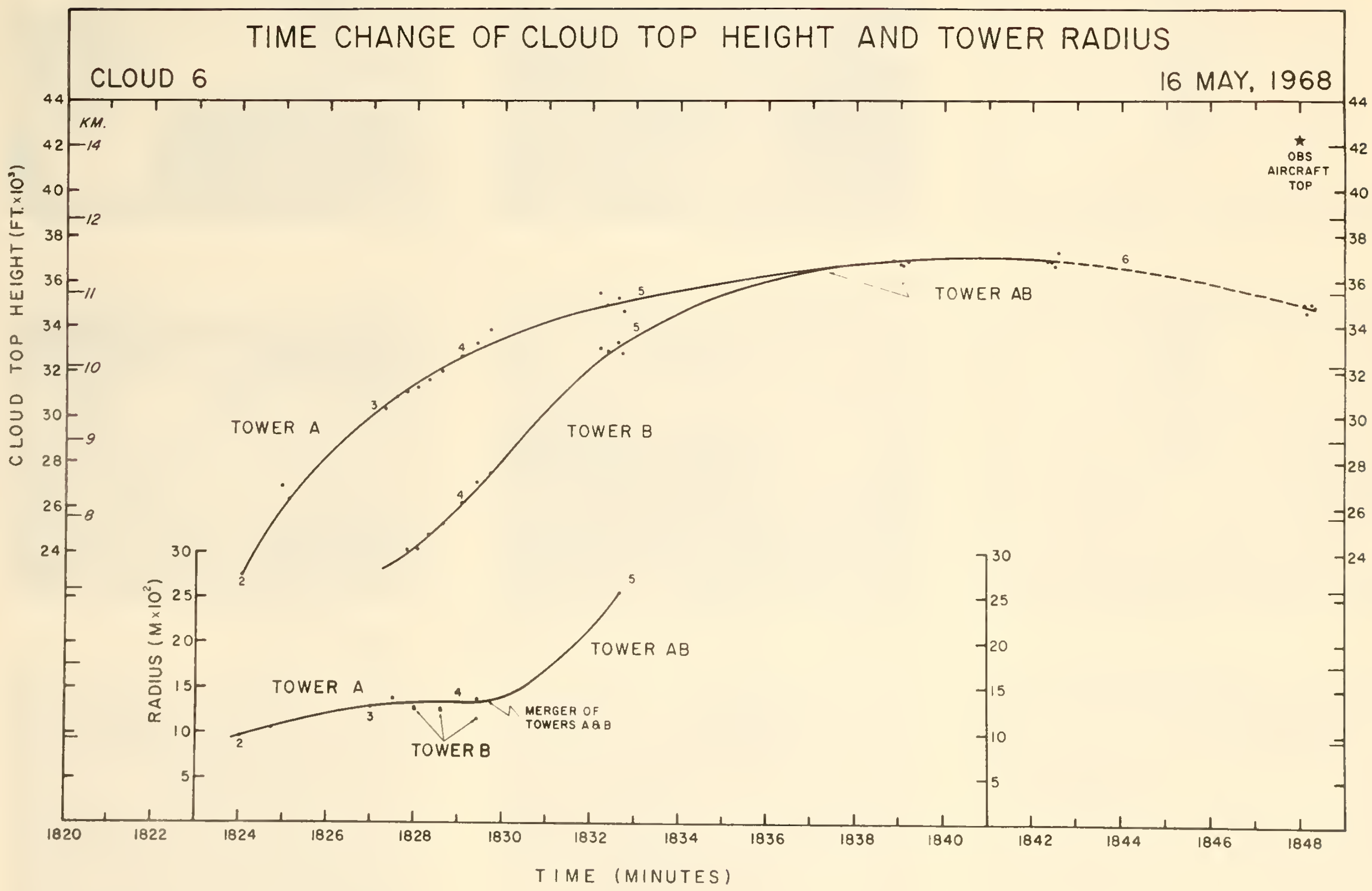

TIME CHANGE OF CLOUD TOP HEIGHT AND TOWER RADIUS
CLOUD 6
16 MAY, 1968
CLOUD TOP HEIGHT (FT.×10³)
KM.
OBS AIRCRAFT TOP
TOWER A
TOWER B
TOWER AB
RADIUS (M×10²)
MERGER OF TOWERS A&B
TIME (MINUTES)

CLOUD 6 MAY 16, 1968

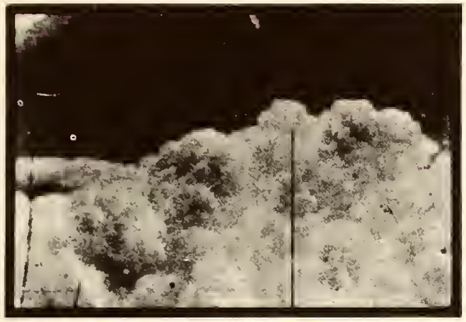

1. 1822Z B-57 NOSE CAMERA

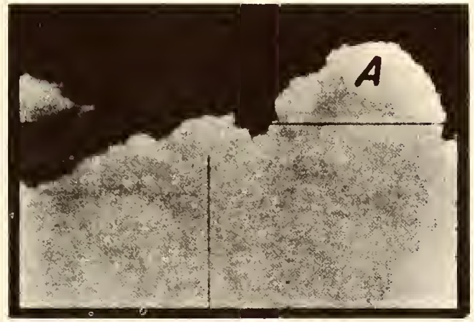

2. 1824Z B-57 NOSE CAMERA. SEEDING PASS I

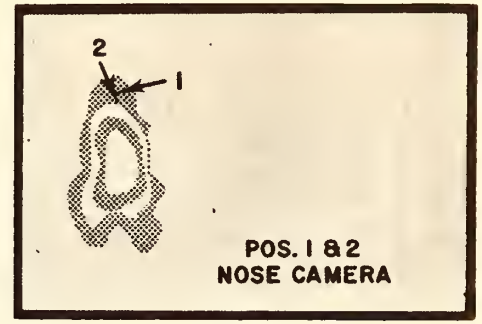

1824Z

3. 1827Z DC-6

4. 1829Z DC-6

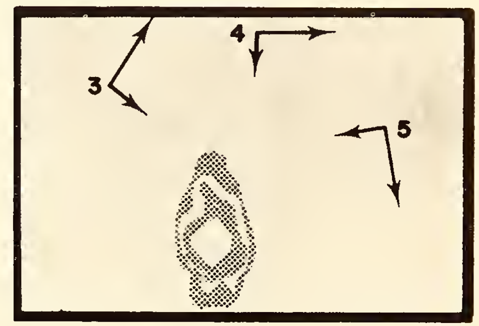

1831Z

5. 1833Z DC-6

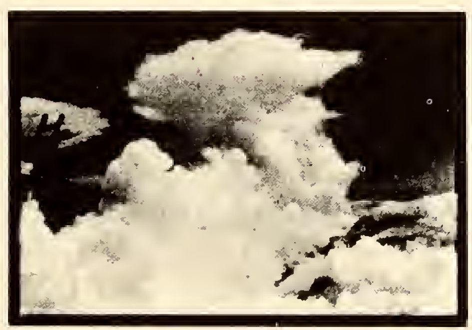

6. 1844Z DC-6

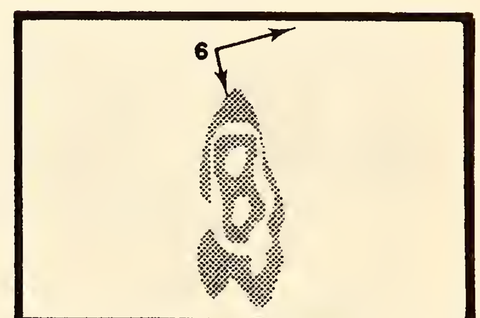

1844Z

Reprinted from Journal of Geophysical
Research, Vol. 74, No. 10, 2590-2596.

Field Occurrences of Induced Multiple Gravity Waves[1]

Robert J. Byrne

ESSA Research Laboratories, Norfolk, Virginia 23510

Field evidence is presented for the occurrence of additional waves arising from an interaction between incident shallow-water waves and submerged shoals. A given additional wave is induced by the passage of an incident wave crest over the crown and downwave flank of a bar. Induced waves were observed under conditions that commonly occur on beaches with wave-built bars. Such waves may significantly influence nearshore processes. Previous discussion or documentation of this interaction is unknown to the author.

Introduction. This report presents field evidence of the occurrence of a particular mode of wave transformation arising, apparently, through the interaction of shallow-water waves and irregular bottom topography, such as submerged bars. This interaction is characterized by the formation of an additional wave that is induced by the passage of the incident wave crest over the crown and downwave flank of the bar.

A number of reports have dealt with other conditions under which multiple wave crests have been observed and studied in the laboratory. These occurrences are limited to conditions of small relative depth ($d/L < 0.1$) wherein multiple crests arise as incident waves: (1) abruptly enter shallow water from deep water [*Mason and Keulegan*, 1944; *Horikawa and Wiegel*, 1959; *Wiegel and Arnold*, 1957]; (2) shoal on a plane beach [*Galvin*, 1967]; (3) travel over a horizontal bottom [*Horikawa and Wiegel*, 1959; *Goda*, 1962; *Galvin*, 1968]. It now appears that these occurrences fit the behavior of some numerical solutions of the Korteweg and de Vries equation for finite-amplitude shallow-water waves [*Zabusky and Kruskal*, 1965; *Zabusky and Galvin*, 1968]. In these solutions and in the experiments, the initial wave decomposes into two or more waves of differing amplitude (called solitons) that initially appear on the upwave flank of the crest. The wave speeds are dependent on their amplitudes. A particularly interesting facet of their nonlinear behavior is that, when the separate waves become 'superimposed,' the net crest elevation is less than the elevation when the waves are isolated.

A case more closely related to the present discussion is that of waves observed in the lee of a submerged finite dock. *Williams* [1964], for example, examined the occurrence of waves incident to a thin rigid barrier, parallel to and below the plane of the free surface. The waves on both sides of the plate were 'deep-water' waves ($d/L > 0.5$) and the plate submergence was less than 20% of the total depth. Among other interesting results, it was demonstrated that the submerged barrier generates, in the downstream region, a system of linear harmonic waves, the fundamental of which is the same frequency as the incident waves. Furthermore, it was found that the amplitude of a given harmonic in the downstream region was proportional to the harmonic content of the same order in the incident wave just before leaving the dock section.

It is, at present, uncertain whether the occurrence discussed by Williams and that presented here arise from the same physical mechanism.

The documentation of the 'multiple' wave phenomenon in the field has, apparently, been rare. *Wiegel* [1964] notes that multiple waves have been observed over reefs and in wave reflections from beaches. Photographs of the process over reefs are shown by *Johnson et al.* [1951, Figure 1] and *Munk and Traylor* [1947, Plate 3]. In both these cases, however, waves are breaking at the reef face and the higher fre-

[1] Contribution 14 of the Land and Sea Interaction Laboratory (LASIL) Atlantic Oceanographic Laboratories, ESSA, Norfolk, Virginia 23510.

quencies may be generated in the breaking process.

It is this paucity of description that motivates the author to publish his observations at this time. It is hoped the description will lead to further field documentation as well as to theoretical and experimental study.

Field site. All observations discussed in this report were obtained on the Outer Beach of Cape Cod, in the immediate vicinity of Cape Cod Lighthouse. An aerial view of the region is shown in Figure 1. The photograph, taken on August 25, 1966, illustrates very clearly the sinuous offshore bar paralleling the beach at a distance between 450 and 600 meters. Also shown is the complex nearshore bar system that during the summer is a quasi-periodic sequence of curved bars.

A bathymetric profile is shown in Figure 2. The offshore bar is a dominant feature that essentially maintains its position throughout the year. Seaward of the offshore bar, the bottom slope is approximately 1 : 100.

Observations. The material presented below is a consequence of two sets of observations, one on September 2, 1966, and the other from early August 1967. Because the August 1967 set offers an explanation of the process, the presentation is given in reverse chronological order.

In August 1967 the author observed waves passing over a curved bar in the nearshore bar complex. The topographic situation is shown schematically in Figure 3. The bar complex, at midtide, was submerged with a uniform swell of approximately 7-second period approaching parallel to the bar axis. The water depth was approximately 1 meter over the bar and was 1.7 meters deep in the trough. It was apparent from casual observations that there were more breakers at area 2 of the foreshore as compared to area 1 (Figure 3). Sighting along the axis of the bar, I counted the number of waves that

Fig. 1. Aerial view of the study area. Photographed August 25, 1966.

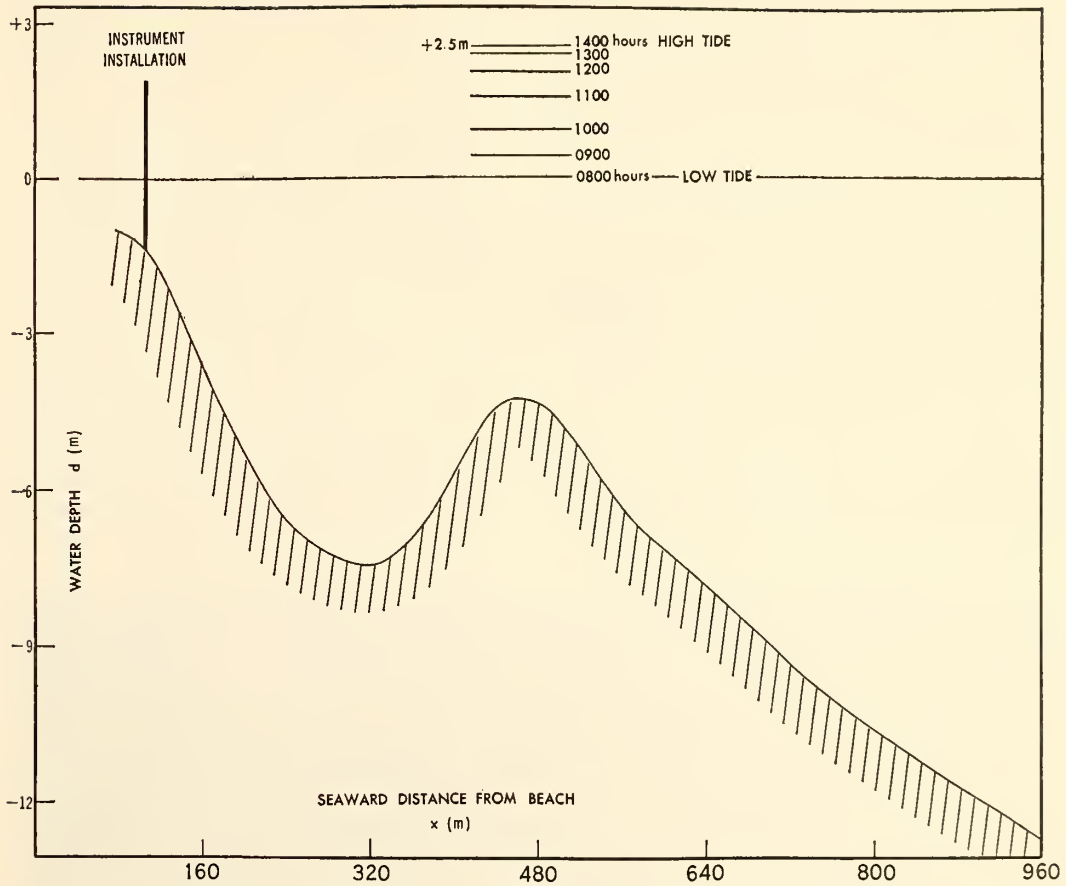

Fig. 2. Bathymetric profile of study area. Sounding in July 1965.

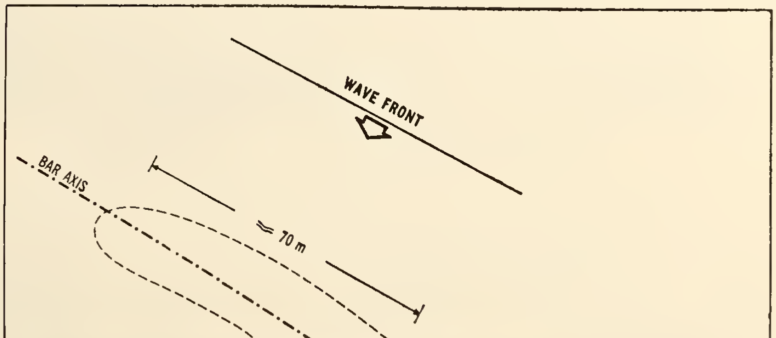

Fig. 3. Schematic (plan view) of nearshore bar.

peaked up on approaching the bar while another observer counted the number of breakers at area 2. The same procedure was used with a second observer at area 1. It was found that the number of breakers at area 1 was the same as the number of waves peaking at the bar, but the number of area 2 was double this number. The wave heights at the crown of the bar were approximately 0.5 meter.

During these observations, an essentially cross-sectional view of the deformation process could be obtained by sighting along the axis of the bar. The various stages are shown diagrammatically in Figure 4. The incident wave (1) peaks up as it approaches the crown of the bar (Figure 4*a*). After the crest passes over the bar, the water surface associated with the trough becomes nearly parallel to the nearshore flank of the bar (Figure 4*b*), and for an instant the seaward flow, associated with the trough, appears to cease. At this point, another wave crest (1a) becomes dissociated from the crown and upper nearshore flank of the bar and propagates shoreward (Figure 4*c*). This separation occurred between 0.3 and 0.5 of a wave period after the incident crest (1) passed the bar.

Similar conditions existed during the observations of September 2, 1966. Then, however, the interaction was between the offshore bar (Figure 2) and the large long-period swell from Hurricane Faith. On that day, a time-lapse motion picture camera and a nearshore wave monitor were operative. The time-lapse camera (16 mm at 26.5 frames per minute) was situated on a bluff behind the beach at an elevation of 40 meters. At the nearshore instrument installation (position shown in Figure 2) the following parameters were measured: surface time history, tide level, and the horizontal component of fluid velocity 0.64 meter above the bottom. Included in Figure 2 is the water depth during a partial tidal cycle for September 2, 1966.

In viewing the time-lapse film it was apparent that the bar was acting as a source area of

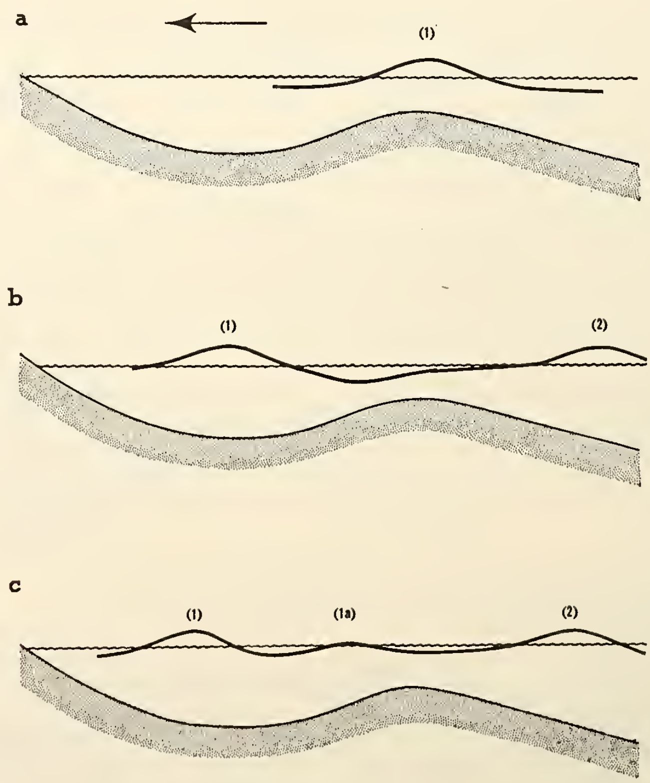

Fig. 4. Schematic representation of induced wave generation over a submerged bar. Figures not to scale.

additional waves. This effect was particularly striking when the film was viewed in reverse motion as the complex inshore waves could be seen to be screened by the bar.

The time-lapse film was run from 0800 hours (low tide) to 1630 hours, encompassing the arrival and passage of high tide. Inspection of the film indicated the waves incident on the bar maintained a rather constant period ($\overline{T}$ = 15 seconds), but, as high tide approached, the number of additional waves, shoreward of the bar, decreased. Under these conditions, only the largest incident waves generated additional waves.

To examine the occurrence in greater detail, sixty-six consecutive frames (149 seconds real time) were enlarged and the number of waves passing at the bar and the number of corresponding waves at the nearshore installation were counted. *Eleven waves* were observed at the bar, whereas *twenty-one waves* were in evidence at the tower. An example from the film enlargement is shown in Figure 5. Inspection of the sixty-six enlarged photographs show that by the time an incident crest is one wavelength shoreward of the bar, a smaller crest is apparent in its following trough.

A segment of the surface wave record, corresponding within minutes to the 2-minute film sampling, is shown in Figure 6. At this time, the water depth at the offshore bar was 5 meters and the mean water level at the sensor was 2 meters. Comparison of the relative direction of pen deflection between the wave sensor (upper trace, Figure 6) and the current meter (lower trace, Figure 6) indicates that a considerable amount of wave energy is reflected from the beach. At the time these recordings were made,

Fig. 5. Photo of incident and induced waves, September 2, 1966. Enlarged from 16-mm color motion picture film.

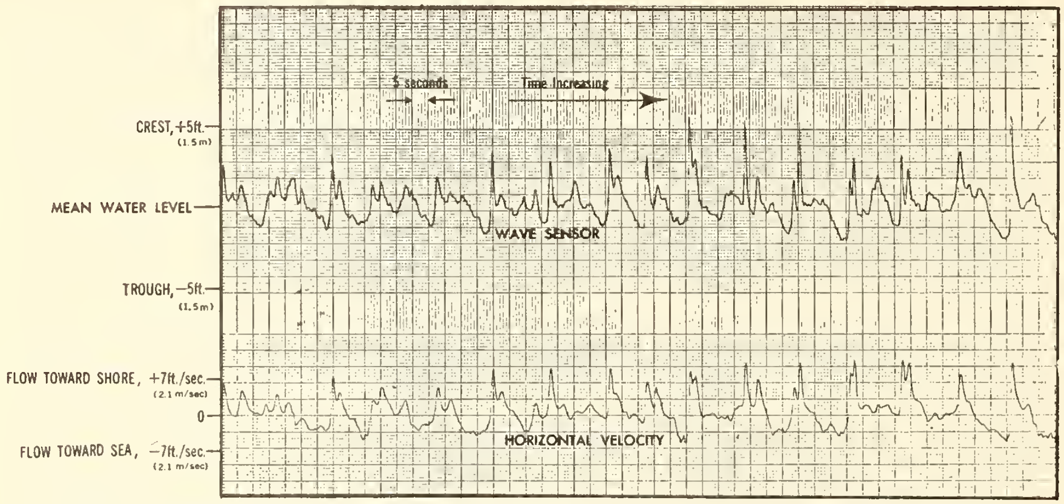

Fig. 6. Oscillograph traces representing surface wave history and horizontal velocity component.

the sensors were near the seaward fringe of the surf zone; thus, the trace contains the incident waves, the additional waves advancing from the bar, reflections, and the frequencies due to breaking. In spite of this, the trace clearly shows the arrival of the incident and additional wave from the bar, separated by a time interval of 1 to 3 seconds. This time lag at the wave gage illustrates the phase speed dependence on wave height, wherein the incident wave has almost caught up with the smaller wave induced from the previous incident wave. This effect is clearly shown in Figure 5.

Discussion. The two occurrences presented in this report represent geometrically similar conditions, and it is assumed that the induced waves arose from the same physical mechanism. A comparison of the relevant dimensions for the two occasions (September 2, 1966, and August 1967) follows.

1. The ratio of bar depth to trough depth was approximately 0.6 in both cases.
2. The relative depth d/L was approximately 0.045 in both cases. These values were derived by using the small-amplitude theory and the bar depth d.
3. The ratio of wave height to bar depth H/d, was approximately 0.4 to 0.5 and 0.5 for the September 2 and the August 1967 observations, respectively. The value for September 2, 1966 (0.4 to 0.5), is a conservative estimate based on visual sighting and consideration of the wave heights at the inshore monitor. By using the results of *Le Méhauté et al.* [1966], an upper limit for wave height at the offshore bar, without breaking, is 3.7 meters ($H_b = 0.8d_b$).

It was previously mentioned that at the higher tidal levels (September 2, 1966) only the largest waves of the groups produced a pronounced induced wave. If the wave periods within the incident wave group are assumed constant, then, to a first approximation, the d/L ratio is likewise constant. This implies that the ratio H/d exerts a strong influence in the formation of the induced waves. From the same estimated values of wave height for low and high tide, the respective H/d ratios are 0.4 to 0.5 and 0.26 to 0.32.

Certainly the observations discussed here are not extensive enough to define the physical mechanism responsible for the induced waves. However, a possible explanation is suggested. After the incident crest passes over the crown of the bar, it accelerates in passing over the steep flank of the bar. As observed, the water surface following the crest becomes nearly parallel to the bar flank. The seaward flow associated with the trough is thus directed parallel to the upward sloping flank of the bar. This flow is brought to rest by the gravitational component parallel to the bed and the water mass, no longer dynamically supported, then surges forward as the leading face of the new crest. If this is the mechanism, the generation process is, in a sense, impulsive.

It should also be recalled, however, that the soliton interaction noted by *Galvin* [1968] occurred when the depth-to-wavelength ratio d/L was less than 0.1. Since the ratios for the cases discussed here are smaller than this limit, it is possible that the interaction of the incident wave with the bar simply amplifies a weak soliton interaction.

The induced wave occurrences discussed in this report were observed under conditions that commonly occur on beaches with wave-built bars. *Shepard* [1950], for example, gives data on wave-built bars for the east and west coast beaches of the United States, the bulk of the information having been acquired from daily measurements of the nearshore profile and waves at Scripps Pier, La Jolla, California. He found an average value of 0.66 for the ratio of bar depth to trough depth. Furthermore, the range of associated wave heights, relative to the bar depth, encompasses the values for the cases reported here. This suggests that the interaction may occur quite frequently. Further study, experimental and theoretical, is needed to define the range of conditions under which an induced wave is to be expected. The interaction may exert a significant influence on nearshore processes as the induced waves redistribute, in time, the energy input to the coastline.

Acknowledgments. The field observations were made while I was affiliated with the Woods Hole Oceanographic Institution. I am indebted to the entire Coastal Studies Group, then under the direction of Dr. John M. Zeigler. Special thanks are due Herman Tasha and William Athearn for their assistance. I thank Drs. G. S. Giese and L. F. McGoldrick for critically reading the manuscript.

References

Galvin, C. J., Classification of breaking waves on three laboratory beaches, unpublished paper available from U.S. Army Coastal Engineering Research Center, 24 pp., Aug. 1967.

Galvin, C. J., Shapes of unbroken periodic gravity waves (abstract) *Trans. Am. Geophys. Union, 49*(1), 206, 1968.

Goda, Yoshimi, A travelling secondary wave crest in a wave channel, Memorandum for seminar at Hydrodynamics Laboratory of Massachusetts Institute of Technology, Cambridge, Mass., 1962.

Horikawa, Kiyoshi, and R. L. Wiegel, Secondary wave crest formation, *Univ. Calif. Wave Res. Lab., Ser. 89,* Issue 4, 23 pp., 1959.

Johnson, J. W., R. A. Fuchs, and J. R. Morison, The damping action of submerged breakwaters, *Trans. Am. Geophys. Union, 32*(5), 704–718, 1951.

Le Méhauté, B. J., G. F. Snow, and L. M. Webb, Gravity waves on bottom slopes, *Natl. Eng. Sci. Co. Rept. S245-A,* Pasadena, Calif., 1966.

Mason, M. A., and C. H. Keulegan, A wave method for determining depths over bottom discontinuities, *U.S. Army Beach Erosion Board Tech. Memo. 5,* 29 pp., 1944.

Munk, W. H., and M. A. Traylor, Refraction of ocean waves: A process linking underwater topography to beach erosion, *J. Geol., 4*(1), 1–26, 1947.

Shepard, F. P., Longshore bars and longshore troughs, *U.S. Army Beach Erosion Board Tech. Memo. 15,* 30 pp., 1950.

Wiegel, R. L., and A. L. Arnold, Model study of wave refractions, *U.S. Army Beach Erosion Board Tech. Memo. 103,* Dec. 1957.

Wiegel, R. L., *Oceanographic Engineering,* 532 pp., Prentice-Hall, Englewood Cliffs, N. J., 1964.

Williams, J. A., A nonlinear problem in surface water waves, *Univ. Calif. Inst. Eng. Res. Tech. Rept. HEL-1-5,* 246 pp., Oct. 1964.

Zabusky, N. J., and M. D. Kruskal, Interaction of 'solitons' in a collisionless plasma and the recurrence of initial states, *Phys. Rev. Letters, 15*(6), 240–243, 1965.

Zabusky, N. J., and C. J. Galvin, Secondary waves as solitons (abstract), *Trans. Am. Geophys. Union, 49*(1), 209, 1968.

(Received August 15, 1968.)

Reprinted from EOS, Transactions, American Geophysical Union, Vol. 50, No. 7, 472-477.

Pelagic Tidal Measurements

A suggested Procedure for Analysis

David Cartwright, Walter Munk, and Bernard Zetler

There has long existed a need for pelagic tide and current measurements, but the technology for making such observations has been developed only recently. In 1965, an international working group on deep-sea tides was formed (now sponsored by IAPSO, SCOR, and Unesco) that would concern itself with the exchange of information on instrumentation and analysis and with the formulation of a worldwide data acquisition program.

Some pelagic tide observations have now been obtained by pressure sensors on the sea bottom connected by cable to the surface [*Eyriès*, 1968] or to shore [*Nowroozi et al.*, 1968] and by self-contained bottom instruments that record internally and are recalled to the surface by an acoustic signal [*Snodgrass*, 1968] and time-release device [*Filloux*, 1968, and *Hicks et al.*, 1965]. The equipment described by Snodgrass and by Nowroozi include current meters measuring speed and direction. The over-all objectives of the deep-sea tide program are described by *Munk and Zetler* [1967] and *Cartwright* [1969].

The working group has recommended records of at least a month's duration. It is quite clear that this requirement entails considerable effort, logistics, and expense (quite aside from many failures), and accordingly it is most important that the analysis of each set of good data be as comprehensive and meaningful as possible.

The authors of this article have been concerned for some time with this very problem. They met in La Jolla, California, in March 1969 to design an analysis program for the pelagic observations. (We are indebted to SCOR for providing travel funds for Cartwright.) This paper describes the method that is recommended and the rationale for some of the steps. The method is suitable for the analysis of tidal disturbances in any geophysical measurements in exposed areas where it is possible to take advantage of data from related, long-established reference stations.

Transfer Functions

The proposed program leans heavily on the 'response method' of tidal analysis; we refer to *Munk and Cartwright* [1966] for a discussion of this method. Here we sketch only the underlying principles.

For any linear system, an input function $x_i(t)$ and an output function $x_o(t)$ can be related according to[1]

$$x_o(t) = \int_0^\infty x_i(t-\tau)w(\tau)d\tau + \text{noise}(t)$$

where $w(\tau)$ is the 'impulse response' of the system, and its Fourier transform

$$Z(f) = \int_0^\infty w(\tau)e^{-2\pi i f\tau}d\tau = R(f)e^{i\phi(f)}$$

is the system's admittance (coherent output/input) at frequency f. In practice, the integrals are replaced by summations; x_i, w, and Z are generally complex. The *discrete* set of w values are termed *response weights.* The basic motive underlying the *response* method for analyzing and predicting tides is to evaluate the station transfer function (w or Z) between a suitable input series and the observed tide. The *classical* method consists of evaluating amplitudes and phases of the princi-

[1] The formalism can be extended to weakly nonlinear systems, but here we shall not be concerned with this generalization.

pal constituents of the observed tide at the station. If input and output are alike, then evidently

$$Z(f) = 1, \qquad \text{or} \qquad w(\tau) = \delta(\tau)$$

and this is called a 'unit transfer function.' In general, $|Z| = R(f)$ and $\operatorname{Arg}(z) = \theta(f)$ measure the relative magnification and phase lead of the station at frequency f. If R and θ vary sensibly across the frequency band of a tidal species, then $w(\tau)$ has to be defined at nonzero values of τ.

In the physical interpretation of the pelagic measurements we find it instructive if the analysis is broken into three steps:

Flow Diagram

The flow diagram (Figure 1) describes five stages of calculation for dealing with pelagic tide and current observations obtained at or near the same location. Stages A, B, and C are response analyses of the tide at a coastal reference station at time t_1, pelagic tides at time t_2, and pelagic currents at time t_3, respectively. Stage B′ is a cross-spectral analysis of predicted coastal tide with observed pelagic tide pressure, and C′ is predicted pelagic pressure with observed pelagic velocity. Stages B′ and C′ are only for decision-making in B and C rather than part of the basic computations.

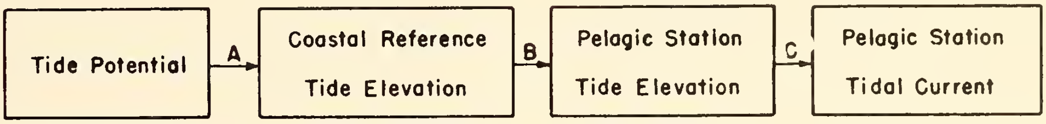

Arrow A represents the transfer function between the tide-producing forces and a coastal tide elevation so chosen as (1) to be in the vicinity of the pelagic station, (2) to be not subject to undue local transformation, and (3) to have available a good record of long duration (> 1 year), enabling one to determine the first transfer function with precision.

Arrow B represents the transfer function between coastal and pelagic tidal elevations; if (1) and (2) above are favorable, this will be nearly proportional to a unit transfer function. Arrow C relates the pelagic tidal elevation to the *local* tidal current, which is an important diagnostic element in determining the wave dynamics. Under favorable circumstances we can also separate the locally coherent tidal currents (associated with the surface, or barotropic tide) from the incoherent currents (associated with the internal, or baroclinic tides).

The pelagic velocity data refer to a time series of a vector in a given azimuth. Ordinarily, northward and eastward orthogonal vectors will be used; the example shown is the northward component.

The sequence of steps following the flow diagram and related discussions are as follows:

A. *Response Analysis of Coastal Reference Station*

1. Prepare time series of observed tides along the coast in the general vicinity of the pelagic pressure observations. The coastal series should be for at least one year.

2. Compute gravitational and 'radiational' tide potentials (merged) for the same period as the coastal observations. We shall refer to such a series as a 'TIDPOT' series after the name

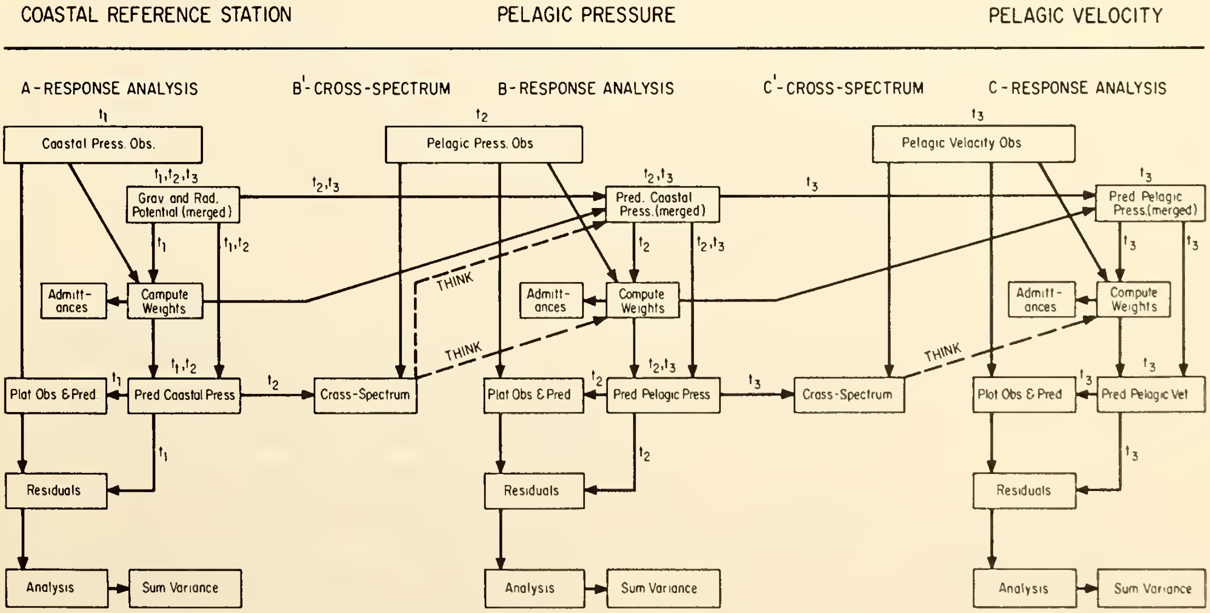

Fig. 1. Flow diagram.

of the BOMM routine used to compute it.

3. Compute 'coastal response weights' for optimum response prediction of the coastal tide.

4. Compute admittances from weights at a resolution of 1 cycle per month (cpm) and at the principal tidal lines.

5. Use coastal response weights and TIDPOT series to predict coastal pressure.

6. Plot sample (15 or 30 days) of observations and predictions.

7. Compute residuals for entire series.

8. Fourier-analyze observations and residuals at record harmonics and cpm resolution.

9. Sum observed and residual variances in the harmonics spanning (1 *cpℓd* − 4½ cpm) to (1 *cpℓd* + 4½ cpm) and similarly for species 2 centered at 2 cycles per lunar day.

B′. *Cross-spectral Analysis of Predicted Coastal Tide with Observed Pelagic Pressure*

The coastal record may not be available for the duration t_2 of the pelagic pressure observations. It can, however, be predicted on the basis of previous observations (time t_1), as in stage A. But even if the coastal observations are available, there is some advantage in using the noise-free predicted tide in the cross-spectral analysis. Any noise residuals are then associated with the pelagic pressure observations. The same consideration holds in subsequent stages; noise-free input functions are particularly attractive in the response method.

1. Predict coastal pressure for time t_2 using the coastal weights and an appropriate TIDPOT series.

2. Compute at cpm resolution the cross spectrum of the predicted ocean tide with observed pelagic pressure. Select a series length that minimizes sidebands (such as 29 solar days). This analysis yields the amplitude ratio and relative phase between observed pelagic pressure and predicted coastal tide for each frequency band.

The results will determine (1) whether the radiational terms should be used for predicting the coastal pressure and (2) how many weights should be used in fitting the pelagic pressure to the coastal pressure predictions.

Radiational potentials were included to allow for non-gravitational changes in coastal sea level (such as winds, tidal atmospheric pressure, or thermal effects). A strong discrepancy between M_2 and S_2 admittances would suggest that the radiational effects were not comparable at the coastal and pelagic stations. In that event it would be better to exclude the radiational terms from the predicted pelagic pressure (*B*2). The radiational terms are included in the examples given here.

The number of pelagic pressure weights for stage B are selected (with due allowance to noise level) on the basis of the variability of the amplitude ratios and relative phases in the tidal bands. Significant variations in admittances call for multiple weights.

B. *Response Analysis of Observed Pelagic Pressure*

1. Prepare time series of the observed pelagic pressure using the complete length of good data.

2. Use appropriate TIDPOT series and coastal weights to prepare predictions for time t_2.

3. Compute response weights for the pelagic pressure.

4. Compute admittances from weights (as in step 4 of stage A).

5. Use pelagic pressure weights and predicted coastal tide to predict pelagic pressure.

6–9. Same as steps 6–9 of stage A.

C′. *Cross-Spectral Analysis of Predicted Pelagic Pressure with Observed Pelagic Velocity (Vector in a Fixed Azimuth)*

As before, it is desirable to use noise-free predictions for the pelagic pressure.

1. Predict pelagic pressure from pelagic pressure weights and coastal pressure predictions. [If t_2 and t_3 are the same, this has already been done in step 5 of stage B. In this case, the predictions are truncated to an appropriate length (see step 2 of stage B′)].

2. Compute the cross-spectrum of predicted pelagic pressure and observed pelagic velocity as in step 2 of stage B′.

The decision on use of radiational potential was made after stage B, and it is not reviewed again at this point. We found large and erratic variations in the amplitude ratios and phase relations across the tidal bands, and we attribute these to baroclinic 'noise.' (This hypothesis was supported by large differences in the cross-spectral analyses of the first and last 29 days of a 37-day series.) We therefore limited the number of weights to one unlagged pair for each species, thus imposing a constant amplitude ratio and a constant phase difference across each of the two tidal bands. We could, of course, improve the current prediction (curve *fitting* would be a better term) for time t_3 at will by allowing additional weights; but if our hypothesis regarding the large noise content is correct then these additional weights could actually lead to a deterioration of a future prediction.

C. *Response Analysis of Observed Pelagic Velocity*

1. Prepare a time series of the observed pelagic velocity using the complete length of good data.

2. Use appropriate coastal pressure predictions and pelagic pressure weights to prepare pelagic pressure predictions for time t_3.

3. Compute response weights for pelagic velocity.

4. Compute admittances from weights (as in step 4 of stage A).

5. Use pelagic velocity weights and pelagic pressure predictions to prepare velocity predictions.

6–9. Same as steps 6–9 of stage A.

Presentation

Our standard presentation of the final results of the analysis as described above aims to satisfy both those who like to think in terms of 'admittances' and those who require only 'amplitudes' and 'phase lags' of major harmonic constituents. Admittances are detailed on the left-hand side of the output list, harmonic constituents on the right.

For each tidal species, the elements of admittance are given at five evenly spaced frequencies, namely

m cycles per lunar day + k cycles per month = $(0.9661368m + 0.0366011k)$cpd

where m is the species number and k takes the values −2, −1, 0, 1, 2 . These frequencies, listed in cpd units (cycles per solar day), approximate to the centers of the principal tidal 'groups' although they do not all belong to major 'constituents.' The admittance function at intermediate frequencies can be assumed to vary smoothly between the given values. Experience has shown that the admittance function is more directly meaningful than corresponding set of 'response weights' since it maintains greater constancy on repeated analysis. We therefore do not list response weights in this presentation.

Below the species admittance is shown the variance of the station series within a band of frequencies from $k = -4.5$ to $k = +4.5$. This variance is derived from a Fourier analysis of the entire series. Below it again is shown the corresponding variance of the residual series when the response convolution ('prediction') is subtracted from the recorded series. These two figures indicate the reliability of the admittance figures. Assuming that the local noise in each tidal group is proportional to the tidal variance of the group (which is approximately true for the major groups), then the relative sampling variance of the real and imaginary parts of the admittance is

$$\sigma^2 = \frac{\text{residual variance}}{2 \times \text{recorded variance}}$$

The relative sampling variance of the admittance amplitudes R and the sampling variance in radians² of their phase leads θ are both approximately

$$\sigma^2 = \sigma'^2 / R^2$$

The harmonic constituent amplitudes for the station are obtained by multiplying the amplitudes for the reference station by the value of R at the appropriate frequency. The Greenwich phase *lags* G (not g) are similarly obtained by subtracting the *leads* θ from the reference G values. All relevant quantities are listed on the right-hand side of the output list. The unbracketed constituents $O1$, $K1$, $M2$, $K2$ are derived directly from the figures on the left and from the 'reference' constituents. For the bracketed constituents $Q1$, $P1$, $N2$, and $S2$, the admittance was re-evaluated from the response weights at the exact frequencies of the constituents.

In the special case when 'reference' is a set of gravitational and radiational potentials, and 'station' is the long-term tide record to be used later as a reference for shorter pressure records, the listed figures have special meanings. The listed admittances relate to the gravitational components a_2^1 and a_2^2 only (see *Munk and Cartwright* [1966]) although the full set of response weights will in general refer to other potentials also. The station harmonic constituents are derived from the complete set of weights and potentials, and reference constituents are not given.

TABLE 1

STATION: Bottom Pressure (La Jolla, 600 m from shore off Scripps Pier), water depth 18 m; sensor buried 3 m below bottom; 418 days; 1961 Dec. 10 to 1963 Feb. 1 (542953.9583 to 552985.9583 Greenwich hours since 1900 Jan. 1, 0^h).

REFERENCE: Gravitational and radiational potentials $c_2^1(0, \pm1, \pm2), c_3^1, \chi_1^1, \chi_2^1, c_2^2(0, \pm1, \pm2), c_3^2, \chi_2^2$.

Admittances (Station / Reference)					Principal Harmonic Constituents			
Intervals 1 cpm (0.0366011 cpd)							Station	
CPD	Real	Imag.	R	ϕ,* deg		CPD	H,cm	G,* deg
0.8929346	0.8454	−0.0986	0.8512	−186.66	($Q1$)	0.8932441	4.18	186.63
0.9295357	0.8218	−0.1737	0.8399	−191.94	$O1$	0.9295357	21.81	192.02
0.9661368	0.6689	−0.2492	0.7138	−200.43	($P1$)	0.9972621	10.85	206.25
1.0027379	0.8332	−0.4205	0.9333	−206.78	$K1$	1.0027379	34.40	206.80
1.0393390	0.8691	−0.5609	1.0343	−212.84				
Recorded variance: 814.04 cm²								
Residual variance: 0.97 cm²								
Ratio: 0.0012								
1.8590714	−0.0322	−0.9968	0.9973	− 91.85				
1.8956725	−0.5233	−0.8650	1.0110	−121.17	($N2$)	1.8959820	12.21	122.92
1.9322736	−0.6433	−0.4903	0.8088	−142.69	$M2$	1.9322736	51.02	142.66
1.9688747	−0.5416	−0.2001	0.5774	−159.72	($S2$)	2.0000000	21.33	137.58
2.0054758	−0.4881	−0.5483	0.7341	−131.68	$K2$	2.0054758	6.08	131.31
Recorded variance: 1682.76cm²								
Residual variance: 0.66cm²								
Ratio: 0.0004								

*G is Greenwich epoch, ϕ is station lead.

TABLE 2

STATION: Bottom Pressure (Josie 175 SW), 31° 01.7′ N, 119° 47.9′ W, Depth 3.64 km, 37 days, 1968 Aug. 1 to Sept. 7 (601201.0833 to 602078.0833 Greenwich hours since 1900 Jan. 1, 0h).

REFERENCE: 'Predicted' Bottom Pressure at La Jolla, 600 M from Shore off Scripps Pier.

Admittances (Station / Reference) Intervals 1 cpm (0.0366011 cpd)					Principal Harmonic Constituents		Station		Reference	
CPD	Real	Imag.	R,	ϕ,* deg		CPD	H, cm	G, deg	H, cm	G,* deg
0.8929346	0.8733	0.1044	0.8795	6.82	($Q1$)	0.8932441	3.68	179.81	4.18	186.63
0.9295357	1.0286	-0.0534	1.0299	-2.97	$O1$	0.9295357	22.46	194.99	21.81	192.02
0.9661368	1.0997	-0.1036	1.1046	-5.38	($P1$)	0.9972621	11.76	209.07	10.85	206.25
1.0027379	1.0720	-0.0360	1.0726	-1.92	$K1$	1.0027379	36.90	208.72	34.40	206.80
1.0393390	0.9511	0.1356	0.9607	8.11						

Recorded variance: 1202.65 cm^2
Residual variance: 2.35 cm^2
Ratio: 0.0020

CPD	Real	Imag.	R,	ϕ,* deg		CPD	H, cm	G, deg	H, cm	G,* deg
1.8590714	0.9212	0.1111	0.9279	6.88						
1.8956725	0.9323	0.0554	0.9339	3.40	($N2$)	1.8959820	11.40	119.52	12.21	122.92
1.9322736	0.9419	0.0239	0.9422	1.45	$M2$	1.9322736	48.07	141.21	51.02	142.66
1.9688747	0.9481	0.0232	0.9484	1.40	($S2$)	2.0000000	20.28	134.74	21.33	137.58
2.0054758	0.9497	0.0535	0.9512	3.22	$K2$	2.0054758	5.78	128.09	6.08	131.31

Recorded variance: 1483.81 cm^2
Residual variance: 0.73 cm^2
Ratio: 0.0005

*G is Greenwich epoch, ϕ is station lead.

TABLE 3

STATION: Bottom Velocity, Northward Component (Josie 175 SW), 31° 01.7′ N, 110° 47.9′ W, Depth, 3.64 km, Sensor 1.70 m above Bottom, 37 Days, 1968 Aug. 1 to Sept. 7 (601201.0833 to 602078.0833 Greenwich hours since 1900 Jan. 1, 0h).

REFERENCE: 'Predicted' Bottom Pressure at Same Position and Time.

Admittances (Station / Reference) Intervals 1 cpm (0.0366011 cpd)					Principal Harmonic Constituents		Station		Reference	
CPD	Real, sec^{-1}	Imag., sec^{-1}	R, sec^{-1}	ϕ,* deg		CPD	H, cm/sec	G, deg	H, cm	G,* deg
0.8929346	0.0165	0.0022	0.0167	7.69	($Q1$)	0.8932441	0.062	172.12	3.68	179.81
0.9295357	0.0165	0.0022	0.0167	7.69	$O1$	0.9295357	0.375	187.30	22.46	194.99
0.9661368	0.0165	0.0022	0.0167	7.69	($P1$)	0.9972621	0.196	201.38	11.76	209.07
1.0027379	0.0165	0.0022	0.0167	7.69	$K1$	1.0027379	0.616	201.03	36.90	208.72
1.0393390	0.0165	0.0022	0.0167	7.69						

Recorded variance: 0.580 (cm/sec)^2
Residual variance: 0.206 (cm/sec)^2
Ratio: 0.355

CPD	Real, sec^{-1}	Imag., sec^{-1}	R, sec^{-1}	ϕ,* deg		CPD	H, cm/sec	G, deg	H, cm	G,* deg
1.8590714	0.0477	-0.0063	0.0481	-7.49						
1.8956725	0.0477	-0.0063	0.0481	-7.49	($N2$)	1.8959820	0.548	127.01	11.40	119.52
1.9322736	0.0477	-0.0063	0.0481	-7.49	$M2$	1.9322736	2.312	148.70	48.07	141.21
1.9688747	0.0477	-0.0063	0.0481	-7.49	($S2$)	2.0000000	0.975	142.23	20.28	134.74
2.0054758	0.0477	-0.0063	0.0481	-7.49	$K2$	2.0054758	0.278	135.58	5.78	128.09

Recorded variance: 3.961 (cm/sec)^2
Residual variance: 0.641 (cm/sec)^2
Ratio: 0.162

*G is Greenwich epoch, ϕ is station lead.

We have included three examples of lists (Tables 1–3) as described above, giving the results of analysis of records recently made by IGPP, La Jolla. The 'reference station' is a high quality pressure record of 14 months' duration taken near Scripps pier. It is applied to a 37-day record of pelagic pressure and velocity from a Snodgrass capsule [*Snodgrass*, 1968] some 325 km southwest of La Jolla at a depth of 3.64 km.

Note that in the third analysis, velocity *versus* pressure, no time lags were allowed for reasons explained in stage C′ of section 3. The resulting admittance figures for each species are therefore constant.

REFERENCES

Cartwright, D., Deep-sea tides, *Sci. J.*, *5*(1), 60–67, January 1969.

Eyriès, M., Maregraphes de grandes profondeurs, *Cahiers Oceanogr.*, *20*(5), 1968.

Filloux, J. H., Deep-sea tide record from the northeastern Pacific, (abstract), *Trans. Amer. Geophys. Union*, *49*, 211, 1968.

Hicks, S. D., A. J. Goodheart, and C. W. Iseley, Observations of the tide on the Atlantic continental shelf, *J. Geophys. Res.*, *70*(8), 1827–1830, 1965.

Munk, W., and D. Cartwright, Tidal spectroscopy and prediction, *Phil. Trans. Roy. Soc. London, A*, 259, 533-581, 1966.

Munk, W., and B. Zetler, Deep-sea tides: a program, *Science*, *158*, 884-886, 1967.

Nowroozi, A. A., M. Ewing, J. E. Nafe, and M. Fleigel, Deep ocean current and its correlation with the ocean tide off the coast of northern California, *J. Geophys. Res.*, *73*, 1921–1932, 1968.

Snodgrass, F., Deep-sea instrument capsule, *Science*, *162*, 78–87, 1968.

David Cartwright is with the National Institute of Oceanography, U. K. Walter Munk is Director of the Institute of Geophysics and Planetary Physics at Scripps Institution of Oceanography, University of California, La Jolla. Bernard Zetler is Director of the Physical Oceanography Laboratory, Atlantic Oceanographic Laboratories, Miami, Florida.

Reprinted from Solar Physics
Vol. 7, 417-433.

BRIGHTNESS VARIATIONS OF THE WHITE LIGHT CORONA DURING THE YEARS 1964–67

RICHARD T. HANSEN, CHARLES J. GARCIA, SHIRLEY F. HANSEN
High Altitude Observatory, National Center for Atmospheric Research, Kamuela, Hawaii, U.S.A.

and

HAROLD G. LOOMIS*
Environmental Science Services Administration, Honolulu, Hawaii, U.S.A.

(Received 4 November, 1968)

Abstract. Observations of the white light corona were made on over 900 days during the years 1964–67 at heights between 1.125 and 2.0 $R_{\odot}$ with the K-coronameter at Mount Haleakala and Mauna Loa, Hawaii. The brightness distribution of the minimum corona was elliptical with average equatorial intensities three times the polar. Coronal features of the new cycle at 1.125 $R_{\odot}$ occurred predominantly in the sunspot zones at 25–30° latitude and in a high latitude zone which migrated toward the North pole before solar maximum. The brightness of the inner corona doubled over this period and a close association is found between the average corona and 10.7-cm solar radio flux. Electron densities in the equatorial regions were nearly twice those of Van de Hulst's model corona, in agreement with the results of recent eclipse observations.

1. Introduction

Systematic observations of the sun's corona have been made at total eclipses for over a century and have well established that the corona changes, possibly in periodic ways, with the solar cycle. Basically, near maximum, it appears relatively circular with streamers extending outward radially from all latitudes but then at sunspot minimum becomes more concentrated along the equatorial plane. LOCKYER (1931) classified the shapes according to latitude distributions of the streamers and showed that three basic structural forms – polar, intermediate and equatorial – are related in a general way to phase of the solar cycle, although even more directly tied to the changing latitude of the prominence zones. LUDENDORFF (1928) introduced the index of ellipticity as a numerical measure of the tendency for coronal isophotes to flatten at sunspot minimum as rifts develop in the polar corona and the equatorial streamers become more pronounced. This trend has been substantiated by observations of a dozen or so eclipses during the past several decades.

However, the extent of changes in total brightness of the corona with the solar cycle has not been clearly established from eclipse observations (summarized by HATA and SAITO, 1966, especially their Figures 6 and 8). This is inherently a difficult study because of differences in size of the moon projected on the sun causing variations in the obscuration of the brighter inner corona, uncertainties as to atmospheric transparency at the time of the eclipse, and, more basically, the fact that the corona

* At Hawaii Institute of Geophysics.

on a specific day is not necessarily truly representative of its place in the solar cycle. One series of visual and photographic observations reported by SYTINSKAYA and SHARONOV (1963) for six eclipses 1936–61 "did not reveal any correlation at all between the integrated coronal brightness and sunspot number or any factor". On the other hand, some convincing evidence for such changes is provided by other observers including the University of Minnesota group whose measurements of the eclipses of 1959 and 1963 with identically the same photoelectric instruments showed a decrease in total intensity in the equatorial direction by 30% between the two dates, which occurred during high and relatively low phases, respectively, of sunspot activity (GILLETT *et al.*, 1964). Also, at the distance of 1.5 $R_{\odot}$ they found the 1959 corona to be 1.5 times brighter at the equator and 2.4 times brighter at the polar regions than the 1963 eclipse.

With Lyot's development of the coronagraph, it has become possible to study coronal variations with a more plentiful supply of data, freed from the coarse sampling procedure imposed by the infrequency of natural eclipses. From his own observations Lyot reached the important conclusion that "the continuous spectrum of the corona (polarized light) has increased between the minimum of 1944 and the maximum in 1947 by a factor of about 2.3 in the polar regions and 2 in the equatorial regions" (from VAN DE HULST, 1953). Presumably this result is for the innermost corona at 1.1 to 1.2 $R_{\odot}$.

Reported here is a new study of the changes in brightness distribution of the inner corona, based upon a highly concentrated series of K-coronameter (WLÉRICK and AXTELL, 1957) observations from February 1964–December 1967, corresponding to solar minimum and the ascending phase of cycle 20. In late 1963, as a cooperative program with the University of Hawaii for the International Quiet Sun Year (IQSY), the High Altitude Observatory's K-coronameter was installed in the Mees Solar Laboratory of the Hawaii Institute of Geophysics on Mount Haleakala, Maui, Hawaii. In November 1965 the instrument was moved to its present location at the Environmental Science Services Administration's Mauna Loa Observatory, 11 150 feet elevation on the Island of Hawaii (HANSEN *et al.*, 1965). Extremely favorable conditions at both sites permitted observations on more than 200 days per year.

Earlier studies with the K-coronameter, then operated at Climax, Colorado, are described by NEWKIRK *et al.* (1958). The basic instrument and reduction procedures remain the same. The measurements are of the quantity pB as the instrument scans around the sun at a selected height above the solar limb, where p is the polarization tangential to the limb and B the radiance of the corona in units of 10^{-8} the radiance of the center of the solar disk.

These observations have two principal limitations as contrasted to those possible at natural eclipse. First, spatial resolution is compromised by the significant size of the scanning aperture used in the telescope. Its diameter is 1.3 min of arc and thus any smaller coronal details are blurred together. Second, even during cloud-free days, reliable measurements are restricted to the inner corona of $R < 2\ R_{\odot}$ but more generally to $R < 1.75\ R_{\odot}$, because of the brightness of the non-eclipse sky and also because of random fluctuations in polarized signal due to atmospheric contaminants which produce a background noise level of at least 1×10^{-8} pB.

2. Representative Daily Observations

Examples of the original K-coronameter measurement at 1.125 $R_{\odot}$ are shown in Figure 1, superposed for the months of July for each year 1964–67. From these it is possible to describe qualitatively the evolution of the corona over this part of the solar cycle. During the solar minimum of 1964, the general level of brightness was

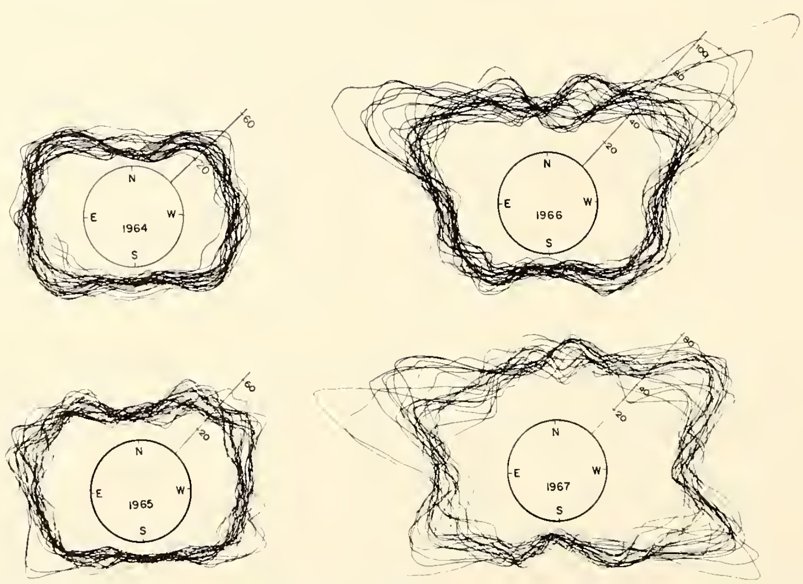

Fig. 1. Superposed polar plots of representative daily observations of the K-corona for successive months of July, 1964–67. The quantity pB is plotted radially as a function of heliographic position angle. – 1.125 $R_{\odot}$.

low with only slight day-to-day changes and the distribution was symmetric about the equator; there was no North-South asymmetry. Recalling that these are polar plots with intensity proportional to radial distance rather than the usually presented isophotes, it is still apparent that the distribution was highly elliptical with equatorial brightness some 3 times greater than polar at the same height. By the next July (1965), K-coronal activity increased slightly as shown by successive East- and West-limb passages of a single distinct feature in the South, but similar features at 20–30° latitude were more numerous in the North. Another zone of activity developed at higher Northern latitudes around 60° which sometimes created the appearance of a polar rift or a deficiency of corona at the pole. In 1966 there was a comparable rift over the South pole, but meanwhile the general level of activity in the North was more advanced. K-coronal features 2 to 3 times brighter than the quiet or minimum phase corona were frequent.* By July 1967, activity in the Southern hemisphere was well-developed at 30° latitude, similar to that in the North, but with a relative void remaining over the South pole.

Comparable daily measurements at the greater height of 1.5 $R_\odot$ are shown in Figure 2 for three years, 1965–67, again for the representative months of July. The

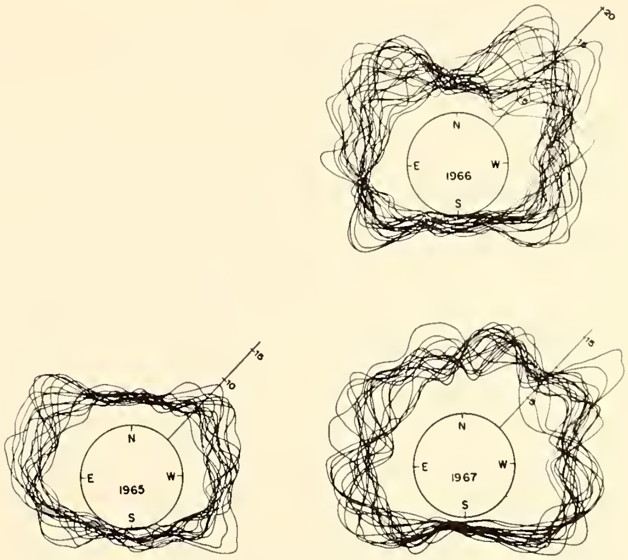

Fig. 2. Same as Figure 1 but for 1.5 $R_\odot$. Observations during 1965–67 only.

general appearance is considerably more chaotic than at 1.125 $R_\odot$ because the dominance of activity at sunspot latitudes did not extend to this height as distinct coronal features occurred at high as well as low latitudes. Features also appeared over the equator at this greater height of 1.5 $R_\odot$, consistent with eclipse photographs which sometimes show coronal arches spanning between the two hemispheres.

The large brightness fluctuations in the vicinity of the North pole are due to projection of high latitude features seen near central meridian passage over the pole. The changing appearance which may be expected from a simple idealized coronal feature is illustrated in Figure 3 and 4 (from Perry, 1967) where radial streamers are assumed to be based on 0°, 30°, 60° North latitude and successive days' observations with the K-coronameter made at a fixed scanning distance. The zero date denotes the observation just at limb passage with minus and plus dates showing the apparent latitude on the days before and after. Relative intensities for each date are represented by the radial distance from the circle. In Figure 3 the sun's axial tilt ($B_\odot$) is zero. A feature based at the equator appears to remain at that latitude and is visible for just 4 days on each side of its limb passage. A high latitude (60°) feature however is

* The very bright coronal feature in the Northwest quadrant was associated with a proton flare region for which electron density models have been constructed (Newkirk *et al.*, 1967).

observable continuously and even when projected over the pole from in front of or behind the visible disk, it remains at about $\frac{1}{4}$ of its true (limb passage) brightness. The extreme situation is shown in Figure 4 with the sun's axial tilt at the maximum of $\pm 7.2^\circ$ (toward or away from the earth) corresponding to the orientation during the months of September and March. At polar passage, the high latitude streamer appears to fluctuate between a low of less than 10% to a maximum of 40% of the brightness observed at limb passage.

Thus, while a high latitude radial coronal feature is based at a specific longitude

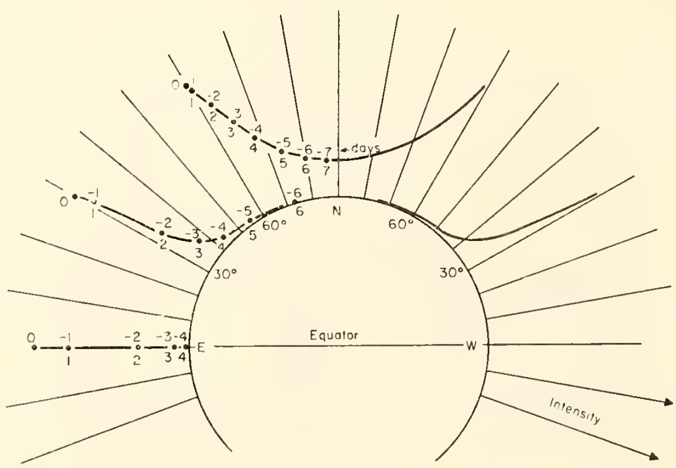

Fig. 3. Variation in apparent latitude and brightness of idealized narrow coronal features based at 0°, 30° and 60° North latitude as they are subjected to the sun's rotation. At zero day, the feature is in the plane of the sky; other numbers indicate the observed latitude on days before and after limb passage with relative intensities represented by the radial distance from the edge of the circle. The sun's axial tilt ($B_\odot$) is assumed to be zero.

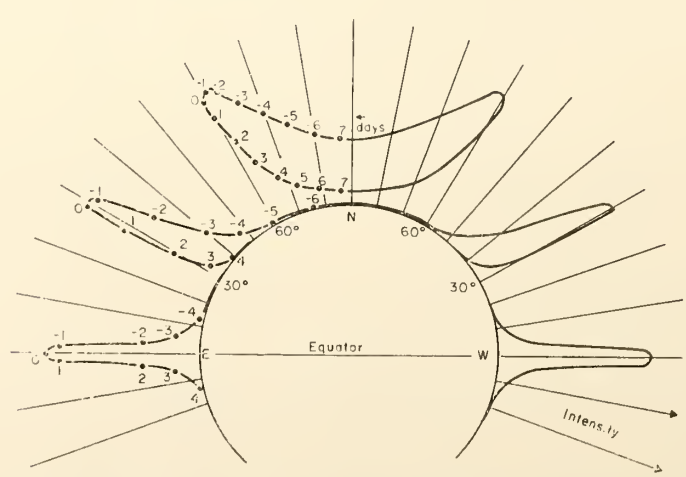

Fig. 4. Same as Figure 3 except that the sun's axial tilt is assumed to be at the maximum of 7.2°.

and latitude, by projection it could appear on the limb at any *higher* latitude. This effect has surely contributed to the difficulty and ambiguity of using eclipse photographs to relate white light coronal features to underlying chromospheric phenomena.

3. Distributions of Average Radiance

The entire 4 years of K-coronal measurements are divided into half-year groupings as listed in Table I with numbers 1–8 designating successive periods. The distribution of average radiance, at 5° increments of latitude, is shown at each height 1.125, 1.25,

TABLE I

Number of daily observations of K-corona at selected heights during successive six-month periods

Dates	1.125	1.25	1.50	1.75 $R_\odot$
1. Feb.–Jun. 1964	75	66	–	–
2. Jul.–Dec. 1964	107	92	–	–
3. Jan.–Jun. 1965	114	88	–	–
4. Jul.–Dec. 1965	117	99	78	–
5. Jan.–Jun. 1966	116	107	109	79
6. Jul.–Dec. 1966	132	114	111	86
7. Jan.–Jun. 1967	113	96	85	80
8. Jul.–Dec. 1967	130	124	115	108

1.5 and 1.75 $R_\odot$ in Figures 5 to 8. During the solar minimum of 1964, the white light corona nearest to the limb of the sun (Figure 5) was nearly symmetric around the equator with uniform brightness of $30–35 \times 10^{-8}$ pB between $\pm 40°$. The first response

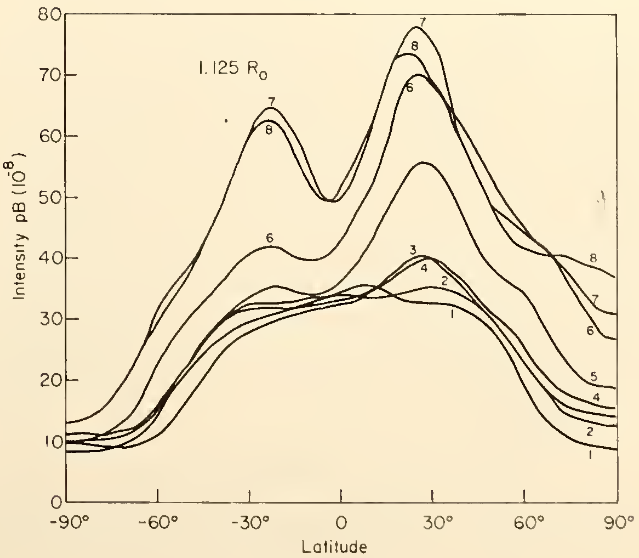

Fig. 5.

to the new solar cycle was the increase in brightness in the sunspot zone at 25–30° North latitude in 1965 which steadily progressed until by the end of 1966 (period 6) the average in this zone was more than double that at solar minimum. A similar brightness increase occurred in the Southern hemisphere about a year later, corresponding to the general lag in development of sunspots and other aspects of activity in the South during the early phase of cycle 20. The polar corona in the North also steadily brightened during this time, reaching an average of 4 times that at minimum.

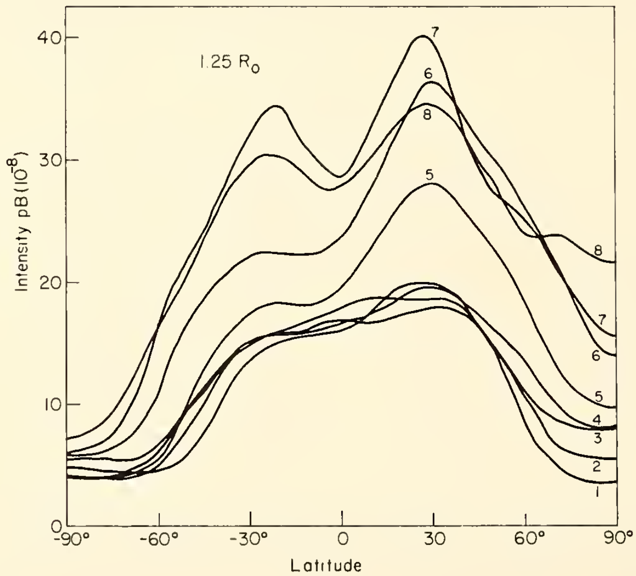

Fig. 6.

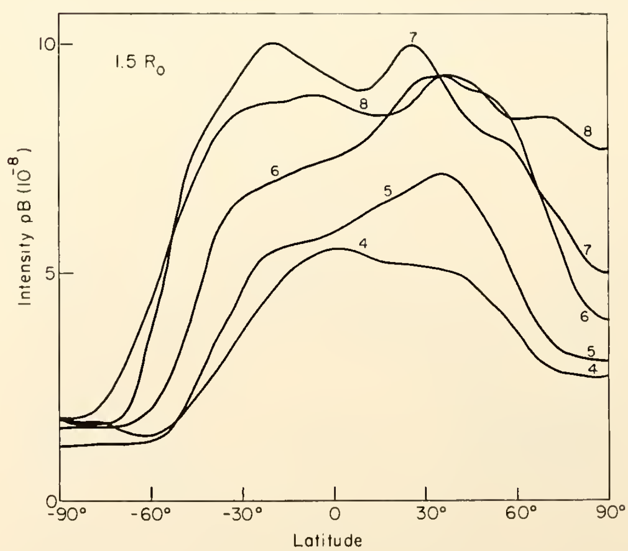

Fig. 7.

By the end of 1967 the North polar corona was brighter than any position around the sun had been during minimum, but the corona over the South pole changed very little during the entire four years. Meanwhile the behavior at 1.25 $R_\odot$ (Figure 6) was essentially parallel to that at 1.125 $R_\odot$ except that the intensities were lower by a factor of 2.

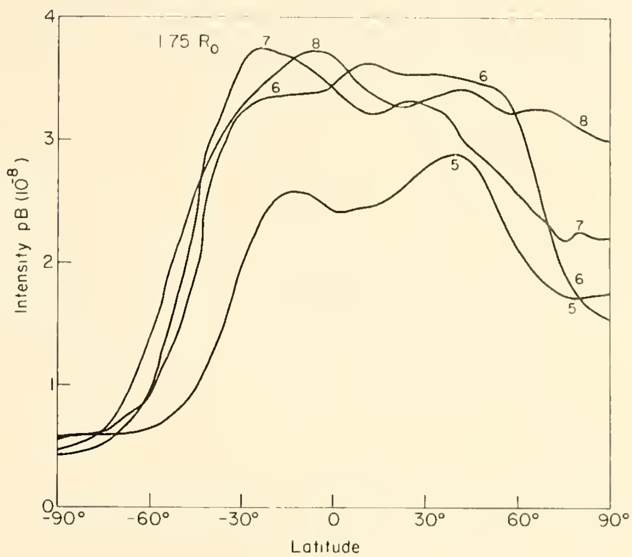

Fig. 8.

Figs. 5–8. Average brightness distributions of the K-corona at 1.125, 1.25, 1.5 and 1.75 $R_\odot$ vs. latitude for each six-month interval from 1964–67 (denoted by numbers 1 to 8). Observations were not made at 1.5 and 1.75 $R_\odot$ during the earlier periods.

At 1.5 $R_\odot$ (Figure 7) and 1.75 $R_\odot$ (Figure 8), K-coronameter measurements were made regularly only from the latter half of 1965 and the beginning of 1966, respectively; thus documentation on the evolution of brightness at these heights is not as complete. Nonetheless, certain patterns are apparent including again the monotonic increase over low latitudes and the North pole but almost complete lack of response to the new cycle at the South pole. However, the marked zonal form of the corona as seen at 1.125 $R_\odot$ did not extend to these heights of half and three quarters radius above the limb. Instead the average increased more uniformly over a wide range of latitude. In fact, by the end of 1967 the average brightness distribution at heights above 1.5 $R_\odot$ was essentially uniform and thereby had achieved the circular form which is considered to be typical of solar maximum – except in the sector 40 to 90° South.

4. Total Radiance at Each Height

We now consider the increase in total light radiated by the electron corona at each of the several standard observing heights. This is based upon simple comparison of the areas under each of the brightness distribution curves of Figures 5 to 8. The totals at 1.125 and 1.25 $R_\odot$ are normalized in terms of 1964, and those for 1.5 and 1.75 $R_\odot$ to the levels during the beginning of 1966 (period 5), and their development is shown in Figure 9. The corona remained practically constant through mid-1965 and then steadily increased in brightness at all heights to twice the minimum level. Less complete and less reliable observations at 2.0 $R_\odot$ indicate that the brightness increased by only 1.5 higher in the corona, but our degree of confidence in this data does not warrant inclusion with the other points of Figure 9.

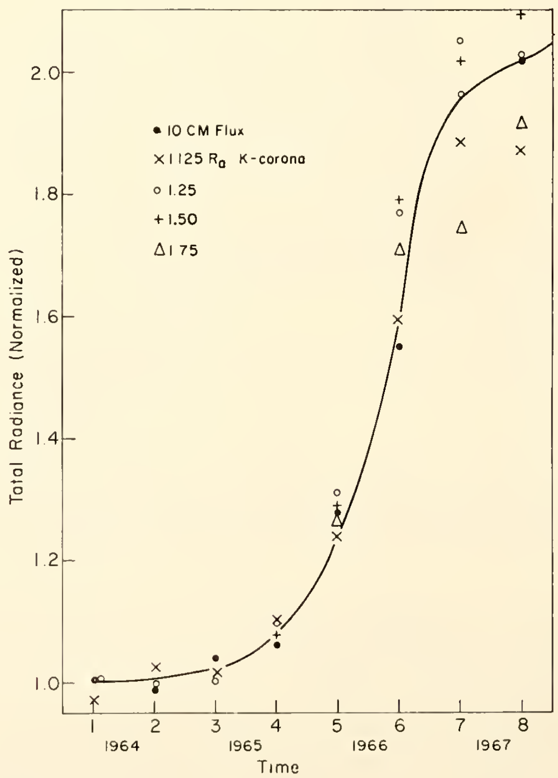

Fig. 9. Variation in total normalized radiance of the K-corona at several heights during the ascending phase of cycle 20. Six-month averages of 10.7-cm radio flux are shown as solid points through which a smooth curve has been drawn.

In order to relate the total radiance to phase of the solar cycle, comparison is made with the half-year averages of 10.7-cm (Ottawa) solar radio flux, known to be closely associated with sunspot and plage areas (KUNDU, 1965). This is shown in Figure 9 by solid circles through which a smooth curve has been passed. It is obvious that the K-coronal brightness, out to a height of 1.75 $R_\odot$, is highly correlated with the slowly varying component of 10.7 solar radio flux. As the radio component increased by 2.0 from 1964 to 1967 the coronal brightness increased by factors 1.9

to 2.1. By extrapolating the radio index to the level at the maximum of cycle 19 in 1958 it appears that the K-corona at great solar activity would have been 3 times brighter than its quiet level as represented by the minimum years of 1964–65.

TABLE II

Determinations of the maximum-minimum ratio in brightness of the K-corona

Source	Period	Height	Ratio
Van de Hulst (6 eclipses, 1918–45)	max/min	1.03–6.00 $R_\odot$	1.8
Hata and Saito	max/min	1.2 $R_\odot$	2.5
(8 eclipses, 1952–63)		1.03–4.00 $R_\odot$	2.5
Lyot (Synoptic coronagraph observations)	1947/1944	1.1–1.2 $R_\odot$	2.1
Hansen, Garcia, Hansen,	1967/1964	1.125 $R_\odot$	1.9
and Loomis		1.25 $R_\odot$	2.0
(Synoptic coronagraph		1.50 $R_\odot$	2.1
observations, six-month averages)		1.75 $R_\odot$	1.9

Several previous determinations of brightness changes in the white light corona during a solar cycle are summarized in Table II. The entry identified with Van de Hulst was actually based largely upon Nikonov's analysis of six eclipses between 1918–45 in which he found an increase of 1.8 from minimum to maximum in the coronal ring bounded by 1.03–6.00 $R_\odot$. Hata and Saito later concluded from their more comprehensive review of all available eclipses (1898–1963) that only observations having absolute photometry, essentially those made since 1952, were useful for demonstrating possible solar cycle variations. And from the 8 eclipses 1952 through 1963 they concluded that at 1.2 $R_\odot$ and also within the ring bounded by 1.03 and 4.00 $R_\odot$ the corona increased in brightness by 2.5. Inspection of Hata and Saito's Figure 8 suggests that their result is derived almost exclusively from the observed variations at 1.2 and 1.5 $R_\odot$ between the maximum eclipses of 1958 and 1959 compared with the minimum of 1954. At the height of 2.0 $R_\odot$ and beyond, the corona is so much fainter (by nearly 2 orders of magnitude) that any cyclic variation would have no significant influence on the total integrated brightness. Thus K-coronameter measurements, even though presently limited to the inner corona of $R < 2\ R_\odot$, are intrinsically as well-suited to answering this question as are measurements at natural eclipse.

5. Zones of Activity and Poleward Migration

The arithmetic averages of the previous section tend to obscure the fact that the K-coronal features occur in discrete latitude zones. The zonal character is rather obvious from inspection of even the small sample of observations of Figure 1 and 2, but is better represented by the statistical standard deviation of intensity from the six-month mean. As an example both parameters, average and standard deviation, are shown together in Figure 10. Clearly the principal zone of 'activity' (in the sense of day-to-day changedness) as well as enhanced brightness for the period occurred in the Northern hemisphere at about 25° latitude. And a similar but considerably

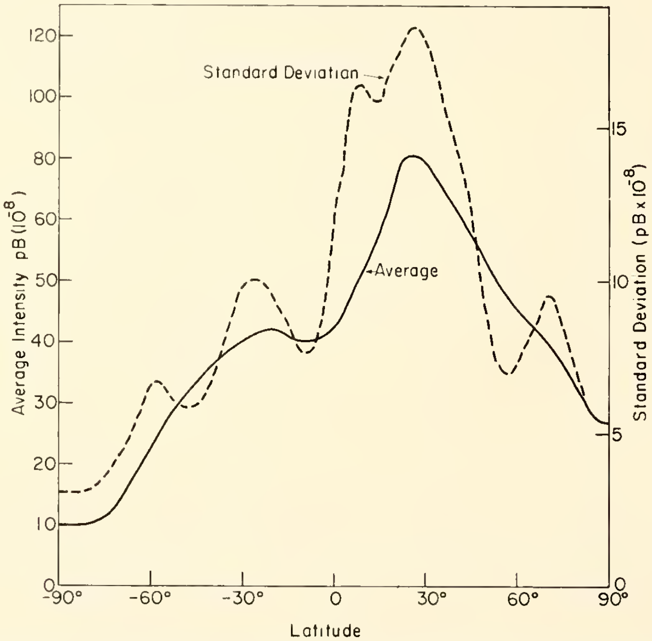

Fig. 10. Comparison of the latitude distribution of average K-coronal brightness and standard deviation from this mean for the period July–December 1966. – 1.125 $R_\odot$.

weaker zone, also associated with sunspot and plage regions, occurred at 25° South. However only the standard deviation curve reveals the high latitude or polar zones at 70° North and 60° South. Because individual coronal features continue to be observed for at least several days as they are carried by solar rotation into and away from the plane of the sky, their apparent position is systematically smeared to higher latitudes. This effect is necessarily greater for the polar zone and the extent is also influenced by the shape and gradient of particular coronal features. Nonetheless, peaks of the standard deviation curve do indicate the approximate latitude of the polar activity zones.

The complete set of standard deviation curves for the entire interval 1964–67 at the observing height 1.125 $R_\odot$ is shown in Figure 11. The general pattern is similar to that found from the averages (Figure 5) with the principal activity developing in the zone at 25° North latitude after 1965. Activity in the Southern hemisphere is again seen to lag by about a year and changes over the poles were slight.

By enlargement of the right hand part of Figure 11 into Figure 12, it is found that the high latitude zone steadily migrated to the pole, beginning at 55° North during

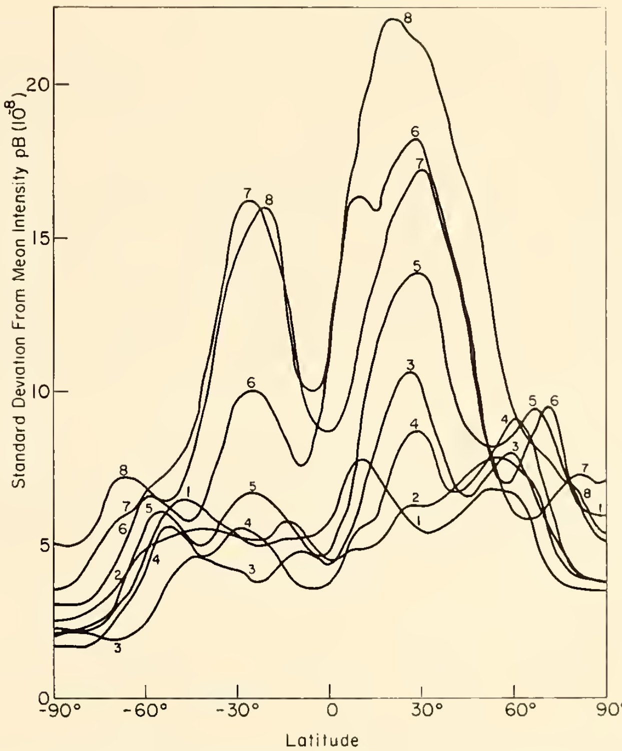

Fig. 11. Latitude distributions of standard deviation from mean brightness for each six-month period 1964–67 (numbered 1 to 8). – 1.125 $R_{\odot}$.

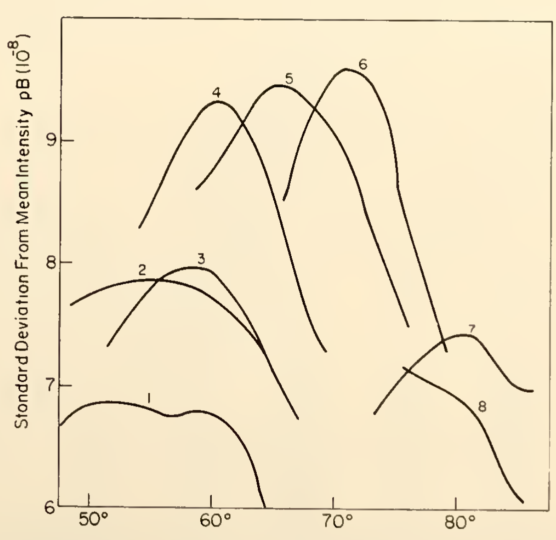

Fig. 12. Enlargement of the right hand portion of Figure 11 showing the poleward migration of the high latitude zone of coronal activity.

the latter half of 1965 and reaching 80° by the first half of 1967. Similar migratory movements of prominences and filaments, culminating in a 'rush to the poles' at the time of solar maximum, have been well established for many years (ANANTHAKRISHNAN, 1954, and references therein). WALDMEIER (1960) further suggested that during the solar maximum of the late 1950's reversal of the sun's polar magnetic fields occurred at the same time that the green corona's high latitude zone reached the poles and prominences reached 68°. HYDER (1965) reported a corresponding synchronism in the rush to the poles of filaments and reversal of the polar magnetic fields for the same cycle. Based on these observations of migration of the white light corona from 1965 to 1967, activity will reach the North and South poles in 1968 and 1969 respectively. Thus one might predict a *reversal* of the North and South polar fields during these years.

6. Electron Densities

The gradients of coronal brightness with increasing distance from the solar limb in the equatorial regions for the minimum year 1964 and the near-maximum year 1967

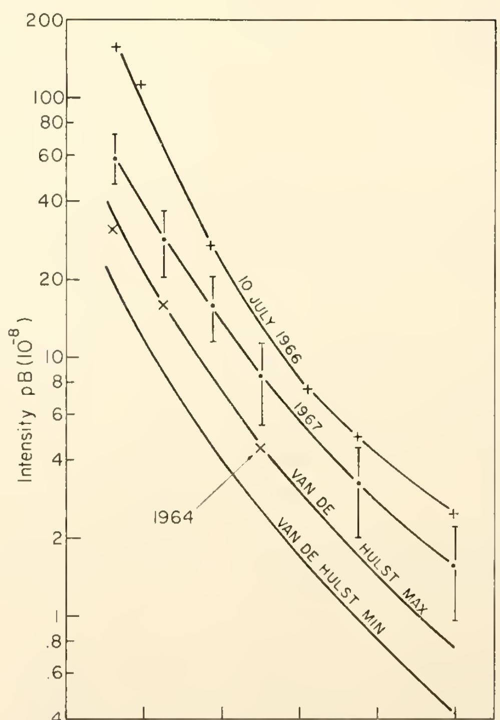

Fig. 13. Gradient of brightness with height for 1964 and 1967 equatorial regions compared with Van de Hulst's models and the exceptional feature of 10 July 1966. Vertical bars on the 1967 points denote one standard deviation above and below the mean. Points for 1964, shown as ×'s, fall almost exactly on the curve for Van de Hulst's maximum.

are shown in Figure 13. We follow the convention of considering the equatorial regions to be between plus and minus 50° latitude. By Figure 5 it is seen that this assumption is reasonable for 1964 in that the average brightness is uniform over a wide range of latitudes, although the somewhat smaller range of $\pm 40°$ might have been more appropriate. During active phase (such as periods 7 and 8) the brighter features of the inner corona are concentrated in zones above the sunspot regions, leaving a trough in the equatorial direction as seen in Figure 5. But this procedure of averaging over $\pm 50°$ to describe the 'equatorial corona' does assure inclusion of most of the bright features of the inner corona. Period 4 is used to represent the minimum corona at 1.5 $R_{\odot}$ for the brightness decrement plot of Figure 13.

Our brightness gradients are compared in this figure with those assumed by Van de Hulst for his classic development of coronal electron models. Van de Hulst's maximum was 1.78 times brighter than his minimum; we find a similar increase (1.9) for the near-maximum year 1967 compared to the minimum year 1964. However our *minimum* brightnesses are essentially identical to those assumed by Van de Hulst for his *maximum* model corona, and the two curves coincide in Figure 13. This is consistent with other recent measurements of the eclipse corona, including those of 1958 (Saito and Yamashita, 1962) and 1959 (Ney *et al.*, 1961) which similarly showed that it is necessary to increase Van de Hulst's model for the equatorial maximum corona by a factor of 2. Vertical bars on the 1967 brightness decrement points denote one standard deviation above and below the means as an indication of the differences one may realistically *expect* from particular eclipse observations during this phase of the solar cycle. During minimum the expected variations are of course much smaller. Also shown for comparison is the gradient of the exceptionally bright feature of 10 July 1966 that was associated with a center of activity producing proton flares (Newkirk *et al.*, 1967).

TABLE III

Comparison of average equatorial electron densities of 1964 and 1967 with other models (units $10^6/cm^3$)

	Hansen, Garcia Hansen and Loomis		Van de Hulst models		Newkirk 1956–58		Proton region 10 July 1966
$r/R_{\odot}$	1964 Min	1967 Max	Min	Max	Quiet	Active	
1.1	–	–	90	160	–	–	–
1.125	120	230	70	125	290	570	820
1.2	71	137	39.8	70.8	160	340	410
1.3	38	72	21.2	37.6	86	176	195
1.4	22	41	12.8	22.5	51	99	105
1.5	14	26.9	8.3	14.8	33	61	63
1.6	–	18.6	5.7	10.0	22	39	40
1.7	–	13.2	4.0	7.1	15	26	27
1.8	–	9.7	2.9	5.0	11	17	19
2.0	–	5.7	1.6	2.8	6	9	11

The derivation of electron densities is standard following Van de Hulst's technique with the assumption that the corona is azimuthally symmetric, an assumption which is well-recognized to be quite good for the minimum corona in the equatorial regions but obviously only a crude approximation to the real corona near solar maximum. Electron densities for 1964 and 1967 are shown in Figure 14 and Table III, again

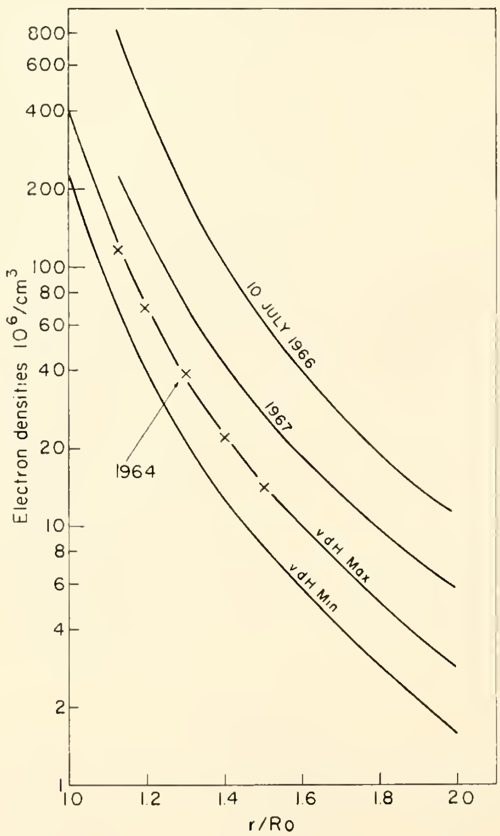

Fig. 14. Electron densities derived from Figure 13 with ×'s again denoting our equatorial minimum of 1964.

compared with those of Van de Hulst and the exceptional isolated feature of July 1966. Also included in the table are Newkirk's models for the quiet corona and the electron density above an active region, based upon some 20 days K-coronameter observations at Climax during the period September 1956 to January 1958 (Newkirk, 1959). This interval covered a pre-maximum phase of the solar cycle similar to 1967. However, the observational data were treated in a somewhat different manner so that the results are not exactly comparable. Ours are based on average K-coronal brightness for every day over the latitude range $\pm 50°$ while Newkirk extracted the contributions of the 10 most active regions (which formed the basis of his active region model) and then averaged all remaining data to within 15° of the poles. Both of these differences work in the direction of depressing his model for the *quiet* corona of 1956–58 as compared to our *average* for 1967.

7. Conclusions

There was a systematic change in brightness of the corona from the solar minimum of 1964 through the pre-maximum year of 1967, as clearly demonstrated by: Appearance of typical daily observations from year to year; average intensities at all latitudes except over the South pole; and total radiation at several concentric heights in the lower corona.

The corona brightened uniformly at all heights in the range 1.125–1.75 $R_{\odot}$ by a factor of 2. A close correlation is found between six-month averages of white light coronal intensity and 10.7-cm solar radio flux. Extrapolation to the radio flux level of the great maximum of cycle 19 in 1958 suggests that the integrated brightness of the corona may have increased by a factor of three at that time.

The brightness variations were due to discrete coronal features in preferred zones, in the sunspot activity belts at 25–30° and in a North polar zone which was observed to migrate from 55° to 80° during the period. Presumably this migration was the coronal manifestation of the 'rush to the poles' that has been well-established for filaments and prominences. Typical coronal features as observed through an aperture giving 1.3 min resolution are 20° to 40° wide in position angle and may appear 4 times brighter than the quiet, minimum-level corona. Their association with other solar phenomena will be discussed in a later paper.

Following the usual assumption of spherical symmetry, our average equatorial coronas for 1964 and 1967 had electron densities nearly twice Van de Hulst's models for the minimum and maximum corona, respectively.

Acknowledgements

This work would not have been possible without the generous cooperation of many staff members at the University of Hawaii's Haleakala Observatory and the Environmental Science Services Administration's Mauna Loa Observatory. We wish to particularly thank Walter Steiger, John Jefferies, Howard Ellis and Lothar Ruhnke.

References

Ananthakrishnan, R.: 1954, *Proc. Indian Acad. Sci.* **40**, 72.
Gillett, F. C., Stein, W. A., and Ney, E. P.: 1964, *Astrophys. J.* **140**, 292.
Hansen, R. T., Hansen, S. F., and Price, S.: 1965, *Publ. Astron. Soc. Pacific* **78**, 14.
Hata, S. and Saito, K.: 1966, *Ann. Tokyo Astron. Observ.*, 2nd Series **10**, 16.
Hyder, C.: 1965, *Astrophys. J.* **141**, 272.
Kundu, M. P.: 1965, *Solar Radio Astronomy*, Interscience, New York.
Lockyer, W. J. S.: 1931, *Monthly Notices Roy. Astron. Soc.* **91**, 797.
Ludendorff, H.: 1928, *Sitz.-Ber. Preuss. Akad. Wiss.* **16**, 185.
Newkirk, G. A.: 1959, *Paris Symposium on Radio Astronomy* (ed. by R. N. Bracewell), p. 149.

Newkirk, G. A., Curtis, G. Wm., and Watson, D. K.: 1958, IGY Solar Activity Report Series No. 4, High Altitude Observatory, Boulder.
Newkirk, G. A., Hansen, R. T., and Hansen, S. F.: 1967, *Annals of the IQSY*, Vol. 3, Paper 8.
Ney, E. P., Huch, W. F., Kellogg, P. J., Stein, W., and Gillett, F.: 1961, *Astrophys. J.* **133**, 616.
Perry, R. N.: 1967, Astro-Geophysical Memorandum No. 175, High Altitude Observatory, Boulder.
Saito, K. and Yamashita, Y.: 1962, *Ann. Tokyo Astron. Observ.* **7**, No. 4, 163.
Sytinskaya, N. N. and Sharonov, V. V.: 1963, in *The Solar Corona* (ed. by J. W. Evans), Academic Press, New York, p. 301.
Van de Hulst, H. C.: 1950, *Bull. Astron. Inst. Neth.* **11**, 135.
Van de Hulst, H. C.: 1953, in *The Sun*, 261 (ed. by G. P. Kuiper), Univ. of Chicago Press, Chicago, p. 261.
Waldmeier, M.: 1960, *Z. Astrophys.* **49**, 176.
Wlérick, G. and Axtell, J.: 1957, *Astrophys. J.* **126**, 253.

Reprinted from Solar Physics
Vol. 10, 135-149.

DIFFERENTIAL ROTATION OF THE SOLAR ELECTRON CORONA

RICHARD T. HANSEN and SHIRLEY F. HANSEN,
High Altitude Observatory, National Center for Atmospheric Research, Kamuela, Hawaii, U.S.A.

and

HAROLD G. LOOMIS*
Environmental Science Services Administration, Honolulu, Hawaii, U.S.A.

(Received 20 May, 1969)

Abstract. Autocorrelation analyses of K-coronameter observations made at Haleakala and Mauna Loa, Hawaii, during 1964–1967 have established average yearly rotation rates of coronal features as a function of latitude and height above the limb. At low latitudes the corona was found to rotate at the same rate as sunspots but at higher latitudes was consistently faster than the underlying photosphere. There were differences as large as 3–4% in the rate at specific latitudes from year to year and between the two hemispheres. In 1967 a nearly constant rotation was found for heights ranging from 1.125 to 2.0 R_0. For 1966 there was a more complicated pattern of height dependence, with the rate generally decreasing with height at low latitudes and increasing at high latitudes.

1. Introduction

More than a hundred years ago on the basis of his observations of the latitude-dependence of the westward drift of sunspots, Carrington demonstrated that the sun does not rotate as a rigid sphere. Sunspots at high latitudes have a longer rotation period than those nearer the equator. His basic result on differential rotation of the photosphere has since been confirmed by many later studies (including Newton and Nunn, 1951; Ward, 1966) and also has been extended to greater heights in the solar atmosphere by investigations of the day-to-day displacements of filaments (D'Azambuja and D'Azambuja, 1948; Bruzek, 1961) and bright coronal regions (Waldmeier, 1955; Trellis, 1957; Cooper and Billings, 1962). Meanwhile, spectroscopic analysis of the Doppler shifts of spectral lines originating in identifiable features and in specific levels of the solar atmosphere has provided independent verification of the differential rotation effect (reviewed by Goldberg, 1953).

Each of these two methods – displacement and spectroscopic – for deriving rotation rates has its own limitations although fortunately few of the limitations are common to both (Delury, 1939; Ward, 1966). Individual sunspots, filaments, and presumably the photospheric faculae undergo *proper motion* and are not truly tracers for the medium in which they are embedded. Similarly these solar phenomena may display an *asymmetric growth* which is superimposed on apparent rotational displacements. A further limitation of this method is that features tend to occur in a limited range of latitudes;

* At Hawaii Institute of Geophysics.

sunspots for example are confined to essentially 5–35°. And since there are practically no spots during solar minimum, it has been necessary to assume that the rotation rate is constant throughout the solar cycle although there is some evidence to the contrary (Evershed, 1945; Livingston, 1969). By the spectroscopic method, rotation rates can be found over a wider range of latitude and throughout the solar cycle. In actual practice however the accuracy is limited by the presence of inhomogeneities of the photospheric velocity field and also by macroscopic motions within coronal and prominence features so that the scatter between repeated measurements is large (Hart, 1954, 1956; De Jager, 1959). Nonetheless the two methods concur on an *average equatorial* rotation rate of $14.4 \pm 0.2°$/day.

The purpose of this paper is to describe the latitude-dependent rotation rate of the electron corona, based on analysis of over 900 daily observations made with the K-coronameter (Wlérick and Axtell, 1958) at Haleakala and Mauna Loa, Hawaii during 1964–1967. The height range of our data extends from 1.125 to $2 R_0$ so that it is possible to search for changes in rotation rate at increasing distances from the solar limb. Some of the characteristics of the K-corona over this period have been discussed earlier (Newkirk *et al.*, 1967; Bohlin 1968; Hansen *et al.*, 1969). Determination of rotation rates is possible because of the occurrence of localized coronal features, as much as two or three times brighter than the quiet corona, and with sufficient stability to reappear at the limb for several rotations. These features thus act as our *tracers* for the corona's rotation.

2. Methodology

Representative examples of the day-to-day brightness variations of the K-corona are shown in Figure 1. Successive observations are joined by line segments wherever the

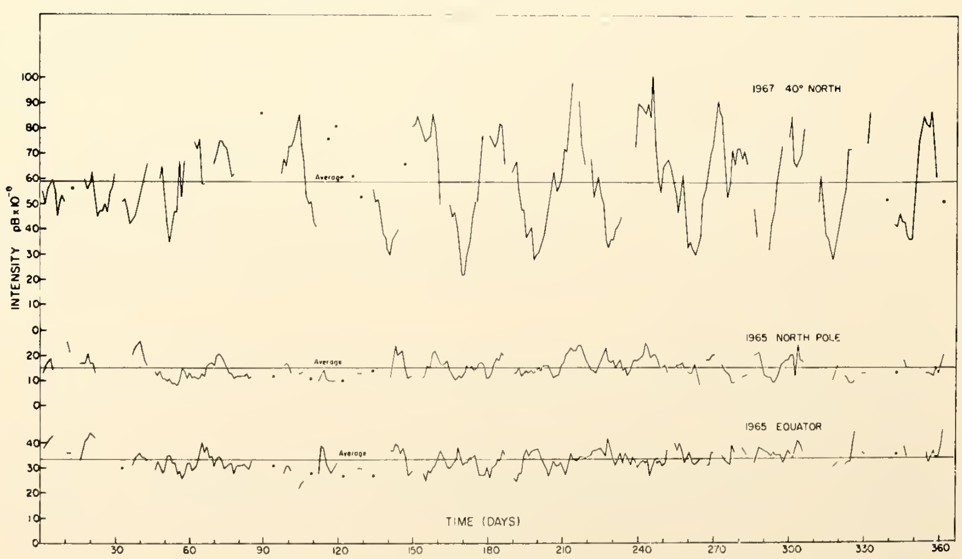

Fig. 1. Representative time sequences of the brightness of the K-corona.

data gaps do not exceed two days. The upper curve (1967, 40° North) is at a latitude where strong and persistent coronal regions reappeared many times during the year, so that a good estimate of the rotation rate is readily found. The autocorrelation for this sequence is shown at the top of Figure 2. The time delay for reappearance of these features after one, two and three rotations is obviously about 30, 60 and 90 days. The strength of the third peak demonstrates the longevity of some coronal features.

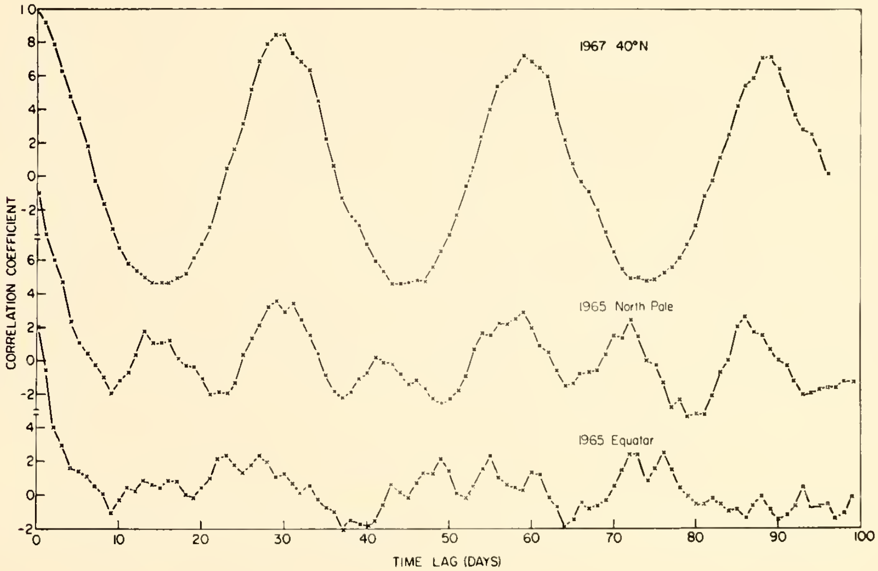

Fig. 2. Autocorrelations of the K-coronal data of Figure 1. The top curve shows the delay times for successive limb passages of strong coronal features at 40° North latitude to be about 30, 60 and 90 days. The maxima at intervals of about 15 days in the middle curve are due to high latitude features that were visible in projection over the North pole twice per rotation. The lower curve confirms that there were no dominant recurring K-coronal features at the equatorial latitude during the year 1965, and without such tracers, no rotation period could be found.

The middle curves of Figures 1 and 2 are for the North pole in 1965. Around midyear there was a high-latitude feature that was continuously visible during complete solar rotations as it appeared to oscillate east and west over polar latitudes. Thus at the polar position it was observed *twice* per rotation, projected alternately from the visible and invisible disk, and the resulting autocorrelation shows distinct maxima at intervals of about fifteen days.

The lower curves are for the Equator in 1965. There appear to be no pronounced recurring coronal features (Figure 1) and accordingly no strongly preferred periodicities in the autocorrelation (Figure 2). Therefore a rotation period is not found for this position for this year.

The detailed procedure that was systematically applied for determining rotation periods from the autocorrelation and for assigning confidence limits is described in Appendix A.

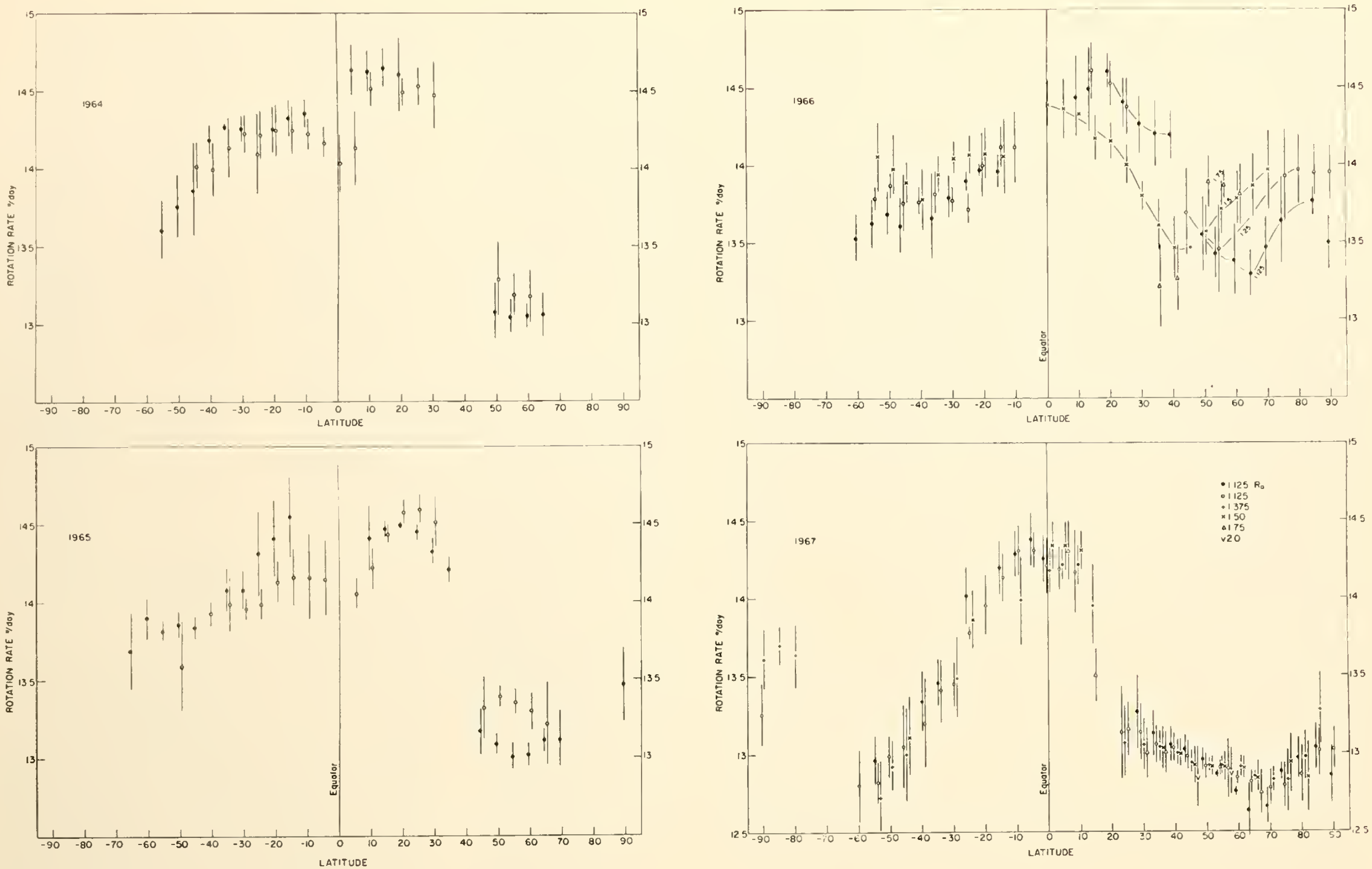

Fig. 3. Latitude dependence of the coronal rotation rate at several heights for separate years 1964–1967. Reliability estimates are shown as vertical bars. Data for 1.125 R_0 are plotted just to the left of each latitude line, higher heights progressively to the right. In 1966 there appears to have been a variation in average angular velocity with distance from the solar limb, but in 1967 the rates were nearly constant with height.

3. Average Coronal Rotation Rate

The entire set of yearly rotation rates by 5° increments of latitude for each year 1964–1967 are shown in Figure 3. Heights are identified by separate symbols and confidence limits by vertical lines. The general trend of a decreasing rotation rate with increasing latitude (differential rotation) is fairly clear. But it is also apparent that the fall-off of rate with latitude is not the same from year to year or between the two hemispheres. For example in 1967 over a broad range of latitude extending from 25° to the North pole, the corona seems to have rotated consistently slower than during 1966. Also the difference between high and low latitude rates was larger in the Northern than in the Southern hemisphere in both 1964 and 1965. These and other variations will be discussed further in later sections of the paper but meanwhile the results for the minimum observed coronal height, $1.125 R_0$, are combined in Figure 4 and their average is shown as the dashed curve.

Consideration is required, however, of the fact that coronal features based at lower latitudes are visible in projection in the plane of the sky at higher latitudes. The extreme case was shown in Section 2; periodicities determined by the autocorrelation analysis at polar latitudes of 85–90° actually represent the rotation rates of features from much lower latitudes. This can be readily verified from the original records by simply

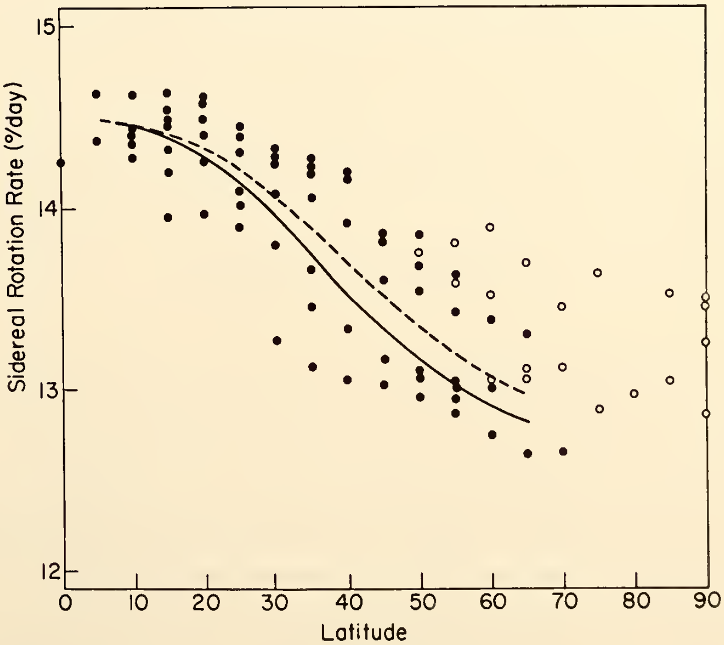

Fig. 4. Individual yearly rotation rates at 1.125 R_0, Northern and Southern hemispheres combined. Certain high latitude rates (open circles) were excluded from the average (dashed line) as explained in text. The adjusted average (solid curve) is based upon consideration of lower latitude coronal features being visible in projection. See also Table I.

tracing the day-to-day displacement in apparent latitude of isolated coronal features around the poles (Bohlin, 1968, Figure 4-14). Also in an earlier study of the 1964–1967 K-coronameter data (Hansen *et al.*, 1969) it was found that the zones of activity at high latitudes steadily migrated toward the poles, and on this basis rates determined for latitudes above the upper boundaries of these zones were *excluded* from the calculated average. The points omitted are shown in Figure 4 as open circles. The upper boundary of the activity zone is estimated to have been at 55° latitude in the North and 45° in the South during 1964, advancing 5° each year to 70° in the North and 60° in the South by 1967.

Similarly rates found by the autocorrelation analyses at other observed positions must be adjusted for the brightness contributions of features projected from lower latitudes. Table I shows this adjustment. Corresponding to each observed position is a

TABLE I

Visibility adjustment to account for projection of features from lower latitudes (see Appendix B)

Observed:	0°	10°	20°	30°	40°	50°	60°	70°
Effective:	0°	10°	19°	28°	37°	46°	55°	63°

somewhat lower (effective) latitude which best represents features having that rate. The table is based on calculations by Perry (1967) of the variation in appearance of an incremental coronal feature as it rotates around the solar limb, considering both the changes in brightness that would be measured with the K-coronameter and also the apparent latitude displacement (See Appendix B for details). The solid curve of Figure 4 is thus the rotation rate adjusted for this projection effect. At equatorial latitudes the difference is insignificant but steadily increases to nearly 0.2°/day at 65°.

4. Comparison with Other Rates

The average coronal rate of Figure 4 is shown in Figure 5 compared with the rates determined from other solar tracers including spots, polar faculae, filaments and regions of bright green coronal emission.

At all latitudes our rates for the K-corona are distinctly greater than those found by Trellis from successive limb passages of green coronal regions during 1943–1955. The faster rate tends to be confirmed by separate studies of long-lived coronal regions at 55° (circle) and 65° (square). Also Bohlin (1968) independently analyzed the K-coronameter data of March–November 1965 and concluded that an extended feature with center of gravity at 53° rotated 13.5°/day.

The filament rate up to 45° latitude is taken from D'Azambuja and D'Azambuja (1948) with Bruzek's (1961) more comprehensive study of polar filaments (during 1956–1959) used to extend the curve to 80°. The general agreement between the *average* K-coronal and filament rates is remarkable. Although the curves do begin to diverge

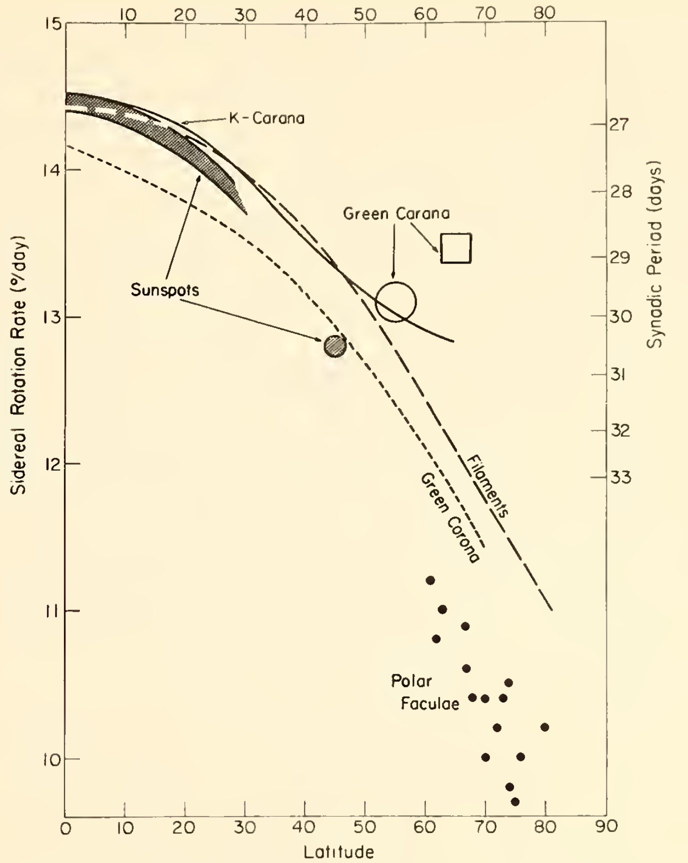

Fig. 5. Comparison of the average rotation rate of the K-corona at 1.125 R_0 (solid curve) with those for all Sunspots (top of grey area, Ward 1966); Recurrent Sunspots (bottom of grey area, Newton and Nunn 1951); High Latitude Spots at 45° (Waldmeier, 1957; Kopecky *et al.*, 1957); Polar Faculae (Muller, 1954; Waldmeier, 1955); Filaments (D'Azambuja and D'Azambuja, 1948; Bruzek, 1961) and Green Corona (dotted curve, Trellis, 1957; circle, Waldmeier, 1950; square, Cooper and Billings, 1962).

at higher latitudes, this difference may not be significant as the mean error in filament rates was estimated by Bruzek at about $\frac{1}{2}$°/day.

Two curves enclosing the grey area at equatorial latitudes are given in Figure 5 for the sunspot rotation rate. In a critical review of the Greenwich sunspot observations (from 1878–1944), Ward (1966) showed the longitudinal motions to be a function of sunspot size and shape with large groups moving up to 2% less rapidly than smaller ones. Since the rates found by Newton and Nunn (lower curve) were derived from recurrent spots which are predominately in large groups, their rate is biased on the low side. Using a random selection of all spots, Ward (upper curve) found rates about 1% higher than Newton and Nunn's.

Our K-coronal analysis is similar to Ward's in that there is no selection of a particular type of feature. However only those having durations sufficiently long to permit successive limb passages could have contributed to the autocorrelation result. Thus the indicated coronal rates are more comparable to those of Newton and Nunn in that they represent recurrent tracers having lifetimes of a month or more. Within an uncertainty of 1 to 2%, all three solar phenomena – spots, filaments and K-coronal features – have the same average rotation rate for latitudes up to about 25°.

At higher latitudes however the difference becomes large. The coronal rate at 60–65° seems to be well-established by the several investigations (excluding Trellis') as being at least 12.8°/day while the filament rate is 12.2 ± 0.5°/day and the photospheric rate found from polar faculae is about 11°/day. It should be noted that there may be a fundamental difference in the nature of these tracers of the sun's rotation. The polar faculae were very short-lived, generally with life-times less than one day, while some of the coronal features and filaments persisted over periods of many months. Thus it is not clear whether these represent real differences in rotation at various levels in the solar atmosphere or instead reflect characteristic behavior of the tracers themselves – such as unequal proper motion or asymmetric growth. But taken at face value these results indicate that the magnitude of the differential rotation of the solar corona is only one half that of the photosphere; the decrease in the K-coronal rate between equatorial latitudes and 60–65° is about $1\frac{1}{2}$°/day while for the photospheric features, the differential is more than 3°/day.

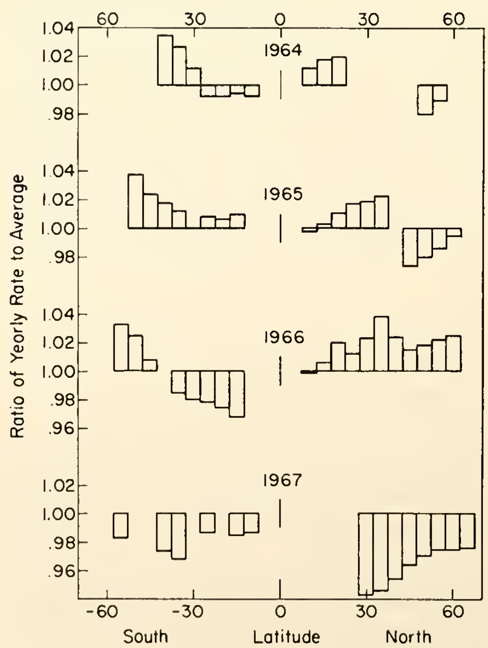

Fig. 6. Time dependence. Individual yearly rates at 1.125 R_0 are shown as a ratio to the average for the entire period.

5. Time Dependence

In Figure 6 rotation rates for individual years are normalized to the average of the entire four years. The pattern seen in the Northern hemisphere for 1964 and 1965 – above average rate at low latitudes and below average at polar latitudes – indicates a larger than average differential rotation. In contrast, the differential in the South was small from 1964 to 1966. Rates in the North in 1966 were all faster than average, but in 1967 were consistently slower in both hemispheres. While these changes from year to year appear to be interesting, there seems to be no obvious relationship with the trend of increasing solar activity during the four years.

Although Newton and Nunn (1951) found no variation in rotation rate of spots between four epochs of the solar cycle, their result was based only upon tracers in the latitude range 10–20°. Similarly the rates for the K-corona are reasonably consistent from year to year over this small range of latitude; the average dispersion from Figure 6 is only 1%. Larger variations in the yearly rates were found for the higher latitudes although part of this scatter is surely due to the approximate nature of our adjustment for projection effects.

6. Height Dependence

Because of the steep gradient of K-coronal brightness with height it is progressively more difficult to attain reliable measurements at greater distances from the limb. For the years 1964 and 1965 our observations were limited primarily to 1.125 and 1.25 R_0

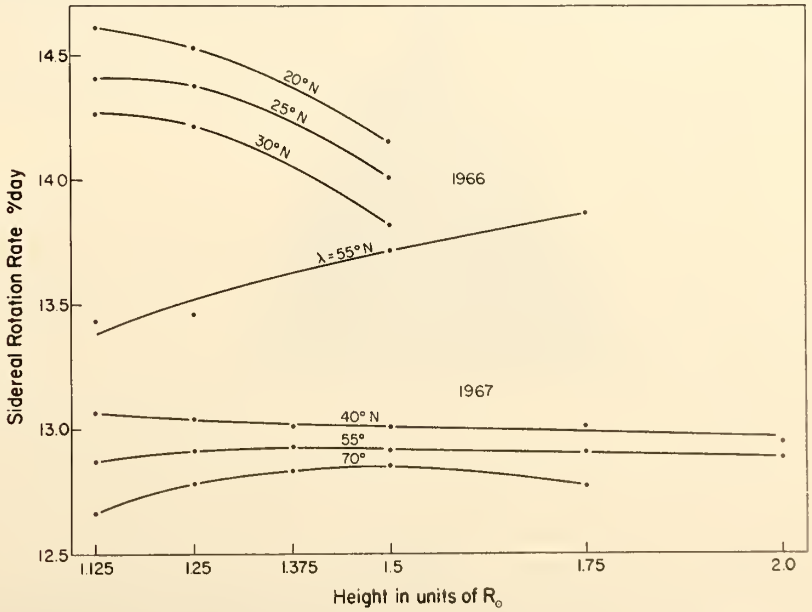

Fig. 7. Height dependence. Examples of the variation of rotation rate with height at several latitudes with well-determined rates during 1966 and 1967. Data taken from Figure 3.

but by steady improvement in experimental techniques, they were extended to 1.5 and even $2\,R_0$ in 1966 and 1967. Thus some information is available on the height dependence of the rotation rate at certain latitudes where strong features occurred. Figure 7 shows that in the Northern hemisphere during 1967 the rate remained nearly constant out to the limit of our observations at two radii from the center of the sun. But at some positions during 1966 (such as 55°N) the rate appeared to steadily increase with radial distance while at other positions (20°N), the rate decreased. Re-examination of Figure 3 shows that for this year there was a latitude, 50°, at which this height dependent effect reversed.

In an earlier discussion on the difference between solar rotation rates deduced from the corona and polar faculae, Billings (1966) suggested that high latitude phenomena are bound to lower latitudes by magnetic fields which join paired regions near the same longitude in the sunspot and polar zones of the sun, constraining the two regions to move nearly at the same rate. Magnetic maps developed by Newkirk *et al.* (1967) suggest that such fields actually do occur in the corona. In addition Billings speculated that not all polar features should rotate at the same rate since those connected to lower latitudes by particularly strong magnetic fields would be influenced to a greater extent by the faster, low latitude, rate.

Our results for the Northern hemisphere during 1966 might be consistent with this hypothesis. The general pattern of decrease in rotation rate with height at low latitudes together with the increase with height at polar latitudes suggests arch-shaped magnetic fields spanning these two zones during at least part of that year. And changes in rotation rate at high latitudes may reflect the degree of interlocking between the two zones by means of the coronal magnetic fields. The implications of this suggestion in terms of the deformation due to shearing of specific coronal features will be discussed in a later paper in the context of the morphology of specific coronal features and their association with other solar phenomena.

7. Conclusions

On the basis of autocorrelation analyses of over 900 daily observations of the white light corona during solar minimum and the ascending phase of cycle 20 we reach the following conclusions about coronal differential rotation:

(I) At equatorial latitudes (to about 25°) the *average* rotation rate of the inner corona is the same as that of the sunspots and filaments, to an uncertainty of 1 to 2%.

(II) At higher latitudes the corona apparently rotates substantially faster than the underlying photosphere. Also our rate for the white light corona 1964–1967 is generally faster than that reported (Trellis, 1957) for the green corona 1943–1955. However the faster rates found from the recurrence of two stable high latitude coronal regions (Waldmeier, 1950; Cooper and Billings, 1962) are confirmed by our results. The general variation of rotation rate of the corona with latitude can be reasonably well approximated by that found for filaments (D'Azambuja and D'Azambuja, 1948; Bruzek, 1961) except possibly for latitudes above 50°.

(III) Differences as large as several percent in the angular velocities are found *at the same latitude* from year to year and between the two hemispheres (Figure 6). These seem not to be related in an obvious way to the increasing solar activity.

(IV) During 1967 some coronal features appeared to rotate at a constant rate to a height of at least $2R_0$. But during 1966 the distribution of rotation rates in the Northern hemisphere was more complicated, decreasing with height at low latitudes and increasing with height at high latitudes (Figures 3 and 7). This may have been due to large arch-shaped coronal magnetic fields spanning between the two zones with the dominant magnetic fields of the low latitude sunspot regions dragging along the high latitude corona as suggested by Billings (1966).

(V) Throughout this study we have compared rotation rates based upon analysis of solar phenomena that occurred at *different* times (such as K-corona 1964–1967, sunspots 1878–1944, filaments 1919–1937 and 1956–1959, and green corona 1943–1955), so that the apparent lack of agreement between the several phenomena might be due to time-dependent changes in the *overall* rotation pattern of the entire sun. Determinations of the rotation rates based upon concurrent sets of data are highly desirable, especially in view of the possibility that the average velocity of the corona changes from year to year (Figure 7).

Appendix A: Determination of Rotation Periods from the Autocorrelations

The highest correlation point was selected within the time lag interval 25–32 days and

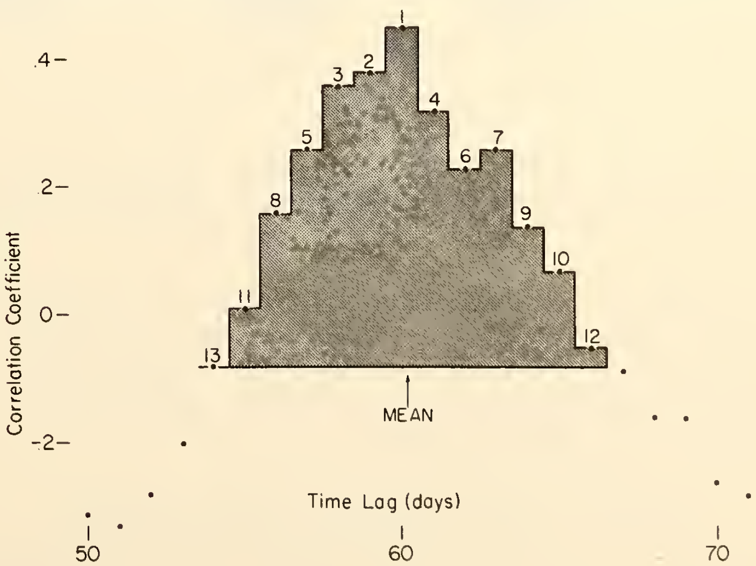

Fig. 8. Sequential selection of the highest autocorrelation values for determination of the coronal rotation period. Each successive point is chosen as the highest adjacent value, either to the left or right. The total number of points included is a function of latitude, increasing from seven at the equator to fourteen at 65°.

then the next highest adjacent points were chosen sequentially, as shown in Figure 8. The first moment of these points (enclosing the grey area of the figure) is taken as a measure of the rotation period. Similar calculations were performed on the autocorrelations at the time lags expected for the next reappearance of coronal features (50–64 days) and for the third reappearance (75–96 days), and these time lags were divided by two and three respectively. Each autocorrelation curve thus provides three estimates of the rotation period, although not strictly independent since they are derived from the same sequence of daily measurements. East and West limb K-coronal observations are analyzed separately and the average of these semi-independent estimates at each latitude is taken as the rotation period for that year (Figure 9).

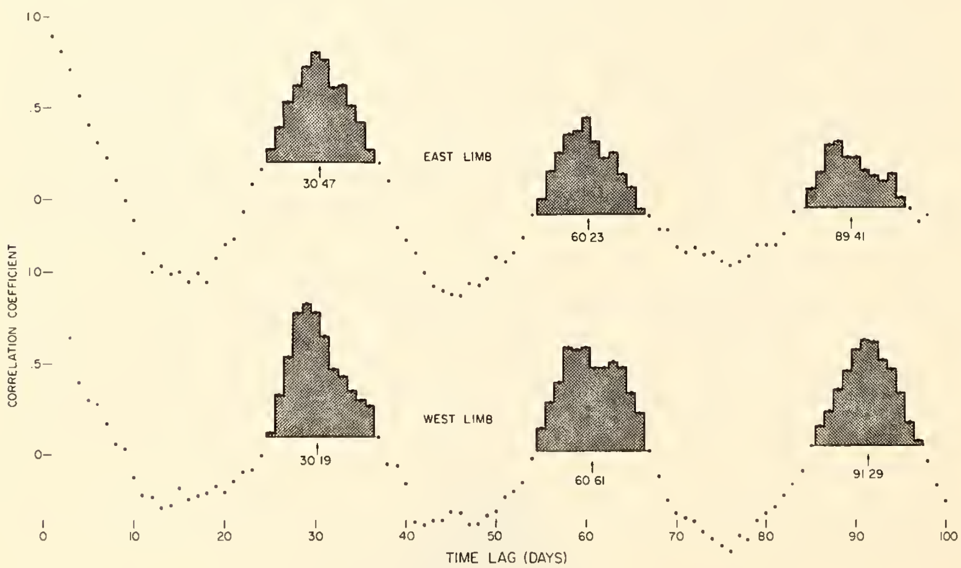

Fig. 9. Autocorrelations for 1.5 R_0 at 60° latitude, 1967. The means of each of the six shaded areas provide estimates of the delay times for successive reappearance of coronal features at the solar limb.

The closeness of agreement of the six values is an indication of the reliability of the average, using Student's t test at the 90% level to establish confidence limits (Hoel, 1947). The rotation periods are then converted to angular velocities (sidereal rotation rate expressed in degrees per day). Only those rates whose confidence limits are less than $\pm 0.3°$/day are discussed in this paper.

Appendix B: Adjustment of Rates for Projection Effects

The rotation rate found at each position is a blend of the rates for features actually based at the observed latitude (λ_0) and of the generally-faster rates of lower latitude features viewed in projection. Thus a rate found by the autocorrelations is more representative of some lower, *effective* latitude which can be estimated by assuming

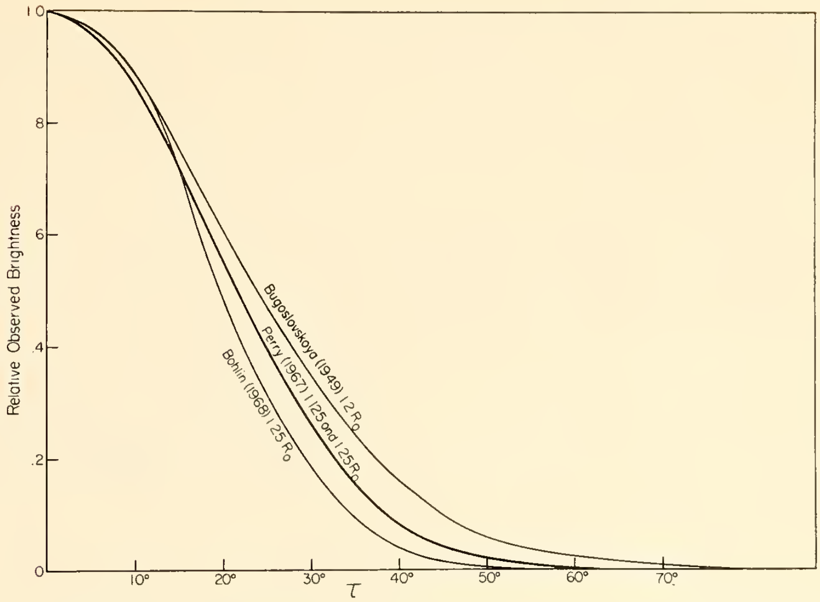

Fig. 10. Variation in observed brightness of an idealized coronal streamer as a function of the angle between the feature and the plane of the sky.

the blended-rate to be established by projected features in direct proportion to their brightness contributions.

The variation in apparent brightness as a coronal feature is observed in projection during limb passage has been calculated by Perry (1967) for an idealized radial feature. The change in brightness with the angle (τ) between the feature and the plane of the sky is shown in Figure 10. Also shown for comparison are results of two similar studies, one by Bugoslavskaya (1949) and another by Bohlin (1968) from K-coronameter observations of a stable feature during 1965. The three curves agree quite well in the range $0<\tau<20°$. At greater angles from the limb the influence is sufficiently small that the choice of a particular model is not crucial.

Assuming that the sun's axial tilt (B_0) is zero, then $\sin\lambda = \sin\lambda_0 \cos\tau$. Using this relationship the relative brightness contributions from features at increments of lower latitude (λ) can be computed for each observed latitude. Examples of this distribution are shown by the histograms of Figure 11. For a K-coronameter observation at low latitudes nearly all of the total brightness is due to features based within a few degrees of the observed position. However foı observations at 60° latitude only about one-half of the brightness is due to features above 55°, while nearly one-fourth is from projection into the plane of the sky of features based below 50°. For each observed latitude there is thus a lower, effective latitude which falls at the midpoint of the brightness contributions, and the rotation rates found by the autocorrelations are better representative of this latitude, as listed in Table I.

This adjustment can be only approximate in that it is based upon the assumption

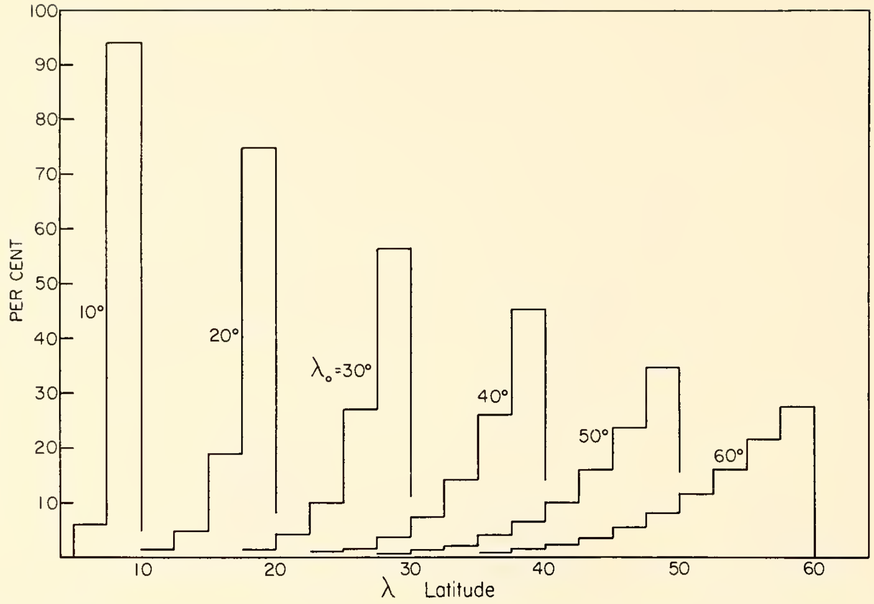

Fig. 11. Histograms showing the relative contributions of coronal features based at increments of lower latitude to the brightness observed at specific latitudes.

that there is a uniform distribution in the number of features and in their average brightness at all latitudes. In actual fact, features of the inner corona are concentrated into discrete latitude zones and those nearer the equator tend to be brighter.

Acknowledgements

It is a pleasure to acknowledge the large contribution of Charles Garcia to the observational program with the K-coronameter. Also we are greatly indebted to Dr. Donald Billings and Dr. Gorden Newkirk for their critical review of the manuscript and to Dr. John Firor for continued encouragement and support.

References

Becker, U.: 1957, *Z. Astrophys.* **42**, 1.
Billings, D. E.: 1966, *A Guide to the Solar Corona*, Academic Press, New York.
Bohlin, J. D.: 1968, 'The Structure, Dynamics and Evolution of Solar Coronal Streamers'. Thesis, University of Colorado, Boulder, Colorado.
Bruzek, A.: 1961, *Z. Astrophys.* **51**, 75.
Bugoslavskaya, E. Y.: 1949, *Publ. Sternberg Inst.* **19**.
Cooper, R. H. and Billings, D. E.: 1962, *Z. Astrophys.* **55**, 28.
D'Azambuja, M. and D'Azambuja, L.: 1948, *Ann. Obs. Paris* **6**.
De Jager, C.: 1959, *Handbuch der Physik*, Vol. 52 (ed. by S. Flugge), Springer-Verlag, Berlin, p. 337.
Delury: 1939, *J. Roy. Astron. Soc. London* **33**, 345.
Evershed, J.: 1945, *Monthly Notices Roy. Astron. Soc.* **105**, 204.

Goldberg, L.: 1953, *The Sun* (ed. by G. P. Kuiper), Chicago Univ. Press, Chicago, p. 19.
Hansen, R. T., Garcia, C. J., Hansen, S. F., and Loomis, H. G.: 1969, *Solar Phys.* **7**, 417.
Hart, A. B.: 1954, *Monthly Notices Roy. Astron. Soc.* **114**, 17.
Hart, A. B.: 1956, *Monthly Notices Roy. Astron. Soc.* **116**, 38.
Hoel, P. G.: 1947, *Introduction to Mathematical Statistics*, John Wiley and Sons, London.
Kopecky, M., Kvicala, J., and Ptacek, J.: 1957, *Bull. Astron. Inst. Czech.* **8**, 106.
Livingston, W. C.: 1969, *Solar Phys.* **7**, 144.
Muller, R.: 1954, *Z. Astrophys.* **35**, 61.
Newkirk, G. A., Hansen, R. T. and Hansen, S. F.: 1967, *Annals of the IQSY*, Vol. 3, 49.
Newkirk, G. A., Altschuler, M. D., and Harvey, J.: 1968, *Structure and Development of Solar Active Regions* (ed. by K. O. Kiepenheuer), Reidel Publ. Co., Dordrecht, p. 379.
Newton, H. W. and Nunn, M. L.: 1951, *Monthly Notices Roy. Astron. Soc.* **111**, 413.
Perry, R. M.: 1967, *Astro-Geophysical Memorandum* No. 175, High Altitude Observatory, Boulder.
Trellis, M.: 1957, *Ann. Astrophys. Suppl. Ser.* **5**.
Waldmeier, M.: 1950, *Z. Astrophys.* **21**, 24.
Waldmeier, M.: 1955, *Z. Astrophys.* **38**, 37.
Waldmeier, M.: 1957, *Z. Astrophys.* **43**, 29.
Ward, F.: 1966, *Astrophys. J.* **145**, 416.
Wlérick, G. and Axtell, J.: 1957, *Astrophys. J.* **126**, 253.

Reprinted from Journal of Marine
Research, Vol. 27, No. 3, 355-357

Anomalous Temperature of Bottom Water in the Panama Basin[1]

Norman P. Laird

Pacific Oceanographic Research Laboratory
Environmental Science Services Administration
Seattle, Washington 98102

In studies of basins along the western rim of the Pacific, Wyrtki (1961 a, b) found no significant differences in bottom potential temperature within individual basins. In the Panama Basin, however, bottom potential temperatures vary about 0.1°C (Fig. 1); bottom water in the western part of the basin is warmer than that to the east. In Fig. 2 it is evident that this trend exists up to a level of about 3000 m.

From a consideration of oceanographic properties and bottom topography, the Panama Basin seems to be filled from a level of about 2500 m through a pass near the coast of Equador. A proposed circulation pattern for the basin consistent with topographic features and available temperature data is shown in Fig. 1.

Temperature variation in the bottom water may result from the topographic isolation of the basin and local heating along the path of flow. Uniformly high geothermal flux has been measured in this area; 15 values averaged 3.2 μg cal/cm^2/sec (P. Grim, personal communication). An alternate explanation for the warmer bottom water in the west is that the western side of the basin is filled from a higher level than the eastern side and that an uncharted topographic barrier separates the two areas below about 3000 m.

Available salinity and oxygen data generally are not precise enough to conclusively resolve this question. Within the limits of the data, it appears that the salinity structure is the same in the eastern and western parts of the basin. This uniformity would indicate a single source of bottom water. A few precise temperature, salinity, and oxygen measurements, with a limited bathymetric survey, are needed to determine the mechanism responsible for these anomalous bottom temperatures.

1. Accepted for publication and submitted to press 23 April 1969.

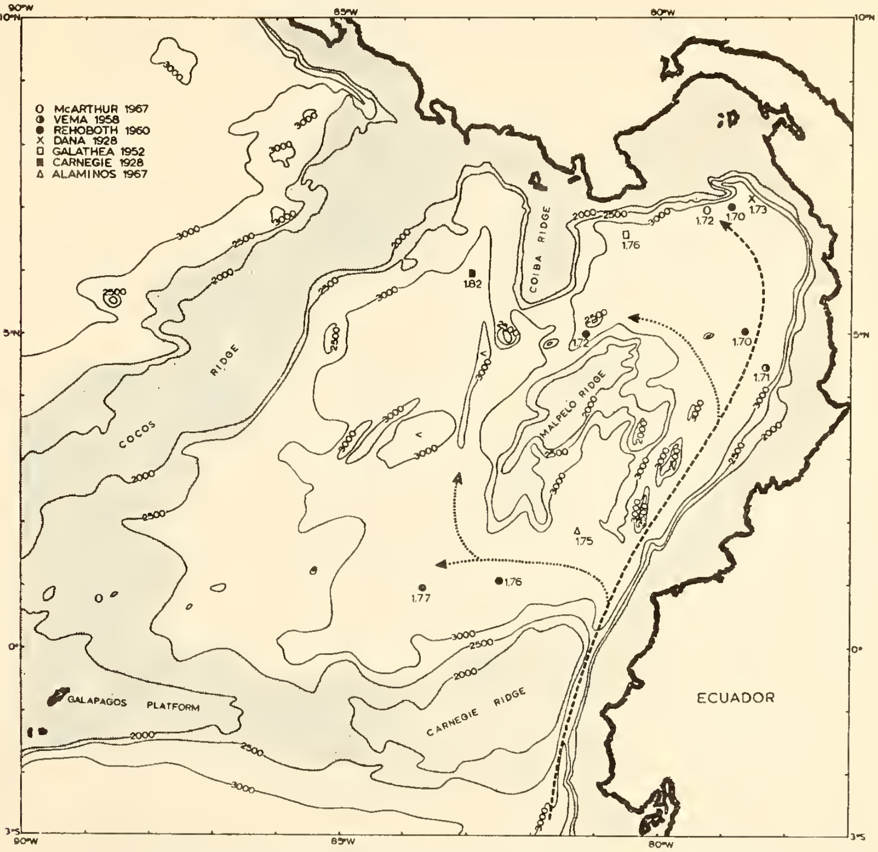

Figure 1. Potential temperature distribution at depths greater than 3000 m and within 200 m of the bottom. Bottom topography is after Chase (1968); shaded areas are less than 2500 m.

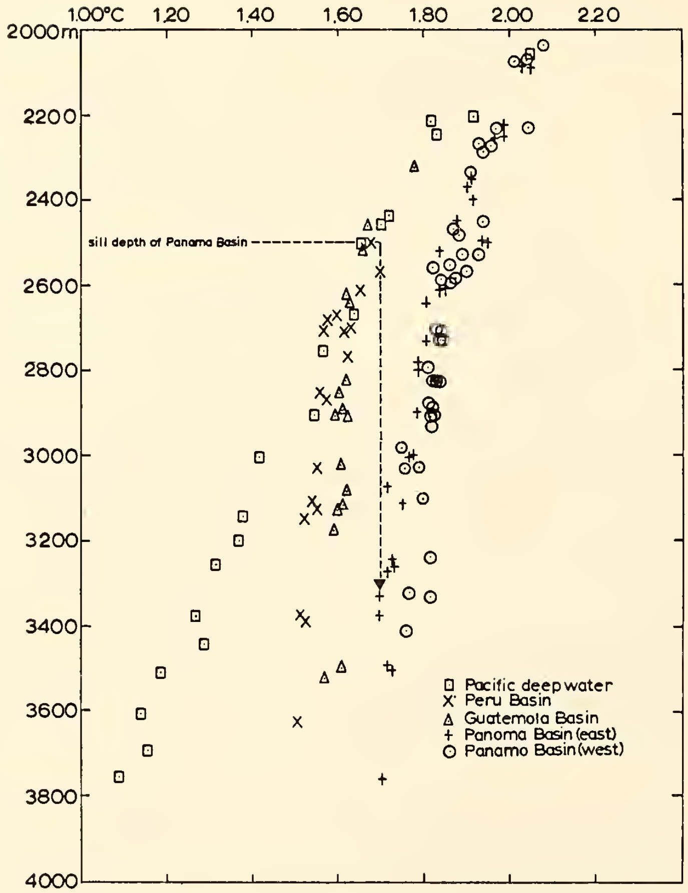

Figure 2. Observed potential temperature in the Panama Basin and adjacent waters.

REFERENCES

Chase, T. E.

1968. Sea floor topography of the central Pacific Ocean. U. S. Bur. Com. Fish., Cir. 291; 33 pp.

Wyrtki, Klaus

1961a. Physical oceanography of the southeast Asian waters. NAGA Report, Vol. 2, University of California, La Jolla; 195 pp.

1961b. The flow of water into deep-sea basins of the western South Pacific Ocean. Aust. J. mar. freshw. Res., *12*: 1–16.

Printed in Denmark for the Sears Foundation for Marine Research,
Yale University, New Haven, Connecticut, U.S.A.
Bianco Lunos Bogtrykkeri A/S, Copenhagen, Denmark

Reprinted from Journal of Geophysical
Research, Vol. 74, No. 23, 5433-5438.

Bottom Current Measurements in the Tasman Sea

N. P. Laird and T. V. Ryan

Pacific Oceanographic Research Laboratory, ESSA
Seattle, Washington 98102

Bottom current velocities of 1 to 9 cm/sec were measured for periods of 0.5 to 1.2 hours at five sites in the Tasman Sea. At four sites a northerly component was present. Bottom photographs indicate stronger currents have occurred at several sites. The results in most cases support previous ideas on flow inferred from water properties.

Introduction. Bottom current observations have been reported by numerous authors and are summarized by *Heezen and Hollister* [1964] and *Knauss* [1965]. No observations have been reported, however, for the Tasman Sea and adjacent areas, although *Rochford* [1960] and *Wyrtki* [1961] have inferred flow in this area from water mass analysis and geostrophic calculations.

In September 1967, five current stations of short duration were occupied between Australia and New Zealand (Figure 1) from the USC&GSS *Oceanographer*. A Geodyne current meter [*Richardson et al.*, 1963], and an EG&G camera were mounted on a frame and lowered to the bottom from the drifting ship [*Pratt*, 1963]. A pinger with a tilt switch was used to indicate bottom contact and system posture. The current meter's sensors were approximately 1 meter above the bottom.

Treatment of data. Current data from periods during which the system was stationary on the bottom for 5 minutes or longer are summarized in Table 1. Directions from the EG&G compass vane were averaged (nearest 5°) from photographs obtained at 8-second intervals. Current direction and speed were calculated from current meter readings and averaged for each series. All tabulated directional data were corrected for magnetic deviation (11° to 15°E). There is generally good agreement between the compass vane and current meter directions except at station 2, series A, where we suspect 'sticking' of the current meter compass. Numerous small-scale fluctuations in both speed and direction were evident in the data, but they were of smaller magnitude than the changes discussed in the following section.

Discussion. Station 1 was located in the Tasman basin, where *Wyrtki* [1961] postulated that bottom water and deep water spread northward with deep water at the 3000-meter level eventually entering the Coral Sea to the north. The observed current direction changed 15° clockwise and speed increased 1 cm/sec over the period of the record (70 minutes). Bottom photographs at this station revealed ripple marks with a wavelength of about 50 cm, which were nearly parallel to the measured current (Figure 2). These may be longitudinal ripples because some current lineations are present that appear to parallel the ripples.

At station 2, an appreciable difference in speed (4 cm/sec) was found between the two series, but the direction and speed of each series were fairly stable. This difference may be due to a slight change in the location of the system after series A. A photograph at this site (Figure 3) shows coarse sediments, which are indicative of active currents. Tidal currents may be strong at this depth, and it is probable that the East Australian current is occasionally present at this site.

At station 3 the current direction rotated 45° counterclockwise, and the speed increased from 1 to 4 cm/sec at a fairly constant rate over the period of the record. The speed appears to increase as the direction becomes more parallel to the major trend of the Lord Howe rise. At depths of this observation, and between latitudes 30° and 40°S, is an area in which two branches of antarctic intermediate water mix, and there is no clearly developed circulation [*Wyrtki*, 1962]. A photograph at this site (Fig-

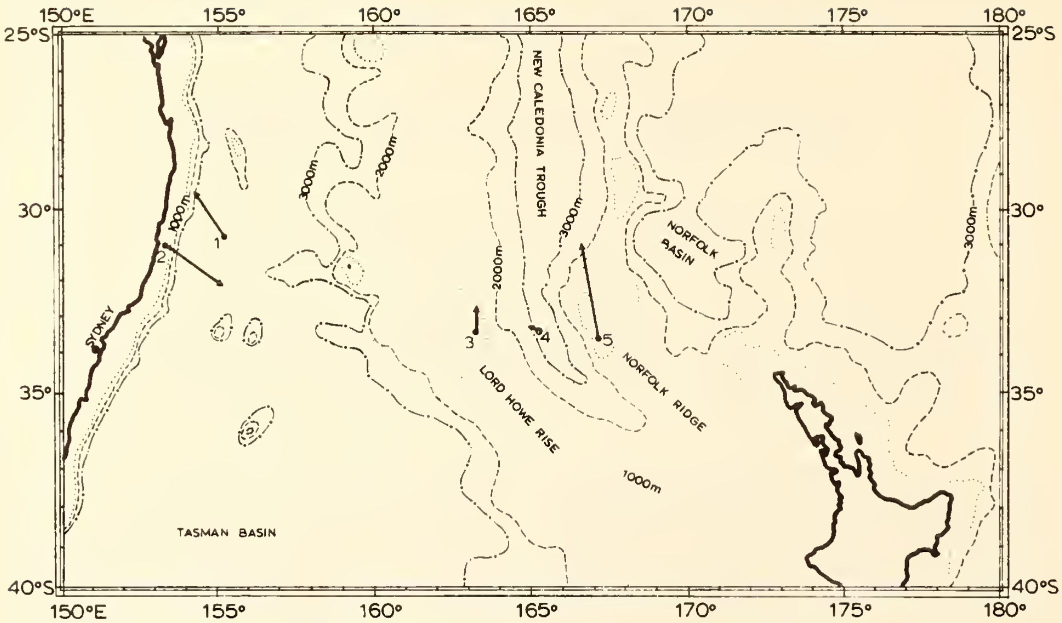

Fig. 1. Bathymetry of the Tasman Sea with station positions. Arrows represent average current direction; the length of the arrow is proportioned to the speed.

ure 4) shows the bottom was disturbed by numerous animal tracks, which indicates sluggish bottom currents.

Station 4 was located in the New Caledonia trough. *Wyrtki* [1961] proposes that water at 3000 meters enters the trough at the northern end and spreads southward, whereas *Rochford* [1960] suggested that it is filled from the southern end. Our records favor neither conclusion as we found a constant westerly direction (290°) with speed increasing from near 0 to 1 cm/sec, which suggests that any flow is very sluggish. The sea floor at this station (Figure 5) seems devoid of any active currents.

TABLE 1. Summary of Current Measurements in the Tasman Sea

Station	Location	Depth, meters	Series	Start (GMT)	Duration, min	Speed, cm/sec	Current Direction, °T	
							Geodyne	EG&G vane
1	30°57.9′S, 155°00.8′E	4572	A	Sept. 24, 1967, 0001 GMT	16	5	315	310
			B	Sept. 24, 1967, 0058 GMT	13	6	330	320
2	31°00′S, 153°18.0′E	336	A	Sept. 24, 1967, 1140 GMT	6	8	90	120
			B	Sept. 24, 1967, 1128 GMT	23	4	150	130
3	33°20.2′S, 163°07.5′E	838	A	Sept. 28, 1967, 0202 GMT	32	3	10	360
4	33°29.9′S, 165°03.5′E	2974	A	Sept. 28, 1967, 1649 GMT	27	1	290	295
5	33°44.7′S, 167°33.6′E	770	A	Sept. 29, 1967, 1012 GMT	18	9	5	355
			B	Sept. 29, 1967, 1044 GMT	10	8	355	355
			C	Sept. 29, 1967, 1058 GMT	13	9	355	345

Fig. 2. Station 1, rippled muddy bottom in the Tasman basin.

Fig. 3. Station 2, coarse sediments on the Australian continental shelf.

Fig. 4. Station 3, photograph on Lord Howe rise. Note animal track and worm holes.

Fig. 5. Station 4, in New Caledonia trough, abundant animal life.

Fig. 6. Station 5, on Norfolk rise, prominent ripple marks in globigerina sand and possibly an animal burrowed in the sand.

At station 5, along the western slope of the Norfolk ridge, the current direction and speed remained fairly constant over 59 minutes. Because this station was also at the level of antarctic intermediate water, the fact that speeds here were much higher than at station 3 suggests that the topography of the Norfolk ridge has a significant effect on flow. Ripple marks photographed in globigerina sand (Figure 6) were oriented normal to the measured current. The recorded velocities (8–9 cm/sec) do not appear to be competent, however, to produce ripples in this type of sediment [*Heezen and Hollister*, 1964], and it is suspected that faster currents must exist at times.

Conclusion. The Tasman Sea is an area of complex topography, with continental slopes, ridges, basins, and troughs occurring in close proximity. These features probably exert a notable influence on the circulation pattern. Although the duration of these measurements does not allow for the isolation of the tidal effect from the net flow, it may be significant that a north to northwesterly component, paralleling the trend of the topographic features, was observed at four of the five stations. A similar correlation between current direction and trend of bathymetric contours has been noted in the western North Atlantic [*Heezen et al.,* 1966].

Acknowledgments. The cooperation of the officers and crew of the USC&GSS *Oceanographer* is gratefully acknowledged. We are indebted to Ronald Reed and James Stephens for assistance and helpful suggestions in the analysis of the data.

References

Heezen, B. C., and C. Hollister, Deep sea current evidence from abyssal sediment, *Mar. Geol.*, *1*(2), 141, 1964.

Heezen, B. C., C. D. Hollister, and W. F. Ruddiman, Shaping of the continental rise by deep geostrophic contour currents, *Science, 152*(3721), 502, 1966.

Knauss, J. A., A technique for measuring deep ocean currents close to the bottom with un-attached current meter, and some preliminary results, *J. Mar. Res., 23*(3), 237, 1965.

Pratt, R. M., Bottom currents on the Blake plateau, *Deep-Sea Res., 10,* 245, 1963.

Richardson, W. S., P. B. Stimson, and C. H. Wilkins, Current measurements from moored buoys, *Deep-Sea Res.,* 10, 369, 1963.

Rochford, D. J., Some aspects of the deep circulation of the Tasman and Coral seas, *Aust. J. Mar. Freshwater Res., 11,* 166, 1960.

Wyrtki, K., The flow of water into the deep sea basins of the western South Pacific Ocean, *Aust. J. Mar. Freshwater Res., 12,* 1961.

Wyrtki, K., The subsurface water masses in the western South Pacific Ocean, *Aust. J. Mar. Freshwater Res., 13,* 18, 1962.

(Received February 27, 1969;
revised May 22, 1969.)

Reprinted from Journal of Marine
Research, Vol. 27, No. 1, 1-6.
SEARS FOUNDATION FOR MARINE RESEARCH
Yale University

Journal of
Marine Research

Volume 27, Number 1

Long Waves along a Single-step Topography in a Semi-infinite Uniformly Rotating Ocean[1]

J. C. Larsen

Joint Tsunami Research Effort
Environmental Science Services Administration
University of Hawaii
Honolulu, Hawaii

ABSTRACT

The dispersion equation for Kelvin-type waves for a single-step topography is derived. Solutions for this equation indicate that, in addition to the Kelvin-type waves, there also exist quasigeostrophic waves that are related to the topography structure.

The lunar semidiurnal tide (12.4206 hour period) along the California coast appears to approximate a Kelvin wave since its amplitude is nearly constant (0.5 ± 0.01 m) while its phase speed (about 200 m/sec) and direction (north) are consistent with the Kelvin-wave solution (Larsen, 1968). In the present paper it is shown how a single-step topography (corresponding to the shelf off California) influences the modification of the Kelvin-wave solution. Other types of waves are also possible, and these are described.

Choose a rectangular coordinate system (x, y, z) such that x is north, y is

1. Accepted for publication and submitted to press 8 July 1968.

west, and z is up, and let the ocean be confined to the space $(-\infty \leqslant x \leqslant \infty, 0 \leqslant y \leqslant \infty)$. The linearized equations of motion for long free waves of small amplitude are

$$\left.\begin{aligned} \frac{\partial u}{\partial t} - fv &= -g\frac{\partial \zeta}{\partial x} \\ \frac{\partial v}{\partial t} + fu &= -g\frac{\partial \zeta}{\partial x}, \end{aligned}\right\} \tag{1}$$

and the continuity equation is

$$\frac{\partial \zeta}{\partial t} = -\frac{\partial}{\partial x}(hu) - \frac{\partial}{\partial y}(hv); \tag{2}$$

here ζ is the wave height, u and v are the horizontal particle velocities in the x and y direction, and f is the Coriolis frequency, assumed to be constant. Let the bottom topography consist of a shelf region $(0 \leqslant y \leqslant \Delta)$ of depth h_1 and of an open-ocean region $(\Delta \leqslant y \leqslant \infty)$ of depth h_2, and seek solutions of the form

$$\left.\begin{aligned} \zeta &= Z(y) \exp[i(kx - wt)] \\ u &= U(y) \exp[i(kx - wt)] \\ v &= V(y) \exp[i(kx - wt)], \end{aligned}\right\} \tag{3}$$

where k is the longshore wave number and w is the radian frequency, which is assumed to be always positive. Then, if $k < 0$, the waves propagate in the negative x direction. The wave amplitude, Z, within each region then satisfies the equation

$$\frac{d^2 Z}{dy^2} - \nu Z = 0, \tag{4}$$

where $\nu = k^2 - (\omega^2 - f^2)/(gh)$ for $h = h_1$ or h_2. The solutions have the form

$$Z = a \exp(-sy) + b \exp(sy) \quad \text{for} \quad s^2 = \nu, \nu > 0$$

or

$$Z = a \sin(sy) + b \cos(sy) \quad \text{for} \quad s^2 = -\nu, \nu < 0.$$

The boundary conditions require that V vanish at the coast, that Z and hV be continuous at the step, and that the solutions remain finite at infinity (Munk et al. 1964). Letting the solutions be Z_1 for the shelf region and Z_2 for the open-ocean region, the boundary conditions require:

(i) $dZ_1/dy + (fk/\omega) Z_1 = 0$ for $y = 0$;
(ii) $Z_1 = Z_2$ and $h_1[dZ_1/dy + (fk/\omega) Z_1] = h_2[dZ_2/dy + (fk/\omega) Z_2]$ for $y = \Delta$;
(iii) Z_2 be finite for $y \to \infty$.

Two types of solutions—trapped and leaky—are possible, depending on the form of the solution in the open-ocean region.

Trapped Mode. For this mode, the solution in the open ocean has the form

$$Z_2 = \exp(-s_2 y)$$

where

$$s_2 = [k^2 - (\omega^2 - f^2)/(gh_2)]^{1/2} > 0.$$

The dispersion relationship is found to be

$$[s_2 - (fk/\omega)]\,[s_1 \coth(s_1 \Delta) - (fk/\omega)] + (h_1/h_2)\,[s_1^2 - (fk/\omega)^2] = 0, \qquad (5)$$

where $s_1^2 = k^2 - (\omega^2 - f^2)/(gh_1)$ may be either positive or negative. The roots were found, numerically, for the three following topographies: (i) $\Delta = 0$, $h_2 = 4.4$ km, (ii) $\Delta = 80$ km, $h_1 = 0.6$ km, $h_2 = 4.4$ km, (iii) $\Delta = 250$ km, $h_1 = 0.6$ km, $h_2 = 4.4$ km. Topography (i) corresponds to a flat ocean depth, topography (ii) corresponds approximately to the shelf and ocean off central California, and topography (iii) corresponds to the ocean off southern California with its broad borderland region. The results are presented in Fig. 1, computed for 35°N. For topographies (ii) and (iii), Fig. 1 shows two types of trapped-mode solutions; one solution (K) corresponds closely to the Kelvin-wave solution, the other (G) corresponds to the quasigeostrophic solution (Reid 1958). [The leaky-mode solutions (R), which correspond to reflected-wave solutions, lie above the hyperbola whose right wing is shown as the dotted line in Fig. 1; see *Leaky Modes* below.]

The Kelvin-type wave for shelf topography ($h_1 < h_2$) and for trench topography ($h_1 > h_2$) propagate only in the positive x directior in the northern hemisphere. For $k\Delta \ll 1$ and $f\Delta/(gh_2)^{1/2} \ll 1$, the solutions for topographies (ii) and (iii) approach the Kelvin-wave solution for topography (i), with the dispersion relationship $\omega/k = (gh_2)^{1/2}$; for $f\Delta/(gh_1)^{1/2} \gg 1$, the solutions approach the Kelvin-wave solution for an ocean of uniform depth, h_1, with the dispersion relationship $\omega/k = (gh_1)^{1/2}$.

The quasigeostrophic waves have relatively lower frequencies and higher wave numbers. Thus an approximate expression for the dispersion relationship for these waves can be obtained by letting $k^2 \gg (\omega^2 - f^2)/(gh_2)$, with the result that $s_1 \approx k$ and $s_2 \approx |k|$. Then the dispersion relationship becomes

$$\coth(k\Delta) = (f/\omega)\,[1 - h_1/h_2] - (|k|/k)\,(h_1/h_2).$$

This puts an upper limit on the frequency, $\omega \leqslant f|h_2 - h_1|/(h_2 + h_1)$, a result that depends only on the absolute sum and the difference of the step. For $k\Delta \ll 1$ and $h_1 \approx h_2$, the longshore phase velocity is approximately $\omega/k = f\Delta(1 - h_1/h_2)$. The waves are then nondispersive and have speeds that are de-

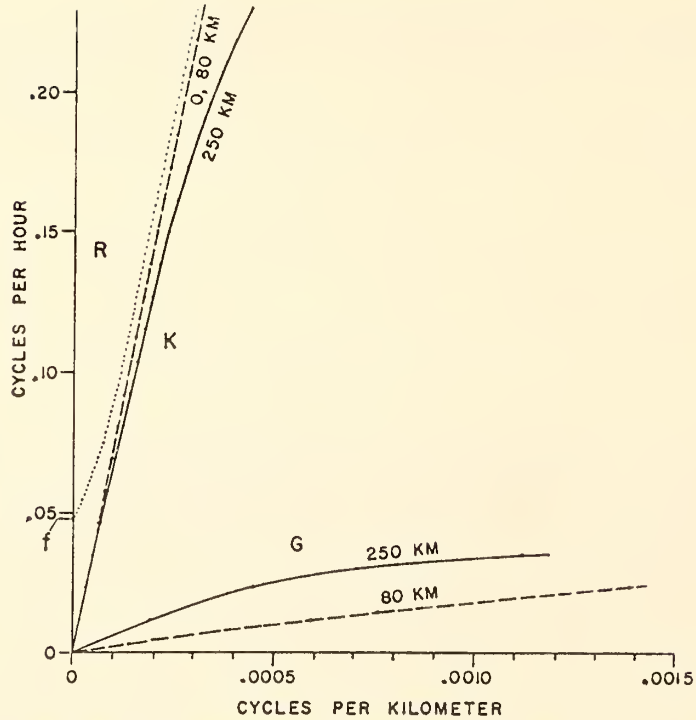

Figure 1. Diagnostic diagram for single-step topography. Plotted is frequency versus longshore wave number in the positive x direction. Reflected-wave solutions, R, lie above the dotted line. The Kelvin-type solutions are K and the quasigeostrophic solutions are G. The width of the shelf is noted; the depth of the shelf is 0.6 km while the offshore depth is 4.4 km. The Coriolis frequency, f, is noted with a value appropriate to 35°N.

pendent on the width of the shelf as well as on the magnitude of the step. For a shelf topography ($h_1 < h_2$), these waves propagate in the positive x direction; for a trench topography ($h_1 > h_2$), the waves propagate in the negative x direction. For a flat topography ($h_1 = h_2$), these waves do not exist. For an infinitely wide shelf ($\Delta = \infty$), coth $(k\Delta) = 1$. Then the dispersion relationship becomes $\omega = f|h_2 - h_1|/(h_2 + h_1)$. This equation has been derived by Longuet-Higgins (1968), who studied in detail the trapping of waves along a discontinuity of depth in an unbounded ocean. (The waves labeled in his paper as the "double Kelvin wave" or "seascarp" wave appear to correspond, in the limit $\Delta = \infty$, to what is labeled here as the quasigeostrophic wave.)

The ratio of the components of the water motion for both types of waves in the open ocean ($y > \Delta$) is

$$v/u = -i(\omega s_2 - kf)/(fs_2 - k\omega).$$

For shelf topography, $kf/\omega < s_2 < k\omega/f$ or $k\omega/f < s_2 < kf/\omega$. Thus the water particles, for the Kelvin-type wave, move in counterclockwise elliptical orbits whereas for trench topography, the water moves in clockwise elliptical orbits. The motion for flat topography is linearily polarized. For the quasigeostrophic waves, which have shorter wavelengths, the motion has a tendency to be circularly polarized, either counterclockwise or clockwise, depending respectively on whether the wave travels in the positive or negative x direction.

Measurements of bottom currents just beyond the borderland region off southern California (Isaacs et al. 1966) have indicated, for most sites, semidiurnal tidal currents of several centimeters per second. The water particles moved in counterclockwise elliptical orbits, with the major axis parallel to the trend of the coast. The ratio of the major axis to the minor axis ranged between 1:2 and 1:6. These observations agree favorably with estimates of semidiurnal tidal currents, using values from coastal tide observations. The Kelvin-type solution just beyond the shelf gives semidiurnal tidal currents of 2 cm/sec; the water particles move in counterclockwise elliptical orbits, with the major axis parallel to the coast; the ratio of the major axis to the minor axis is 1:6. However, there is a possibility that the current measurements also include internal wave motion of tidal frequency and thus confuse the interpretation.

Leaky Mode. For this mode, the solution in the open ocean has the form $Z_2 = \cos(s_2 y + \theta)$, where $s_2^2 = (\omega^2 - f^2)/(gh_2) - k^2 > 0$. This mode corresponds closely to the reflected-wave solution for an ocean of uniform depth. The dispersion relationship is found to be

$$[s_2 \tan(s_2 \Delta + \theta) - (fk/\omega)][s_1 \coth(s_1 \Delta) - (fk/\omega)] + (h_1/h_2)[s_1^2 - (fk/\omega)^2] = 0, \tag{6}$$

where $s_1^2 = k^2 - (\omega^2 - f^2)/(gh_1)$ may be either positive or negative. Discrete solutions, in terms of the longshore wave number k, do not occur, but the ratio of coastal amplitude over incident amplitude could be contoured (Munk et al. 1964); this has not been attempted here. The low-frequency cut-off is $\omega^2 = f^2 + gh_2 k^2$, which, in Fig. 1, is the dotted hyperbola above which the leaky modes lie.

REFERENCES

ISAACS, JOHN, JOSEPH REID, GEORGE SCHICK, and RICHARD SCHWARTZLOSE
1966. Near-bottom currents measured in 4 kilometers depth off the Baja California coast. J. geophys. Res., *71*: 4297–4303.

LARSEN, J. C.
1968. Electric and magnetic fields induced by deep sea tides. Geophys. J. R. astr. Soc., *16*: 47–70.

Reprinted from Journal of Geophysical
Research, Vol. 74, No. 13, 3408-3414.

Heat Transfer in the Top Millimeter of the Ocean

E. D. McAlister and William McLeish[1]

Scripps Institution of Oceanography, University of California, San Diego
La Jolla, California 92037

Different mechanisms of heat transfer to the ocean surface dominate within different depth regions. Under suitable weather conditions, radiation dominates within the upper micron of depth. Turbulence is dominant at greater depths, but the evidence indicates that, with wind speeds less than 10 m/sec, it dominates only at depths greater than 0.5 mm. A region in which heat is transferred almost entirely by conduction lies between. Radiometric measurements of the total heat flow to the ocean surface may be made in this region.

Introduction

The mechanisms of heat transfer in the top millimeter of the ocean are not well known, partly because of the experimental difficulties in obtaining temperature measurements in this region and partly because of the theoretical problems in predicting properties of the water near a wind-disturbed wavy surface. *Neumann and Pierson* [1966] emphasize that this region has not been studied adequately. However, the temperature profile through this region is critical to important areas of current research. It introduces a significant difference between the bulk water temperature and the airborne or satellite infrared radiometric readings of sea surface temperature [*Saunders*, 1967]. Furthermore, a knowledge of the mechanisms of heat transfer is necessary for interpretation of the readings of an infrared radiometer developed in this laboratory to measure the heat flow to the ocean surface through measurement of water temperature at two different depths [*McAlister*, 1964, 1967]. The present paper is a compilation of results of various studies that examine the different mechanisms. Through these results rough quantitative estimates of the temperature profile and of its influence on the radiation emitted from the ocean are found. Thus, a basis for the calculation of heat flow from radiation measurements is provided.

[1] Now at ESSA Atlantic Oceanographic Laboratories, Sea-Air Interaction Laboratory, Miami, Florida 33130.

Heat within the ocean is transferred to the surface through turbulence, conduction, and radiation. Turbulence tends to produce an approximately logarithmic temperature profile, and conduction gives a linear one, whereas radiation from the ocean gives a decrease in temperature gradient (Figure 1). Direct laboratory measurements of the mean temperatures in the upper few millimeters beneath smooth water surfaces have shown a region of linear profiles such as given by conduction [*Häussler*, 1956]. However, these experiments apparently had not allowed the formation of wind-induced turbulence in the water, and *Timofeev* [1966] suggested that the conduction region does not exist in the ocean with appreciable wind speeds. *Kanwisher* [1963] in laboratory experiments on gas exchange rates between air and water showed the existence of a lamellar diffusion layer at the water surface under moderate wind speeds (his Figure 4, p. 202). Several investigators have hypothesized the existence of this region [e.g., *Saunders*, 1967], and *McAlister* [1964] showed it to be present with light winds. We know of no observation demonstrating its existence in the ocean under a moderate wind. Without the present calculations it is conceivable that the regions with significant radiation and turbulent transfer could merge. The present studies provide additional evidence that the conduction region exists and give estimates of its minimum thickness.

Radiation

The influence on the temperature profile of the nighttime exchange of infrared radiation be-

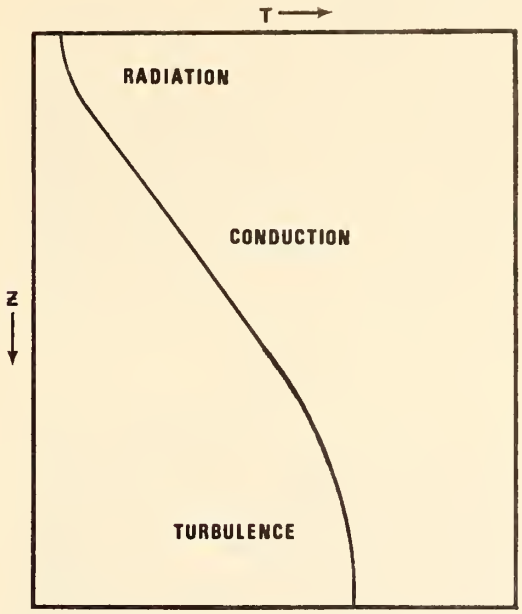

Fig. 1. Schematic representation of temperature profile near the sea surface.

tween the sky and the water beneath the ocean surface is estimated through sample numerical calculations. In these calculations, the sky is assumed to be a blackbody having a constant temperature, so that the influence of the atmosphere in modifying radiation intensities at different wavelengths and from different directions is ignored. The effect of waves in changing the field of view of a surface element is considered to have a negligible effect on the mean temperature profile, and the influence on this profile of the alternate surface convergence and divergence induced by waves is also small [*O'Brien,* 1967]. In an investigation begun in this laboratory, *Lick* [1965] examined transient effects on the temperature profile of a radiating and conducting medium. Such effects can be neglected in the present problem. Calculations in the next section indicate that turbulence is not significant in this region. The radiational transfer of heat from one level to another within the water is negligible in comparison with the transfer by conduction and the radiational exchange with the sky. Also, the variation in temperature of the water within the radiation exchange region is small when compared with the temperature difference between the water and the sky.

With these conditions, the radiational heat exchange with the sky through any level is just that for the transfer between two parallel plates, attenuated by the intervening water:

$$q_{\text{net}}(z) = 2\pi \int_0^\infty [B_\nu(T_w) - B_\nu(T_s)]E_3(k_\nu z)\, d\nu \tag{1}$$

where $B_\nu(T)$ is Planck's function and the exponential integral $E_3(k_\nu z)$ represents the attenuation of diffuse radiation by the water above the level [*Goulard and Goulard,* 1960]. The temperature gradient is given by the conductive heat flow

$$H_c(z) = \delta\, dT/dz \tag{2}$$

and, since the total heat flow is constant with depth,

$$\frac{dT}{dz} = \frac{1}{\delta}(H_T - q_{\text{net}}(z)) \tag{3}$$

Substituting (1) into (3) and integrating, we have the temperature profile

$$T(z) = T_0 + \frac{H_T z}{\delta} - \frac{2\pi}{\delta}$$

$$\cdot \int_0^z \int_0^\infty [B_\nu(T_w) - B_\nu(T_s)]E_3(k_\nu z)\, d\nu\, dz \tag{4}$$

For convenience of introduction into a computer, the kernel $\frac{1}{2}$ exp $(-3k_\nu z/2)$ was substituted for $E_3(k_\nu z)$ [see *Lick,* 1965]. Values of k_ν were derived from *Plyler and Acquista* [1954]. Observations at sea with a total-wavelength net radiometer and a 7- to 12-μ radiation thermometer indicated that, with a clear sky, T_s was at times as low as 0°C. Calculations of $T(z)$ using values of T_s near this value and $T(0) = 15°$C showed little influence of radiation on the temperature profile. An extremely low value of T_s of $-20°$C led to a departure of the temperature profile from a linear one of only 0.0015°C at the surface. Thus the over-all temperature changes resulting directly from emitted radiation are small.

The distribution with depth of radiation and conductive heat flow was examined in further calculations by using (1). A value of 0.34 cal/cm²/min was taken for H_T, in accord with the maximum value reported by *McAlister*

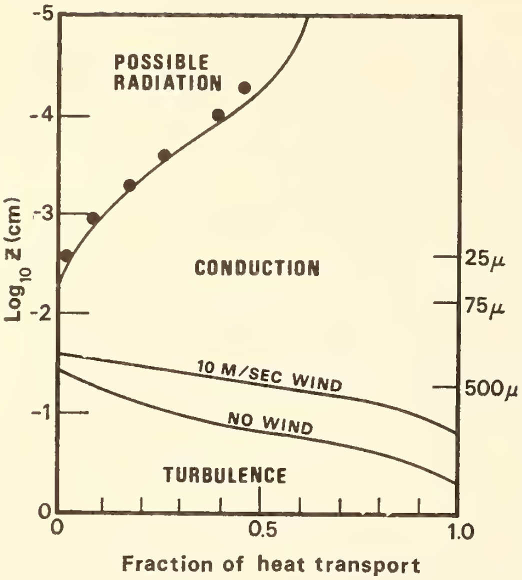

Fig. 2. Mechanisms of heat transport to the sea surface at different depths.

[1964], and $T_s = -20°C$, so that the radiational heat transfer at the surface was 63% of the total. Figure 2 shows the fraction of transport by radiation as a function of depth. Radiation may be negligible at any depth, but even with an extremely cold sky it would generally constitute less than 10% of the total heat flow at depths greater than 10 μ.

The above calculations were completed in 1964; since then the compilation of optical properties of water by *Irvine and Pollack* [1968] has become available. They presented absorption coefficients that are significantly smaller in the 12- to 20-μ region than were used above. An approximate recalculation of the radiation curve in Figure 2 has been performed with these data and an infrared slide rule. The sky temperature for wavelengths shorter than 15 μ was taken to be $-20°C$, as before, but for longer wavelengths a sky temperature of 10°C was assumed in order partially to represent atmospheric emission. Sky radiation in these longer wavelengths is largely emitted from the lower atmosphere, where the temperature is seldom much below the water temperature. The recalculated values, shown by solid dots in Figure 2, show a profile similar in shape to the previous one. Changes in the wavelength distribution of sky radiation appear to have only a limited effect on the shape of the heat transfer profile.

Although the total solar radiation reaching the sea surface is at times much greater than the total heat loss, calculations based on the values of Irvine and Pollack indicate that only about 10% of it is absorbed within the upper 1 mm. Thus, even when the insolation is 2–3 times as great as the heat loss, there is only a small departure from a linear temperature profile.

Turbulence

The water near the ocean surface is commonly in turbulent motion induced either by wind (forced turbulence) or by gravitational instability resulting from evaporation and surface cooling (free turbulence). *Häussler* [1956] measured the mean temperature profile beneath a laboratory water surface where gravitational instability appeared to be responsible for the turbulence. The mean profile with rates of heat loss comparable with the values at sea was linear to depths of 1–2 mm. A theoretical calculation by J. Pierce (1962, unpublished report in this laboratory) is in accord with Häussler's profile. These measurements indicate that at sufficiently low wind speeds and rates of heat loss turbulence is not dominant in the heat transfer in the upper 1 mm. At higher wind speeds, however, forced turbulent transfer can become dominant within some of this region, and the present effort is directed to estimating extent. This estimate is made through an examination of the temperature profile and equation 2.

It was observed by *McLeish* [1967] that the initiation of wind-driven turbulence in the water near the surface was always accompanied by the formation of steep capillary waves, and a direct measurement of the temperature profile near the surface under these conditions would appear to be difficult. A limiting form of the temperature profile may, however, be estimated by an indirect method, in which the temperature profile at a solid boundary expected for a given surface stress is determined. There is evidence that the linear region extends at least as deep into the fluid at a free surface as at a solid boundary on which the surface stress is equal to the wind stress on the water. The disruption of the surface by whitecaps is not considered here.

Stresses on the water at wind speeds of 2–10 m/sec have been estimated from empirical relationships. The temperature profiles corresponding to these stresses for a given rate of heat flow at a solid boundary were calculated from the 'universal' temperature profile of *Deissler* [1955]. The profile for 2 m/sec is similar to the profile derived by Pierce, but the profile for 10 m/sec remains linear only to about 0.4 mm. The no wind (Pierce) and 10-m/sec temperature profiles were transformed into heat transfer profiles with equation 2 and are presented in Figure 2.

The evidence that the conductive region extends deeper at a free boundary than at a solid one with the same total stress is derived from measurements of the velocity profile near the water surface. Techniques given by *Schraub et al.* [1964] were used to produce lines of small hydrogen bubbles in the water by intermittent electrolysis along a thin vertical wire extending through the surface of the water in a laboratory wind-water tunnel. The lines of bubbles were carried downstream by the current, and side-view cine photographs recorded their positions to indicate water speeds. The mean current near the surface increased with the length of time that the air had been flowing, but the mean shear at any level within the upper centimeter soon attained a nearly steady state.

Figure 3 shows the average of twenty-five sets of velocity readings at different fixed distances beneath the mean water level, denoted by open circles. The air speed was 6 m/sec and the fetch was 1 meter. This fetch was sufficient for the development of small-scale waves and turbulence that appeared to be similar to the conditions in the ocean. The velocities at fixed distances near the surface could not be determined because of the waves, and a second series of measurements near the surface was obtained in which the depths were measured from the instantaneous position of the water surface in each photograph. The two methods of measurement were somewhat different; the deeper measurements were made of the distances between bubble lines, whereas the near-surface measurements had to be made of the distance from the wire that a bubble line traveled in a known number of cine frames. The latter values were about 20% less in the region of overlap, presumably because of the slower flow in the wake of the wire [*Schraub et al.*, 1964]. These values were corrected by this amount and are denoted by solid dots in the figure.

The wind stress for the measured air speed in that experiment was estimated as 0.4 dyne/cm². A velocity profile for a solid boundary at this stress was derived from Deissler's profile and fitted to the measurements in the lower portion of the region (the solid line in Figure 3). This curve differs markedly from the measurements nearer to the surface. A velocity profile for a stress of 0.1 dyne/cm² (dashed line) fits the measurements more closely. Possibly much of the momentum transported vertically from the air to the water, representing the stress of 0.4 dyne/cm², passes into the waves through pressure variations instead of into surface currents through viscosity [*Stewart*, 1961, and personal communication, 1968]. If so, a given wind speed produces less shear stress in the water at the surface than assumed in these calculations. Since the thicknesses of both the viscous and the conduction regions are expected to vary in an inverse manner with the shear stress, the conduction region

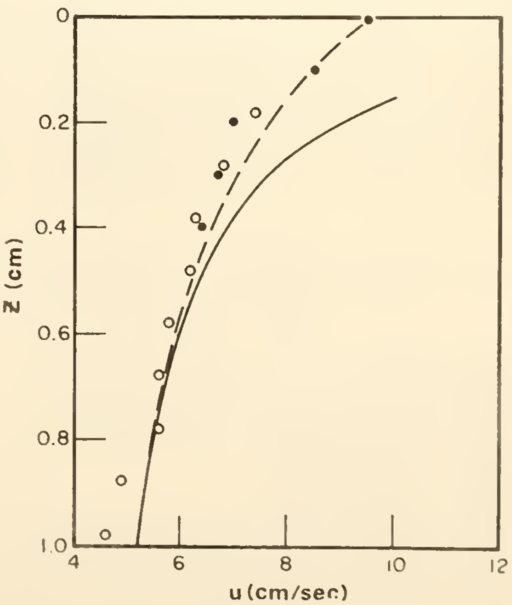

Fig. 3. Velocity profile in the top centimeter of water under a 6-m/sec wind.

at a wind speed of 10 m/sec should extend deeper than shown in Figure 2.

The diffusion to the surface of dissolved gases and other materials would also be inhibited by this factor.

Conduction

The depth region in which conduction is dominant has an especial significance to infrared radiometric measurements of the ocean since this region is largely responsible for the temperature difference between the surface and the bulk water and since it forms the basis for radiometric heat flow measurements. Conversely, it is also a region that can be studied with infrared radiometers. In particular, a heat flow radiometer has demonstrated the existence of this layer under some conditions found in the ocean. A radiometer measuring temperatures at effective depths of 75 and 500 μ obtained values of heat flow to the ocean surface with 2- to 3-m/sec winds that averaged within 20% of the value obtained from empirical formulas [*McAlister*, 1964].

The turbulence near the ocean surface during the radiometric measurement might have been produced by gravitational instability rather than by the wind at these low speeds. A series of laboratory experiments has shown, however, that a conductive layer exists at higher wind speeds with wind-driven turbulence similar to that at sea. An air flow of 4.5 m/sec was passed over a 70 $\times$ 220 $\times$ 4 cm laboratory water surface. Three distinct regions of the water surface could be distinguished: a smooth upwind region containing small-amplitude regular waves; a rough central region containing steep, irregular capillary and gravity waves; and a slick at the downwind end. Wind-driven turbulence began at the upwind end of the rough region and continued into the slick. The water container was insulated from heat loss, and the water was maintained at an approximately constant temperature with electrical heaters. The electrical power input, corrected for small rates of change of the water temperature, represented the total heat flow through the water surface. A different infrared radiometer than mentioned above, measuring temperatures at 25- and 75-μ effective depths, recorded the heat flow through the three distinct regions of the surface in separate experiments. A description of this instrument will appear in a separate publication.

Table 1 shows the experimental conditions and the results of these measurements. The decrease in the heat flow with increasing fetch is attributed to the development of a warm, moist boundary layer in the air. An abrupt change in the temperature near the surface at the beginning of the slick is illustrated by the increased difference between the temperature of the bulk water and that at 25-μ depth. This increase is attributed to a reduction in the turbulence beneath the slick resulting from the rigidity of the slick. The heat flow to the entire surface was obtained from the radiometric measurements with the assumption that the heat flow was constant within each region. The radiometric measurement of heat flow was 93% of the input heat flow. The difference could be ascribed to errors in the experiments. Thus, in

TABLE 1. Measurement of Heat Flow through Different Regions of a Water Surface

	Smooth	Rough	Slick
Fetch distance, cm	0–70	70–160	160–220
Air temperature, °C	17.4	17.1	16.8
Wet-bulb temperature, °C	11.1	11.0	10.7
Bulk water temperature, °C	31.4	31.3	32.7
Radiometer distance, cm	20	110	180
Temperature at 75-μ depth, °C	30.48(3)	30.21(8)	30.44(9)
Temperature at 25-μ depth, °C	30.35(4)	30.11(4)	30.36(4)
Temperature difference, bulk water − 25-μ depth, °C	1.0	1.2	2.3
Radiometric heat flow, cal/cm²/min	2.27	1.83	1.50
Total heat flow, cal/cm²/min	1.96	1.96	2.28
Ratio	1.16	0.93	0.66

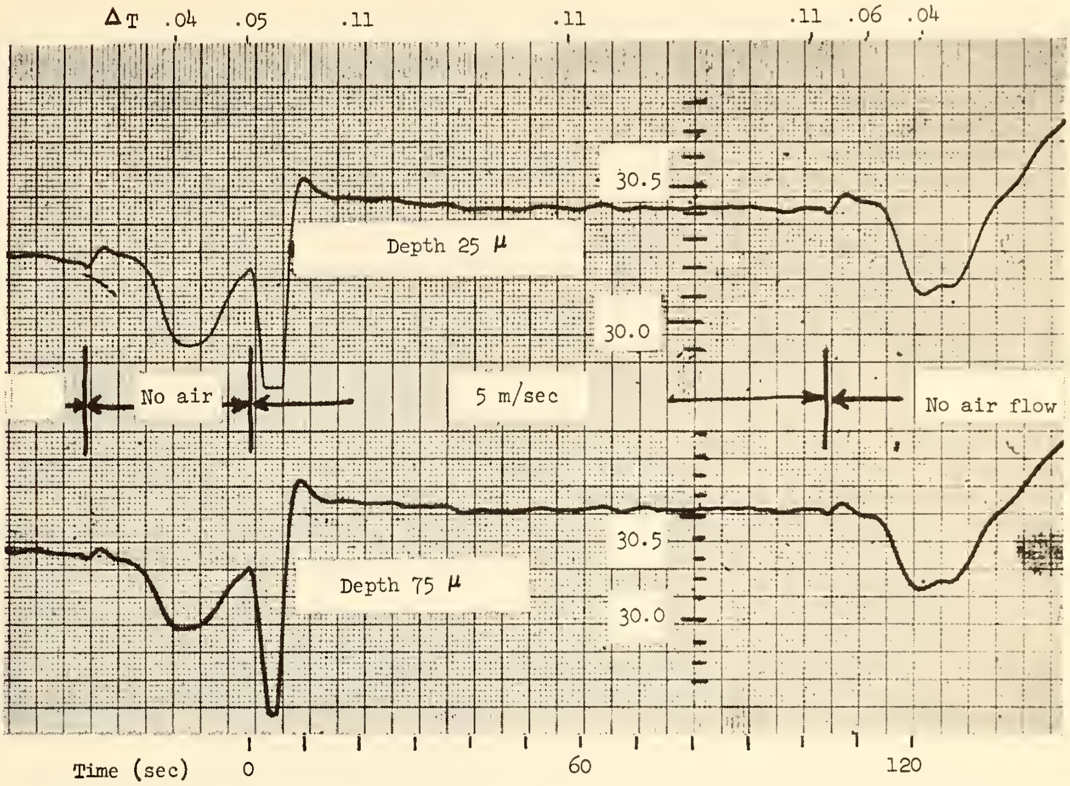

Fig. 4. Two-wavelength radiometer measurements from a laboratory water surface when an air flow is started and stopped. The heat flow is proportional to ΔT.

spite of the wind-driven turbulence and a heat flow several times larger than that commonly occurring in the ocean, the conductive layer was adequately thick for the radiometric measurement of heat flow.

Some relationships between the conductive and the turbulent mechanisms of heat transport are illustrated by radiometric measurements of heat flow in laboratory experiments in which the air flow is started and stopped (Figure 4). The results are interpreted in terms of the structure of the flow near the surface. In these experiments, the air temperature was lower than the water temperature, so that heat was being transferred from the water. The radiometer viewed the 'rough' portion of the surface. The surface temperature decreased rapidly when the air flow was started. This cooling was associated with the development of a nearly laminar flow near the surface. However, the surface temperature rose rapidly when the steep waves and wind-driven turbulence appeared, then remained nearly constant. (*Kanwisher* [1963] observed a decrease in the thickness of the lamellar layer occurring at the onset of capillary waves.) The heat flow was small without air flow and larger during the steady air flow. When the air flow was stopped, the heat removal from the water was seen to be decreased, and the surface temperature rose slightly. With the decay of the wind-driven turbulence in the water, however, the surface again became cooler and the heat flow decreased further. Later, the electrical heaters caused the surface water temperature to rise again. Thus the heat flow and the surface temperature show a close relationship to the air flow and to the state of turbulence in the water near the surface.

Limiting temperature profiles derived from the previous sections may be used to predict some ranges of conditions under which an infrared radiometer can measure the heat flow to a water surface. Radiation with wavelengths near 2.2, 3.8, and 4.8 μ with effective depths near 500, 75, and 25 μ has been used in such measurements. Clearly the transfer of heat by radiation from near the surface will have negligible influence on the measurement, but the turbulent transfer of heat may be significant. Calculations of the errors in heat flow measurements with wavelengths giving 75- and 500-μ effective depths have been made for different intensities of turbulence near the surface. With the approximation of a linear relationship between intensity of radiation and temperature over the small range of temperature near the surface,

$$B_\nu(T) - B_\nu(T_0) = a(T - T_0) \qquad (5)$$

the intensity of radiation within a narrow bandwidth received by a radiometer is

$$I_\nu = ak_\nu \int_0^\infty T(z) \exp(-k_\nu z)\, dz - aT_0 + B_\nu(T_0) \qquad (6)$$

and the temperature read by the radiometer is

$$T_r = k_\nu \int_0^\infty T(z) \exp(-k_\nu z)\, dz \qquad (7)$$

The expected reading for each of the two wavelengths with a given temperature profile was calculated by a computer summation, and the expected error in a heat flow measurement was determined. Temperature profiles taken from *Deissler* [1955] with stresses expected for wind speeds of 2, 3.5, 5, and 10 m/sec gave predicted errors of 0, 0, 14, and 35%, respectively, with the 75- and 500-μ effective depths. If the conduction layer were no thicker than that at a solid boundary with the same total stress, these results would indicate that either the 500-μ effective depth infrared region should not be used with wind speeds of 5 m/sec or more, or else a correction factor based on the wind speed should be applied. No significant error from turbulence would be expected at these wind speeds with a radiometer using effective depths of 25 and 75 μ.

Acknowledgments. We are indebted to R. W. Stewart for advice in the interpretation of the velocity profile. R. C. Steinbach wrote the computer programs, and J. Cook assisted in the measurement of the velocity profile.

This research was supported by the Office of Naval Research, codes 461 and 481; Naval Oceanographic Office, code 7007; and National Science Foundation, Atmospheric Sciences Section, grants GA-854 and GA-1491.

References

Deissler, R. G., Analysis of turbulent heat transfer, mass transfer, and friction in smooth tubes at high Prandtl and Schmidt numbers, *NACA Rept. 1210,* 14 pp., 1955.

Goulard, R., and M. Goulard, One-dimensional energy transfer in radiant media, *Intern. J. Heat Mass Transfer, 1,* 81–91, 1960.

Häussler, I. W., Über die temperaturprofile beiderseits einer verdunstenden wasseroberfläche, *Wiss. Z. Tech. Hochsch. Dresden, 5,* 435–450, 1956.

Irvine, W. M., and J. B. Pollack, Infrared optical properties of water and ice spheres, *Icarus, 8*(2), 324–360, 1968.

Kanwisher, J., On the exchange of gases between the atmosphere and the sea, *Deep-Sea Res., 10,* 195–207, 1963.

Lick, W., Transient energy transfer by radiation and conduction, *Intern. J. Heat Mass Transfer, 8,* 119–127, 1965.

McAlister, E. D., Infrared optical techniques applied to oceanography, 1, Measurement of total heat flow from the sea surface, *Appl. Optics, 3*(5), 609–612, 1964.

McAlister, E. D., Using infrared to measure heat flow from the sea, *Ocean Ind., 2*(5), 35–39, 1967.

McLeish, W. L., On the mechanism of wind-slick generation, Ph.D. thesis, University of Washington, Seattle, 1967.

Neumann, G., and W. J. Pierson, *Principles of Physical Oceanography,* pp. 255 and 421, Prentice-Hall, Englewood Cliffs, N. J., 1966.

O'Brien, E., On the flux of heat through laminar wavy liquid layers, *J. Fluid Mech., 28,* 295–303, 1967.

Plyler, E. K., and N. Acquista, Infrared absorption of liquid water from 2 to 42 microns, *J. Opt. Soc. Am., 44*(6), 505, 1954.

Saunders, P. M., The temperature at the ocean-air interface, *J. Atmospheric Sci., 24,* 269–273, 1967.

Schraub, F. A., S. J. Kline, J. Henry, P. W. Runstadler, Jr., and A. Littel, Use of hydrogen bubbles for quantitative determination of time dependent velocity fields in low speed water flows, Thermosciences Division, Department of Mech. Engineering, Stanford University, 1964.

Stewart, R. W., The wave drag of wind over water, *J. Fluid Mech., 10,* 189–194, 1961.

Timofeev, Yu. M., Thermal sounding of surface water layers by means of thermal radiation, *Izv. Atmospheric Oceanic Phys., 2*(7), 772–774 (translated by F. Goodspeed), 1966.

(Received August 5, 1968;
revised January 27, 1969.)

Reprinted from "Oceans from Space,"
Gulf Publishing Co., Houston, Texas, 38-45.

3. The potential application of remote sensing to selected ocean circulation problems

Raymond M. Nelson, *General Physical Scientist, Institute for Oceanography, Environmental Science Services Administration.*

Introduction

As part of its mission, Environmental Science Services Administration (ESSA) has the long-term problem of monitoring the ocean and the related physical environment. Its purpose is to understand the physical processes and improve prediction techniques so that it can enhance its existing scientific services and anticipate new ones, emphasizing the problem of environmental hazards. It is obvious that to do this job, all facets of oceanography will have to advance on a broad front, such as the development of new tools, the inception of new ideas, the refinement and broadening of the various theories, and a worldwide continuous measurement program.

We believe in an integrated program of coordinated data collection, using each tool where it can perform best, applying as many parameters and dimensions as appropriate. A major part of this problem is ocean circulation, and we look forward to the prospect of using air/space as a surveillance and data collection medium.

Therefore, ESSA is experimenting with remote sensing (in addition to many other techniques) as an additional method to apply to the various problems. Stommel,[9] McAlister,[4] Gifford Ewing[3] and others have pioneered in applying aerial photography and airborne infrared radiation devices to oceanography. This work has been continued by many, both in and out of government. We are interested in aircraft and spacecraft capability, but at present we are in the experimentation and problem defining stage, exploring potential usage.

Another phase of remote data collection is the interrogation of buoys from air or space, where the buoys are either stationary, or free floating, such as surface and subsurface types. Although ESSA is interested in all phases of such instrument application, this chapter is confined to potential usage of remote sensing to certain aspects of ocean currents and circulation problems.

Nimbus 2 imagery

An examination of Nimbus 2 high resolution infrared (HRIR) line scan imagery shows that high thermal contrasts on the water surface are discernible. Nimbus 2 was designed to be a meteorological satellite, and since the ground spot size is approximately 23 miles,[6] any data about the water surface is a distinct bonus. Allison, Foshee, and Warnecke at NASA, Goddard, and Wilkerson at the Naval Oceanographic Office[1] collaborated on determining water surface temperatures from such data. Although the problems of clouds and radiation transmission losses are obvious, the Nimbus 2 HRIR imagery as compared with correlated ESSA satellite photography shows periods of cloudless skies off the east coast of the United States where the high contrast, thermal surface and boundary of the Gulf Stream can be detected, and point temperature distributions could be measured between clouds. Time-sequence analyses of such quasi-synoptic coverage over large areas of the ocean could show surface thermal drift, possibly boundary regions for currents, and may reveal previously undisclosed surface circulation effects.

For example, Figure 3-1A is an ESSA-1 television picture of the east coast of the United States and was exposed at 17:38Z (Z represents Greenwich Civil Time) on June 2, 1966. Figure 3-1B, a Nimbus 2 HRIR photograph, was exposed at 04:26Z (night), June 3, 1966, 11 hours after the ESSA-1 photograph. The front line appears to have moved farther east on the infrared photograph, and some cloud patterns, imaged near the coast on the ESSA-1 photograph, are not discernible on the Nimbus exposure. Aircraft coverage at the time of this Nimbus orbit proved that the local sky was free of clouds.

The surface effects of another western boundary current are also discernible. Figures 3-2A and B are two Nimbus 2 HRIR images of the extension of the Agulhas Current (see arrows) south of the Cape of Good Hope, Africa. Figure 3-2A was exposed September 18, 1966 at night, and Figure 3-2B the next night.

An example of Nimbus 2 HRIR daylight effects are provided in the next series of illustrations. Figure 3-3A, B, and C are ESSA-1 television pictures exposed May 24, 1966. Figure 3-3A and B at approximately 17-55Z, Figure 3-3C at 16:17Z (day). Figure 3D is a Nimbus 2 HRIR photograph collected on the same date at approximately 14:57Z (day). An imagery comparison shows similar cloud patterns. If the boundary lines and the possible warm cell (arrows on Figure 3-3D) are really water surface effects (the ESSA-1 photographs are remarkably free of clouds in

Figure 3-1A: ESSA-1 television photo of U.S. east coast and adjacent waters of Atlantic Ocean.

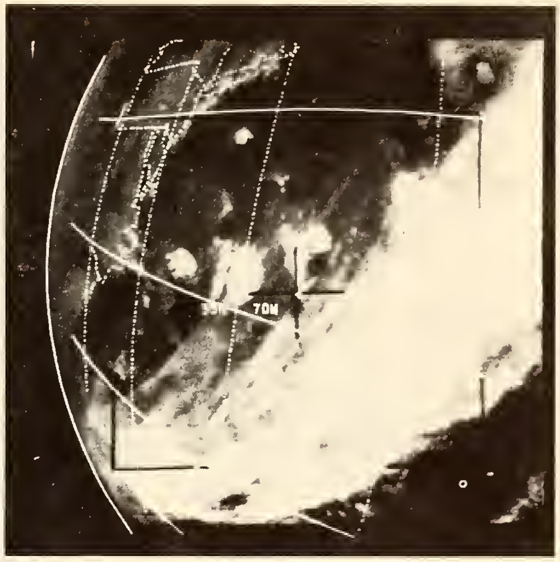

these areas), we would like to have ships and buoys out there monitoring such effects in depth. However, this kind of comparison when no ground check is available, indicates a need for multiple simultaneous sensors to reduce the problem of ambiguity.

Meteorological thermal discontinuities have been collected in a visually transparent atmosphere with airborne infrared systems, causing an ambiguity in attempts to analyze the water surface. Oshiver, et al,[7] in an aircraft/ship experiment with infrared radiometers and meteorological data collectors over continental shelf water southeast of New York City, discovered a low altitude visually transparent atmospheric lens that created a sharp discontinuity in the data from the airborne radiometer. This discontinuity was not observed with a similar radiometer mounted over the bow of the ship. The discontinuity was identified as a lens from information supplied by meteorological instruments attached to a captive balloon as it was raised and lowered from the ship. Similarly, Clark[2] at the U. S. Naval Research Laboratory used airborne infrared radiometers to record and assemble a statistical history of low altitude visually transparent convection cells over north Atlantic and Gulf Stream water. The apparent temperature discontinuities of such cells are no more than approximately 1° C, and the horizontal dimensions range from 1-10 miles.

In addition to such low altitude phenomena, there are other effects, such as small cloud patches, haze, and thin stratus and cirrus cloud patterns, within the noise level of existing ESSA and Nimbus satellite television camera systems. Such phenomena cannot be resolved on Nimbus 2 HRIR data, on either day or night exposures.

Many theories of the Gulf Stream hold that meanders can be expected almost anywhere. Therefore, high spatial resolution, multi-sensor surveil-

Figure 3-1B: Nimbus 2 high resolution infrared photo of U.S. east coast and gulf stream.

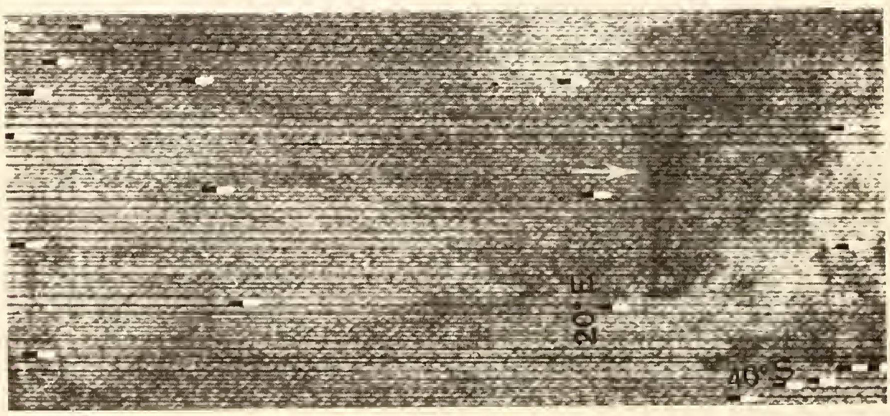

Figure 3-2A: Nimbus 2 photo off the southern tip of the Cape of Good Hope, Africa. Arrows show extension of Agulhas Current.

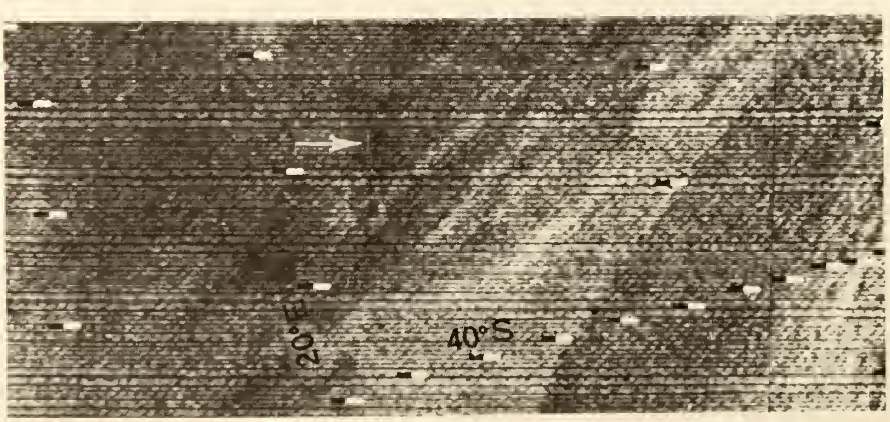

Figure 3-2B: Nimbus 2 photo off the southern tip of the Cape of Good Hope, Africa. Exposure about 24 hours after Figure 3-2A.

Figure 3-3A (left): ESSA-1 television photo of area off the U.S. east coast. Figure 3-3B (right): ESSA-1 television photo of area south of Nova Scotia.

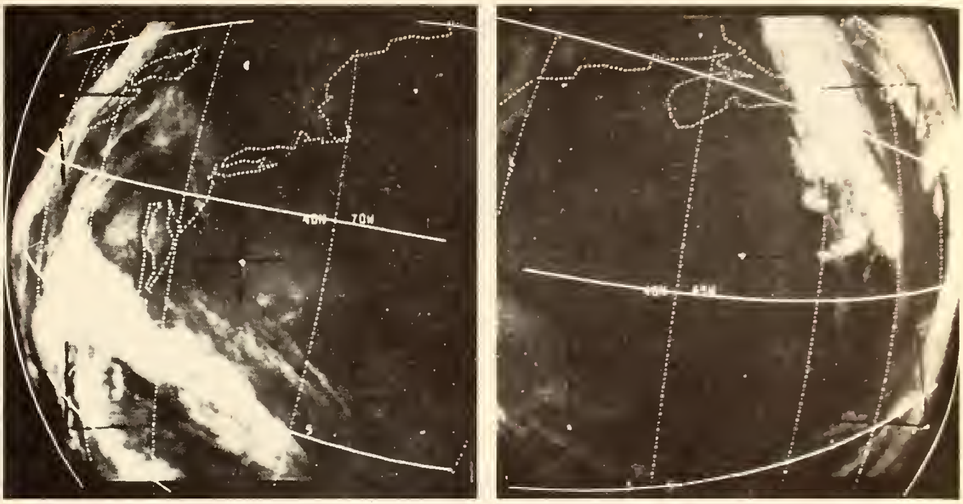

lance systems, including microwave with a cloud penetration capability, are necessary to detect meanders, at which time ships and aircraft could be sent to monitor them in greater detail. Information from both satellite and aircraft may contribute to reducing the ambiguity of interpretation of both remote sensing and ship recorded data. A time-sequence analysis of the evolutionary pattern could show the rate and size of growth, and the pinching off into an eddy, and decay. In time, we would like to predict the development, location, and size of meanders, as well as their likelihood of invading the banks and the fishing grounds. We would also like to know if meander dynamics are the same for the right as for the left side of the Gulf Stream.

Time-sequence charting of surface currents boundaries, as to shape, size, and location, will be another element toward understanding the total dynamics, in addition to providing data for the shipping industry. The interface of the Gulf Stream with the Labrador current and the transmission into the North Atlantic current are particularly interesting.

The capability of an aircraft infrared line scan system to detect an ocean eddy is illustrated in Figure 3-4. After detecting an eddy, a ship can make surface and subsurface profile passes at the same time an aircraft collects such imagery. Thermal profiles generated from microdensitometer cans across the image can be correlated with a ship-towed surface thermistor for calibration and comparison. Time-sequencing by the aircraft, such as at 15-20 minute intervals, could reveal the motion within the eddy, assuming the eddy shape effects are maintained and move during the time period. From short-time-sequence data collection by both ship and aircraft, information on eddy motion and its three dimensional size and shape could be obtained, and probably reduce ambiguity of data interpretation. Longer time-sequencing could show changes in position, size, and shape.

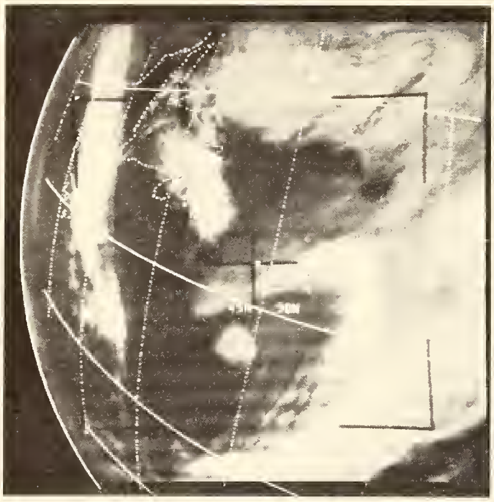

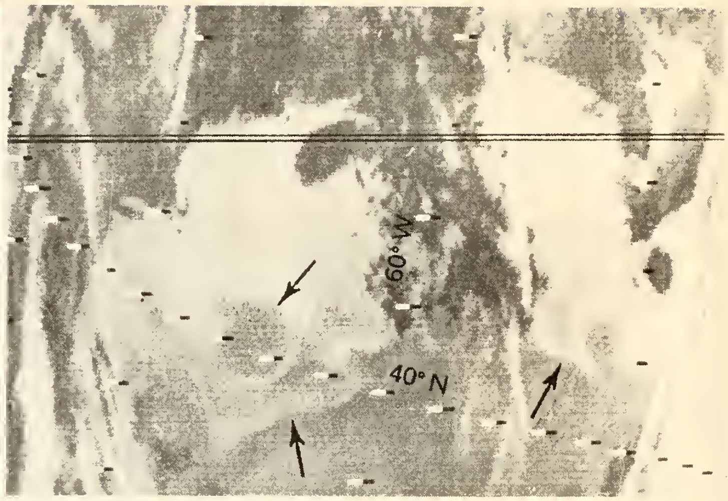

Figure 3-3C (left): ESSA-1 television photo south and east of Newfoundland. Figure 3-3D (right): Nimbus 2 photo of north Atlantic south of New England, Nova Scotia and Newfoundland.

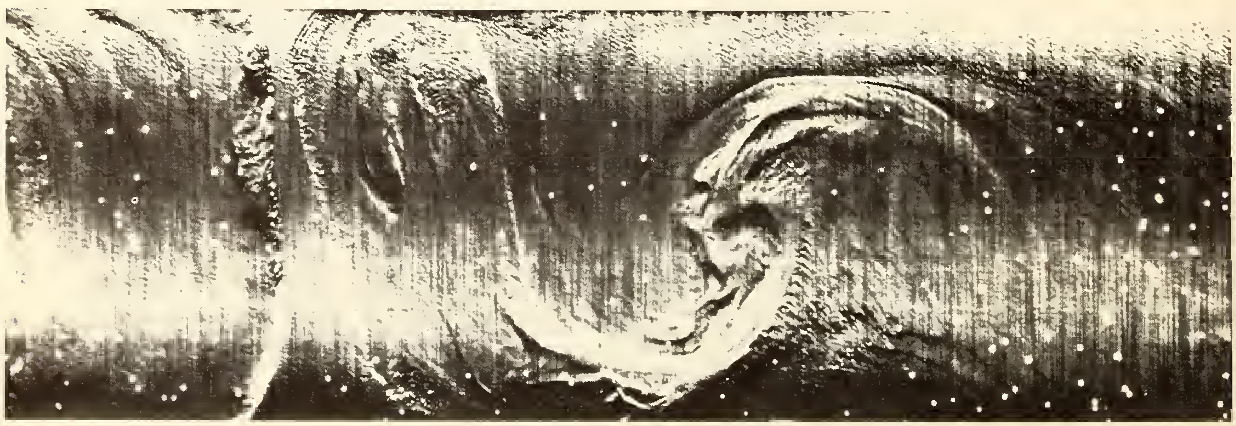

Figure 3-4: Taken 200 miles east of Cape Cod, this photo clearly illustrates the capability of an aircraft infrared line scan system to detect an ocean eddy.

Figure 3-5, is an aircraft color photo of an eddy in the Caribbean, north of St. John, Virgin Islands. Again a time sequencing of 10-15 minutes between photographs may reveal eddy motion. An additional goal with aircraft sensors is to examine the complex structure of eddy mixing, as well as boundary current interfaces with other water masses.

In some areas, such effects as eddies, meanders, and major changes in current direction will require a continuous surveillance capability just to

Figure 3-5: Aircraft photo of an eddy in the Caribbean, north of St. John, Virgin Islands.

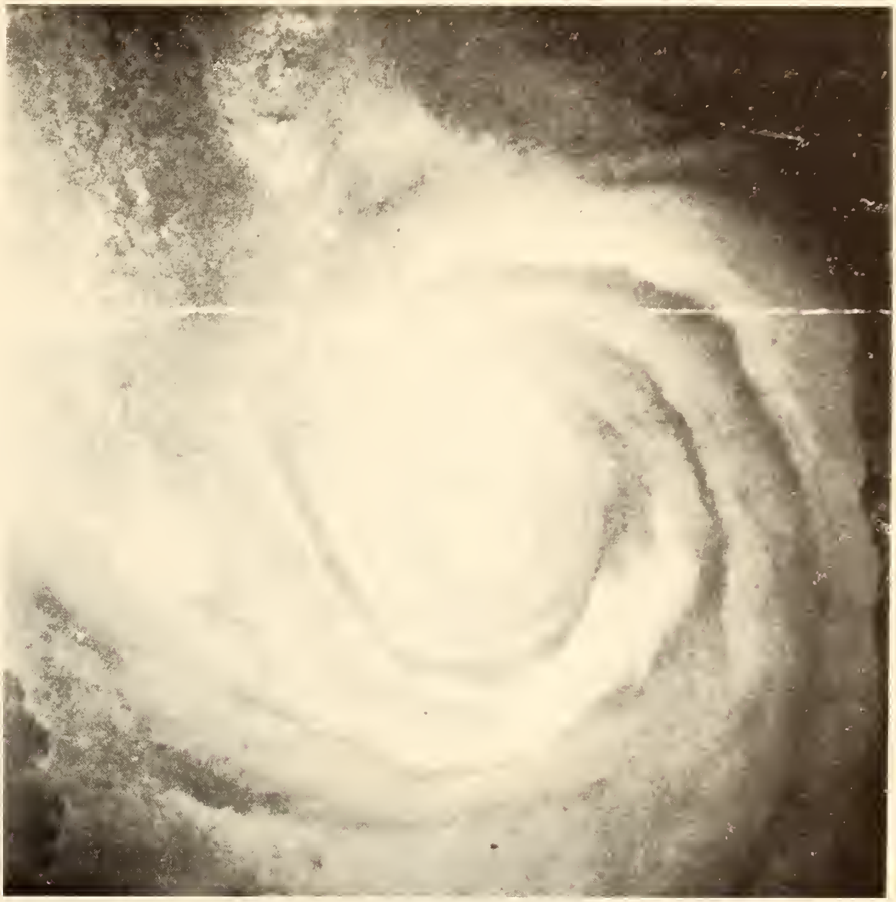

find them. Space sensors will do yeoman's work in this regard, but aircraft systems will also have their place.

Plans for the future

What are ESSA's plans for the near future? First, aircraft/ship experimentation programs will continue. Then in 1969, the ESSA Barbados Oceanographic and Meteorological Experiment will take place during the summer, covering a part of the eastern Caribbean and a small section of the Atlantic due east of the Antilles arc. Present plans are to use sensors ranging in heights from satellite altitudes down to the sea floor. The experiment is designed to serve as a pilot field study for the Global Atmospheric Research Program (GARP) of the World Weather Watch. Later, in the early 70's, the Tropical Meteorological Experiment (Tromex) is scheduled, and some consideration is being given to expanding it to a Tropical Environmental Experiment. In FY 1971, the satellite systems Improved TOS N and O and Advanced Polar Orbiting Satellites (APOS) A and B may carry laser altimeters for determining variations of sea level for geodetic purposes.

The distant future, however, is more nebulous. For example, since the cost of keeping aircraft in the air is extremely high, we have considered the concept of "aircraft of opportunity" as a possible means of reducing such long-term costs. Many airlines run over the oceans on daily schedules, both night and day. The possibility of equipping such aircraft with sensors where all the commercial pilot has to do is flip a few switches to turn them on and off has a certain amount of merit.

However, the ocean is an international problem, and to exploit the global surveillance capability of spacecraft will require international cooperation, possibly under a central cooperative control, where as automated data are displayed and critical changes in meteorological and oceanographic effects or patterns are detected aircraft and ships in the area can be sent to monitor a region in greater detail.

It is understood that the problems are many, and industry's scientific effort is needed just as much as its tools. There is a long way to go, but we feel that a start has been made.

References

1. Allison, L. J., L. L. Foshee, G. Warnecke, and J. C. Wilkerson, 1966: "An Analysis of the North Wall of the Gulf Stream Utilizing Nimbus 2 High Resolution Infrared Measurements," Gulf Stream Symposium, Am. Geophysical Union, April 17-21.

2. Clark, H., 1967: (Private Communication), U. S. Naval Research Laboratory, Applied Oceanography Branch, Washington, D.C., "Clear Air Convection Cells," March.

3. Ewing, Dr. G. C., 1966: "The Use of Film as a Sensor," Minutes of the Fourth Meeting Ad Hoc Spacecraft Oceanography Advisory Group, Spacecraft Oceanography Project, U. S. Naval Oceanographic Office, October 18-19, p. 12.

4. McAlister, E. D., 1964: "Infrared-Optical Techniques Applied to Oceanography: I Measurement of Total Heat Flow from the Sea Surface," Applied Optics, 3, pp. 609-612.

5. McAlister, E. D. and W. L. McLeish, 1965: "Oceanographic Measurements with Airborne Infrared Equipment and Their Limitations," Oceanography from Space, Woods Hole Oceanographic Institution, Woods Hole, Mass., pp. 189-214.

6. NASA, Goddard Space Flight Center, (Private Communication).

7. Oshiver, A. H., G. A. Berberian, J. R. Clark and R. B. Stone, 1965: "Factors in Measurement of Absolute Sea Surface Temperature by Infrared Radiometry," Proceedings of the Third Symposium on Remote Sensing, Univ. of Mich., Ann Arbor, pp. 737-762.

8. Smith, G., 1963: "Color - A New Dimension in Photogrammetry," Photogrammetric Engineering, Nov. 1963, Figure 7, pp. 999-1013.

9. Stommel, H. M., W. S. Von Arx, D. Parson, and W. S. Richardson, 1953: "Rapid Aerial Survey of Gulf Stream with Camera and Radiation Thermometer," Science, 117, pp. 639-640.

Reprinted from Hot Brines and Recent Heavy Metal Deposits in the Red Sea, Springer-Verlag, New York, 18-21.

A Fourth Brine Hole in the Red Sea?

FEODOR OSTAPOFF

Atlantic Oceanographic Laboratories
Sea Air Interaction Laboratory
Miami, Florida

Abstract

This paper discusses some of the results of the **OCEANOGRAPHER** (USC & GSS) crossing of the Red Sea. A possible new hot hole was observed 617km north-northwest of the original hot brine area. Three reflecting layers were observed in the Atlantis II Deep that are apparently related to the different brine layers.

Recently a number of publications (Swallow and Crease, 1965; Krause and Ziegenbein, 1966; Miller *et al.*, 1966; Hunt *et al.*, 1967; Ross and Hunt, 1967; and Munns *et al.*, 1967) have dealt with the interesting problem of the hot brine holes in the Red Sea. Three such hot brine holes were discovered, documented and subsequently named Atlantis II Deep, Discovery Deep and Chain Deep. All three are located in a small area of less than 10 by 10 nautical miles.

In May, 1967 the USC & GSS **OCEANOGRAPHER** traversed the Red Sea on her scientific Global Expedition. A station in the Atlantis II Deep was occupied at the position 21°25′02″N and 38°03′03″E to obtain large volume water samples and cores for specialized analysis. The depth recorder was operating all the time. Positions were determined by satellite fixes taken every few hours.

The **OCEANOGRAPHER** is equipped with a General Electric narrow beam (2.66° at 3db) mechanically stabilized sound transducer system and operates on 19KHz. The recording is made on a precision fathometer recorder (Raytheon PFR-193A). The calibration is set at 1,463msec^{-1}. Fig. 1 is a sample of the PFR record, recorded while on station in the Atlantis II Deep. Three characteristic sound reflections indicate the presence of the hot brine. The weakest reflection at 1,034 fathoms (1,891m), and two stronger reflections are found at 1,041 and 1,057 fathoms (1,904 and 1,933m), respectively. All depths quoted in this paper are uncorrected.

The **OCEANOGRAPHER's** fathogram may be compared with a number of similar records which were obtained by **METEOR**

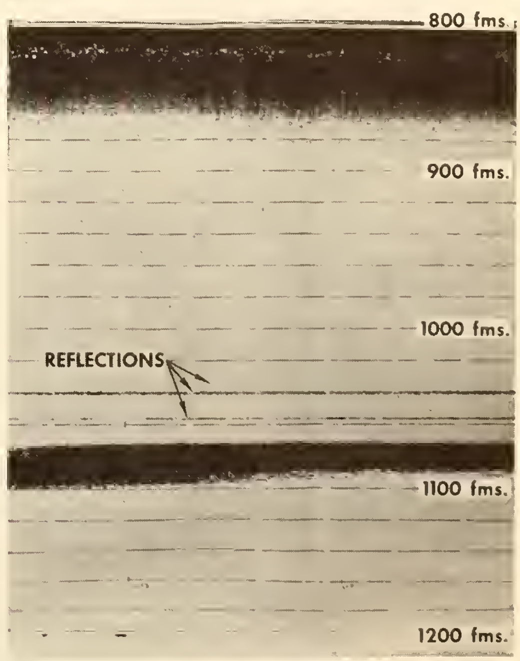

Fig. 1. Narrow-beam echo-sounder record obtained on **OCEANOGRAPHER** while on station in Atlantis II Deep at 21°25′2″N and 38°13′13″E. Depth scale uncorrected.

and published by Krause and Ziegenbein (1966). The **METEOR** carried the ELAC narrow-beam sounder 1 CO operating at the frequency of 30KHz with a beam width of 2.8° at 3db. The transducer is mechanically stabilized and calibrated for a sound speed of 1,500$msec^{-1}$.

Considering the instrumental limitations and differences, the agreement between the **OCEANOGRAPHER's** PFR record and the **METEOR's** PDR record is rather good. The travel time of the sound waves between the surface and the first reflection for the **METEOR** instrument and the **OCEANOGRAPHER** instrument are about the same (estimated as less than 4m). The **METEOR** station was located less than 4km to the south-southwest of the **OCEANOGRAPHER's** station. Thus, the **OCEANOGRAPHER** found, about two years later, conditions similar to those observed by the **METEOR** as far as the layering structure is concerned.

Table 1 presents scaled distances in meters between the identifiable reflectors. Individual differences appear to be relatively large, although the distance between the first and the third reflecting surface is very little. The differences may arise from the fact that one echo-sounder operates on 19KHz, the other on 30KHz; thus, different scatterers may have been involved.

The three different reflecting layers correlate well with the temperature structure observed by Ross (1969). These layers occur at depths of large temperature and salinity changes (Table 2) and are probably due to the increase in density associated with these changes.

The narrow-beam deep echo-sounding systems used on the **METEOR** and **OCEANOGRAPHER** thus proved to be useful tools in detecting, among other things, the hot brine holes. Scanning the PFR records for specific characteristic features revealed an interesting reflection in a very narrow hole located some 617km north-northwest of the original hot brine area. It was named Oceanographer Deep. A reproduction of the original record is presented in Fig. 2. The bottom of the hot hole was observed at 785 fathoms (1,446m). The Oceanographer Deep measures on top 5.5km and is at the bottom about 1.0km wide along the trackline. East-west dimensions are unknown. Possibly the course of the **OCEANOGRAPHER** may have crossed the hole as its outer edge. The reflection can

Table 2 Comparison of Depths of Reflecting Layers and Temperature Structure as Observed by Ross, 1969

(All depths uncorrected fathoms)

Reflecting Layers	Depth	Temperature Structure	Depth
1	1,034	Start of hot brine	1,025
2	1,041	Start of 44°C water	1,037
3	1,057	Start of 56°C water	1,054

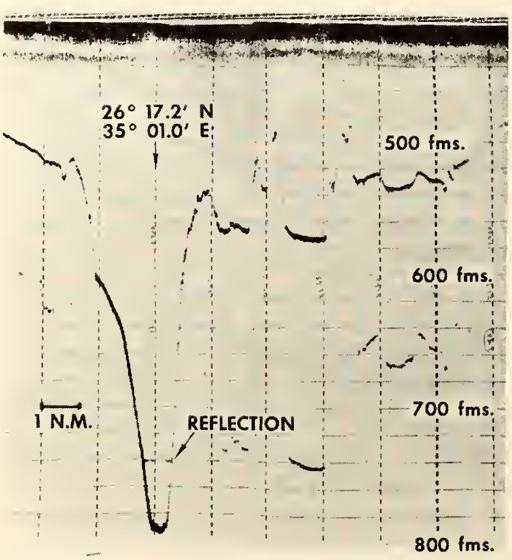

Fig. 2. Narrow-beam echo-sounder record obtained on **OCEANOGRAPHER** showing one reflecting layer. Depth scale uncorrected.

Table 1 Distances in Meters Between Reflecting Layers for the METEOR and OCEANOGRAPHER Records

	1st–2nd layer	2nd–3rd layer	1st–3rd layer
METEOR	8m	31m	39m
OCEANOGRAPHER	13m	29m	42m

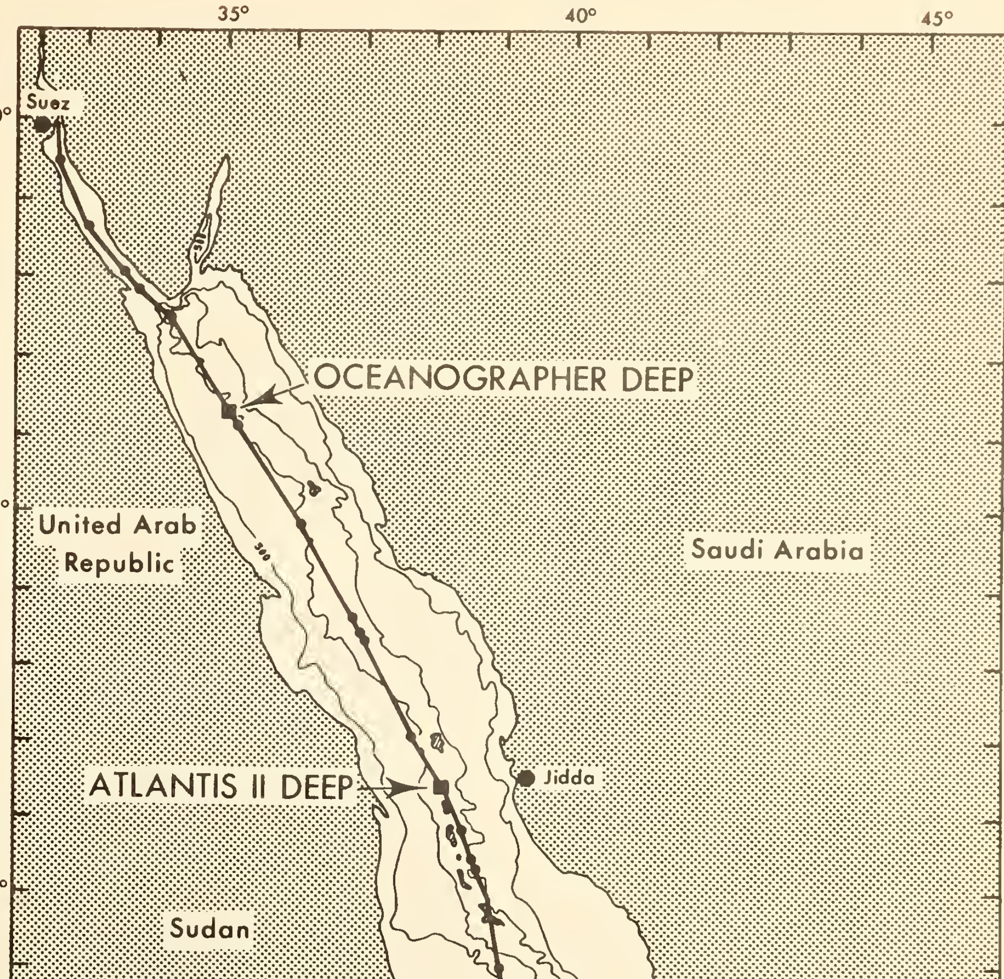

Fig. 3. Trackline of the **OCEANOGRAPHER** through Red Sea showing geographic locations of Atlantis II Deep and Oceanographer Deep; 500m and 1,000m contour lines after Drake and Girdler (1964).

be clearly identified and seems rather strong, raising the suspicion of a possible hot hole in an unsuspected area and at a shallower depth than the other three known holes.

Most of the available records from the other holes show multiple reflections unlike the one from the Oceanographer Deep, which reveals only one reflecting layer at an uncorrected depth of 741 fathoms or 1,355m (Fig. 2). Krause and Ziegenbein (1966) published a record obtained at Meteor station 28 (21°17.2′N, 38°02.5′E) from the eastern edge of the Discovery Deep with only one reflecting layer.

Fig. 3 shows the trackline of the **OCEANOGRAPHER**, the location from which the PFR record (Fig. 2) was obtained in relation to the Atlantis II Deep where the record (Fig. 1) was obtained. Indeed, if the Oceanographer Deep does contain hot brine, for the proof of which we must await further research, then a new area of hot holes has been found, probably belonging to a separate system.

Acknowledgment

The author would like to thank participating scientists and the crew of the USC & GSS **OCEANOGRAPHER** for their efforts; in particular, Mr. W. Moore of New York State University at Stony Brook, Long Island and Dr. J. Swinnerton of the Naval Research Laboratory, Washington, D.C., for their assistance searching the voluminous records.

References

Drake, C. L. and R. W. Girdler: A geophysical study of the Red Sea. Geophys. J. Royal Astro. Soc., **8**, 473 (1964).

Hunt, J. M., E. E. Hays, E. T. Degens, and D. A. Ross: Red Sea: detailed survey of hot brine areas, Science, **156**, 514 (1967).

Krause, G. and J. Ziegenbein: Die structur des heissen salzreichen Tiefenwassers im Zentralen Rotem Meer. METEOR-Forschungsergebnisse Reihe A. **1**, Gebr. Borntraeger, 53 (1966).

Miller, A. R., C. D. Densmore, E. T. Degens, J. C. Hathaway, F. T. Manheim, P. F. McFarlin, R. Pocklington, and A. Jokela: Hot brines and recent iron deposits in deeps of the Red Sea. Geochimica et Cosmochimica Acta, **30**, 341 (1966).

Munns, R. G., R. J. Stanley, and C. D. Densmore: Hydrographic observations of the Red Sea brines. Nature, **214**, 1215 (1967)

Ross, D. A.: Temperature structure of the Red Sea brines. *In: Hot brines and recent heavy metal deposits in the Red Sea*, E. T. Degens and D. A. Ross (eds.). Springer-Verlag New York Inc., 148–152 (1969).

Ross, D. A. and J. M. Hunt: Third brine pool in the Red Sea. Nature, **213**, 687 (1967).

Swallow, J. C. and J. Crease: Hot salty water at the bottom of the Red Sea. Nature, **205**, 165 (1965).

Reprinted from Journal of Marine
Research, Vol. 27, No. 1, 24-31.

Deep Water Properties and Flow in the Central North Pacific[1]

R. K. Reed

Pacific Oceanographic Research Laboratory
Environmental Science Services Administration
Seattle, Washington 98102

ABSTRACT

Values of potential temperature, salinity, and dissolved oxygen at deep levels in the central North Pacific are presented and discussed, and the direction of flow is inferred. Deep water from the south appears to spread into the northern region by way of a western route rather than directly through the central region.

Introduction. The flow of Pacific deep water has been inferred by Knauss (1962) from the distribution of temperature, salinity, and radioactive carbon. He concluded that all water below 2500 m in the Pacific is from a single source to the south, that the flow is predominantly northward, and that the return flow occurs in the upper layers as a result of rising water in the North Pacific. At a given depth, the general trend is for temperature to increase and for salinity and dissolved oxygen to decrease toward the north, primarily because of mixing with overlying water that is warmer, less saline, and contains less oxygen than the source water. The effect of heat flow from the earth's interior was deemed by Knauss to be of less importance than a modification by upper water.

Recently, numerous deep measurements have been made in the central North Pacific. Many of the measurements were taken by the Coast and Geodetic Survey (C & GS) and by the Pacific Oceanographic Research Laboratory (PORL) as part of an ocean-survey program (SEAMAP). Although plans call for further work in this area and for an extension to the entire Pacific, it seems desirable at this time to present the results derived from existing data.

Methods. The C & GS-PORL cruises were designed so that certain sites were reoccupied during the 1961–1966 period. Table I is a summary of the

1. Accepted for publication and submitted to press 14 August 1968.

Table I. Deviations from the means of potential temperature, salinity, and dissolved oxygen at reoccupied sites (C&GS-PORL cruises, 1961–1966) at levels of 3, 4, and 5 km. The sites are indicated in Figs. 1 and 2 by bars over the plotted values.

Potential temperature (°C)		Salinity (‰)		Dissolved oxygen (ml/l)	
Deviation from mean	Number of values	Deviation from mean	Number of values	Deviation from mean	Number of values
0.00	33	0.000–0.004	52	0.00–0.04	36
0.01	38	0.005–0.008	29	0.05–0.08	33
0.02	16	0.009–0.012	4	0.09–0.12	12
0.03	4	total	85	0.13–0.16	3
0.04	2			0.17–0.18	2
total	93			total	86
Number of values exceeding 0.02°C = 6% of total.		Number of values exceeding 0.008‰ = 5% of total.		Number of values exceeding 0.12 ml/l = 6% of total.	

deviations from the mean values found at these sites at depths of 3, 4, and 5 km. Approximately 95% of the temperatures do not vary from the means by more than 0.02°C; comparable values for salinity and dissolved oxygen are 0.008‰ and 0.12 ml/l. These values, except for dissolved oxygen, are close to most estimates of the random errors in these oceanographic measurements. Carritt and Carpenter (1966), however, showed that random and systematic errors in oxygen data may be as great as 1 ml/l; thus a value of 0.12 ml/l, coupled with the absence of trends, does not appear significant. Furthermore, temperature data taken over a span of more than a decade revealed no temporal changes of sufficient magnitude to influence the following analysis. Consequently, data from various periods and sources were used. Examination of all of the data allowed some random and systematic errors to be detected.

The data are identified in Table II and Fig. 1. Figs. 1 and 2 show the distribution of potential temperature (computed according to Fofonoff 1962), salinity (obtained with a salinometer), and dissolved oxygen at 5 and 4 km. The bathymetry shown is from Rechnitzer and Terry (1965).

Discussion. Fig. 1 shows that water colder than 1.05°C occurs in the southern sector of the area. Temperatures lower than 1.10°C appear in zones just north of the Hawaiian Rise and just south of the Aleutian Islands; between these areas the water is about 0.05°C warmer. As expected, the less-saline and less-oxygenated water generally coincides with the warmer water. Although dissolved oxygen is subject to change by biological processes, the fact that its distribution pattern is very similar to the distribution of temperature and salinity suggests that oxygen may be treated as a conservative property


170°
180°
170°
160°
150°
60°
50°
40°
30°
20°
10°
3.60
3.50
3.40
3.40
3.50
3.60
3.70
1.00
Oxy

Table I. Deviations from the means of potential temperature, salinity, and dissolved oxygen at reoccupied sites (C&GS-PORL cruises, 1961–1966) at levels of 3, 4, and 5 km. The sites are indicated in Figs. 1 and 2 by bars over the plotted values.

Potential temperature (°C)		Salinity (‰)		Dissolved oxygen (ml/l)	
Deviation from mean	Number of values	Deviation from mean	Number of values	Deviation from mean	Number of values
0.00	33	0.000–0.004	52	0.00–0.04	36
0.01	38	0.005–0.008	29	0.05–0.08	33
0.02	16	0.009–0.012	4	0.09–0.12	12
0.03	4	total	85	0.13–0.16	3
0.04	2			0.17–0.18	2
total	93			total	86
Number of values exceeding 0.02°C = 6% of total.		Number of values exceeding 0.008‰ = 5% of total.		Number of values exceeding 0.12 ml/l = 6% of total.	

deviations from the mean values found at these sites at depths of 3, 4, and 5 km. Approximately 95% of the temperatures do not vary from the means by more than 0.02°C; comparable values for salinity and dissolved oxygen are 0.008‰ and 0.12 ml/l. These values, except for dissolved oxygen, are close to most estimates of the random errors in these oceanographic measurements. Carritt and Carpenter (1966), however, showed that random and systematic errors in oxygen data may be as great as 1 ml/l; thus a value of 0.12 ml/l, coupled with the absence of trends, does not appear significant. Furthermore, temperature data taken over a span of more than a decade revealed no temporal changes of sufficient magnitude to influence the following analysis. Consequently, data from various periods and sources were used. Examination of all of the data allowed some random and systematic errors to be detected.

The data are identified in Table II and Fig. 1. Figs. 1 and 2 show the distribution of potential temperature (computed according to Fofonoff 1962), salinity (obtained with a salinometer), and dissolved oxygen at 5 and 4 km. The bathymetry shown is from Rechnitzer and Terry (1965).

Discussion. Fig. 1 shows that water colder than 1.05°C occurs in the southern sector of the area. Temperatures lower than 1.10°C appear in zones just north of the Hawaiian Rise and just south of the Aleutian Islands; between these areas the water is about 0.05°C warmer. As expected, the less-saline and less-oxygenated water generally coincides with the warmer water. Although dissolved oxygen is subject to change by biological processes, the fact that its distribution pattern is very similar to the distribution of temperature and salinity suggests that oxygen may be treated as a conservative property

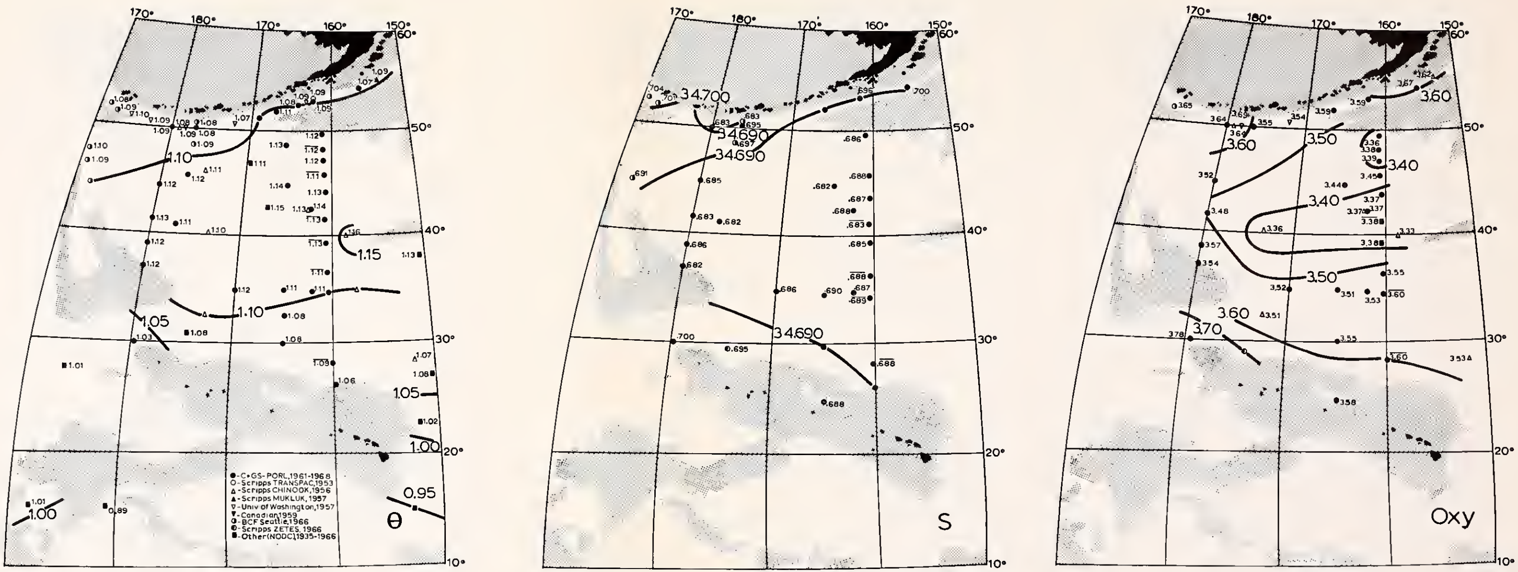

Figure 1. The distribution of potential temperature (θ), salinity (S), and dissolved oxygen (Oxy) at 5 km. Values on all charts representing the average from reoccupied sites are denoted by overbars.

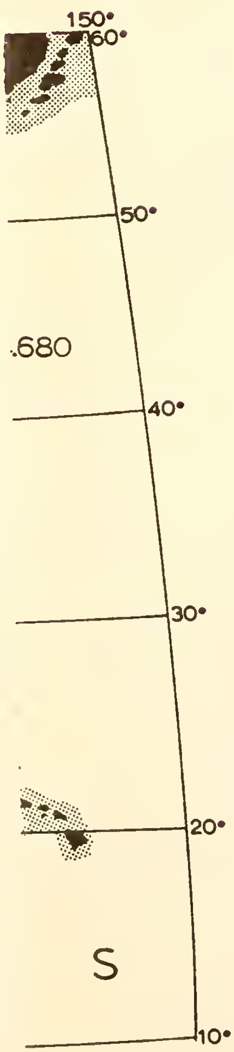

isolved oxygen (Oxy)

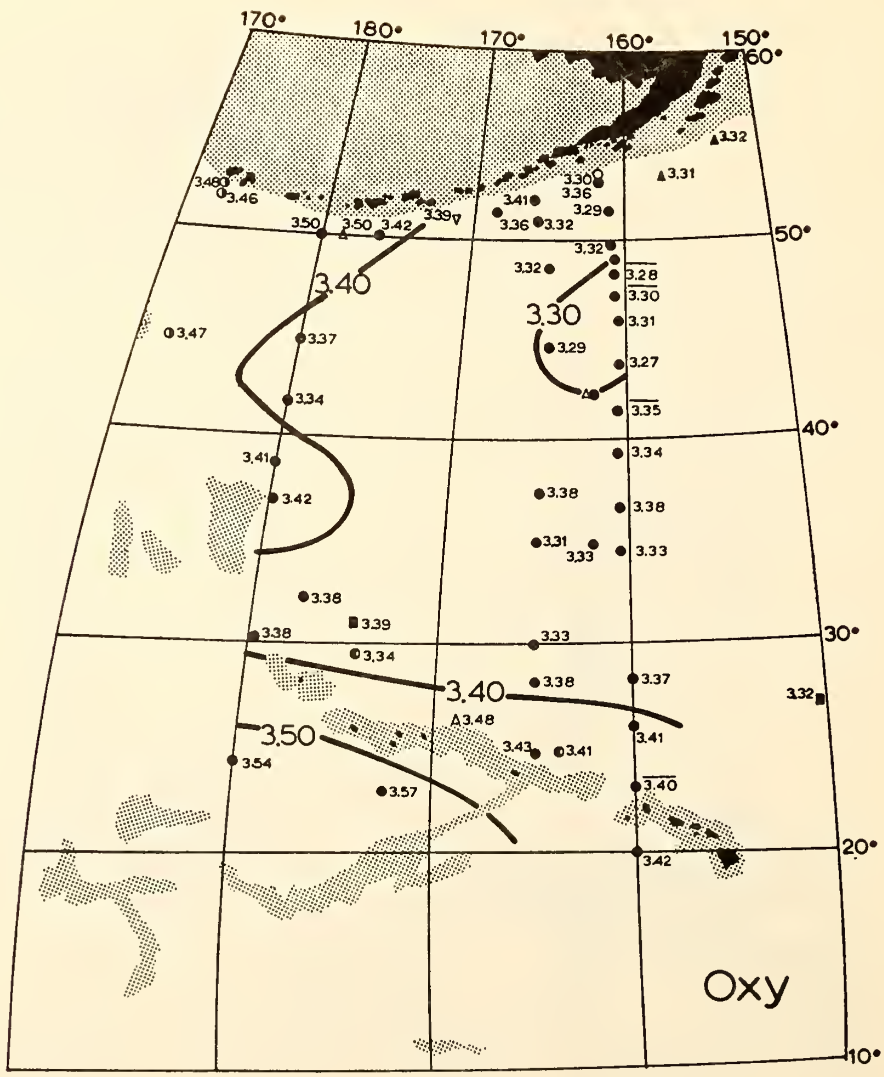

Table II. Identification of data used.

Data	Year(s)	Source
C&GS-PORL	1961–1968	PORL files (unpublished; available at NODC)
Scripps TRANSPAC........	1953	*Oceanic Observations of the Pacific
Scripps CHINOOK	1956	*Oceanic Observations of the Pacific
Scripps MUKLUK.........	1957	*Oceanic Observations of the Pacific
Univ. of Washington......	1957	*Oceanic Observations of the Pacific
Canadian	1959	*Oceanic Observations of the Pacific
BCF Seattle.............	1966	Bureau of Commercial Fisheries Report (unpublished)
Scripps ZETES	1966	Unpublished report, SIO Ref. 66–24
Other (NODC)..........	1935–1966	†National Oceanographic Data Center

* Scripps Instituion of Oceanography, Univ. of Calif. Press, Berkeley and Los Angeles.
† Various stations: Japanese, Swedish, Scripps, Russian, and U.S. Navy.

in the deep water in this region. Ranges of salinity and dissolved oxygen are about 0.02‰ and 0.4 ml/l, respectively, over the area north of the Hawaiian Islands.

The distribution at 4 km is shown in Fig. 2. A significant difference in the potential temperature patterns in Figs. 1 and 2 is the lack of a widespread cold zone south of 30°N at 4 km. Except for one value, the temperature increase from south to north at 4 km is only a few hundredths of a degree compared with a temperature range of at least 0.15°C at 5 km. Perhaps the water at 4 km is more uniform because of the lack of major bathymetric impediments to the flow. A 3-km chart was also prepared, but it is not shown because of its similarity to the distribution at 4 km.

Because all of the deep water is from a single source region, the differences in observed properties are usually considered to be a result of residence time in the Pacific, and the path of flow is assumed to be from areas of colder (newer) to areas of warmer (older) water. The temperature distribution at 5 km indicates that the warmer water in the central region cannot be the source of the colder water to the north, but this distribution does not preclude a northward flow below this level. The deepest water in the central region, however, is not as cold as water in the northern region at the bottom or at a depth of 5 km (see Figs. 3 and 1). Thus the deeper water in the northern region must arrive by way of a route other than one that would pass directly through the central region.

Figs. 1 and 2 reveal an increase in temperature from west to east between 45°N and 50°N. Salinity and oxygen exhibit comparable decreases toward the east. This fact, plus the marked similarity in properties on either side of the rise along 170°E (Bureau of Commercial Fisheries, unpublished data, 1966), suggests that the deeper water found near the Aleutians entered from the west, through a break in the rise between 46°N and 48°N. The inferred circulation is summarized in Fig. 4.

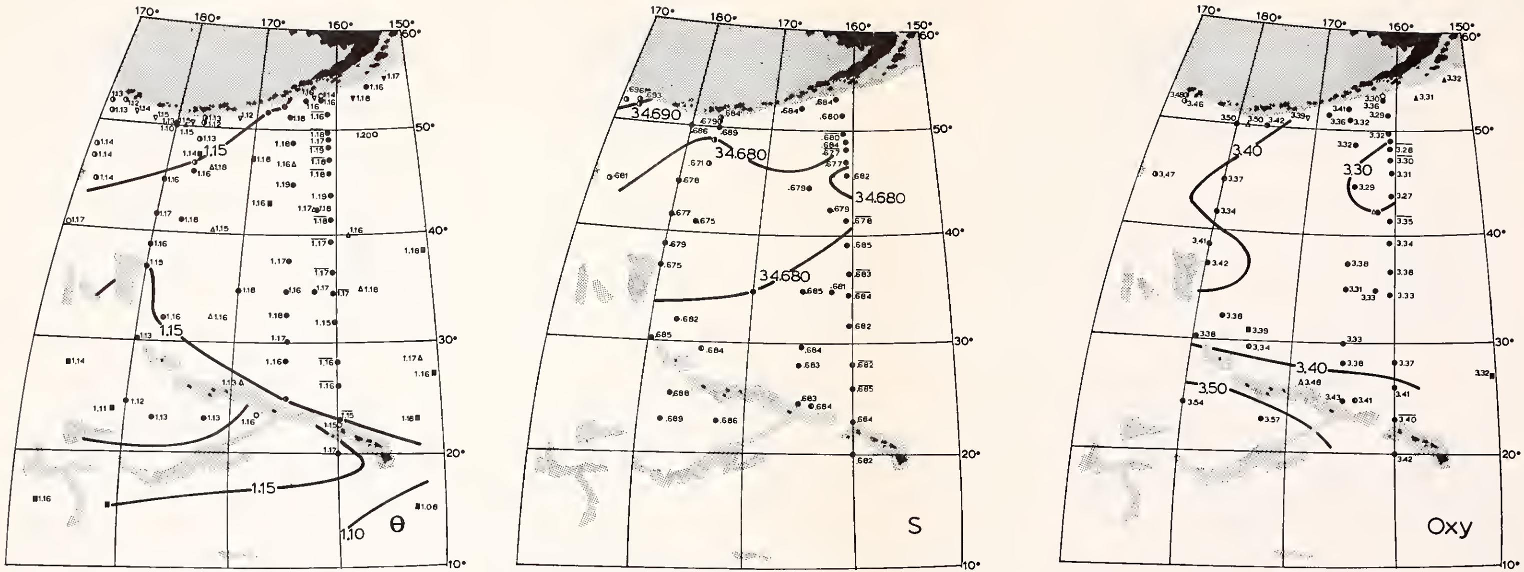

Figure 2. The distribution of potential temperature (θ), salinity (S), and dissolved oxygen (Oxy) at 4 km.

Table II. Identification of data used.

Data	Year(s)	Source
C&GS-PORL	1961–1968	PORL files (unpublished; available at NODC)
Scripps TRANSPAC	1953	*Oceanic Observations of the Pacific
Scripps CHINOOK	1956	*Oceanic Observations of the Pacific
Scripps MUKLUK	1957	*Oceanic Observations of the Pacific
Univ. of Washington	1957	*Oceanic Observations of the Pacific
Canadian	1959	*Oceanic Observations of the Pacific
BCF Seattle	1966	Bureau of Commercial Fisheries Report (unpublished)
Scripps ZETES	1966	Unpublished report, SIO Ref. 66–24
Other (NODC)	1935–1966	†National Oceanographic Data Center

* Scripps Instituion of Oceanography, Univ. of Calif. Press, Berkeley and Los Angeles.
† Various stations: Japanese, Swedish, Scripps, Russian, and U.S. Navy.

in the deep water in this region. Ranges of salinity and dissolved oxygen are about 0.02‰ and 0.4 ml/l, respectively, over the area north of the Hawaiian Islands.

The distribution at 4 km is shown in Fig. 2. A significant difference in the potential temperature patterns in Figs. 1 and 2 is the lack of a widespread cold zone south of 30°N at 4 km. Except for one value, the temperature increase from south to north at 4 km is only a few hundredths of a degree compared with a temperature range of at least 0.15°C at 5 km. Perhaps the water at 4 km is more uniform because of the lack of major bathymetric impediments to the flow. A 3-km chart was also prepared, but it is not shown because of its similarity to the distribution at 4 km.

Because all of the deep water is from a single source region, the differences in observed properties are usually considered to be a result of residence time in the Pacific, and the path of flow is assumed to be from areas of colder (newer) to areas of warmer (older) water. The temperature distribution at 5 km indicates that the warmer water in the central region cannot be the source of the colder water to the north, but this distribution does not preclude a northward flow below this level. The deepest water in the central region, however, is not as cold as water in the northern region at the bottom or at a depth of 5 km (see Figs. 3 and 1). Thus the deeper water in the northern region must arrive by way of a route other than one that would pass directly through the central region.

Figs. 1 and 2 reveal an increase in temperature from west to east between 45°N and 50°N. Salinity and oxygen exhibit comparable decreases toward the east. This fact, plus the marked similarity in properties on either side of the rise along 170°E (Bureau of Commercial Fisheries, unpublished data, 1966), suggests that the deeper water found near the Aleutians entered from the west, through a break in the rise between 46°N and 48°N. The inferred circulation is summarized in Fig. 4.

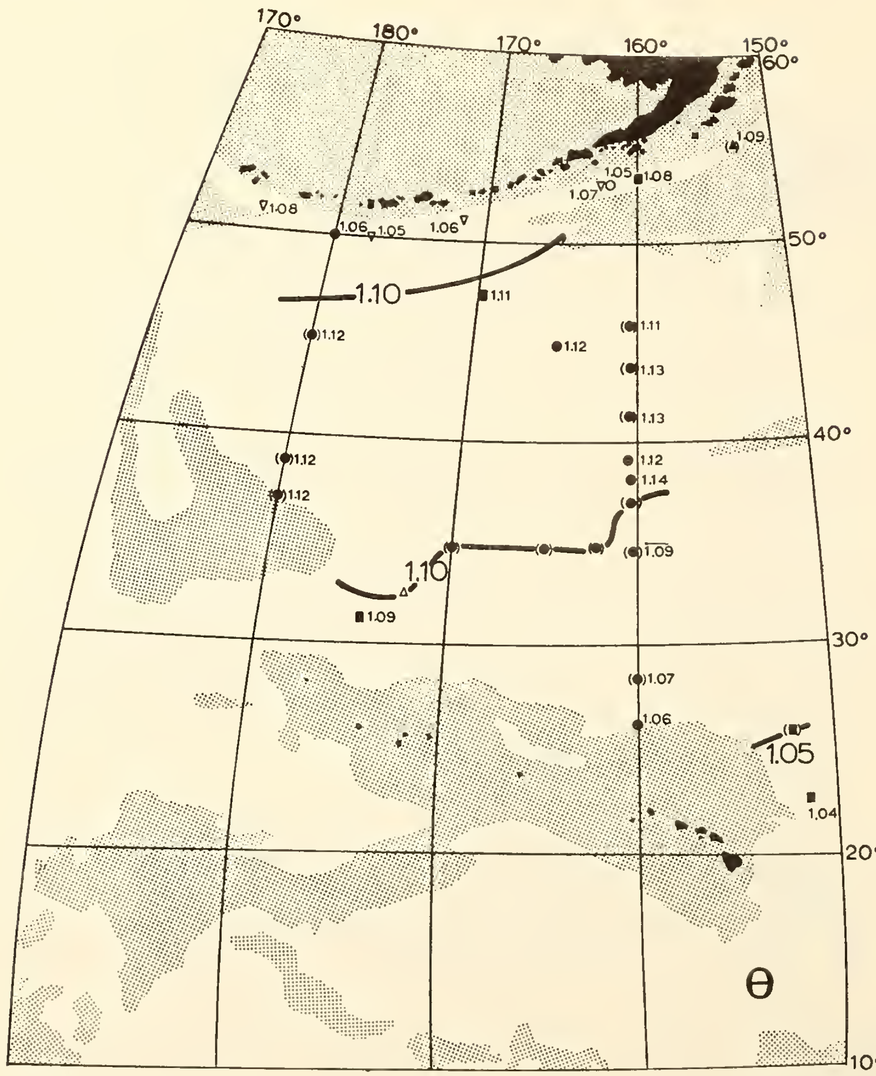

Figure 3. Bottom potential-temperature distribution. Prepared from temperature data obtained within 300 m of the bottom. Values for depths of less than 100 m from the bottom are denoted by the station symbol in parentheses. Water depths at these stations generally ranged from 5500 to 6000 m, except in the Aleutian Trench, where depths exceed 7000 m in the western part.

Considerations for the Future. Although direct current measurements have yielded interesting results, they have not given reliable values of the net transport of Pacific deep water. Because of fluctuating barotropic flows of 1 cm/sec

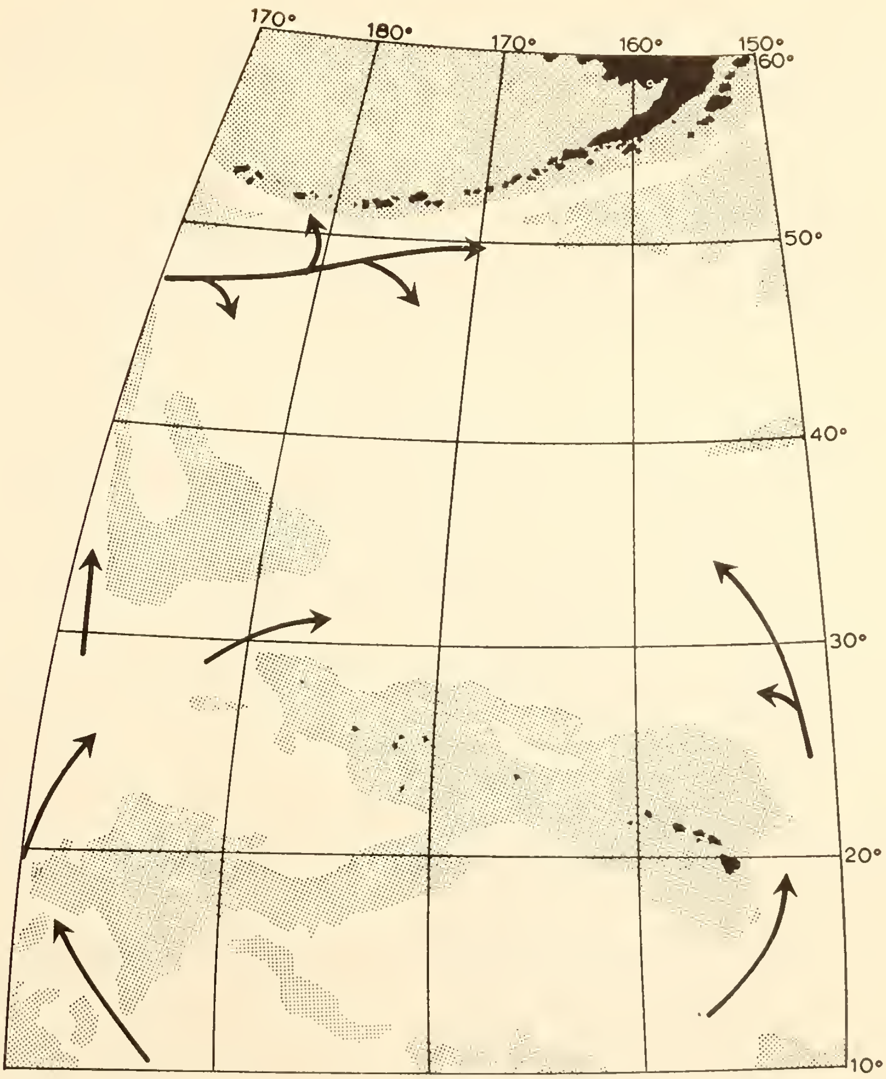

Figure 4. Schematic representation of the inferred circulation at 5 km and below.

or more (Barbee 1965) and deep tidal currents probably at least this great, it is very difficult to resolve net velocities on the order of 0.1 cm/sec (Knauss 1962, Bien et al. 1965). Thus the distributions of physical and chemical properties, plus results from isotope dating, are likely to remain for some time our main source of information on deep circulation in the Pacific.

The data presented here suggest an interesting and unanticipated path for the deep water; northern water appears to arrive from the west instead of from the south. Ultimately, very precise measurements from strategic locations throughout the Pacific may yield a convincing circulation pattern for the entire basin.

Acknowledgments. I wish to thank W. James Ingraham, Jr., Bureau of Commercial Fisheries, Biological Laboratory, Seattle, for use of data from the RV George B. Kelez cruise, winter 1966. Dr. Kilho Park, Oregon State University, kindly furnished unpublished oxygen data. Cdr. W. D. Barbee, N. P. Laird, and T. V. Ryan read the manuscript and offered helpful suggestions.

REFERENCES

Barbee, W. D.
1965. Deep circulation, Central North Pacific: 1961, 1962, 1963. Cst. geod. Surv. Res. Pap.; 104 pp.

Bien, G. S., N. W. Rakestraw, and H. E. Suess
1965. Radiocarbon in the Pacific and Indian oceans and its relation to deep water movements. Limnol. Oceanogr., *10* (Redfield Suppl.): R25-R37.

Carritt, D. E., and J. H. Carpenter
1966. Comparison and evaluation of currently employed modifications of the Winkler method for determining dissolved oxygen in seawater; a NASCO report. J. mar. Res., *24* (3): 286–318.

Fofonoff, N. P.
1962. Physical properties of sea-water, *in* The Sea, Vol. 1, pp. 3–30. M. N. Hill, Editor. Interscience, N.Y. 864 pp.

Knauss, J. A.
1962. On some aspects of the deep circulation of the Pacific. J. geophys. Res., *67* (10): 3943–3954.

Rechnitzer, A. B., and R. D. Terry
1965. Bathymetry of the Pacific Basin. Printed by North American Aviation/Autonetics, Anaheim, California, 1 p.

Printed in Denmark for the Sears Foundation for Marine Research,
Yale University, New Haven, Connecticut, U.S.A.
Bianco Lunos Bogtrykkeri A/S, Copenhagen. Denmark

Reprinted from Journal of Acoustic Society of America, Vol. 46, No. 5, 1382-1384.

Received 30 August 1969 11.2; 13.4, 13.5

Diffraction of a Plane Acoustic Pulse by a Free Orthogonal Trihedron (Three-Dimensional Corner)

RICHARD P. SHAW* AND DANIEL F. COURTINE

Division of Interdisciplinary Studies and Research, State University of New York at Buffalo, Buffalo, New York 14214

The normal velocity field on arbitrary three-dimensional scattering surfaces struck by a weak acoustic plane wave, is considered. A numerical solution for a right-angle corner (i.e., three orthogonal edges of infinite length) is found for a step-incident pressure wave, while the wavefront normal is taken to form equal angles with the three orthogonal edges. The scattering obstacle is assumed to have a free surface (i.e., pressure is zero).

WE CONSIDER HERE A NUMERICAL SOLUTION TO THE PROBLEM OF A plane weak shock wave striking a three-dimensional exterior right-angled corner, i.e., an orthogonal trihedron (see Fig. 1), with a pressure-release (free) boundary condition. The incident wave is taken to be symmetric with respect to the three orthogonal sides. The approach is described elsewhere[1] (in a report form of this paper) and is based on an integral equation formulation[2] of wave problems, which allows for solution on the scattering surface separately from the remainder of the solution.

The total velocity potential, φ, at an arbitrary field point, $\bar{r}$, and time, t, for an incident wave potential, φ_W, satisfies[3,4]

$$\varphi(\bar{r},t)=\varphi_W(\bar{r},t)-\frac{1}{4\pi}\iint_S \frac{1}{R}[v(\bar{r}_0,t_0)]ds_0, \qquad (1)$$

where S is that portion of the scattering surface capable of affecting the field point, $\bar{r}\equiv(x,y,z)$, at time t; R is the distance from a point of integration $\bar{r}_0\equiv(x_0,y_0,z_0)$ to the field point; and $[v]$ is the normal surface velocity evaluated at $t_0=t-R/c=$ the retarded time, with c the acoustic sound speed.

For an incident wave representing a unit step in pressure,

$$\varphi \;=ct-(1/\sqrt{3})(x+y+z). \qquad (2)$$

By taking the field point on the scattering surface, e.g., $y=0$, where φ is zero, there is no contribution from the singular point

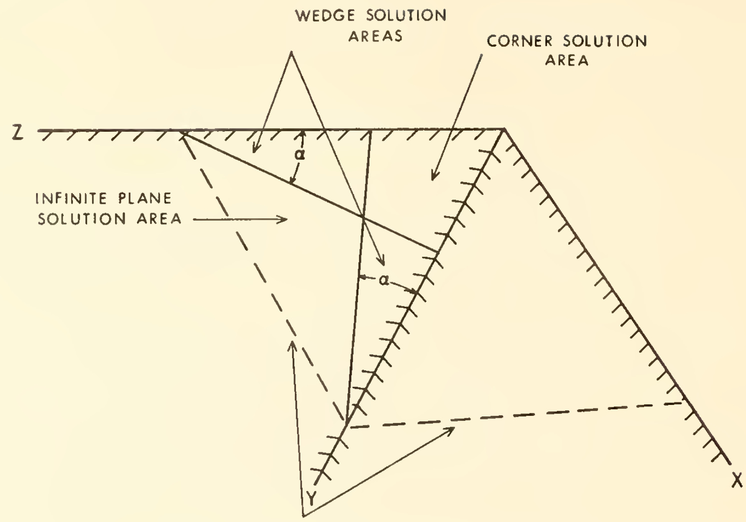

FIG. 1. Corner solution areas.

$R=0$, and Eq. 1 becomes[1,3]

$$4\pi\varphi_W=\iint_S \frac{[v]}{R}dS_0, \tag{3}$$

on which the numerical solution is based.

The integral in Eq. 3 can be replaced by a finite sum if v is assumed to be constant over a specified region and time interval, leading to a finite set of linear algebraic equations for these values of v in terms of velocity values at other locations and previous values of time (due to the time retardation), which will then have already been calculated. This set of equations is then uncoupled, i.e., successive rather than simultaneous.

Unfortunately, this numerical procedure has a possible shortcoming. When Eq. 3 is approximated, regardless of the method of subdividing the integration area, the resulting form is, for $y=0$,

$$4\pi\varphi_W-\sum_{j\neq i}\alpha_j[v_j]=\alpha_i v_i(x,0,z,t), \tag{4}$$

where α_j represents the coefficients corresponding to given source areas, $[v_j]$ is the corresponding retarded velocity (and is positive), and v_i is the field-point velocity with its own source area coefficient, α_i.

The left-hand side of Eq. 4 then represents a small difference of large numbers, since both φ_W and the summation grow with time and distance behind the wavefront. Therefore, a relatively fine grid must be used and particular care must be taken to include the appropriate portion of the discretized source areas that fall on the boundary of S. For the geometry considered, the areas of integration (S) are defined by:

$$(x-x_0)^2+(z-z_0)^2\leq[ct-(x_0+y_0)/\sqrt{3}]^2, \quad \text{on} \quad y_0=0, \tag{5}$$

with similar expressions on $x_0=0$ and $z_0=0$—with the restriction that all values of x_0, y_0, z_0 remain positive (or zero). A rectangular area of width Δx and height Δz over a time interval t to $t+\Delta t$ is used with a velocity value corresponding to that calculated at the center of the rectangle and time t. Areas that fall completely within S are included directly, but those through which the boundary

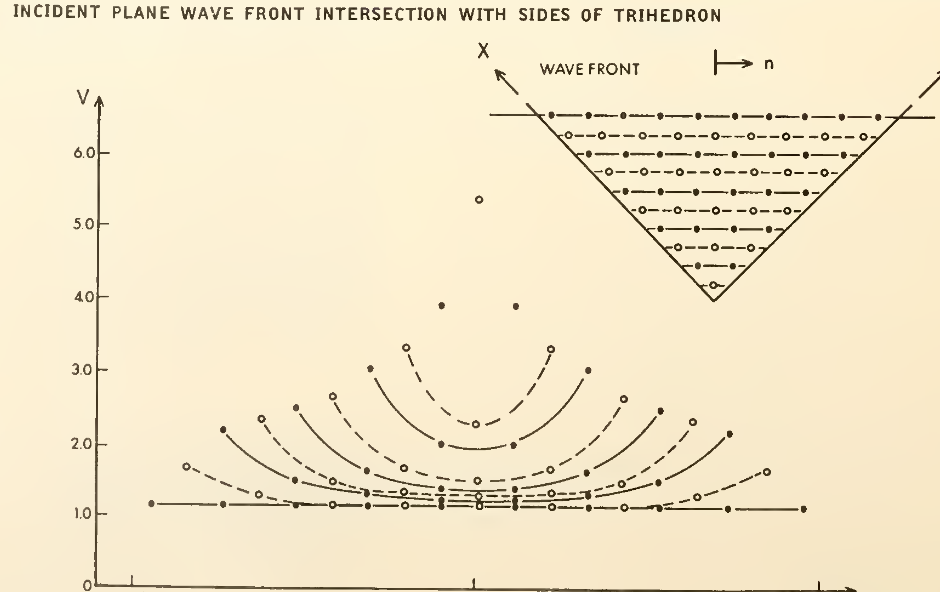

FIG. 2. Velocity at $t=10$ sec.

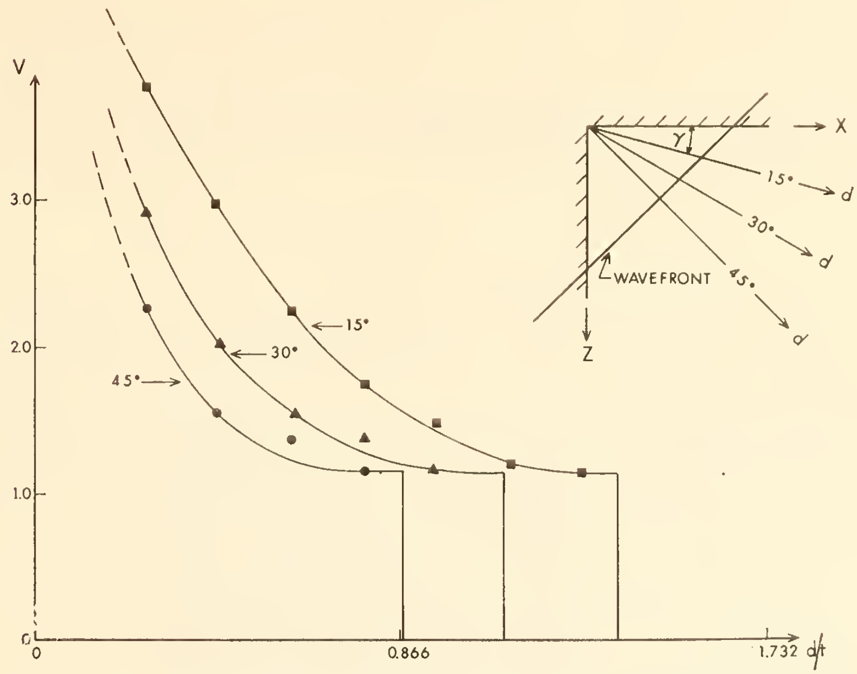

FIG. 3. Free corner: $t=10$ sec; $\gamma=15°$ 30°, 45°.

defining the domain of dependence, Eq. 5, passes must be treated as special cases in order to include that portion of the source area which lies within S in the calculations, as mentioned above.

For the corner problem, three distinct types of solution are expected in three different regions. They are the "infinite-plane solution" in that region of the surface not affected by any of the edges of the trihedron, the "infinite-wedge solution" in that region affected by only one edge, and the solution for those remaining areas that are affected by more than one edge (see Fig. 1). The results obtained are in very good agreement with known solutions in the areas corresponding to the infinite-plane and the infinite-wedge solutions. There is no exact solution to which the corner area may be compared, but the results (see Figs. 2 and 3) show higher velocities than those in the corresponding infinite-wedge solution, as would be expected. For fixed arbitrary γ, where γ is the angle between the x axis and an arbitrary line passing through the origin on the xz face, and d is the distance from the origin along this line, plots of velocity against d/t yield essentially the same results for several different valus of t (e.g., see Fig. 4 for $\gamma=45°$), as they should, since time and space dimensions are coupled; i.e., there is no representative length in the problem.[5]

FIG. 4. Free corner,: $\gamma=45°$, $t=8$, 9, 10 sec.

Acknowledgment: This research was supported in part by the Office of Naval Research.

* Presently on leave at Hawaii Inst. of Geophys., Univ. of Hawaii, Honolulu, Hawaii 96822.

[1] R. P. Shaw and D. F. Courtine, "Diffraction of a Plane Acoustic Pulse by a Free Orthogonal Trihedron," Rep. No. 32, Div. of Interdisciplinary Studies and Res., State Univ. of New York at Buffalo (May 1968).
[2] M. B. Friedman and R. Shaw, "Diffraction of Pulses by Cylindrical Obstacles of Arbitrary Cross Section," J. Appl. Mech. 29, 40–46 (1962).
[3] R. P. Shaw, "Diffraction of Pulses by Obstacles of Arbitrary Shape with a Robin Boundary Condition: Part B: Semi-Free Case," Rep. No. 12, Div. of Interdisciplinary Studies and Res., School of Eng., State Univ. of New York at Buffalo (April 1966); J. Acoust. Soc. Amer. 41, 855–859 (1967).
[4] R. P. Shaw and M. B. Friedman, "Diffraction of Pulses by Deformable Cylindrical Obstacles of Arbitrary Cross Section," Proc. U. S. Nat. Congr. Appl. Mech., 4th, June 1962, pp. 371–376.
[5] J. B. Keller and A. Blank, "Diffraction and Reflection of Pulses by Wedges and Corners," Commun. on Pure and Appl. Math. 4, 75–94 (1951).

Received 13 January 1969 12.3, 12.3i

Damping-Material Effectiveness Measured by the Geiger-Plate and Composite-Beam Tests

T. J. DUDEK

Lord Manufacturing Company, Erie, Pennsylvania 16512

The Geiger thick-plate test and the vibrating composite-beam test for the evaluation of vibration damping materials are briefly reviewed, and the advantages and disadvantages of both methods are analyzed. The results

Reprinted from Journal of Acoustic Society of America, Vol. 46, No. 3, 649-654.

Received 10 June 1968 11.2, 11.3, 11.7

Transmission of Plane Waves through Layered Linear Viscoelastic Media

R. P. Shaw and P. Bugl

Division of Interdisciplinary Studies and Research, State University of New York at Buffalo, Buffalo, New York 14214

The two-dimensional propagation of time-harmonic plane waves through a plane horizontally layered viscoelastic medium is discussed. The problem is formulated as the equivalent elastic plane-strain case with modified Lamé constants, which are complex and frequency dependent, replacing the usual elastic Lamé constants. Rather than use potentials, incident angles, etc., we formulate the problem directly in terms of stresses and displacements and solve it by using matrix methods. This approach is felt to be more direct and leads to some interesting conclusions. If the incident wave is not attenuated in the direction parallel to the layering, interface waves can be generated only if one of the layers is "pseudoelastic," i.e., has at least one real wave speed. In this case, the interface waves are generated in the same manner as in the purely elastic case. Such a physical problem would exist, for example, if the incident waves were to travel through a semi-infinite elastic half-space before striking the plane viscoelastic layers. If the incident wave is attenuated in the direction parallel to the layering, interface waves can be generated at specific angles of incidence and specific combinations of material parameters.

INTRODUCTION

The transmission of time-harmonic plane waves through layered linear elastic media is a problem of great interest and much study.[1,2] In addition, there has been much recent interest in the reflection and transmission of plane waves in a linear viscoelastic medium.[3] It is a relatively straightforward task to combine these topics into a single treatment. Insofar as the mathematical manipulations are concerned, the primary distinction between the elastic and the viscoelastic cases is that the latter will have modified Lamé constants, $\tilde{\lambda}$ and $\tilde{\mu}$, which are complex and frequency dependent.[4] The governing equations, continuity conditions at the interface between layers, etc., remain unchanged, except that some care must be taken in physical interpretation of the results.

A modification of the usual technique of solution for the elastic (or viscoelastic using $\tilde{\lambda}$ and $\tilde{\mu}$) problem is introduced in an attempt to clarify the mathematical manipulations involved. Results are left in a form relating the displacements and stresses in any layer to those at the uppermost ($z=0$) interface that separates the layered media, $z>0$, from a half-space, $z<0$, through which some incident wave travels. Since the displacements and stresses at this $z=0$ interface also depend on the waves transmitted from below ($z>0$) by reflections at other interfaces, these "initial" values cannot be determined until the entire problem has been specified, i.e., the number of layers, the appropriate physical parameters in each layer, etc. Nevertheless, some useful conclusions can be drawn regarding interface waves directly.

I. ELASTIC CASE

Consider a stratified medium consisting of parallel plane-homogeneous elastic layers of different thickness and material properties (Fig. 1). The z axis is oriented

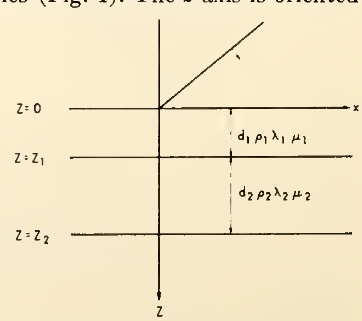

Fig. 1. Geometry of layered medium.

[1] L. M. Brekhovskikh, *Waves in Layered Media* (Academic Press Inc., New York, 1960).
[2] M. Ewing, W. Jardetsky, and F. Press, *Elastic Waves in Layered Media* (McGraw-Hill Book Co., New York, 1957).
[3] H. F. Cooper, Jr., "Reflection and Transmission of Oblique Plane Waves at Plane Interface Between Viscoelastic Media," J. Acoust. Soc. Amer. 42, 1064–1069 (1967).
[4] W. Nowacki, *Dynamics of Elastic Systems* (John Wiley & Sons, Inc., New York, 1963), p. 315.

in a direction normal to these planes with x and y forming a right-handed Cartesian-coordinate system. The problem considered will be restricted to a plane-strain case, such that none of the variables depend on the coordinate y. This uncouples the SH wave, which is not considered. In any one layer, the displacement $(\mathbf{u})$ equation of motion is given as

$$\rho_j \ddot{\mathbf{u}} = (\lambda_j+\mu_j)\nabla(\nabla\cdot\mathbf{u})+\mu_j\nabla^2\mathbf{u}, \tag{1}$$

where ρ_j is the density, and λ_j, μ_j are the Lamé constants for the jth layer. Along the upper surface $z=0$, the displacements and stresses of an incoming plane wave are given. Using the continuity of the normal stress, shear stress, normal displacement, and tangential displacement at the interface between layers, the reflected and transmitted fields may be calculated.

The assumption of a solution in the form

$$\begin{aligned} u_x &= U(z)\exp\{ik[ct-x]\}, \\ u_y &= 0, \\ u_z &= W(z)\exp\{ik[ct-x]\}, \end{aligned} \tag{2}$$

implies a frequency $\omega=kc$ and a phase velocity c in the x direction. The normal and shear stresses are, respectively,

$$\begin{aligned} \tau_{xz} &= \mu[u_{x,z}+u_{z,x}] = S(z)\exp\{ik[ct-x]\}, \\ \tau_{zz} &= \lambda u_{x,x}+(\lambda+2\mu)u_{z,z} = T(z)\exp\{ik[ct-x]\}. \end{aligned} \tag{3}$$

In any given layer (leaving out the j subscript for convenience at this point), a set of four coupled first-order ordinary different equations on U, W, S, and T can be found. In matrix form, these are

$$\begin{bmatrix} U_{,z} \\ W_{,z} \\ S_{,z} \\ T_{,z} \end{bmatrix} = \begin{bmatrix} 0 & ik & \dfrac{1}{\mu} & 0 \\ \dfrac{ik\lambda}{\lambda+2\mu} & 0 & 0 & \dfrac{1}{\lambda+2\mu} \\ \dfrac{-k^2[\lambda^2+\rho c^2(\lambda+2\mu)-(\lambda+2\mu)^2]}{\lambda+2\mu} & 0 & 0 & \dfrac{ik\lambda}{\lambda+2\mu} \\ 0 & -k^2\rho c^2 & ik & 0 \end{bmatrix} \begin{bmatrix} U \\ W \\ S \\ T \end{bmatrix} \tag{4}$$

or, in a condensed form,

$$(d/dz)X = \mathbf{A}X, \tag{5}$$

where X is a vector whose components are (U, W, S, T) and $\mathbf{A}$ is the coefficient matrix given above in Eq. 4.

While Eq. 5 can be solved directly, a transformation is convenient. Consider

$$V=\mathbf{B}X \quad \text{or} \quad X=\mathbf{B}^{-1}V. \tag{6}$$

Equation 5 is then

$$dV/dz = \mathbf{B}dX/dz = \mathbf{B}(\mathbf{A}X) = \mathbf{BAB}^{-1}V = \mathbf{E}V. \tag{7}$$

If $\mathbf{B}$ can be determined so as to make $\mathbf{E}$ diagonal,

$$\mathbf{E} = \mathrm{diag}[\gamma_i], \tag{8}$$

then V could be obtained directly from Eq. 7:

$$V = \mathrm{col}[K_i \exp\gamma_i z] = \mathbf{Q}K, \tag{9}$$

where

$$K = \mathrm{col}[K_i] = V(0) = \mathbf{B}X(0) \tag{10}$$

and

$$\mathbf{Q} = \mathrm{diag}[\exp(\gamma_i z)]. \tag{11}$$

If the first layer is between $z=0$ and $z=z_1$, $X(z_1)$ can be evaluated;

$$X(z_1) = \mathbf{B}_1^{-1}V(z_1) = \mathbf{B}_1^{-1}\mathbf{Q}_1(z_1)\mathbf{B}_1X(0), \tag{12}$$

where the subscript 1 indicates that $\mathbf{B}$, $\mathbf{Q}$, etc., are evaluated using the material properties of Layer 1. Similarly, $X(z_2)$ may be found in terms of $X(z_1)$ and therefore in terms of $X(0)$. This may be generalized to

$$X(z_n) = \prod_{j=1}^{n} \mathbf{B}_j^{-1}\mathbf{Q}_j(z_j-z_{j-1})\mathbf{B}_jX(0) = \prod_{j=1}^{n}\mathbf{R}_jX(0), \tag{13}$$

where z_j is the coordinate of the interface between the jth and $(j+1)$th layers.

The eigenvalues γ_1, γ_2, γ_3, and γ_4 and the matrix $\mathbf{B}$ can be determined directly from the condition that

$$\mathbf{BAB}^{-1} = \mathbf{E}. \tag{14}$$

A straightforward calculation gives

$$\gamma_{1,2} = \pm iak, \; \gamma_{3,4} = \pm ibk, \tag{15}$$

where

$$a^2 = c^2/\alpha^2-1, \; b^2 = c^2/\beta^2-1, \tag{16}$$

with $\alpha=[(\lambda+2\mu/\rho)]^{\frac{1}{2}}$, the dilational wave speed, and $\beta=(\mu/\rho)^{\frac{1}{2}}$, the rotational wave speed.

Furthermore,

$$\mathbf{B} = \begin{bmatrix} 2a\mu ik & -ik\xi & +1 & -a \\ 2a\mu ik & +ik\xi & -1 & -a \\ ik\mu(b^2-1) & 2ik\mu b & +b & +1 \\ ik\mu(b^2-1) & -2ik\mu b & -b & +1 \end{bmatrix} \tag{17}$$

and

$$\mathbf{B}^{-1}=\frac{-1}{2kab\rho c^2}\begin{bmatrix} ib & ib & iab & iab \\ -iab & iab & ia & -ia \\ -2kab\mu & 2kab\mu & -ka\xi & ka\xi \\ +k\mu b(b^2-1) & k\mu b(b^2-1) & -2kab\mu & -2kab\mu \end{bmatrix}, \tag{18}$$

where $\xi=\lambda+a^2(\lambda+2\mu)$.

Finally, the matrix $\mathbf{R}$ can be written in component form from the definition

$$\mathbf{R}=\mathbf{B}^{-1}\mathbf{Q}(z)\mathbf{B}. \tag{19}$$

If this is done, the components are found to agree with those obtained previously by other authors[1,5,6] and are given in detail in Ref. 7. Unfortunately, the equations obtained in Ref. 5, and repeated in Ref. 1, make the severely restrictive assumption that the shear modulus is constant throughout all layers and use continuity of shear strain at the interfaces rather than the appropriate shear stress. This was apparently first corrected in Ref. 6. Using the notation of Ref. 6, $\gamma=2\beta^2/c^2$ and $1-\gamma=\beta^2(b^2-1)/c^2=\xi/\rho c^2$ (where γ is NOT an eigenvalue as defined here, and noticing that the dependent variables of Ref. 6 are (ikV, ikW, T, S) the equations are found to check completely.

The solution, Eq. 13, has been formulated in terms of $X(0)$, which involves not only the incident wavefront, which is known, but also the reflected wavefronts that are unknown but that can be described in terms of two amplitude coefficients. The entire problem can then be solved once the number of layers and their properties are specified. Assuming $N+2$ layers with N layers of finite width bounded by semi-infinite layers, it can readily be seen that the coefficients of the terms $\exp(-iakz)$, $\exp(-ibkz)$ in the last semi-infinite layer must vanish, since these would represent reflections returning from infinity. These two conditions will then determine the two unknown reflection amplitude coefficients in $X(0)$ and thereby completely determine the solution.

At this point, there may be a question as to the necessity of rederiving results that are already available, albeit by a slightly different technique. As will be apparent in the next Sections on viscoelastic layered media, the formulation given here has a definite advantage over the usual method in that the z dependence is given directly and simply by the term $\mathbf{Q}(z)$ rather than in an involved manner by $\mathbf{R}(z)$, as is usually done. This allows a very simple interpretation, for example, of the conditions under which interface waves may exist rather than requiring the complicated arithmetic of a complex Snell's law, as discussed in Ref. 3.

II. VISCOELASTIC CASE

If the material considered is assumed to have a viscoelastic response, the governing equation will be identical to Eq. 1 with λ and μ replaced by complex frequency-dependent parameters $\tilde{\lambda}$ and $\tilde{\mu}$, respectively. Reference 8 defines $\tilde{\lambda}=\frac{1}{3}[Y_v-Y_s]$ and $\tilde{\mu}=\frac{1}{2}Y_s$, where Y_s and Y_v are the deviatoric and dilational complex modulii for the viscoelastic material, i.e., $s_{ij}=Y_s e_{ij}$ and $\tau_{kk}=Y_v\epsilon_{kk}$ in the time-harmonic case, where s_{ij}, e_{ij} are deviatoric stress and strain, respectively. The same analysis as carried out above will hold, then, for the viscoelastic case.

In a typical layer, e.g., the jth, the z dependence of the displacements and stresses will be given by the $\mathbf{Q}$ term; i.e.,

$$X(z)=\mathbf{B}_j^{-1}\mathbf{Q}_j(z-z_{j-1})\mathbf{B}_jX(z_{j-1}), \tag{20}$$

where $X(z_{j-1})$ represents the boundary conditions at $z=z_{j-1}$ and is independent of the coordinate z, as are $\mathbf{B}_j^{-1}$ and $\mathbf{B}_j$.

If $\tilde{\lambda}$ and $\tilde{\mu}$ are complex, then α and β will also be complex as will be a and b. Although it may appear that some physical "feeling" has been lost by working directly with displacements and stresses rather than dilational and rotational potentials, as is customary,[3] there seem to be advantages to this direct approach.

A main purpose of this paper is to investigate those conditions under which interface waves may be generated. Before this specific problem is considered, however, some interesting general conclusions may be drawn concerning the types of reflected and transmitted waves that may exist in this case. These waves will have a form proportional to $\exp\{i\omega t-ikx+ikaz\}$ for $\gamma_1=+ika$ with similar expressions arising from γ_2, γ_3, and γ_4. Clearly, this represents combinations of general attenuated or inhomogeneous plane waves, where the direction of attenuation is not the same as the direction of propagation leading to plane waves whose amplitude is not constant along the wavefront. Such a wave may, in general, be written as proportional to $\exp[i\omega t-il_s\times(x\sin\theta-z\cos\theta)-l_s'(x\sin\theta'-z\cos\theta')]$ for a wave traveling in the $+x$ and $-z$ directions such that a surface of constant phase makes an angle θ with respect

[5] W. Thomson, "Transmission of Elastic Waves Through a Stratified Solid Medium," J. Appl. Phys. 21, 89–93 (1950).

[6] N. Haskell, "The Dispersion of Surface Waves in Multilayered Media," Bull. Seismol. Soc. Amer. 43, 17–34 (1953).

[7] R. P. Shaw and P. Bugl, "On the Transmission of Plane Waves Through Layered Linear Viscoelastic Media," DISR Rep. No. 42, State University of New York at Buffalo, (Aug. 1968).

[8] D. Bland, *The Theory of Linear Viscoelasticity* (Pergamon Press, Inc., New York, 1960), p. 59.

to the x axis, and attenuated in the $+x$ and $-z$ directions such that a plane of constant amplitude makes an angle θ' with respect to the x axis (assuming l_s, l_s' to be positive). A simple comparison of this general form with the solution obtained above leads directly to

$$\theta=\tan^{-1}\{\mathrm{Re}[k]/\mathrm{Re}[ka]\}, \tag{21a}$$

$$\theta'=\tan^{-1}\{\mathrm{Im}[k]/\mathrm{Im}[ka]\}, \tag{21b}$$

which are, in general, not the same. Similar conclusions hold for the γ_2, γ_3, and γ_4 terms. Therefore, regardless of the form of incident wave, these transmitted dilational and rotational waves (γ_2, γ_4, respectively) and reflected dilational and rotational waves (γ_1, γ_3) will be inhomogeneous waves unless Eqs. 21a and 21b give θ equal to θ', in which particular case the wave becomes an ordinary damped wave, i.e., one attenuated only in the direction of propagation.

The actual speed of propagation of plane surfaces of constant phase (wavefronts) can also be found and is given (for dilational or P waves) by

$$\alpha_{\mathrm{actual}}^2=\frac{\omega^2}{\{\mathrm{Re}[k]\}^2+\{\mathrm{Re}[(\omega^2/\alpha^2-k^2)^{\frac{1}{2}}]\}^2}, \tag{22}$$

which has α_{actual} equal to the elastic wave speed α only if α and k are real. (A similar equation holds for rotational waves with β replacing α.) Thus, the actual wave speed will depend, in general, on the angles of the incident wave, θ and θ', as well as the material properties of the layers.

The conditions under which interface waves may exist are now considered.

A. Viscoelastic Layers under an Elastic Half-Space

If the half-space $z<0$ through which the incident waves travel is elastic, k and c will be real quantities, e.g., $k=k_s\cdot\sin\theta$ and $c=\omega/k$, where k_s is the wavenumber for elastic rotational waves, θ is the angle of incidence, and c is the phase velocity in the x direction for an incident rotational wave, with similar expressions for an incident dilational wave.

Then, the existence of interface waves is specified by having terms in the dependent variables that have only a real exponential dependence on z; i.e., in the $\mathbf{Q}$ term, at least one of the eigenvalues γ_i must be a pure real number. Obviously, this implies that γ_1, γ_2, and/or γ_3, γ_4 must be real and that, by Eq. 15, a and/or b must be pure imaginary. This requires that α_j^2 and/or β_j^2 be real, positive, and less than c^2 or that α_j^2 and/or β_j^2 be real, negative, and greater than $-c^2$. The former case corresponds to the usual elastic case. The latter appears physically unrealistic, since it would require $\tilde{\mu}$ and/or $\tilde{\lambda}+2\tilde{\mu}$ to be pure imaginary. If $\tilde{\mu}$ is imaginary, so is Y_s. This implies that rotational waves will not propagate in such a material. Similarly, if $\tilde{\lambda}+2\tilde{\mu}$ is imaginary, so is $\frac{1}{3}[Y_v+2Y_s]$. But this implies that dilatational waves will not propagate. Therefore, neither of these latter possibilities is considered.

Therefore, for the case of viscoelastic layers lying under an elastic half-space through which the incident wave travels, it is concluded that interface waves cannot be generated unless one of the layers is "pseudoelastic," in which case they may be generated under the same conditions as in the usual elastic case.

B. Viscoelastic Layers under a Viscoelastic Half-Space

The primary distinction between this case and the previous one is that the incident wave may now be attenuated in the x direction, and, therefore, k and c in Eq. 2 will be complex such that $kc=\omega$ is real. The same requirement as before on γ_i holds for the existence of interface waves, but, since k is complex, some γ_i can be real by having ka and/or kb a pure imaginary number. This implies that $(ka)^2$ and/or $(kb)^2$ is a real negative number. From Eq. 16,

$$(ka)^2=(\omega/\alpha)^2-k^2;\ (kb)^2=(\omega/\beta)^2-k^2. \tag{23}$$

First consider the "dilatational" interface wave. The requirement is then

$$\mathrm{Re}[(\omega/\alpha)^2-k^2]<0, \tag{24a}$$

$$\mathrm{Im}[(\omega/\alpha)^2-k^2]=0. \tag{24b}$$

This corresponds to

$$\rho^{(L)}\omega^2\,\mathrm{Re}[\lambda^{(L)}+2\mu^{(L)}]/|\lambda^{(L)}+2\mu^{(L)}|^2<\{\mathrm{Re}[k]\}^2-\{\mathrm{Im}[k]\}^2, \tag{25a}$$

$$\rho^{(L)}\omega^2\,\mathrm{Im}[\lambda^{(L)}+2\mu^{(L)}]/|\lambda^{(L)}+2\mu^{(L)}|^2=2\,\mathrm{Re}[k]\cdot\mathrm{Im}[k]. \tag{25b}$$

The corresponding equations for the "rotational" interface wave are

$$\rho^{(L)}\omega^2\,\mathrm{Re}[\mu^{(L)}]/|\mu^{(L)}|^2<\{\mathrm{Re}[k]\}^2-\{\mathrm{Im}[k]\}^2, \tag{26a}$$

$$\rho^{(L)}\omega^2\,\mathrm{Im}[\mu^{(L)}]/|\mu^{(L)}|^2=2\cdot\mathrm{Re}[k]\cdot\mathrm{Im}[k], \tag{26b}$$

where the superscript L denotes the material properties of the layer in question, while values without a superscript refer to properties of the "incident" half-space.

Consider an incident SV wave decaying in the direction of propagation, i.e., a "damped" plane wave. The exponential dependence of the incident potential, displacement, stress, etc., will have the form $\exp\{i[\omega t-k_s(x\sin\theta+z\cos\theta)]\}$, where k_s is a complex, shear wavenumber and θ is a real angle of incidence. An equivalent form would be $\exp\{i[\omega t-\mathrm{Re}[k_s](x\sin\theta+z\cos\theta)]-\mathrm{Im}[k_s](x\sin\theta+z\cos\theta)\}$, such that $\mathrm{Re}(k_s)\sin\theta$ expresses the real phase velocity in the x direction, while $\mathrm{Im}(k_s)\sin\theta$ is the attenuation factor in the x direction. Clearly, from Eq. 2,

$$k=k_s\cdot\sin\theta, \tag{27}$$

such that $\mathrm{Re}(k)=\mathrm{Re}(k_s)\sin\theta$ and $\mathrm{Im}(k)=\mathrm{Im}(k_s)\sin\theta\cdot k_s$

are known in terms of the complex Lamé parameters for the "incident" half-space and may be written as

$$k_s^2 = \{\mathrm{Re}[k_s]\}^2 - \{\mathrm{Im}[k_s]\}^2 + 2i\,\mathrm{Re}[k_s]\,\mathrm{Im}[k_s] = \omega^2\rho[\mathrm{Re}[\tilde{\mu}] - i\,\mathrm{Im}[\tilde{\mu}]]/|\tilde{\mu}|^2. \quad (28)$$

Equations 25 and 26 can then be examined in detail. Equation 25b requires

$$\rho^{(L)}\omega^2\,\mathrm{Im}[\lambda^{(L)}+2\mu^{(L)}]/|\lambda^{(L)}+2\mu^{(L)}|^2 = \rho\omega^2\,\mathrm{Im}[\tilde{\mu}]\sin^2\theta/|\tilde{\mu}|^2, \quad (29)$$

which, in turn, requires a definite relationship between the angle of incidence θ of the incident plane wave and the material properties of the various layers. Equation 25a requires

$$\rho^{(L)}\omega^2\,\mathrm{Re}[\lambda^{(L)}+2\mu^{(L)}]/|\lambda^{(L)}+2\mu^{(L)}|^2 < \sin^2\theta\cdot\rho\omega^2\,\mathrm{Re}[\tilde{\mu}]/|\tilde{\mu}|^2, \quad (30)$$

whereupon, using Eq. 29 to define the appropriate angle θ,

$$\mathrm{Re}[\lambda^{(L)}+2\mu^{(L)}] < \mathrm{Re}[\tilde{\mu}]\cdot\mathrm{Im}[\lambda^{(L)}+2\mu^{(L)}]/\mathrm{Im}[\tilde{\mu}]. \quad (31)$$

A similar result will apply for the "rotational" interface case, i.e., for Eqs. 26a and 26b

$$\rho^{(L)}\omega^2\,\mathrm{Im}[\mu^{(L)}]/|\mu^{(L)}|^2 = \sin^2\theta\cdot\rho\omega^2\,\mathrm{Im}[\tilde{\mu}]/|\tilde{\mu}|^2 \quad (32)$$

and

$$\mathrm{Re}[\mu^{(L)}] < \mathrm{Re}[\tilde{\mu}]\cdot\mathrm{Im}[\tilde{\mu}^{(L)}]/\mathrm{Im}[\tilde{\mu}]. \quad (33)$$

These equations then define the circumstances under which an interface wave may be generated.

Finally, the case of a general attenuated plane incident wave[3] may be discussed. Such a wave is assumed to decay both in the direction of propagation and along the direction of the wave front and, for an incident SV wave, will have an exponential dependence on the form $\exp\{i\omega t - il_s(x\sin\theta + z\cos\theta) - l_s'(x\sin\theta' + z\cos\theta')\}$, where k in Eq. 2 is given by $l_s\sin\theta - il_s'\sin\theta'$. The governing differential equation would require that

$$k_s^2 = l_s^2 - l_s'^2 - 2il_sl_s'\cos(\theta-\theta'), \quad (34)$$

which implies

$$l_s^2 - l_s'^2 = \rho\omega^2\,\mathrm{Re}[\tilde{\mu}]/|\tilde{\mu}|^2, \quad (35a)$$

$$2l_sl_s'\cos(\theta-\theta') = \rho\omega^2\,\mathrm{Im}[\tilde{\mu}]/|\tilde{\mu}|^2. \quad (35b)$$

Then Eqs. 25b and 26b become

$$\frac{\rho^{(L)}\omega^2\,\mathrm{Im}[\lambda^{(L)}+2\mu^{(L)}]}{|\lambda^{(L)}+2\mu^{(L)}|^2} = \frac{\rho\omega^2\sin\theta\cdot\sin\theta'\,\mathrm{Im}[\tilde{\mu}]}{\cos(\theta-\theta')|\tilde{\mu}|^2} \quad (36)$$

and

$$\frac{\rho^{(L)}\omega^2\,\mathrm{Im}[\mu^{(L)}]}{|\mu^{(L)}|^2} = \frac{\rho\omega^2\sin\theta\cdot\sin\theta'\,\mathrm{Im}[\tilde{\mu}]}{\cos(\theta-\theta')|\tilde{\mu}|^2}, \quad (37)$$

respectively. Given θ and θ', these equations will determine the material properties in the layers such that an interface wave can be generated (or vice versa). The corresponding restrictions of Eqs. 25a and 26a require

$$\rho^{(L)}\omega^2\,\mathrm{Re}[\lambda^{(L)}+2\mu^{(L)}]/|\lambda^{(L)}+2\mu^{(L)}|^2 < l_s^2\sin^2\theta - l_s'^2\sin^2\theta' \quad (38)$$

and

$$\rho^{(L)}\omega^2\,\mathrm{Re}[\mu^{(L)}]/|\mu^{(L)}|^2 < l_s^2\sin^2\theta - l_s'^2\sin^2\theta', \quad (39)$$

where l_s and l_s' are determined from Eqs. 33. Similar results hold for an incident P wave with $\tilde{\lambda}+2\tilde{\mu}$ replacing $\tilde{\mu}$.

C. Examples of Interface Waves

It is assumed that the bulk modulus is real (i.e., no volume viscosity), requiring that $\mathrm{Im}[\tilde{\lambda}] = -\frac{2}{3}\,\mathrm{Im}[\mu]$. This appears to be a very good assumption at moderate frequencies, although in the ultrasonic range (e.g., 1–10 Mc/sec) experiments indicate some volume viscous effects for some polymers,[9] although other experiments indicate no such effect for a Buna-N rubber[10] or very little effect for a natural rubber.[11] For metals and other "hard" materials, this effect again does not appear significant.[12]

An additional assumption that is often used for "soft" polymers and rubbers is that of incompressibility, which implies that the bulk modulus is much larger than the shear modulus. With these two assumptions, no volume viscosity and incompressibility, only two parameters are required to describe the mechanical behavior of a material. These parameters are usually obtained by means of a shear test and correspond to the real and imaginary parts of the shear modulus, e.g., Refs. 11 and 13, although some measurements are available on longitudinal behavior giving the complex Young's modulus, e.g., Refs. 11 and 14.

Consider then a "semi-infinite" layer of "soft" material (i.e., incompressible), in which ordinary damped incident SV waves travel with underlying finite-width layers of other "soft" materials, and examine Eqs. 29, 31, 32, and 33 for possible interface waves at moderate frequencies. This problem may be considered without requiring the complete solution—i.e., without specifying all of the layers and their properties and determining all of the reflected and transmitted waves. A simple calculation based on Eq. 33 requires that, assuming

[9] R. Marvin, R. Aldrich, and H. Sack, "The Dynamic Bulk Modulus of Polyisobutylene," J. Appl. Phys. **25**, 1213–1218 (1954).

[10] A. Nolle and P. Sieck, "Longitudinal and Transverse Ultrasonic Waves in a Synthetic Rubber," J. Appl. Phys. **23**, 888–894 (1952).

[11] J. D. Ferry, *Viscoelastic Properties of Polymers* (John Wiley & Sons, Inc., New York, 1961), Chap. 18.

[12] C. Zener, *Elasticity and Anelasticity of Metals* (University of Chicago Press, Chicago, Ill., 1948), p. 56.

[13] W. Philippoff, "Mechanical Investigations of Elastomers in a Wide Range of Frequencies," J. Appl. Phys. 24, 685–689 (1953).

[14] D. Jones, "Material Damping," Air Force Mater. Lab., Wright-Patterson AFB, Ohio (presented at ASA Damping Conference, Nov. 1968).

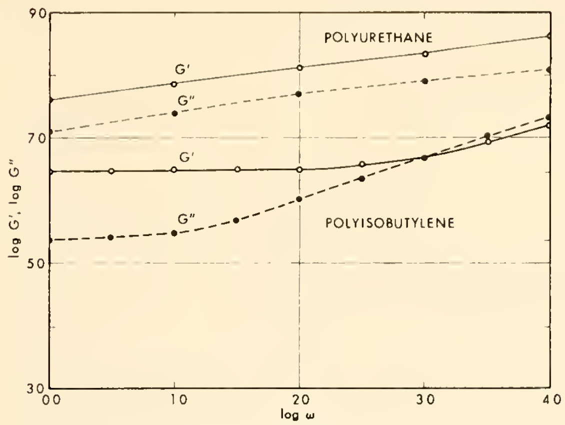

FIG. 2. Log G', log G'' (G in dynes/square centimeter) vs log ω (ω in radians/second) for polyurethane and polyisobutylene.

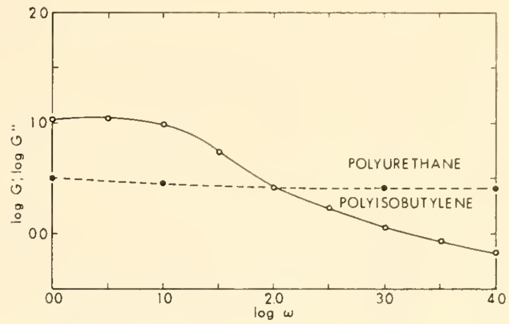

FIG. 3. Comparison of log (G'/G'') for polyurethane, ●, and polyisobutylene, ○.

$\mathrm{Im}[\mu]>0,$

$$\tan\arg[\tilde{\mu}]=\mathrm{Im}[\tilde{\mu}]/\mathrm{Re}[\tilde{\mu}] < \mathrm{Im}[\mu^{(L)}]/\mathrm{Re}[\mu^{(L)}]=\tan\arg[\mu^{(L)}]$$

or

$$\log G'-\log G''>\log G'^{(L)}-\log G''^{(L)}, \qquad (40)$$

where $G'=\mathrm{Re}[\mu]$ and $G'=\mathrm{Im}[\mu]$ in terms of Ref. 11. Clearly, the results will not be particularly accurate in those regions where log G' and log G'' are close in magnitude, and this reservation must be considered in evaluating the conclusions. Reference 11 gives data for several materials in Appendix D, but unfortunately at different reference temperatures. These may be reduced to the same reference temperature[11] or may be compared to other materials measured at the same reference temperature. As an illustration of Eq. 40, compare polyisobutylene[11] with a polyurethane propellant[15] at 25°C. Values of G' and G'' are given in Fig. 2, while $\log G'-\log G''$ is plotted in Fig. 3, over a frequency range $0<\log\omega<4$. Clearly, the quantity $\log G'-\log G''$ for polyisobutylene is larger than that for polyurethane for $0<\log\omega<2$ and smaller for $2<\log\omega<4$, indicating that a finite layer of polyurethane under a semi-infinite "incident" layer of polyisobutylene could support an interface wave for $0<\log\omega<2$, while the reverse would be true for $2<\log\omega<4$. If several materials were to be considered, a similar figure would quickly indicate which material should be the "incident" layer and which the underlying layer to have the possibility of an interface wave.

Of course, Eq. 32 must also be satisfied in order to have an interface wave. This requires an incident angle such that

$$\sin\theta=\left[\frac{\rho^{(L)}}{\rho}\cdot\frac{|\tilde{\mu}|^2}{|\mu^{(L)}|^2}\cdot\frac{\mathrm{Im}[\mu^{(L)}]}{\mathrm{Im}[\tilde{\mu}]}\right]^{\frac{1}{2}}. \qquad (41)$$

If no such real angle exists, an interface wave cannot exist for an ordinary damped incident wave, and the case of a general inhomogeneous incident wave must be considered, e.g., Eqs. 36–39. For the particular example used, ρ (polyisobutylene) $\simeq 1.0$ while ρ (polyurethane) (Ref. 15) $\simeq 1.7$. Thus, for $\omega=1.0$ rad/sec, $\theta=\sin^{-1}(0.68)\simeq 43°$.

For inhomogeneous incident waves or for compressible materials, the calculations would be somewhat more complicated but follow directly from the equations developed.

III. CONCLUSION

A method has been presented for the calculation of stresses and displacements resulting from a time-harmonic plane wave propagating through a layered linear viscoelastic medium. Some general conclusions have been drawn concerning the types of waves transmitted and reflected, and a simple example of the conditions under which an interface wave may occur has been given. It is felt that this direct approach has an advantage over usual approaches, e.g., Ref. 3, in that the complex arithmetic involved in the application of a complex Snell's law is avoided, giving, it is hoped, a clearer understanding of the conclusions drawn. These are that general inhomogeneous reflected and transmitted waves will be formed even if the incident waves are not of this form (i.e., see Eq. 21), that the actual speed of propagation of wavefronts differs from the usual wave speed, (i.e., see Eq. 22), that interface waves cannot exist in viscoelastic layers under an elastic half-space unless one of the wave speeds in the layer is real (i.e., the layer is "pseudoelastic"), and that interface waves can exist in viscoelastic layers under a viscoelastic half-space under specific conditions of material properties and incident angle.

ACKNOWLEDGMENT

This research was supported in part by a contract with the Office of Naval Research.

[15] T. Smith, L. Hiam, and J. Smith, "Viscoelastic Properties of Solid Propellants and Propellant Binders," Stanford Res. Inst., Quart. Rep. 5, 6 (Jan. 1963).

Reprinted from Journal of American Ceramic Society
Vol. 52, No. 10, 539-542 (Also HIG 287).

Adiabatic Elastic Moduli of Vitreous Calcium Aluminates to 3.5 Kilobars

T. J. SOKOLOWSKI

Environmental Science Services Administration, Pacific Oceanographic Laboratories,
Joint Tsunami Research Effort, Honolulu, Hawaii 96822

and

M. H. MANGHNANI

Hawaii Institute of Geophysics, University of Hawaii, Honolulu, Hawaii 96822

"Pulse superposition" ultrasonic interferometry was used to measure elastic wave velocities and related elastic parameters of four vitreous calcium aluminate specimens at pressures up to 3.5 kbars at 25°C. The values obtained for the bulk (K_s) and shear (μ) moduli and for Poisson's ratio (σ) were much higher than those reported for silicate glasses. The bulk moduli for the calcium aluminates, however, fit quite well with the relation between bulk modulus and specific volume per ion pair suggested by Soga and Anderson for 29 glasses. The (dv_p/dP) value was highest (8.9×10^{-3} km/(s·kbars)) for the SiO_2-doped vacuum-melted calcium aluminate and lowest (6.8×10^{-3} km/(s·kbars)) for the BaO-doped air-melted specimen. The BaO doping seemed to cause anomalous behavior in the shear wave velocity vs pressure relation; the (dv_s/dP) value for the BaO-doped air-melted specimen was -4.1×10^{-3} km/(s·kbars). The differences in the compressibility at 1 bar and the rate of change of compressibility with pressure appear to be related to composition and melt conditions. The (dK_s/dP) values ranged from 4.0 to 4.7 and the ($d\sigma/dP$) values from 6.8 to 7.5×10^{-4}/kbars.

I. Introduction

The elastic behavior of noncrystalline solids under pressure has been studied by several workers. Bridgman[1] first noted that elastic behavior was anomalous, in the sense that the compressibility increased with pressure, in several natural and artificial silica-rich glasses. Other investigators[2-6] reported that the moduli of such glasses decreased with pressure. Recently, it was shown[4] that the anomalous behavior of silica-rich glasses under pressure is quantitatively related to silica content.

The purpose of this study was to better understand the effect of composition and conditions of glassmelting on the elastic constants of vitreous calcium aluminates by comparing the elastic parameters at normal and high pressures. Properties were measured by ultrasonic wave propagation. The elastic behavior of four specimens of vitreous calcium aluminate subjected to pressures up to 3.5 kbars at 25°C is reported.

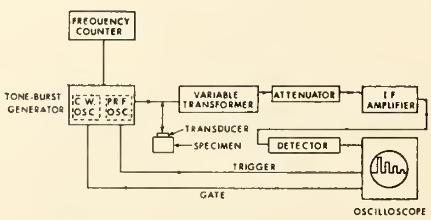

Fig. 1. Diagram of electronic equipment (adapted from Ref. 8).

II. Method of Investigation

Ultrasonic interferometry ("pulse superposition" method) was described in detail by McSkimin[7] and by Schreiber and Anderson.[8] Figure 1 is a diagram of the electronic equipment used. The major components are a tone-burst generator, consisting of a carrier wave (CW) oscillator and a pulse repetition frequency (prf) oscillator, a Tektronix 545A oscilloscope, a frequency counter (Hewlett-Packard model 5246L), and an amplifier. An rf pulse from the tone-burst generator is applied to a quartz transducer; the frequency of the CW pulse is equal to the natural frequency of the transducer. The transducer is attached to one of the two parallel faces of the specimen to

Received November 29, 1968; revised copy received March 24 1969. Contribution No. 287 from the Hawaii Institute of Geophysics.
Supported by the Office of Naval Research under Contract N-00014-68-A-0387-0005 to the University of Hawaii.

Table I. Elastic Wave Velocity Measurements and Related Parameters for Calcium Aluminate Glasses at 1 Bar and 25°C

Parameter	Relation	Units	Glass No.*			
			BS37A–A	BS37A–V	BS39B–A	BS39B–V
Longitudinal velocity	v_p	km/s	6.934	6.923	6.832	6.746
Shear velocity	v_s	km/s	3.784	3.760	3.758	3.659
Density	ρ	g/cm³	2.960	2.996	3.089	3.170
Bulk modulus	$K_s = \rho(v_p^2 - \frac{4}{3} v_s^2)$	kbars	857.9	871.2	860.3	876.6
Shear modulus	$\mu = \rho v_s^2$	kbars	423.8	423.6	436.3	424.4
Compressibility	$\beta_s = 1/K_s$	Mbars⁻¹	1.166	1.148	1.162	1.141
Young's modulus	$E = 9K_s\mu/(3K_s + \mu)$	kbars	1091.6	1093.5	1119.6	1096.2
Poisson's ratio	$\sigma = \frac{1}{2}\left\{\left[\frac{(V_p)^2}{v_s} - 2\right] / \left[\frac{(v_p)^2}{v_s} - 1\right]\right\}$		0.2879	0.2908	0.2831	0.2916
Mean atomic wt†	$m = M/p$	g	24.40	24.40	25.08	25.08
Vol/ion pair†	$V = 2M/p\rho$	cm³/mol	16.49	16.28	16.23	15.82

* BS37A–A and BS39B–A were melted in air; BS37A–V and BS39B–V were melted in vacuum.
†Calculated from known chemical composition.

generate elastic wave pulses. The waves so generated travel through the specimen, are reflected, and are then received by the transducer. When the interval between the applied rf pulses is equal to an integral multiple (p) of the round-trip transit time of the wave pulses, the echoes are superimposed (in the present case, p is equal to 1). By properly gating the incident pulses, the echo pulses are received. The signal of these pulses is then matched with an impedance matching device, amplified, and displayed on the oscilloscope. The prf of the applied pulse is measured with a frequency counter. Elastic wave velocity is calculated from the prf; 30-MHz X-cut and Y-cut quartz transducers were used for measuring longitudinal and shear wave velocities. The transducers were bonded to the specimen by a thin film of Dow Corning resin 276 V9.

The pressure-generating system included a two-stage nitrogen gas pumping system, a pressure vessel, a Harwood manganin pressure cell, and a Carey-Foster resistance bridge. The latter was used to measure and monitor the pressure in the vessel containing the specimen. The manganin coil was calibrated with a Harwood DWT–300 dead-weight tester to 4 kbars.

The prf data were obtained at 4000 psi intervals of increasing and decreasing pressure; 20 to 25 min were allowed after the pressure was changed for the specimen to reach equilibrium with the pressure and temperature in the vessel.

The temperature of the specimen was maintained at 25° ±0.1°C by a constant-temperature water jacket around the vessel and was monitored with a Chromel-Alumel thermocouple and a K–4 Leeds & Northrup potentiometer.

III. Specimens

The vitreous calcium aluminates* were those used by Levengood[9] in his studies. One glass (BS37A) is doped with SiO_2 and the other (BS39B) with BaO.

Two specimens of each composition were prepared by the manufacturer: those identified as BS37A–A and BS39B–A were melted and cooled in air at 1 bar; those identified as BS37A–V and BS39B–V were melted and cooled at reduced pressure (100 μm air pressure), so that most of the interstitial dissolved gases were removed from the melt. Each sample was prepared for wave propagation velocity measurements by grinding and polishing the two parallel faces to within 1 part in 1×10^4 parts. The specimens were 10 to 11 mm long between the parallel faces.

*Specimens were obtained from W. C. Levengood at the University of Michigan; they were produced by the Barr and Stroud Company, Glasgow, Scotland. Composition of glass BS37A is CaO 57, Al_2O_3 28, MgO 7, SiO_2 7; glass BS39B is CaO 50, Al_2O_3 34, MgO 9, and BaO 7 mol%.

IV. Measurements at 1 Bar and 25°C

The pulse repetition frequencies (prf) gave the longitudinal wave velocity (v_p) and shear wave velocity (v_s) according to the relation $v=2lf$, where v is the velocity in the specimen, l the length of the specimen, and f the prf. The effect of the phase shift due to reflection at the specimen-seal interface is less than 1° for a properly prepared seal and was neglected in the calculations. The data at 1 bar and 25°C are presented in Table I.

V. Measurements at Higher Pressures

The sound velocity variation in a specimen subjected to pressure is obtained from the relation $v/v_0=(f/f_0)\,(l/l_0)$. The zero subscript denotes initial (1 bar) conditions. The prf data were obtained at regular pressure intervals to approximately 3.5 kbars. The results for both longitudinal and shear modes are shown in the plots of (f/f_0) vs pressure (Fig. 2).

The length ratio (l_0/l) at a given pressure can be calculated from Cook's formula[10]:

$$(l_0/l) = 1 + \frac{1+\Delta}{\rho_0} \int_0^P \frac{dP}{3A - 4B}$$

where $(1+\Delta)$ is the ratio of the adiabatic bulk modulus to the isothermal bulk modulus, ρ_0 the initial density, $A=(v_{p0}f/f_0)^2$ for longitudinal waves, and $B=(v_{s0}f/f_0)^2$ for shear waves. The quantity Δ is equal to $\alpha\gamma T$, where α is the coefficient of volumetric expansion, γ the Grüneisen parameter, and T the temperature (°K). Since α is a small quantity ($<10^{-5}$/°C for calcium aluminate glasses), the quantity Δ was ignored in the computations.

The pressure derivatives of the elastic parameters are presented in Table II.

VI. Results and Discussion

As seen in Table I, the bulk densities and bulk moduli for vacuum-melted glasses are slightly higher than those for air-melted glasses of the same composition. This relation is consistent with the fact that interstitial gas and water vapor are removed from the glass when it is melted under reduced pressure.

Several investigators[11-14] have attempted to correlate bulk modulus of glasses with the various structural parameters that are basically related to the bonding forces of the atomic linkages. One such correlation of bulk modulus, K_s, shear modulus, μ, and specific volume/ion pair, V ($V=2M/p\rho$, where M is the molecular weight, p the number of atoms in the molecule, and ρ the density), was suggested by Soga and Anderson.[14] They showed that, for 29 glasses, the bulk

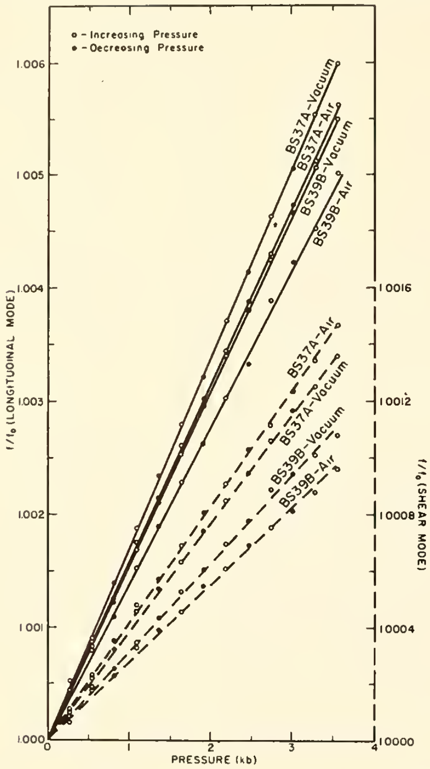

Fig. 2. Longitudinal (*solid line*) and shear (*dashed line*) frequency ratios (f/f_0) vs pressure for vitreous calcium aluminates. Melt condition for each specimen follows the specimen number.

modulus is inversely proportional to the specific volume; their data fit a line parallel to a relation for various crystalline solids (see Ref. 14, Fig. 1). Our data for vitreous calcium aluminate, if plotted on this figure, would fall reasonably close to an extension of the line for the glasses. The bulk moduli of the BaO-doped specimens are slightly higher than those of the SiO_2-doped specimens (Table I). It has been suggested[16] that there could be a significant effect on the elastic modulus of a glass when high-field-strength modifying ions, such as Ba, are introduced.

In the present study, the bulk moduli for the glasses which contain appreciable amounts of CaO are higher than those for the silicate glasses listed in Refs. 1, 2, 4, 5, and 14.

Poisson's ratio for the glasses studied varied from 0.283 to 0.292 (Table I), which is quite high compared to the values for glasses such as borosilicate[6] and fused silica and for fused quartz.[5] One explanation for relatively high Poisson's ratios (>0.25) for glasses containing appreciable amounts of large alkali and alkaline-earth ions was given by Smyth[12]: "...when the modifying ions are large, they fill the interstices in which they are located so that any change in the shape of the glass means a deformation of these ions as well as the distortion of the network."

The relations between compressional and shear wave velocities and pressure are shown in Fig. 3. The longitudinal velocities increase linearly with pressure within experimental error for all the specimens. Values of (dv_p/dP) are higher for the vacuum-melted specimens than for the air-melted specimens of the same composition (Table II). Also, the (dv_p/dP) values for the SiO_2-doped vacuum-melted and air-melted specimens are higher than for the BaO-doped specimens. The relations among the shear velocities and among

Table II. Pressure Derivatives of the Elastic Parameters of the Calcium Aluminate Glasses

Derivative	Glass No.			
	BS37A–A	BS37A–V	BS39B–A	BS39B–V
$\frac{dv_p}{dP}$ (km/(s·kbar)×10³)	8.1	8.9	6.8	7.8
$\frac{dv_s}{dP}$ (km/(s·kbar)×10⁴)	1.1	0.3	−4.1	−2.3
$\frac{dK}{dP}$	4.31	4.71	4.00	4.42
$\frac{d\mu}{dP}$	0.51	0.48	0.40	0.42
$\frac{d\sigma}{dP}$ (kbars⁻¹×10⁴)	6.9	7.5	6.8	7.1

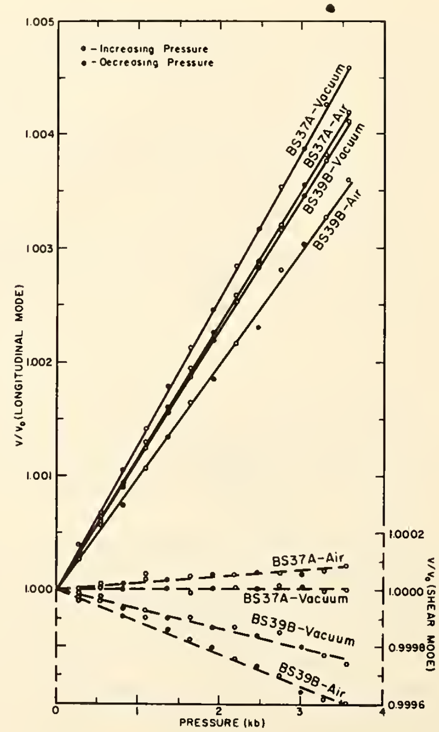

Fig. 3. Longitudinal (*solid line*) and shear (*dashed line*) velocity ratios (v/v_0) vs pressure for vitreous calcium aluminates.

their pressure derivatives are not simple, however. Figure 3 shows that in the BaO-doped vacuum-melted and air-melted specimens the behavior of the shear velocity under pressure is anomalous, i.e. decreasing with pressure, and also that the behavior of the air-melted specimen is relatively more anomalous. The (dv_s/dP) values for the SiO_2-doped specimens are normal (positive) but low and are higher for the air-melted specimen. Anomalous behavior of shear velocity with pressure[4–6] has been found previously only in silicate glasses with a high silica content (>70%).

Poisson's ratio is plotted vs pressure in Fig. 4. The ($d\sigma/dP$) values for the calcium aluminate glasses lie between 6.8×10^{-4} and 7.5×10^{-4} kbars⁻¹ (Table II).

The relations between bulk modulus and pressure are shown in Fig. 5. Since interstitial gas and water vapor are removed in vacuum-melting, these glasses were expected to be less compressible than air-melted specimens, and this was confirmed: the vacuum-melted specimens had higher bulk moduli (low compressibility), and, further, the pressure derivatives of their bulk moduli (dK_s/dP) are higher: 4.7 (SiO_2-doped) and 4.4 (BaO-doped) for vacuum-melted compared with 4.3 (SiO_2-doped) and 4.0 (BaO-doped) for air-melted glasses. The data also show that for both melt conditions, the BaO-doped specimen is less compressible than the SiO_2-doped specimen.

VII. Summary and Conclusions

1. The calcium aluminate glasses studied are characterized by higher bulk and shear moduli and Poisson's ratios, in general, than the values reported for various silicate glasses.

2. The data for the calcium aluminate glasses fit well with the bulk modulus vs specific volume/ion pair relation reported for other glasses.

3. The elastic parameters of the calcium aluminate glasses and the pressure derivatives of these parameters are influenced by composition and melt condition. However, more data are needed to quantitatively evaluate the parameters in terms of compositional variation and melt condition.

4. At 1 bar, the vacuum-melted BaO-doped glass is the least compressible (highest K_s), whereas the air-melted SiO_2-doped glass is the most compressible (lowest K_s).

5. The anomalous behavior of shear velocity with respect to pressure in certain glasses has been attributed to high silica content; this study indicates that calcium aluminates with low silica content doped with BaO also exhibit anomalous behavior.

6. The (dK_s/dP) values of the calcium aluminate glasses examined range from 4.0 to 4.7, depending on composition and melt condition. The vacuum-melted and SiO_2-doped specimens have relatively higher (dK_s/dP) values.

Acknowledgments

The authors thank W. C. Levengood of the University of Michigan for providing the specimens and G. R. Miller and G. H. Sutton for constructive criticism of the paper.

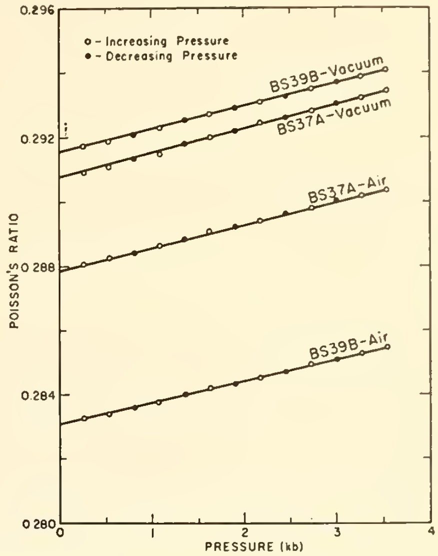

Fig. 4. Poisson's ratio as function of pressure for vitreous calcium aluminates.

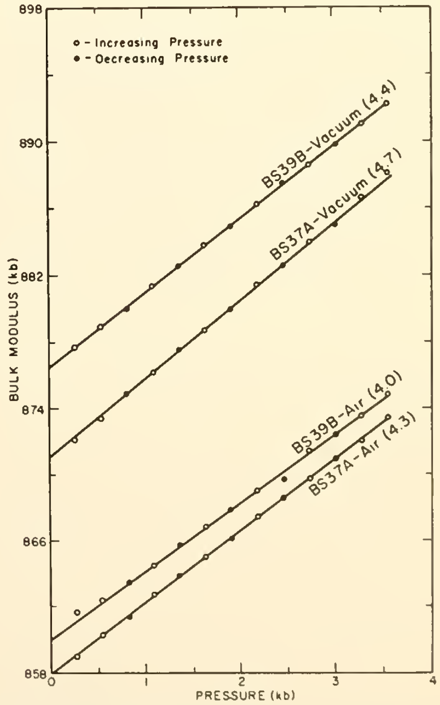

Fig. 5. Absolute values for adiabatic bulk modulus as function of pressure for vitreous calcium aluminates. The (dK_s/dP) values are given in parentheses.

References

[1] P. W. Bridgman, "Compressibility of Several Artificial and Natural Glasses," *Am. J. Sci.*, 10, 81–102 (1924).
[2] Francis Birch, "Effect of Pressure on the Modulus of Rigidity of Several Metals and Glasses," *J. Appl. Phys.*, 8, 129–33 (1937).
[3] O. L. Anderson and G. J. Dienes; Chapter 18 in Noncrystalline Solids. Edited by V. D. Frechette. John Wiley & Sons, Inc., New York, 1960.
[4] M. H. Manghnani, "Role of Silica Content in the Anomalous Elastic Behavior of Silicate Glasses Under Pressure"; presented at the 71st Annual Meeting, The American Ceramic Society, Washington, D. C., May 5, 1969 (Glass Division, No. 10–G–69); for abstract see *Am. Ceram. Soc. Bull.*, 48 [4] 434 (1969).
[5] Louis Peselnick, Robert Meister, and W. H. Wilson, "Pressure Derivatives of Elastic Moduli of Fused Quartz to 10 Kilobars," *J. Phys. Chem. Solids*, 28 [4] 635–39 (1967).
[6] M. H. Manghnani and W. E. Benzing, "Pressure Derivatives of Elastic Moduli of Vycor Glass to 8 Kilobars," *ibid.*, 30 [9] (1969).
[7] H. J. McSkimin, "Pulse Superposition Method for Measuring Ultrasonic Wave Velocities in Solids," *J. Acoust. Soc. Am.*, 33 [1] 12–16 (1961).
[8] Edward Schreiber and O. L. Anderson, "Pressure Derivatives of the Sound Velocities of Polycrystalline Alumina," *J. Am. Ceram. Soc.*, 49 [4] 184–90 (1966).
[9] W. C. Levengood, "Stress-Induced Defects in Vitreous Calcium Aluminates," *J. Appl. Opt.*, 5 [12] 1906–10 (1966).
[10] R. K. Cook, "Variation of Elastic Constants and Static Strains with Hydrostatic Pressure: Method for Calculation from Ultrasonic Measurements," *J. Acoust. Soc. Am.*, 29 [4] 445–49 (1957).
[11] R. J. Charles; pp. 1–38 in Progress in Ceramic Science, Vol. 1. Edited by J. E. Burke. Pergamon Press, New York, 1961.
[12] H. T. Smyth, "Elastic Properties of Glasses," *J. Am. Ceram. Soc.*, 42 [6] 276–79 (1959).
[13] C. J. Phillips, "Calculation of Young's Modulus of Elasticity from Composition of Simple and Complex Silicate Glasses," *Glass Technol.*, 5 [6] 216–23 (1964).
[14] N. Soga and O. L. Anderson; Paper No. 37 in Proceedings of the Seventh International Congress on Glass, Brussels, Belgium, 1965, Vol. I; 9 pp. Institut National du Verre, Charleroi, Belgium, 1966.
[15] G. Y. Onada and S. D. Brown, "High Modulus Glasses Based on Ceramic Oxides," Final Report, Contract N 00019–67–C–301, Rocketdyne, Canoga Park, California, 1–53, 1968.

Reprinted from Marine Technological Society
Journal, Vol. 3, No. 3, 41-46.

TIDAL MODULATION OF THE FLORIDA CURRENT SURFACE FLOW

John A. Smith[2], *Bernard D. Zetler*[3], *and Saul Broida*[2]

ABSTRACT

A tidal current analysis has been made of surface current observations obtained by the General Dynamics Monster Buoy in 1965 in the Florida Current off Hollywood, Florida. The analysis of 15 days of hourly speeds shows that the diurnal constituents K_1 and O_1 have larger amplitudes than the semidaily M_2 and S_2, this in sharp contrast to the predominantly semidaily tide in the area. The amplitudes and phases of the diurnal constituents support the hypothesis of a diurnal standing wave oscillating between the open ocean and the Gulf of Mexico with a node in the Florida Straits near the latitude of Miami. The tidal analysis indicates that the tidal modulation accounts for roughly one fifth of the variance in the observations.

INTRODUCTION

The pulsations of tidal origin in the Florida Current have long been a subject of interest and speculation. Pillsbury (1891) found monthly current variations related to the declination of the moon, and daily oscillations amounting in some instances to as large as 128 cm/sec. He reported two periods of increase and two periods of decrease during a lunar day. Parr (1937) reported current speed fluctuations up to 50 cm/sec. apparently caused by tidal forces, both diurnal, and more dominantly, semidiurnal. From studies of electric potential measurements between Key West, Florida and Havana, Cuba, Wertheim (1954) was able to show evidence of the diurnal tidal influence on the transport through the Florida Straits. He cited the dependence of the transport on both the semidiurnal Atlantic tide and the diurnal Gulf of Mexico tide. Webster (1961) analyzed a large amount of GEK data for both the Straits of Florida and off Onslow Bay, North Carolina. He concluded that although it was probably rash to ascribe the velocity fluctuation of the Florida Current predominantly to tidal causes, the periods of the fluctuations observed were on the order of one day.

Recently Schmitz and Richardson (1967) utilized a least-squares harmonic analysis of transport data (acquired over a period of three years using the free-fall instrument technique) across a section of the Florida Current. Based on the limited data available, they indicate that it is possible for fluctuations of tidal period to be the major modulation of the Florida Current transport. Their estimates of transport amplitudes are 3.5 ± 1 ($10^6 m^3 sec^{-1}$) for tidal coefficients M_2, K_1 and O_1, and 1.5 ± 1 ($10^6 m^3 sec^{-1}$) for S_2.

MONSTER BUOY DATA

Late in 1965, a General Dynamics ocean buoy was moored for testing and evaluation in the Straits of Florida at

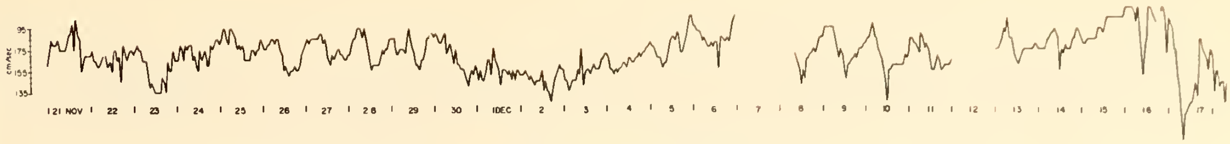

Figure 1. Current Velocity versus Time

Lat. 26°01'N and Long. 79°51.2'W. From November 20 to December 18, 1965, the buoy was equipped with a rotary current meter placed immediately beneath the water surface. Current speed data for one-minute averages taken approximately each hour were telemetered to the mainland and recorded. Also available for this period are wind speed, wind direction, barometric pressure and the significant wave height at the time of recording. Current direction is considered as directionally steady in the north-south orientation of the Florida Current at this location. A plot of current velocity versus time (Figure 1) reveals fluctuations of current speed on the order of 30 cm/sec. with apparent periodicity of 24 hours. Harmonic analysis of the data was conducted to determine if the fluctuations were indeed due largely to tidal effects.

HARMONIC ANALYSIS

Comparative tests show that the harmonic constants for the same set of constituents are slightly more accurate utilizing the least-squares method as opposed to the classical approach (Zetler and Lennon, 1967). The greatest advantage in using the least-squares method, however, is that it requires neither equally spaced data nor a synodic period, whereas the traditional Fourier tidal analysis requires both equally spaced data and a quasi-synodic period of the principal constituents (Zetler, *et al,* 1965). The least-squares method has been adopted by the Coast and Geodetic Survey for the analysis of long data series but, for 15 and 29 day series, a computer program based on Fourier analysis is now in use.

Also, Parseval's Theorem states that the energy of a composite wave is composed of the sum of the energies of each of the distinct harmonic constituents of the waves of different frequencies making up the basic wave. Thus, from the current fluctuation data, the percentage of total energy due to periodic variations was calculated and compared to the total energy of all of the fluctuations; and the total energy contributed by individual periodic components was determined.

RESULTS

Figure 2 presents a plot of current velocity versus time with a superimposed plot of the predicted tidal component of the current from the results of this analysis. The predicted tidal current is plotted about the mean current (167.05 cm/sec.) indicating the predicted Florida Current in the absence of fluctuations of a non-tidal nature. The hourly predictions were prepared by the Coast and Geodetic Survey using a least count of 0.1 knot, hence the step characteristic of the plotted curve. Figure 3 is a plot of the residual after the predicted tidal modulation of the Florida Current has been removed.

As can be seen from Figure 1, the second half of the current data series is of much poorer quality than the first half. Gaps in the record were due to telemetry and recording failure. The intense abrupt fluctuations seem to be indicative of a gradual failure of the current meter. Data obtained from the first fifteen days of this period are continuous, and the current meter one-minute speed averages were available for each hour.

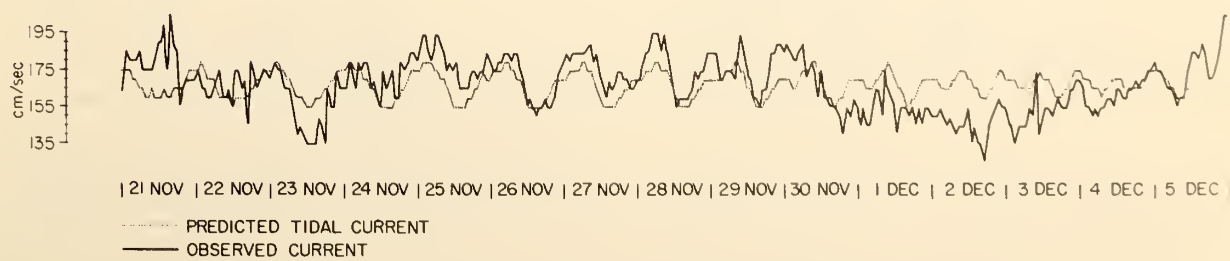

Figure 2. Current Velocity versus Time with Superimposed Plot of Predicted Tidal Modulation

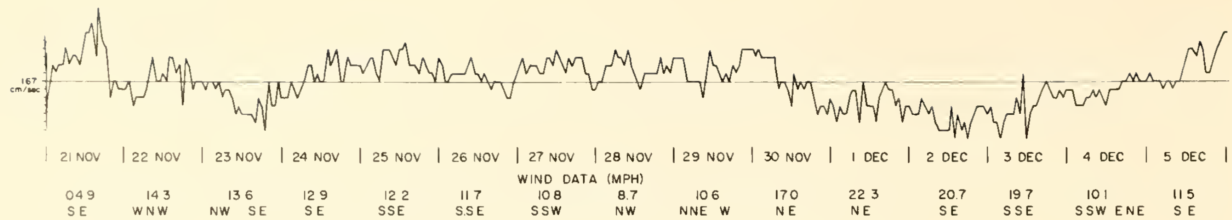

Figure 3. Plot of the Residual After Tidal Modulation is Removed

An initial computer analysis of the entire data series utilizing a least-squares program indicated that the diurnal tidal constituents, K_1 and O_1, are the predominant contributors to the tidal fluctuations of the current. The results of the least-squares analysis for the diurnal constituents for the first fifteen days and the entire period are compared in Table 1. That the amplitudes and phase angles agree reasonably well in the two separate analyses is indicative that the diurnal tidal components are in fact significant and that our results are not due to random fluctuations. Because the second half of the data series was of marginal reliability, it is not included in the remainder of the analysis.

Table 2 indicates that three techniques for solving for the major tidal constituents produce relatively small differences. These can be accounted for based on the method of each technique. The Fourier computer analysis was selected for determining the harmonic constants contained in Table 3. A total of 24 constituents, of which 15 were inferred from the 4 major constituents, were then recombined to produce the predicted tidal modulation of the Florida Current for the period 21 November through 5 December 1965.

TABLE 1

Comparison of least-squares harmonic analysis of the first half of the data series with that of the entire series

	K1		O1	
	Amplitude*	Phase	Amplitude*	Phase
1. 15 DAY ANALYSIS (360 Data Entries)	0.11	59.8°	0.12	273.5°
2. ENTIRE DATA SERIES (596 Data Entries)	0.15	43.5°	0.13	296.5°

*Amplitude is in knots.

Note: Amplitudes and phases are values prior to correcting for equilibrium argument, interference effects, etc. These comparative results will slightly differ from those found elsewhere in this paper as during the above analysis the constituent N_2 was included in the calculations.

TABLE 2

Comparison of results of harmonic analysis on the first 15 day data period using different analysis methods

METHOD	M_2		S_2		K_1		O_1	
	Amp*	Phase	Amp*	Phase	Amp*	Phase	Amp*	Phase
1. Hand Analysis (C&GS Spec. Pub. No. 98)	0.063	55.73°	0.048	300.07°	0.125	60.43°	0.103	277.27°
2. Least-Squares Analysis	0.066	57.2°	0.047	301.8°	0.115	59.6°	0.119	274.0°
3. Fourier Computer Analysis	0.063	59.64°	0.047	301.46°	0.132	55.94°	0.106	281.42°

*Amplitude is given in knots.

Note: The amplitudes and phases given are values prior to correcting for equilibrium argument, interference effects, etc.

TABLE 3

Harmonic constants from Florida current data

CONSTITUENT**	AMPLITUDE (H) (cm/sec)	KAPPA***
(a) DIURNAL CONSTITUENTS		
K_1	5.710	24.49°
O_1	5.551	12.25°
P_1	1.888	24.49°
Q_1	1.075	6.13°
J_1	0.437	30.61°
M_1	0.396	18.37°
OO_1	0.237	36.74°
RHO_1	0.211	6.98°
$2Q_1$	0.144	0.00°
(b) OTHER CONSTITUENTS		
M_2	3.400	114.95°
S_2	2.500	309.40°
S_6	1.101	159.88°
K_2	0.679	309.40°
M_6	0.664	277.76°
N_2	0.658	203.68°
S_4	0.458	236.23°
M_4	0.304	41.08°
M_8	0.278	290.55°
T_2	0.149	309.40°
NU_2	0.129	191.79°
L_2	0.098	26.22°
$2N_2$	0.087	292.41°
$LAMBDA_2$	0.026	38.13°
R_2	0.020	309.40°

**Nomenclature and constituent speeds are in accordance with the classical Doodson classification.

***The phases are referred to tidal flow to the north; for a south direction apply ±180°. To convert to Greenwich Epoch (G), add the product of the longitude (79.85°) times the value of the constituent subscript.

Astronomical data for the period are given in Table 4. It can be seen that the predicted tidal modulation is in agreement with the astronomical data for the period. The additive effect of M_2 and S_2 on November 22 is not readily apparent due to the semi-diurnal components being over-shadowed by K_1 and O_1 as they approach phase agreement on November 26. The predominant diurnal modulation becomes negligible as K_1 and O_1 come into opposition on December 3, leaving only semi-diurnal tidal modulation of less than usual amplitude because M_2 and S_2 were in phase opposition on December 1.

TABLE 4

Astronomical data for period
21 November through 17 December 1965*

22 November	New moon
26 November	Moon farthest south of equator
29 November	Moon in apogee
1 December	Moon in first quarter
3 December	Moon at equator
8 December	Full moon
10 December	Moon farthest north of equator
11 December	Moon in perigee
15 December	Moon in last quarter
16 December	Moon at equator

*From *American Ephemeris and Nautical Almanac.*

Fluctuations of the observed and predicted current are in excellent agreement and clearly show that the tidal modulation is the major periodic fluctuation of the current during the period 23 through 30 November. During the remainder of the data series, correlation with the predicted tidal modulation remains fairly good, but the mean current speed is raised or lowered, apparently in response to local wind stress, or possibly in response to atmospheric variations over the water regions which are coupled to the Florida Straits.

Figure 3 is a plot of the residual after the predicted tidal modulation has been removed from the data. Included is the mean local wind speed and average wind direction at the buoy location in the Straits during each day from midnight to midnight. It would appear that response of the current to wind stress from either the east or west is negligible, and further that the current responds fairly rapidly to winds from a southerly direction. Response of the current to northerly winds appears more complicated, with the indication from this limited data series being that the current initially is slow to respond to northerly winds; but once the response commences, the current speed is greatly lowered and recovery to normal conditions is quite gradual. The seemingly erratic period, November 30 through December 3, contained the highest wind speeds, and rough seas were prevalent.

Table 5 presents statistical results from the 15 day analysis of the current data. During this period the tidal modulation accounted for 21.35 per cent of the total fluctuations, with the remainder being fluctuations of an apparent non-periodic nature.

DISCUSSION

The analysis of the surface current data reveals large diurnal tidal modulation of the Florida Current. This is in agreement with the tidal analysis performed on the transport of the Florida Current by Richardson and Schmitz *(op. cit.)* and tidal analysis of transport fluctuations from studies of electric potential measurements by Wertheim *(op. cit.)*. It is further in agreement with Project MIMI's results, where underwater acoustic signals transmitted across the Straits of Florida over long periods of time have shown prominent diurnal phase changes (Steinberg and Birdsall, 1966), (Clark and Yarnall, 1967).

Recently, Zetler (1968) calculated the amplitude of the K_1 tidal current in the Florida Straits required to conform to observations of the oscillating diurnal tidal water transport in the Gulf of Mexico. The K_1 amplitude of 0.11 knots found from the harmonic analysis of the Monster Buoy data is remarkably close to his calculated value of 0.12 knots. Zetler concluded, after consideration of the known K_1 and O_1 amplitudes and phase angles at shore stations along either side of the Straits of Florida, that there is a strong indication of a longitudinal standing wave for the major diurnal tidal components in the Straits of Florida, with a node close to the latitude of Miami. The large amplitudes of the diurnal constituents of the tidal modulation of the Florida Current at the Hollywood latitude are in agreement with this concept, as the tidal current should be maximum at the node. Zetler and Hansen (1968) have used the K_1 phase of the tidal current observed at the Monster Buoy as additional evidence of a standing wave. The current observations near the node should have a phase 90° earlier than the observed tide in the Gulf of Mexico. Because of differences in longitude, it is more meaningful to use phase angles referred to the same meridian, usually Greenwich. An approximate generalized Greenwich phase for K_1 in the Gulf of Mexico is 20°. The comparable phase of 284° for the tidal current at the Monster Buoy is about 90° earlier than the tide in the Gulf and therefore supports the hypothesis of a standing wave.

TABLE 5

Statistical results and energy calculations for the 15 day period

1. Mean Current Velocity	167.05 cm/sec
2. Standard Deviation	15.42 cm/sec
3. Average Fluctuation	9.23 per cent
4. Total Current Variance	237.90 cm^2/sec^2
5. Predicted Tidal Current Variance	50.79 cm^2/sec^2
6. Fluctuations Due to Tidal Components	21.35 per cent
7. Per cent of Item 6 Due to Major Diurnal Tidal Components (K_1 and O_1)	71 per cent
8. Per cent of Item 6 Due to Major Semi-Diurnal Tidal Components (M_2 and S_2)	20 per cent
9. Energy Contributed by Individual Tidal Constituents (cm^2/sec^2)	
K_1	16.30
O_1	15.40
M_2	5.78
S_2	3.12
P_1	1.78
S_6	0.60
Q_1	0.58
Remainder Semi-Diurnal Constituents	0.88
Remainder Diurnal Constituents	0.24

SUMMARY AND CONCLUSIONS

Harmonic analysis of Monster Buoy data covering 15 complete days confirms that the tidal influence on the Florida Current surface flow does not conform to the usual Atlantic coastal tidal configuration. Instead, the influence is transitional between the semi-diurnal Atlantic tide and the diurnal Gulf of Mexico tide. The tidal coupling between the Gulf of Mexico and the Atlantic Ocean, with pronounced diurnal features, can be explained at present only by a heretofore overlooked longitudinal, diurnal, standing wave oscillating through the Florida Straits. The obtainment and subsequent analysis of tide observations at additional points along the lower third of the east coast of Florida should confirm the presence of this diurnal, standing wave.

A fluctuation of 10 per cent of the mean surface current is given as representative of the Florida Current. Slightly more than one-fifth of this modulation is attributed to tidal influence.

ACKNOWLEDGMENTS

The authors wish to thank R. A. Cummings, C. B. Taylor, and other Coast and Geodetic Survey, ESSA, personnel at Rockville, Md. for providing tidal predictions and analysis. The Florida Current data were made available by General Dynamics Corp. and W. S. Richardson of Nova University. This work was supported by the Office of Naval Research under Contract Nonr 4008 (02).

LT. Smith, U.S. Navy, is currently an instructor in the Naval Science Department at the U.S. Naval Academy, Annapolis. He has a B.S., 1961, from the USNA, and an M.S. (Oceanography), 1968, from the University of Miami.

Bernard D. Zetler is Director of the Physical Oceanography Laboratory, Atlantic Oceanographic Laboratories, ESSA in Miami. He has a B.S. from Brooklyn College, and has done graduate work at George Washington University and the Department of Agriculture Graduate School. He has been with the Federal Government since 1938, serving in the Hydrographic Office and the Coast and Geodetic Survey.

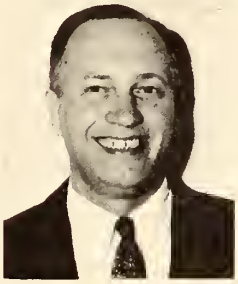

Saul Broida has been on the faculty of the Institute of Marine Sciences, University of Miami, since 1961. He has a PhD in physical oceanography. He has done extensive research in the dynamics and kinematics of the Florida Current, and has participated in Equalant II, International Cooperative Investigation of the Tropical Atlantic.

[1]Contribution No. 1022 from the Institute of Marine Sciences, University of Miami.

[2]Institute of Marine Sciences, University of Miami, Miami, Florida.

[3]Physical Oceanography Laboratory, Atlantic Oceanographic Laboratories, ESSA, Miami, Florida

REFERENCES

1. Clark, John G. and J. R. Yarnall, 1967. "Long Range Ocean Acoustics and Synoptic Oceanography, Straits of Florida Results," Contribution No. 798, Institute of Marine Sciences, University of Miami. Unpublished Manuscript.

2. Parr, Albert E., 1937. "Report of Hydrographic Observations at a Series of Anchor Stations Across the Straits of Florida," Bulletin Bingham Oceanographic Laboratory, Yale University. 6 pp. 1-62.

3. Pillsbury, John E., 1891. "The Gulfstream – A Description of the Methods Employed in the Investigation and the Results of the Research," Report of the Superintendent of the U. S. Coast and Geodetic Survey, Appendix 10, 461-620.

4. Schmitz, William J. and W. S. Richardson, 1967. "On the Transport of the Florida Current," Nova University. Unpublished Manuscript.

5. Steinberg, John C. and T. G. Birdsall, 1966. "Underwater Sound Propagation in the Straits of Florida," Journal Acoustical Society of America, 39 (2), p. 301-315.

6. Webster, F., 1961. "The Effect of Meanders on the Kinetic Energy Balance of the Gulfstream," Tellus 13 (3), p. 392-401.

7. Wertheim, G. K., 1954. "Studies of the Electric Potential Between Key West, Florida and Havana, Cuba," Trans-American Geophysical Union, 35 (6), p. 872-882.

8. Zetler, Bernard D., M. D. Schuldt, R. W. Whipple and S. D. Hicks, 1965. "Harmonic Analysis of Tides from Data Randomly Spaced in Time", Journal of Geophysical Research, 70 (12), p. 2805-2811.

9. Zetler, Bernard D. and G. W. Lennon, 1967. "Some Comparative Tests of Tidal Analytical Processes," International Hydrographic Review, 44 (1), p. 139-147.

10. Zetler, Bernard D., 1968. "Tides in the Gulf of Mexico," Physical Oceanography Laboratory, ESSA, Miami. Preliminary Report. Unpublished Manuscript.

11. Zetler, Bernard D. and D. V. Hansen, 1968. "Proposed Tide Program – Gulf of Mexico," Physical Oceanography Laboratory, ESSA, Miami. Unpublished Manuscript.

Deep-Sea Research, 1969, Supplement to Vol. 16, pp. 447 to 470. Pergamon Press. Printed in Great Britain.

Fluctuations of the Florida Current inferred from sea level records

C. Wunsch*, D. V. Hansen† and B. D. Zetler†

Abstract—Power spectra and coherences were computed from simultaneous tide records at Miami, Florida; Cat Cay, Bimini Islands; Key West, Florida; and Havana, Cuba, as a measure of statistical variability of the Florida Current. Diurnal and semi-diurnal tides account for most of the power in sea level variations at all stations, and approximately half of the remaining power is in the annual variation. Power levels are generally higher on the left side of the current but no significant power peaks were found between the annual and tidal frequencies. Coherence is generally low between all stations, but where significant coherence is found, it occurs with essentially zero phase, indicating that sea level tends to rise or fall together on opposite sides of the Florida Straits. The zero-phase coherence suggests a common response to local weather events. Low coherence was found between atmospheric pressure and sea level, with essentially an inverse barometer response for fluctuations of period greater than ten days. At shorter periods the response is direct barometric. Coherence between vector wind and sea level was also low, so that removal of linear weather effects (by a Wiener multichannel filter) accomplished little reduction of total power, and did not materially change coherence amplitudes or phases. A sharp result is obscured by the general lack of coherence between records, but the major conclusions are that the Florida Current is fairly steady, r.m.s. modulation at all periods between two days and one year amounting to perhaps 25% of the mean, the annual fluctuations accounting for about 10%, and linear weather effects have only a minor influence on statistical sea level. The instantaneous fluctuations of the transport could be considerably larger, but the low r.m.s. values indicate that extreme transport values are unusual if they occur at all.

INTRODUCTION

Using ship-drift data, Fuglister (1951) has documented an annual cycle in surface current speed in the Gulf Stream system, with a range of approximately one-third the mean current speed, as shown in Fig. 1. Pillsbury (1890) observed fortnightly and higher frequency tidal modulation of flow in the Straits of Florida. Von Arx, Bumpus and Richardson (1955) suggested that visual and thermal "shingle" structures observed along the edge of the Gulf Stream northward from the Straits of Florida might be caused by fluctuations of the flow through the Straits. Dominant periods of approximately four and seven days were found in 28 days of GEK data from this region analyzed by Webster (1961). These results were all based on short records however, and therefore no conclusions could be drawn about the significance of the observed fluctuations.

The only intensive study of fluctuations in flow rate and transport appears to be that of Wertheim (1954) who obtained electrical potential measurements by means of an underwater telegraph cable between Key West and Havana. The potential measurements were converted to volume transport T, by the relation

$$T = \frac{d}{H} \Delta\phi \tag{1.1}$$

*Department of Earth and Planetary Sciences, Massachusetts Institute of Technology, Cambridge, Massachusetts.

†Physical Oceanography Laboratory, Atlantic Oceanographic Laboratories, ESSA, Miami, Florida.

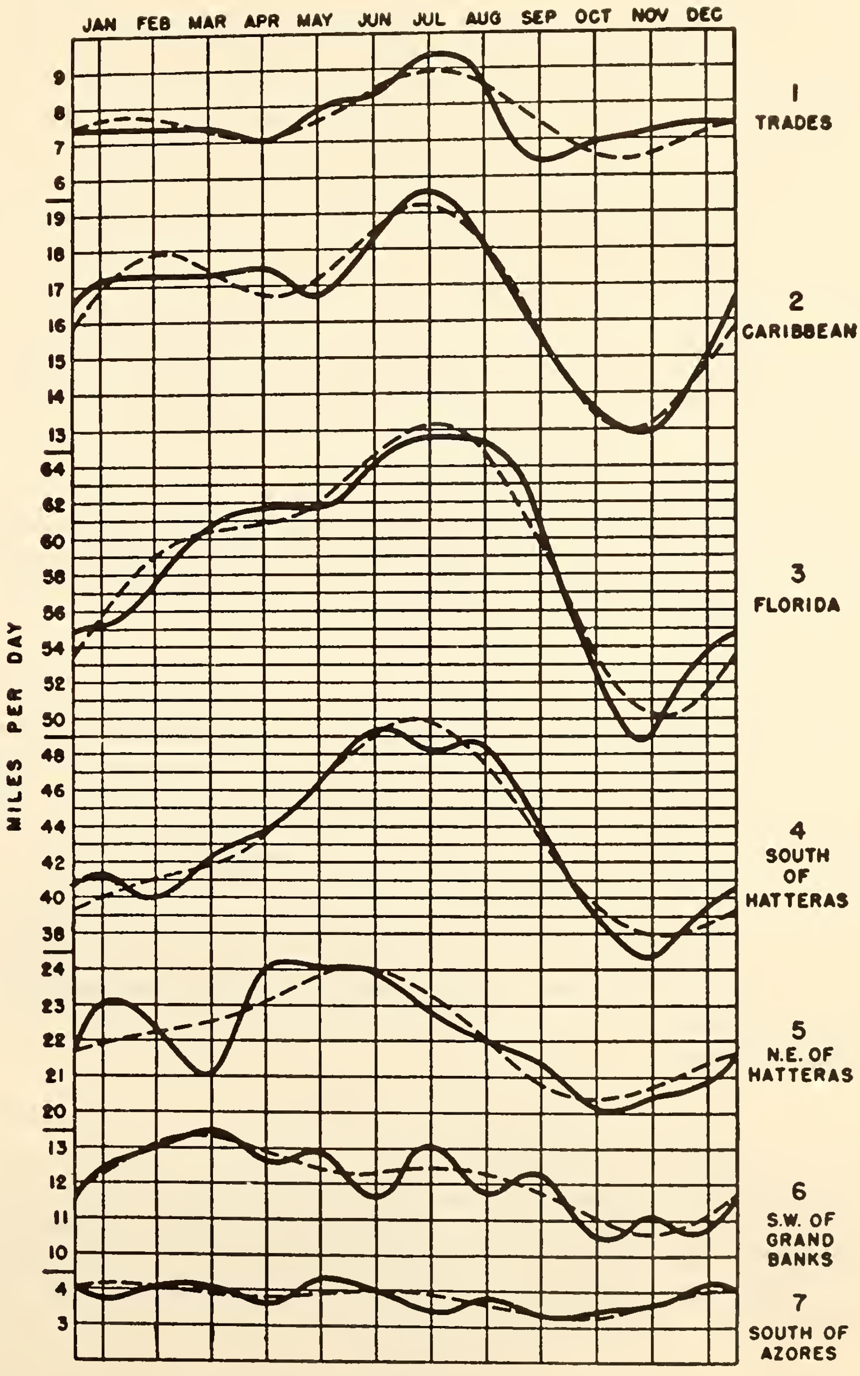

Fig. 1. Annual cycle in surface currents of the Gulf Stream system. After FUGLISTER (1951). Included is the annual variation of the Trade Wind system. Broken line represents fitted sinusoids.

where H is the vertical component of the earth's magnetic field, d is the mean depth of the channel, and $\Delta\phi$ is the electrical potential difference measured across the channel. Annual means of the transports so obtained varied only moderately from 25 $\times$ 10^6 m^3/sec over several years (cf. STOMMEL, 1957, 1959, 1961, and BROIDA, 1962, 1963, for later reports of these measurements). This figure is about 80% of that found in recent direct measurements by SCHMITZ and RICHARDSON (1968), which suggests that the potential difference generated by the current is partially short-circuited by the conducting bottom. In addition to tidal period modulations, the data show large erratic transport fluctuations (Fig. 2). Changes as large as the mean transport occuring within a few days occasioned speculation about transport switching between the Florida Current and Antilles Current branches of the Gulf Stream. But the Florida Current does not fill the strait between Key West and Havana in the same sense that it does between Miami and the Bahama Banks, and there remains the possibility (raised and dismissed by Wertheim) that some of the variation observed is due to partial short-circuiting of the electrical potential by lateral movement of the axis of the stream into regions of varying depth.

A series of papers by MONTGOMERY (1938, 1941a, b) lays the foundation for our own analysis of fluctuations of the Florida Current. The first consideration, and the only one for which Montgomery had suitable data for application to the Straits of Florida, is that of the Bernoulli relation between sea level and the speed of the flow on a surface streamline,

$$V_s^2 + 2g\zeta = \text{constant}, \tag{1.2}$$

where V_s denotes surface current speed in the stream axis, g is gravitational acceleration and ζ is local sea level. MONTGOMERY (1938, 1941a) in applying (1.2) to the Straits of Florida between Key West and Miami found that the mean sea level difference between these stations determined by a precise leveling survey was substantially less than required to explain the observed acceleration of the current between these stations. The monthly means of sea level difference between the two places occasionally indicated a negative slope, leading to the conclusion that sea level variations on one coast are not a useful indication of the strength of the Florida Current. Nonetheless, assuming sea level is relatively invariable somewhere upstream and that the speed of the stream in the axis of the current is the controlling measure of the strength of the flow, we expect local sea level to respond to changes in current speed approximately as

$$\frac{\partial\zeta}{\partial V_s} = \frac{-V_s}{g} \sim -0{\cdot}2 \text{ sec}$$

more or less uniformly across the stream.

Tide gauges installed at Havana, Cuba and Cat Cay, B.I., provide data, unavailable to Montgomery, on variations of sea level across as well as along the current. In a geostrophic flow, the Coriolis effect associated with the surface current is in near balance with the transverse pressure gradient, requiring a difference in sea level across the stream,

$$\Delta\zeta = \frac{fL}{g}\bar{V}_s \tag{1.3}$$

where the overbar denotes the average value across the stream, L is the width of the stream, and f is the Coriolis parameter. Studies by ISELIN (1940), HELA (1952), and

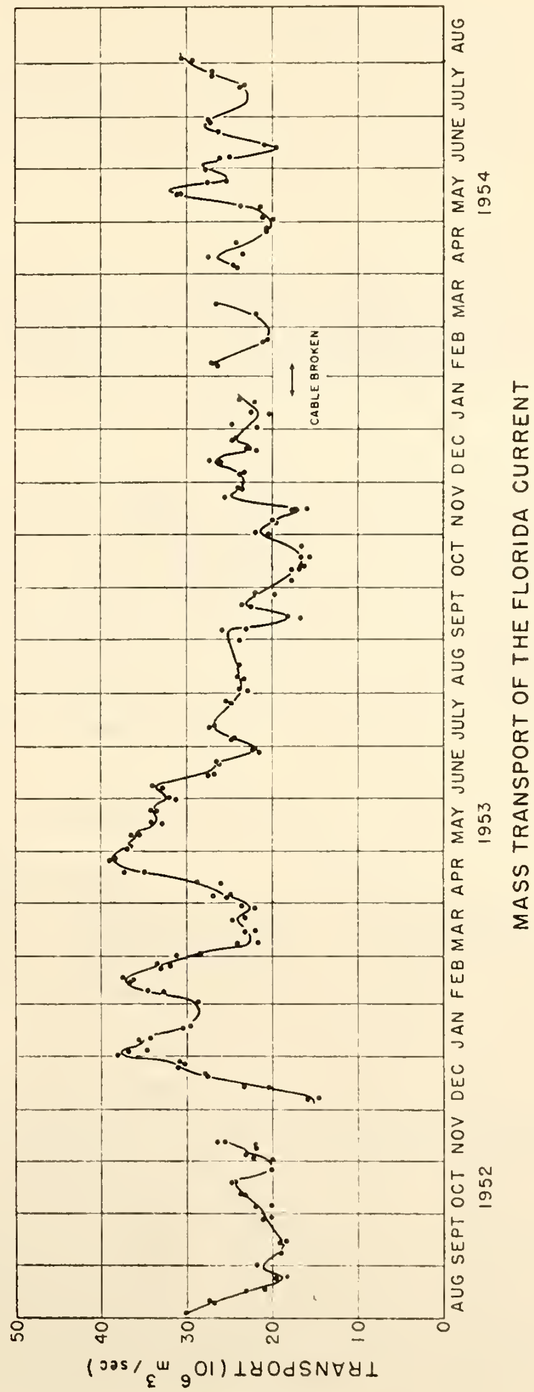

Fig. 2. Apparent changes in Gulf Stream transport as deduced from cable data, after Wertheim (1954).

STOMMEL (1953) of monthly mean sea level at these stations are summarized by STOMMEL (1965). Sea level at all stations and cross-stream differences of sea level are greatest in July when the flow is strongest.

Geodetic leveling does not span the Florida Straits with sufficient precision to enable direct determination of absolute differences in sea level, so we consider only the variation of sea level difference implied by the geostrophic relation

$$\frac{\partial \zeta}{\partial \bar{V}_s} = \frac{fL}{g},$$

which amounts to approximately 0·5 sec and 0·8 sec at Miami–Cat Cay and Key West–Havana respectively. In the simplest interpretation, the sea level change should be of the same amplitude and opposite sign on the two sides of the channel.

Curvature associated with meandering of the stream within the straits introduces perturbations

$$\pm \frac{L}{g} \frac{(\overline{V_s^2})}{R}$$

into (1.3), where R is the radius of curvature of the flow. Since very little is known of the magnitude and cross-stream coherence of curvature occuring in the stream, we have estimated the possible importance of this effect from 17 six-hour drogue trajectories from the Gulf Stream at mean Lat. 32°N.*, where the flow is presumably subject to less severe lateral constraint than in the Straits of Florida. The mean curvature in these trajectories is 0·0056 km^{-1}, in accord with that of the eastward turning of the stream at this latitude, and the standard deviation is 0·004 km^{-1}. Using $\overline{V_s^2} \sim 1$ m^2/sec^2, the perturbation of sea level difference is estimated as

$$\Delta\zeta = \frac{\partial \zeta}{\partial \left(\frac{1}{R}\right)} \Delta \left(\frac{1}{R}\right) = \overline{V_s^2} \left(\frac{L}{g}\right) \Delta \left(\frac{1}{R}\right) \sim 5 \text{ cm}$$

a potentially significant contribution, but probably an overestimate.

The absolute difference of sea level across the Straits of Florida is useful as a reference against which to measure the observed fluctuations. By applying (1.3) to the current measurements by PILLSBURY (1890), MONTGOMERY (1941b) and HELA (1952) estimated the cross stream difference in sea level at Havana and Miami as 52 and 58 cm, respectively. Using the recent transport measurements reported by SCHMITZ and RICHARDSON (1968) we compute a sea level difference of 66 cm at Miami. Little is known about the representativeness of these measurements except that monthly mean sea level at Miami was near normal at about 5 cm below the annual mean when most of the observations by Schmitz and Richardson were made.

We have investigated in greater detail the question of variation of the Florida Current as evidenced in sea level records. In particular, we have used hourly values instead of monthly means to seek fluctuations of comparatively high frequencies.

The record pairs are not simultaneous. Although HICKS and SHOFNOS (1965) show that smoothed secular trends at Miami and Key West are quite similar, the annual sea level values fluctuate greatly over short periods and therefore the spectral

*These observations were made by the U.S. Coast and Geodetic Survey Ship *Peirce*, 1965–1966. The data is on file at Atlantic Oceanographic Laboratories, ESSA, Miami, Fla.

estimates in the very low frequencies may vary considerably depending on the epoch being used.

We wish to re-emphasize that the sea level differences strictly relate only to surface speed of the current, but the assumption will be made throughout that this is a reflection of total transport changes.

The geostrophic assumption is applied only to changes of sea level with periods exceeding two days. For shorter periods we have not attempted to relate sea level changes to transport, as geostrophy is unlikely to be valid.

2. Methods of analysis and discussion of results

The discussion of our results is divided into parts. In the first part we work only with the observed sea level variations across and along the Florida Current axis. In the second part we attempt to improve our results by taking the effects of local weather into account. The conclusions change very little.

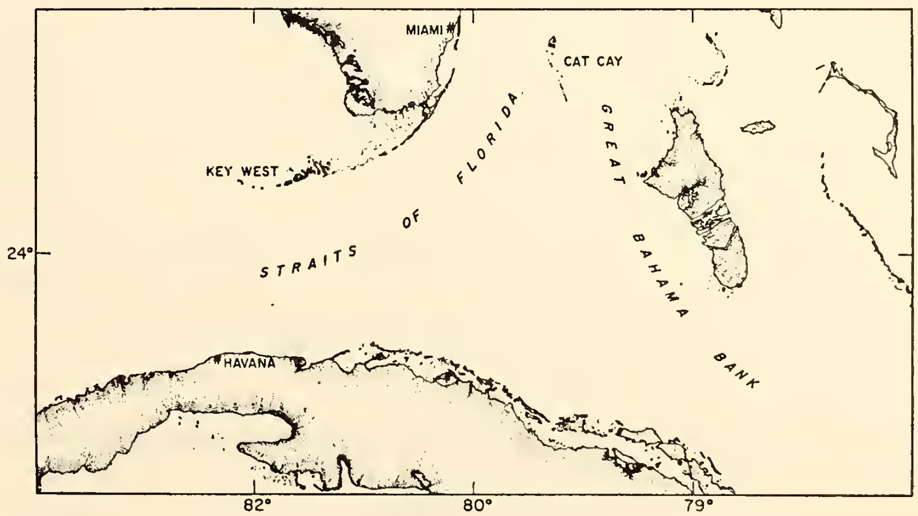

Fig. 3. The Florida Current region of the Gulf Stream.

The records at our disposal were hourly values of sea level from the tide gauges at Miami and Cat Cay (1938–1939), Key West and Havana (1953–1956), and Key West and Miami (1957–1962). A chart of the general area and detail charts of tide-gauge location are shown in Figs. 3 and 4.

Our time-series methods are nearly standard, and we will only outline the procedures here. The hourly sea level values were edited for miscellaneous errors by a procedure described in Zetler and Groves (1964). Daily values of sea level were then obtained in a two-step procedure. An ordinary 35-term convolution filter was first used to remove the semi-diurnal and diurnal tides [the so-called D_{35}, described by Groves (1955)]. In order to avoid aliasing the continuum between the tidal lines, a recursive low-pass filter was then applied.

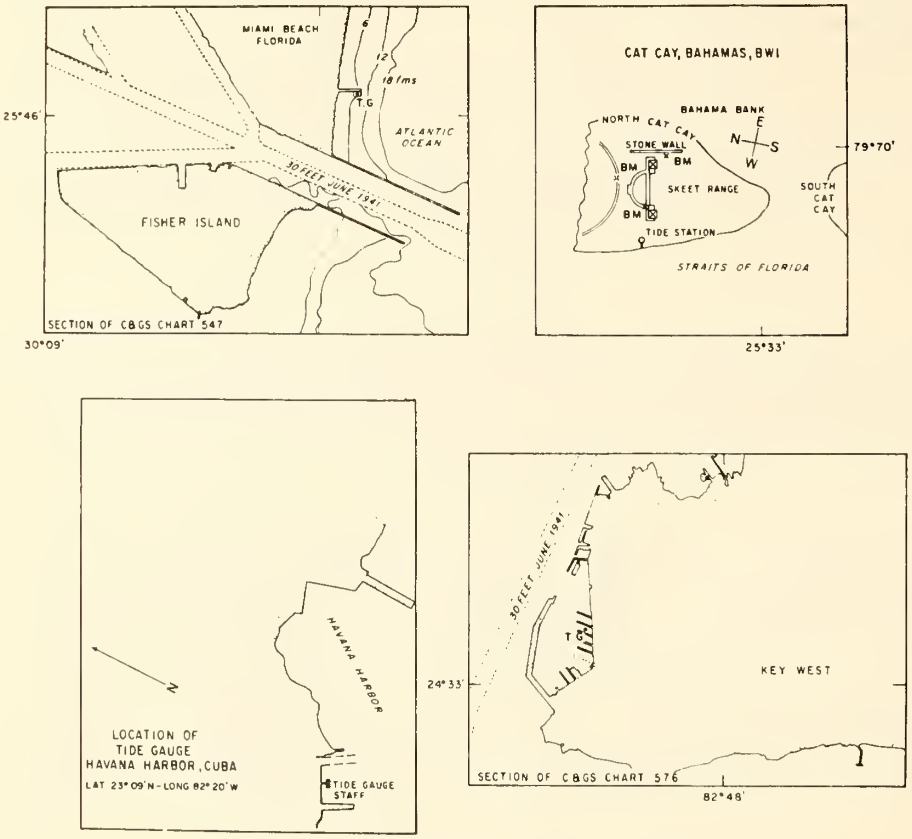

Fig. 4. Locations of tide gauges used in this study.

Let $\hat{f}(\omega)$ be the Fourier transform of the filter. Then the filter transfer function was

$$|\hat{f}(\omega)|^2 = \frac{C}{1 + \epsilon^2 T_3^2(\omega)} \tag{2.1}$$

where $T_3(\omega)$ is the 3rd order Chebyschev polynomial, C is a normalization constant and ϵ is a constant controlling the degree of " ripple " in the filter pass-band. For a discrete time low-pass filter we put

$$\omega = \frac{2(1-z)}{(1+z)} \tag{2.2}$$

z being the discrete-time z-transform variable. A discussion of the high-speed recursion (feed-back) application of the filter may be found in SHANKS (1967). The Chebyschev response is discussed in WEINBERG (1962), and the distortion due to the mapping (2.2) is discussed in GOLDEN and KAISER (1964).

The doubly filtered, hourly values were then resampled at 24-hour increments yielding the working time series.

The spectra and coherences were all computed from Cooley–Tukey Fourier transforms, using the perfect Daniell (rectangular) frequency window. Owing to the rapid low-frequency rise of the sea level power, the transforms were, in practice, computed in two sections to avoid a leakage of power from the low-to-high frequency end of the spectrum. The low-frequency transforms were performed directly on the 24-hour samples. The high-frequency transforms were performed on the 24-hour samples after they had first been filtered with a high-pass filter of the form of (2.1). To obtain a high-pass recursive filter from (2.1) one simply lets

$$\omega = \frac{(1 + z)}{2\,(1 - z)}\,. \tag{2.3}$$

The effects of the three filters involved have been removed from the spectra. All spectra are shown as power instead of the more common power density. They may be converted to power/cpd by multiplication by 128/cpd for the spectra based on daily values, and by 3152/cpd (Fig. 5 only) for the ones based on hourly values.

Approximate 95% confidence limits are shown on all spectra, and the 95% significance levels for the zero-hypothesis are shown on the coherences. These are from the

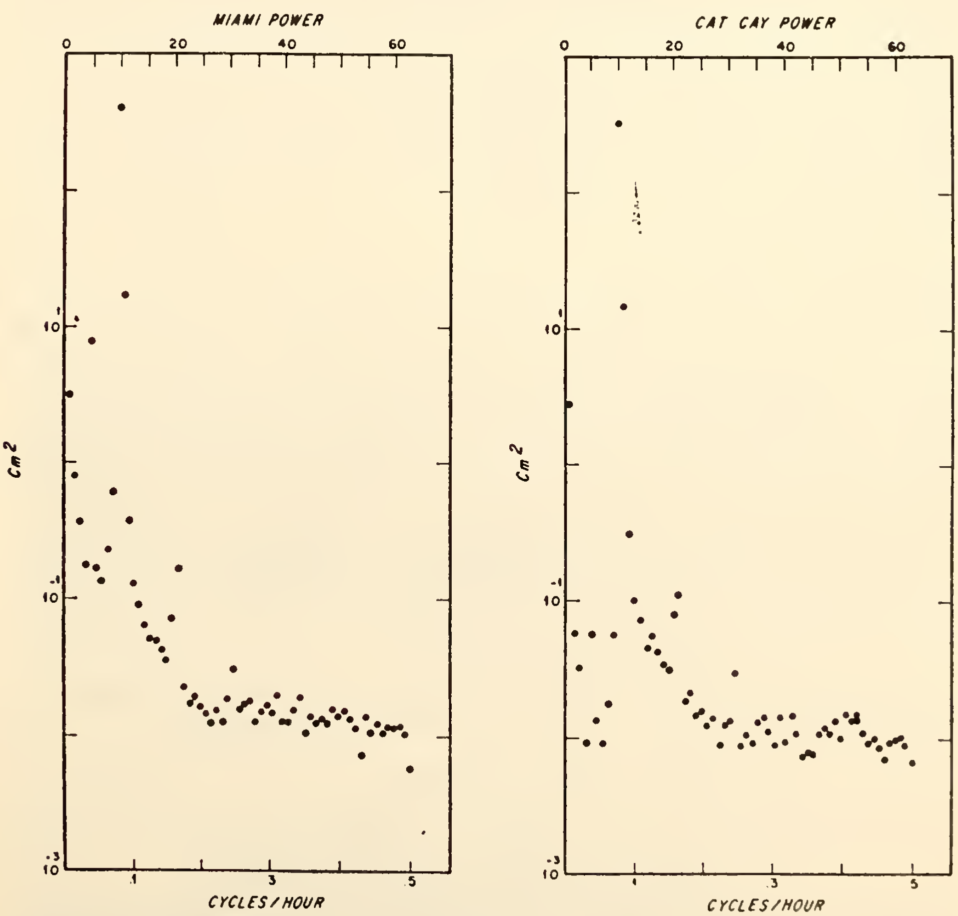

Fig. 5. High frequency pair spectra at Miami and Cat Cay. Peaks are due to semi-diurnal tides and their harmonics. Miami shows a small diurnal peak.

tables of AMOS and KOOPMANS (1963). The confidence limits for coherence phase and amplitude are large and depend upon the values of the coherence amplitude. They may be estimated from the tables of AMOS and KOOPMANS (1963) and GROVES and HANNAN (1968). We have not corrected the small positive bias in the coherence amplitude estimates; the phase estimates are unbiased.

In retrospect the spectra and coherences were run at too high a resolution. We were searching for a nonexistent frequency structure and might as well have sacrificed resolution for statistical reliability. The consequences of this are most severe for the coherences, as indicated by the high 95% level for the hypothesis of zero coherence. The scatter in the phases of coherence give good eye estimates of true level of coherence.

Table 1. The total power and r.m.s. amplitude for each station over the entire record.

Spectrum	*Root-mean-square amplitude* (cm)	*Non-seasonal r.m.s.* (cm)
Miami	10·0	8·1
Cat Cay	5·9	5·2
Miami- Cat Cay	8·7	—
Havana	8·7	5·5
Havana residual	7·6	5·3
Key West	9·1	6·8
Key West residual	8·9	6·5
Havana–Key West	8·4	7·1
Havana–Key West residual	7·2	6·3
Key West–Miami	9·4	—
Bermuda	11·4	—

In each section, Miami–Cat Cay, Key West–Havana, and Key West–Miami, we have shown in Table 1 the r.m.s. amplitude of each station over the entire record. This includes the energy lying in periods from the total record length to two days (the filter cutoff). We also show the difference power between the station pairs, and in some cases the "annual" power and amplitude. As a comparison with a totally different oceanic regime, we have included similar results at Bermuda.

The power in the difference is explicitly related to the coherence. Let $\xi_1(\omega)$ and $\xi_2(\omega)$ be the transforms of two tide records $\zeta_1(t)$ and $\zeta_2(t)$. Then the power spectra are

$$\Phi_{ij}(\omega) = \langle \xi_i \, \xi_j^* \rangle \quad i, j = 1, 2$$

the brackets denoting ensemble averages (in practice, of course, we use frequency-band averages). Then the power spectrum of the difference of ζ_1 and ζ_2 is

$$\begin{aligned} \langle (\xi_1 - \xi_2)(\zeta_1 - \zeta_2)^* \rangle &= \Phi_D(\omega) \\ &= \Phi_{11}(\omega) + \Phi_{22}(\omega) - 2\, R1\, \Phi_{12}(\omega) \\ &= \Phi_{11}(\omega) + \Phi_{22}(\omega) - 2\, R1\, \mathrm{Coh}_{12} \sqrt{(\Phi_{11}\Phi_{22})} \end{aligned}$$

where Coh_{12} is the coherence between ζ_1 and ζ_2.

The difference power in the case of zero-coherence is the sum of the powers. If ζ_1 and ζ_2 tend to be coherent with 180° phase, $\Phi_D(\omega)$ will approach $\Phi_{11} + \Phi_{22}\, 2 \sqrt{\Phi_{11}\Phi_{22}})$, an upper bound. If they are coherent with zero phase, $\Phi_D(\omega)$ approaches

$\Phi_{11} + \Phi_{22} - 2\sqrt{(\Phi_{11}\Phi_{22})}$, a lower bound, which will be zero if $\Phi_{11} = \Phi_{22}$. We discuss the sections in turn.

(*a*) *Miami–Cat Cay* 1938–1939

These records are very short (512 days used), and the spectra and coherence (Fig. 6) should be taken as indicative rather than definitive. The spectra are generally monotone and featureless. The slight rise in power at the very high frequencies is a small residual aliasing effect and not a physical feature. The coherences are not significant at the very lowest frequencies where most of the power lies. The average coherency phase is much closer to zero than 180 degrees and is manifest in the difference power which is less than the sum of the power. The table indicates that Miami is noisier than Cat Cay, mostly due to the smaller annual contribution at Cat Cay.

In the r.m.s. amplitudes, about 20% is due to the annual or seasonal effect. If we accept the SCHMITZ and RICHARDSON (1968) values for mean surface current speed through this section, the mean difference in sea level must be about 66 cm. The double r.m.s. amplitude difference between Cat Cay and Miami is then about 25% of the mean, of which about 1/4 is seasonal.

The power spectra of Miami and Cat Cay based on hourly values are shown in Fig. 5. The tidal lines are very apparent. Based upon these determinations of tidal amplitude, we find that approximately 80% of the sea level power at these two locations is tidal. The tidal variations in sea level cannot, of course, be directly related to transport variation.

(*b*) *Key West–Havana* 1953–1957

These records are based on nearly three years of data (1024 days), and the results are statistically more reliable than for the Miami–Cat Cay section. The spectra (Fig. 7) are essentially the same as in the other section, fifteen years earlier: monotone, structureless spectra with low coherence at the low-frequency, high-power end. We can estimate the average coherence to be no more than about 0·4; the power in Key West that is coherent with Havana is then no more than 16% of the total power in Key West.

The coherence phase is again essentially zero and reflected in the difference power. We find a double amplitude here in the difference power of 25% of the mean difference, of which about 1/5 is annual. The power in Havana is somewhat less (about 80% of Key West). On the average, it would appear that there is a slight tendency for Key West to lead Havana. Owing to the smaller tides here, the non-tidal power is about 23% of the total sea level power due to tides plus low-frequency oscillations.

(*c*) *Key West–Miami* 1957–1963

These are the statistically most reliable records; the transforms are on 2048 days of sea level. We obtain the characteristic spectra and low coherence (Fig. 8) with a small coherence peak at 5·3 days. The r.m.s. difference amplitude differs little from that obtained by MONTGOMERY (1941a) from the monthly means. We obtain the same paradoxical result that the r.m.s. head fluctuation exceeds the apparent mean head required to drive the current. We note, however, that the fluctuations are very incoherent, except in a few isolated regions of the spectrum where the phase is essentially zero. There is no indication of a systematic phase difference between the two locations.

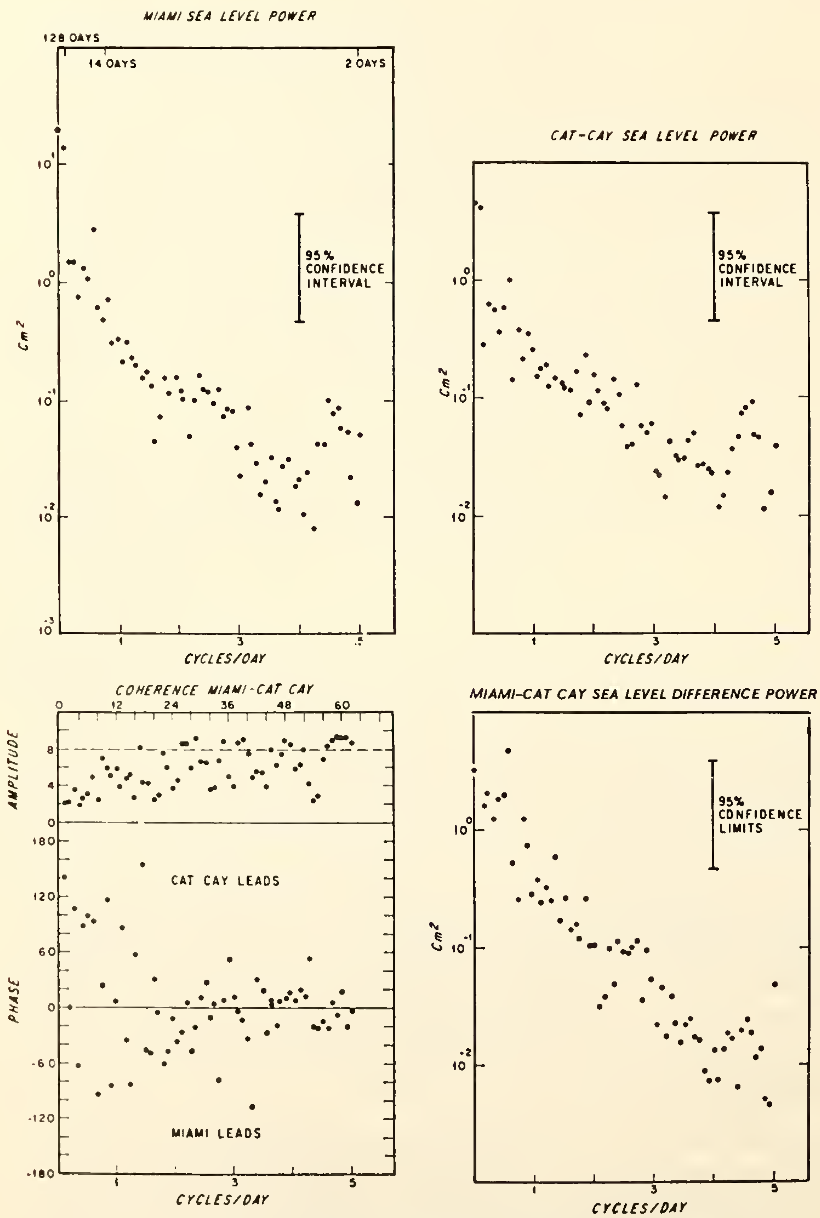

Fig. 6. Results at Miami and Cat Cay.

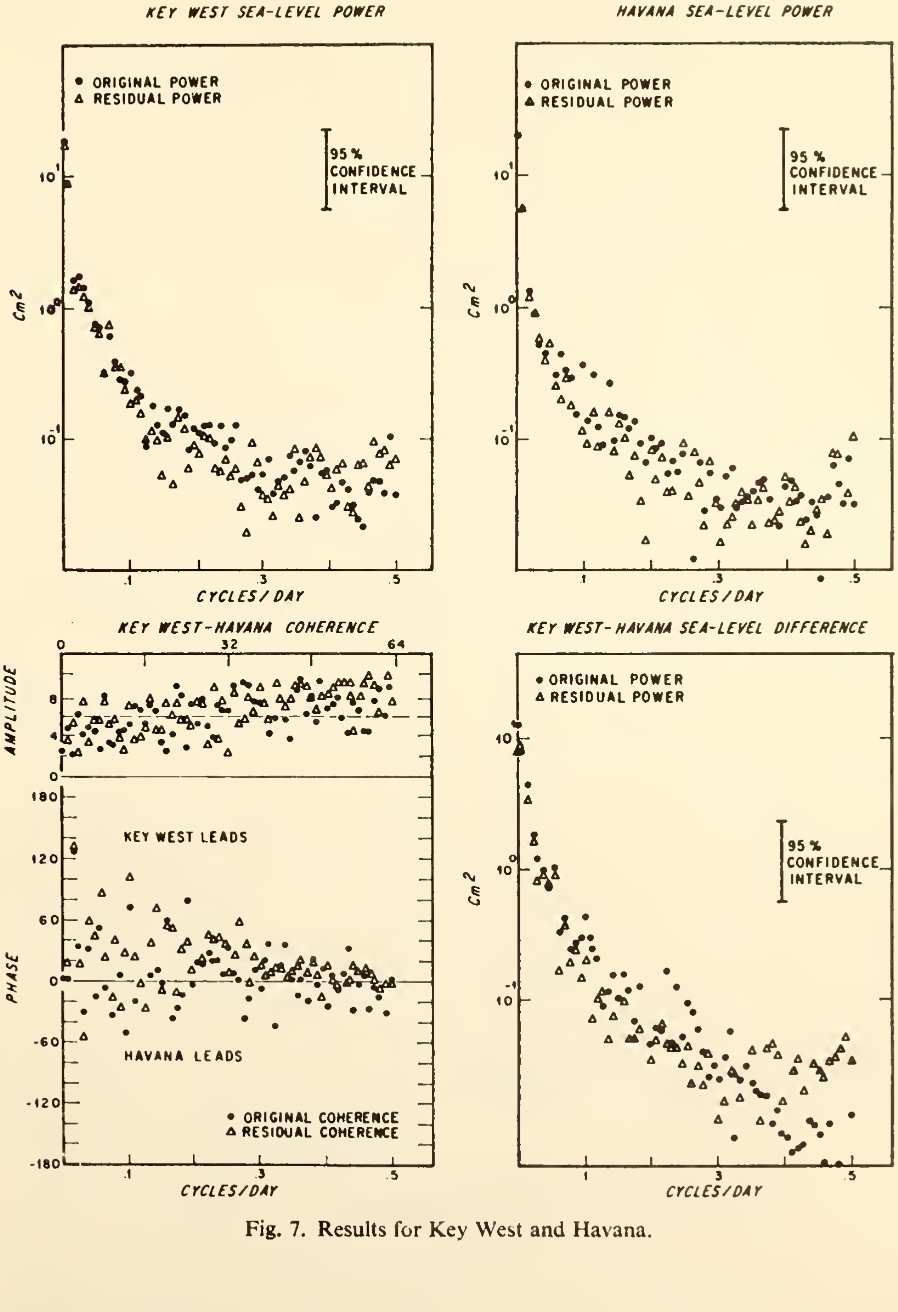

Fig. 7. Results for Key West and Havana.

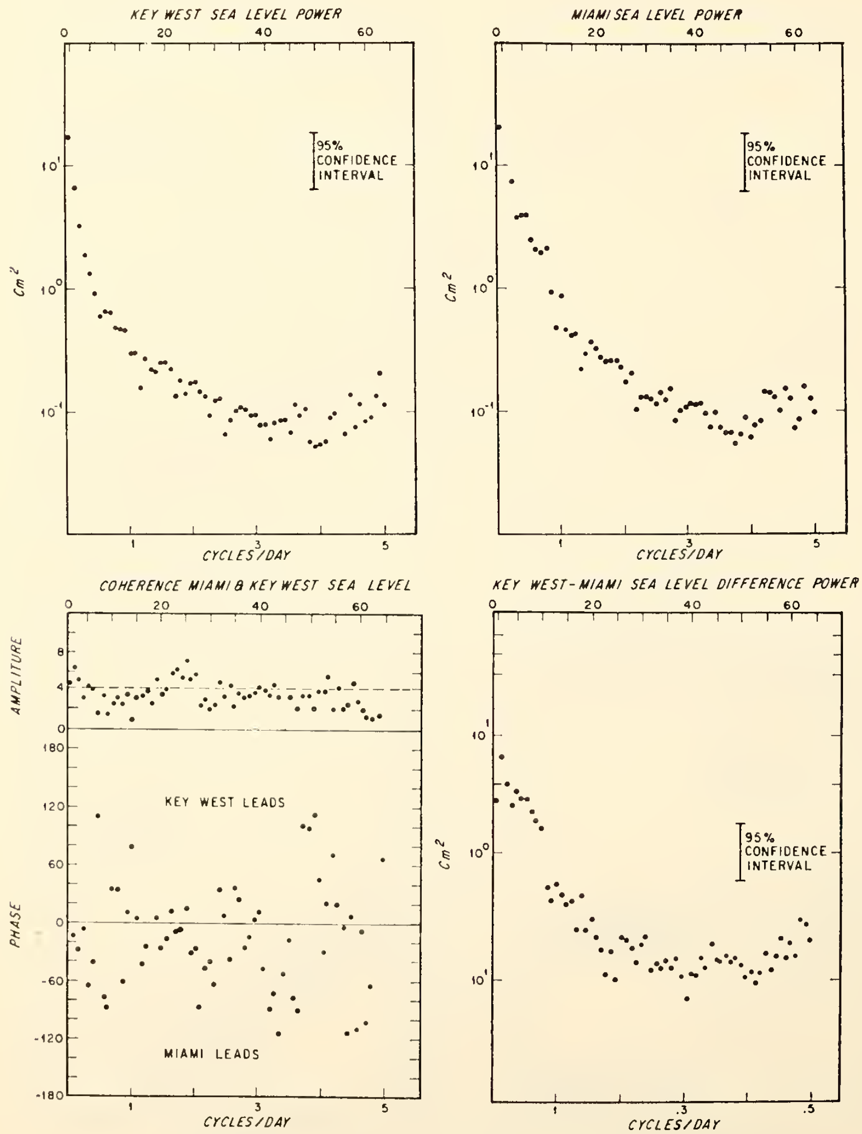

Fig. 8. Results for Key West and Miami.

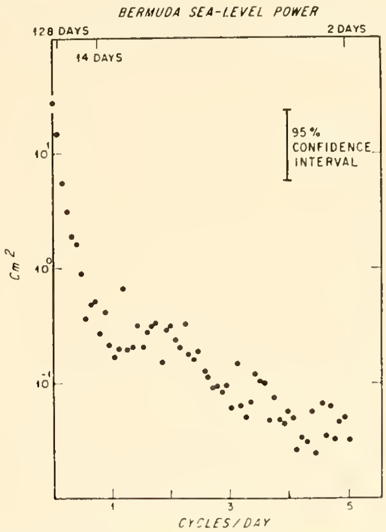

Fig. 9. The Bermuda sea level spectrum.

(*d*) *Bermuda* 1953–1957

This result is in Fig. 9 as a comparative study. The spectral levels are about the same as for the other four locations, with slightly greater energy at periods of 5–10 days.

Discussion

There are three obvious conclusions we can draw from the results thus far:

(1) The power levels are very low. There is no possibility of 50% fluctuations of the Gulf Stream transport as suggested by Wertheim (1954). If the sea-surface slope measurements reflect transport changes, then the transport varies by at most 25%, of which about 1/4 is a seasonal change. This is in agreement with the findings of Schmitz and Richardson (1968) drawn from wholly different methods and data.

(2) There is no real structure in the fluctuations; there are no distinct fortnightly or other major frequency components. The monotonic rise in power toward lower frequencies is a demonstration that calculations based upon monthly means are a good indicator of the long-period fluctuations. In particular, the seasonal oscillation we have found is in good agreement in amplitude and phase with that calculated by Pattullo, Munk, Revelle and Strong (1955) (Fig. 10) and with the surface currents tabulated by Fuglister (1951), (Fig. 1).

(3) The small fluctuations that do exist appear to be basically incoherent. To the extent that cross-stream records are coherent (in particular Havana–Key West for periods of 2–10 days), the phase is zero, indicating that the two sides of the stream oscillate up and down together, perhaps as a result of the Bernoulli effect.

Let us postulate a model of the Gulf Stream in which the sea surface is fixed at Havana and permitted to oscillate at Key West. Then the power is zero at Havana. Now suppose that the Havana side moves only in response to the Bernoulli effect so

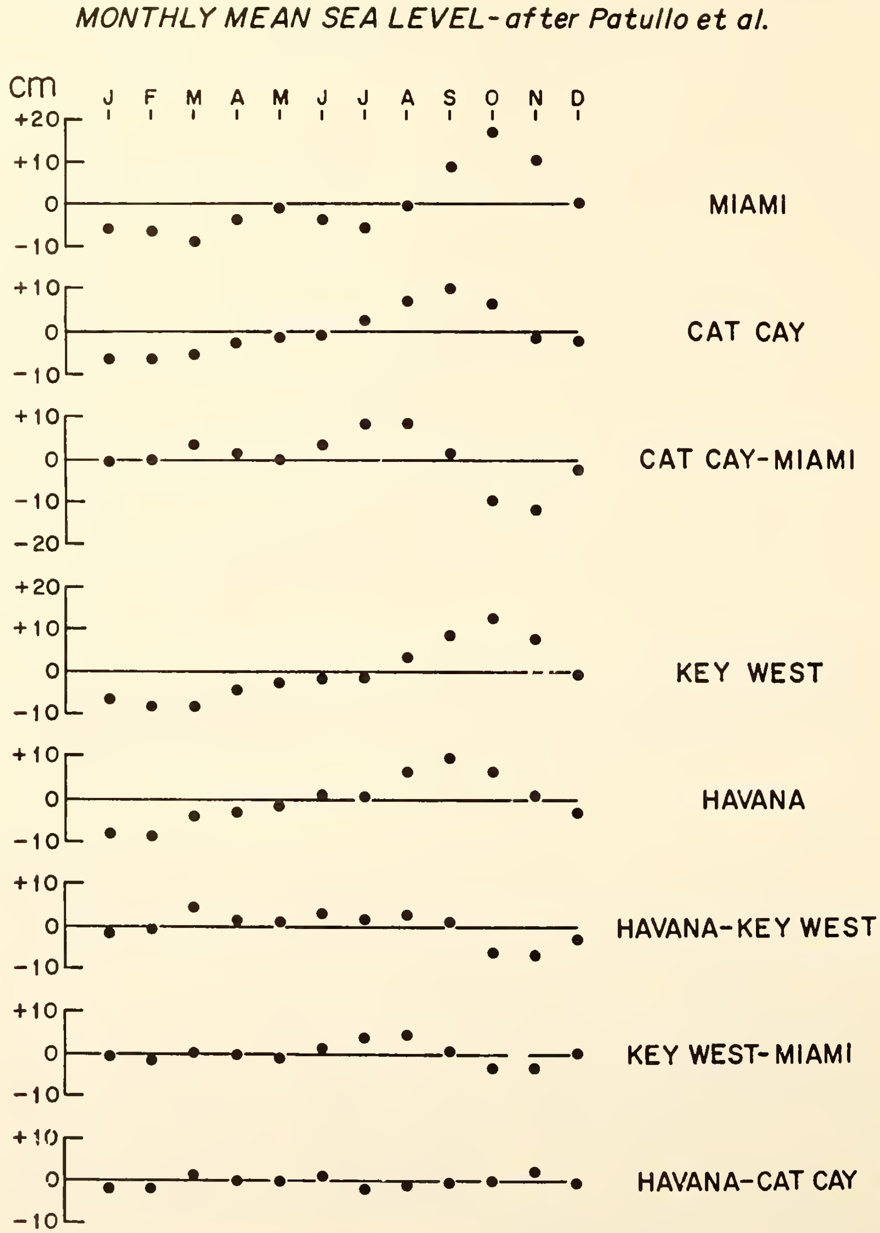

Fig. 10. Annual changes in sea level based on monthly means. After PATTULLO, MUNK, REVELLE and STRONG (1955).

that Havana fluctuations are due only to the non-linearity. Associated with a core speed of twice the mean surface speed, we then expect that Havana sea level will move up and down with Key West with about 33% of the Key West amplitude. Let us now write

$$\zeta_H(t) = A\zeta_{KW}(t) + n(t)$$

where ζ_H is Havana sea level, ζ_{KW} is Key West sea level, and $n(t)$ is that part of Havana sea level unrelated to (incoherent with) Key West. A is a constant scale factor. If Havana responds primarily to Bernoulli effects, we expect that the power at Havana coherent with Key West should be about 10% of the power at Key West. In fact, the coherence is about 0·4 on the average, and thus the coherent power at Havana is about 16% of the Key West power. A is about 0·36, which is a reasonable value under the Bernoulli hypothesis. One could equally well postulate that the Key West side is geostrophically anchored and Havana moving; we cannot choose between these possibilities or some intermediate case on the basis of the available data, as long as the nature of the incoherent fluctuations remains obscure.

The lack of downstream coherence, Key West–Miami, can be rationalized in several ways. One interesting idea is as follows: due to the shoaling and narrowing of the channel from Key West to Miami, the current accelerates downstream. Using a mean current speed (over the whole water column) at Key West of 25 cm/sec, the speed at Miami is 63 cm/sec. Suppose there exist disturbances in the stream at Key West with a frequency σ (to an observer at rest) with a characteristic wavelength of $\lambda = 250$ km. Then the apparent frequency to an observer fixed at Miami is

$$\sigma' = \sigma + U2\pi/\lambda$$

where U is the difference between the surface speeds at the two locations.

Putting in the numbers, we find a shift in frequency

$$\Delta\sigma \asymp 2\pi\frac{U}{\lambda} = 10^{-6}/\text{sec}. \tag{2.5}$$

The coherencies were computed with a resolution frequency

$$\delta\sigma = \frac{2\pi}{2048\ \text{days}} = 3{\cdot}6 \times 10^{-8}/\text{sec} \tag{2.6}$$

almost two orders of magnitude sharper than the frequency shift. Depending upon the generation mechanism for stream disturbance, *i.e.* the Q of the system, the coherence could be totally destroyed. This Doppler shifting could be an important effect, but it should be pointed out that there are several other ways to destroy coherence between two records.

In particular, the cyclostrophic effects discussed in the introduction need not be coherent with transport changes. If meandering within the straits is important (and this is the best explanation of Wertheim's large voltage fluctuations), the coherence we measure both across and downstream is reduced; the power in the sea level variations then also overestimates the transport changes. We have no quantitative measure of these effects of meandering.

3. WEATHER

The zero-phase difference between the record pairs suggests that sea level is responding to local weather effects, perhaps the barometric fluctuations. The low coherence amplitude between stations suggests that one station might be responding to one component of wind, and the other station to the other component. To the extent that the wind components are incoherent, the sea level records would be incoherent, and might account for the occasional negative slope between Key West and Miami.

In an attempt to explore the relationship between weather and sea level, we obtained hourly values of wind and atmospheric pressure at Key West and Miami. Before proceeding we would like to emphasize that we are dealing with small numbers

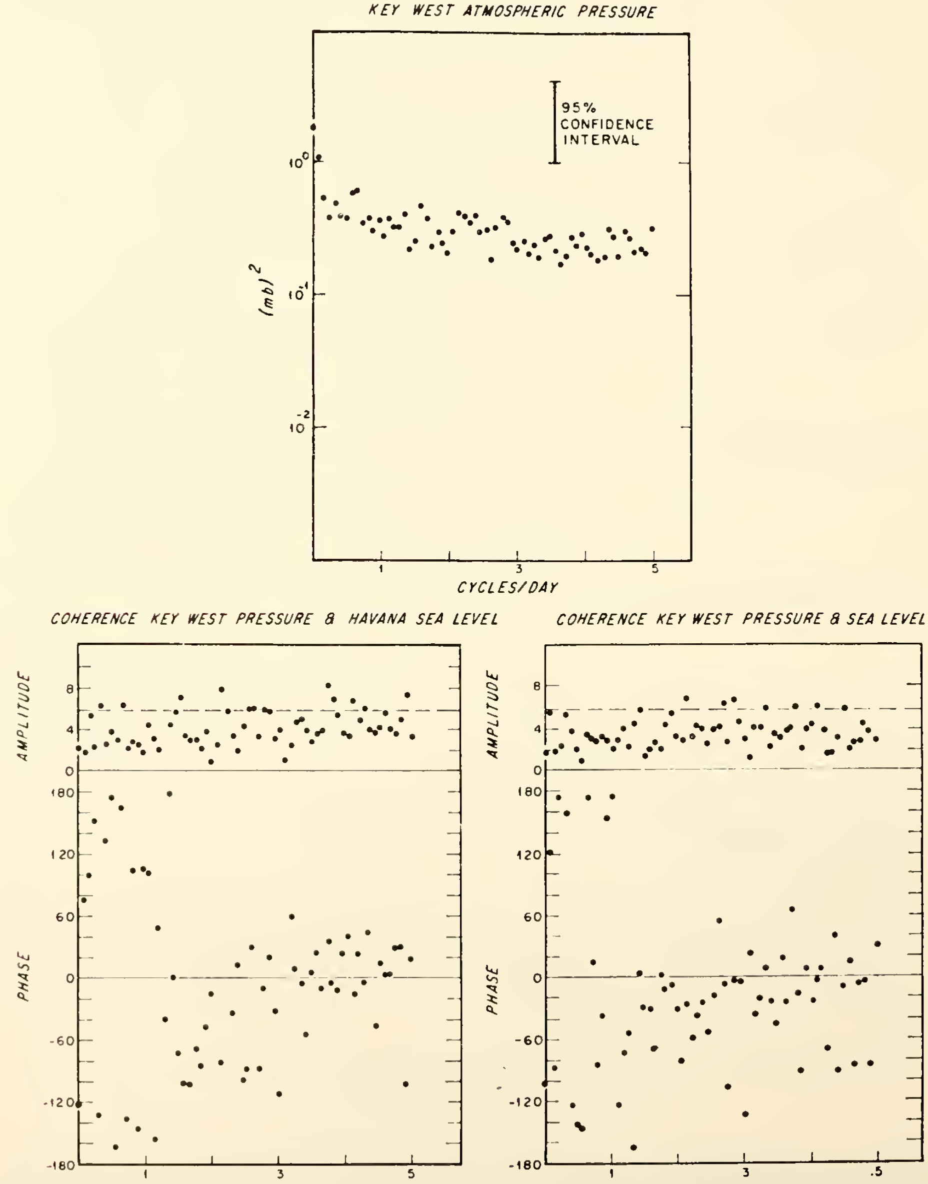

Fig. 11. Pressure power spectrum from Key West and the coherence with sea level at Key West and Havana.

in proportion to the mean difference in sea level across the Florida Current. Any " removal " of weather effects will reduce the power in what is already a very small fluctuation of the current, but perhaps will unmask frequency structure in these fluctuations.

The wind records are reported on the basis of hourly speed and a 16-point compass direction code. These were converted to east and north component of wind. The 16-point code introduces a high background noise—the least count error. Owing to the erratic behavior of the wind, the error checking was abandoned. It was extremely difficult to determine when a change in wind direction and speed was not real. There

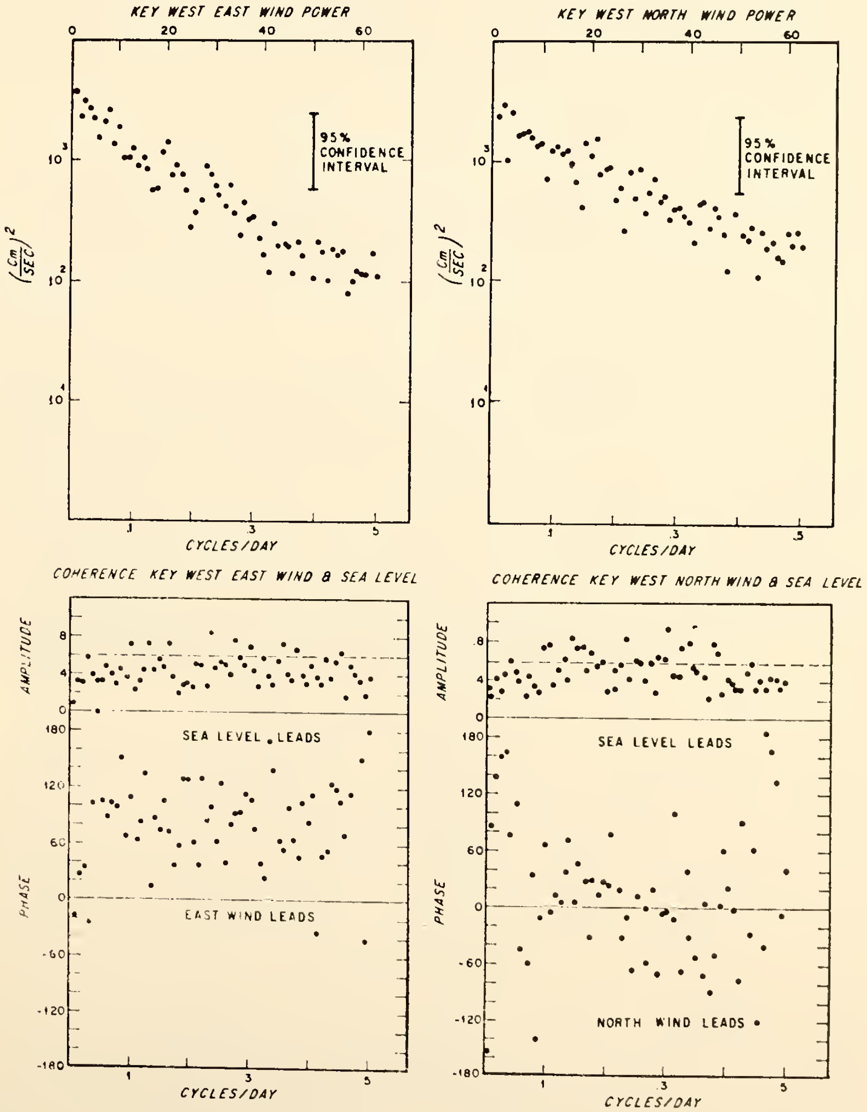

Fig. 12. Power in the two components of wind at Key West and the coherence with the sea level there.

is a possibility, which we cannot evaluate, of aliasing from high frequency wind changes.

The pressure records are probably more reliable, as the spectrum of pressure computed by GOSSARD (1960) shows a steep rise toward low frequencies.

We deal primarily with the weather record at Key West in the period 1953–1957. As the Havana weather record was unavailable, we have used Key West weather to compare with the Havana tide gauge.

The power spectrum of Key West pressure is shown in Fig. 11; the most obvious feature is that it is much flatter than the equivalent sea level spectrum. Coherence with Key West sea level and Havana sea level is shown in the figure as well, and is quite low. At the lower frequencies, periods about 128 days to 10 days, the phase tends to be near $\pm$ 180°, indicating an isostatic inverted barometer effect at both locations. The coherence level is too low to make calculations of the actual " barometer factor " meaningful.

At the higher frequencies on the contrary, the average phase tends to be zero, a direct barometer effect. The cause of this change is not apparent and is in distinction to the results of GROVES and HANNAN (1968), who found an essentially isostatic response at all frequencies, for two Pacific islands. On the other hand, HAMON (1966) found non-static barometer effects at some Australian locations. We note that the coherence involved is low; and, in general, the contribution of atmospheric pressure to the sea level oscillations is small.

The coherence between the two components of wind and sea level is shown in Figs. 12 and 13. The level is about the same as for pressure. We note that the phase between Key West sea level and east component of wind is generally positive at high frequencies, indicating that either sea level fluctuations lead the wind or that an increase in wind leads to a drop in sea level. The latter conclusion would appear to

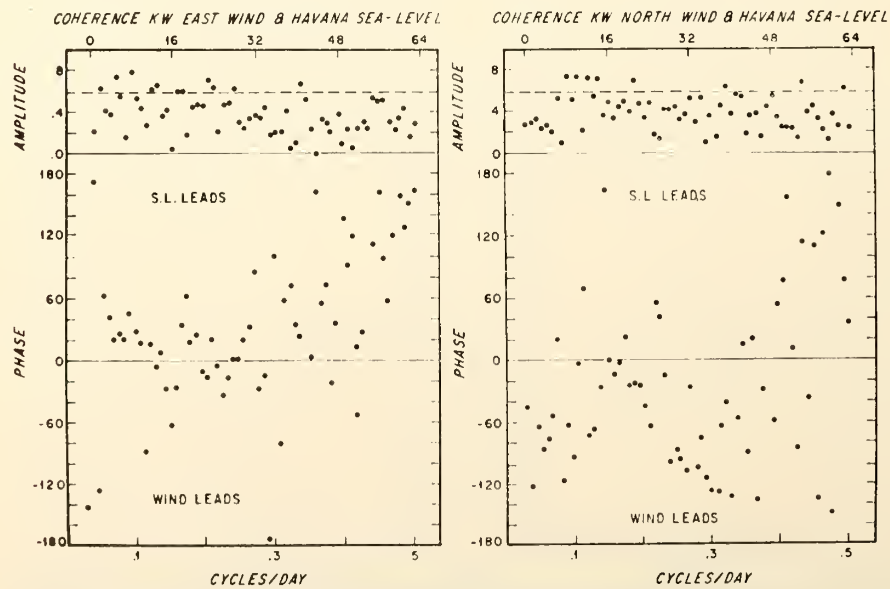

Fig. 13. Coherence of Key West wind and Havana sea level.

be more acceptable except that it is difficult to reconcile with the chart in Fig. 4, which places the gauge on the eastern side of the harbor. At Havana there is a change over from 180° (acceptable for a gauge on the western side of the harbor) to zero-phase at intermediate frequencies. At the highest frequencies there is a trend back toward 180° but with reduced coherence. It is difficult to generalize about these results.

In a variation on the coherence calculation, and in an effort to raise the coherence between these two stations, we removed the linear wind effects from sea level by constructing the Wiener optimum filters relating sea level and wind at each location. We then computed the residuals at each location and compared the power and coherence with the nonresidual results.

In particular, let ζ_t^i be discrete-time sea level at the ith place, and let e_t and n_t be east and north wind at Key West. Then using the daily values we put

$$\zeta_j^i = \sum_{K=0}^{N_e} a_K^i \, e_{t-K} + \sum_{K=0}^{N_n} b_K^i \, n_{t-K} + \xi_t^i \tag{3.2}$$

where $f_t^i = \{a_t^i, b_t^i\}$ is a finite approximation to the multi-channel Wiener optimum filter and ξ_t^i is " noise," or that part of sea level incoherent with the wind. In practice N_e and N_n were equal, and after a little experimentation were chosen as either 9 or 10, corresponding to a maximum time lag of sea level response to wind of nine days.

Note that the a_t^i and b_t^i are zero for t less than 0, requiring that sea level respond only to past or present values of wind and not to future values. The validity of this causal assumption depends upon the absence of an " ocean-driven wind circulation," investigation of which is outside the scope of this paper.

A discussion of the finite, discrete, Wiener optimum filter, and the recursive solution for it may be found in LEVINSON (1947) and in WIGGINS and ROBINSON (1965). Due to the finite filter length, the filter characteristics are principally determined by the spectral components of the data with the most power. For this reason the operation of removing the wind was performed on both the low- and high-passed versions of sea level discussed above, and the power spectra patched together as before.

In each case equation (3.2) is solved for the residual noise

$$\xi_t^i = \zeta_t^i - \left(\sum_K a_K^i \, e_{t-K} + \sum_K b_K^i \, n_{t-K}\right). \tag{3.3}$$

Since the filters are of necessity of finite length, they are broad-band in frequency, operating in those frequency bands where sea level and weather may be incoherent. For this reason, we expect that the power in ξ_t^i will exceed the power in ζ_t^i in regions of sea level wind coherence. The power should be less where there is true coherence, and the wind correctly removed.

The results are shown in Fig. 7 where the residual power is plotted for comparison with the original results. Generally speaking the power has decreased by a small amount; the totals are given in Table 1. The decrease is at most 20%, a figure we could have anticipated from the coherence levels. The small increase in power at the high frequencies indicates that here the filters were ineffective, presumably due to the very small power levels associated with these frequencies. The remedy for this is to high-pass the data, leaving only these frequencies, and compute a Wiener filter for this region of the spectrum. We deemed this unnecessary since the power involved is very small. The total decrease in power is of the same order as found for Kwajalein and Eniwetok in the mid-Pacific by GROVES and HANNAN (1968), using a much more elaborate procedure and dispensing with the causality condition.

The coherence between the residuals dropped slightly at low and high frequencies with the phases remaining scattered about zero degrees. At intermediate frequencies there was a slight increase in coherence with a subsequent small decrease in the phase scatter about zero degrees. The residual difference power in Fig. 7 reflects these changes. The very slight change we made in the power levels led us to drop any further experimentation along these lines.

Discussion

The weather variables account for no more than 20% of the total sea level variation or about 5% of the total mean cross-stream pressure head. At the lowest frequencies, the weather effects are essentially static; they are definitely nonstatic at periods shorter than about ten days. It is plainly possible to explain these results in terms of a dynamic model of the response of this region to large scale weather systems, but we will not pursue the subject further here.

The weather regression could undoubtedly be improved by using longer filters, more weather variables from more locations, and perhaps by using the geostrophic wind as well as observed wind. There is little reason to anticipate any qualitative improvement; however, we did make one attempt at exploring another approach as described below.

4. A STRESS EXPERIMENT

The calculation of coherences and convolution relations between sea level and wind depend for their interpretation upon an assumption of a linear response of water to wind. A commonly accepted relation for stress on the sea surface is the expression

$$\boldsymbol{\tau} = 0{\cdot}0025\, \rho_a\, \mathbf{w}\, |\mathbf{w}| \tag{4.1}$$

$\mathbf{w}$ being vector wind, $\boldsymbol{\tau}$ the vector stress, ρ_a the density of air. Steady winds are normally implied. This is, of course, a nonlinear relation, and (4.1) represents a complicated transformation of the frequency structure of the non-steady winds. To the extent that sea level responds to stress and not to wind directly, there would be a low coherence between wind and sea level. On the other hand, if the stress law (4.1) can be linearized, there will be no difference between stress and wind coherence with sea level. Note that (4.1) tends to emphasize the importance of strong winds.

To study the applicability of (4.1), we used the 2048 days of available Miami wind and sea level. The unnormalized time series

$$(\tau_{et}, \tau_{nt}) = (e_t, n_t)\, (e_t^2 + n_t^2)^{\frac{1}{2}} \tag{4.2}$$

were computed from the daily values of the wind. The filtering involved in computing the daily values is involved in a complicated way in the frequency structure of (4.2).

The power in each component of stress and the coherence between wind and stress (east stress on east wind, north stress on north wind) and coherence between stress and sea level at Miami and at Key West were computed. Some of the results, which are puzzling, are shown in Fig. 14.

For north stress (not shown) there is no problem. The coherence with sea level is low, and the coherence with north wind is high. Since the coherence of north wind with sea level is also low, north stress is apparently sufficiently represented by a linearization of (4.1).

For east stress the picture is quite different (Fig. 14). The stress–sea level coherence is markedly higher than the wind–sea level coherence, in several peaks. But most striking is the essentially linear-phase relationship between stress and sea level, as indicated by the dashed lines on the coherence-phase plot. Such a law is characteristic of a system with pure delay. Let $\tau(t)$ be a stress component with Fourier transform $\hat{\tau}(\omega)$, and let $\zeta(t) = -\tau(t - t_0)$ be sea level. It is easy to see that $\hat{\zeta}(\omega) = -e^{-i\omega t_0}\hat{\tau}(\omega)$ yielding a coherence phase difference, $\phi(\omega) = -\omega t_0 + \pi$, linear in frequency with value π (180 degrees) at $\omega = 0$. t_0 is ambiguous up to multiples of 2π. From the slope of the phase curves in Fig. 14, we find the smallest possible value of t_0 is about thirteen days. Such a delay time is difficult to rationalize, but STOMMEL (1965) estimates that a change in the North Atlantic wind system would be reflected in the Florida Current

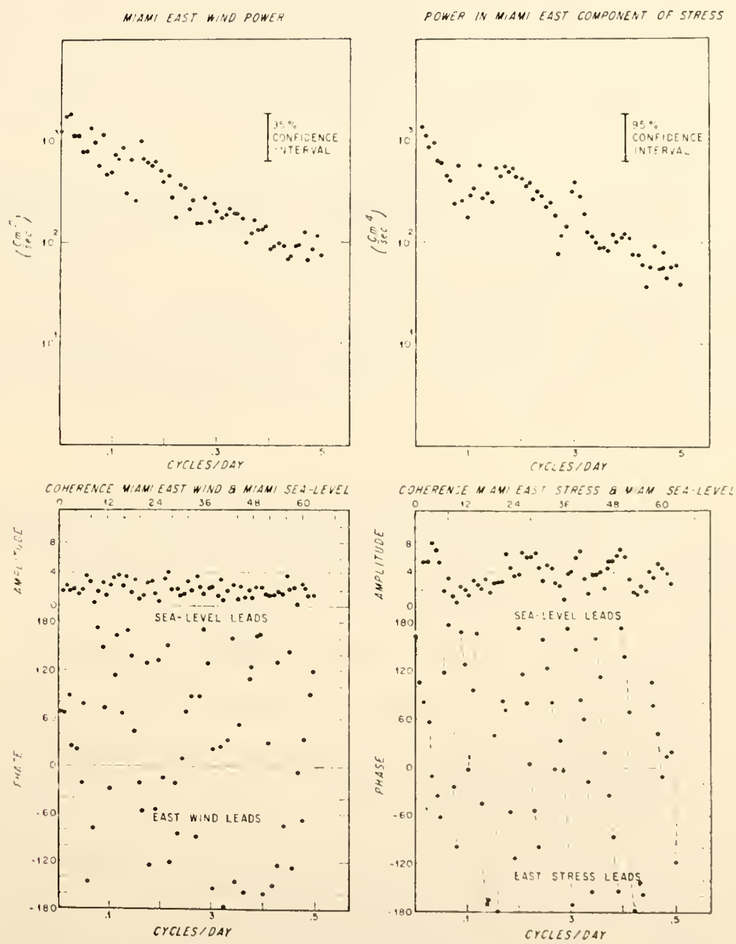

Fig. 14. Results of the computation on stress and sea level at Miami (see text).

about fifteen days later. The agreement is presumably fortuitous. If Stommel's idea were correct, we would expect a similar relationship between Miami stress and Key West sea level. We found no significant coherence, which we could have anticipated from the low Key West–Miami sea level coherences. The result remains a puzzle.

There is a low coherence between east stress and east wind at Miami in the range where the stress–sea level coherence is highest, and a somewhat higher coherence where the stress–sea level coherence is lower. This is consistent with the low wind–sea level coherence.

Since the filtering effects from computing daily values of wind are included in a complicated way in the computation of (4.1) and (4.2) (and the spectra are uncorrected for this effect), we attempted to investigate the effects of this on the results by computing stress from hourly values of wind, and then low-pass filtered to obtain daily east stress values. The result was a very low coherence between stress and sea level, and the phase was essentially random, implying that high frequency wind fluctuations are not effective in exerting a stress on the ocean. If, in fact, stress is directly related to sea-state as is often hypothesized, and if sea-state is primarily determined by winds of many hours' duration, then our result is reasonable.

Since the law (4.1) is postulated for steady winds and is of itself somewhat arbitrary, any further exploration of stress–sea level effects should be done systematically to determine empirically the best form of stress law. We are currently investigating techniques to do so.

Acknowledgements—This work was supported by the National Science Foundation through Grant GA–434 with the Massachusetts Institute of Technology. We are indebted to the United States Coast and Geodetic Survey, Rockville, Maryland, for making the sea level records available, and for their continued cooperation throughout.

Prof. Henry M. Stommel contributed a great deal to this study in continual discussions of our results and we are highly indebted to him.

The data analysis was performed at the Information Processing Center at MIT. The bulk of the work was done while we were visiting the Woods Hole Oceanographic Institution and we thank them for their hospitality.

REFERENCES

Amos D. E. and L. H. Koopman (1963) Tables of the Distribution of the coefficient of coherence for stationary bivariate Gaussian processes. *Sandia Corp. Monogr*, SCR-483.

Broida S. (1962) Florida Straits transports. April 1960–January 1961. *Bull. mar. Sci. Gulf Carib.*, **12**, 168.

Broida S. (1963) Florida Straits transports. May 1961–September 1961. *Bull. mar. Sci. Gulf Carib.*, **13**, 58.

Fuglister F. C. (1951) Annual variations in current speeds in the Gulf Stream System. *J. mar. Res.*, **10**, 119–127.

Golden R. M. and J. F. Kaiser (1964) Design of wideband sampled—data filters. *Bell Syst. tech. J.*, **43**, 1533–1545.

Gossard E. E. (1960) Spectra of atmospheric scalars. *J. geophys. Res.*, **65**, 3339–3351.

Groves G. W. (1955) Numerical filters for discrimination against tidal periodicities. *Trans. Am. geophys. Un.*, **36** (6), 1073–1084.

Groves G. W. and E. J. Hannan (1968) Time series regression of sea level on weather. *Rev. Geophys.*, **6** (2), 129–174.

Hamon B. V. (1966) Continental Shelf waves and the effects of atmospheric pressure and wind stress on sea level. *J. geophys. Res.*, **71** (12), 2883–2893.

Hela I. (1952) The fluctuations of the Florida Current. *Bull. mar. Sci. Gulf Carib.*, **4**, 241–248.

Hicks S. D. and W. Shofnos (1965) Yearly sea level variations for the United States. *J. Hydraul. Div.*, ASCE, **91**, (Proc. Pap. 4468) 23–32.

ISELIN C. O'D. (1940) Preliminary report on long period variations in the strength of the Gulf Stream System. *Pap. Phys. Oceanogr. Meteorol.*, **8** (1), 1–40.
LEVINSON N. (1947) The Wiener r.m.s. error criterion in filter design and prediction, appendix to N. WIENER (1947) *Extrapolation, Interpolation and Smoothing of Stationary Time Series, MIT Press*, 163 pp.
MONTGOMERY R. B. (1938) Fluctuations in monthly sea level on eastern U.S. coast as related to dynamics of western North Atlantic Ocean. *J. mar. Res.*, **1** (2), 165–185.
MONTGOMERY R. B. (1941a) Sea level difference between Key West and Miami, Florida. *J. mar. Res.*, **4** (1), 32–37.
MONTGOMERY R. B. (1941b) Transport of the Florida Current off Havana. *J. mar. Res.*, **4** (3), 198–220.
PATTULLO J., W. MUNK, R. REVELLE and E. STRONG (1955) The seasonal oscillation in sea level. *J. mar. Res.*, **4** (2), 88–155.
PILLSBURY J. E. (1890) The Gulf Stream—A description of the methods employed in the investigation, and the results of the research. *U.S. Coast Geodetic Survey Rep.* for 1890, Appendix No. 10, 461–620.
SCHMITZ W. J., JR and W. S. RICHARDSON (1968) On the transport of the Florida Current. *Deep-Sea Res.*, **15**, 679–693.
SHANKS J. L. (1967) Recursion filters for digital processing. *Geophysics*, **32** (1), 33–51.
STOMMEL H. M. (1953) Examples of the possible role of inertia and stratification in the dynamics of the Gulf Stream System. *J. mar. Res.*, **12**, 184–195.
STOMMEL H. M. (1957) Florida Straits transports, 1952–1956. *Bull. mar. Sci. Gulf Carib.*, **7**, 252–254.
STOMMEL H. M. (1959) Florida Straits transports : June 1956–July 1958. *Bull. mar. Sci. Gulf Carib.*, **9**, 222–223.
STOMMEL H. M. (1961) Florida Straits transports : July 1958–March 1959. *Bull. mar. Sci. Gulf Carib.*, **11**, 318.
STOMMEL H. M. (1965) *The Gulf Stream.* University of California Press, 2nd. edn.
VON ARX W. S., D. F. BUMPUS and W. S. RICHARDSON (1955) On the fine-structure of the Gulf Stream front. *Deep-Sea Res.*, **3**, 46–65.
WEBSTER F. (1961) A description of Gulf Stream meanders off Onslow Bay. *Deep-Sea Res.*, **8**, 130–143.
WEINBERG L. (1962) *Network Analysis and Synthesis.* McGraw-Hill Co., New York, pp. 692.
WERTHEIM G. K. (1954) Studies of the electrical potential between Key West, Florida, and Havana, Cuba. *Trans. Am. geophys. Un.*, **35** (6), 872–882.
WIGGINS R. A., and E. A. ROBINSON (1965) Recursive solution to the multichannel filtering problem. *J. geophys. Res.*, **70** (8), 1885–1891.
ZETLER B. D. and G. W. GROVES (1964) A program for detecting and correcting errors in long series of tidal heights. *Int. Hydrogr. Rev.*, **41** (2), 103–107.

Reprinted from Handbook of Ocean and Underwater Engineering
North American Rockwell, Inc., (McGraw-Hill Inc. New York).

TIDES

B. D. Zetler

Tides and tidal currents give rise to periodic changes in the ocean level and are the result primarily of lunar and solar gravity influences on the water masses of the oceans.

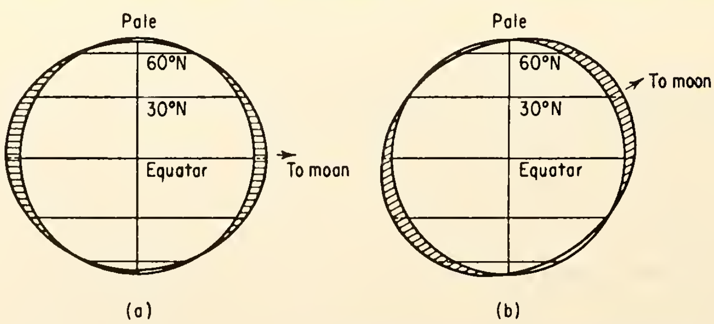

Fig. 1-38 Lunar tidal effects: (*a*) moon on equator; (*b*) moon at maximum declination.

A simplified (although fictitious) model permits a useful delineation of the forces involved in tidal theory. If a rigid earth is considered to be completely covered by a deep layer of ocean, the magnitude and direction of the tidal forces can be related to the various motions of the moon and sun.[47,53] Friction and inertia are disregarded, so it is assumed that the waters respond instantly to the attraction of the tide-producing body.

In the earth-moon system there is a high-water bulge at both points where the line connecting the centers of earth and moon intersects the surface of the earth. There is a low-tide belt circling the earth between these points (Fig. 1-38). There is a similar tide caused by the sun, but its amplitude is only 46 percent of the lunar tide. From a fixed point on earth, both the moon and sun vary in longitude, declination, and distance. These changes are cyclical, and therefore the tide at a given time and place can be calculated as the sum of a series of cosine curves representing tidal constituents whose amplitudes, periods, and phases are known. These are the bases of some tidal constants used in tide prediction.

However, the earth does not have a surface of water that is either uniform or of the required depth to validate this equilibrium theory. Furthermore, friction, inertia, viscosity, and the continental masses make meaningless any theoretical determinations of amplitude and phase. Mathematicians have made remarkable use of the identification of tidal frequencies. With this knowledge and a sufficiently high signal/noise ratio, sophisticated analysis techniques have been developed. Tidal records that are ordinarily continuous hourly heights (Fig. 1-39) are subjected to a Fourier analysis modified by the knowledge of tidal frequencies and utilizing theoretical ratios of amplitudes and phase relationships for a refinement of results.

Although methods have been developed for obtaining harmonic constants from a tidal series as short as only a few days, a year of hourly heights is desirable for a satisfactory determination and resolution of the tidal components.

Tidal Components

The U.S. Coast and Geodetic Survey considers 37 components in its analysis and prediction procedures.[54] Some European tide-predicting agencies use more than 60 components, the larger number being related primarily to additional shallow-water tidal components (nonlinear combinations of tidal frequencies) that are found significant in their home waters. The following important tidal components are described to illustrate the concept.

Lunar and Solar Components. The principal lunar semidiurnal component has an average period of 12 hr and 25 min; the principal solar semidiurnal component has a period of 12 hr. These two components will be in phase at new and at full moon, causing *spring tides* (high waters appreciably higher than average and low waters lower than average) about every 15 days. They are opposed (out of phase) at the first and last quarters of the moon; the resulting smaller than average ranges are called *neap tides.* The moon does not remain at a fixed distance from the earth. A lunar elliptic semidiurnal component with a period of 12.66 hr is in phase with the principal lunar constituent at perigee (moon closest to the earth) and out of phase at apogee (moon farthest from the earth). Perigean and apogean ranges are approximately 20 percent larger and smaller, respectively, than the mean range. In Fig. 1-39 the larger spring ranges for New York at times of new and full moon are quite apparent.[46] Perigee occurs at the same time as full moon, making the ranges appreciably larger than the spring tides 2 weeks earlier, when new moon and apogee are just 1 day apart.

To take care of diurnal inequalities in the tide associated with large declinations of moon and sun, diurnal components are introduced whose periods are such that they are in phase at extreme declination and opposed when the moon (or sun) is on the equator. Figure 1-39 illustrates the importance of extreme declination of the moon in the larger inequalities at Seattle, Los Angeles, and Honolulu. At Pakhoi the tide is completely diurnal, except for a few days when the moon is near the equator.

Nonastronomical Components. Some tidal components do not have astronomical causes. Estuaries may be considered to consist of various superimposed basins, each of which has a vibration period determined by its length and depth. Although the period of an enclosed basin is $2L/(gh)^{1/2}$, where L is the length, g is gravity, and h the depth, a bay open to the ocean has a period twice as long. If the opening of the bay is large compared to the basin length, its period is even longer.[2] When the period of a basin approximates a harmonic of a tidal period, it introduces a repetitive disturbing wave that more or less persistently distorts the shape of the tidal curve. The irregular dimensions of real basins make it difficult to estimate their effect on the tide.

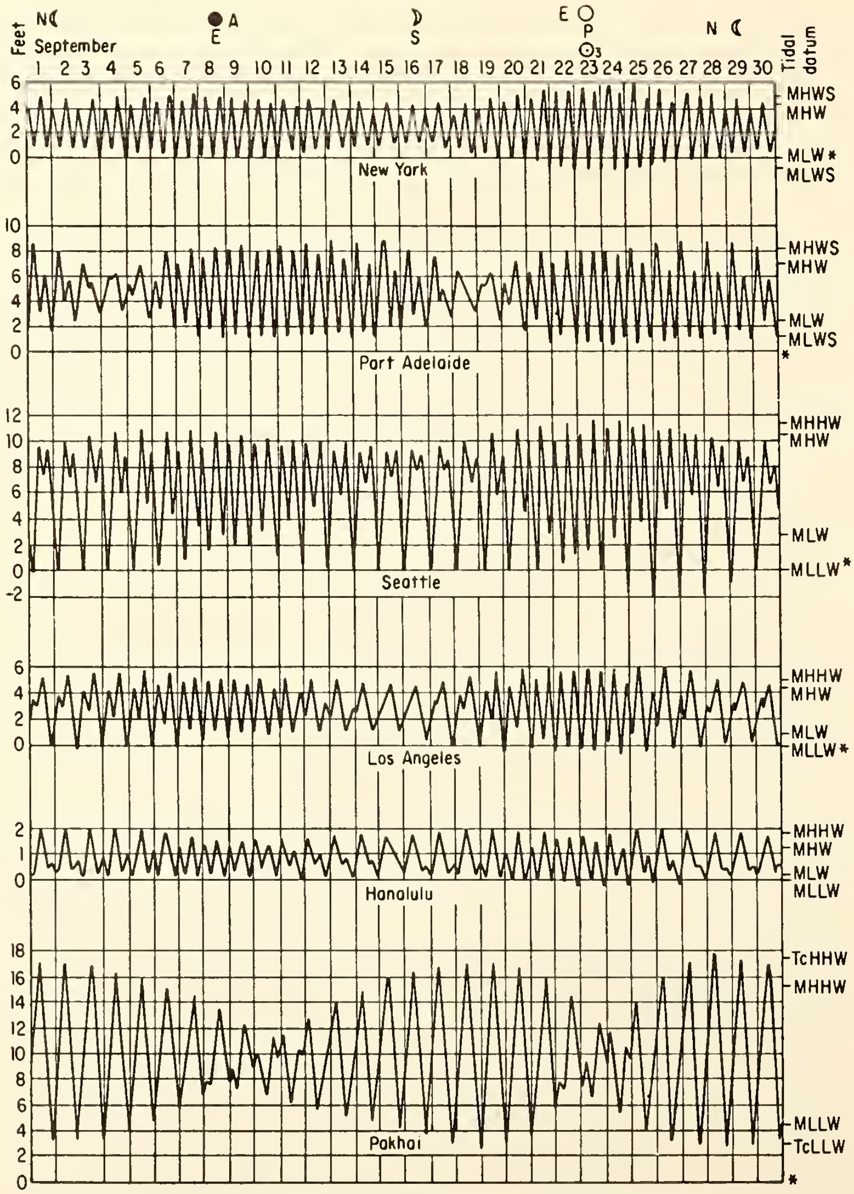

●, new moon; ☽, first quarter; ○, full moon; ☾, last quarter; E, moon on the Equator; N,S, moon farthest north or south of the Equator; A,P, moon in apogee or perigee; $\odot_3$, sun at autumnal equinox. x=chart datum

Fig. 1-39 Tidal variations at various places during a month.

Higher harmonics of the largest components are caleulated and introduced in the predictions to simulate the observed shape of the curve.

In general, the tide in an estuary is a progressive wave, high water oecuring later with distance upstream. The range of tide depends on the cross-section dimensions, the phasing of the ineoming wave with a reflected wave from the head of the estuary, and the damping eoefficients.[52] The tidal current floods upstream and ebbs downstream, going through slaek water before each reversal. Ordinarily the charaeteristies of the tide or tidal current for a particular place are best determined from observations.

See Hurricanes and Typhoons for a discussion of storm tides.

Cotidal Charts

After tides were observed and analyzed at many places, tidal mathematicians found they could draw cotidal charts, which have lines indicating places at whieh high waters of a particular component occur simultaneously. Many fit the data with the concept of a progressive wave (wave advancing horizontally with a fixed period between successive crests). Others used superimposed stationary waves (the back-and-forth sloshing observed on a rectangular pan of water, one end of which is raised and quickly lowered). In the latter concept, when it is high water at one end of a basin, it is low water at the other, and at the middle there is a nodal line with no rise or fall of the water. Dietrieh[3] favors the progressive-wave idea in theoretically projecting the tidal lines offshore.

Along some eoasts the cotidal lines are thickly clustered and thereby describe large changes in time of tide in relatively short distances. On the East Coast of the United States the semidiurnal cotidal line is more or less parallel to the shoreline, showing that high water occurs almost simultaneously all along the outer coast. On the West Coast these lines are somewhat normal to the coast, showing a progressive ehange in time of high water with distance along it. Thus these charts can be used for estimating the tidal regime at plaees for which no observations are available, whereas estimating from only a few nearby stations may be extremely unreliable.

Measurement of Tides

Tide Level. Tides are ordinarily measured by gages whieh use floats in wells to orient the position of a pencil or stylus on an analog record. A limited orifice at the bottom of the well dampens the high-frequeney wind-wave effect. These gages can be portable or permanent, and various types of pressure sensors are used when a pier or piling is not available for mounting the equipment above the water surface. If necessary, hourly observations can be made visually in a graduated vertical scale, averaging crest and trough splash marks for an observation at any given time. A short series obtained in any of these ways furnishes a rough estimate of average range and sea level, particularly if obtained during ordinary meteorological conditions. Inasmuch as a very short series may inelude only a limited period, such as spring tides, more reliable values can be obtained if the observations are redueed by eomparison with data for a station of similar tidal characteristics for whieh better-determined mean values are available.

Chart Datum. The datum of a nautical chart is the level to which all soundings on the chart are referred. In principle, it is desirable to have a level such that the tide seldom or never drops below it. In that ease we would not have negative-tide predictions, and the mariner could always count on having at least the charted depth of water. For historic, legal, and engineering reasons, the U.S. Coast and Geodetic Survey[61] has not followed this principle, using mean low water on the East Coast and mean lower low water on the West Coast. Thus on the East Coast half of all low waters fall below ehart datum; on the West Coast, half of all of the lower of the two low tides a day fall below the datum. Many countries use appreeiably lower datums, some using a level ehosen arbitrarily sueh that the tide is unlikely to fall below it.

Seasonal changes in various meteorological parameters (wind, pressure, and temperature) result in slow eyclieal ehanges in sea level. Monthly mean values of sea level averaged over a number of years are analyzed for an annual and a semiannual variation, which are in turn introduced in the predictions to reproduce the seasonal change in sea level.

Tidal Currents. There has not been an intensive effort on the part of oceanographers to measure tidal currents in the ocean because these measurements are not only expensive but also somewhat unreliable. Instrumental contributions to the observations may be almost as great as the relatively low velocities observed. Unlike tidal-current predictions in estuaries and rivers, tidal currents in most of the ocean have little or no significance to navigators.

Theoretically it is possible to predict tidal currents in the open ocean from cotidal charts if water depth and Coriolis force are considered.[2] This prediction assumes that the tide is a progressive wave with maximum current occurring at times of high and low

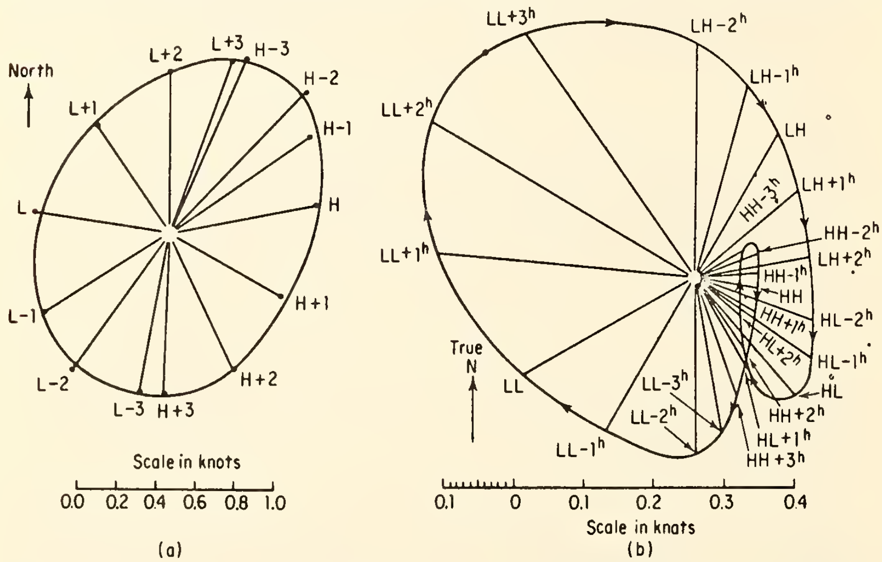

Fig. 1-40 Rotary-current plot (*current rose*): (*a*) mean current curve, Nantucket Shoals Light Vessel, July, 1920; (*b*) tidal-current curve, San Francisco Lightship referred to predicted time of tide at San Francisco (Golden Gate), California.

water. However, in a stationary wave maximum current occurs at mean water level, exactly out of phase with a progressive wave. If the tides in the open ocean are considered to be some combination of progressive and stationary waves, there is no satisfactory method of inferring the tidal current from cotidal charts.

There have been numerous long series of surface-current observations obtained from lightships in coastal waters.[49,50] Analysis of these data shows a rotary change in direction and a cyclical change in velocity during a tidal period. The simpler type of semidiurnal rotary current can be drawn as a *current rose*, a series of hourly vectors starting from a fixed point whose extremities can be described by an ellipse (Fig. 1-40*a*). The major axis of the ellipse describes the maximum flood and ebb of the tidal current; the minor axis represents the minimum currents in lieu of the slack water found with reversing currents. When rotary tidal currents are diurnal or have a large diurnal component, the current rose is unsymmetric and very complex (Fig. 1-40*b*).[50]

REFERENCES

General

1. Coker, R. E.: "This Great Wide Sea," University of North Carolina Press, Durham, N.C., 1949; reprinted by Harper & Row, Publishers, Incorporated, 1962.

2. Dietrich, G.: "General Oceanography," Interscience Publishers, Inc., New York, 1963.
3. Hill, M. N. (ed.): "The Sea," vol. I, Physical Oceanography; vol. II, Composition of Sea Water; vol. III, The Earth Beneath the Sea; Interscience Publishers, Inc., New York, 1962, 1963.
4. King, C. A. M.: "An Introduction to Oceanography," McGraw-Hill Book Company, New York, 1962.
5. "Handbook of Oceanographic Tables, 1966," U.S. Navy Oceanographic Office Special Publication #68, 1967.
6. Sears, M. (ed.): *Progress in Oceanography*, Pergamon Press, New York (published annually).
7. Sverdrup, H. U., M. W. Johnson, and R. H. Fleming: "The Oceans: Their Physics, Chemistry, and Biology," Prentice-Hall, Inc., Englewood Cliffs, N.J., 1942.
8. Weigel, R. L.: "Oceanographical Engineering," Prentice-Hall, Inc., Englewood Cliffs, N.J., 1964.
9. "Climatological & Oceanographic Atlas for Mariners," U.S. Government Printing Office, Washington, D.C., 1961.

Physical Oceanography

10. Defant, A.: "Physical Oceanography," Pergamon Press, New York, 1961. A large two-volume work with examples, theory, and thoroughness.
11. Fuglister, F. C.: "Atlantic Ocean Atlas: Temperature and Salinity Profiles and Data from the International Geophysical Year," Woods Hole Oceanographic Institute, Woods Hole, Mass., 1960. A graphical summary of extensive series of temperature and salinity measurements made in the Atlantic during the International Geophysical Year. A comprehensive and well-printed collection of actual data.
12. LaFond, E. C.: Processing Oceanographic Data, *U.S. Navy Oceanog. Off. Publ.* 614, 1951. A convenient set of instructions for computing densities and currents from classical temperature and salinity values.
13. Neumann, G., and W. J. Pierson, Jr.: "Principles of Physical Oceanography," Prentice-Hall, Inc., Englewood Cliffs, N.J., 1966. Physical oceanography with a strong slant toward meteorology and waves. A big modern book with much information and mathematical material, both descriptive and pictorial.
14. Pickard, G. L.: "Descriptive Physical Oceanography," Pergamon Press, New York, 1963. An excellent paperback book on the title subject.
15. Pounder, E. R.: "The Physics of Ice," Pergamon Press, New York, 1965. An excellent paperback description of ice and its properties in the laboratory and at sea.
16. von Arx, W. S.: "An Introduction to Physical Oceanography," Addison-Wesley Publishing Company, Inc., Cambridge, Mass., 1962. An introduction to oceanography that was written by an oceanographer with the engineering student in mind.

Chemical Oceanography

17. Barnes, H.: "Apparatus and Methods of Oceanography," pt. 1, Interscience Publishers, Inc., New York, 1965.
18. Harvey, H. W.: "Chemistry and Fertility of Sea Water," Cambridge University Press, Cambridge, England, 1957.
19. Mero, J. L.: "The Mineral Resources of the Sea," American Elsevier Publishing Company, New York, 1965.
20. Riley, J. P., and G. Skirrow (eds.): "Chemical Oceanography," vols. 1 and 2, Academic Press, New York, 1965.

Geological Oceanography

21. Bascom, W.: "Waves and Beaches," Anchor Books, Doubleday & Company, Inc., Garden City, New York, 1964.

22. Krumbein, W. C., and F. J. Pettijohn: "Manual of Sedimentary Petrography," Appleton-Century-Crofts, Inc., New York, 1938.
23. Kuenen, Ph. H.: "Marine Geology," John Wiley & Sons, Inc., New York, 1950.
24. Menard, H. W.: "Marine Geology of the Pacific," McGraw-Hill Book Company, New York, 1964.
25. Shepard, F. P.: "Submarine Geology," Harper & Row, Publishers, Incorporated, New York, 1963.

Meteorological Oceanography

26. Bolin, B. (ed.): "The Atmosphere and the Sea in Motion," Rockefeller Institute Press, Oxford University Press, New York, 1959.
27. Gentry, R. C.: Current Hurricane Research, *Weatherwise*, **17**: 180 (1964).
28. Petterssen, S.: "Introduction to Meteorology," McGraw-Hill Book Company, New York, 1958.
29. Redfield, A. C., et al: "Interaction of Sea and Atmosphere," *Meteorol. Monographs*, **2** (10) (1957).
30. Sverdrup, H. U.: "Oceanography for Meteorologists," Prentice-Hall, Inc., Englewood Cliffs, N.J., 1943.
31. Taylor, G. F.: "Elementary Meteorology," Prentice-Hall, Inc., Englewood Cliffs, N.J., 1954.
32. Annual Tropical Storm Report, 1963, *U.S. Navy Fleet Weather Facility, Miami, Rept.*, OPNAV 3140-9, 1964.
33. Annual Typhoon Report, 1963, *U.S. Fleet Weather Central/Joint Typhoon Warning Center Rept., Guam*, 1964.
34. "The Application of Oceanography to Subsurface Warfare," chaps. 5 and 7, National Defense Research Council, reprinted by Commission on Undersea Warfare of the National Research Council with Office of Naval Research, 1951

Sea Motion

Waves

35. Bretschneider, C. L.: Wave Variability and Wave Spectra for Wind-generated Gravity Waves, *U.S. Army Corps Engrs. Beach Erosion Board Tech. Memo.* 118, 1959.
36. Bretschneider, C. L.: "Modification of Wave Spectra over the Continental Shelf," *Proc. Eighth Conf. Coastal Eng.*, 1963.
37. Bretschneider, C. L.: Generation of Wind: State of the Art, *Natl. Eng. Sci. Co. Rept.* SN 134-6, 1965.
38. Cornish, V.: "Ocean Waves and Kindred Physical Phenomena," Cambridge, England, 1934.
39. Darbyshire, J.: The Generation of Waves by Wind, *Proc. Roy. Soc.* (*London*), *Ser. A*, **215**: 299 (1952).
40. Jeffreys, H.: On the Formation of Water Waves by Wind, *Proc. Roy. Soc.* (*London*), *Ser. A*, **107**: 189 (1924).
41. Kelvin, Lord: On the Waves Produced by a Single Impulse in Water of Any Depth, or in a Dispersive Medium, *Proc. Roy. Soc.* (*London*), **42** (1887).
42. Kitaigorodski, S. A., and S. S. Strekalov: Contribution to the Analysis of the Spectra of Wind-caused Wave Action, *I. Izv. Geophys.*, 1962, p. 1221.
43. Pierson, W. J., Jr., and L. Moskowitz: A Proposed Spectral Form for Fully Developed Wind Seas Based on the Similarity Theory of Kitaigorodski, *N.Y. Univ. Tech. Rept.* 63-12, 1963.
44. Russell, R. C. H., and D. H. MacMillan: "Waves and Tides," Hutchinson's Scientific and Technical Publications, New York, 1952.

Tides and Currents

45. Stommel, H.: "The Gulf Stream: A Physical and Dynamical Description," University of California Press, Berkeley, Calif., 1965.
46. Bowditch, N.: "American Practical Navigator," U.S. Navy Oceanographic Office, Washington, D.C., 1958.

47. Darwin, G.: "The Tides and Kindred Phenomena in the Solar System," W. H. Freeman and Company, San Francisco, 1962.
48. Doodson, A. T., and H. D. Warburg: "Admiralty Manual of Tides," Admiralty Hydrographic Department, London, 1941.
49. Haight, F. J.: Coastal Currents along the Atlantic Coast of the United States, *U.S. Coast Geodet. Sur. Spec. Publ.* 230, 1942.
50. Marmer, H. A.: Coastal Currents along the Pacific Coast of the United States, *U.S. Coast Geodet. Sur. Spec. Publ.* 121, 1926.
51. Marmer, H. A.: "Tidal Datum Planes," *U.S. Coast Geodet. Sur. Spec. Publ.* 135, 1951.
52. Redfield, A. C.: The Analysis of Tidal Phenomena in Narrow Embayments, *MIT Woods Hole Oceanog. Inst. Papers Phys. Oceanog. Meteorol.*, **11**(4) (1950).
53. Russell, R. C. H., and D. H. MacMillan: "Waves and Tides," Hutchinson's Scientific and Technical Publications, New York, 1952.
54. Schureman, P.: "Manual of Harmonic Analysis and Prediction of Tides," *U.S. Coast Geodet. Surv. Spec. Publ.* 98, 1958.
55. Eckart, C.: "Hydrodynamics of Oceans and Atmospheres," Pergamon Press, New York, 1960.

TIDE FORECASTING

B. D. Zetler

Prediction of tides and tidal currents is a highly specialized technique which an engineer ordinarily will not wish to master. He will generally use the published tables and tidal-current charts to obtain required predictions. These tables and charts furnish a time-dependent correction to the depths published on nautical charts by the U.S. Coast and Geodetic Survey and the U.S. Navy Oceanographic Office.

The tables,[31] in four volumes covering different geographic areas, are published by the U.S. Coast and Geodetic Survey and may be purchased from that agency and various sales agents. There are two related tidal-current tables published annually and a series of tidal-current charts for specific areas, showing current speeds and direction at various points for each hour in the tidal cycle. A list of publications relating to tides and currents and a list of sales agents may be obtained by writing directly to the U.S. Coast and Geodetic Survey, Rockville, Maryland 20852.

Table 1 of the *tide tables* (Fig. 11-50*a*), an example of which is reproduced here from Ref. 31, furnishes the times and heights of high and low waters for a number of places in the area of coverage. The heights are added to the depths shown on nautical charts to obtain the total depth at the particular time. Note that if the tidal height is a minus quantity it should be subtracted from the charted depth. Table 2 (Fig. 11-50*b*), an example of which is reproduced here from Ref. 31, furnishes tidal differences (time differences and height differences or ratios) for many additional places. The differences are applied to the predictions for a designated reference station in Table 1. Regardless of the time zone listed for the reference station, the predicted time of high and low water for a place in Table 2 will be in the time zone listed in Table 2 for that place. Supplemental tables are furnished for estimating the height of the tide at times in between high and low water. Predicted heights in these tables are compatible with the chart datum on the largest-scale nautical chart of the place for which the predictions are prepared.

Table 1 of the *tidal-current tables* (Fig. 11-51*a*) furnishes daily predictions for a limited number of stations. The predictions consist of times of slack water and times and velocities of maximum floods and ebbs. "Flood" refers to the current movement from the ocean into an estuary, and "ebb" refers to the opposite current movement. In some complex geographical locations, as in a strait between two basins both connected directly to the ocean, the designated flood and ebb directions are chosen somewhat arbitrarily. Table 2 (Fig. 11-51*b*) permits daily predictions for additional places by listing differences to be applied to the daily predictions for designated reference stations.

In some places the tidal current turns cyclically in a clockwise or counterclockwise direction, during which it has maximum and minimum speeds rather than maximum and slack water of the reversing currents described in the previous paragraph. The tidal-current tables furnish hourly values of direction and speed for these rotary currents. The extremities of these plotted hourly vectors describe the current rose (see Tidal Currents in Sec. 1).

The tidal-current charts are referred to predicted tides (high and low waters) or predicted currents (either maximum flood and ebb or slack waters). They are used in conjunction with predicted tables for the particular year in which the information is needed. The charts, which supply a visual generalized composite of currents in an area, are a useful supplement to the tables. However, inasmuch as they are referred to only two phases in the tidal cycle, as opposed to four in the tidal-current tables, they are not ordinarily so accurate as the latter.

NEW YORK (THE BATTERY), N.Y., 1968

TIMES AND HEIGHTS OF HIGH AND LOW WATERS

JANUARY

DAY	TIME H.M.	HT. FT.	DAY	TIME H.M.	HT. FT.
1	0248	-0.7	16	0236	-0.2
M	0906	5.2	TU	0842	4.8
	1530	-1.0		1518	-0.7
	2136	4.0		2112	3.7
2	0336	-0.6	17	0312	-0.3
TU	0954	5.0	W	0918	4.7
	1618	-0.9		1554	-0.7
	2230	4.0		2154	3.8
3	0424	-0.4	18	0354	-0.4
W	1048	4.7	TH	1006	4.6
	1700	-0.7		1630	-0.6
	2324	4.0		2236	4.0
4	0512	-0.1	19	0430	-0.3
TH	1136	4.4	F	1048	4.5
	1748	-0.4		1706	-0.6
				2324	4.1
5	0012	3.9	20	0512	-0.2
F	0600	0.2	SA	1136	4.3
	1224	4.1		1742	-0.4
	1836	-0.1			
6	0100	3.8	21	0012	4.2
SA	0700	0.5	SU	0606	-0.1
	1306	3.8		1230	4.1
	1930	0.1		1830	-0.3
7	0148	3.8	22	0106	4.3
SU	0806	0.6	M	0718	0.1
	1354	3.5		1318	3.9
	2024	0.2		1936	-0.1
8	0236	3.8	23	0200	4.4
M	0906	0.7	TU	0842	0.1
	1442	3.3		1418	3.6
	2118	0.3		2048	-0.1
9	0324	3.8	24	0306	4.4
TU	1000	0.6	W	0948	0.0
	1542	3.1		1530	3.5
	2206	0.3		2154	-0.1
10	0418	3.9	25	0412	4.5
W	1054	0.4	TH	1054	-0.2
	1636	3.1		1648	3.5
	2254	0.2		2300	-0.3
11	0512	4.0	26	0518	4.7
TH	1142	0.2	F	1148	-0.4
	1736	3.1		1754	3.6
	2336	0.2		2354	-0.4
12	0600	4.3	27	0618	4.9
F	1230	0.0	SA	1248	-0.6
	1824	3.2		1848	3.8
13	0024	0.1	28	0054	-0.5
SA	0642	4.5	SU	0712	5.1
	1312	-0.2		1336	-0.8
	1912	3.4		1942	4.0
14	0112	0.0	29	0142	-0.6
SU	0724	4.6	M	0800	5.1
	1400	-0.4		1424	-0.9
	1954	3.5		2030	4.2
15	0154	-0.1	30	0236	-0.7
M	0800	4.7	TU	0848	5.0
	1436	-0.6		1512	-1.0
	2030	3.6		2118	4.2
			31	0318	-0.6
			W	0936	4.8
				1548	-0.9
				2206	4.2

FEBRUARY

DAY	TIME H.M.	HT. FT.	DAY	TIME H.M.	HT. FT.
1	0400	-0.5	16	0336	-0.8
TH	1018	4.6	F	0942	4.8
	1630	-0.7		1600	-0.9
	2248	4.2		2212	4.6
2	0442	-0.3	17	0418	-0.7
F	1100	4.3	SA	1030	4.6
	1706	-0.5		1642	-0.8
	2336	4.1		2300	4.7
3	0524	0.0	18	0506	-0.6
SA	1142	4.0	SU	1118	4.4
	1742	-0.2		1718	-0.6
				2348	4.7
4	0018	4.0	19	0554	-0.3
SU	0606	0.4	M	1212	4.1
	1224	3.7		1806	-0.3
	1824	0.1			
5	0100	3.9	20	0042	4.6
M	0706	0.6	TU	0706	0.0
	1306	3.4		1306	3.8
	1912	0.4		1912	0.0
6	0142	3.8	21	0142	4.9
TU	0812	0.8	W	0824	0.2
	1348	3.1		1412	3.5
	2012	0.6		2030	0.2
7	0224	3.7	22	0248	4.4
W	0918	0.8	TH	0936	0.1
	1442	2.9		1524	3.4
	2118	0.7		2148	0.2
8	0324	3.7	23	0400	4.4
TH	1018	0.6	F	1042	0.0
	1554	2.8		1642	3.4
	2212	0.6		2248	0.0
9	0424	3.8	24	0512	4.5
F	1106	0.4	SA	1136	-0.2
	1700	2.9		1748	3.7
	2306	0.5		2348	-0.2
10	0524	4.0	25	0612	4.7
SA	1200	0.1	SU	1230	-0.4
	1800	3.2		1842	4.0
11	0000	0.3	26	0042	-0.4
SU	0612	4.3	M	0700	4.9
	1248	-0.1		1318	-0.6
	1848	3.5		1930	4.3
12	0048	0.0	27	0130	-0.5
M	0700	4.6	TU	0748	4.9
	1330	-0.4		1406	-0.8
	1924	3.8		2012	4.4
13	0130	-0.2	28	0218	-0.6
TU	0742	4.8	W	0830	4.9
	1412	-0.6		1442	-0.8
	2006	4.0		2054	4.5
14	0212	-0.5	29	0300	-0.6
W	0818	4.9	TH	0906	4.7
	1448	-0.8		1524	-0.7
	2048	4.3		2130	4.5
15	0300	-0.7			
TH	0900	4.9			
	1524	-0.9			
	2124	4.5			

MARCH

DAY	TIME H.M.	HT. FT.	DAY	TIME H.M.	HT. FT.
1	0342	-0.5	16	0318	-1.0
F	0948	4.5	SA	0924	4.9
	1554	-0.6		1536	-0.9
	2212	4.4		2142	5.2
2	0418	-0.3	17	0406	-0.9
SA	1024	4.2	SU	1012	4.7
	1630	-0.3		1612	-0.7
	2248	4.3		2236	5.2
3	0448	0.0	18	0448	-0.7
SU	1106	3.9	M	1106	4.4
	1654	0.0		1654	-0.5
	2330	4.2		2330	5.0
4	0530	0.3	19	0542	-0.4
M	1142	3.6	TU	1200	4.1
	1724	0.3		1748	-0.1
5	0006	4.0	20	0024	4.8
TU	0606	0.6	W	0648	0.0
	1218	3.3		1300	3.8
	1748	0.6		1854	0.3
6	0042	3.9	21	0130	4.6
W	0706	0.8	TH	0812	0.2
	1300	3.1		1406	3.6
	1818	0.8		2024	0.5
7	0124	3.8	22	0236	4.4
TH	0830	0.9	F	0924	0.2
	1354	2.9		1518	3.5
	2012	1.0		2136	0.4
8	0224	3.7	23	0348	4.3
F	0936	0.8	SA	1024	0.1
	1506	2.9		1630	3.7
	2136	1.0		2242	0.3
9	0336	3.8	24	0454	4.4
SA	1036	0.6	SU	1118	-0.1
	1624	3.0		1730	4.0
	2236	0.8		2336	0.0
10	0442	4.0	25	0554	4.5
SU	1124	0.3	M	1206	-0.3
	1724	3.4		1824	4.3
	2330	0.4			
11	0542	4.3	26	0024	-0.2
M	1212	0.0	TU	0642	4.7
	1812	3.8		1254	-0.4
				1906	4.6
12	0018	0.1	27	0112	-0.3
TU	0630	4.6	W	0724	4.7
	1254	-0.3		1336	-0.5
	1854	4.2		1948	4.8
13	0106	-0.3	28	0154	-0.4
W	0712	4.8	TH	0800	4.6
	1336	-0.6		1412	-0.5
	1936	4.6		2024	4.8
14	0154	-0.7	29	0236	-0.4
TH	0754	5.0	F	0842	4.5
	1418	-0.8		1448	-0.4
	2018	4.9		2100	4.8
15	0236	-0.9	30	0318	-0.4
F	0836	5.0	SA	0918	4.3
	1454	-0.9		1524	-0.3
	2100	5.1		2136	4.7
			31	0348	-0.2
			SU	0954	4.1
				1554	-0.1
				2206	4.6

TIME MERIDIAN 75° W. 0000 IS MIDNIGHT. 1200 IS NOON.
HEIGHTS ARE RECKONED FROM THE DATUM OF SOUNDINGS ON CHARTS OF THE LOCALITY WHICH IS MEAN LOW WATER.

Fig. 11-50a Representative Table 1 from "Tide Tables: High and Low Water Predictions," U.S. Coast and Geodetic Survey, Rockville, Maryland (published annually).

TABLE 2.—TIDAL DIFFERENCES AND OTHER CONSTANTS

No.	PLACE	POSITION		DIFFERENCES				RANGES		Mean Tide Level
				Time		Height				
		Lat.	Long	High water	Low water	High water	Low water	Mean	Spring	
		° ′	° ′	h. m.	h. m.	feet	feet	feet	feet	feet
	NEW YORK—Continued	N.	W.	on SANDY HOOK, p.70						
	Long Island, South Side—Continued									
				Time meridian, 75°W.						
	Hempstead Bay									
1451	Deep Creek Meadow	40 36	73 32	+1 02	+1 09	*0.52	*0.52	2.4	2.9	1.2
1453	Green Island	40 37	73 30	+1 22	+1 29	*0.41	*0.41	1.9	2.3	0.9
1455	Cuba Island	40 37	73 31	+1 08	+1 20	*0.50	*0.50	2.3	2.8	1.1
1457	Bellmore, Bellmore Creek	40 40	73 31	+1 29	+1 56	*0.43	*0.43	2.0	2.4	1.0
1459	Neds Creek	40 37	73 33	+0 50	+0 52	-1.9	0.0	2.7	3.3	1.3
1461	Freeport Creek	40 38	73 34	+0 34	+0 27	-1.5	0.0	3.1	3.8	1.5
1463	Freeport, Baldwin Bay	40 38	73 35	+0 38	+0 53	-1.6	0.0	3.0	3.6	1.5
1465	Long Beach	40 36	73 39	+0 19	0 00	-0.7	0.0	3.9	4.7	1.9
1467	Long Beach, outer coast	40 35	73 39	-0 29	-0 35	-0.1	0.0	4.5	5.4	2.2
	Hempstead Bay—Continued									
1469	East Rockaway	40 38	73 40	+0 42	+0 45	-0.7	0.0	3.9	4.7	1.9
1471	Woodmere, Brosewere Bay	40 37	73 42	+0 35	+0 48	-0.7	0.0	3.9	4.7	1.9
1473	East Rockaway Inlet	40 36	73 44	-0 06	-0 16	-0.5	0.0	4.1	5.0	2.0
	Jamaica Bay									
1475	Plumb Beach Channel	40 35	73 55	+0 03	-0 05	+0.3	0.0	4.9	5.9	2.4
1477	Barren Island, Rockaway Inlet	40 35	73 53	0 00	-0 06	+0.4	0.0	5.0	6.0	2.5
1479	Beach Channel (bridge)	40 35	73 49	+0 38	+0 22	+0.5	0.0	5.1	6.2	2.5
1481	Motts Basin	40 37	73 46	+0 40	+0 46	+0.8	0.0	5.4	6.5	2.7
1483	Norton Point, Head of Bay	40 38	73 45	+0 39	+0 43	+0.8	0.0	5.4	6.5	2.7
1485	New York International Airport	40 37	73 47	+0 26	+0 43	+0.7	0.0	5.3	6.4	2.6
1487	Grassy Bay (bridge)	40 39	73 50	+0 44	+0 45	+0.6	0.0	5.2	6.3	2.6
1489	Canarsie	40 38	73 53	+0 28	+0 06	+0.6	0.0	5.2	6.3	2.6
1491	Mill Basin	40 37	73 55	+0 29	+0 02	+0.6	0.0	5.2	6.3	2.6
	NEW YORK and NEW JERSEY									
	New York Harbor									
1493	Coney Island	40 34	73 59	-0 03	-0 19	+0.1	0.0	4.7	5.7	2.3
1495	Norton Point, Gravesend Bay	40 35	74 00	-0 03	+0 01	+0.1	0.0	4.7	5.7	2.3
1497	Fort Wadsworth, The Narrows	40 36	74 03	+0 02	+0 12	-0.3	0.0	4.3	5.2	2.1
1499	Fort Hamilton, The Narrows	40 37	74 02	+0 03	+0 05	+0.1	0.0	4.7	5.7	2.3
				on NEW YORK, p.62						
1501	Bay Ridge	40 38	74 02	-0 24	-0 24	+0.1	0.0	4.6	5.5	2.3
1503	St. George, Staten Island	40 39	74 04	-0 21	-0 18	0.0	0.0	4.5	5.4	2.2
1505	Bayonne, New Jersey	40 41	74 06	-0 19	-0 08	0.0	0.0	4.5	5.4	2.2
1507	Gowanus Bay	40 40	74 01	-0 19	-0 15	-0.1	0.0	4.4	5.3	2.2
1509	Governors Island	40 42	74 01	-0 11	-0 06	-0.1	0.0	4.4	5.3	2.2
1511	NEW YORK (The Battery)	40 42	74 01	Daily predictions				4.5	5.4	2.2
	Hudson River‡									
1513	Jersey City, Pa. RR. Ferry, N. J	40 43	74 02	+0 07	+0 07	-0.1	0.0	4.4	5.3	2.2
1515	New York, Desbrosses Street	40 43	74 01	+0 10	+0 10	-0.1	0.0	4.4	5.3	2.2
1517	New York, Chelsea Docks	40 45	74 01	+0 17	+0 16	-0.2	0.0	4.3	5.2	2.1
1519	Hoboken, Castle Point, N. J	40 45	74 01	+0 17	+0 16	-0.2	0.0	4.3	5.2	2.1
1521	Weehawken, Days Point, N. J	40 46	74 01	+0 24	+0 23	-0.3	0.0	4.2	5.0	2.1
1523	New York, Union Stock Yards	40 47	74 00	+0 27	+0 26	-0.3	0.0	4.2	5.0	2.1
1525	New York, 130th Street	40 49	73 58	+0 37	+0 35	-0.5	0.0	4.0	4.8	2.0
1527	George Washington Bridge	40 51	73 57	+0 46	+0 43	-0.6	0.0	3.9	4.6	1.9
1529	Spuyten Duyvil, West of RR. bridge	40 53	73 56	+0 58	+0 53	-0.7	0.0	3.8	4.5	1.9
1531	Yonkers	40 56	73 54	+1 09	+1 10	-0.8	0.0	3.7	4.4	1.8
1533	Dobbs Ferry	41 01	73 53	+1 29	+1 40	-1.1	0.0	3.4	4.0	1.7
1535	Tarrytown	41 05	73 52	+1 45	+1 54	-1.3	0.0	3.2	3.7	1.6

*Ratio.

‡Values for the Hudson River above George Washington Bridge are based upon averages for the six months May to October, when the fresh water discharge is a minimum.

Fig. 11-50b Representative Table 2 from "Tide Tables: High and Low Water Predictions," U.S. Coast and Geodetic Survey, Rockville, Maryland (published annually).

THE NARROWS, NEW YORK HARBOR, N.Y., 1968

F-FLOOD, DIR. 340° TRUE E-EBB, DIR. 160° TRUE

MARCH

DAY	SLACK WATER TIME H.M.	MAXIMUM CURRENT TIME H.M.	VEL. KNOTS	DAY	SLACK WATER TIME H.M.	MAXIMUM CURRENT TIME H.M.	VEL. KNOTS
1		0206	2.1E	16		0148	2.5E
F	0536	0806	1.7F	SA	0518	0748	2.0F
	1112	1424	2.1E		1054	1406	2.4E
	1754	2030	1.7F		1724	2012	2.2F
	2336				2318		
2		0248	2.0E	17		0236	2.5E
SA	0618	0848	1.5F	SU	0606	0836	1.9F
	1148	1506	2.0E		1136	1448	2.3E
	1836	2112	1.7F		1812	2100	2.2F
3	0018	0330	1.9E	18	0012	0324	2.4E
SU	0706	0930	1.4F	M	0700	0930	1.7F
	1230	1542	1.9E		1224	1536	2.2E
	1918	2154	1.6F		1900	2154	2.1F
4	0100	0412	1.8E	19	0106	0418	2.2E
M	0800	1018	1.2F	TU	0800	1024	1.5F
	1306	1618	1.7E		1318	1630	2.0E
	2006	2242	1.5F		2000	2248	2.0F
5	0148	0500	1.6E	20	0200	0512	2.0E
TU	0900	1106	1.1F	W	0906	1124	1.4F
	1354	1706	1.5E		1412	1730	1.8E
	2054	2330	1.5F		2106	2348	1.9F
6	0236	0554	1.5E	21	0300	0624	1.9E
W	0954	1154	1.0F	TH	1012	1224	1.2F
	1442	1806	1.4E		1512	1842	1.7E
	2148				2212		
7		0018	1.4F	22		0048	1.7F
TH	0330	0700	1.5E	F	0406	0730	1.8E
	1054	1248	0.9F		1118	1336	1.2F
	1536	1912	1.3E		1624	1948	1.7E
	2242				2318		
8		0112	1.4F	23		0206	1.7F
F	0430	0800	1.5E	SA	0512	0836	1.9E
	1148	1342	0.9F		1218	1500	1.2F
	1642	2006	1.4E		1736	2054	1.8E
	2336						
9		0206	1.4F	24	0018	0330	1.7F
SA	0530	0854	1.6E	SU	0618	0930	2.0E
	1242	1454	0.9F		1312	1612	1.4F
	1742	2100	1.5E		1836	2148	1.9E
10	0030	0312	1.5F	25	0118	0430	1.8F
SU	0624	0942	1.8E	M	0712	1024	2.0E
	1330	1600	1.1F		1400	1700	1.6F
	1836	2148	1.7E		1930	2242	1.9E
11	0124	0412	1.6F	26	0212	0518	1.8F
M	0712	1024	1.9E	TU	0800	1112	2.1E
	1412	1642	1.4F		1448	1742	1.7F
	1924	2236	1.8E		2018	2330	2.0E
12	0212	0500	1.8F	27	0306	0600	1.8F
TU	0800	1112	2.1E	W	0842	1154	2.1E
	1454	1724	1.6F		1530	1818	1.8F
	2012	2330	2.0E		2100		
13	0300	0542	2.0F	28		0018	2.1E
W	0842	1154	2.2E	TH	0348	0636	1.8F
	1536	1800	1.9F		0918	1236	2.1E
	2100				1606	1848	1.9F
					2142		
14		0018	2.2E	29		0100	2.1E
TH	0348	0618	2.1F	F	0436	0706	1.7F
	0924	1242	2.3E		1000	1318	2.0E
	1612	1842	2.0F		1642	1918	1.8F
	2142				2224		
15		0100	2.4E	30		0142	2.1E
F	0430	0700	2.1F	SA	0518	0736	1.6F
	1006	1324	2.4E		1036	1354	2.0E
	1648	1924	2.2F		1718	1954	1.8F
	2230				2306		
				31		0224	2.0E
				SU	0600	0812	1.4F
					1112	1430	1.9E
					1754	2030	1.7F
					2348		

APRIL

DAY	SLACK WATER TIME H.M.	MAXIMUM CURRENT TIME H.M.	VEL. KNOTS	DAY	SLACK WATER TIME H.M.	MAXIMUM CURRENT TIME H.M.	VEL. KNOTS
1		0300	1.9E	16		0306	2.5E
M	0642	0854	1.3F	TU	0648	0906	1.7F
	1154	1506	1.7E		1206	1518	2.2E
	1836	2118	1.6F		1836	2130	2.2F
2	0030	0342	1.8E	17	0048	0400	2.3E
TU	0736	0942	1.1F	W	0748	1006	1.5F
	1236	1548	1.6E		1300	1612	2.0E
	1918	2200	1.5F		1942	2230	2.0F
3	0112	0424	1.7E	18	0142	0454	2.1E
W	0830	1036	1.0F	TH	0848	1112	1.4F
	1324	1630	1.4E		1400	1712	1.8E
	2012	2254	1.5F		2048	2330	1.8F
4	0200	0518	1.6E	19	0242	0600	1.9E
TH	0924	1124	1.0F	F	0954	1218	1.3F
	1412	1724	1.3E		1500	1824	1.6E
	2106	2342	1.4F		2154		
5	0254	0618	1.5E	20		0036	1.7F
F	1018	1218	0.9F	SA	0342	0712	1.9E
	1506	1830	1.3E		1054	1330	1.3F
	2206				1612	1936	1.6E
					2300		
6		0036	1.4F	21		0148	1.6F
SA	0348	0724	1.5E	SU	0448	0812	1.9E
	1112	1312	1.0F		1148	1442	1.4F
	1612	1936	1.3E		1718	2036	1.7E
	2306						
7		0130	1.4F	22	0006	0306	1.5F
SU	0448	0818	1.7E	M	0548	0906	1.9E
	1200	1412	1.1F		1242	1542	1.5F
	1712	2030	1.5E		1818	2130	1.8E
8	0000	0230	1.4F	23	0100	0406	1.6F
M	0548	0906	1.8E	TU	0642	0954	2.0E
	1248	1512	1.3F		1330	1636	1.7F
	1806	2124	1.7E		1912	2224	1.9E
9	0054	0336	1.6F	24	0154	0454	1.6F
TU	0636	0954	2.0E	W	0724	1042	2.0E
	1330	1606	1.5F		1412	1718	1.8F
	1900	2212	2.0E		1954	2306	2.0E
10	0148	0424	1.7F	25	0248	0536	1.6F
W	0724	1036	2.1E	TH	0806	1124	1.9E
	1412	1648	1.8F		1454	1754	1.9F
	1948	2300	2.2E		2036	2354	2.0E
11	0236	0512	1.9F	26	0330	0612	1.6F
TH	0806	1124	2.2E	F	0848	1206	1.9E
	1454	1730	2.1F		1536	1818	1.9F
	2030	2348	2.4E		2118		
12	0324	0554	2.0F	27		0036	2.0E
F	0854	1206	2.3E	SA	0412	0642	1.5F
	1536	1812	2.3F		0924	1242	1.9E
	2118				1612	1848	1.9F
					2154		
13		0042	2.5E	28		0118	2.0E
SA	0412	0642	2.0F	SU	0454	0712	1.4F
	0936	1254	2.4E		1006	1324	1.8E
	1612	1900	2.4F		1648	1918	1.8F
	2206				2236		
14		0130	2.6E	29		0200	2.0E
SU	0500	0724	2.0F	M	0536	0748	1.3F
	1024	1342	2.4E		1042	1400	1.7E
	1654	1942	2.4F		1724	2000	1.8F
	2300				2318		
15		0218	2.6E	30		0236	2.0E
M	0548	0812	1.8F	TU	0624	0830	1.2F
	1112	1430	2.3E		1124	1442	1.6E
	1742	2036	2.3F		1800	2042	1.7F
	2354						

TIME MERIDIAN 75° W. 0000 IS MIDNIGHT. 1200 IS NOON.

Fig. 11-51*a* Representative Table 1 from "Tidal Current Tables," U.S. Coast and Geodetic Survey, Rockville, Maryland (published annually).

TABLE 2.—CURRENT DIFFERENCES AND OTHER CONSTANTS

No	PLACE	POSITION		TIME DIFFERENCES		VELOCITY RATIOS		MAXIMUM CURRENTS			
								Flood		Ebb	
		Lat.	Long.	Slack water	Maximum current	Maximum flood	Maximum ebb	Direction (true)	Average velocity	Direction (true)	Average velocity
		° ′	° ′	*h. m.*	*h. m.*			*deg.*	*knots*	*deg.*	*knots*
	LONG ISLAND, South Coast—Continued	N.	W.	on THE NARROWS, p.52 *Time meridian, 75°W.*							
2250	Shinnecock Inlet	40 51	72 29	−0 20	−0 40	1.5	1.2	350	2.5	170	2.3
2255	Fire I. Inlet, 0.5 mi. S. of Oak Beach	40 38	73 18	+0 15	0 00	1.4	1.2	80	2.4	245	2.4
2260	Jones Inlet	40 35	73 34	−1 00	−0 55	1.8	1.3	35	3.1	215	2.6
2265	Long Beach, inside, between bridges	40 36	73 40	−0 10	+0 10	0.3	0.3	75	0.5	275	0.6
2270	East Rockaway Inlet	40 35	73 45	−1 25	−1 35	1.3	1.2	40	2.2	225	2.3
2275	Ambrose Channel Lightship	40 27	73 49	See table 5.							
2280	Sandy Hook App. Lighted Horn Buoy 2A	40 27	73 55	See table 5.							
	JAMAICA BAY										
2285	Rockaway Inlet	40 34	73 56	−1 45	−2 15	1.1	1.3	85	1.8	245	2.7
2290	Barren Island, east of	40 35	73 53	−2 00	−2 25	0.7	0.9	5	1.2	190	1.7
2295	Canarsie (midchannel, off Pier)	40 38	73 53	−1 35	−1 50	0.3	0.3	45	0.5	220	0.7
2300	Beach Channel (bridge)	40 35	73 49	−1 20	−1 20	1.1	1.0	60	1.9	225	2.0
2305	Grass Hassock Channel	40 37	73 47	−1 10	−1 00	0.6	0.5	50	1.0	230	1.0
	NEW YORK HARBOR ENTRANCE										
2310	Ambrose Channel entrance	40 30	73 58	−1 10	−1 05	1.0	1.2	310	1.7	110	2.3
2315	Ambrose Channel, SE. of West Bank Lt	40 32	74 01	(1)	−0 25	0.8	0.9	310	1.3	170	1.8
2320	Coney Island Lt., 1.6 miles SSW. of	40 33	74 01	−0 10	(2)	0.5	0.8	330	0.8	145	1.5
2325	Ambrose Channel, north end	40 34	74 02	+0 05	+0 15	0.8	0.9	330	1.3	175	1.9
2330	Coney Island, 0.2 mile west of	40 35	74 01	−0 55	−0 55	0.9	1.0	330	1.5	170	2.0
2335	Ft. Lafayette, channel east of	40 36	74 02	(3)	(3)	0.6	0.5	345	1.1	195	0.9
2340	THE NARROWS, midchannel	40 37	74 03	Daily predictions				340	1.7	160	2.0
	NEW YORK HARBOR, Upper Bay										
2345	Tompkinsville	40 38	74 04	−0 10	+0 20	0.9	1.0	5	1.6	170	2.0
2350	Bay Ridge Channel	40 39	74 02	−0 35	−0 45	0.6	0.6	40	1.0	220	1.1
2355	Red Hook Channel	40 40	74 01	−0 35	−0 35	0.6	0.4	355	1.0	170	0.7
2360	Robbins Reef Light, east of	40 39	74 03	+0 10	+0 20	0.8	0.8	15	1.3	205	1.6
2365	Red Hook, 1 mile west of	40 41	74 02	+0 45	+1 00	0.8	1.2	25	1.3	205	2.3
2370	Statue of Liberty, east of	40 42	74 02	+0 55	+1 00	0.8	1.0	30	1.4	205	1.9
	HUDSON RIVER, Midchannel [4]										
2375	The Battery, northwest of	40 43	74 02	+1 30	+1 35	0.9	1.2	15	1.5	195	2.3
2380	Desbrosses Street	40 43	74 01	+1 35	+1 40	0.9	1.2	10	1.5	----	2.3
2385	Chelsea Docks	40 45	74 01	+1 30	+1 40	1.0	1.0	20	1.7	185	2.0
2390	Forty-second Street	40 46	74 00	+1 35	+1 45	1.0	1.2	30	1.7	----	2.3
2395	Ninety-sixth Street	40 48	73 59	+1 40	+1 50	1.0	1.2	30	1.7	----	2.3
2400	Grants Tomb, 123d Street	40 49	73 58	+1 45	+1 55	0.9	1.2	25	1.6	----	2.3
2405	George Washington Bridge	40 51	73 57	+1 45	+2 00	0.9	1.1	20	1.6	200	2.2
2410	Spuyten Duyvil	40 53	73 56	+2 00	+2 10	0.9	1.1	20	1.6	----	2.1
2415	Riverdale	40 54	73 55	+2 05	+2 20	0.8	1.0	15	1.4	200	2.0
2420	Dobbs Ferry	41 01	73 53	+2 25	+2 40	0.8	0.9	10	1.3	----	1.7
2425	Tarrytown	41 05	73 53	+2 40	+2 55	0.6	0.8	0	1.1	----	1.5
2430	Ossining	41 10	73 54	+2 55	+3 10	0.5	0.7	320	0.9	----	1.3
2435	Haverstraw	41 12	73 57	+3 05	+3 15	0.5	0.7	335	0.8	----	1.3
2440	Peekskill	41 17	73 57	+3 20	+3 35	0.5	0.6	0	0.8	----	1.2
2445	Bear Mountain Bridge	41 19	73 59	+3 25	+3 40	0.5	0.6	0	0.8	----	1.1
2450	Highland Falls	41 22	73 58	+3 35	+3 50	0.6	0.6	5	1.0	185	1.2
2455	West Point, off Duck Island	41 24	73 57	+3 40	+3 55	0.5	0.6	10	1.0	----	1.1

[1] Current is rotary, turning clockwise. Minimum current of 0.9 knot sets SW. about time of "Slack, flood begins" at The Narrows. Minimum current of 0.5 knot sets NE. about 1 hour before "Slack, ebb begins" at The Narrows.

[2] Maximum flood, $-0^h\ 50^m$; maximum ebb, $+0^h\ 55^m$.

[3] Flood begins, $-2^h\ 15^m$; maximum flood, $-0^h\ 05^m$; ebb begins, $+0^h\ 05^m$; maximum ebb, $-1^h\ 50^m$.

[4] The values for the Hudson River are for the summer months, when the fresh-water discharge is a minimum.

Fig. 11-51b Representative Table 2 from "Tidal Current Tables," U.S. Coast and Geodetic Survey, Rockville, Maryland (published annually).

Safety Afloat

13. "Recreational Boating Guide," CG-340, U.S. Coast Guard, Washington, D.C., 1961.
14. "Harbor Craft Crewman's Handbook," TM 55-501, U.S. Army, Washington, D.C., 1958.
15. SCUBA Suits, *U.S. Coast Guard Commandant Instruct.* 10126.1A, July, 1963.
16. Powder Actuated Tools, *U.S. Coast Guard Commandant Instruct.* 10290.1A, September, 1963.
17. "U.S. Navy Safety Precautions," Government Printing Office, Washington, D.C., 1961.
18. "U.S. Navy Diving Manual," Government Printing Office, Washington, D.C., July, 1953.
19. Knight, A. M., "Modern Seamanship," D. Van Nostrand Company, Inc., Princeton, N.J., 1966.
20. "Aids to Navigation Manual," CG-222, U.S. Coast Guard, Washington, D.C., 1953.
21. "National Search and Rescue Manual," CG-308, U.S. Coast Guard, Washington, D.C., July, 1959.
22. "Accident Prevention Manual for Industrial Operations," National Safety Council, Chicago, 1959.
23. "Fire Protection Handbook," National Fire Protection Association, Boston, 1962.
24. "Bureau of Ships Technical Manual," chap. 88, Damage Control, U.S. Navy Bureau of Ships, Washington, D.C., April, 1959.
25. "Bureau of Ships Technical Manual," chap. 93, Fire Fighting, U.S. Navy Bureau of Ships, Washington, D.C., April, 1959.

Marine Communications

26. Bennett, W. R., and J. R. Davey: "Data Transmission," McGraw-Hill Book Company, New York, 1965.
27. Davies, K.: "Ionospheric Radio Propagation," National Bureau of Standards, 1965.
28. International Radio Consultative Committee, *CCIR Doc. Ninth Plen. Sess., Los Angeles*, 1959.
29. "Fundamentals of Single Sideband," Collins Radio Company, Cedar Rapids, Iowa, 1960.
30. "Point-to-point Radio Relay Systems," Radio Corporation of America, Camden, N.J., 1962.

Tide, Wave, and Weather Forecasting

31. "Tide Tables: High and Low Water Predictions," U.S. Coast and Geodetic Survey, Rockville, Maryland (published annually).
32. Bretschneider, C. L.: Revision in Wave Forecasting: Deep and Shallow Water, *Proc. Sixth Conf. Coastal Eng.*, 1957, p. 30.
33. Neumann, G.: On Ocean Wave Spectra and a New Method of Forecasting Wind-generated Sea, *U.S. Army Corps Engrs. Beach Erosion Board Tech. Memo.* 43, 1952.
34. Pierson, W. J., Jr., G. Neumann, and R. W. James: Observing and Forecasting Ocean Waves by Means of Wave Spectra and Statistics, *U.S. Navy Hydrographic Off. Publ.* 603, 1955.
35. Sverdrup, H. U., and W. H. Munk: Wind, Sea, and Swell: Theory of Relations for Forecasting, *U.S. Navy Hydrographic Off. Publ.* 601, 1947.
36. Wilson, B. W.: Graphical Approach to the Forecasting of Waves in Moving Fetches, *U.S. Army Corps Engrs. Beach Erosion Board Tech. Memo.* 73, 1955.
37. Petterssen, S.: "Introduction to Meteorology," McGraw-Hill Book Company, New York, 1958.
38. Taylor, G. F.: "Elementary Meteorology," Prentice-Hall, Inc., Englewood Cliffs, N.J., 1954.

Reprinted from Proceedings of the Symposium on Tides organized by the International Hydrographic Bureau, Monaco, 1967, with permission UNESCO and the International Hydrographic Bureau.

COMPUTER APPLICATIONS TO TIDE AND CURRENT ANALYSIS IN THE COAST AND GEODETIC SURVEY

Bernard D. ZETLER

Physical Oceanography Laboratory, Institute for Oceanography, ESSA

The U.S. Coast and Geodetic Survey is now using a digital tide gage (Barbee, 1965which outputs a punched paper tape with information on tidal height in a stilling well every six minutes (each tenth of an hour). The paper tape is fed through a translator which converts the information to punched cards suitable for processing in electronic computers.

The availability of the data in this format led to the development of computer programs to routinely do the reduction processing previously done manually from the traditional analog tide records. A changeover of this type must be done carefully. The data must be edited to insure that erroneous values are not included in the processing ; previously a man had scaled a continuous curve and would have detected a malfunction in the gage or the recording equipment. Furthermore, the temptation to do the processing exactly as it had been done before must be resisted. Sometimes the standard procedures are based on man's limitations and opportunities to do things better with our new powerful tools must be sought. For example, we get into the habit of looking up information in tables to save the time involved in obtaining the answer from a formula. Unless a table is used repeatedly, it may be more efficient for an electronic computer to work with a formula and, in addition, precious space in the memory core is not used for storing the table.

The editing procedures are primarily to compute third differences in the data, a process which multiplies an error by three, thereby making it stand out above small random fluctuations. In the initial testing, errors were found due to failure of the punch to pierce the paper tape for certain digits and to translator errors. The editing procedure checks time and date sequence on successive cards and outputs a diagnostic if the cards are arranged wrong and if values are missing. The format of each card is also checked in the routine editing. The tide heights are read to four significant digits (hundredths of a foot) and the editing by differences is not likely to find an error in the last digit. A program was written that counts the number of times each digit occurs in the last place and severe departures from a rectangular distribution for the about 7,000 values each month can be interpreted as evidence of a systematic failure. However, the information furnished by the program is not considered sufficiently significant to be used routinely.

The major problem in the reduction lay in deciding on a method of choosing times of high and low waters. In preparing tide tables, the predicted heights are routinely compared to select the extremes (high and low waters). However, the presence of noise makes this method unacceptable with observations. Serious consideration was given to using a low pass filter to smooth high frequency noise but this was rejected on the basis that this modifies the data on a subjective basis (the choice of filter) and it is not possible now to anticipate future uses of the data that might be affected by the choice of the filter. Furthermore, there is the problem that the records are frequently used as legal records and a smoothed value might have a questionable value in a court of law. In addition, the response of the smoothing function must be exactly unity in the tidal frequencies ; otherwise the analysed ranges would be incorrect. It appeared logical and simple to identify a limited period of an extreme and then to fit a parabola by least squares to these data. The first derivative of $Y = ax^2 + bx + c$, in which a, b, and c are the unknowns to be obtained by a least square procedure, can be set equal to zero ($2ax + b = 0$) to obtain a linear solution for the times of high or low water. However, this implies a model curve symmetric to a line parallel to the Y axis, a solution that is not valid for the skewed curve found in many estuaries where the duration of rise is shorter than the duration of fall. Instead, we settled on a tilting board type of approach, using a given time as a fulcrum, adding four adjacent heights on either side and subtracting one sum from the other. At times of extremes, this difference is closest to zero. The method stemmed from an approach of fitting a line to the same data by a regression formula and choosing the slope closest to zero but the latter method weights each height by its distance from the fulcrum, making the distant points most important. The method accepted gives equal weight to each height used in the computation.

Times are treated cumulatively during a month and the program sums these times for both high and low waters. The sum of the moon's transits for the month has already been prepared on the same basis using a formula which takes into account the dates of the two days with only one transit due to the lunar progression in solar time. The instruction card which precedes the data contains this sum of transits as well as the number of days in the month. Also included is the designated option of reducing the data as (1) semidiurnal, (2) mixed, and (3) diurnal (only one high and low water during some days of the month).

With the first option, the output lists times and heights of all high and low waters, mean lunitidal intervals, mean high water, mean low water, mean tide level, mean sea level (river level in estuaries), mean range, hourly heights (these are outputted on punched cards as well) and monthly extremes. Option two chooses the higher high and lower low water and the inequalities to the output. It had been customary in U.S. Coast and Geodetic Survey procedures (1965) to check the higher high and lower low of each solar day, adding a check or omitting it on the days of one tide per solar day in accordance with sequence on either side (day before and after). This led invariably to either 29 or 31 higher highs in a 60 tide month, an expedient but unsatisfactory result of tabulating a lunar phenomenon in solar time. It would have been difficult to program this method ; furthermore it was not good science. It was easier and more satisfactory to pair the high waters in sets of two (two per lunar day) and to select the higher of each pair for inclusion as higher high. A comparable treatment is applied to the low waters. With both of these options, the program damands the proper number of high and low waters (2 less than twice the number of days). It does not sum the last tide in a month if it is superfluous and it advances to the early hours of the first day of the following month if another tide is needed. A diagnostic is outputted if there are too many or too few calculated high and low waters in a given month. The diagnostic includes information identifying the problem dates.

With the third option (sometimes diurnal), the program calculates the times and heights of all high and low waters and outputs them according to day of month. It also outputs and punches hourly heights and lists monthly extreme high and low. It does not reduce the data nor does it check the number of highs and lows.

The procedures used in the program to locate times of extremes makes it possible to identify other anomalous tide conditions. Inasmuch as it is impossible to anticipate and correct for any possible contingency, the program outputs diagnostics giving the approximate time of the occurrence and categories of what may be wrong. Thus, if a float sticks to the side of the well, the resulting straight line is detected and reported. If a storm surge obliterates a high or low tide, the failure to change sequence or the wrong number of tides is reported. Under these circumstances, a man must examine the data and decide on how the processing must proceed. Simple points of inflection or stands are handled within the program.

Numerous changes have been made in the analysis procedures as well. Some of these have already been described (Harris et al., 1963) but they will be summarized here. A least square analysis program is used routinely for series of one year, solving for 37 traditional harmonic constants (Schureman, 1958). The decision to adopt the program was supported by some comparative tests (Zetler and Lennon, 1967). The program is dimensioned for 41 constituents and when a larger number is needed, more than one analysis is made (Zetler and Cummings, 1967). This is done without loss of significant accuracy by including all frequencies in a particular species (cycles per day) in the same solution. The Vo + u phase corrections and the node factors are applied to the results as they have been in the past.

An evaluation of the least squares approach was made with twelve consecutive 29 day series, using the results from the year as the criteria for accuracy, but the results were not significantly better than comparable analyses made by traditional methods, now programmed for an electronic computer (both 29 and 15 day analyses).

Unlike the analysis for a year, only M_2, S_2, N_2, K_1, and O_1, are in the 29 day solution and corrections must be made in the results for contributions from nearby frequencies (those with synodic periods greater than the length of series being analyzed). These include P_1 on K_1, K_2 and T_2 on S_2 (R_2 is disregarded), and Nu_2 on N_2. Equilibrium ratios and phase relationships were used in the corrections in the calculations made thus far. It may be that if local relationships established from nearby places are used, the results could be improved sufficiently to warrant a change in procedure. In a few cases where the data are obtained in random time, a least square solution is a method whereby the harmonic constants can be obtained (Zetler et al., 1965).

A comparable automation in the processing of tidal current observations has been achieved. Current speed and direction are obtained every ten minutes for a 29 day series on a Geodyne meter. The photographic record is translated under contract and the Coast and Geodetic Survey is furnished a magnetic tape with the data in BCD code. A plot and a non-harmonic reduction provide the azimuth of the major axis of the current ellipse. This direction is subtracted from the observed directions and by multiplying the speeds by the cosine and sine respectively of the resulting angles, we obtain series of vectors parallel to and normal to the major axis. These are then analysed using the computer program to furnish harmonic constants in the two orthogonal directions. It has been found that it is more satisfacotry to align the axis of the solution to match the tidal ellipse rather than north and east components because, if the amplitudes along the minor axis are small, these constants may be disregarded and satisfactory predictions may be prepared from the harmonic constants for the vectors parallel to the major axis. The analysis also furnished the non-tidal current in both directions. These are the algebraic means for each set of vectors. Sometimes the clock is not precise and an adjustment is needed for a sampling interval that is not exactly ten minutes. A simple compensation for clock error is made by adjusting the frequencies sought to correspond to the true sampling interval.

Some of the procedures described in this paper represent radical departures from the practices described in various U.S. Coast and Geodetic Survey manuals. The need to update the manuals appears to be imperative but I have strong doubts that we have reached a new plateau of achievement that will result in stabilized procedures for even a few years. Tidal authorities in many countries are going through similar changes in their programs. It is good that we are getting together to discuss these changes and all of us should benefit by this exchange of ideas.

REFERENCES

BARBEE, W.D. (1965) - Tide Gages in the U.S. Coast and Geodetic Survey, unpublished manuscript, U.S. Coast and Geodetic Survey.

HARRIS, D.L., PORE, N.A., and CUMMINGS, R. (1963) - The Application of High Speed Computers to Practical Tidal Problems, Abstracts of Papers, VI, IAPO, XIII General Assembly, IUGG, Berkeley.

SCHUREMAN, Paul (1958) - Manual of Harmonic Analysis and Prediction of Tides, U.S. Coast and Geodetic Survey Spec. Pub. No. 98.

U.S. Coast and Geodetic Survey (1965) ; Manual of Tide Observations, Pub. No. 30-1.

ZETLER, B.D. and CUMMINGS, R.A. (1967) - A Harmonic Method for Predicting Shallow water Tides, Journal of Marine Research, Vol. 25, No. 1, pp. 103-114.

ZETLER, B.D. and LENNON, G.W. (1967) - Some Comparative Tests of Tidal Analytical Processes, International Hydrographic Review, Vol. XLIV, No. 1, pp. 139-147.

ZETLER, B.D., SCHULDT, M.D., WHIPPLE, R.W., and HICKS, S.D. (1965) - Harmonic Analysis of Tides from Data Randomly Spaced in Time, J. Geophy. Res., 70 pp. 2805-2811.

DISCUSSION

Le PRESIDENT remercie M. Zetler de sa communication et propose d'entendre les exposés de M. A.C.M. Van ETTE et du Pr SCHOEMAKER, qui se rapportent, comme les deux premières communications, à l'utilisation pratique des ordinateurs pour l'analyse des marées. Voir ci-après.

Reprinted from Proceedings of the Symposium on Tides organized by the International Hydrographic Bureau, Monaco, 1967, with permission UNESCO and the International Hydrographic Bureau.

SHALLOW-WATER TIDE PREDICTIONS

Bernard D. ZETLER

An objective method for identifying significant hidden frequencies and thereby developing a harmonic method of predicting shallow-water tides is described by Zetler and Cummings (1967). The method was devised to improve predictions at Anchorage, Alaska, where the tidal range is about eight meters and the routine tide predictions were not sufficiently accurate for the navigation needs of deep-draft oil tankers.

Inasmuch as the port freezes during the winter, the available length of record was 192 days of hourly heights, too short for Doodson's method (1957) of shallow water analysis or that of the German Hydrographic Office. The paper describes a standard U.S. Coast and Geodetic Survey analysis of the data, a prediction for the same period that is subtracted from the data, a power spectrum analysis of the residuals, and a high resolution Fourier analysis of the frequency bands in which the spectral energy is high. Wherever large values stood out above the continuum in a plot of the Fourier amplitudes, an effort was made to identify an integral combination of frequencies of constituents known to be important that closely matched the frequencies of these peaks. The least square analysis program was then repeated using the larger set of constituents, the number in this study being 114. The resulting predictions (with 114 constituents) matched the observed high and low waters better in times and mean range, the difference between tide level and sea level was better, and the residual variance (using hourly heights) was sharply reduced.

The question of consistency of phase was considered in the paper by applying the same approach to tide data at Philadelphia for the years 1946, 1952 and 1957. It was found that the phases were not sufficiently consistent for a number of constituents that included the sum of K_2 and N_2 but that, if the sum of M_2 and L_2 is substituted (a difference of .009°/hour or one cycle in about 4.5 years), the phases matched satisfactorily and the residual variances were reduced. The paper questions why L_2, theoretically a small constituent, should be so large at Philadelphia that it contributes significantly to the interaction constituents.

Since publication of the paper, it has come to my attention that Horn (1960) determined that the large amplitudes found for the L_2 frequency in shallow water ports are primarily for the compound term, $2MN_2$, which has exactly the same speed. This does not change the solution by least squares but it does modify the "f and u" nodal factors and phase corrections. Consequently all of the affected constituents shown in the paper should be changed, deleting L_2 and adding $(2M_2 - N_2)$ in the source column. The Doodson numbers and the speeds are unchanged. It is interesting to note that the method followed in this study forced a consideration of a particular frequency even though the inadequate physics in the original model omitted this particular frequency as a possible contributor to the compound constituents.

Another aspect of the solution would be considered if the study was re-examined. No attempt was made to seek significant constituents in the low frequencies (species zero) because a previous study, Groves and Zetler (1964), had failed to find any significant additional frequencies although about fifty years of data and an extremely high resolution (.0005 cpd) were used. However, this was done with stations having very little shallow-water effect ; I am informed that with stations such as Anchorage, it is very likely that a number of compound terms would be found with amplitudes significantly above the continuum.

The residual variance would be appreciably reduced if these constituents are included in the least square solution but the effect on the accuracy of future daily predictions would be very small. When a line extends above a continuum, the solution gives the amplitude and phase of a trigonometric identity which is the vectorial sum of the signal and the white noise (continuum). The relationship of the phase lags of the two is unknown and cannot be resolved. Therefore, all that is known is that the true amplitude of the signal lies somewhere in between the sum of the analyzed amplitude and the continuum level in the vicinity of the line and their difference. The most likely value is probably in the middle of this range, namely the analyzed value, but the level of the continuum (highest in the low frequencies and peaking at or near zero) is a good index of possible error. Furthermore, the phase of the particular continuum sample contaminates the determined phase of the constituent. Hence, although the residual variance of a self-predictor is reduced by introducing the added constituent, there is little expectation that the use of the constituent for a future prediction would provide a comparable reduction in the variance. With reference to tide predictions, the species zero constituents are not important in determining the times of high and low waters because the first derivatives are weighted by the constituent speeds, so their only significant contribution is to the heights.

Finally, it appears that the computing effort in searching for significant hidden frequencies could be greatly reduced by using the "Fast Fourier Transform" (Cooley and Tukey, 1965) on the residuals rather than the power spectral analysis of the residuals followed by the high resolution Fourier analysis in particular frequency bands. The estimated number of computer operations for the "Fast Fourier Transform" is estimated as $2N \operatorname{Log}_2 N$ whereas the traditional Fourier method requires N^2 operations, where N is the number of data points. Therefore the relative computing time is the factor $2N \operatorname{Log}_2 N/N^2$. There are 4 608 hours in 192 days. If the data are normalized in the sense that the mean is made equal to zero, the ends tapered, and enough zeros are added at both ends to bring the total number of points to 8 192 (the next power of 2), the factor becomes about 1/300. In this particular study, the savings would not have been quite as great because only particular portions of the spectrum were examined, but nevertheless it appears that the savings in computer time would have been quite large.

I thank D.E. Cartwright, G.W. Lennon and W. Horn for calling some of the above points to my attention.

REFERENCES

COOLEY, J.W. and TUKEY, J.W. (1965) - An Algorithm for the Machine Calculation of Fourier Series, Mathematics of Computation, 19 : pp. 297-301.

DOODSON, A.T. (1957) - The Analysis and Prediction of Tides in Shallow Water, International Hydrographic Review, 34, pp. 5-46.

GROVES, G.W. and ZETLER, B.D. (1964) - The Cross Spectrum of Sea Level at San Francisco and Honolulu, Journal of Marine Research, 12, pp. 269-275.

ZETLER, B.D. and CUMMINGS, R.A. (1967) - A Harmonic Method for Predicting Shallow-water Tides, Journal of Marine Research, 25, pp. 103-114.

DISCUSSION

Mr. van ETTE (Netherlands) wanted to ask a question about the Fourier analysis, because there was a registration of a certain time which consisted not only of tidal constituents but also of all kinds of noise. It was true that when the Fourier analysis had been made results were found, and since every result had to have a variable the results had a certain standard deviation. It was well known that the standard deviation of results obtained by means of harmonic analysis, in its proper sense, was very high and could be approximated by a Chi^2 distribution with only 2 degrees of freedom. What value, therefore, could be attached to the results of a calculation of that Fourier analysis ? Was anything known about the statistical behaviour of the results ? If not, the following device might be considered.

A long series of results might be split up into equal parts and the same computation done for each of the parts. If that were done, were approximately the same results obtained for each of the parts ?

Mr. ZETLER (U.S.A.) replied that the data at Anchorage had been too short to truncate and they had needed the utmost resolution that they could possibly get. What they had had was barely enough and so they had not been able to afford the luxury of that particular test.

The frequencies of the Fourier analysis had not been used ; they were merely a guide. Obviously the non-linear terms which the had been looking for would not fall on the accidental exact harmonics of a particular record length. They had been looking for values which obviously extended significantly above the continuum. When they had been found they were not necessarily on a line ; in fact, ordinarily they were distributed between lines and it was obvious that there was energy there of a frequency of approximately so much. That could be determined from the frequency assigned to each harmonic.

They had then looked for a combination of significant frequencies such as the $2MS_6$ which had been a new frequency to them. When they found energy that apparently corresponded to what they would get by adding twice the frequency of M_2 to that of S_2, and it appeared to be approximately right, they had merely included that in their model for the next least square analysis. Had they been wrong they would have got a side band of what they were looking for and not the true thing. However, it was a somewhat systematic search in that there were a very limited number of terms which they had attempted to use as input to the search. They had used only the important ones. That was why they had been off on L_2 when they added L_2 and M_2 in place of K_2 and N_2 on the fourth, sixth and eighth diurnal terms that they had happened to correct. When a subsequent residual analysis had been done it had been found that the residual energy had been reduced in the three different species by the change that had been made. There was, therefore, satisfactory documentation that the renaming of the constituents was an improvement.

With regard to the question of what was a significant amount over the continuum, that again was something which had to be judged by eye and there seemed to be a difference of opinion in the group as to how good a tool an eye was. So far as the fifth diurnal was concerned, those particular points stood out well above the continuum and it was not a normal distribution with an occasional value 3 sigma away from the mean. They were more than that.

There was, therefore, a geophysical reason for the changes. There was a tidal line, and they were allowed to identify it and put it into their solution.

Mr. van ETTE (Netherlands) referred to the fact that Mr. Zetler had only had a fairly short period of 192 days and had really had to use them all, and suggested that between computations it would be worth while to try to split them up and consider whether the results which had been obtained did indeed have some value. In the end, of course, all the data available could be used.

Mr. ZETLER (U.S.A.) made the point that subsequently they had succeeded in putting a bottom recorder in the location, substituting it for a tide gauge, and had obtained a year of data of which only about three months overlapped with the 192 days which had been described in the paper. It was a pleasant surprise that the analyzed constants for the full year agreed very well with what had been done previously.

Mr. HORN (Federal Republic of Germany) wanted first to congratulate Mr. Zetler because he had a laboratory which they would all like to have with a range of 10 metres and tides of an almost fixed character. This was desirable for analyzing tides and doing research. Unfortunately it froze up, and Mr. Horn wondered whether something could be done through international cooperation to make it permanent. A careful comparison had been made between Mr. Zetler's results and the German results over a period of 25 years and there was a range of only 3 metres. They could not go as far as Mr. Zetler had done, but they had also included the twelfth order species. What was perhaps remarkable was that they had found more or less the same orders of magnitude for the individual constituents that he had found. They had called some of them by different names, but the wording was something which would soon have to be gone into.

As to the identification of L_2, 2M and N_2, that was something to which Mr. Horn had drawn attention in 1958 and it was one of the outstanding points. L_2 was only 10 per cent of the total amplitude. It was really surprising that Mr. Zetler had found results from such a short series which could be confirmed by such a long analysis, and it seemed probable that he was perfectly right in what he had done.

Mr. GODIN (Canada) suspected that the proof of the analysis was in the prediction, and asked how the prediction went.

Mr. HORN (Federal Republic of Germany) replied that in analyzing the tides they had found a twelfth order species. According to Sei's law, which had often been quoted by Dr. Doodson, the number of constituents of almost the same order in one species should increase as any three in the order of the species. The table of results which had been shown was not in harmony with that law because the number decreased instead of increasing indefinitely. It was obvious that they were all mixed up with the noise. If the high and low water times were to be investigated, where there had to be a differentiation with respect to time, the combined influence of those things would be found in the high and low water intervals.

That was one of the reasons why he had given up the direct harmonic analysis and had decided to analyze high and low waters directly, or lunar or hourly heights.

Mr. ZETLER (U.S.A.) agreed completely with what Mr. Horn had said. It was apparent that the combinations multiplied up very rapidly. That was obvious even in the spread in frequency within species. The species were no longer so far apart in the higher order of species. At the same time they tended to get smaller in size. There were more of them but they tended to get smaller and one began to wonder whether they were not merging with the continuum to form part of it. There were so many and they were small, so that instead of having a random meteorological process there might be a process which was not random but was hardly worth working with to extract all of the additional terms.

It came back to the problem which Mr. Zetler had mentioned at the beginning. One wondered at what point to stop punching holes in the continuum in the hope that one was doing something meaningful. Any set of data could obviously be described by a Fourier transform and there would be no residuals. One could therefore keep punching the continuum had getting more and more constituents. The imagination could run wild in the higher species on the number of combinations which one could allow oneself to use. It became a subjective process. Mr. Zetler had tried to limit himself in most cases to something that obviously protruded. He believed that, in what Mr. Horn was saying, the continuum was part of the non-harmonic grouping in the higher species.

Mr. LENNON (United Kingdom) commented that he had done an exercise very similar to Dr. Zetler's when dealing with two ports in the River Thames. It had been found that, as one proceeded into the higher species, the situation was not that one had more and more constituents which merged with the noise but that one had relatively few constituents which stuck out bright and clear above the noise. In fact, the highest species were the easiest to handle and the most difficult ones were the semi-diurnals and the fourth-diurnals where there was considerable pseudo-tidal noise.

Mr. HORN (Federal Republic of Germany) replied that that did not entirely meet the point which he had made. Mr. Lennon was perfectly correct when he spoke of approximating to the total tide curve, but the higher species had an influence on the times of high and low waters that could not be represented by that method. That was why he had said that it was necessary to choose the things that they wanted to predict in a tide table and try to represent them directly. Dr. Doodson had always said that if eight diurnals had to be included the situation would probably become hopeless because there would be too many. Mr. Lennon had said that he did not entirely agree, which implied that he did partly agree. Mr. Horn himself agreed with Dr. Doodson to a somewhat higher degree. The situation became difficult if there were too many shallow water corrections which all influenced the high water times, because in the derivative with respect to times they appeared multiplied by a factor of 3, 4, 6, 8 and so on. That was of importance. They could be found, but only by finding their combined effect not the individual effect.

Mr. ZETLER (U.S.A.) recalled the statement of Dr. Doodson's which Mr. Horn had quoted, but he also remembered that in his Manual he had talked about the convergence and the possibility of working with higher order terms. He had specifically stated that there was a physical limitation on how many constituents could be used on a mechanical tide predicting machine. Using the cut-off that he used he had thought that it was virtually impossible to go beyond 60 constituents on a tide predicting machine without introducing so much friction that the tide predictions suffered in the process.

Mr. CARTWRIGHT (United Kingdom) thought that the list of high order interaction terms was impressive, but it had occurred to him that there was one type of interaction term which could not be included in that scheme. Many people had observed, as he had done himself around Great Britain or in the North Sea, that many of the important tidal lines had a seasonal modulation. That meant that if one took a special analysis one found, surrounding the M_2 line, some lines at one cycle per year difference. Admittedly, in the full development of the potential, there was a seasonal change, or a change which depended on the sun's perigee for its true expansion, but it was very small and the observed modulation was larger than that. It would be almost impossible when choosing the dominant tidal terms to choose a combination of terms which would give one cycle per year difference among them. Possibly in many sea areas that was not at all important, but in certain areas where, for some reason, there was a large seasonal modulation, another type of interaction would have to be introduced, possibly something which involved the product of SA, the annual term and the leading lineal terms.

Reprinted from GO Boating, Miami

GO JANUARY 1969

TIDE TALK

By Bernard D. Zetler
Atlantic Oceanographic Laboratories, Miami.

January Tide Talk

The Coast and Geodetic Survey recently completed one hundred years of providing published tide predictions to navigators. As early as 1844, the Coast Survey provided information (mean high water lunitidal intervals and ranges) that could be used with a nautical almanac to provide an approximate tide prediction. Although reasonably accurate tide predictions are taken very much for granted today, the development of the science was an outstanding scientific achievement in the nineteenth century.

This is another illustration of necessity being the mother of invention. The Coast Survey was given the responsibility of preparing nautical charts for the safety of navigation. A chart shows the depth of water at any particular place within the geographic limits of the chart. But, the water column does not remain fixed. Instead it rises and falls in some periodic fashion related to the transits of the moon and sun. How does one measure something that won't stand still? Obviously, one needs to correct the measurement at a given time to some fixed datum; on our east coast, we use mean low water. In the same sense, the navigator must apply (add or subtract, depending on the sign) a tide prediction to a charted depth to know the depth of water at the time he plans to be there.

GO FEBRUARY 1969

TIDE TALK

By Bernard D. Zetler
Atlantic Oceanographic Laboratories, Miami.

During World War II an intensive effort was made to improve tide predictions, particularly for amphibious operations in strategic areas. Landing craft moving onto a beach needed as much water as possible in order to carry both men and supplies as far up on the beach as possible. However, it was desirable to come in just before high water so that if a boat did run aground on a shoal, after a short wait a little more water was available to make it float again. The heavy toll in the Tarawa landing, when many landing craft were hung up for long periods on shoals, emphasized the need for more accurate tide predictions.

Needless to say, the improvement was given a high priority. The tide tables contain daily predictions for a few particular places and Table 2 lists differences and ratios for many subordinate places. The choice of a reference station for these subordinate places frequently involves a compromise, that is a selected best possible reference station but one which may not be a satisfactory one. Furthermore a reference station which may be adequate for ordinary navigation may not be acceptable for a military landing operation. As an example, the pre-war tide tables used two reference tables, Manila and Cebu, for the Philippines. This was expanded to six reference stations in special military reports. Predicting the additional four stations on a crash basis was not a tremendous task but remaking Table 2 to go along with the augmented coverage required a considerable effort, first deciding on the appropriate reference stations and then recomputing the time and height differences.

The post-war tide tables included many of the additional reference and subordinate stations prepared for military purposes during the war.

****

GO MARCH 1969

TIDE TALK

By Bernard D. Zetler
Atlantic Oceanographic Laboratories, Miami.

In 1965 the Coast and Geodetic Survey's tide prediction machine finally yielded to electronic computers after more than a half century of distinguished service. Those of us who were involved in the changeover to an electronic computer felt some measure of remorse for terminating its remarkable career.

The tide predicting machine, completed in 1910, was designed to sum continuously 37 cosine curves, draw a combined curve and select automatically its maxima and minima (times and heights of high and low waters). Although the periods involved in the tide calculations varied from one cycle per year to eight cycles per day, the gearing for these various input curves was so precise that the maximum allowable error was 2 degrees in a year. A man could set the dials on the machine, turn a hand crank (stopping to record each high and low water) and complete a year of predictions in an eight hour day.

Because the machine was both unique and indispensible, there was considerable anxiety during World War II and in the post-war years that it might be harmed by bombing or sabotage. Although special tables were prepared to facilitate crude predictions that could be computed on a desk calculator, the only significant safeguard was achieved by running the machine overtime to build up a stockpile of four years of advance predictions.

Needless to say, when the Coast Survey purchased its first electronic computer, an IBM 650, about fifteen years ago, designing a program for predicting tides was given careful consideration. I remember meeting an IBM executive about a year later at a social event where I described the tide-predicting machine. When he asked incredulously whether the almost fifty year old machine had a hand crank, I replied in the affirmative with the further comment that it turned out tide predictions faster than his men had been able to achieve on the 650.

It was a losing battle, however, as electronic computers rapidly became faster and cheaper to operate. In 1965 the Coast and Geodetic Survey changed over to a computer program that predicts a year of tides in three minutes and outputs the data in a format ready for reproduction. Furthermore there is greater flexibility in that there is no longer a constraint to a unique 37 periods (114 have been used in a special research study) and there is far greater security in no longer depending on one unique set of hardware. Nevertheless --- it was a wonderful machine!

****

GO APRIL 1969

TIDE TALK

By Bernard D. Zetler
Atlantic Oceanographic Laboratories, Miami.

Tides generally are classified in three categories, semidaily, mixed and daily. Miami residents are somewhat uniquely in a position to see a all three without going far from home.

The semidaily tides are found closest, at Miami Beach, Biscayne Bay and nearby waters. There is very little difference between the heights of the two high waters or between the two low waters on a particular day. Tidal ranges are largest at times of new and full moon and at times of perigee (moon closest to the earth, about once a month). If new or full moon and perigee come on about the same day, the ranges are particularly large.

If we go west across the Tamiami Trail to Naples or Marco Island, we find the diurnal tides are much more important and when the moon is near extreme declination, there may be only one high and one low tide a day. The tide tables use St. Marks River Entrance as the reference station for predictions in this area; the predictions for April 9, 1969 call for only one high and one low tide. Farther to the north at St. Petersburg the tides are even more diurnal and, at Pensacola, the diurnal tide is so predominant that one finds two highs and two lows only on a few days each month when the moon is near the equator.

If we go south to Key West, we find the mixed type of tide. Both the daily and semidaily tides are important and usually there is a significant difference between the height of the two highs on a particular day and/or between the two lows on that day. This inequality will be greatest when the moon is near extreme declination and smallest when the moon is near the equator.

These sharp changes in type of tide within short distances demonstrate the problem implicit in setting up Table 2 in the tide tables. Obviously, the changes in type are not abrupt but rather gradual in a geographic sense. Nevertheless, in preparing Table 2, it is necessary to have arbitrary limits which indicate that all places to some point A fit Miami, from there on to point B, Key West is used, beyond B St. Marks is used, etc.

****

GO MAY 1969

TIDE TALK

By Bernard D. Zetler

Atlantic Oceanographic Laboratories, Miami.

The Miami Herald on April 13, had a feature article on a significant lowering of the world temperature due primarily to man-made contamination. It made me wonder if a related trend has been recorded on tide gauges spanning the world's oceans.

We have known for some time that mean sea level is a misleading term for geodetic purposes because sea level does not stand still, even on an average basis. If we average hourly tidal heights over a period of a year (about 9,000 values), this should average out reasonably well tides, waves, storm induced changes, etc. But not only do annual means show large variations from year to year but, over the past fifty years, there has been a significant upward trend, about 0.01 foot per year on our east coast. It has not been the same along all coastlines and an approximation of a world rate would be somewhat smaller, possibly 0.005 foot per year. Areal differences in trend have generally been attributed to differential land sinking or uplift.

The principal point, however, is that sea level has been rising. The usual explanation has been that the earth has been warmed by the increased supply of carbon dioxide and this warming has reduced the polar ice-caps. In support of this theory has been some documentation of the retreat of glaciers and similar phenomena.

The scatter (non-systematic variation) between annual sea level values is sufficiently large that a valid trend cannot be determined from just the past few years. Oceanographers will be watching annual sea level values even more carefully in the next decade looking for evidence of a continuance, leveling off, or even a reversal of the rising trend that has been recorded so far in this century.

GO JUNE 1969

TIDE TALK

By Bernard D. Zetler
Atlantic Oceanographic Laboratories, Miami.

Most people viewing an earth-moon diagram for the first time have little or no trouble in accepting on faith the tidal bulge on the earth directly beneath the moon. However, the cause of the comparable bulge (high tide) on the opposite side of the earth is far less obvious and usually leads to questions, primarily, "How come?"

We know from physics that the earth and moon attract each other and that it requires an equal and opposite force to keep them apart. The latter is centrifugal force directed away from the moon. However, this centrifugal force is the same at all points on the earth's surface whereas the gravitational force is greatest at that point on the earth just under the moon and least at a point on the other side farthest from the moon. The difference between the attractive force and the centrifugal force is therefore a small net force toward the moon just under the moon, zero at the center of the earth, and a small net force away from the moon on the far side of the earth. These net differences are responsible for the two high water bulges (two high tides each lunar day as the earth rotates under the moon).

There are similar high waters on either side of the earth due to the sun but the much greater distance of the sun than the moon makes the solar tide slightly less than half the lunar tide.

****

electronic computer permitted the use of any reasonable set and, in this case, we went from 37 to 114 periods to achieve our results.

Shortly after our improved prediction program was ready for use, English tidal experts arrived at virtually the same solution for a comparable problem in the Thames.

GO JULY 1969

TIDE TALK

By Bernard D. Zetler
Atlantic Oceanographic Laboratories, Miami.

I note with interest the recent proposal to deepen the channel into Dodge Island to permit larger draft vessels to use the Port of Miami. There is a strong trend toward building larger ships, particularly oil tankers for the trip around Africa since the closing of the Suez Canal.

In some ports where the tidal range is large, the advent of these larger ships has led to a requirement for increased accuracy in tide predictions. If channel depth combined with the tide adds up to marginal clearance, the need for extreme accuracy becomes obvious. It was such a requirement that recently led to some quite interesting research.

The tide at Anchorage, Alaska, averages about 25 feet. For many years the Coast and Geodetic Survey prepared predictions for Anchorage based on summer observations only as the port freezes in winter. Then oil was discovered in Cook Inlet bringing deep-draft oil tankers into the area. The published tide tables were found to be not sufficiently accurate for navigational purposes and all existing techniques were investigated and found inadequate.

A technique was developed for identifying and analyzing significant additional tide constituents and these were then incorporated into the prediction method to achieve improved accuracy. In this case, the timing was very fortunate. Less than two years before, the Coast and Geodetic Survey had changed from using its mechanical tide prediction machine to an electronic computer. The mechanical machine used 37 predetermined tidal periods for prediction and there was virtually no way to add additional periods to the calculation without years of precise preparation of appropriate gears. The

TIDE TALK

By Bernard D. Zetler
Atlantic Oceanographic Laboratories, Miami.

A frequent question on tides is whether a particular body of water is large enough to have a tide and my response is that you can have a tide in a tea cup. This means that the tide producing forces act on any body of water and, if measurements could be made sufficiently precise and if all other forces affecting the level of water are eliminated, we would indeed find a tide in any basin.

The smallest basin in which, to my knowledge, a tide has been documented is the David Taylor Model Basin, an enclosed rectangular tank about 2700 feet long, 52 feet wide and 22 feet deep, along the Potomac River near Washington, D.C. The tank is used for extremely precise measurement of the characteristics of ship models towed in the tank, The demand for precision is so great that the tracks used for the towing vehicles were leveled to the curvature of the earth rather than purely horizontal.

I recall that in 1947 when we were asked to compute the theoretical tide in the basin, we made a quick calculation of "less than .005 inch." We were quite surprised by the response, "Yes, but how much?"

During a seven day period when the basin was not used, we installed registering floats at either end and had volunteers bicycle back and forth around the clock reading the gauges each half hour. The observed mean range was .00181 inch and the plotted tide curve was quite smooth, the only other bvious change being a downward drift due to seepage.

Tides have been measured on the Great Lakes but it requires a long record to clearly identify the small tidal range that is usually masked by other changes due to meteorological variables.

****

Using tide table on Page 2 which is Miami Beach (ocean), Port Everglades entrance (jetties), and Miami Harbor entrance, add or subtract as indicated.

Differences

Place	High Water	Low Water
Miami Harbor Entrance	--	--
Fort Pierce Inlet	-0 14	-0 18
St. Lucie Inlet	-0 20	-0 21
Jupiter Inlet	+1 04	+1 38
Palm Beach (ocean)	-0 21	-0 18
Hillsboro Inlet	+0 13	+0 36
Port Everglades	+0 02	+0 02
Cape Florida	+0 49	+1 02
Fowey Light	+0 03	+0 02
Pumpkin Key, Card Sound	+2 53	+3 03
Molasses Reef	+0 16	+0 11
Alligator Reef Light	+0 13	+0 26
Key West Channel	+2 10	+1 34
Sombrero Light	+0 51	+0 44
American Light	+0 58	+0 38
Sand Key Light	+1 08	+0 50
East Cape Sable	+5 59	+6 11
Shark River	+5 23	+6 06
Pavilion Key	+5 29	+5 45
Barron River	+6 58	+8 19
Cape Romano	-7 16	-7 00
Marco	-7 03	-7 05
Naples	-8 00	-8 06
Fort Myers	-3 39	-3 37
Pine Island	-6 17	-7 05
Captiva Island	-6 33	-6 41
Boca Grande	-6 59	-8 17
Miami Yacht Basin	+1 28	+1 47
79th St. Csywy	+1 45	+2 13
Ft. Laud. (Andrews Ave. Bridge)	+1 06	+1 28
Cape Fla. (west side)	+0 49	+1 02
Riviera (Lake Worth)	•	•
Key Biscayne	+0 49	+1 02
Card Sound	+2 53	+3 03
Key Largo (Garden Cove)	+0 36	+1 09
Plantation Key (Tavernier)	+0 34	+0 39
Key West	+2 10	+1 34
Sombrero Key Light	+0 51	+0 44
Marathon (No. side)	+7 32	+6 15
Flamingo	+7 38	+8 56
Big Sable Creek	•	•
White Water Bay	•	•

•No data

GO SEPTEMBER 1969

TIDE TALK

By Bernard D. Zetler

Atlantic Oceanographic Laboratories, Miami

The tide measurements described last month for the David Taylor Model Basin introduced me for the first time to tidal variations in the crust of the earth. When we compared a computed tide curve with the observations, there were consistent small variations in phase and in range. A study showed the reason was the yielding of the earth's crust to the tidal forces.

At the latitude of Washington, D.C., the earth tide averages about six inches. It would not be possible to measure this by ordinary geodetic instrumentation because the extent of the tidal bulges is so great that the differential change that can be measured directly between any two points is much less than the possible error of the observation. As with ocean tides, the semidaily ranges are larger at new and full moon and when the moon is at perigee. The diurnal tides are larger when the moon is at extreme declination.

The earth also responds in a more devious and indirect way to tide-producing forces because the crust yields due to tidal loading on the sea floor. The degree to which the earth yields depends on the geological structure in the area and to the range and extent of the ocean tide. Although Washington, D.C. is about a hundred miles from the ocean, the loading effect was found to be 5 to 10% of the tide-producing force. At some places near the coast where the tidal ranges are quite large, the loading effect has been found to be the most important contributor to the observed earth tide.

The principle benefit of earth tide measurements is that by documenting the response of the earth to known forces, it becomes possible to evaluate the structural strength of the earth's crust.

GO OCTOBER 1969

TIDE TALK

By Bernard D. Zetler

Atlantic Oceanographic Laboratories, Miami

Engineers are constantly trying to harness the energy of the oceans, usually concentrating on tides although attempts have also been made to use wave motion and temperature gradients. There has never been a question of the engineering possibilities of tidal power; the principal restraining consideration has been econmonics.

In places where the tidal range is large, such as the Bay of Fundy where the average range exceeds 35 feet, it is readily feasible to trap the water at high tide and use the head as water level falls on the outside to generate power. This is the simplest form of tidal power and the principle defect is that the power supply is intermittent. A more complex system of multiple basins can be designed so that a sufficient head always exists somewhere in the system, thereby making possible a continuous supply of power. Other more complex systems are conceivable such as using power during the available periods to pump water into a storage basin and thereby establishing a head as a source of supply during other periods in the tidal cycle. The recently constructed French power plant produces power from the current as the waters in Rance River rush upstream and then uses the trapped head to produce power on the falling tide.

****

"We are just on the threshold of our knowledge of the oceans. Knowledge of the oceans is more than a matter of curiosity. Our very survival may hinge on it." *- John F. Kennedy*

GPO 830-693